

# **Multi-scale multiphase modelling of granular flows**



**Krishna Kumar Soundararajan**

Department of Engineering  
University of Cambridge

This dissertation is submitted for the degree of

*Doctor of Philosophy*

King's College

September 2014



I would like to dedicate this thesis to my loving parents



## **Declaration**

I hereby declare that except where specific reference is made to the work of others, the contents of this dissertation are original and have not been submitted in whole or in part for consideration for any other degree or qualification in this, or any other university. This dissertation is the result of my own work and includes nothing which is the outcome of work done in collaboration, except where specifically indicated in the text. This dissertation contains fewer than 65,000 words including appendices, bibliography, footnotes, tables and equations and has fewer than 150 figures.

Krishna Kumar Soundararajan  
September 2014



## Acknowledgements

My deepest gratitude goes to my supervisor, Prof. Kenichi Soga, for his generous help, support, guidance and encouragement throughout my PhD research. I feel privileged to have worked with him; thank you so much for a very inspiring and an interesting four years of research.

I would like to express my sincere thanks to my advisor Prof. Malcolm Bolton, for his valuable advice and comments following my first year report.

I am extremely grateful to Prof. Jean-Yves Delenne, Université Montpellier 2, France for his support and guidance in developing coupled Lattice Boltzmann - Discrete Element Model. I owe a debt of gratitude to Prof. Farhang Radjai, Université Montpellier 2, France for stimulating discussions and guidance for this work. I would like to thank Patrick Mutabaruka, Université Montpellier 2, France for the collaborative research work and for his support during my stay in Montpellier. I owe a debt of gratitude to Samila Bandara, EPFL for her continuous support, both as a friend and as a work colleague, for her assistance in bringing me up to speed with Material Point Method and for her continuous support and discussions.

I would like to express my sincere gratitude to Prof Boominathan, Indian Institute of Technology, Madras for his continuous support throughout my research career. I sincerely thank my professors at Indian Institute of Technology Madras and at Thiagarajar College of Engineering for their support, encouragement and for their prior teaching. I would like to thank Dr Vidya Bhushan Maji for all his support and for his constant encouragement to pursue my PhD at the University of Cambridge, during my research at IITM. A very special thanks to Dr. Nagan, Dr. Sivagurunathan, and Dr. Sugunaseelan for their constant support and motivation throughout my engineering career. I'm greatly indebted to them for my research life.

I owe a very special thanks to my aunt Chitra for all her support, care and affection she has showered on me and for always being there for me. I can never forget these four years in my life, thank you for making it so special and wonderful. Also an extra special thanks to her for getting me started on my computing journey. A special thanks to my uncle Sankar and my cousin Karthik for their encouragement and making these four years a very memorable experience.

Coming from India, particularly as this was my first time outside the country, my friends have always been around to make these four years a wonderful experience and making my stay at Cambridge feel like home. A very special thanks to Alex Ridge for being such a great friend and for being there for me pretty much every single day of my four years of PhD. I would like to thank Adam Reid for all his support in easing me in to this new country and introducing me to table football. A special thanks to Adam for staying with me and supporting me even beyond the visiting hours of the hospital after my surgery. A sincere thanks to my extra special friend Nicole Grunstra for all our wonderful time together. Extra special thanks to Steven Kaneti, who has always been there for me and for all the interesting discussions about computing. A special thanks to my friend Charlotte Houldcroft for being such a great friend, and for proof-reading the chapters of my thesis. I owe an extra special thanks to my friends Renate Fellinger, Katie Fitzpatrick, Wis Wang-Koh, Anne Musset, James Taylor, Max Hewkin-Smith, Marilena Frisone, Auerélie Petiot, Isabell Frank, Sarah Williams, Anna Bachmann, Stewart Forshaw and all the others, for making my time so far at Cambridge such an enjoyable one!

A special thanks again to Alex Ridge, Nicole Grunstra and Steven Kaneti for spending sleepless nights to help me format the proceedings of the International Symposium on Geomechanics from Micro to Macro.

I would like to extend my sincere thanks to my friends Karthik, Sundaralingam, Meenakshi Sundaram, SME Karthik, Sonu Thomas, Varun Thangamani, Anjana Bhashi, Selvaganesh and Aruna Prasath who have always been there for me and for their continuous support and encouragement.

My time at the geotechnical research group would not have been so enjoyable without my friends and colleagues. Thank you Tina Schwamb, Denis Garber, Francesca Burali, Samila Bandara, Ouge Wang, Kirk Ellison, Paul Shepley, and Ermao Xu. I am very grateful for the memorable time, for the support and encouragement from all of you. A special thanks to the Div-D computer officer, Tim Ablett for all his support.

Words cannot express the inspiration, understanding, patience and moral support of my parents Soundararajan and Meenakshi, my sister Shenbagam and my grandparents, not only in completing my PhD research work but also in all aspects of my life. Above all I thank the Gods for their abundant blessings showered upon me throughout my life.

Furthermore, I would like to sincerely acknowledge the support of Cambridge Commonwealth, European and International Trust for my personal funding during this PhD, without which this research would not have been possible. I would like to acknowledge the Lundgren Research Award for their financial support during the final year of my PhD.

## Abstract

Geophysical hazards usually involve flow of dense granular solids and water as a single-phase system. Understanding the mechanics of granular flow is of particular importance in predicting the run-out behaviour of debris flows. The dynamics of a homogeneous granular flow involve three distinct scales: the microscopic scale, the meso-scale, and the macroscopic scale. Conventionally, granular flows are modelled as a continuum because they exhibit many collective phenomena. Recent studies, however, suggest that a continuum law may be unable to capture the effect of inhomogeneities at the grain scale level, such as orientation of force chains, which are micro-structural effects. Discrete element methods (DEM) are capable of simulating these micro-structural effects, however they are computationally expensive. In the present study, a multi-scale approach is adopted, using both DEM and continuum techniques, to better understand the rheology of granular flows and the limitations of continuum models.

The collapse of a granular column on a horizontal surface is a simple case of granular flow, however a proper model that describes the flow dynamics is still lacking. In the present study, the generalised interpolation material point method (GIMPM), a hybrid Eulerian – Lagrangian approach, is implemented with Mohr-Coloumb failure criterion to describe the continuum behaviour of granular flows. The granular column collapse is also simulated using DEM to understand the micro-mechanics of the flow. The limitations of MPM in modelling the flow dynamics are studied by inspecting the energy dissipation mechanisms. The lack of collisional dissipation in the Mohr-Coloumb model results in longer run-out distances for granular flows in dilute regimes (where the mean pressure is low). However, the model is able to capture the rheology of dense granular flows, such as run-out evolution of slopes subjected to impact loading, where the inertial number  $I < 0.1$ .

The initiation and propagation of submarine flows depend mainly on the slope, density, and quantity of the material destabilised. Certain macroscopic models are able to capture simple mechanical behaviours, however the complex physical mechanisms that occur at the grain scale, such as hydrodynamic instabilities and formation of clusters, have largely been ignored. In order to describe the mechanism of submarine granular flows, it is important to consider both the dynamics of the solid phase and the role of the ambient fluid. In the present study, a two-dimensional coupled Lattice Boltzmann LBM – DEM technique is developed

to understand the micro-scale rheology of granular flows in fluid. Parametric analyses are performed to assess the influence of initial configuration, permeability, and slope of the inclined plane on the flow. The effect of hydrodynamic forces on the run-out evolution is analysed by comparing the energy dissipation and flow evolution between dry and immersed conditions.

# Table of contents

|   |              |
|---|--------------|
| <b>List of figures</b>  | <b>xv</b>    |
| <b>List of tables</b>   | <b>xxiii</b> |
| <b>1 Introduction</b>   | <b>1</b>     |
| 1.1 Modelling the granular flows . . . . .                      | 4            |
| 1.2 Objectives . . . . .  | 6            |
| 1.3 Overview of this work . . . . .                             | 7            |
| <b>2 Granular flows</b>   | <b>9</b>     |
| 2.1 Introduction . . . . .                                      | 9            |
| 2.2 Modelling the granular flows . . . . .                      | 11           |
| 2.2.1 Continuum models . . . . .                                | 13           |
| 2.2.2 Kinetic theory . . . . .                                  | 14           |
| 2.2.3 Rheology . . . . .  | 15           |
| 2.2.4 Shallow-water approximation . . . . .                     | 21           |
| 2.3 Studies on granular flows . . . . .                         | 23           |
| 2.3.1 Granular column collapse . . . . .                        | 24           |
| 2.3.2 Flow down an inclined plane . . . . .                     | 34           |
| 2.3.3 Saturated and submerged granular flows . . . . .          | 37           |
| 2.4 Summary . . . . .   | 45           |
| <b>3 Numerical modelling of granular flows</b>                  | <b>47</b>    |
| 3.1 Introduction . . . . .                                      | 47           |
| 3.2 Continuum modelling of granular flows . . . . .             | 47           |
| 3.2.1 Mesh-based and mesh-free techniques . . . . .             | 51           |
| 3.3 Material Point Method (MPM) . . . . .                       | 53           |
| 3.3.1 Discrete formulation of the governing equations . . . . . | 54           |
| 3.3.2 Boundary conditions . . . . .                             | 57           |

---

|          |  |            |
|----------|--|------------|
| 3.3.3    | Integration scheme . . . . .   | 57         |
| 3.3.4    | Solution scheme . . . . .  | 59         |
| 3.3.5    | Effect of mesh size and number of material points per cell . . . . .           | 63         |
| 3.3.6    | GIMP method . . . . .  | 70         |
| 3.3.7    | Application of MPM in geomechanics . . . . .                                   | 74         |
| 3.4      | Particulate modelling of granular flows . . . . .                              | 78         |
| 3.5      | Discrete Element Method . . . . .  | 81         |
| 3.5.1    | The Forces . . . . .   | 82         |
| 3.5.2    | Numerical algorithm and integration scheme . . . . .                           | 87         |
| 3.5.3    | Boundary conditions . . . . .  | 92         |
| 3.5.4    | Validation of DEM . . . . .  | 95         |
| 3.5.5    | Cumulative beta distribution . . . . .   | 95         |
| 3.5.6    | Particle assembling methods . . . . .  | 98         |
| 3.5.7    | Voronoi tessellation . . . . .   | 99         |
| 3.6      | Summary . . . . .  | 102        |
| <b>4</b> | <b>Multi-scale modelling of dry granular flows</b>                             | <b>105</b> |
| 4.1      | Introduction . . . . .   | 105        |
| 4.2      | Granular column collapse . . . . .   | 106        |
| 4.2.1    | Numerical set-up . . . . .   | 107        |
| 4.2.2    | Deposit morphology . . . . .   | 115        |
| 4.2.3    | Flow evolution and internal flow structure . . . . .                           | 116        |
| 4.2.4    | Energy dissipation mechanism . . . . .   | 125        |
| 4.3      | Role of initial grain properties on the collapse of granular columns . . . . . | 130        |
| 4.4      | Slopes subjected to impact loading . . . . .                                   | 139        |
| 4.4.1    | Numerical set-up . . . . .   | 141        |
| 4.4.2    | Evolution of pile geometry and run-out . . . . .                               | 142        |
| 4.4.3    | Decay of kinetic energy . . . . .  | 148        |
| 4.4.4    | Effect of friction . . . . .   | 156        |
| 4.4.5    | Comparison with granular column collapse . . . . .                             | 158        |
| 4.5      | Summary . . . . .  | 163        |
| <b>5</b> | <b>Numerical modelling of fluid–grain interactions</b>                         | <b>167</b> |
| 5.1      | Fluid simulation using lattice Boltzmann method . . . . .                      | 167        |
| 5.1.1    | Formulation . . . . .  | 169        |
| 5.1.2    | Lattice Boltzmann - Multi-Relaxation Time (LBM-MRT) . . . . .                  | 173        |
| 5.1.3    | Boundary conditions . . . . .  | 176        |

|                   |   |            |
|-------------------|---|------------|
| 5.2               | Validation of the lattice Boltzmann method . . . . .            | 179        |
| 5.3               | Turbulence in lattice Boltzmann method . . . . .                | 183        |
| 5.4               | Coupled LBM and DEM for fluid-grain interactions . . . . .      | 188        |
| 5.4.1             | Draft, kiss and tumbling: Sedimentation of two grains . . . . . | 193        |
| 5.5               | GP-GPU Implementation . . . . .                                 | 194        |
| <b>6</b>          | <b>Underwater granular flows</b>                                | <b>203</b> |
| 6.1               | Introduction . . . . .  | 203        |
| 6.2               | LBM-DEM permeability . . . . .                                  | 204        |
| 6.3               | Granular collapse in fluid . . . . .                            | 209        |
| 6.3.1             | LBM-DEM set-up . . . . .  | 210        |
| 6.3.2             | Collapse in fluid: Flow evolution . . . . .                     | 212        |
| 6.3.3             | Effect of permeability . . . . .                                | 225        |
| 6.3.4             | Effect of initial packing density . . . . .                     | 235        |
| 6.4               | Submarine granular flows down incline plane . . . . .           | 246        |
| 6.4.1             | Effect of initial density . . . . .                             | 246        |
| 6.4.2             | Effect of permeability . . . . .                                | 256        |
| 6.5               | Tall columns . . . . .  | 260        |
| 6.6               | Summary . . . . .   | 270        |
| <b>7</b>          | <b>Conclusions and recommendations for future research</b>      | <b>273</b> |
| 7.1               | Conclusions . . . . .   | 273        |
| 7.1.1             | Multi-scale modelling of dry granular flows . . . . .           | 273        |
| 7.1.2             | Granular flows in fluid . . . . .                               | 275        |
| 7.2               | Recommendations for future research . . . . .                   | 278        |
| 7.2.1             | Development of numerical tools . . . . .                        | 278        |
| 7.2.2             | Understanding the rheology of granular flows . . . . .          | 280        |
| <b>References</b> |   | <b>283</b> |



# List of figures

|      |   |    |
|------|---|----|
| 1.1  | Debris slide in Las Colinas, El Salvador, January 2001 . . . . .  | 2  |
| 1.2  | The extent of the Storegga landslide . . . . .  | 3  |
| 2.1  | Particle size range and their predominant characteristics . . . . .   | 10 |
| 2.2  | The modes of viscous dissipation in a granular flow . . . . .   | 12 |
| 2.3  | Plane shear stress distribution under a constant pressure and shear rate for a granular assembly . . . . .  | 17 |
| 2.4  | Dependence of frictional coefficient $\mu$ with dimensionless shear rate $I$ . . . . .  | 18 |
| 2.5  | Variation of dimensionless parameter $I$ for different flow regimes . . . . .   | 20 |
| 2.6  | Illustration of the Savage-Hutter model . . . . .   | 23 |
| 2.7  | Schematic view of the experimental configuration of a 2-D collapse in a rectangular channel (Lajeunesse et al., 2004) . . . . .   | 25 |
| 2.8  | Normalised final run-out and height as a function of initial aspect ratio for plane-strain and axisymmetric collapse . . . . .  | 27 |
| 2.9  | Collapse of granular column simulation using DEM and Shallow-water approximation . . . . .  | 29 |
| 2.10 | Final deposit profiles for granular column collapse experiments with different initial aspect ratios (Lube et al., 2005). . . . .   | 31 |
| 2.11 | The extent of the failure surface for granular columns with initial aspect ratio of 0.4 and 3 at time $t = 0.4\tau_c$ (Lajeunesse et al., 2004). Short columns show truncated conical deposit at the end of the flow, while tall columns exhibit conical deposit. . . . . | 32 |
| 2.12 | Rough inclined plane: (a) Set-up, and (b) $h_{stop}(\theta)$ (black symbols) and $h_{start}(\theta)$ (white symbols). Reproduced after (Midi, 2004). . . . .  | 35 |
| 2.13 | Complex interactions in a submarine landslide . . . . .   | 38 |
| 2.14 | Experimental set-up of granular collapse in fluid (Rondon et al., 2011). . . . .  | 39 |
| 2.15 | Evolution of run-out and pore-water pressure at the bottom for granular column collapse in fluid for dense and loose conditions (Rondon et al., 2011). . . . .  | 40 |

|  |     |
|--|-----|
| 2.16 Pore pressure feedback mechanism: effect of density (Iverson, 2000). . . . .  | 42  |
| 2.17 Normalised run-out distance as a function of the peak value of the horizontal kinetic energy per grain. (Topin et al., 2011). . . . .                                       | 44  |
| 2.18 Sketch of the motion of a grain $z(t)$ during a simple shear $\dot{\gamma}$ under a confining pressure $P_g$ . . . . .  | 44  |
| 3.1 Schematic representation of different scales of description involved in the multi-scale modelling of granular materials . . . . .  | 48  |
| 3.2 Difference between mesh-based and mesh-free techniques in modelling large deformation flow. . . . .  | 52  |
| 3.3 Typical discretisation of a domain in MPM . . . . .  | 54  |
| 3.4 Illustration of the MPM algorithm . . . . .  | 62  |
| 3.5 Evolution of run-out with time for varying material points per cell for a slope subjected to an impact velocity. . . . .   | 64  |
| 3.6 Effect of number of material points on cell on the run-out behaviour $E_0 = 12.7mgd$ . Velocity profile (m/s) of granular pile subjected to gradient impact loading. . . . . | 66  |
| 3.7 Effect of number of material points on cell on the run-out behaviour $E_0 = 152mgd$ . Velocity profile (m/s) of granular pile subjected to gradient impact loading. . . . .  | 67  |
| 3.8 Evolution of kinetic with time for varying material points per cell for a slope subjected to an impact velocity. . . . .   | 68  |
| 3.9 Evolution of run-out and duration of flow for varying material points per cell for a slope subjected to an impact velocity. . . . .  | 69  |
| 3.10 Schematic description of occurrence of cell crossing noise in MPM . . . . .   | 71  |
| 3.11 Schematic view of 1-D basis functions used in MPM (Steffen et al., 2008). .   | 73  |
| 3.12 Comparison between GIMP method and conventional MPM on the flow morphology of a granular column collapse ( $a = 0.4$ ). . . . .   | 76  |
| 3.13 Comparison between GIMP method and conventional MPM on the evolution of run-out and height with time for a granular column collapse ( $a = 0.4$ ). .                        | 77  |
| 3.14 Calculation of normal force in DEM . . . . .  | 83  |
| 3.15 Verlet list algorithm for neighbourhood search . . . . .  | 88  |
| 3.16 Checking the validity of Verlet list in DEM simulations . . . . .   | 89  |
| 3.17 Verlet integration scheme . . . . .   | 92  |
| 3.18 A 2D periodic simulation cell $\omega$ with its basis vectors in an absolute frame .  | 94  |
| 3.19 Validation of DEM using a disk rolling down an inclined plane . . . . .   | 96  |
| 3.20 Generation of a poly-disperse sample using ballistic deposition technique .   | 100 |

|  |     |
|--|-----|
| 3.21 A poly-dispersed DEM sample generated using ballistic deposition technique . . . . .                            | 101 |
| 3.22 Fortune sweep line algorithm for generating Voronoi Tessellation . . . . .                                      | 102 |
| 3.23 Voronoi tessellation of a run-out profile showing the local packing density . .                                 | 103 |
| <br>   |     |
| 4.1 DEM sample used for the granular column collapse and its grain size distribution curve . . . . .                 | 109 |
| 4.2 DEM set-up of a granular collapse simulation ( $a = 0.8$ ) . . . . .   | 111 |
| 4.3 Periodic shear test using DEM to obtain macroscopic friction angle . . . . .                                     | 112 |
| 4.4 MPM initial mesh and vertical stress for a granular column collapse simulation ( $a=1$ ) . . . . .               | 114 |
| 4.5 Normalised final run-out distance for columns with different initial aspect ratios. . . . .                      | 117 |
| 4.6 Normalised final collapse height for columns with different initial aspect ratios. . . . .                       | 117 |
| 4.7 Velocity profile of a granular column collapse ( $a = 0.4, t = \tau_c$ ) . . . . .                               | 120 |
| 4.8 Velocity profile of a granular column collapse ( $a = 0.4, t = \tau_c$ ) . . . . .                               | 121 |
| 4.9 Velocity profile of a granular column collapse ( $a = 6, t = \tau_c$ ) . . . . .                                 | 122 |
| 4.10 Velocity profile of a granular column collapse ( $a = 6, t = 3 \times \tau_c$ ) . . . . .                       | 123 |
| 4.11 Flow evolution of granular column collapse ( $a = 0.4$ and $6$ ) . . . . .                                      | 126 |
| 4.12 Scheme of collapse for small aspect ratio columns. . . . .  | 127 |
| 4.13 Energy evolution of granular column collapse ( $a=0.4$ and $6$ ) . . . . .                                      | 129 |
| 4.14 Flow evolution of granular column collapse using $\mu(I)$ rheology ( $a=0.4$ and $6$ )                          | 131 |
| 4.15 MPM simulation of evolution of inertial number with time for columns with $a = 0.4$ and $a = 6$ . . . . .       | 132 |
| 4.16 Effect of density on the run-out evolution $a = 0.8$ . . . . .  | 134 |
| 4.17 Evolution of local packing density with time $a = 0.8$ . . . . .  | 135 |
| 4.18 Effect of density on the energy evolution $a = 0.8$ . . . . .   | 136 |
| 4.19 Effect of density on run-out evolution $a = 0.8$ (poly-dispersity $r = 6$ ) . . . . .                           | 137 |
| 4.20 Snapshots of granular column collapse at $t = 6\tau_c$ ( $a = 0.8$ ) . . . . .                                  | 137 |
| 4.21 Effect of density on the evolution of energy and packing fraction $a = 0.8$ (poly-dispersity ‘r’ = 6) . . . . . | 138 |
| 4.22 Effect of density on the run-out behaviour and energy evolution $a = 0.6$ . .                                   | 140 |
| 4.23 Initial geometry and dimensions of the pile subjected to an impact velocity .                                   | 141 |
| 4.24 Initial configuration for the MPM simulation of a pile subjected to impact velocities. . . . .                  | 143 |
| 4.25 Periodic shear test using CD (Mutabaruka, 2013). . . . .  | 144 |
| 4.26 MPM simulation of the initial stages of granular pile subjected to a gradient impact energy. . . . .            | 145 |

|      |   |     |
|------|---|-----|
| 4.27 | CD simulation of the initial stages of granular pile subjected to a gradient impact energy. (Mutabaruka, 2013). . . . .               | 146 |
| 4.28 | Evolution of run-out and time as a function of the normalised input energy for a pile subjected a gradient impact energy . . . . .    | 147 |
| 4.29 | Evolution of kinetic energy with time (MPM) for a pile subjected to gradient input velocities . . . . .                               | 149 |
| 4.30 | Evolution of normalised kinetic energy with normalised time for a pile subjected to gradient input velocities . . . . .               | 150 |
| 4.31 | Evolution of packing density with time $E_0 = 152mgd$ (DEM) . . . . .   | 150 |
| 4.32 | Evolution of vertical and horizontal kinetic energy with time (MPM) for a pile subjected to gradient input velocities . . . . .       | 152 |
| 4.33 | Evolution of the normalised horizontal kinetic energy as function of time since the transient phase . . . . .                         | 153 |
| 4.34 | Evolution of the normalised horizontal kinetic energy as function of the normalised time since the transient phase . . . . .          | 154 |
| 4.35 | Decay time and run-out time as a function of the normalised kinetic energy $E_{kx0}$ . . . . .  | 155 |
| 4.36 | MPM simulations of effect of friction on the run-out behaviour of slopes subjected to impact velocities. . . . .                      | 157 |
| 4.37 | Snapshots of MPM simulations of the evolution of granular pile subjected to a gradient impact energy $E_0 = 61 mgd$ . . . . .         | 159 |
| 4.38 | Snapshots of DEM simulations of the evolution of granular pile subjected to a gradient impact energy $E_0 = 61 mgd$ . . . . .         | 160 |
| 4.39 | Effect of input velocity distribution on the run-out behaviour of slopes subjected to impact velocities. . . . .                      | 161 |
| 4.40 | Comparison of the normalised run-out between the collapse of granular columns and granular slope subjected to impact loading. . . . . | 162 |
| 5.1  | The lattice Boltzmann discretisation and D2Q9 scheme . . . . .  | 169 |
| 5.2  | Illustration of the streaming process on a <i>D2Q9</i> lattice . . . . .  | 172 |
| 5.3  | Illustration of the collision process on a <i>D2Q9</i> lattice . . . . .  | 172 |
| 5.4  | Half-way bounce back algorithm for the <i>D2Q9</i> model . . . . .  | 178 |
| 5.5  | Velocity profile obtained from a LBM Simulation of a laminar flow through a channel. . . . .  | 181 |
| 5.6  | Finite Volume mesh used in the CFD analysis of laminar flow through a channel. . . . .  | 181 |

|      |   |     |
|------|---|-----|
| 5.7  | Velocity profile obtained from a CFD analysis of laminar flow through a channel. . . . .  | 181 |
| 5.8  | Comparison between LBM and CFD on the development of the Poiseuille velocity profile in time . . . . .                            | 182 |
| 5.9  | LBM simulation of velocity profile for a laminar flow through a pipe with an obstacle at L/4. . . . .                             | 183 |
| 5.10 | CFD simulation of velocity contour for a laminar flow through a pipe with an obstacle at L/4. . . . .                             | 184 |
| 5.11 | LBM and CFD simulation of the velocity contour at L/2 for a flow around an obstacle at L/4. . . . .                               | 185 |
| 5.12 | Development of Kármán vortex street around a circular obstacle, for different Reynolds number. . . . .                            | 187 |
| 5.13 | LBM bounce back boundaries for different values of $\delta$ . . . . .   | 192 |
| 5.14 | Time series of draft, kiss and tumble of two grains during sedimentation in a viscous fluid. . . . .                              | 195 |
| 5.15 | Time history of sedimentation of two circular grains. . . . .   | 196 |
| 5.16 | Schematics of a heterogeneous CPU/GPU system. . . . .   | 198 |
| 5.17 | GPU scalability with increase in LBM nodes . . . . .  | 202 |
| 6.1  | Schematic representation of the hydrodynamic radius in LBM-DEM computation. . . . .   | 206 |
| 6.2  | Evaluation of the horizontal permeability for a hydrodynamic radius of 0.7 R. 207   |     |
| 6.3  | Variation of the mean flow velocity with pressure gradient for different hydrodynamic radius. . . . .                             | 208 |
| 6.4  | Relation between permeability and porosity for different hydrodynamic radius and comparison with the analytical solution. . . . . | 210 |
| 6.5  | Underwater granular collapse set-up. . . . .  | 211 |
| 6.6  | Discretisation of solid grains in LBM grid. Shows the step-wise representation of circular disks in the lattice. . . . .          | 213 |
| 6.7  | Flow evolution of a granular column collapse in fluid ( $a = 0.4$ ) . . . . .   | 214 |
| 6.8  | Evolution of height and run-out with time for a column collapse in fluid ( $a = 0.4$ ). . . . .                                   | 216 |
| 6.9  | Evolution of kinetic energies with time for a granular column collapse in fluid ( $a = 0.4$ ) . . . . .                           | 217 |
| 6.10 | Evolution of the potential energy with time for a granular column collapse in fluid ( $a = 0.4$ ) . . . . .                       | 218 |
| 6.11 | Flow evolution of a granular column collapse in fluid ( $a = 4$ ) . . . . .   | 220 |

|  |     |
|--|-----|
| 6.12 Evolution of run-out and height with time for a column collapse in fluid ( $a = 4$ ) . . . . .  | 221 |
| 6.13 Evolution of the potential energy with time for a granular column collapse in fluid ( $a = 4$ ) . . . . .   | 222 |
| 6.14 Evolution of kinetic energies with time for a granular column collapse in fluid ( $a = 4$ ) . . . . .   | 223 |
| 6.15 Comparison of run-out and height between dry and submerged collapse for columns with different initial aspect ratios . . . . .  | 224 |
| 6.16 Effect of permeability on the evolution of run-out for a column collapse in fluid ( $a = 0.8$ ) . . . . .   | 225 |
| 6.17 Effect of permeability on the excess pore water pressure distribution for a granular column collapse in fluid ( $a = 0.8$ & dense packing) at $t = \tau_c$ along the horizontal direction at a height of $10d$ from the base. . . . . | 227 |
| 6.18 Effect of permeability on the evolution of the potential energy with time for a granular column collapse in fluid ( $a = 0.8$ ) . . . . .   | 228 |
| 6.19 Effect of permeability on the evolution of kinetic energies with time for a granular column collapse in fluid ( $a = 0.8$ ) . . . . .   | 229 |
| 6.20 Effect of permeability on the excess pore water pressure distribution along the bottom plane for a granular column collapse in fluid ( $a = 0.8$ & dense packing) at $t = 2\tau_c$ . . . . .  | 230 |
| 6.21 Effect of permeability on the evolution of packing density for a granular column collapse in fluid ( $a = 0.8$ & dense initial packing) . . . . .   | 231 |
| 6.22 Effect of permeability on the deposit morphology of a granular column collapse in fluid ( $a = 0.8$ ) . . . . .   | 232 |
| 6.23 Normalised final run-out distance for columns with different initial aspect ratios. Comparison of dry and submerged granular column collapse for different hydrodynamic radius ( $0.7 R$ , $0.8 R$ and $0.9 R$ ). . . . .             | 233 |
| 6.24 Normalised final run-out distance for columns as a function of peak kinetic energy in dry and submerged conditions . . . . .  | 234 |
| 6.25 Effect of permeability on the evolution of run-out for a column collapse in fluid ( $a = 0.8$ & loose packing) . . . . .  | 236 |
| 6.26 Effect of permeability on the excess pore water pressure distribution along the base of a granular column collapse in fluid ( $a = 0.8$ & loose packing) at $t = \tau_c$ . . . . .  | 237 |
| 6.27 Effect of permeability on the excess pore water pressure distribution for a granular column collapse in fluid ( $a = 0.8$ & loose packing) at $t = 2\tau_c$ . . . . .   | 238 |

|   |     |
|---|-----|
| 6.28 Effect of permeability on the evolution of the potential energy with time for a granular column collapse in fluid ( $a = 0.8$ & loose packing) . . . . .                                     | 239 |
| 6.29 Effect of permeability on the evolution of kinetic energies with time for a granular column collapse in fluid ( $a = 0.8$ & loose packing) . . . . .   | 240 |
| 6.30 Effect of permeability on the evolution of packing density for a granular column collapse in fluid ( $a = 0.8$ & loose initial packing) . . . . .  | 241 |
| 6.31 Particle tracking of the deposit morphology for a granular column collapse in fluid ( $a = 0.8$ & loose packing), influence of permeability . . . . .  | 242 |
| 6.32 Effect of permeability on the normalised effective stress for loose initial packing at $t = 2\tau_c$ . . . . .   | 243 |
| 6.33 Effect of initial density on the deposit morphology for a granular column collapse in fluid ( $a = 0.8$ ) . . . . .  | 244 |
| 6.34 Evolution of packing fraction at $t = \tau_c$ for dense and loose initial packing fraction. Black means dense packing, while white colour denotes loose packing in the voronoi cell. . . . . | 245 |
| 6.35 Evolution of run-out and kinetic energy with time (dense) . . . . .  | 248 |
| 6.36 Flow morphology at $t = 3\tau_c$ for different slope angles (dense) . . . . .  | 249 |
| 6.37 Evolution of run-out and kinetic energy with time (loose) for different slope angles . . . . .   | 251 |
| 6.38 Flow morphology at time $t = 3\tau_c$ for different slope angles (loose) . . . . .   | 252 |
| 6.39 Evolution of packing density with time for different slope angles . . . . .  | 253 |
| 6.40 Comparison between dry and submerged granular column on the effect of slope angle on the run-out distance (Dense and Loose). . . . .   | 254 |
| 6.41 Effect of slope angle on the run-out behaviour for different initial packing density. . . . .  | 255 |
| 6.42 Evolution of run-out and height with time for different permeability (loose slope $5^\circ$ ) . . . . .  | 257 |
| 6.43 Evolution of kinetic energy and packing density with time for different permeability (loose slope $5^\circ$ ) . . . . .  | 258 |
| 6.44 Evolution of the flow front at $t = 3\tau_c$ for different permeabilities (loose slope $5^\circ$ ). . . . .  | 259 |
| 6.45 Comparison between dry and submerged granular column for a slope angle of $0^\circ$ and $5^\circ$ on the effect of permeability on the run-out distance (Dense and Loose). . . . .           | 261 |
| 6.46 Effect of permeability on the run-out behaviour for different slope angle and the initial packing density. . . . .   | 262 |

|  |     |
|--|-----|
| 6.47 Flow evolution of a granular column collapse in fluid ( $a = 6$ ) on a horizontal surface . . . . .   | 263 |
| 6.48 Flow evolution of a granular column collapse in fluid ( $a = 6$ ) on a slope of $5^\circ$ . . . . .   | 266 |
| 6.49 Packing density of a granular column collapse in fluid ( $a = 6$ ) on a slope of $5^\circ$ .266   |     |
| 6.50 Evolution of run-out and height for a column collapse in fluid ( $a = 6$ ) on a slope of $5^\circ$ . . . . .                                      | 267 |
| 6.51 Evolution of the kinetic and the potential energy with time for a granular column collapse in fluid ( $a = 6$ ) on a slope of $5^\circ$ . . . . . | 268 |
| 6.52 Evolution of the kinetic energies with time for a granular column collapse in fluid ( $a = 6$ ) on a slope of $5^\circ$ . . . . .                 | 269 |

# List of tables

|     |   |     |
|-----|---|-----|
| 3.1 | Comparison of theoretical and DEM result for a disk on an inclined plane of 45° . . . . .                   | 95  |
| 4.1 | Material properties of glass ballotini used in granular column collapse (Lajeunesse et al., 2004) . . . . . | 108 |
| 4.2 | Micro-mechanical parameters used in DEM simulations of granular column collapse . . . . .                   | 110 |
| 4.3 | Parameters used in continuum simulations of granular column collapse . . . . .                              | 113 |
| 5.1 | LBM parameters used in simulating laminar flow through a circular pipe. . . . .                             | 180 |
| 5.2 | Computed Strouhal number for fluid flows with different Reynolds number . . . . .                           | 188 |
| 5.3 | GPU vs CPU parallelisation . . . . .  | 201 |
| 6.1 | Configurations for LBM-DEM simulations of granular collapse in fluid . . . . .                              | 205 |



# Chapter 1

## Introduction

Avalanches, debris flows, and landslides are geophysical hazards which involve rapid mass movement of granular solids, water and air as a single phase system. The presence of water in a granular flow distinguishes '*mud and debris flow*' from '*granular avalanches*'. Debris flow is a rapid mass movement of liquefied, unconsolidated, saturated soil. The speed of the debris flow varies from 50 km/h to 80 km/h in extreme cases, transporting 100 to 100,000 cubic meters of unconsolidated sediments down very steep slopes. Figure 1.1 shows the catastrophic effect of a debris flow that occurred during an earthquake-triggered landslide in Las Colinas, El Salvador. On the other hand, submarine landslides transport sediments across continental shelves even on slopes as flat as 1° and can reach speeds of 80 km/h. Figure 1.2 shows the Storegga Landslide, the largest recorded continental slope failure, which struck off the coast of central Norway, transporting materials over 500 km (Ward and Day, 2002).

Granular avalanches, debris flow and submarine landslides cause significant damage to life and property. Globally, landslides cause billions of pounds in damage, and thousands of deaths and injuries each year. On 2 May 2014, a pair of mudslides killed at least 2000 people, burying 3000 houses and over 14,000 people were affected after a landslide hit the north-east Afghan province of Badakhshan. Rescuers responding to the initial mudslide were struck by a second mudslide which trapped or killed a large proportion of potential rescuers (Source: BBC, 2014). The consecutive slides levelled the village, and left the area under 10 to 30 metres of mud. A week of torrential rain might be a plausible reason for the mud flows. Understanding the triggering mechanism and the granular flow process provides an insight into the force and velocity distribution in a granular flow, enabling us to design appropriate defensive measures.



Figure 1.1 Initiation, channelling, spreading and deposition of debris slide in Las Colinas, El Salvador, January 2001. The debris flow buried as many as 500 homes. (Source: USGS report on '*Landslides in Central America*', 2001)

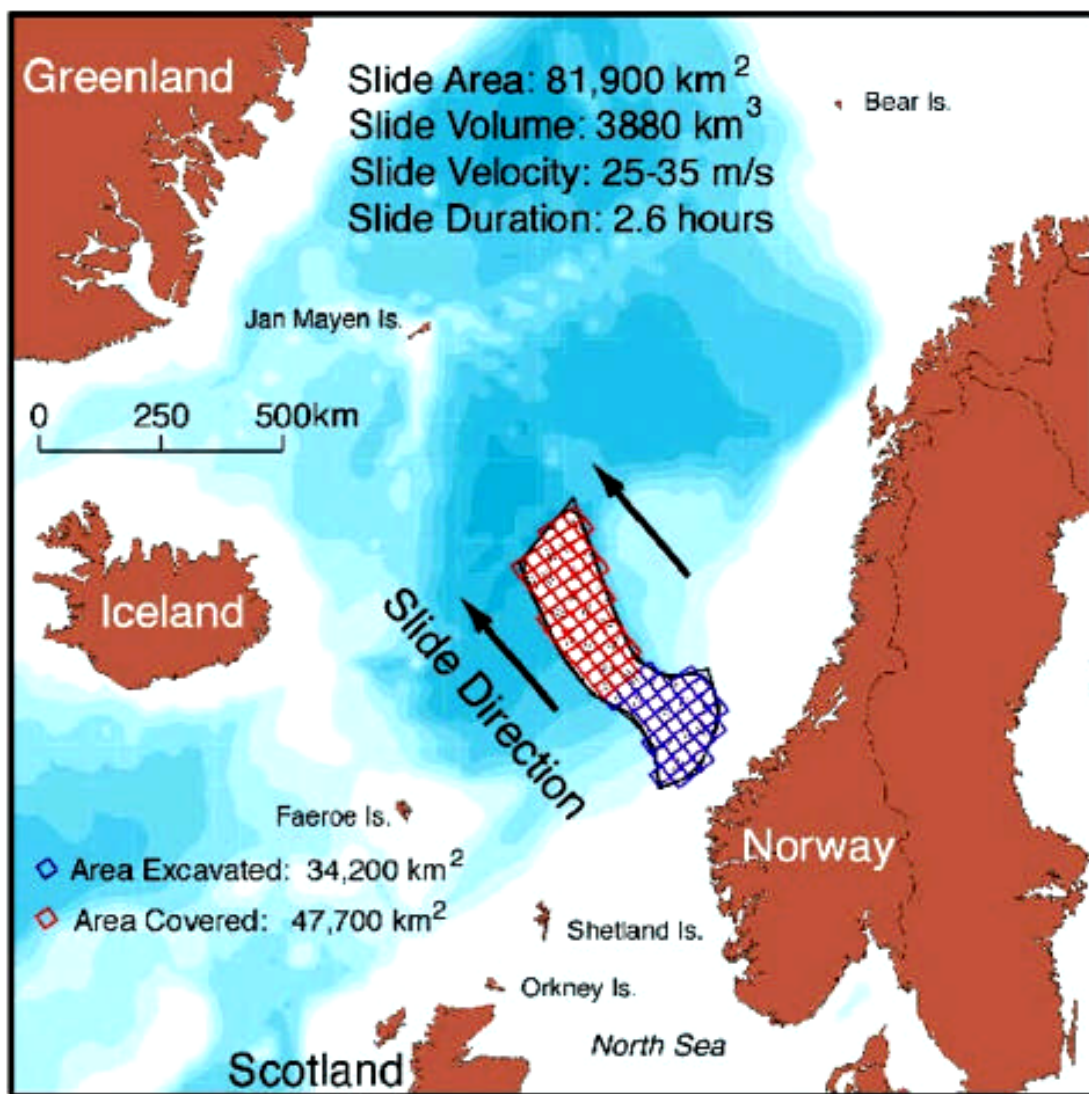


Figure 1.2 The extent of the Storegga landslide (Source: School of geoscience, University of Sydney)

## 1.1 Modelling the granular flows

The dynamics of a homogeneous granular flow involve at least three distinct scales: the *microscopic scale* which is characterized by the contact between grains, the *meso-scale* which represents micro-structural effects such as grain rearrangement, and the *macroscopic scale*. The flow of submarine landslides, which is of  $100.000 \text{ km}^3$  in volume, is influenced by the grain-grain interactions and the dynamics happening at the scale of a few micrometers to millimetres. This poses a question of how to effectively model the various scales of behaviour observed in a granular flow?

Typically, continuum laws are only used when there is a strong separation of scales between the micro-scale and the macro-scale sizes of the flow geometry. Although granular materials are composed of discrete grains which interact only at contacts, the deformations of individual grains are negligible in comparison with the deformation of the granular assembly as a whole. Hence, the deformation is primarily due to the movements of grains as rigid bodies. Therefore, continuum models are still widely used to solve engineering problems associated with granular materials and flows.

Conventional mesh-based approaches, such as Finite Element (FE) and Finite Difference (FD) methods, involve complex re-meshing and remapping of variables, which cause additional errors in simulating large deformation problems. Mesh-free methods, such as the Material Point Method (MPM) and Smooth Particle Hydrodynamics (SPH), are not constrained by the mesh size and its distortion, and are effective in simulating large deformation problems such as debris flow and submarine landslides. The analytical and finite-element-like techniques which consider granular materials as a continuum cannot take into account the local geometrical processes that govern the mechanical behaviour of non-homogeneous soils, and pose subtle problems for statistical analysis (Mehta and Barker, 1994).

The grain level description of the granular material enriches the macro-scale variables that happen to poorly account for the local rheology of the materials. Numerical tools such as the Discrete Element Method (DEM) allow us to evaluate quantities which are not accessible experimentally, thus providing useful insight into the flow dynamics. Grain-fluid interactions can be simulated by interfacing discrete-element methods with a lattice Boltzmann solver or a computational fluid dynamics solver, however these methods have their inherent limitations. Even though millions of grains can be simulated, the possible size of such a grain system is generally too small to regard it as '*macroscopic*'. Therefore, methods to perform a micro-macro transition are important and these '*microscopic*' simulations of a small sample, i.e. the '*representative volume element*', can be used to derive a macroscopic theories which describes the material within the continuum framework.

Granular flows have been extensively studied during the past two decades through experimental and numerical simulations (Andersen and Andersen, 2010; Denlinger and Iverson, 2001; Iverson et al., 1997; Jaeger et al., 1996; Tang et al., 2013). In most cases, granular flows exhibit three distinct regimes: the slow quasi-static regime, a dilute collisional regime and an intermediate regime. Many theories and phenomenological models have been developed to model the behaviour of different flow regimes. One approach is to use the Kinetic theory (Jenkins and Savage, 1983; Savage and Jeffrey, 1981), which assumes binary collision between particles. Kinetic theory is able to capture the rapid-collisional regime, however is incapable of predicting the dense quasi-static behaviour. Under certain conditions, granular flows exhibit some fluid-like behaviour, using a simple analogy from fluid dynamics one can model granular flows as non-Newtonian fluids using a variant of the Navier-Stokes equation (Savage and Hutter, 1991). The depth-averaged shallow water equation has been applied to solve granular flow dynamics with a reasonable amount of success. However, the basic assumption of neglecting the effect of vertical acceleration restricts the approach from describing the triggering mechanism, such as the collapse of a vertical cliff.

In certain cases, classical theories are incapable of describing the flow kinematics. Hence, rheologies have been used to describe the mechanical behaviour of granular flows through an empirical relation between deformations and stresses. Midi (2004) proposed a new rheology for granular flows based on extensive experimental and numerical investigation on gravity-driven flows. The  $\mu(I)$  rheology describes the granular behaviour using a dimensionless number, called the *inertial number I*, which is the ratio of inertia to the pressure forces. Small values of  $I$  correspond to the critical state in soil mechanics and large values of  $I$  corresponds to the fully collisional regime of the kinetic theory. The spreading dynamics are found to be similar for the continuum and grain-scale approaches, however the rheology falls short in predicting the run-out distance for steeper slopes and in the transition regime where the shear-rate effect diminishes. The use of rheologies to describe the flow of granular materials in fluids remains largely unexplored.

In addition to the scale-effects, most geophysical hazards usually involve multi-phase interactions. The momentum transfer between the discrete and continuous phases significantly affects the dynamics of the flow. In order to describe the mechanism of multi-phase granular flows, it is important to consider both the dynamics of the solid phase and the role of the ambient fluid. Most models which simulate submarine landslides assume a single homogeneous grain-fluid mixture governed by a non-Newtonian fluid behaviour (Denlinger and Iverson, 2001; Iverson, 2000). Although successful in accounting for the general phenomenology on analytical grounds, such models fail to capture certain phenomena such as porosity gradient and fluid-induced size-segregation. Moreover, application of these

models involves additional assumptions about the boundary/interface between the grains and the fluid, and the transition between high and low shear stresses.

The simple  $\mu(I)$  rheology is found to capture the dense submarine granular flows, if the inertial time scale in the rheology is replaced with a viscous time scale (Pouliquen et al., 2005). However, the transition from a rapid granular flow down a slope to the quasi-static regime when the granular mass ceases to flow, where the shear rate vanishes, is not captured by the simple model. The flow threshold or the hysteresis characterizing the flow or no-flow condition is also not correctly captured by this model. When the scale of the system is larger than the size of the structure, a simple rheology is expected to capture the overall flow behaviour, however in granular flows, the size of the correlated motion has the same size as the system, causing difficulties in modelling the flow behaviour. Hence, it is essential to study the behaviour of granular flows at various scales, i.e. microscopic, meso-scale and continuum-scale levels, in order to describe the entire granular flow process.

## 1.2 Objectives

This study is motivated by a simple question: If a granular column collapses and flows in a dry condition and within a fluid, in which case would the run-out be the farthest? The collapse in a fluid experiences drag forces which tend to retard the flow, this might result in a longer run-out distance in the case of dry condition. However, the collapse in fluid might experience lubrication effects due to hydroplaning and this reduces the effective frictional resistance, which might result in a longer run-out distance in the case of fluid than the dry condition. Would the effect of lubrication overcome the drag forces and result in the farthest run-out in fluid? Or would the drag forces predominate resulting in dry case having the farthest run-out distance? Although, a simple problem by description, the influence of various properties such as slope angle, initial packing density, and permeability on the run-out behaviour makes it a complex phenomenon.

The other important question is how to model the granular flow behaviour, which exhibits complex fluid-like and/or solid-like behaviour depending on the initial state and the ambient conditions. This research aims to provide an insight into the mechanics of granular flows in dry and submerged conditions, using a multi-scale approach, so as to describe the behaviour of geophysical hazards such as avalanches, debris flows and sub-marine landslides.

## 1.3 Overview of this work

This PhD makes advances in the field of numerical modelling of granular flows. Granular materials exhibit complex flow behaviour that often involves multiphase interactions. Development of sophisticated numerical tools that are capable of modelling the different scales of description in a granular flow and the multiphase interaction between the soil grains and the fluid is thereby the focus of this PhD. This study addresses the following areas of granular flow modelling and behaviour:

**Development of numerical tools for modelling dry granular flows (Chapter 3)** The Material Point Method, a continuum based Eulerian - Lagrangian approach, is developed to describe the dynamics of the various granular flow behaviours (described in Chapter 2). The grain-scale response of the granular flow kinematics is captured using Discrete Element Method (DEM). The implementation of DEM and development of tessellations tools for extracting macro-scale properties are also discussed.

**Dry granular flows (Chapter 4)** Multi-scale analyses using MPM and DEM are performed to understand the suitability of MPM as a continuum approach in modelling collapse of a granular column. Energy evolution studies are carried out to study the difference in the dissipation mechanism between both approaches. The influence of various initial material properties on the run-out behaviour is investigated. The run-out behaviour of a granular slope subjected to an impact loading is analysed using MPM and DEM. The effect of distribution of kinetic energy on the run-out behaviour of granular slopes is also discussed.

**Numerical modelling of fluid - grain coupling (Chapter 5)** A coupled lattice Boltzmann - DEM approach is implemented in this work to understand the micro-scale interactions between the soil grains and the ambient fluid. Due to the computational demand of this approach, the LBM - DEM technique is implemented in GPUs. A turbulent model is incorporated to capture the interaction of vortices with the granular surface. The validation of the developed LBM-DEM model under different flow conditions is also discussed.

**Granular flows in fluid (Chapter 6)** The fundamental question of the difference in the mechanism of collapse and flow between the dry and the submerged granular columns is addressed. The role of initial granular properties such as packing density, permeability and slope angle on the run-out behaviour of the dry and the submerged granular flows is investigated. This chapter provides an insight into the flow dynamics of submerged granular flows under different initial conditions.

The videos of simulations performed in this study can be viewed at <http://vimeo.com/kks32/videos>.

# **Chapter 2**

## **Granular flows**

### **2.1 Introduction**

A granular material is a conglomeration of a large number of discrete solid grains of sizes greater than  $1\mu m$  whose behaviour is governed by frictional contacts and inelastic collisions. A schematic representation of the size range of the granular materials is presented in figure 2.1. Granular materials, characterized by the interaction between individual grains, lie between two extremes scales: the molecular-scale range predominated by the electrostatic force, i.e. Van der Waals forces, and the continuum scale which is described by the bulk property of the material. In various soil classification systems, sand is classified as a granular material having grain sizes greater than  $75\mu m$ . A grain size of  $75\mu m$  is an important transition point, where the frictional effect starts to dominate the material behaviour and the effect of the electrostatic Van der Waals forces diminishes. The extent of the grain size range of the granular materials from the molecular size to a continuum scale indicates that they have a complex behaviour, demonstrating a mix of grain-like and continuum-like behaviour.

The physics of non-cohesive granular assemblies is intriguing. Despite being ubiquitous in nature, granular materials are the most poorly understood materials from a theoretical standpoint. For such a poorly understood area, the flow of granular materials has a surprising range of geo-hazard predictions and industrial applications. For years, granular materials have resisted theoretical development, demonstrating non-trivial behaviour that resembles solid and/or fluid-like behaviour under different circumstances. Even in the simplest of situations, granular materials can exhibit surprisingly complex behaviour. Macroscopically, the complex mix of solid and fluid-like behaviour can be illustrated by a simple example; while one walks on the beach, the solid-like behaviour of soil becomes evident as it supports one's weight, but if we scoop a handful of soil and allow it to run through the fingers, the fluid-like nature becomes obvious.

Microscopically this complex behaviour has various reasons. The range of the grain size gives rise to complex interactions between grains constituting the granular media. Unlike other micro-scale particles, soil grains are insensitive to thermal energy dissipation (Mehta, 2011), because the thermal energy dissipation in a granular material is several orders of magnitude smaller in comparison with the energy dissipation due to interaction between the grains. The thermal energy scales are small when compared to the energy required to move the grains. The granular material reaches the static equilibrium quickly due to its dissipative nature, unless an external source of energy is constantly applied (Choi, 2005).

Our knowledge of the behaviour of granular assemblies is restricted to two extremes: the solid-like behaviour of dense granular assemblies that resist the shearing force by undergoing plastic deformations, and the fluid-like flow behaviour characterized by high shear rates. Granular media are *a priori* simple systems made of solid grains interacting through their contacts. However, they still resist our understanding and no theoretical framework is available to describe their behaviour (Pouliquen et al., 2006). The strong dependency of the behaviour of granular material on its surrounding environment makes it difficult to have a unified theoretical framework. When strongly agitated, the granular material behaves like a dissipative gas, and kinetic theories have been developed to describe this regime (Popken and Cleary, 1999; Xu et al., 2003). On the other hand, during slow deformations, the quasi-static regime is dominated by steric hindrance and friction forces are often described using plasticity theories. In between the two regimes, the material flows like a fluid, and the grains experience enduring contacts, which is incompatible with the assumptions of the kinetic theory (Pouliquen et al., 2006) that describes the dilute regime of a granular flow. Typical granular flows are dense and hence a fundamental statistical theory is not appropriate to describe their properties. Moreover, during the process of granular flow, the material can exist in all the above-mentioned states, which further complicates our understanding of granular flows.

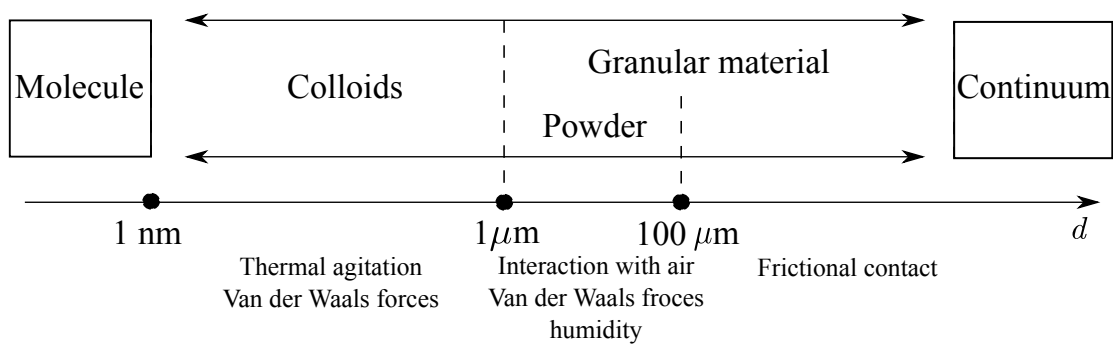


Figure 2.1 Particle size range and their predominant characteristics

## 2.2 Modelling the granular flows

Different approaches have been used to model the granular flows at different scales of description. The dynamics of a homogeneous granular flow involve at least three distinct scales: (1) the *microscopic scale* characterized by small time and length scales representing contact/grain interactions, (2) the *mesoscopic scale*, where grain rearrangements, development of micro-structures and shear rates have a dominant influence on the granular flow behaviour, and (3) the *macroscopic scale* which involves large length scales that are related to geometric correlations at even larger scales. The interesting issue is whether one should consider or neglect a particular scale while modelling the granular dynamics (Radjai and Richefeu, 2009). However, the difficulty in modelling the granular flows originates from the fundamental characteristics of the granular matter such as negligible thermal fluctuations, highly-dissipative interactions, and a lack of separation between the microscopic grain scale and the macroscopic scale of the flow (Goldhirsch, 2003).

Granular flows display a large span of grain concentrations and therefore exhibit different behaviour at different concentrations (figure 2.2). Granular flows can be classified into three different regimes (Jaeger et al., 1996): (a) in the dilute part of the flow, grains randomly fluctuate and translate, this form of viscous dissipation and stress is named as the *kinetic regime*. This regime is characterized by grains moving freely between successive collisions (Goldhirsch, 2003). (b) at higher concentration, in addition to the previous dissipation form, grains can collide shortly, this gives rise to further dissipation and stress, called as the *collisional regime*. This intermediate fluid-like regime is dense but still flows like a fluid and the grains interact both by collision and through friction (Midi, 2004; Pouliquen and Forterre, 2002). Transfer of grain kinetic energy and momentum within a rapidly flowing granular medium occurs during these collisions (Popken and Cleary, 1999). (c) at very high concentration (more than 50% in volume), grains start to endure long, sliding and rubbing contacts, which gives rise to a totally different from of dissipation and stress, *frictional regime*. This dense slow quasi-static regime is characterized by long duration between contacts and grain interaction via frictional contact (Roux and Combe, 2002).

The momentum and energy transfer will be different according to the granular regimes. For the granular phase, it is clear that any mathematical model attempting to model the granular flow must account for the above mechanisms, at any time and anywhere within the flow. The mathematical models require a comprehensive unified stress tensor able to adequately describe stress within the flow for any of these regimes, and this without imposing what regime will dominate over the others. Several theoretical frameworks have been used to describe the granular flow behaviour. Frictional behaviour predominates in most granular flows. Hence, continuum models based frictional properties of the granular mass have been

widely adopted to discuss the granular flow behaviour. Alternatively, dilute granular flow behaviour is conventionally modelled using the kinetic theory, while the dense granular flows are described using the  $\mu(I)$  rheology. In certain conditions, where the lateral extent of the flow is significantly larger than the vertical component, shallow-water approximation is used. The capability and limitation of the various frameworks are discussed below.

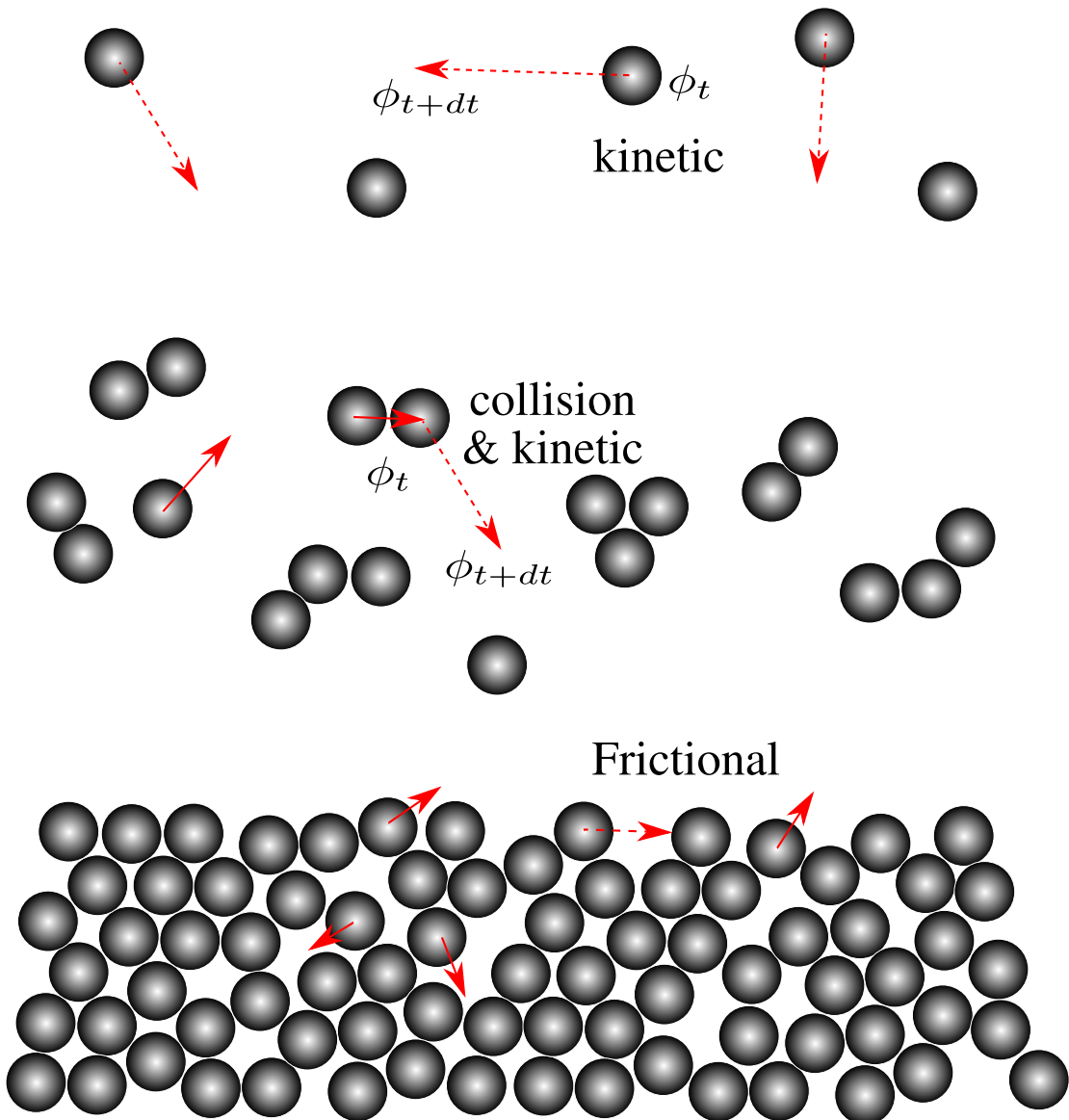


Figure 2.2 The modes of viscous dissipation in a granular flow

## 2.2.1 Continuum models

In frictional regime, grains experience long and permanent contacts in rubbing, rolling on each other. Hence a stress tensor based on the mechanical law of friction must be developed. Granular flow modelling began as early as 1776 with Coulomb's paper describing the yielding of granular material as a frictional process. Although it was not about granular flows, *per se*, the prediction of soil failure for civil engineering applications describes the onset of structural collapse leading to catastrophe (Campbell, 2006). Mohr-Coulomb's yield criterion along with a flow rule from metal plasticity is sufficient to describe the behaviour of granular flow as a continuum process, without considering the interaction of individual grains.

Advanced models based on the critical state concept (Schofield and Wroth, 1968) provides further insight into continuum description of granular flows. According to the critical state theory, the 'under consolidated' or loose soil tends to increase in density upon shearing, while the dense 'over consolidated' soil dilates when sheared, until it reaches the critical state. As dense granular flow involves large shear stresses, it is reasonable to assume that the shearing occurs at the critical state. Large applied stress can cause the granular solids to deform at the grain scale and squeeze them into the inter-grain pores. However, the critical state is independent of the applied stress. In granular flows, the applied stress during the actual flow is less in comparison to the stress on the soil underneath a structure, where the soil is subjected to large shear strains. It is therefore reasonable to assume that the flow is incompressible and takes place at the critical state (Campbell, 2006).

The main limitation of the continuum approach is the assumption that the friction angle,  $\phi$  is a constant material parameter (Potapov and Campbell, 1996). Although the mechanism of dense granular flow is attributed to the bulk friction, it is the formation of force chains and the rearrangement of internal structure of the granular assembly that causes friction-like behaviour. Experiments (Savage and Sayed, 1984; Savage, 1984) and computer simulations (Campbell and Brennan, 1985) indicate a weak relation between the bulk friction and the packing density, due to the micro-structural rearrangement of grains (Campbell, 1986). As the packing density increases, the grains tend to arrange themselves in a regular order when sheared. In order to understand the development of micro-structure, it is important to look at the grain-level interactions. Bagnold (1954) was the first to try and model granular materials as individual grains. Bagnold's theory of motion of individual grains in a shear flow and inter-grain friction inducing random velocities is reminiscent of the thermal motion of molecules in the kinetic theory of gases.

## 2.2.2 Kinetic theory

The gas kinetic theory assumes that the particles interact by instantaneous collisions, which implies only binary (two-particle) collisions. The particles are modelled using a single coefficient of restitution, to represent the energy dissipated by the impact normal to the point of contact between the particles, and for the most part, the surface friction or any other particle interactions tangential to the point of contact are ignored (Campbell, 1990). Jenkins and Savage (1983) extended the kinetic theory for thermal fluids to idealized granular mixtures to predict the rapid deformation of granular material by including energy dissipation during collision for nearly inelastic particles. Savage and Jeffrey (1981) extended the kinetic theory to predict simple shear flow behaviour for a wide range of coefficients of restitution. The kinetic theory is capable of predicting the shear flow behaviour only for mixtures composed of particles with identical density and size (Iddir and Arastoopour, 2005), however real systems are composed of particles that vary in size, and segregation of particles can occur.

The formulation of the gas kinetic theory can be used to derive a set of equations for granular flow if the particles are assumed to be rigid. In turn, the rigid particle assumption implies that all contacts occur instantaneously. Thus, there is vanishing probability of multiple simultaneous contacts and only binary contacts are considered. From there, kinetic theory formulation yields a set of Navier – Stokes like equations. Conservation of mass is written as

$$\frac{d\rho v}{dt} + \rho v \nabla \cdot \mathbf{u} = 0. \quad (2.1)$$

Conservation of momentum

$$\rho v \frac{d\mathbf{u}}{dt} = \nabla p(\rho, v, T, \varepsilon) + \nabla \cdot (\eta(p, \rho, v, T, \varepsilon) \nabla \mathbf{u}). \quad (2.2)$$

Conservation of granular energy (granular temperature)

$$\rho v \frac{dT}{dt} = \nabla \cdot (\alpha(p, \rho, v, T, \varepsilon) \nabla T) + \tau : \nabla \mathbf{u} - \Gamma(p, \rho, v, T, \varepsilon). \quad (2.3)$$

where  $\alpha$  is the conductivity,  $\tau : \nabla \mathbf{u}$  is the temperature production by shear work,  $p$  is the pressure, concentration is  $v$ ,  $\rho$  is the density,  $\varepsilon$  is the coefficient of restitution,  $T$  is the granular temperature and  $\Gamma$  is the dissipation through inelastic collisions. There are several problems that should be immediately apparent with this formulation. The most obvious is that the range of applicability of rapid flow theory is limited. The solid phase stresses are viscous in nature (eq. 2.2), which results in no-force condition when the granular mass is static (Campbell, 2006).

The kinetic theory is valid for dispersed granular flows (Ng et al., 2008). Van Wachem et al. (2001) observed that the numerical simulations of dense granular flow based on kinetic theory were poor in comparison with the experimental data on fluidised bed expansion. Confined granular flows are usually dense, because of their mechanism of energy dissipation and their tendency to form clusters. The dense granular flows lie in an intermediate regime, where both the grain inertia and the contact network has significant influence on the flow behaviour (Pouliquen and Forterre, 2002). Thus, a part of the force is transmitted through the force network, which contradicts the two basic assumptions in the kinetic theory, i.e. binary collision and the molecular chaos.

For dense granular flow conditions, the total stress transmission in the flow regime is the sum of the rate-dependent (collision-transition) and the rate-independent (friction) components (Ng et al., 2008). Addition of frictional stress component (Schaeffer, 1987) to the kinetic theory improves the ability of the model to predict the dense granular flows. The main advantage of kinetic theories is that they can be used to derive deterministic constitutive laws to describe the behaviour of granular flows in a theoretical framework (Jenkins and Savage, 1983). Kinetic theories formulated on the assumption of solid phase stress as a viscous response have limitations when applied to granular flows. A viscous material produces no force unless it is in motion, hence the kinetic theory based on viscous solid phase cannot explain the static force exerted by the granular materials on the walls, as observed in experiments. The frictional component that is based on long-duration contact is added to the instantaneous collision contact term, which is self-contradictory. Also, the rapid-flow models based on gas kinetic theory assume that the molecular collisions are elastic, which means that they do not dissipate energy (Campbell, 2006), which is in contrast to the reality. Finally, the important assumption of gas kinetic theory is molecular chaos, which assumes no correlation between the velocities or positions of the colliding particles, which is not true especially in a dense granular flow where the particles interact many times with their neighbours and a strong correlation between their velocities is inevitable.

### 2.2.3 Rheology

Rheology is the science of flow of materials with solid and fluid characteristics. In practice, rheology is principally concerned with describing the mechanical behaviour of those materials that cannot be described by the classical theories, by establishing an empirical relation between deformation and stresses. Consider a granular assembly of grains having diameter  $d$  and density  $\rho_d$  under a confining pressure  $P$  (see figure 2.3). If the material is sheared at a constant shear rate,  $\dot{\gamma} = V_w/L$  is imposed by the relative movement of the top plate with a velocity  $V_w$ . In the absence of gravity, the force balance implies that the shear stress,

$\tau = \sigma_{xy}$ , and normal stress,  $P = \sigma_{xx}$ , are homogeneous across the cell. This configuration is the simplest configuration to study the rheology of granular flow, i.e. to study the effect of the strain rate,  $\dot{\gamma}$ , and pressure,  $P$  on the volume and shear stress,  $\tau$ .

Even though the granular materials have been extensively researched at microscopic level, the continuum representation of granular materials in terms of conservation of mass and momentum is still an area of concern (Daniel et al., 2007; Midi, 2004). The prediction of rheology of granular materials even in the simplest case is complicated as they exhibit rate-dependent behaviour and no single constitutive equation is able to describe the behaviour over a range of shear stress rates. Da Cruz et al. (2005) developed a very famous rheology for granular flows, that is based on the simple two-dimensional shear in the absence of gravity and establishes that the flow regime and rheological parameters scale with a dimensionless number that represents the relative strength of inertia forces with respect to the confining pressure (Daniel et al., 2007), along the lines of Savage and Hutter (1991). The shear stress,  $\tau$ , is proportional to the confining pressure,  $P$ , and is written as

$$\tau = P\mu(I). \quad (2.4)$$

The friction coefficient  $\mu$  depends on the single non-dimensional parameter  $I$ , expressed as

$$I = \frac{\dot{\gamma}d}{\sqrt{P\rho_p}}. \quad (2.5)$$

The parameter  $I$  can be interpreted in terms of different time scales controlling the grain flow. If the grains are rigid, i.e. neglecting the elastic properties of the grains, then  $I$  is the only non-dimensional parameter in the problem. Hence, the shear stress,  $\tau$ , has to be proportional to the pressure,  $P$ , times a function of  $I$ . Comparing the shape of the function  $\mu(I)$  with the experimental results of flow down an inclined plane, Jop et al. (2006) observed that the frictional coefficient increases from a minimal value of  $\mu_s$  to an asymptotic value of  $\mu_2$ , when the value of  $I$  increases. The variation of friction coefficient with  $I$  is shown in figure 2.4. The friction coefficient can be related to the inertial number  $I$  as

$$\mu(I) = \mu_s + \frac{\mu_2 - \mu_s}{I_0/I + 1}, \quad (2.6)$$

where  $I_0$  is constant, typically in the range of 0.25 - 0.3.

To formulate a complete constitutive model, it is essential to describe the volumetric behaviour. Based on the dimensional analysis, it can be argued that the volume change is also a function of dimensionless parameter  $I$  and that it also depends on the maximum and the minimum possible void ratios and the time for microscopic rearrangement of grains.

Consider two rows of mono-dispersed grains. When a grain is located on the gap formed by two adjacent grains, it is assumed to have a maximum packing fraction. As the grain is sheared along the bottom row of grains, it moves out of the gap resulting in a minimum packing fraction. The duration required for this rearrangement is directly proportional to the volume fraction. The dimensionless shear rate, expressed as the ratio between the duration of re-arrangement to the mean duration (see figure 2.18), has a linear relationship with the volume fraction.

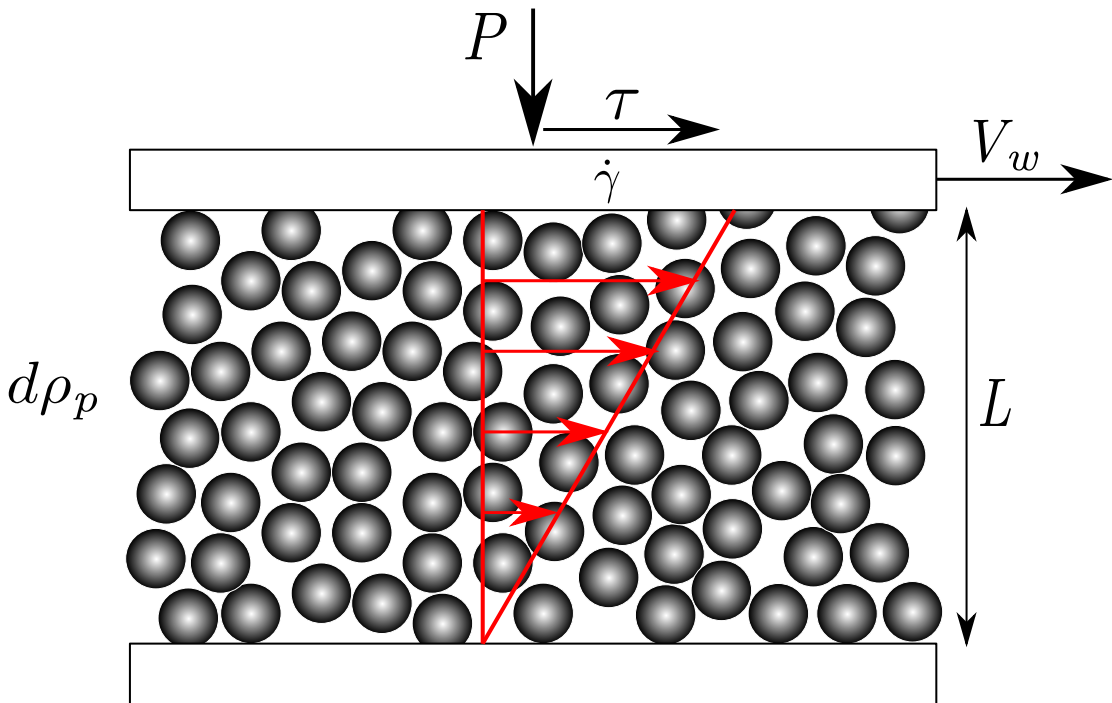


Figure 2.3 Plane shear stress distribution under a constant pressure and shear rate for a granular assembly

In general, the flow regimes can be classified based on the dimensionless number  $I$  (Da Cruz et al., 2005). Figure 2.5 shows the variation of frictional coefficient  $\mu$  and packing fraction with dimensionless number  $I$  for different flow regimes under simple shearing. Dilute or “collisional” flow occurs for  $I > 10^{-1}$  and the grain collision is chiefly binary, accompanied by additional “bounce-back” akin to gases (Kamrin, 2008). In the dilute flow regime, the grains are rarely in long-duration contacts and can be described by dissipative Boltzmann kinetics. The “quasi-static” regime occurs at the other extreme of the spectrum,  $I < 10^{-3}$ , where the intermittent motion is prevalent. The inertial time is always small enough for the grains to align to a dense compaction, without significant collisional dissipation. The frictional sliding and stick-slip dynamics dominate the dissipation mechanism. The stress/strain-rate relationship becomes singular; driving the system with a range of quasi-

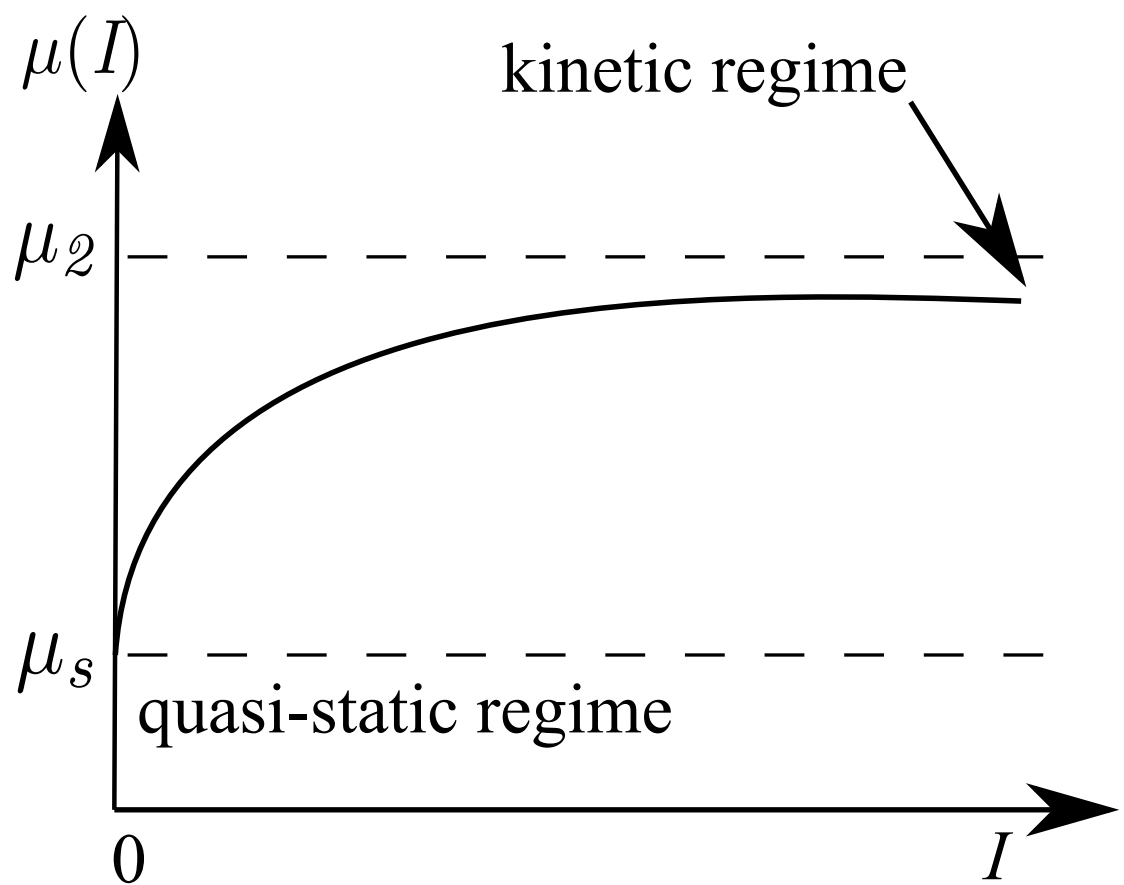


Figure 2.4 Sketch of dependence of frictional coefficient  $\mu$  with dimensionless shear rate  $I$ , reproduced after Pouliquen et al. (2006)

static normalized shear rates all give the same time-average value for  $\mu$ . In this regime the dissipation is primarily frictional and rate-independent. Packing fraction appears independent of  $I$ , and grain-level specifics are more important to flow dynamics. The moderate-flow regime is observed for  $I$  between  $10^{-3}$  and  $10^{-1}$ , characterized by faster flows, with a high rate of contact formation and more energy dissipation per impact. In this regime,  $I$  has a one-one relationship with  $\mu$  and is large enough for rate dependence, but small enough for the flow to remain dense. Moderate flows also exhibit the property of *shearing dilation*, where an increase in the normalized flow rate causes the steady-state packing fraction to decrease, which is different from *shear dilation*, which refers to a decrease in the packing density as a function of total shear. Flows which are too slow to be moderate still undergo shear dilation due to geometric packing constraints, but shearing dilation occurs only in faster flows due to rate effects (Kamrin, 2008). In moderate flows, the dissipation is primarily rate-sensitive due to energy loss during contact formation, yet packing remains dense

Campbell (2002) described the “Moderate regime” as an elastic granular flow regime, where the inter-grain stiffness governs the overall flow behaviour of the granular assembly. At high concentration, the stresses are proportional to the contact stiffness, and the streaming stiffness is negligible. When a dense granular assembly is sheared, the force chains that transmit the forces continue to rotate until it becomes unstable and collapses. As the force-chain rotates, the granular material tend to dilate, however it is restricted due to the constant volume constraint; instead, the rotation compresses the chain, generating an elastic response (Campbell, 2006). Campbell (2002) divided the flow into the elastic and the inertial regimes. In the Elastic regime, the force is transmitted principally through the deformation of force chains with a natural stress scaling of  $\tau d/k$ . The force chain forms when the grains are sheared at the rate of  $\dot{\gamma}$ , and hence the rate of chain formation is proportional to the shear rate  $\dot{\gamma}$ . This transition regime can be explained using the force-chain concept. The lifetime of a force chain is proportional to  $1/\dot{\gamma}$ , consequently the product of rate of formation and the lifetime of the force chain is independent of  $\dot{\gamma}$ , and the stresses generated are quasi-static. However at higher shear rates, the elastic forces in the chain have to absorb the additional inertial force of the grains, requiring extra force to rotate the chain proportional to the shear rate. Even though the grains are locked in force chains, the forces generated must reflect the grain inertia. The ratio of elastic to inertial effects is governed by a dimensionless parameter

$$k^* = \frac{k}{\rho d^3 \dot{\gamma}^2}, \quad (2.7)$$

where  $k/\rho d^3 \dot{\gamma}^2 = (\tau/\rho d^2 \dot{\gamma}^2)/(\tau d/k)$  is the ratio of Bagnold’s inertial to the elastic stress scaling. The important dimensionless parameter is  $k^*$ , which is a measure of inertially-

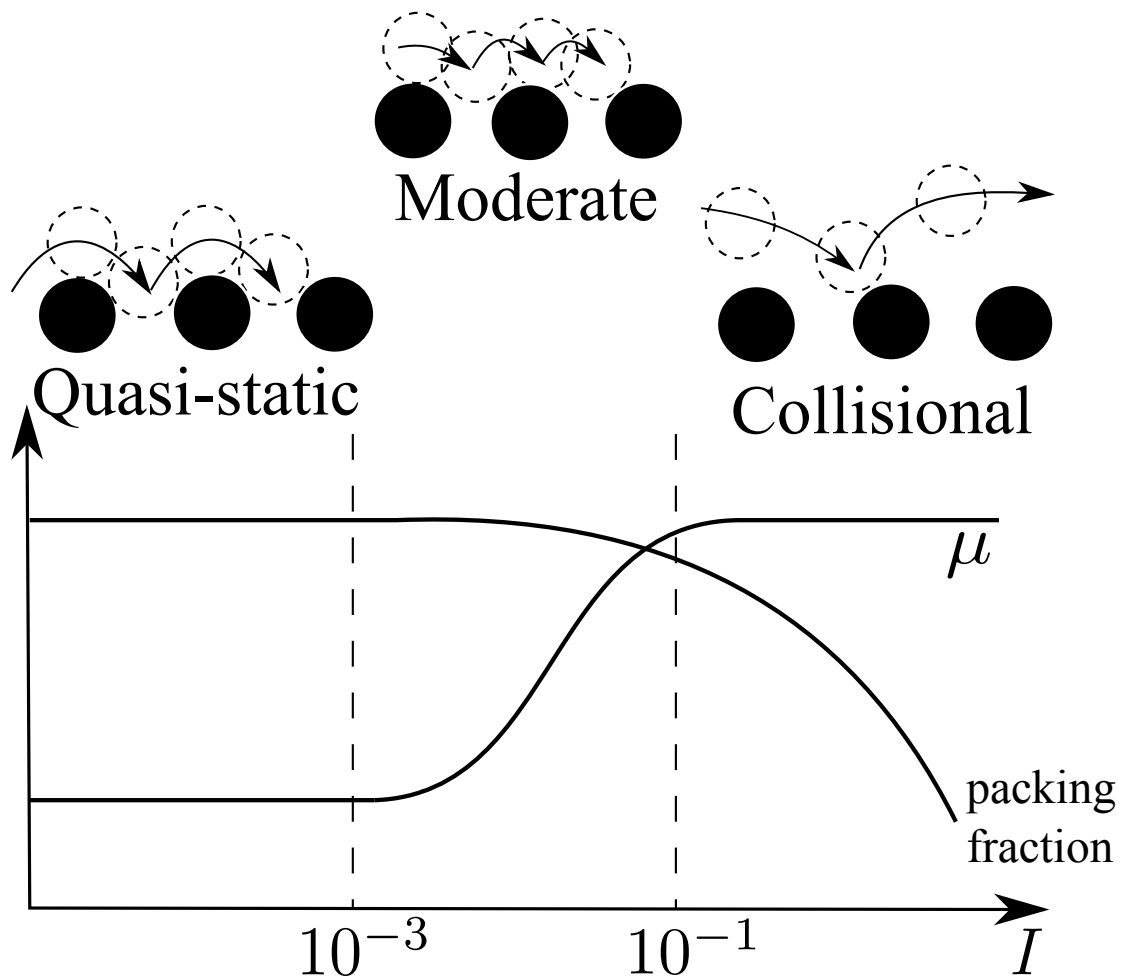


Figure 2.5 Variation of dimensionless parameter  $I$  for different flow regimes under simple shearing. (a) *Quasi-static* ( $I < 10^{-3}$ ): Dissipation is primarily frictional and rate-independent. Packing fraction appears independent of  $I$ , and grain-level specifics are more important to flow dynamics; (b) *Moderate* ( $10^{-3} < I < 10^{-1}$ ): the dissipation is primarily rate-sensitive due to energy loss during contact formation, yet packing remains dense; (c) *Collisional* ( $I > 10^{-1}$ ): Flow becomes dilute and gas-like. Dynamics modelled best by dissipative Boltzmann kinetics. Redrawn after (Kamrin, 2008)

induced deformation, reflects the relative effects of elastic to inertial forces, i.e. at large  $k^*$ , the elastic forces dominate and at small  $k^*$ , inertial forces dominate (Campbell, 2006). Campbell (2002) observed a strong correlation between the coefficient of friction and the dimensionless parameter,  $k$  as the flow progresses through different regimes, similar to the observation made by Kamrin (2010).

Constitutive laws, which describe the dilatancy and friction, allow us to deduce the dependency of pressure and shear stress on shear rate and solid fraction. In contrast to the observation of Campbell (2002), Da Cruz et al. (2005) found that the elastic stiffness has little effect on the constitutive law, for values greater than  $10^4$ , however that it does affect the coordination number. Da Cruz et al. (2005) also observed that the microscopic friction coefficient,  $\mu$ , has a significant influence on the dilatancy, and the solid fraction remains a linearly-decreasing function of  $I$ . The frictional properties of the material are found to control the solid fraction, from the critical state to the collisional regime (Da Cruz et al., 2005).

Although the rheology tends to describe the behaviour of granular flows, the mechanism of granular flows was found to vary with time, position and feedback mechanism (Iverson, 2003). Rheology summarizes the mechanical behaviour at scales smaller in comparison with the Representative Elemental Volume (REV), for a substance modelled as a continuum. Rheology-based descriptions are generally restricted to homogeneous materials that exhibit time-independent behaviour, hence are unsuitable for describing granular flows where the stress history has a significant effect on the flow dynamics. The estimation of debris flow yield strength highlights the limitation of rheologies which do not consider the development of strength with evolution of time and space. Johnson (1965) emphasized that debris yield strength is predominantly a frictional phenomenon analogous to the Coulomb strength of granular soils, and that strength consequently varies with effective normal stress. Treatment of yield strength as an adjustable rheological property contradicts the basic understanding that the strength evolves as the debris-flow motion progresses. Frictional behaviour implies no explicit dependence of shear resistance on shear rate, whereas rheological formulas commonly used to model debris flows generally include a viscous component that specifies a fixed functional relationship between shear resistances and shear rate. Although rate-dependent shear resistance is observed in debris flows, its magnitude and origin indicate that it is ancillary rather than essential (Iverson, 2003).

#### 2.2.4 Shallow-water approximation

Developing constitutive laws valid from the quasi-static to dilute regimes remains a serious challenge. Simple elasto-plastic approach fails to model the collisional regimes in a granular flow. On the other hand, the original kinetic theory based on binary collisions does not

capture the correct behaviour in the dense regime. In configurations where the flowing layer is thin, a different theoretical framework is adopted. One such approach is the depth-averaged shallow-water equation, which has been applied to solve granular flow dynamics with a reasonable amount of success. The Savage-Hutter model (Savage and Hutter, 1991), is a depth-average continuum-mechanics based approach which consists of hyperbolic partial differential equations to describe the distribution of the depth and the topography of an avalanching mass of cohesion-less granular media (Hutter et al., 2005). This approach is based on the assumption that the horizontal length scale is very large in comparison with the vertical length scale, which allows us to neglect the horizontal partial derivatives relative to the vertical partial derivatives. Field observations of natural avalanches indicate an aspect ratio of  $10^{-3}$  to  $10^{-4}$  (Cawthor, 2006). By neglecting the vertical length scale, the continuum equation for conservation of mass and momentum can be written as

$$\partial_x u + \partial_y v = 0, \quad (2.8)$$

$$\partial_t u + u \partial_x u + v \partial_y u = (\nabla \cdot \boldsymbol{\sigma})_x + \mathbf{F}_x. \quad (2.9)$$

The continuum equation requires determining the components of the stress tensor and a suitable constitutive law. *Savage-Hutter (SH) model* uses the Mohr-Coulomb law to describe the constitutive relation. The conservation of mass and momentum in the SH model is based on the assumption of granular flow as an incompressible fluid flow, which means that throughout the avalanche, the density of the avalanching material remains constant. Although Hutter et al. (1995) observed the density of the granular flow to remain almost constant in a flow down a curved chute, the destructive nature of landslides and avalanches restricts us from inferring a conclusive result. The SH model involves the following assumptions: (1) Coulomb-type sliding takes place with a bed friction angle  $\delta$ , (2) Mohr-Coulomb frictional behaviour occurs inside the material with internal angle of friction,  $\phi \geq \delta$ , and (3) the velocity profile is assumed to be uniform throughout the avalanche depth. The granular flow over a rigid plane inclined at an angle,  $\theta$  is shown in figure 2.6. The mass and momentum balance in the SH model is written as

$$\frac{\partial H}{\partial T} + \frac{\partial}{\partial X}(HU) = 0, \quad (2.10)$$

$$\frac{\partial U}{\partial T} + U \frac{\partial U}{\partial X} = (\sin \theta - \tan \delta \operatorname{sgn}(U) \cos \theta) - \beta \frac{\partial H}{\partial X}, \quad (2.11)$$

where capital letters denote non-dimensional quantities with respect to the typical horizontal and vertical length scales ( $L^*, H^*$ ) and the time scale  $\sqrt{L^*/g}$ . The key feature in the shallow water approximation is the Mohr-Coulomb constitutive law, which is applied at the free

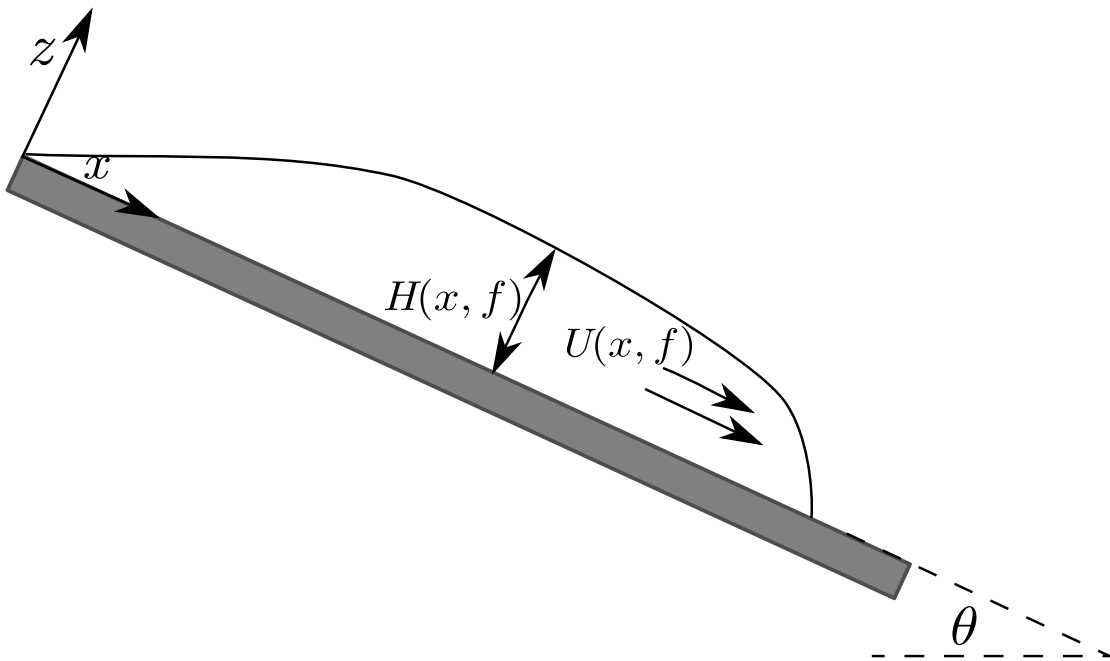


Figure 2.6 Illustration of the Savage-Hutter model

surface and at the base, to describe the granular flow. Comparison of the model with the post-calculation of Madlein avalanche in Austria indicates that the Coulomb basal friction is insufficient and requires an additional viscous component. The SH model's predictions were not satisfactory for granular flows down gentle slopes of inclination angle  $\leq 30^\circ$ , where granular materials exhibit premature stop (Hutter et al., 2005). The SH model has not yet been tested in cases where the granular flow interacts with obstacles.

The two main modelling techniques that are commonly employed to describe the granular flow are the continuum approach and the discrete element approach. The continuum approach involves treating granular assembly as a continuum and describing its response using constitutive laws, while the discrete approach involves considering the individual grains of the granular material and applying Newton's laws of motion to describe the deformation of the granular material. These approaches are adopted in the present study and detailed discussions are provided in chapter 3.

## 2.3 Studies on granular flows

The flow of dense granular material is a common phenomenon in engineering predictions, such as avalanche, landslides, and debris-flow modelling. Despite the huge amount of research that has gone into describing the behaviour of granular flow, a constitutive equation

that describes the overall behaviour of a flowing granular material is still lacking. To model geo-physical scale problems, the depth-averaged constitutive equations have been employed along with an empirical friction coefficient and a velocity profile deduced from experiments (Iverson, 2003; Midi, 2004; Pouliquen, 1999). Although this approach has been successful to a certain extent in predicting geophysical flows (Hutter et al., 1995; Pouliquen and Chevoir, 2002), it presents two important shortcomings (Lajeunesse et al., 2005): first, the depth-average method is true only if the thickness of the flowing layer is thin in comparison with the lateral dimension, and second, the empirical laws are deduced from experiments performed under steady-flow conditions. These cast doubts on the validity of the depth-averaged approach. Two simple granular flow studies, granular column collapse and granular flow down an inclined plane, carried out by various researchers to understand the flow behaviour are discussed below.

### 2.3.1 Granular column collapse

Lube et al. (2005) and Lajeunesse et al. (2004) have carried out experimental investigations on the collapse behaviour of granular columns on a horizontal plane. Both the experiments involved filling a cylinder of height  $H_0$  and radius  $L_0$  with granular material of mass  $m$ . Figure 2.7 shows the schematic view of the experimental configuration of a 2-D granular column collapse in a rectangular channel. The granular column is then released *en masse* by quickly removing the cylinder, thus allowing the granular material to collapse onto the horizontal surface, forming a deposit having a final height  $H_f$  and radius  $L_f$ . Although the experiment is simple and attractive allowing us to explore the limitations of depth-average modelling techniques, a constitutive law that could describe the entire flow behaviour is still lacking. The primary aim of these experiments was to determine the scaling laws for the run-out distance.

#### Deposit morphology

##### *Experimental findings*

Lajeunesse et al. (2005) observed that the flow dynamics and the final deposit remain independent of the volume of granular material that is released, but depend only on the initial aspect ratio  $a$  of the granular column. The experiment was carried out to understand the effect of the geometrical configuration on the run-out, the mechanism of initiation of the flow, the evolution of flow with time, and to understand how such complex flow dynamics could produce deposits obeying simple power laws. Lube et al. (2005) explored the effect of density

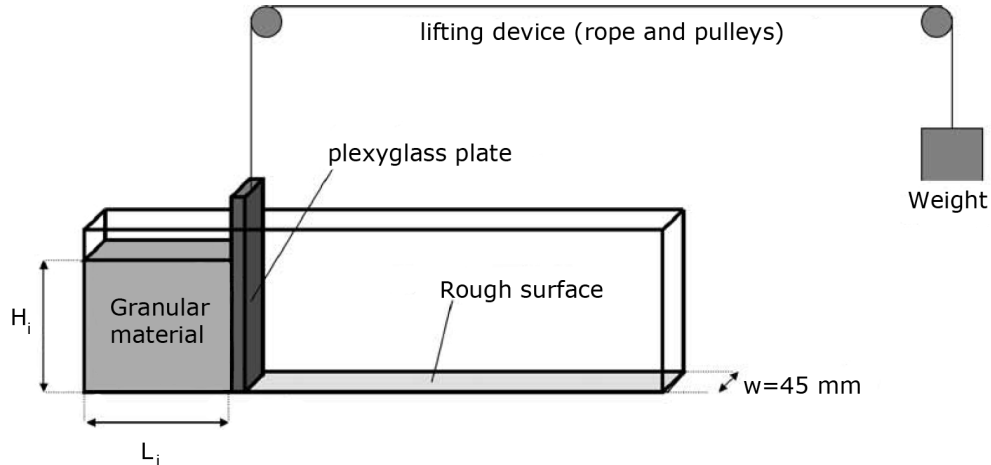


Figure 2.7 Schematic view of the experimental configuration of a 2-D collapse in a rectangular channel (Lajeunesse et al., 2004)

and shape of grains on flow dynamics, whereas Lajeunesse et al. (2004) worked with glass beads to study the influence of bead size and substrate properties on the deposit morphology. Surprisingly, both drew the striking conclusion that the flow duration, the spreading velocity, the final extent of the deposit, and the fraction of energy dissipated during the flow can be scaled in a quantitative way independent of substrate properties, bead size, density, and shape of the granular material and released mass,  $m$  (Lajeunesse et al., 2005).

The normalised final run-out distance as a function of the initial aspect ratios of the granular column under plane-strain and axisymmetric conditions is shown in figure 2.8a. Lube et al. (2005) scaled the run-out distance as

$$\frac{L_f - L_0}{L_0} \approx \begin{cases} 1.24a, & a \lesssim 1.7 \\ 1.6a^{1.2}, & a \gtrsim 1.7 \end{cases} \quad (2.12)$$

while Lajeunesse et al. (2005) scaled run-out as

$$\frac{L_f - L_0}{L_0} \approx \begin{cases} 1.35a, & a \lesssim 0.74 \\ 2.0a^{1.2}, & a \gtrsim 0.74 \end{cases} \quad (2.13)$$

The final run-out distance is found to have a linear relation ship for short columns and exhibit a power-law relation with the initial aspect ratio of tall columns.

The normalised final height as a function of the initial aspect ratios of the granular column under plane-strain and axisymmetric conditions is shown in figure 2.8b. The evolution of the final scaled deposit height  $H_f/L_0$  with the initial aspect ratio  $a$  for the axisymmetric

collapse (Lajeunesse et al., 2005) is given as

$$H_f/L_0 \approx \begin{cases} a, & a \lesssim 0.74 \\ 0.74, & a \gtrsim 0.74 \end{cases} \quad (2.14)$$

and for two-dimensional collapse

$$H_f/L_0 \approx \begin{cases} a, & a \lesssim 0.7 \\ a^{1/3}, & a \gtrsim 0.7 \end{cases} \quad (2.15)$$

The final height of collapse is unaffected in both 2D collapse and axisymmetric collapse for short columns. In the case of tall columns, axisymmetric collapse show a constant final height whereas a power-law relation with the initial aspect ratio is observed in 2D collapse.

#### *Axisymmetric versus two-dimensional collapse*

Quasi-two-dimensional collapse of a granular column on a horizontal surface reveals that the geometric configuration influences the scaling of the run-out distance (Lajeunesse et al., 2005). The run-out in a quasi-two-dimensional collapse of a granular column in a rectangular channel scales as

$$\frac{L_f - L_0}{L_0} \approx \begin{cases} 1.2a, & a \lesssim 2.3 \\ 1.9a^{2/3}, & a \gtrsim 2.3 \end{cases} \quad (2.16)$$

Balmforth and Kerswell (2005) studied the collapse of granular columns in rectangular channels with a narrow (width  $W$  of the slot = 10 \* diameter  $d$ ) and a wide slot ( $W = 200 * d$ ), and focused on the deposit shape. Lacaze et al. (2008) observed that slots whose width  $W \geq 1.2 \times d$  avoids crystallisation and wider slots  $W \geq 2 \times d$  overcomes the effect of jamming. As in the axisymmetric case, Balmforth and Kerswell (2005) observed that the run-out is well represented at large aspect ratios by a simple power-law dependence, which depends on the width of the channel. The run-out distance can be scaled as:  $\Delta L/L_0 \approx \lambda a^{0.65}$  for narrow channels and  $\Delta L/L_0 \approx \lambda a^{0.9}$  for wide channels. The scaling found for quasi-two-dimensional experiments in the narrow gap configuration gives similar results as Lube et al. (2005) and roughly a scaling of  $(L_f - L_0)/L_0 \propto a^{2/3}$ . However, these laws are influenced by the presence of sidewalls and depend, albeit only in the numerical coefficient of proportionality, on the frictional properties of the granular material.

Balmforth and Kerswell (2005) observed that the constant of proportionality  $\lambda$  in the power-law relation is found to vary with the internal friction angle of the granular material,

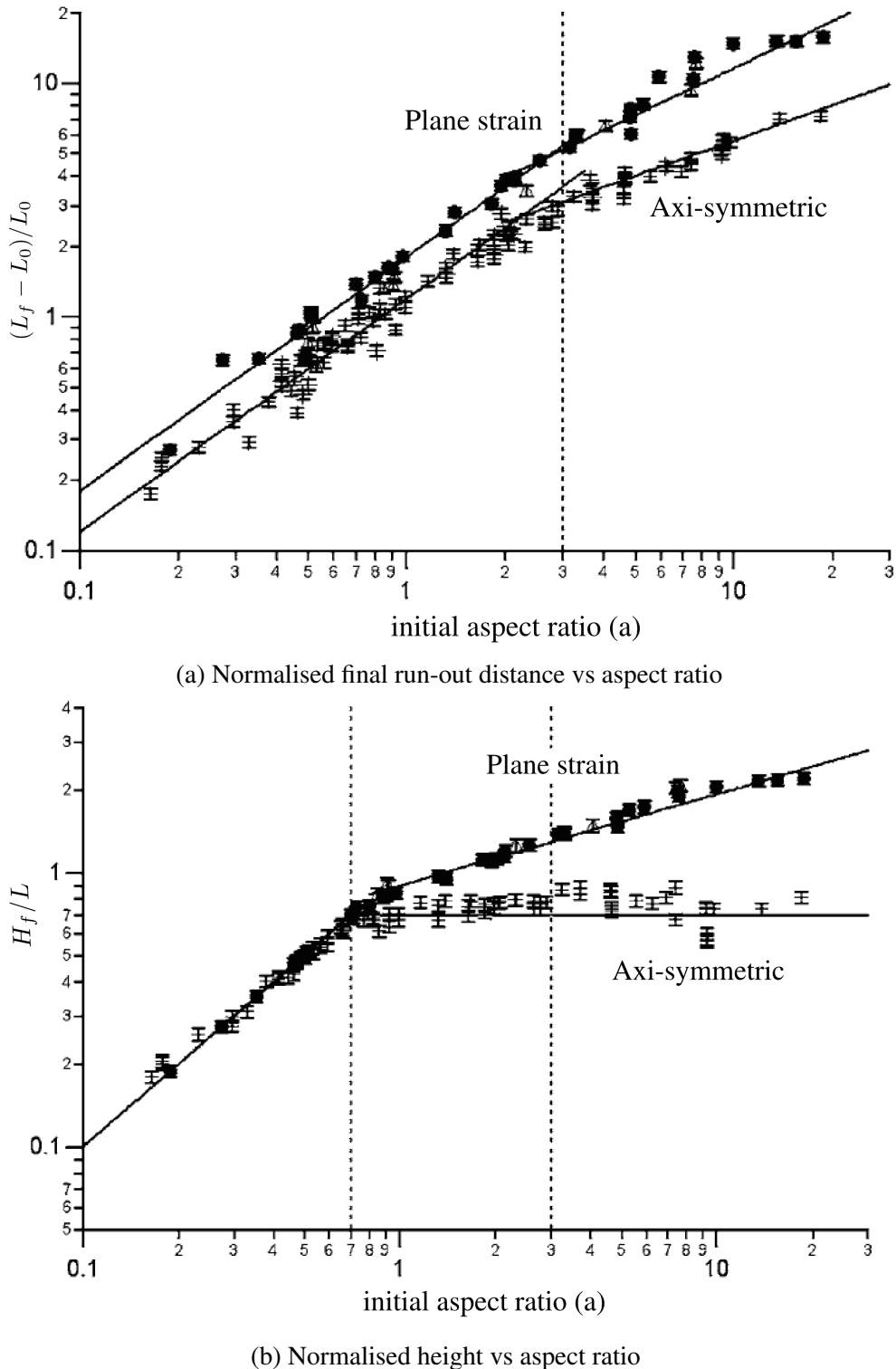


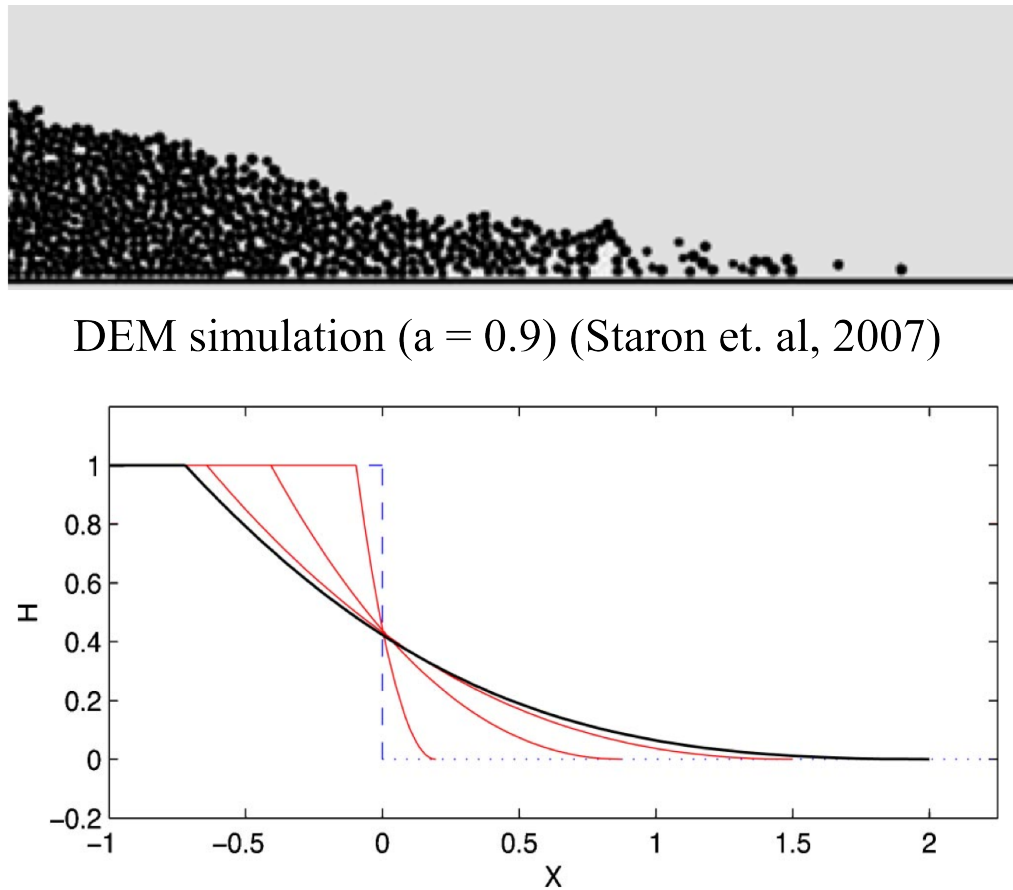
Figure 2.8 The normalised final run-out distance and final height as a function of the initial aspect ratios of the granular column under plane-strain and axisymmetric conditions (Lajeunesse et al., 2004).

which contradicts the findings of previous authors, especially Lube et al. (2005) who found that the scaling of run-out is independent of the granular material. This may perhaps be due to a narrow range of experimental materials restricted to mono-dispersed grain size considered in the previous studies. Balmforth and Kerswell (2005) found that the material properties have almost no influence on the exponent of the normalised run-out as a function of the initial aspect ratio. The numerical constant of proportionality, however, showed clear material dependence. This corroborates the conclusions of Lajeunesse et al. (2004). Daerr and Douady (1999) also observed strong influence of initial packing density and the internal structure on the behaviour of granular flows. By comparing the initial and final cross-section areas of the pile, Balmforth and Kerswell (2005) observed that the granular material experienced dilation (by about 10%) as the flow progressed to form the final deposit (Balmforth and Kerswell, 2005). Although, internal packing structure and density is found to have an influence on the run-out behaviour, a proper understanding of the effect of density on the run-out and evolution of packing fraction is still lacking.

### *Numerical modelling*

Numerical simulations of granular column collapse by Zenit (2005) and Staron and Hinch (2007) yielded similar scaling of run-out with aspect ratio  $a$ . Unlike other authors, Zenit (2005) did not observe any transition in the run-out behaviour of a granular column collapse with the aspect ratio  $a$ . The origin of the exponents is still under discussion. No model has yet achieved a comprehensive explanation of the complex-collapse dynamics. For higher aspect ratios, the free fall of the column controls the dynamics of the collapse and the energy dissipation at the base is attributed to the coefficient of restitution. Thus, the initial potential energy stored in the system is dissipated by sideways flow of material and the mass ejected sideways is found to play a significant role in the spreading process, i.e. as  $a$  increases, the same fraction of initial potential energy drives an increasing proportion of initial mass against friction, thus explaining the power-law dependence of the run-out distance on  $a$ .

Taking advantage of the similarity between granular slumping and the classical “*dam break*” problem in fluid mechanics, Kerswell (2005) solved both the axisymmetric and two-dimensional granular-collapse problem using the shallow-water approximation. Although the results of the shallow-water approximation have good agreement with experimental results, the shallow-water approximation overestimates the run-out distance for columns with aspect ratio  $a$  greater than unity. The shallow-water equation does not take into account the effect of vertical acceleration (Lajeunesse et al., 2005), which has been found to play a significant role in controlling the collapse dynamics (Staron and Hinch, 2007), thus resulting in overestimation of the run-out distance. The evolution of run-out predicted



Shallow water approximation ( $a = 1.0$ ) (Kerswell, 2005)

Figure 2.9 Collapse of granular column simulation using DEM (Staron and Hinch, 2007) and Shallow-water approximation (Kerswell, 2005).

using shallow-water approximation and DEM are shown in figure 2.9. Tall columns showed significantly longer run-out distances when using continuum approaches like material point method (Bandara, 2013; Mast et al., 2014a). It was observed that a simple friction model cannot effectively describe the collapse dynamics (Staron and Hinch, 2007). However, the reason for difference in the run-out behaviour is not known.

The final collapse height observed in the numerical simulations of granular collapse is found to be similar to the experimental results (Balmforth and Kerswell, 2005; Lube et al., 2005). Numerical simulation of granular column collapse (Lacaze et al., 2008; Staron and Hinch, 2007) showed a transition in the flow behaviour at  $a \geq 10$ , which was not observed in granular collapse experiments (Balmforth and Kerswell, 2005; Lajeunesse et al., 2004; Lube et al., 2005). In the depth-averaged shallow-water model, which integrates over the depth, the

emphasis was on capturing the scaling of the final deposit, rather than trying to reproduce the internal structure of the flow. The shallow-water model captures well the final deposit scaling for lower aspect ratios, however fails to capture the flow dynamics for granular columns with higher aspect ratios, where the flow is governed mainly by the vertical collapse of the granular column as a whole. The run-out distance predicted is clearly erroneous in the collapse regime where there is a sudden drop in efficiency by which the initial potential energy of the system is converted into the kinetic energy for spreading. Even a more sophisticated basal drag law will not be sufficient to model the mechanism of granular column collapse realistically using the shallow-water approximation (Kerswell, 2005). Considering the large spectrum of theoretical frameworks, no consensus exist on the origin of the power-law and finding constitutive laws valid from the quasi-static to dilute regimes remains a serious challenge.

## Flow dynamics

### *Experimental findings*

The variation of final scaled deposit with the aspect ratio  $a$  shows a transition in the run-out behaviour for an aspect ratio of 1.7, indicating a transformation in the spreading process or the collapse mechanism. To understand the collapse mechanism, it is insufficient to study only the final scaled profile, and hence the entire flow process should be analysed. Lajeunesse et al. (2005) observed the flow regime and deposit morphology for a quasi-two-dimensional granular collapse in a rectangular channel. The flow phenomenology of a granular column collapse in a rectangular channel was surprisingly similar to that observed in the axisymmetric collapse (Lajeunesse et al., 2004; Lube et al., 2005), depending mainly on the initial aspect ratio  $a$  (section 2.3.1).

The flow dynamics involve spreading of granular mass by avalanching of flanks producing a truncated cone for  $a \lesssim 0.74$  and a cone for  $a \gtrsim 0.74$ ; the transition of flow dynamics occurs as the value of  $a$  is increased (figure 2.10). The evolution of the deposit height remains independent of the flow for  $a \lesssim 0.7$ , however it exhibits significant dependence on the geometrical configuration for  $a \gtrsim 0.7$ . In rectangular channels, the effect of side-wall on the run-out behaviour was observed; the surface velocity profile between the side walls is that of a plug flow with a high slip velocity at the wall and low shear along the direction transverse to the flow. Systematic measurements indicate that the ratio of the maximum surface velocity to the surface velocity at the wall is between 1.2 and 1.4. Lajeunesse et al. (2005) observed that the difference between the evolution of  $H_f$  in the axisymmetric geometry and in the rectangular channel is not an experimental artefact due to the side wall friction, but is a *geometrical effect*.

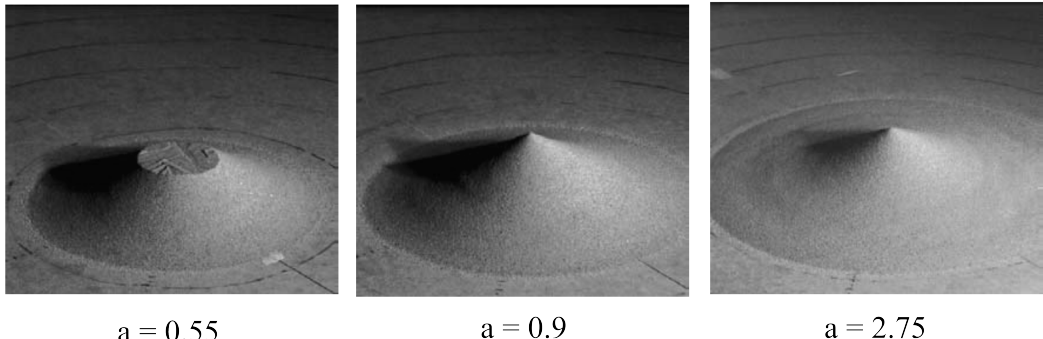


Figure 2.10 Final deposit profiles for granular column collapse experiments with different initial aspect ratios (Lube et al., 2005).

Understanding the internal flow structure will provide an insight into the complex collapse dynamics. The failure surface observed at  $t = 0.4\tau_c$  for granular columns with initial aspect ratio of 0.4 and 3 are shown in figure 2.11. For smaller values of aspect ratio  $a \leq 0.7$ , the flow is initiated by a failure at the edge of the pile along a well-defined shear-failure surface above which material slides down and below which the grains remain static. The grains located above the shear-failure surface move “*en masse*” and most of the shear is concentrated along this surface forming a “*truncated-cone-like*” deposit with a central motionless plateau figure 2.11. For columns with larger aspect ratios, the flow is still initiated by failure along a well-defined surface, an inclined plane in two-dimensional geometry or a cone in the axisymmetric case. However, the initial height of the column is much higher than the top of the failure surface, causing a vertical fall of grains until they reach the summit where they diverge along the horizontal direction, dissipating a lot of kinetic energy, resulting in a final conical deposit. Interestingly, the final deposit height coincides with the summit of the failure surface in the axisymmetric geometry, whereas in the rectangular channel, the deposit summit always lies above the top of the failure surface (Lajeunesse et al., 2005). Shallow-water approximations shows a truncated cone-like deposit, while DEM simulations show a cone like deposit for  $a = 1.0$  (figure 2.9). This shows the inability of shallow-water approximation in modelling tall columns.

Identification of the static region is an important task, as it is a prime component in describing the collapse mechanism. Regardless of the experimental configuration, for all values of  $a$  the flow is initiated by rupture along a well-defined failure surface and the failure angle remains of the order of  $50^\circ$  to  $55^\circ$  (figure 2.11). The failure angle is consistent with an interpretation of *active Coulomb failure*, which leads to a failure angle  $\phi_f = 45^\circ + \delta/2$ , where  $\delta$  is the internal friction angle of the granular material. Estimating the internal friction angle of glass beads from the angle of repose as  $22^\circ$ , the failure angle is estimated as  $56^\circ$ , which is in good agreement with the experimental findings. Contrary to the suggestion

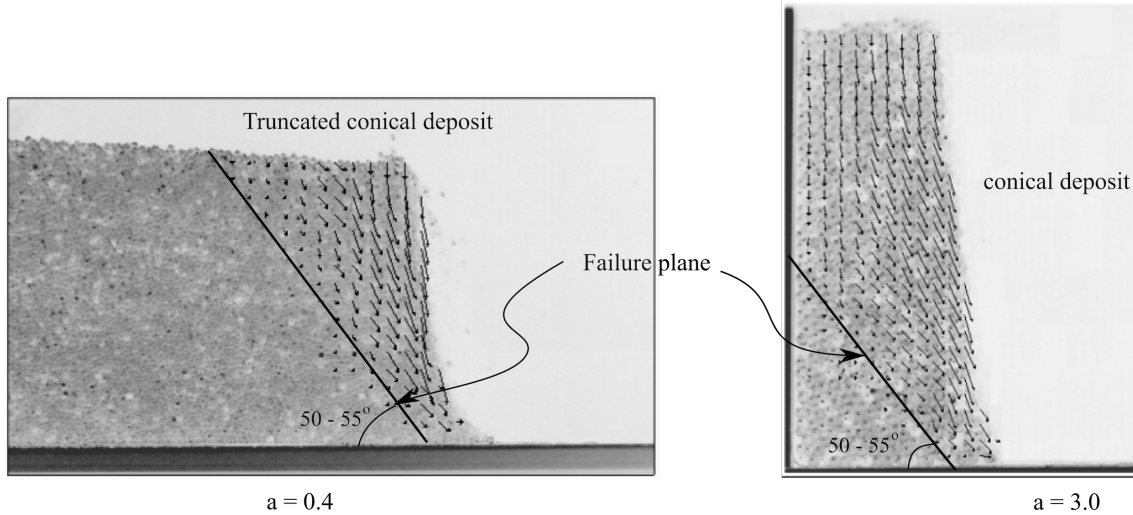


Figure 2.11 The extent of the failure surface for granular columns with initial aspect ratio of 0.4 and 3 at time  $t = 0.4\tau_c$  (Lajeunesse et al., 2004). Short columns show truncated conical deposit at the end of the flow, while tall columns exhibit conical deposit.

of Lajeunesse et al. (2004), the shear-failure angle was found to have no direct effect on the transition between truncated cone and conical deposit occurring at aspect ratio  $a$  of 0.7 (Lajeunesse et al., 2005). Schaefer (1990) observed the onset of instability in a narrow wedge of  $56^\circ$  to  $65^\circ$ , which corresponds to the angle of shear bands. A rate-dependent constitutive relationship (Jop et al., 2006) for dense granular flows indicates the angle of shear-band orientation depends on the inertial number  $I$ . For small to moderate values of  $I$ , the orientation of shear bands is found to vary from the Roscoe and the Coulomb solutions to a unique admissible angle (Lemiale et al., 2011). Daerr and Douady (1999) observed active Coulomb-type yielding in transient surface flows for granular materials having a packing density of 0.62 to 0.65.

### *Numerical findings*

In order to describe the complex flow dynamics, it is important to understand the internal structure and the flow behaviour. The flow evolution involves three stages (Staron and Hinch, 2007). The first stage involves conversion of the initial potential energy of the grains into vertical motion, resulting in downwards acceleration of grains. In the second stage, the grains undergo collision with the base and/or neighbouring grains, and their vertical motion is converted into horizontal motion. The velocity field depends on the position of grains along the pile. In the region above the static core, the flow is locally parallel to the failure surface and has an upper linear part and a lower exponential tail near the static bed (figure 2.11). The velocity flow profile is similar to that of a steady granular flow (Midi, 2004). In the

final stage, the grains eventually leave the base area of the column and flow sideways. At the front, the flow involves the entire thickness of the pile and corresponds to a plug flow in the horizontal direction. The typical velocity observed at the front of the ejecting mass is  $v = \sqrt{2gL_0}$ . As the pile spreads, interface separation occurs as the flow diverges and the static region starts to move inwards; this effect is predominant in the case of granular flows in a rectangular channel.

The typical time required for the flow to cease and form the final deposit, from the instant of its release, is  $T = \sqrt{2H_0/g}$  (Staron and Hinch, 2007). While plotting the variation of normalized potential and kinetic energy with normalized time, Staron and Hinch (2007) observed that the flow ceases when the normalized time  $t/T_0$  is 2.5, i.e. the flow is assumed to have stopped when the total normalized energy is almost zero. This observation is consistent with the experimental results of Lube et al. (2005) and Lajeunesse et al. (2005). The transition of the flow occurs when the normalized time  $t/T_0$  is 1.0 or at critical time  $\tau_c$ , which is defined as the time at which the flow is fully mobilized.

### Comments on modelling

In order to have a detailed understanding of the final profile of the collapsed granular column, it is important to solve the collapse problem as an *initial-value problem* (Balmforth and Kerswell, 2005), beginning from the instant of release and extending to the time when the material finally ceases to flow, forming the final deposit. As the process of granular collapse involves collective dynamics of collisions and momentum transfer, the prediction of the trajectory of a single grain is difficult. In fact, there are quantitative disagreements between theory and experiments; the final shapes are reproducible, but not perfectly. Some of the disagreement arises because the experiments did not have exactly the same amount of materials; it is indeed difficult to fill the pile with exactly the same amount of material, which results in differences in packing. However, the theoretical errors are due to the incapability of the models to capture the physics that governs the flow dynamics (Balmforth and Kerswell, 2005).

Shallow water models fail to account for the vertical acceleration, which is responsible for the momentum transfer and, in turn, the spreading process. This restricts the shallow water model to capture the mechanism of collapse until the critical time  $\tau_c$ . Surprisingly, shallow-water models capture certain experimental aspects for columns with lower aspect ratios (Balmforth and Kerswell, 2005; Kerswell, 2005; Mangeney et al., 2010), even though the contrast between surface flows and the static region is important in this range of aspect ratio. Thus, the assumption of plug flow in the horizontal direction is not critical in cap-

turing the run-out behaviour, especially if the basal friction coefficient is used as a fitting parameter (Lajeunesse et al., 2005).

Simple mathematical models based on conservation of horizontal momentum capture the scaling laws of the final deposit, however they fail to describe the initial transition regime, indicating that the initial transition has negligible effect on the run-out, which is incorrect. Models based on the initial potential energy show promise, but the effect of material properties, such as basal friction and coefficient of restitution, on the run-out behaviour is still unclear and produces non-physical run-outs. The  $\mu(I)$  rheology predicts the normalized run-out behaviour quite well in comparison with the experimental results, for lower aspect ratios. The spreading dynamics is found to be similar for the continuum and grain approaches; however, the rheology falls short in predicting the run-out distance for higher aspect ratios.

Unlike Lube et al. (2005), many researchers (Balmforth and Kerswell, 2005; Kerswell, 2005) observed strong dependency of material properties on the run-out distance, moistening the materials or the sides of the channel even by a small amount leads to markedly different results. Staron and Hinch (2007) observed that the friction has little effect on the run-out for granular column collapse for high aspect ratios, which are driven mainly by the free vertical fall of grains. The initial conditions have a significant impact on the overall behaviour of the granular system, indicating the significance of the triggering mechanism in case of the natural flows (Staron and Hinch, 2007). A theoretical framework that is capable of describing the influence of material properties on the run-out behaviour is still lacking. Numerical investigations, such as Discrete Element Method techniques, allow us to evaluate these quantities which are not accessible experimentally, thus providing useful insight into the flow dynamics. Subsequent chapters discuss the methodology and modelling of granular column by continuum- and discrete-element approaches. Effect of initial packing fraction and the internal structure on the run-out behaviour are also discussed. The difference in the mechanism of modelling the granular flows in continuum and discrete approaches are presented in chapter 4.

### 2.3.2 Flow down an inclined plane

Most contemporary research on granular materials deals with the steady-state flows. Transients and inhomogeneous boundary conditions are much less amenable to observation and analysis, and have thus been less extensively studied despite their primary importance in engineering practice. Studies on the flow of granular materials down inclined planes are important to understand the mechanism of geophysical hazards, such as granular avalanches, debris flows and submarine landslides. Large scale field tests on dry and saturated granular

materials were carried out to capture the mechanism of granular flows down an inclined plane (Denlinger and Iverson, 2001; Okada and Ochiai, 2008).

### Experimental findings

The granular material stored in a reservoir at the top of the inclined plane is released by opening a gate (figure 2.12). The flow rate is controlled by the height of the opening. The material flows down and develops into a dense granular flow. An initially static granular layer of uniform thickness ' $h$ ' starts to flow when the plane inclination reaches a critical angle,  $\theta_{start}$ , the material reaches a sustained flow until the inclination is decreased down to a second critical angle,  $\theta_{stop}$  (Midi, 2004). The occurrence of two critical angles indicates the hysteretic nature of granular materials. Reciprocally, the critical angle thresholds can be interpreted in terms of critical layer thickness  $h_{stop}(\theta)$  and  $h_{start}(\theta)$ . The measurement of  $h_{stop}(\phi)$  is easier as it corresponds to the thickness of the deposit remaining on the plane once the flow has ceased.

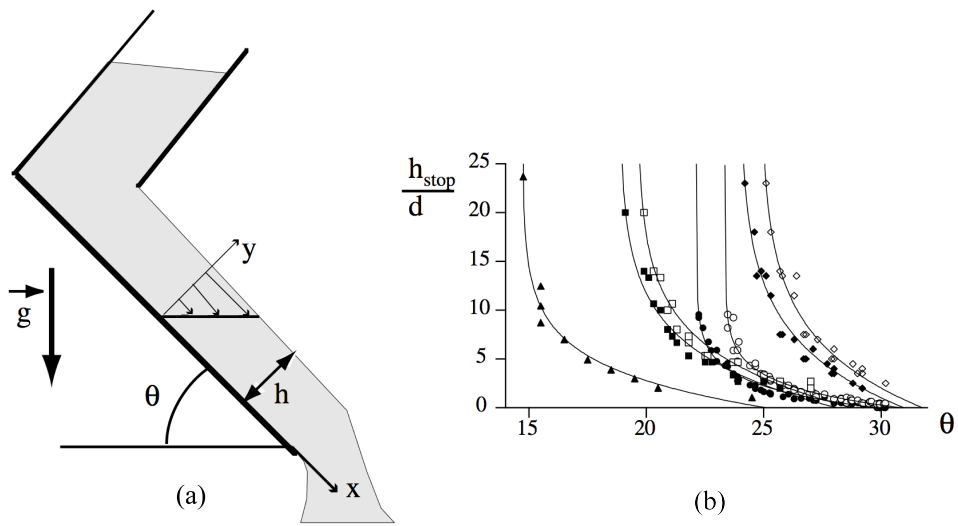


Figure 2.12 Rough inclined plane: (a) Set-up, and (b)  $h_{stop}(\theta)$  (black symbols) and  $h_{start}(\theta)$  (white symbols). Reproduced after (Midi, 2004).

The two curve  $h_{stop}(\theta)$  and  $h_{start}(\theta)$  divides the phase diagram ( $h, \theta$ ) into three regions: a region where no flow occurs, ( $h < h_{stop}(\theta)$ ), a sub-critical region where both static and flowing layers can exist ( $h_{stop}(\theta) < h < h_{start}(\theta)$ ) and a region where flow always occurs, ( $h > h_{start}(\theta)$ ). In the flow regime, i.e. ( $h > h_{start}(\theta)$ ), the flow is steady and uniform for moderate inclination, but accelerates along the plane for large inclinations (Midi, 2004). The critical angle controlling the flow behaviour tends to increase when the thickness of

the bed decreases (Daerr and Douady, 1999; Pouliquen and Chevoir, 2002), which can be attributed to the non-trivial finite-size effects and/or boundary effects that are not well understood (Forterre and Pouliquen, 2008). There exists a value of roughness for which a maximum thickness of deposit is observed, which might correspond to a maximum of effective friction at the bottom (Midi, 2004).

For thick enough piles flowing on a rough inclined plane, say  $h \geq 20 \times d$ , the velocity profiles and rheology follow Bagnold scaling. As the height of the flowing pile reduces, a continuous transition from Bagnold rheology to linear velocity profiles through to avalanche-like dynamics occurs, until finally, one reaches the angle of repose  $\theta_r$ , and the flow ceases. This transition behaviour is difficult to model.

### Numerical modelling

Fast moving granular flows can undergo a motion-induced self-fluidisation process under the combined effects of front instabilities setting on at large values of the Froude number which are responsible for extensive air entrainment, and small deflation rates associated with small incipient fluidisation velocities and longer collapse time of the bed solids. Self-fluidisation results in enhanced mobility of the solids, causing an inviscid flow to an extent that may largely exceed the establishment of a “*granular liquid*” state in purely granular flow (Bareschino et al., 2008). It is understood that, for a granular material to flow, it has to exceed a certain critical threshold, i.e. the friction criterion: the ratio of shear stress to normal stress. As there is no internal stress scale for a granular material, granular materials exhibit solid-fluid transition behaviour based on the friction criterion (Forterre and Pouliquen, 2008). The stress ratio in the flowing regime above the static bed indicates the solid-to-fluid transition is a yielding phenomenon and can be described by Mohr-Coulomb-like failure criterion (Zhang and Campbell, 1992). This is in contrast to the mechanism of behaviour of other complex fluids, where there is an internal stress scale linked to the breakage of microscopic structure. From a microscopic point of view, the strength of the granular materials is due to the internal friction between grains, but packed frictionless materials still exhibit macroscopic friction.

Constitutive laws based on Plasticity-theories relate the micro-structure to the macroscopic behaviour (Roux and Combe, 2002), which provide useful insight into the mechanism of granular flow. However, at present they are limited to initiation of deformation and do not predict the quasi-static flow. Continuum approach such as Material Point Method simulation of granular flow down an inclined plane (Abe et al., 2006; Bandara, 2013) captures the flow behaviour in the initial stages, however it exhibits inconsistent behaviour when the granular

material ceases to flow. This may be due to the application of small deformation theory to a large deformation problem and the use of zero dilation.

Alternatively by using the  $\mu(I)$  rheology we can capture the velocity profile and the localization at the free surface. However, it fails to model the transition from a continuous flow to an avalanching regime as the flow rate is decreased (Pouliquen et al., 2006). The rheology predicts no-flow below a critical angle  $\theta_s = \arctan(\mu_s)$  independent of the thickness. In experiments, it is observed that the critical angle increases when the thickness of the flow decreases (Pouliquen, 1999). The granular flow down rough inclined planes exhibit strong Coulomb shear stresses on a plane normal to the basal flow boundary. The stresses dissipate the energy along the rough surface; models that lack multi-dimensional momentum transport or Coulomb friction cannot represent this energy dissipation and lodging.

### Comments on modelling

Granular flow down inclined planes exhibit a transient behaviour. Various velocity profiles and flow behaviours can be obtained not only through changing the height of the flowing granular mass, but also by varying the inclination of the chute, such that there is an overlap region where one can obtain similar flow properties through either procedure. These features can be used to better predict the evolution of an avalanche surface. The experimental configuration is ideal to study the effectiveness of various theoretical frameworks in modelling the granular flows especially the transition from solid-like to fluid-like behaviour. The  $\mu(I)$  rheology and models that are based on Coulomb friction are able to predict the energy dissipation along the rough surface. However, they fail to capture the transient from static to a flowing behaviour and again when it ceases to flow. In large scale granular flow down slopes, only those grains that are located on the surface of will have higher  $I$  values, due to lower mean pressures. However, grains located within the main flowing mass would experience higher mean pressure and thus resulting in smaller  $I$  values. Hence,  $\mu(I)$  rheology is less effective in large scale problems and a simple Mohr-Coulomb model will be yield a similar response. It can be suggested that the flow is governed by its momentum. It is important to carry out DEM simulations to understand the mechanics of the flow transition behaviour. This will enable us to describe the continuum response of phase transition more efficiently.

#### 2.3.3 Saturated and submerged granular flows

Submarine mass movements pose a significant threat to the off-shore structures, especially oil and gas platforms. Geophysical hazards, such as debris flows and submarine landslides, usually involve flow of granular solids and water as a single-phase system. Modelling

the multi-phase interaction poses a serious challenge. The momentum transfer between the discrete and the continuous phases significantly affects the dynamics of the flow as a whole (Topin et al., 2011). The complex interactions between the soil and the ambient fluid is shown in figure 2.13. For a given granular mass, the energy balance can be written as

$$E_p + E_s = E_k + E_f + E_D + E_v + E_r, \quad (2.17)$$

where  $E_s$  is the seismic energy resulting from an earthquake,  $E_f$  is the friction loss,  $E_D$  the friction loss due to drag effects on the upper surface of the flow,  $E_v$  the loss due to viscous effects and  $E_r$  the energy used to remold or transform the intact material. During the course of a submarine slide event (or also a sub-aerial slide), there appears to be a process by which there are some changes in solid to water ratio which provides a sufficiently low strength to allow flow to take place (Locat and Lee, 2002). Whatever the exact nature of the phenomenon, it is embedded in the remoulding energy ( $E_r$ ). In both sub-aerial and submarine landslides the triggering energy is the same (initial potential energy). It appears as though the submarine landslides experience more dissipation  $E_D$  and  $E_v$  than sub-aerial landslides, but one shouldn't prematurely conclude that the run-out in submarine landslide will be shorter due to more dissipation. The effect of hydroplaning and fluidisation of the flowing mass result in complex interactions, which makes it difficult to predict the exact mechanism of run-out and the length of run-out in submarine conditions for a given initial state.

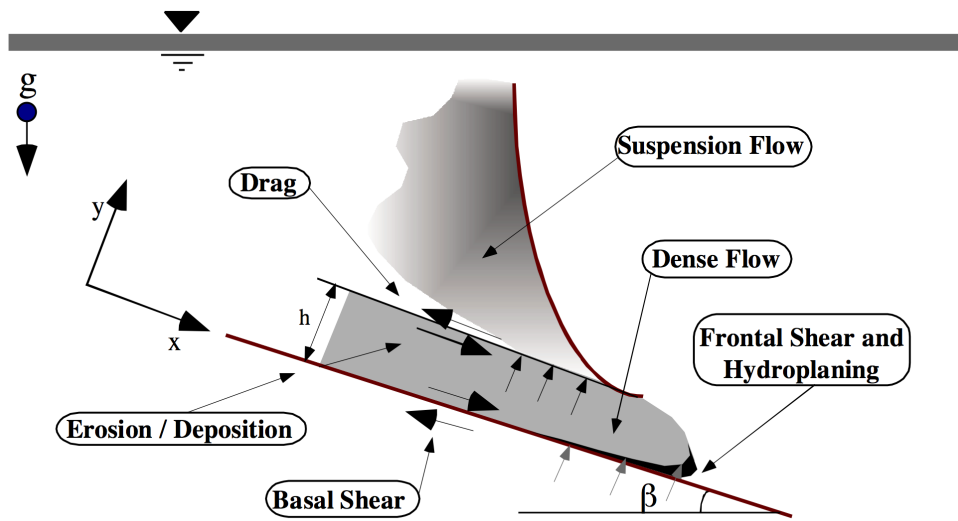


Figure 2.13 Schematic diagram showing the generation of a turbidity current (suspension flow) for drag forces on the surface, potential lifting of frontal lobe leading to the process of hydroplaning, the basal shear stress causing erosion and deposition (Locat and Lee, 2002).

### Experimental findings

The collapse of a granular column, which mimics the collapse of a cliff, has been extensively studied in the case of dry granular material, when the interstitial fluid plays no role. The case of the collapse in presence of an interstitial fluid has been less studied (Topin et al., 2012). Rondon et al. (2011) performed granular column collapse experiments in fluid to understand the role of initial volume fraction. The experimental set-up of granular collapse in fluid performed by Rondon et al. (2011) is shown in figure 2.14.

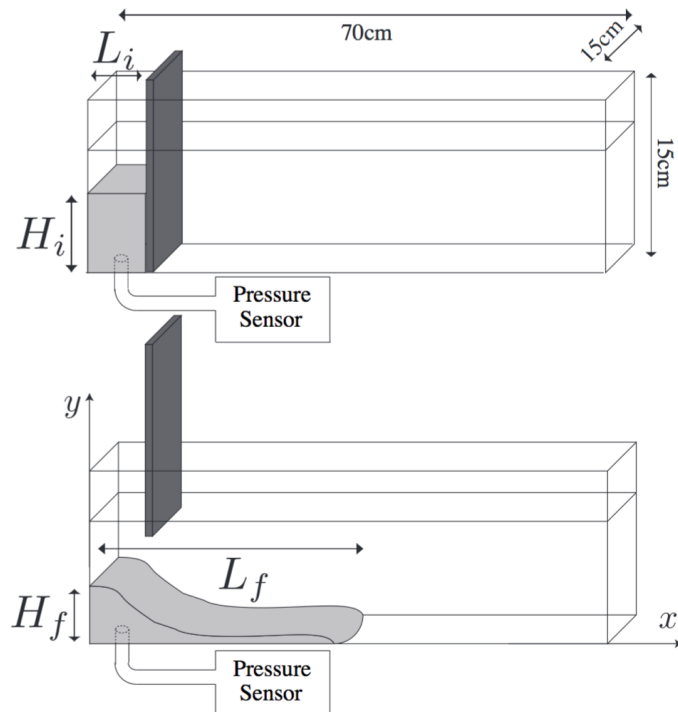


Figure 2.14 Experimental set-up of granular collapse in fluid (Rondon et al., 2011).

Figure 2.15 shows the evolution of run-out and pore-pressure at the bottom of the granular flow. The whole loose column is mobilised immediately, in contrast to the dense case. The loose column in fluid spreads almost twice than the dense case. The collapse of a granular column in a viscous fluid is found to be mainly controlled by the initial volume fraction and not by the aspect ratio of the column. The role of the initial volume fraction observed in the viscous collapse can be understood by the pore pressure feedback mechanism proposed by (Iverson, 2000; Schaeffer and Iverson, 2008) in the context of landslides.

Iverson (2000) observed in the large-scale field tests that the soil prepared in a loose state on a slope and subjected to a rainfall flows rapidly like a liquid when it breaks, whereas a dense soil only slowly creeps (figure 2.16). The underlying mechanism is related to the

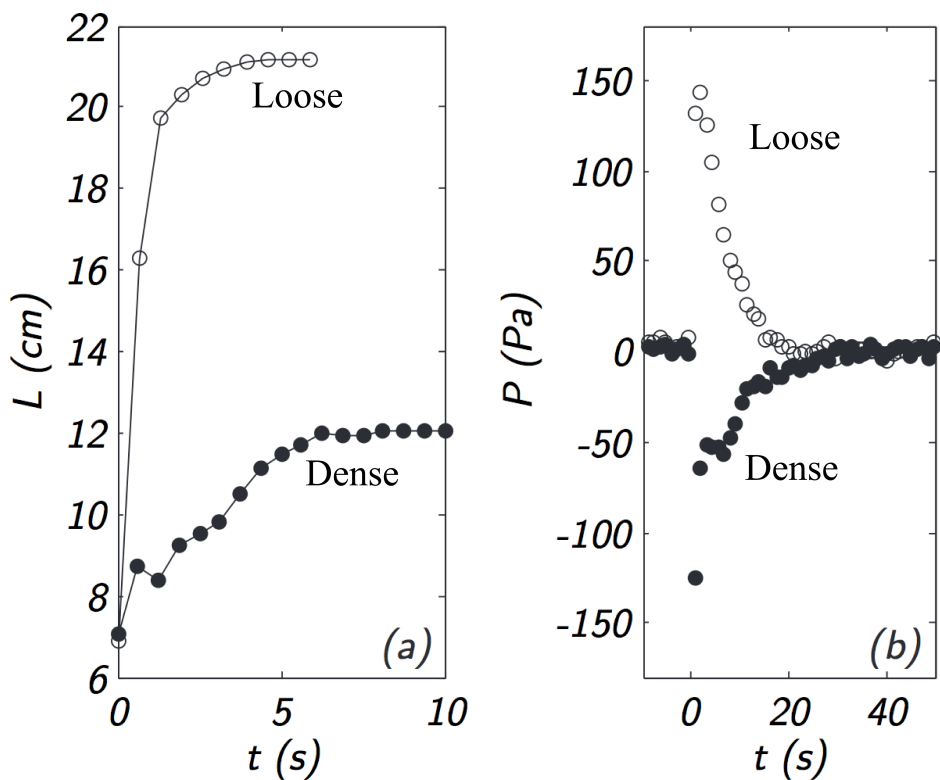


Figure 2.15 Evolution of run-out and pore-water pressure at the bottom for granular column collapse in fluid for dense and loose conditions (Rondon et al., 2011).

dilation or contraction character of the granular material, which the authors described as the “pore pressure feedback”. The compaction or dilation of grains can cause additional stress in the grains which can stabilise or destabilise the soil. The loose sediment experience high positive pore-pressure and low shear stresses resulting in a quicker flow, while the large negative pore-pressure in the dense case delays the run-out. The flow is controlled by the coupling between the dilatancy of the granular layer and the development of pore pressure in the fluid phase (Pailha et al., 2008).

The dense column needs to dilate in order to flow. When it starts to fall, liquid is then sucked into the column, which is then stabilized by the additional viscous drag (Rondon et al., 2011; Topin et al., 2012). In the dense condition, large negative-pore pressures are developed in the initial stages of collapse, they collapse has to overcome the large negative pore-pressure before it starts to flow. This results in a slow flow evolution as seen by the flatness of the initial run-out curve in dense condition in comparison to the steep slope in the loose case (figure 2.15). By opposition the loose column when it starts flowing expands and ejects liquid, leading to a partial fluidisation of the material. The large positive pore-pressure developed at the bottom of the flow in loose condition indicates water entrainment and hydroplaning. The entrainment of water at the basal flow front lubricates the frictional effect and along with hydroplaning it results in longer run-out distance.

Very few research has been carried out to understand the difference in mechanism of dry and submerged granular flow. Cassar et al. (2005) carried out experimental investigation on the flow of dense granular material down an inclined plane fully-immersed in water. The velocities observed in the submarine case were found to be a magnitude smaller than the dry condition. This is in contrast to the idea that the submarine landslides tend to flow longer than its sub-aerial counterpart. In order to compare the dry collapse with the submarine collapse, it is important to start with the same initial configuration. Packing soil grains to the same initial density is difficult. Hence, it is important to perform numerical studies and develop theoretical framework that can explain the submarine granular flow behaviour.

### Numerical modelling

Although certain macroscopic models are able to capture simple mechanical behaviours, the complex physical mechanisms occurring at the grain scale, such as hydrodynamic instabilities, formation of clusters, collapse, and transport (Peker and Helvacı, 2007; Topin et al., 2011), have largely been ignored. In particular, when the solid phase reaches a high volume fraction, the strong heterogeneity arising from the contact forces between the grains, and the hydrodynamic forces, are difficult to integrate into the homogenization process involving global averages (Topin et al., 2011).

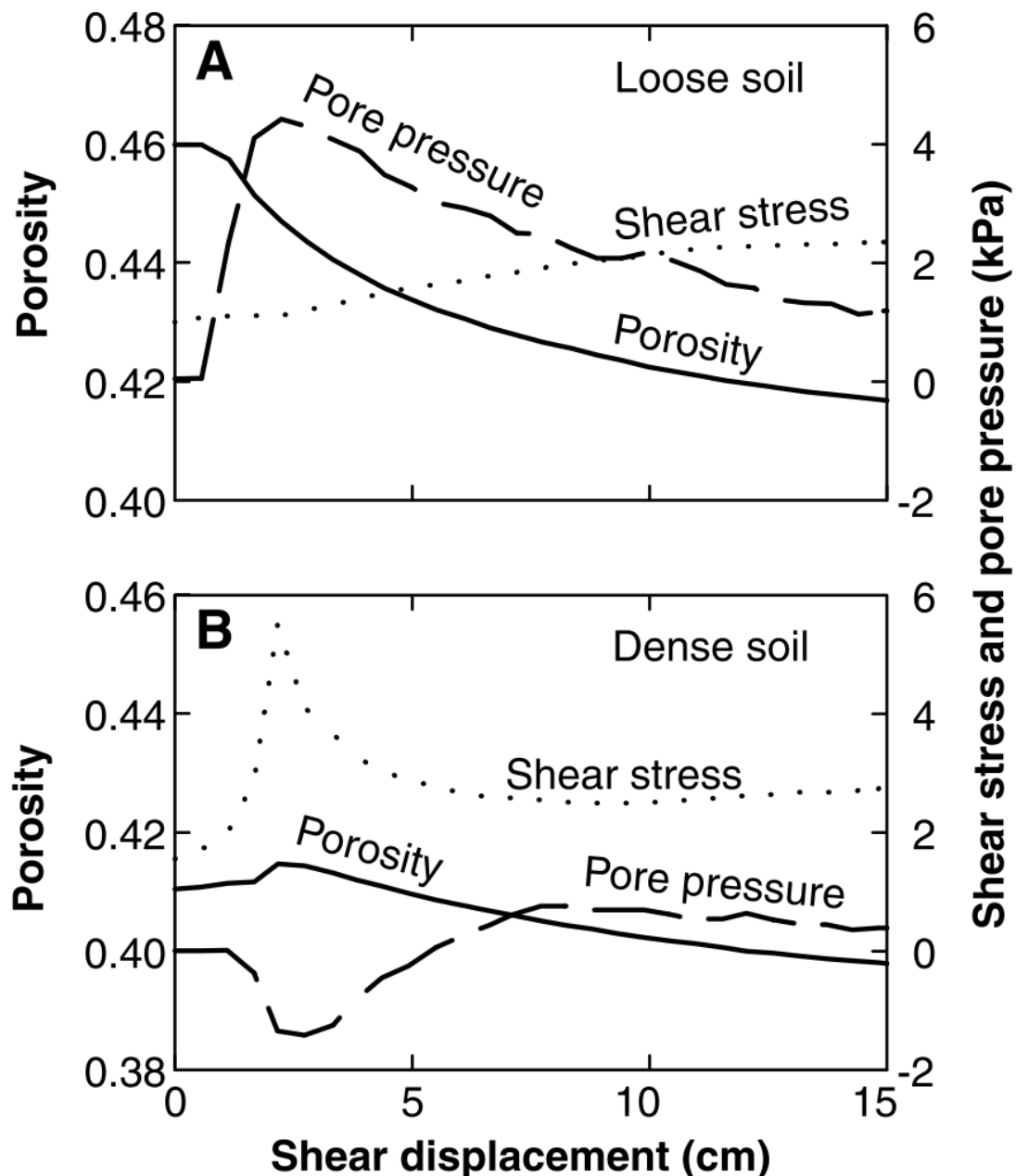


Figure 2.16 Pore pressure feedback mechanism: effect of density (Iverson, 2000).

In two-phase models (Pitman and Le, 2005), the momentum transfer between the grains and the suspension fluid depends on the momentum equations of both the phases. In case of mixture theory based models (Meruane et al., 2010), the shear-induced migration and grains collisions are considered in an average sense. In order to describe the mechanism of saturated and/or immersed granular flows, it is important to consider both the dynamics of the solid phase and the role of the ambient fluid (Denlinger and Iverson, 2001; Iverson, 1997). The dynamics of the solid phase alone are insufficient to describe the mechanism of granular flow in a fluid; it is important to consider the effect of hydrodynamic forces that reduce the weight of the solids inducing a transition from dense-compacted to dense-suspended flows, and the drag interactions which counteract the movement of the solids (Meruane et al., 2010).

Topin et al. (2011) performed granular collapse in fluid using Non-Smooth Contact Dynamics coupled with distributed Lagrange multiplier/fictitious domain (DLM/FD) method. The mechanism of collapse of granular columns in dry and submerged conditions were compared. Topin et al. (2011) observed that for a given initial geometry the run-out distance in the dry case is significantly higher than the submerged condition, this observation is similar to the experimental results of Cassar et al. (2005). In the dry case, inertia is responsible for the enhanced mobility at high aspect ratio. However in submerged conditions, i.e., in the viscous regime, the inertial effects remain negligible, which could explain why the important parameter controlling the dynamics is the initial volume fraction and not the initial aspect ratio. Topin et al. (2011) observed that the run-out exhibit a power-law relation with the peak kinetic energy and the largest value of run-out in fluid inertial regime, and the lowest in grain-inertial and intermediate value for the viscous-regime (figure 2.17). The viscous regime is where the grain reaches the viscous limit velocity, the Stoke's number  $S_t \ll 1$  and the density ratio  $r \gg S_t$  (Courrech du Pont et al., 2003). However, the role of the volume fraction on dry granular collapse has not been precisely studied and the preparation of the pile may also play a role Daerr and Douad (1999).

The  $\mu(I)$  rheology relates the non-dimensionless number  $I$  to the shear rate through a characteristic time. In the case of dry granular flows, the parameter  $I$  is defined as the ratio between the time taken for a grain to fall into the hole,  $t_{micro}$ , and the meantime,  $t_{mean}$ , which is inversely related to the shear rate. Cassar et al. (2005) observed that the run-out behaviour collapse on to a single friction law, which shows that the major role of the fluid is to change the time it takes for a grain to fall into a void-space. The  $\mu(I)$  rheology for dry dense flows can be modified to capture the behaviour of dense submarine granular flows, if the inertial time scale in the rheology is replaced with a viscous time scale. Pitman and Le (2005) observed that if the fluid inertial effects are small enough, then a simpler model can be adopted. Sketch of the motion of a grain  $z(t)$  during a simple shear  $\dot{\gamma}$  under a confining

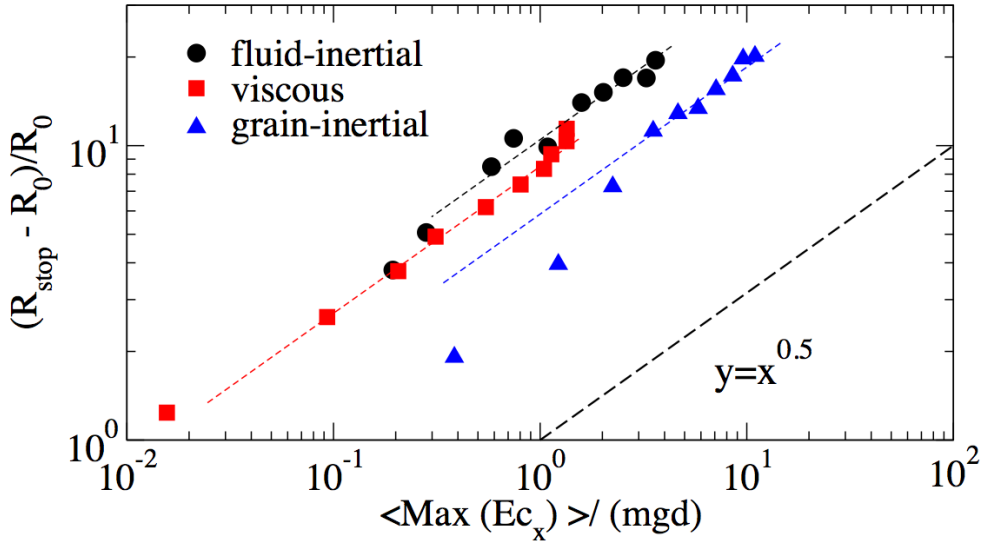


Figure 2.17 Normalised run-out distance as a function of the peak value of the horizontal kinetic energy per grain. (Topin et al., 2011).

pressure  $P_g$  is shown in figure 2.18. Hence, assuming that the fluid velocity is low enough for the contact interaction between grains to be significant, the time taken by the grain to fall into a hole,  $t_{micro}$ , is then controlled by the viscosity of the ambient fluid. Thus, the dimensionless parameter can be modified to incorporate the viscous time to describe granular flow in a fluid (Pouliquen et al., 2005). In short time scales, the grain initially accelerates but because of the drag force, the grain eventually reaches a limit viscous velocity  $v_{\infty v}$ . The time required to travel a diameter  $d$  is given as  $t_{fall} = d/v_{\infty v}$ . This new viscous time is used to define the dimensionless number.

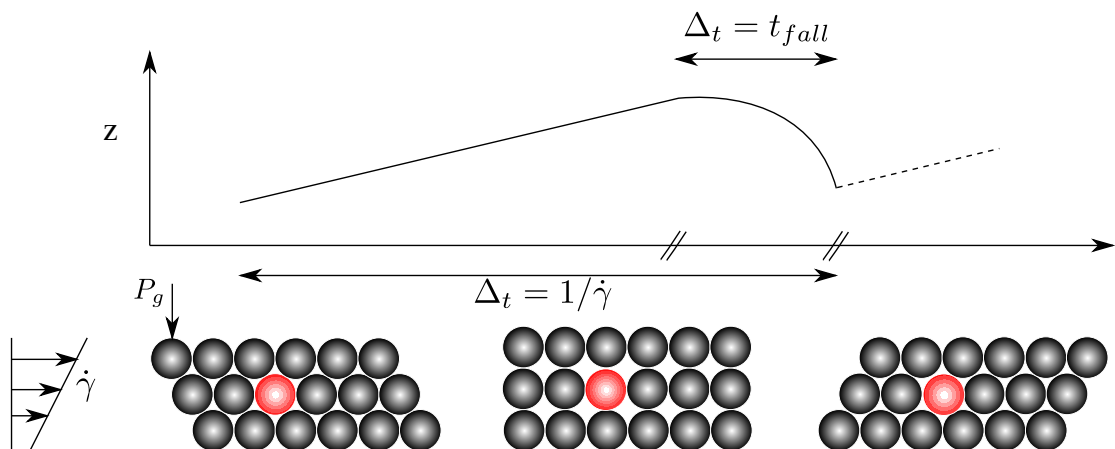


Figure 2.18 Sketch of the motion of a grain  $z(t)$  during a simple shear  $\dot{\gamma}$  under a confining pressure  $P_g$ .

### Comments on modelling

The  $\mu(I)$  rheology is found to be valid only for the steady uniform regime; unsteady phenomena such as the triggering of avalanches result in coupling between the granular grains and the ambient fluid, which are much more complex to model. Transient regimes characterized by change in solid fraction, dilation at the onset of flow and development of excess pore pressure, result in altering the balance between the stress carried by the fluid and that carried by the grains, thereby changing the overall behaviour of the flow (Denlinger and Iverson, 2001). The  $\mu(I)$  rheology seems to predict well the flow of granular materials in the dense regime. However, the transition to the quasi-static regime where the shear rate vanishes is not captured by the simple model. Also, shear band formation observed under certain flow configurations is not predicted. The flow threshold or the hysteresis characterizing the flow or no-flow condition is not correctly captured by the model, which can be due to the discrepancies between the physical mechanism controlling the grain level interactions, clustering, and vortex formations. When the scale of the system is larger than the size of the structure, a simple rheology is expected to capture the overall flow behaviour, however the size of the correlated motion is the same as that of the system, causing difficulties in modelling the flow behaviour (Pouliquen et al., 2005). Hence, it is essential to study the behaviour of granular flows at various scales, i.e. microscopic, meso-scale and at continuum level, in order to develop a constitutive model that captures the entire flow process.

## 2.4 Summary

Granular flow involves three distinct regimes: the dense quasi-static regime, the rapid and dilute flow regime, and an intermediate regime. The dynamics of homogeneous granular flow also involve at least three different scales, making it difficult to describe the mechanics of granular flow by simple theories. It is important to describe the granular dynamics as an initial-value problem. Experimental conditions are too difficult to reproduce precisely, resulting in inherent inconsistencies in the results. Numerical models, such as the shallow-water approximation, kinetic theory approach, and rheologies have captured the basic flow dynamics, but have failed to describe the complete mechanics of the granular flow.

Collapse of a granular column is a simple case of granular flow. Experimental results have shown that the run-out exhibit a power-law dependence with the initial aspect ratio of the column. Although, numerical simulations and theoretical frameworks were able to recover the power-law behaviour, they were unable to explain the origin of the power law or capture the various stages of the flow. The initial conditions have a significant impact on the overall behaviour of the granular system, however, a theoretical framework that is capable

of describing the influence of material properties on the run-out behaviour is still lacking. In the present study the capability of continuum models such as the Mohr-Coulomb model and  $\mu(I)$  rheology in modelling the granular column collapse is investigated by comparing it with the discrete-element simulations. The role of initial packing fraction on the run-out behaviour is also investigated in the present study.

Submarine granular flows exhibit complex interactions between the soil grains and the ambient fluid. The presence of fluid causes drag which slows down the run-out, while the entrainment at the flow front causes hydroplaning and longer run-out distance. The run-out distance is found to be controlled by the initial volume rather than the aspect ratio of the column. Loose granular column is found to flow longer than the dense condition. However, researchers observed longer run-out in dry condition in comparison with the submerged collapse. The difference in the mechanism of dry and submerged granular flows is not well researched. The role of initial volume fraction on the run-out behaviour is not precisely known. This study focuses on the effect of initial packing and permeability on the run-out by performing grain-scale simulations. This study investigates the influence of grain-scale quantities, which are otherwise not accessible experimentally, on the run-out behaviour thus providing useful insight into the flow dynamics, thereby enabling us to develop better constitutive laws.

# Chapter 3

## Numerical modelling of granular flows

### 3.1 Introduction

Most of the geotechnical analysis involves failure prediction and design of structures that can safely withstand applied loads. However, it is very important to study the post-failure behaviour to mitigate risk posed by geophysical and gravity-driven flows such as landslides, avalanches, slope failures, and debris flows. Granular flows are complex problems in continuum mechanics for which no closed-form solution exists. Hence it is essential to develop alternative solution schemes, which are capable of simulating failure mechanisms and post-failure dynamics of the granular media.

The dynamics of a homogeneous granular flow involve at least three distinct scales: the *microscopic scale*, which is characterised by the contact between grains, the *meso-scale* that represents micro-structural effects such as grain rearrangement, and the *macroscopic scale*, where geometric correlations can be observed (figure 3.1). Conventionally, granular flows are modelled as a continuum because they exhibit many collective phenomena. However, on a grain scale, the granular materials exhibit complex solid-like and/or fluid-like behaviour. Recent studies, however, suggest that a continuum law may be unable to capture the effect of inhomogeneities at the grain scale level, such as orientation of force chains, which are micro-structural effects. Discrete element methods (DEM) are capable of simulating these micro-structural effects, however they are computationally expensive.

### 3.2 Continuum modelling of granular flows

The most powerful way of modelling the granular assembly is through numerical techniques. It is important to argue, why it is acceptable to model the granular materials as a continuum.

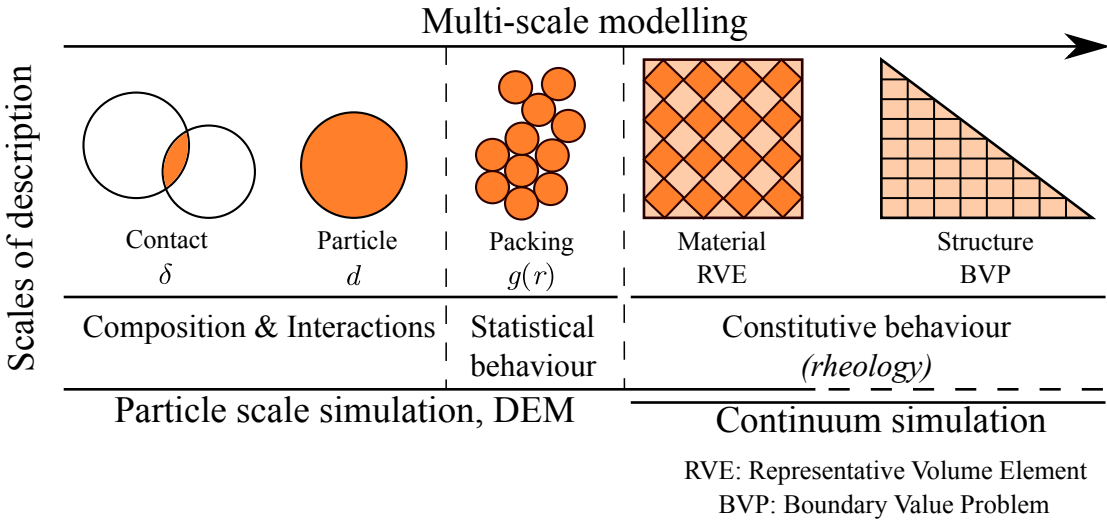


Figure 3.1 Schematic representation of different scales of description involved in the multi-scale modelling of granular materials

At the outset, it may even appear for some reasons why such a treatment is objectionable. Most obvious is the fact that the micro-constituents of granular matter, i.e. the individual grains are not small enough to warrant a continuum description (Kamrin et al., 2007). Typical continuum laws are only expected to apply when there is a strong separation of scales, i.e. separation of the micro-scale from the macro-scale, in the flow geometry. Continuum mechanics relies on the fundamental notion of a representative volume element, in which, properties averaged over discrete grains exhibit deterministic relationships. Recent works on granular materials suggest that a continuum law may be incapable of revealing in-homogeneities at the grain-scale level (Rycroft et al., 2009a). Microscopic features of dense granular materials, which seem to defy a simple continuum description include (i) complex, fractal networks of force chains, which are inhomogeneous down to the grain level (Goldschmid, 2003), (ii) anomalous, non-collisional particle dynamics with very slow cage breaking (Rycroft et al., 2006), (iii) proximity to the jamming transition, where geometrical packing constraints suppress any dynamics, (iv) a lack of thermal equilibrium in the conventional sense, since grains only move in response to external forces, motivating new definitions of temperature, and (v) wide range of dynamical response, from liquid-like to solid-like behaviour (Aranson and Tsimring, 2001, 2002; Jaeger et al., 1996). The first four points cast serious doubt on the prospects of a continuum law. The fifth point means that the full stress tensor must be described, and it may depend on strain, deformation rate, and material variables that can evolve during the process (Rycroft et al., 2009a).

Granular materials exhibit many collective phenomenon (Jaeger et al., 1996). However, no continuum model is still capable of describing the parabolic flow, the plug flow (Rycroft

et al., 2006) and the occurrence of localized shear bands in the granular materials. Most constitutive models, even in the simple case of dry granular flows, cannot describe the entire range of flow from solid to fluid. In certain cases, the granular flow is modelled as a fluid behaviour. Continuum models that are based on averaging techniques applied to a representative volume elements have been applied mostly to problems involving quasi-static conditions. The fundamental question is how to model granular materials which exhibit complex phenomenon, meaningfully.

The oldest approach involves modelling the granular material as a rigid solid, which behaves as an ideal Coulomb material and undergoes failure if the ratio of the shear stress to the normal stress in any plane reaches a critical value of the Coulomb internal friction coefficient  $\mu$ . The stress is determined based on the mechanical equilibrium of the system along with the hypothesis of *incipient yield*, i.e. the yield criterion is attained everywhere at all times (in a “*limit-state*”). In limit-state Mohr–Coulomb plasticity, these conditions are assumed to hold even if boundary conditions allow for plastic yielding. In that case, the velocity follows from the assumption of coaxiality, which asserts that the stress and deformation rate have the same eigen directions (Rycroft et al., 2009a). The fundamental assumption of a limit-state stress field at incipient yield everywhere is questionable. Granular flows can contain regions of stresses lying within the yield surface. For example, in the case of a granular column collapse the central cone remains stagnant, and thus cannot be considered as yielded. In fact, discrete-element simulations show that the grains in this region essentially remain static (Staron et al., 2005). Mohr–Coulomb plasticity have been used extensively in engineering applications (Nedderman, 1992), but the general solution requires sophisticated numerical techniques to capture shock-like discontinuities in stress and velocity, which arise even in relatively simple geometries.

The coaxiality feature of Mohr–Coulomb plasticity is useful in describing the debris flow. The principle of coaxiality claims that material should flow by extending along the minor principal stress direction and contracting along the major principal stress direction; the principal planes of stress are aligned with the principal planes of strain-rate. Granular material deforms solely based on the alignment of the principle plane. In general, the major principle plane is usually vertical due to gravity, and the coaxiality rule requires the material to expand horizontally, which is the case for granular column collapse. However, the coaxiality can be troubling depending on the circumstances. Suppose we have a flat-bottomed quasi-2D silo with smooth side-walls. Under standard filling procedures, the walls provide only enough pressure to keep the grains from sliding farther out. For example, in a slow dense granular flow through a silo, the principle plane remains vertical and the coaxiality requires the granular material to expand horizontally, thus making it geometrically impossible for

the granular material to converge and exit through the orifice. Depending on the boundary conditions, Mohr-Coulomb plasticity can result in discontinuity or jumps in the velocity and stress fields (Rycroft et al., 2006). Coaxiality can also violate principles of thermodynamics. Coaxiality only ensures there is no shear strain-rate in the principal stress reference frame and actually does not directly enforce that of the two principal strain-rate axes, the axis of maximal compression (i.e. the major principal strain-rate direction) must align with the major principal stress direction.

Roscoe (1970) showed that the principal axes of strain rate and of stress are generally not coincident during simple shear tests of sand. Despite the plastic character of the flow, the flow rules obtained by employing the rheological concept of perfect plasticity to granular materials (perfect soil plasticity) are definitely inadequate for a description of fully developed shear flow. The non-coaxiality of the tensors of stress and strain increment is able to explain the shear flow behaviour. The rotations of the principal stress and the principal plastic strain rate are found to be non-coaxial particularly at the early stage of loading. However, the axes tend to become coincident at large shear strains (Yu and Yuan, 2006), which is common in geophysical flows.

Advanced elasto-plastic models based on the *critical state* theory provide a better representation of granular flows in quasi-static regime, but do not have any rate-dependent effects that are associated with rapid granular flows. At large shear strains, such as geophysical flows, the granular mass is considered to be in critical state. Another continuum based model is the partial fluidisation model, which uses a set of equations that describes the flow velocity and the shear stresses along with a auxiliary order parameter to predict the granular flow behaviour. The order parameter of the granular media controls the size of the viscous-like contribution to the stress tensor, and describes the transition between the flowing and the static components of the granular system (Aranson and Tsimring, 2001). A constitutive model, which considers the solid fraction as the main microscopic parameter for describing dense granular flow was proposed by Josserand et al. (2004). The stress in the granular material is divided into rate-dependent part representing the rebound-less impact between grains, and a rate-independent part associated with longer contacts, i.e. quasi-static regime. Although, the model captures shear localization behaviour, it fails to describe the granular flow behaviour at rough boundaries. In the basal or frictional layer, the grain rotation plays an important role. This causes the grain stress tensor to be non-symmetric and results in a perturbed profile in the solid fraction, these phenomena would require specific modelling (Josserand et al., 2004).

In the case of saturated/submerged soil conditions, most of the continuum techniques do not consider the fully coupled behaviour. Instead, they consider the soil-fluid mixture as a single phase material. However, modelling of pore pressure dissipation is important

to capture accurate flow behaviour, especially in submarine conditions, where they play a crucial role in the flow dynamics. Presence of ambient fluid may retard the flow due to viscous drag or accelerate the flow through lubrication effect. Fully coupled constitutive models are essential to realistically capture the initiation and propagation of rapid granular flows.

Granular materials are composed of distinct grains, which interact only at the contact points. It is assumed that the deformations of individual grains are negligible in comparison with the deformation of the granular assembly as a whole. The latter deformation is primarily due to the movement of the grains as a rigid body. Therefore, it can be argued that precise modelling of grain deformation is not necessary to obtain a good approximation of the overall mechanical behaviour. An Eulerian grain-level continuum model describes the response of individual grains to the applied loads. However, continuum mechanics solves over the whole domain using initial and boundary conditions appropriate for the problem. Hence, continuum models are still widely used to solve engineering problems associated with granular materials and flows.

### 3.2.1 Mesh-based and mesh-free techniques

In continuum mechanics, there are two different view points describing the deformation of a continuum, namely Lagrangian and Eulerian description. In the Lagrangian description the movement of the continuum is specified as a function of the material coordinates and time. This is a particle description that is often applied in solid mechanics. On the other hand, the Eulerian description focuses on the current configuration, giving attention to what is occurring at a fixed point in space as time progresses, instead of giving attention to individual particles as they move through space and time. The Eulerian description is commonly used for describing fluid flows where kinematic properties are of great interest.

Conventional mesh based Lagragian approaches, such as Finite Element Method or Finite Difference Method are capable of modelling history dependant material behaviour and have well-defined free surface. However, they require complex re-meshing and remapping of variables, which cause additional errors in simulating large deformation problems (Li and Liu, 2002). Unlike Lagrangian FEM, in Eulerian FEM the computational mesh is kept spatially fixed while the material is deforming in time. This allows the capability of handling large deformation without the problem of mesh distortion. As the computational mesh is completely decoupled from the material, convective terms appear in Eulerian FEM, introducing numerical difficulties because of their non-symmetrical properties (Donea et al., 1982). Additionally, Eulerian FEM is difficult to use with history dependent constitutive models. Coupled Eulerian–Lagrangian (CEL) method is an arbitrary Lagrangian-Eulerian

that attempts to capture the advantages of both the Lagrangian and the Eulerian method in modelling large deformation problems in geomechanics (Qiu et al., 2011). This approach involves solving the governing equation in the Lagrangian step and thus obtaining the material displacement followed by the Eulerian step where a new mesh is generated and the variables are transferred to the the new mesh. Thus requiring higher computational time.

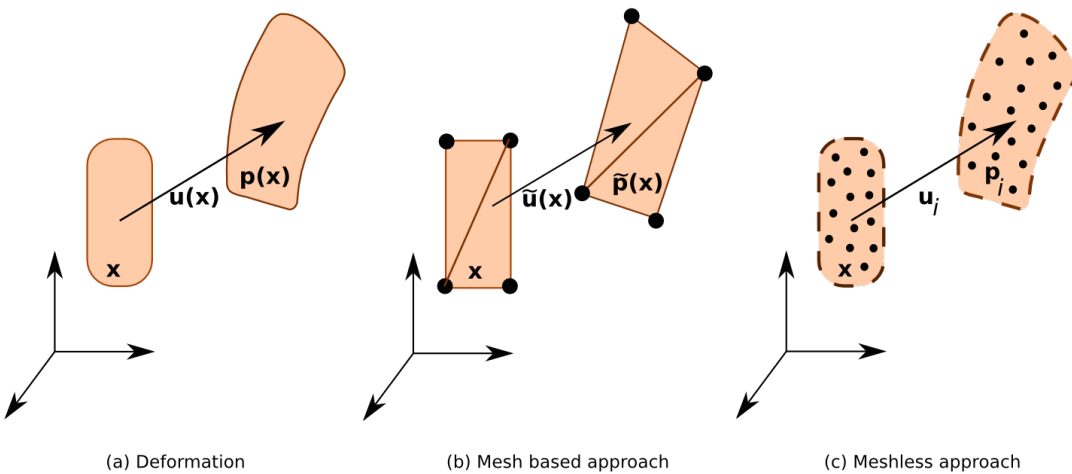


Figure 3.2 Difference between mesh-based and mesh-free techniques in modelling large deformation flow.

An alternative to the mesh-based approach is using mesh-less Lagrangian methods (figure 3.2) where the nodes representing the solid transforms as the continuum deforms, avoiding the problem of mesh distortion, i.e., the nodes representing the solid can move freely within the domain. Mesh free methods such as Smooth Particle Hydrodynamics and Material Point Method are not constrained by the mesh size and mesh distortion effects, and hence can be effectively used in simulating large deformation problems, such as debris flow and submarine landslides.

The element-free Galerkin (EFG) method is a relatively new mesh-less method, in which the trial functions for the weak form are constructed using moving least squares interpolation (Belytschko et al., 1994). The particle finite element method (PFEM) is another mesh-less method that involves the mesh-less finite element interpolation. In PFEM, the nodal points represent the particles and the computational mesh is constructed by connecting these points. The mesh is then used to solve the governing equations in Lagrangian fashion. In PFEM, large deformation requires frequent re-meshing (Kafaji, 2013).

Smooth Particle Hydrodynamics is the oldest mesh-free technique, in which the domain is discretised into particles that have a spatial distance, called the *smoothing length* over which the material properties are “smoothed” by a kernel function. SPH was developed to solve

astrophysical problem (Monaghan, 2005). SPH has been widely applied in geomechanics for solving large deformation problem (Augarde and Heaney, 2009; Maeda and Sakai, 2010; Mori, 2008). Although SPH has been widely adopted, it has a few drawbacks: SPH exhibits spatial instabilities, as a consequence of the point-wise integration (Bonet and Kulasegaram, 2000), insufficient neighbouring particles causes inconsistencies and is computationally expensive as a result of search for the neighbouring particles (Bandara, 2013).

### 3.3 Material Point Method (MPM)

Material Point Method (MPM) (Sulsky et al., 1994, 1995) is a particle based method that represents the material as a collection of *material points*, and their deformations are determined by *Newton's laws of motion*. Sulsky et al. (1994) extended the Particle-in-Cell (PIC) method (Harlow, 1964) to computational solid mechanics by taking advantage of the combined Eulerian-Lagrangian approach. Material Point Method is a hybrid Eulerian-Lagrangian approach, which uses moving material points, and computational nodes on a background mesh. This approach is very effective particularly in the context of large deformations (Andersen and Andersen, 2010; Bandara, 2013; Mackenzie-Helnwein et al., 2010; Mast et al., 2014a; Shin, 2010; Zhang et al., 2009). Although, not derived directly from what is classically considered as mesh-free or mesh-less methods, MPM is still considered as a mesh-free approach, primarily because the initial discretisation of the material does not involve a polygonal tessellation, as in Finite Element Method. However, MPM utilizes a background mesh to perform differentiation, integration, and to solve equations of motions (Steffen et al., 2008). The background mesh can be of any form, however for computational efficiency a Cartesian lattice is adopted. A typical 2D discretisation of a solid body is shown in figure 3.3.

The grey circles are the material points  $x_p$ , where 'p' represents a material point, and the computational nodes are the points of intersection of the grid (denoted as  $X_i$ , where  $i$  represents a computational node). MPM involves discretising the domain  $\Omega$  with a set of material points. The material points are assigned an initial value of position, velocity, mass, volume, and stress denoted as  $\mathbf{x}_p$ ,  $v_p$ ,  $m_p$ ,  $\mathbf{V}_p$  and  $\sigma_p$ . Depending on the material being simulated, additional parameters, like pressure, temperature, pore-water pressure, etc., are specified at the material points. The material points are assumed to be within the computational grid, which for the ease of computation, is assumed to be a Cartesian lattice (figure 3.3). At every time step  $t_k$ , MPM computation cycle involves projecting the data, such as position, mass, and velocity from the material points to the computational grid using the standard nodal basis functions, called the *shape functions*, derived based on the position of particle with respect to the grid. Gradient terms are calculated in the computational grid

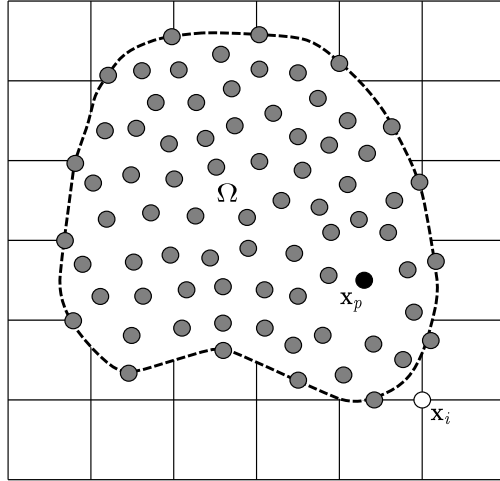


Figure 3.3 Typical discretisation of a domain in MPM. The dotted line represents the boundary of the simulated object  $\Omega$  and each closed point represents a material point used to discretise  $\Omega$ . The square mesh represents the background grid. Each square in the background grid is a grid cell, and grid nodes are located at the corners of grid cells.

and the governing equation, i.e. the equation of motion, is solved and the updated position and velocity values are mapped back to the material points. The mesh is reinitialized to its original state and the computational cycle is repeated.

### 3.3.1 Discrete formulation of the governing equations

The governing differential equation for a continuum is derived from the conservation of mass and momentum:

$$\frac{\partial \rho}{\partial t} \rho \Delta \cdot v = 0, \quad (3.1)$$

$$\rho a = \Delta \cdot \sigma + \rho b, \quad (3.2)$$

where  $\rho(\mathbf{x}, t)$  is the mass density,  $\mathbf{v}(\mathbf{x}, t)$  is the velocity,  $\mathbf{a}(\mathbf{x}, t)$  is the acceleration,  $\sigma(\mathbf{x}, t)$  is the Cauchy's stress tensor, and  $\mathbf{b}(\mathbf{x}, t)$  is the body force. The vector  $\mathbf{x}$  represents the current position of any material point in the continuum, at time  $t$ . In MPM, the continuum body is discretised into finite number of material points  $N_p$ . Let  $\mathbf{x}_p^t$  ( $p = 1, 2, \dots, N_p$ ) denote the current position of material point  $p$  at time  $t$ . Each material point, at any given time  $t$ , has an associated mass  $m_p^t$ , density  $\rho_p^t$ , velocity  $v_p^t$ , Cauchy stress tensor  $\sigma_p^t$ , strain  $\epsilon_p^t$ , and other necessary internal state variables based on the adopted constitutive model. These material points provide a Lagrangian description of the continuum body, since material points have a fixed mass at all times, eq. 3.1 is satisfied. The data from the material points are mapped on

to the nodes of the computational grid, where the discrete form of eq. 3.2 is described. The weak form of eq. 3.2 is obtained by multiplying eq. 3.2 with a test function  $w(\mathbf{x}, t)$ :

$$\int_{\Omega} \rho \mathbf{w} \cdot a d\Omega = - \int_{\Omega} \rho \boldsymbol{\sigma}^s : \Delta \mathbf{w} d\Omega + \int_{\partial\Omega_\tau} w \cdot \boldsymbol{\tau} dS + \int_{\Omega} \rho w \cdot \mathbf{b} d\Omega, \quad (3.3)$$

where  $\boldsymbol{\sigma}^s$  is the specific stress (i.e. stress divided by mass density,  $\boldsymbol{\sigma}^s = \boldsymbol{\sigma}/\rho$ ),  $\Omega$  is the current configuration of the continuum,  $\boldsymbol{\tau}$  is the traction. eq. 3.3 is obtained by applying the divergence theorem, similar to the standard procedure adopted in Finite Element Methods (Chen and Brannon, 2002; Sulsky et al., 1994, 1995). The differential volume and the surface elements are denoted by  $d\Omega$  and  $dS$ , respectively.

As the whole continuum is discretised into a finite set of material points, the mass density can be written as

$$\rho(\mathbf{x}, t) = \sum_{p=1}^{N_p} M_p \delta(x - x_p^t), \quad (3.4)$$

where  $\delta$  is the Dirac delta function. Substituting eq. 3.4 in eq. 3.3, the sum of quantities of material points can be evaluated as

$$\begin{aligned} \sum_{p=1}^{N_p} M_p [w(x_p^t, t) \cdot \mathbf{a}(x_p^t, t)] &= \sum_{p=1}^{N_p} M_p [-\boldsymbol{\sigma}^s(x_p^t, t) : \Delta w|_{x_p^t} \\ &\quad + w(x_p^t, t) \cdot \boldsymbol{\tau}^s(x_p^t, t) h^{-1} + w(x_p^t, t) \cdot \mathbf{b}(x_p^t, t)], \end{aligned} \quad (3.5)$$

where  $h$  is the thickness of the boundary layer. It can be noted from eq. 3.5 that the interactions between different material points are reflected only through the gradient terms. In MPM, a background computational mesh is used to calculate the gradient terms. The computational mesh is constructed using 2-node cells for 1-D, 4-node cells for 2-D, and 8-node cells for 3-D problems. These elements are used to define the standard nodal basis functions,  $N_i(\mathbf{x})$ , associated with the spatial nodes  $x_i(t), i = 1, 2, \dots, N_n$ , where  $N_n$  represents the total number of mesh nodes. The nodal basis functions are assembled by using the conventional finite-element shape functions (Chen and Brannon, 2002). The co-ordinates of any material point in a cell can be represented by

$$x_p^t = \sum_{i=1}^{N_n} x_i^t N_i(\mathbf{x}_p^t). \quad (3.6)$$

Similarly the nodal displacements, velocity and acceleration of any material point in a cell are represented using the basis functions. Thus, the test function has to be of the form

$$w_p^t = \sum_{i=1}^{N_n} w_i^t N_i(\mathbf{w}_p^t). \quad (3.7)$$

The equations (3.6) and (3.7) ensures that the associated vectors are continuous across the cell boundary. However, the gradient of these functions are not continuous, due to the use of linear shape functions. Substituting, eq. 3.6 and eq. 3.7 into eq. 3.5, the weak form of the equation of motion reduces to

$$\sum_{j=1}^{N_n} m_{ij}^t \mathbf{a}_j^t = \mathbf{f}_i^{int,t} + \mathbf{f}_i^{ext,t}, \quad (3.8)$$

where the nodal mass,  $m_{ij}^t$  is represented as

$$m_{ij}^t = \sum_{p=1}^{N_p} M_p N_i(x^t) N_j(x^t). \quad (3.9)$$

The nodal internal force,  $\mathbf{f}_i^{int,t}$  and the nodal external force,  $\mathbf{f}_i^{ext,t}$  are defined as

$$\begin{aligned} \mathbf{f}_i^{int,t} &= - \sum_{p=1}^{N_p} M_p \mathbf{G}_{ip}^t \cdot \boldsymbol{\sigma}_p^{s,t} \\ \mathbf{f}_i^{ext,t} &= - \sum_{p=1}^{N_p} M_p \mathbf{b}_p^t N_i(\mathbf{x}_p^t) + \sum_{p=1}^{N_p} M_p N_i(\mathbf{x}_p^t) \tau_p^{s,t} h^{-1} \end{aligned} \quad (3.10)$$

where  $\mathbf{G}_{ip}^t = \Delta N_i(x)|_{x=X_p^t}$ . The nodal accelerations are obtained by explicit time integration of eq. 3.8. To obtain stable solutions, the time step used in the analysis should be less than the critical time step, which is defined as the ratio of the smallest cell size to the wave speed (Chen and Brannon, 2002). The critical time increment is obtained as

$$\Delta t_{crit} = L/c, \quad (3.11)$$

$$c = \frac{K + \frac{4}{3}G}{\rho_s}, \quad (3.12)$$

where  $L$  is the background cell size,  $c$  is the pressure wave velocity,  $K$  and  $G$  are the bulk modulus and the shear modulus of the solid and  $\rho_s$  is the density of the soil skeleton. The boundary conditions are enforced on the cell nodes and the nodal velocities are obtained by

solving the equation of motion at each node. The strain increment for each material point is determined using the gradients of the nodal basis functions. The corresponding stress increments are computed using the adopted constitutive law. After updating all the material points, the computational mesh is discarded, and a new mesh is defined for the next time step.

### 3.3.2 Boundary conditions

The Material Point Method uses standard shape functions, similar to those used in the Finite Element Methods, hence the essential and the natural boundary conditions can be applied to the background grid nodes in the same way as in the traditional FEM. The free surface boundary conditions are satisfied, as MPM is formulated in the weak form. Implementation of traction boundary conditions requires a set of material points to represent the boundary layer. Bandara (2013) proposed a friction interaction for the planar boundary condition, using Coulomb's friction criterion. The friction boundary algorithm for solid phase adopted in the present study is shown in section 3.3.2. The friction boundary conditions are applied on the mesh nodes by controlling the nodal acceleration tangential to the boundary. The nodal accelerations are considered to include the frictional effects instead of the forces, as the forces are proportional to the corresponding accelerations. Both static and kinetic friction are considered, and are applied only when the particles are in contact with the boundary. The static and kinematic frictions are applied in the direction tangential to the nodal boundary. Friction forces are applied, only if the particles are in contact. The normal velocity and acceleration on the boundary plane is zero. Displacement boundary conditions are applied as velocity constrains on the nodes in the background mesh.

### 3.3.3 Integration scheme

Love and Sulsky (2006) investigated the energy consistency of MPM and observed that MPM algorithm is more suited to flow calculations than Lagrangian finite element methods. Since, energy consistent MPM formulation is effective in simulating materials that exhibit localised dissipative mechanisms. In dynamic MPM, the explicit time integration scheme is adopted to advance the solution. Bardenhagen (2002) studied the energy consistency of MPM using two different explicit integration schemes. The *update stress first* USF involves updating the strain and the stress at the beginning of the time step from the velocities of the previous time step. In the *update stress last* USL approach the updated particle momentums are used to calculate the nodal velocities, which are then used to update the particle strain and stress. Bardenhagen (2002) observed that the USL approach performed better than the

**Algorithm 1** Friction boundary algorithm for solid phase in MPM (Bandara, 2013)

---

```

if  $a_{sI,t}^{k+1} < 0.0$  then
     $v_{sI,t}^{k+1,tmp} = v_{sI,t}^k + \Delta a_{sI,t}^{k+1}$ 
    if  $v_{sI,t}^{k+1,tmp} = 0$  then                                ▷ static friction condition
        if  $a_{sI,t}^{k+1} \leq \mu_s |a_{sI,n}^{k+1}|$  then
             $a_{sI,t}^{k+1} = 0.$ 
        else                                         ▷ friction acts in the direction opposite to the tangential force
             $a_{sI,t}^{k+1} = a_{sI,t}^{k+1} - \mu_s |a_{sI,n}^{k+1}| \frac{a_{sI,t}^{k+1}}{|a_{sI,n}^{k+1}|}$ 
        end if
    else                                         ▷ Kinetic friction condition
        if  $v_{sI,t}^{k+1} \leq \mu_k |a_{sI,n}^{k+1}| \Delta t$  then
             $a_{sI,t}^{k+1} = -\frac{v_{sI,t}^k}{\Delta t}$ 
        else                                         ▷ friction acts in the direction opposite to the movement
             $a_{sI,t}^{k+1} = a_{sI,t}^{k+1} - \mu_k |a_{sI,n}^{k+1}| \frac{v_{sI,t}^{k+1}}{|v_{sI,n}^{k+1}|}$ 
        end if
    end if
end if

```

---

USF. The USL approach dissipates the energy slowly, while the USF approach is found to gain energy (Kafaji, 2013). The USL approach yields almost the same result as using the central difference scheme that is second order in time (Wallstedt and Guilkey, 2008). The *update stress last* approach is used in the present study, due to its dissipative nature, which in certain conditions simulate artificial damping, and the numerical stability.

In problems involving slow rate of loading, i.e., quasi-static problems, the flow of the material is much slower than the speed of wave propagation in the material. Hence, employing an implicit time integration scheme reduces the computational time considerably (Kafaji, 2013). Guilkey and Weiss (2003) proposed an implicit time integration method for MPM using quasi-static governing equations, using the Newmark integration scheme. Love and Sulsky (2006) showed that the implicit time integration in MPM to be unconditionally stable. Although, MPM did not suffer from the limitations of FEM in simulating large deformations, more research is required for applying implicit time integration for large deformation problems. The present study focuses on large deformation problems, hence an explicit time integration scheme with the USL approach is adopted.

### 3.3.4 Solution scheme

A step-by-step solution scheme for Material Point Method is described below:

- A continuum body is discretised into a finite set of material points corresponding to the original configuration of the body. The number of material points corresponds to the resolution of the mesh size adopted in Finite Element Method. The material points are followed throughout the deformation of the material, which gives a Lagrangian description of the motion.
- An arbitrary computational grid is initialized to describe the natural coordinates of the material points. For the purpose of simplicity, a Cartesian grid is usually adopted.
- The state variables (mass/density, velocity, strain, stress, other material parameter corresponding to the adopted constitutive relation) are initialized at every material point.
- The shape function  $N_{ip}^t(x_p)$  and the gradient of the shape function  $G_{ip}^t$  for each material point is computed.
- The information and properties carried by each material point is projected on to the background mesh using the shape functions computed from the particle position.
- The nodal mass matrix is obtained as

$$m_i^t = \sum_{p=1}^{N_p} m_p N_{ip}^t(x_p^t), \quad (3.13)$$

where  $m_i^t$  is the mass at node  $i$  at time  $t$ ,  $m_p$  the particle mass,  $N_i$  the shape function associated with node  $i$ , and  $x_p^t$  the location of the particle at time  $t$ .

- The nodal velocity is obtained by mapping the particle velocity to the nodes using the shape functions. If necessary, the boundary conditions for the nodal velocities are applied.

$$\mathbf{v}_i^t = \sum_{p=1}^{N_p} m_p \mathbf{v}_p^t N_{ip}^t(x_p^t) / m_i^t. \quad (3.14)$$

- The momentum balance equation for the solid phase is solved and the nodal acceleration is computed as

$$a_i^t = \frac{1}{m_i^t} \left( - \sum_{p=1}^{N_p} G_{ip}^t \sigma_p^t \Omega_p^t + \sum_{p=1}^{N_p} m_p^t \mathbf{b}_p^t N_{ip}^t(x_p^t) \right). \quad (3.15)$$

If necessary, the boundary conditions for the nodal accelerations are applied.

- The nodal velocity at the end of the Lagrangian time step ( $L$ ) is obtained from the computed nodal acceleration as:

$$v_i^L = \mathbf{v}_i^t + a_i^t \Delta t. \quad (3.16)$$

where  $\Delta t = (t + 1) - t$ .

- The particle position and its velocity are updated according to:

$$\begin{aligned} \mathbf{x}_p^{t+1} &= \mathbf{x}_p^t + \Delta t \sum_{i=1}^{N_n} v_i^L N_{ip}^t, \\ \mathbf{v}_p^{t+1} &= \mathbf{v}_p^t + \Delta t \sum_{i=1}^{N_n} a_i^t N_{ip}^t. \end{aligned} \quad (3.17)$$

- Strain increment  $\Delta \boldsymbol{\epsilon}_p^{t+1}$  for particle is then computed as

$$\Delta \boldsymbol{\epsilon}_p^{t+1} = \frac{\Delta t}{2} \sum_{i=1}^{N_n} G_{ip}^t \mathbf{v}_i^t + (G_{ip}^t \mathbf{v}_i^t)^T. \quad (3.18)$$

- The stress increment for the particle  $\Delta \boldsymbol{\sigma}_p^{t+1}$  is computed from the strain increment using the constitutive model adopted in the simulation

$$\Delta \boldsymbol{\sigma}_p^{t+1} = \mathbf{D} : \Delta \boldsymbol{\epsilon}_p^{t+1}. \quad (3.19)$$

In large deformation problems, the Jaumann rate is used to update the effective stress of the solid particles

$$\boldsymbol{\sigma}_p^{t+1} = \Delta t (\boldsymbol{\sigma}_p^t - \mathbf{W}_p^t - \mathbf{W}_p^t \boldsymbol{\sigma}_p^t) x + \mathbf{D} : \Delta \boldsymbol{\epsilon}_p^{t+1}, \quad (3.20)$$

$$\mathbf{W}_p^t = \sum_{i=1}^{N_n} \left[ \mathbf{G}_{ip}^t \mathbf{v}_i^t - (\mathbf{G}_{ip}^t \mathbf{v}_i^t)^T \right]. \quad (3.21)$$

- The stress and the strain of the material points are updated based on

$$\begin{aligned} \boldsymbol{\sigma}_p^{t+1} &= \boldsymbol{\sigma}_p^t + \Delta \boldsymbol{\sigma}_p^{t+1}, \\ \boldsymbol{\epsilon}_p^{t+1} &= \boldsymbol{\epsilon}_p^t + \Delta \boldsymbol{\epsilon}_p^{t+1}. \end{aligned} \quad (3.22)$$

- In large deformation the volume of solid material points  $\Omega_p$  is updated using the determinant  $J$  of the deformation gradient  $\mathbf{F}_p^{t+1}$ :

$$\Omega_p^{t+1} = J\Omega_p^{t_0}. \quad (3.23)$$

- The material point density is then updated as

$$\rho_p^{t+1} = \frac{\rho_p^t}{\{1 + \text{tr}(\Delta\boldsymbol{\varepsilon}_p^{t+1})\}}. \quad (3.24)$$

- At the end of every time step, all the variables on the grid nodes are initialized to zero. The material points carry all the information about the solution and the computational grid is re-initialised for the next step.

Figure 3.4 illustrates the steps involved in a MPM analysis.

### Post processing

The post-processing stage, as in any analysis, involves visualization and extraction of the data from the analysis. In mesh-less methods, like the material point method, structures are generally represented as points which describe a discrete region of the body. MPM facilitates representation of arbitrarily complex geometries and has advantages over strictly grid based methods especially in simulations involving large deformations (Bardenhagen et al., 2000). MPM poses a whole new set of visualization problem, it is essential to visualize the general configuration of the body as well as observe the finer details like development of cracks or separation of chunks of material from the body. The body is discretised into conceptual material points, which carry all the relevant information of the corresponding segment. The unique qualities of MPM necessitate the need to visualize the particle data in a way that is informative and appropriate.

In MPM, the particle data represents the finite portion of a larger continuum, and the ability to see and interpret the macroscopic structure created by these particles is vital (Bigler et al., 2006). There are two main aspects in visualizing MPM data: (1) visualization of the structure represented by the material points, and (2) understanding the qualitative trend associated with the material points like mass, velocity or stress.

The MPM output data contains both the material point and the grid data, and one approach in visualizing MPM data is by rendering the interpolated particle values on grid nodes using *iso-surfacing* (Lorensen and Cline, 1987) or *volume rendering* (Levoy, 1988) technique. In regions where the material points are sparse, it is necessary that the grid resolution to

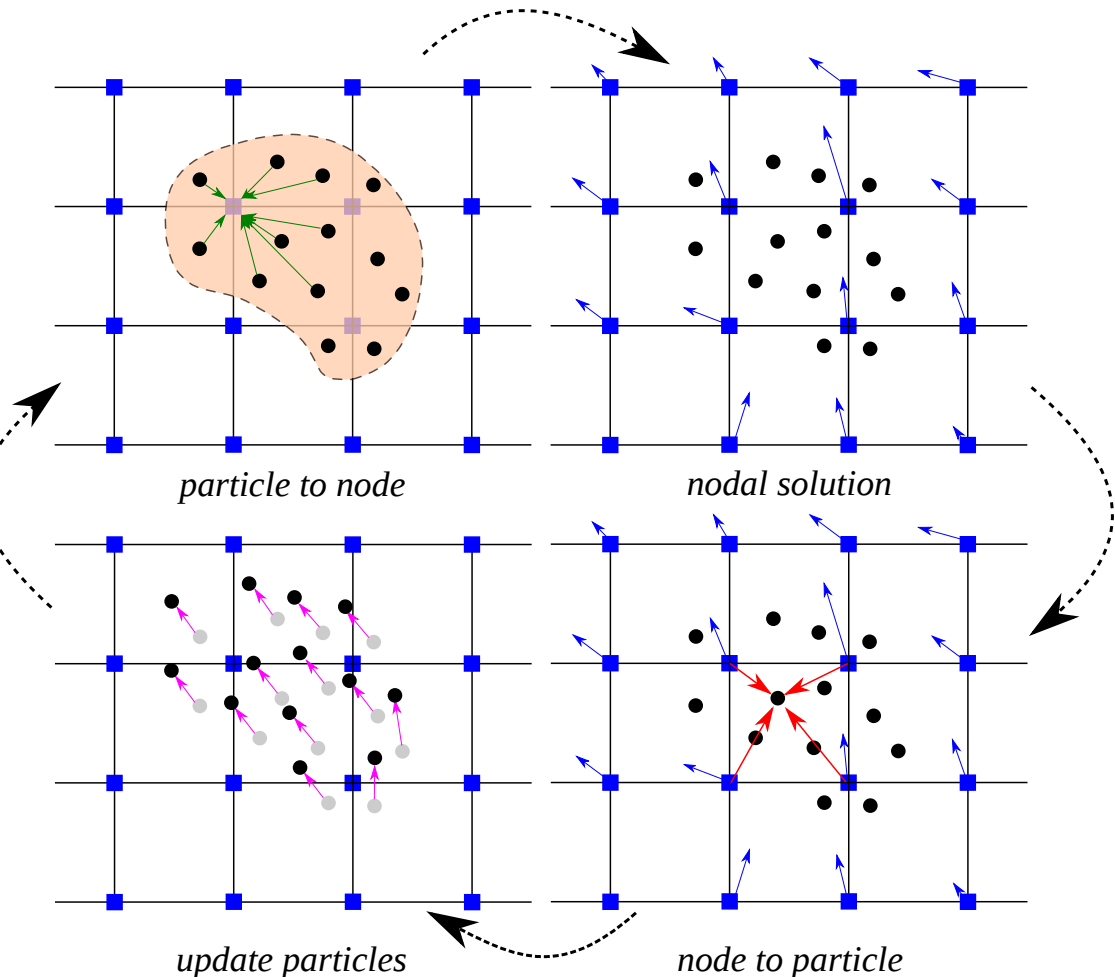


Figure 3.4 Illustration of MPM algorithm (1) A representation of material points overlaid on a computational grid. Arrows represent material point state vector (mass, volume, velocity, etc.) being projected to the nodes of the computational grid. (2) The equations of motion is solved on the nodes, resulting in updated nodal velocities and positions. (3) The updated nodal kinematics are interpolated back to the material points. (4) The state of the material points are updated and the computational grid is reset.

be sufficiently fine to compensate for the missing features. This results in storing large amount of unnecessary data in regions where sufficient material points are present. Thus, it is advantageous to visualize MPM data of the material points as particles (Bigler et al., 2006). Particle visualization involves rendering the particles as a sphere or an ellipsoid representing the size and location of the fraction of the continuum (Gumhold, 2003; Krogh et al., 1997; Kuester et al., 2001). In the present study, MPM data points are represented as spheres. Colour mapping of scalar quantities such as mass, velocity, or stress of a material point are applied to provide additional qualitative understanding of the data.

### 3.3.5 Effect of mesh size and number of material points per cell

The accuracy of MPM simulations largely depends on the number of material points representing the continuum. MPM utilizes a grid to compute the deformation of a continuum, hence the size of the cells affects the accuracy of the results. Generally in MPM, the number of particles per cell controls the accuracy of the simulation. Guilkey et al. (2003) recommends higher particle density, such as 4 particles per cell, for large deformation problems. Very low particle density will result in non-physical opening of cracks in large deformation simulations. However, a higher value of particle density affects the computational time.

Abe et al. (2013) observed that for a coarse mesh, the numerical error decreases with increase in the number of material points per cell. In contrast, they observed an opposite trend for the fine meshes. The influence of numerical noise due to particles crossing the background mesh is not observed in coarse meshes. Coetzee et al. (2005) also found that the numerical error decreases with increase in mesh refinement.

In the present study, the effect of mesh size and the number of material points per cell on the run-out behaviour is investigated. The run-out behaviour of a granular slope of length 0.8 m and height 0.2 m is subjected to a gradient impact velocity is studied. The initial static slope is set into motion by applying a horizontal gradient velocity  $v_{0x}(y) = k(y_{max} - y)$  with  $k > 0$ . Figure 4.24c shows the initial configuration and distribution of initial horizontal impact velocity of 50J in the granular mass. Detailed description of this problem and the material properties used in the simulations are found in section 4.4. A mesh size of 0.0125 m is adopted. The number of material points per cell (PPC) is varied as 4, 16, 25, 36, 64, 81 and 100.

The effect of number of material points on the run-out behaviour is presented in figure 3.5. At a low input energy of 50 J, 4 and 16 material points per cell result in a longer run-out distance, where as the run-out distance converges when the number of PPC is more than 25. While at a high input energy of 500 J, both 4 and 16 PPC predict almost the same run-out distance, but is higher than the run-out predicted with more than 25 material points per cell.

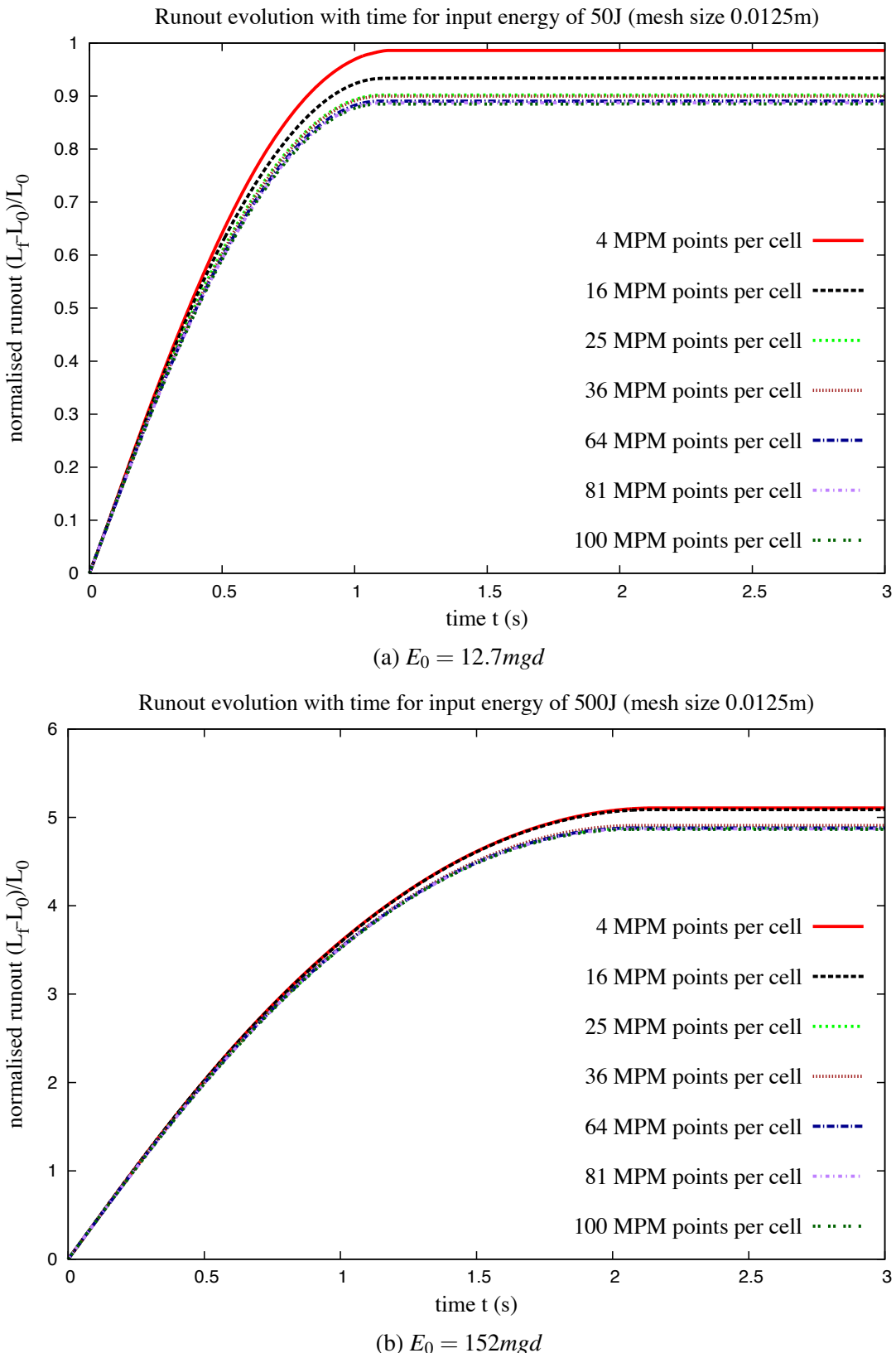


Figure 3.5 Evolution of run-out with time for varying material points per cell for a slope subjected to an impact velocity.

The evolution of the granular pile during the initial stage of flow is shown in figure 3.6 for different number of material points per cell. At low input energy, fewer material points per cell results in larger separation of the spreading mass from the left wall. Distinct shear bands can be observed for more than 16 PPC. The flow structure remains unchanged with increase in PPC of more than 25. At a higher input energy (figure 3.7), almost all cases predict similar flow structure, except in the case of 4 PPC.

Figure 3.8 shows the evolution of kinetic energy with time for varying number of material points per cell. At low input energy, the horizontal kinetic energy evolution is identical for all cases. A slightly quicker run-out evolution during the spreading phase can be observed for the case of 4 PPC. However, increase in the number of material points per cell significantly affects the evolution of the vertical kinetic energy  $E_{ky}$ . At low energy, a large proportion of the input energy is dissipated in the destabilisation process. This results in material points falling behind the spreading mass to fill the cavity. Fewer material points per cell results in cell crossing noise as the material points filling the cavity experience free-fall due to gravity. The effect of cell-crossing noise can be seen in the oscillation of vertical kinetic energy for fewer material points per cell. However, at high input energy, most of the input velocity is dissipated during the spreading process. This means that only a small fraction of energy is available in the vertical component resulting in almost similar behaviour for all cases. Four material points per cell predicts a higher peak vertical kinetic energy in comparison with other cases, unlike the low energy case, no oscillations are observed for the high input energy.

The effect of mesh size on the flow kinematics is studied by comparing two mesh sizes: 0.01 m and 0.0125 m (figure 3.9). It can be observed that the run-out distance converges with an increase in the number of material points per cell in both cases. Less than 1% difference in the run-out distance is observed between a mesh size of 0.0125 m and 0.01 m. The final run-out duration is almost unaffected by the increase in the number of material points per cell.

This shows that the run-out distance is affected by the number of material points per cell. However, the duration of the run-out is independent of the number of material points per cell. The computation time increases with increase in the number of material points per cell and decrease in the mesh size. However, the run-out distance converges with increase in number of material points per cell. Hence, an optimum number of 25 material points per cell is adopted in this case. In summary, for conducting a successful MPM analysis, a careful selection of the mesh size and the number of particles is necessary.

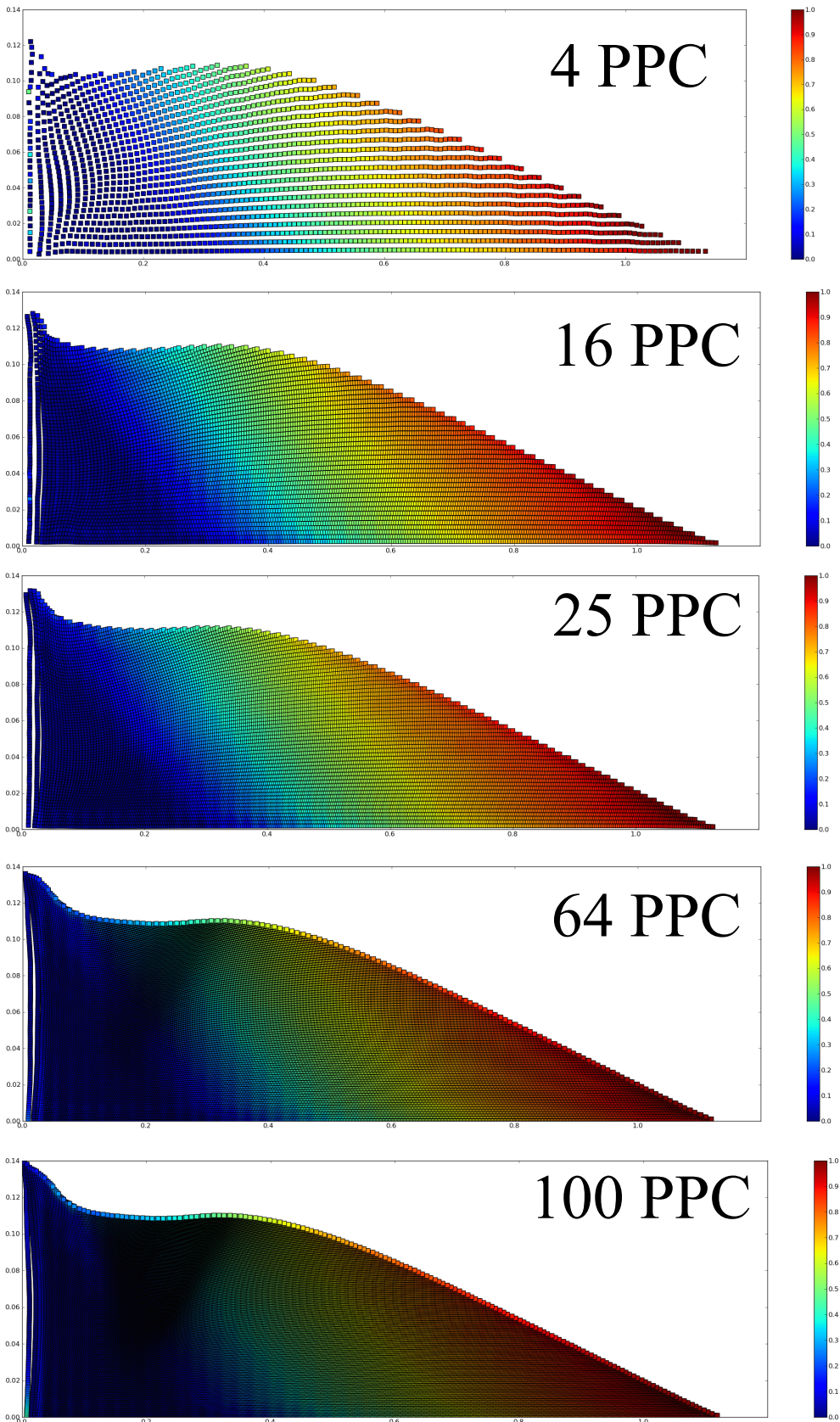


Figure 3.6 Effect of number of material points on cell on the run-out behaviour  $E_0 = 12.7mgd$ . Velocity profile (m/s) of granular pile subjected to gradient impact loading.

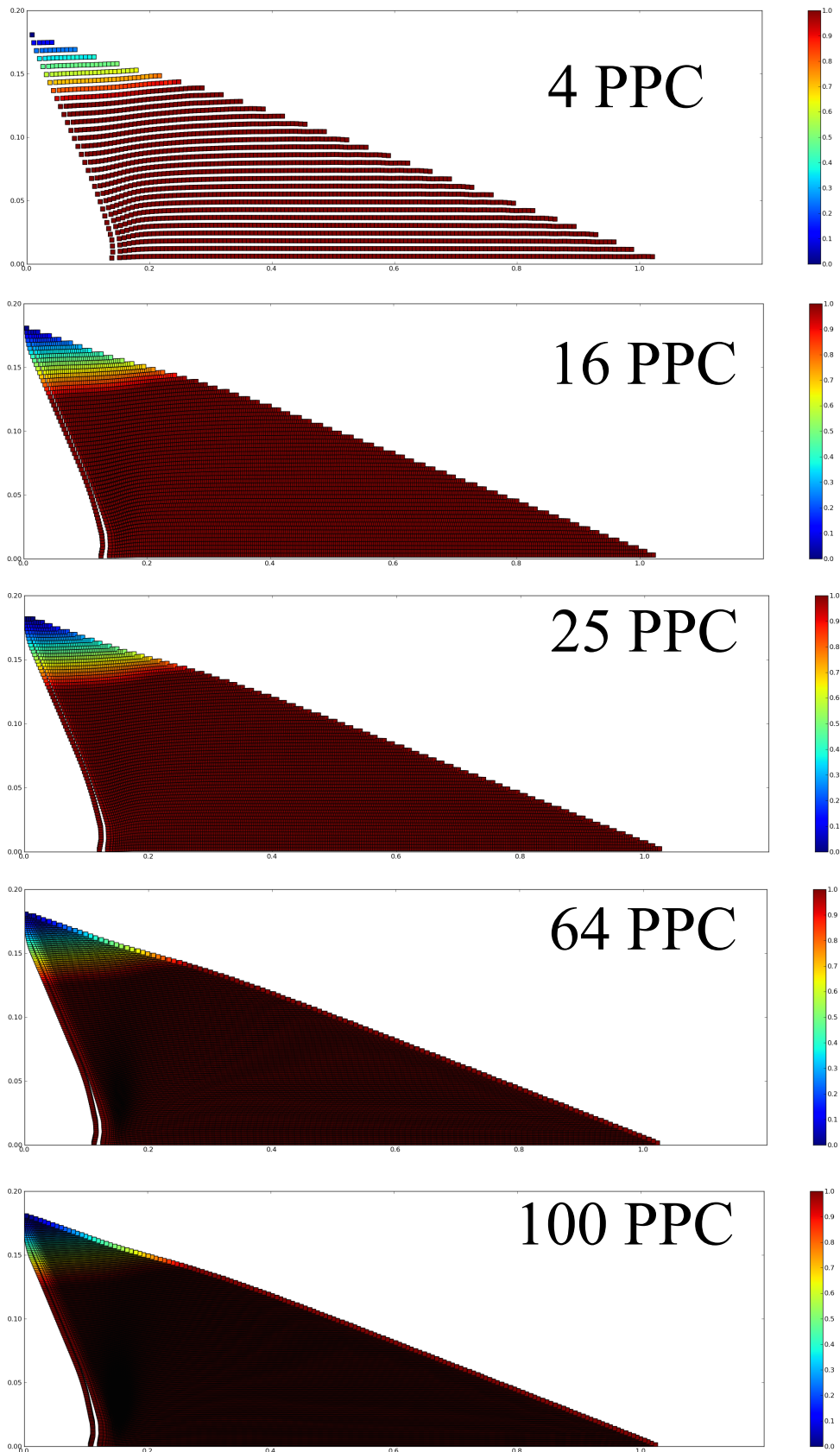


Figure 3.7 Effect of number of material points on cell on the run-out behaviour  $E_0 = 152mgd$ . Velocity profile (m/s) of granular pile subjected to gradient impact loading.

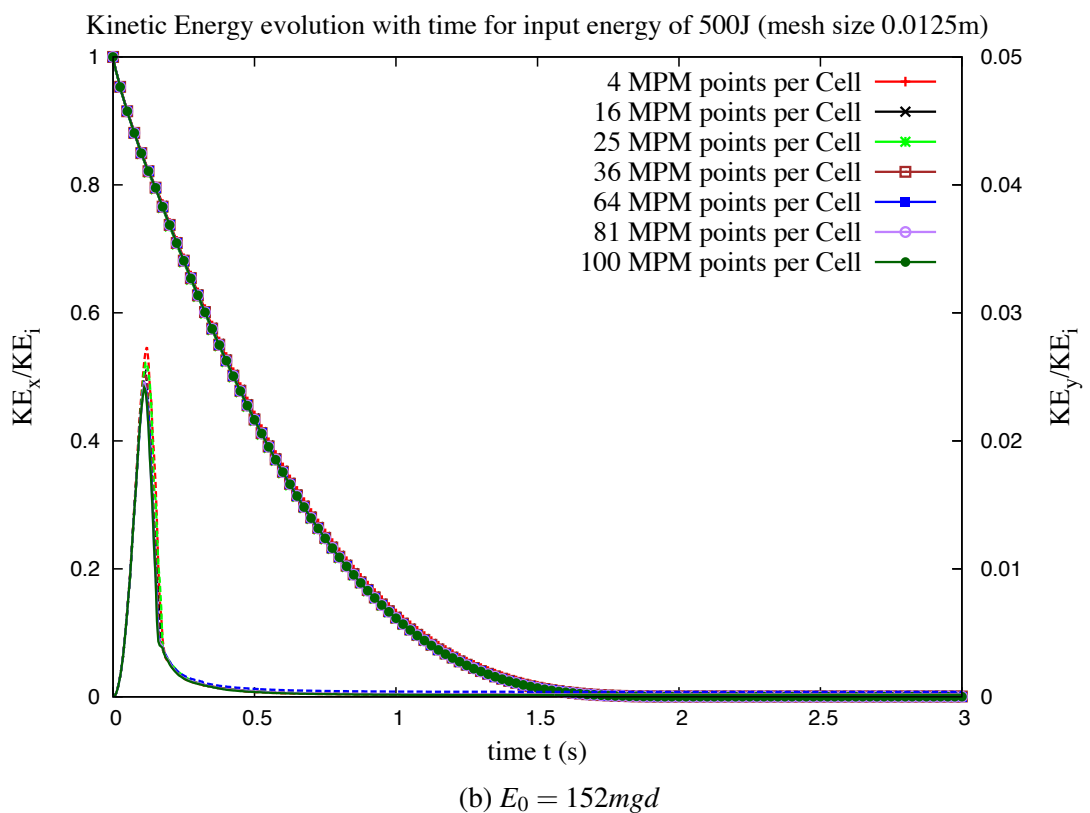
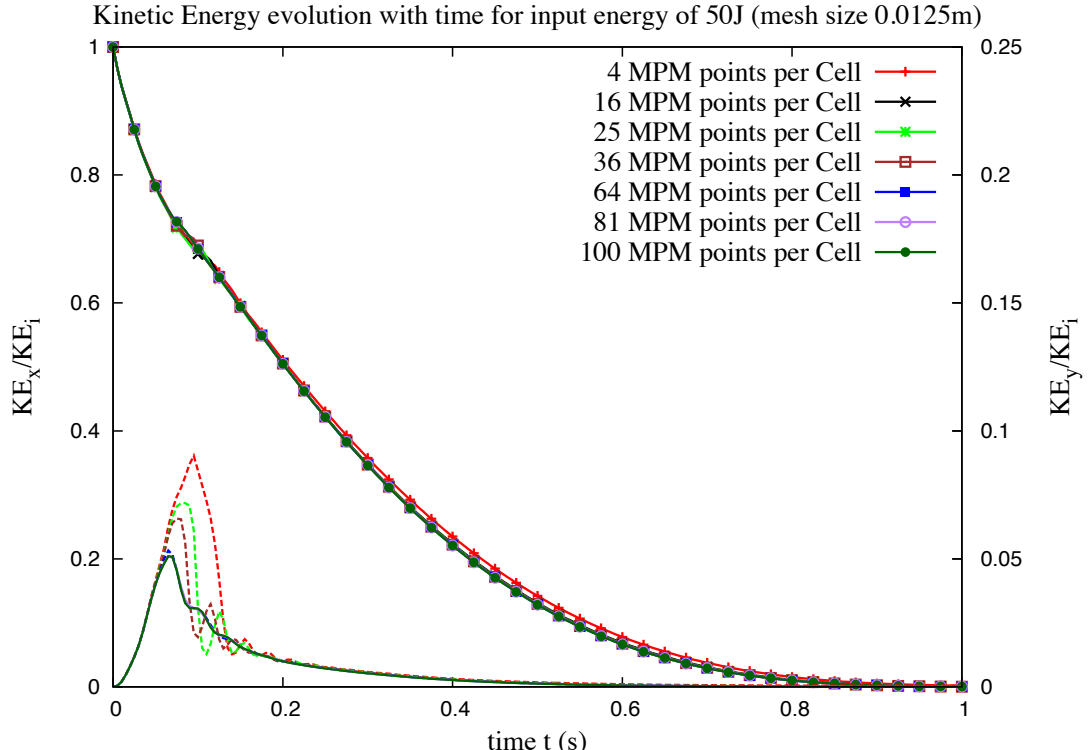


Figure 3.8 Evolution of kinetic with time for varying material points per cell for a slope subjected to an impact velocity.

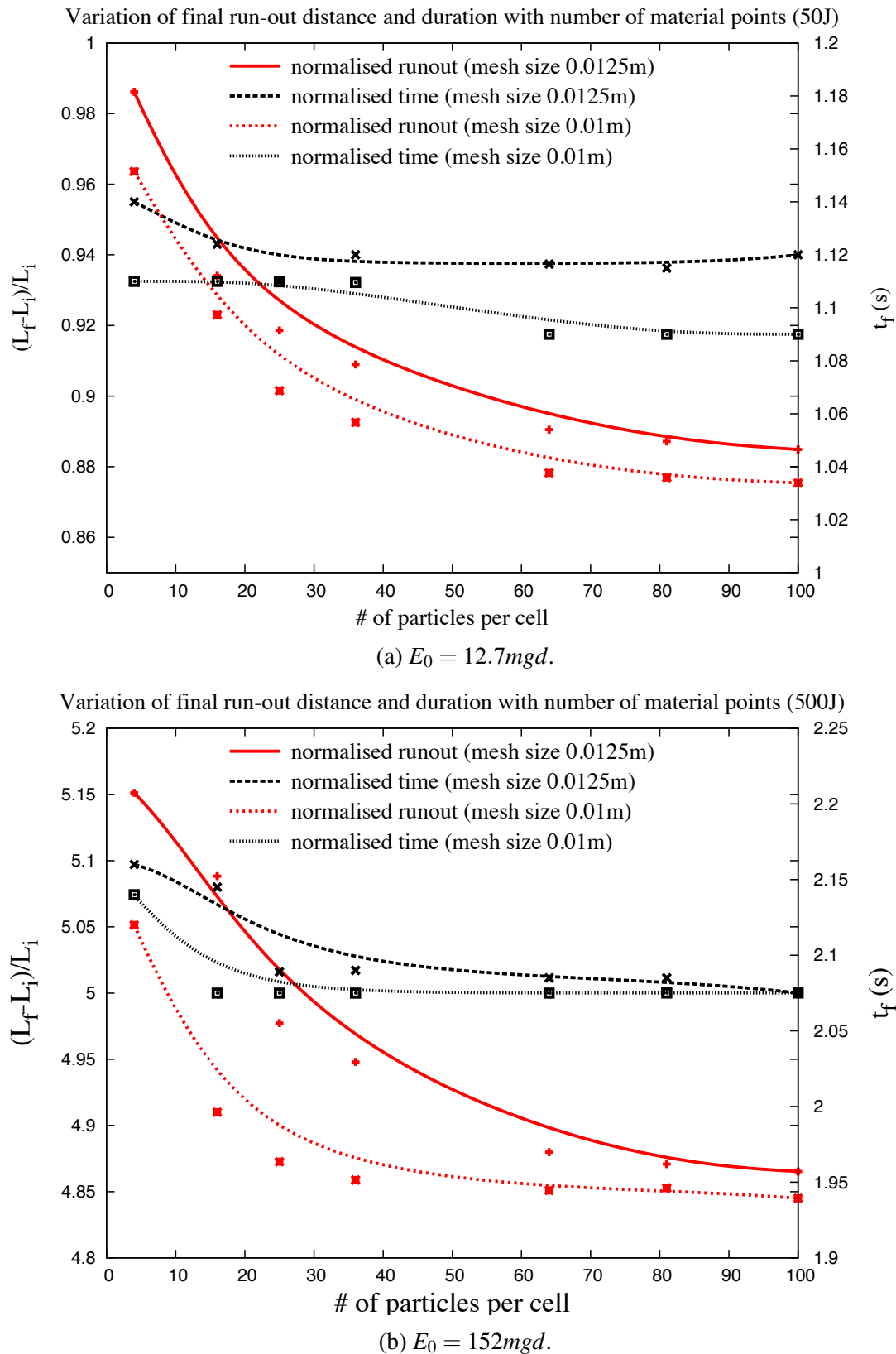


Figure 3.9 Evolution of run-out and duration of flow for varying material points per cell for a slope subjected to an impact velocity.

### 3.3.6 GIMP method

The shape functions used in MPM are continuous, and hence penetration between bodies are handled automatically without the need for any supplemental contact algorithm (Chen and Brannon, 2002). In MPM, the continuum body deforms and moves in an arbitrary computation grid and all the boundary conditions are carried by the boundary particles. If a boundary particle is present in a cell, then the cell boundary becomes a part of the continuum body, and the cell size represents the thickness of the boundary. However, in certain cases both the boundary particle and an interior particle can be found in a cell, in which case the cell is still treated as a boundary cell, and the interior particle temporarily acts as a boundary particle. To avoid numerical errors, it is essential to consider smaller cell size along the boundary (Chen and Brannon, 2002).

In MPM simulations, numerical noises are observed when the material points crosses the cell boundaries as the body deforms, this is termed as *cell crossing noise*. If a material point is located very close to the cell boundary, it results in discontinuous gradient of the weighing function causing a force imbalance on the grid (Bardenhagen and Kober, 2004). This results in large non-physical acceleration values resulting in separation of material points from the continuum (Sulsky et al., 1995). Figure 3.10 illustrates the problem of cell crossing noise. The main reason for the occurrence of cell crossing noise is the use of piecewise linear shape functions. However, this problem, which is predominant when using fine mesh size, can be overcome by changing the order of arithmetic operation as proposed by Sulsky et al. (1995).

To overcome the problem of cell crossing noise, Bardenhagen and Kober (2004) proposed an alternate method called the Generalized Interpolation Material Point Method that uses smoother shape functions and a larger influence region for each grid node. This approach minimizes the cell crossing noise. A piecewise-linear grid basis functions are written as

$$\phi_x = \begin{cases} 1 - |x|/h & : |x| < h \\ 0 & : \text{otherwise}, \end{cases} \quad (3.25)$$

where  $h$  is the grid spacing. The basis function associated with grid node  $i$  at position  $x_i$  is then  $\phi_i = \phi(x - x_i)$ . The basis functions in 3-D are separable functions constructed as  $\phi_i(x) = \phi_i^x(x)\phi_i^y(y)\phi_i^z(z)$ . GIMP is often implemented using the standard piecewise-linear grid basis functions and piecewise-constant particle characteristic functions:

$$\chi_p = \begin{cases} 1 & : |x| < \frac{1}{2}l_p \\ 0 & : \text{otherwise}, \end{cases} \quad (3.26)$$

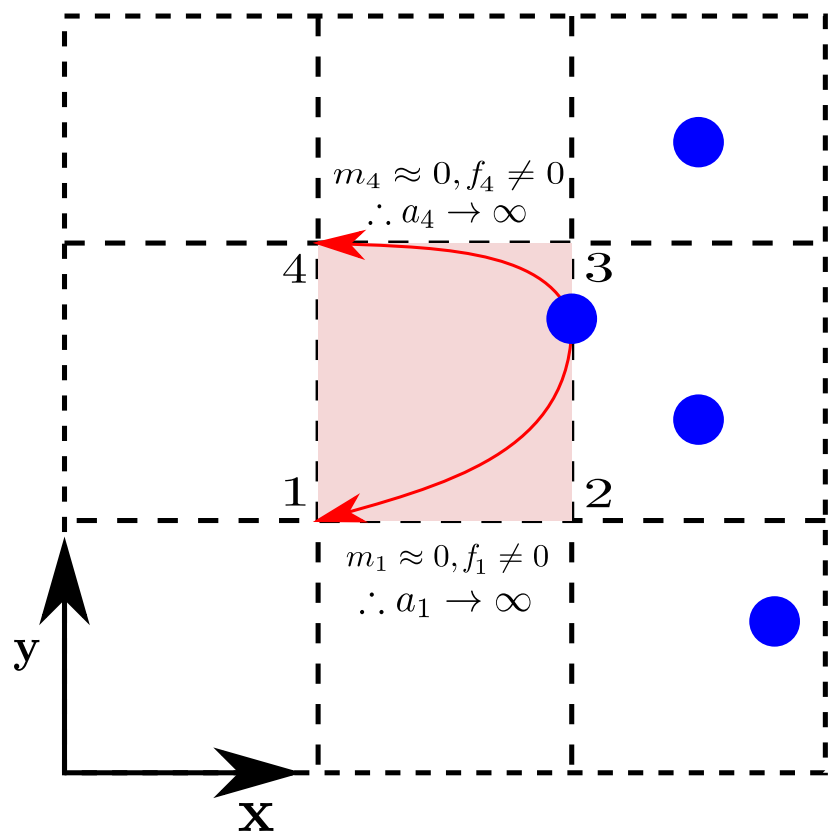


Figure 3.10 Schematic description of occurrence of cell crossing noise in MPM

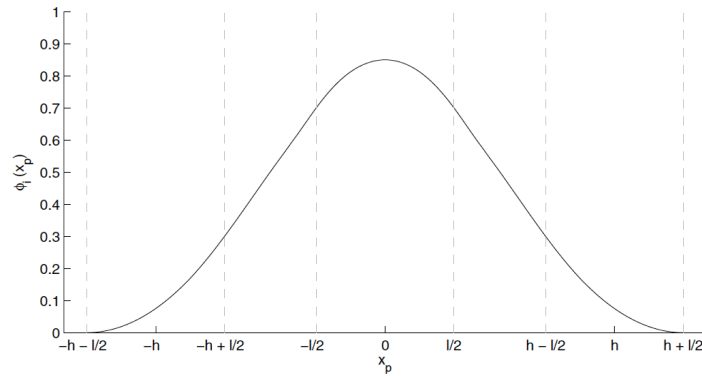
in which case the 1-D MPM and GIMP weighting functions can be grouped together in the general form

$$\phi = \begin{cases} 1 - (4x^2 + l_p^2)/(4hl_p) & : |x| < \frac{l_p}{2} \\ 1 - |x|/h & : \frac{l_p}{2} \leq |x| < h - \frac{l_p}{2} \\ \left(h + \frac{l_p}{2} - |x|\right)^2/(2hl_p) & : h - \frac{l_p}{2} \leq |x| < h + \frac{l_p}{2} \\ 0 & : otherwise, \end{cases} \quad (3.27)$$

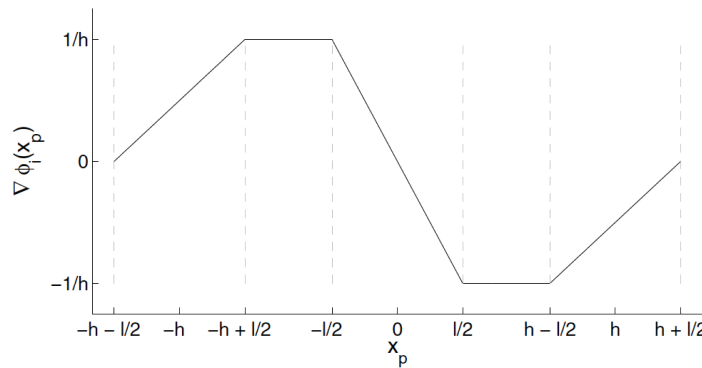
where  $l_p$  is the width of the particle characteristic function  $\chi_p$ . figure 3.11a shows a 1-D GIMP weighting function  $\bar{\phi}_{ip}$  and gradient weighting function  $\nabla\bar{\phi}_{ip}$  for a piecewise-constant  $\chi_p$  with a characteristic length of  $l$ . The GIMP weighting function is smooth, however a discontinuity is observed in the gradient weighting function.

In traditional MPM, boundary conditions only need be applied on those nodes which coincide with the extents of the computational domain. As illustrated in figure 3.11c nodes beyond those boundaries are not influenced by particles within the domain. This can be considered a result of the zero width of the Dirac delta characteristic functions. However, special attention is required to simulate the boundaries in the Generalized Interpolation Material Point Method (GIMP). Namely, because of their increased extents, it is possible for particles to influence, and be influenced by, nodes that lie outside of the simulation domain (figure 3.11b). These extra nodes are referred to as the “ghost” nodes. Boundary condition treatment of these nodes for Dirichlet conditions is the same as for the regular boundary nodes, namely, their computed values are replaced by prescribed values (Steffen et al., 2008).

In the present study, the influence of GIMP method on the run-out behaviour of a granular column collapse experiment is investigated. A granular column of height  $H_0$  and length  $L_0$  is allowed to collapse and flow on a horizontal plane (figure 2.7). The run-out distance observed is proportional to the initial aspect ratio of the column ( $H_0/L_0$ ). Further details about the granular collapse experiment and the material properties used in the simulations are presented in section 4.2. A granular column with an initial aspect ratio of 0.4 is considered for the comparison. The granular column is represented by 32,000 material points arranged uniformly on a regular lattice with a particle spacing of 0.25 mm. Since, the scale of the problem being modelled is small and it is important to precisely define the flow surface, a larger number of material points are used to represent the geometry. However when modelling geophysical problems, where the tolerance in defining the flow surface is in the order of few millimetres, each material point shall represent individual grains or orders of magnitude larger than the grain size. A grid size of 1 mm is adopted with 16 material points per cell. In order to understand the influence of the number of material points on the accuracy

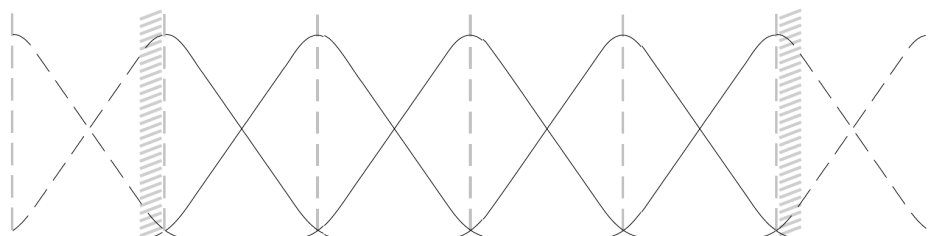


GIMP Weighting Function

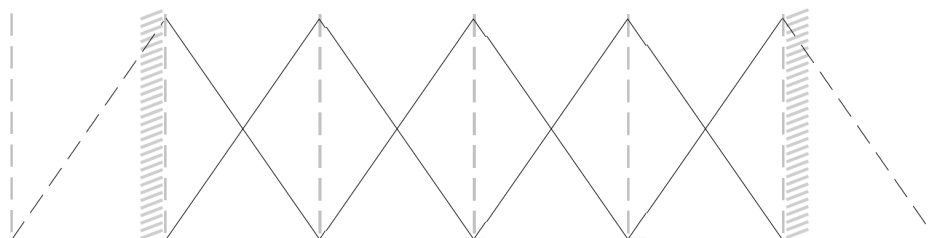


GIMP Gradient Weighting Function

(a) Example GIMP weighting function  $\bar{\phi}_{ip}$ , and gradient weighting function  $\nabla \bar{\phi}_{ip}$  centered at 0 using piecewise linear grid basis functions and piecewise constant particle characteristic functions  $\chi_p$ . Dotted lines denote breaks in the continuity of the functions.



(b) GIMP



(c) Piecewise-Linear

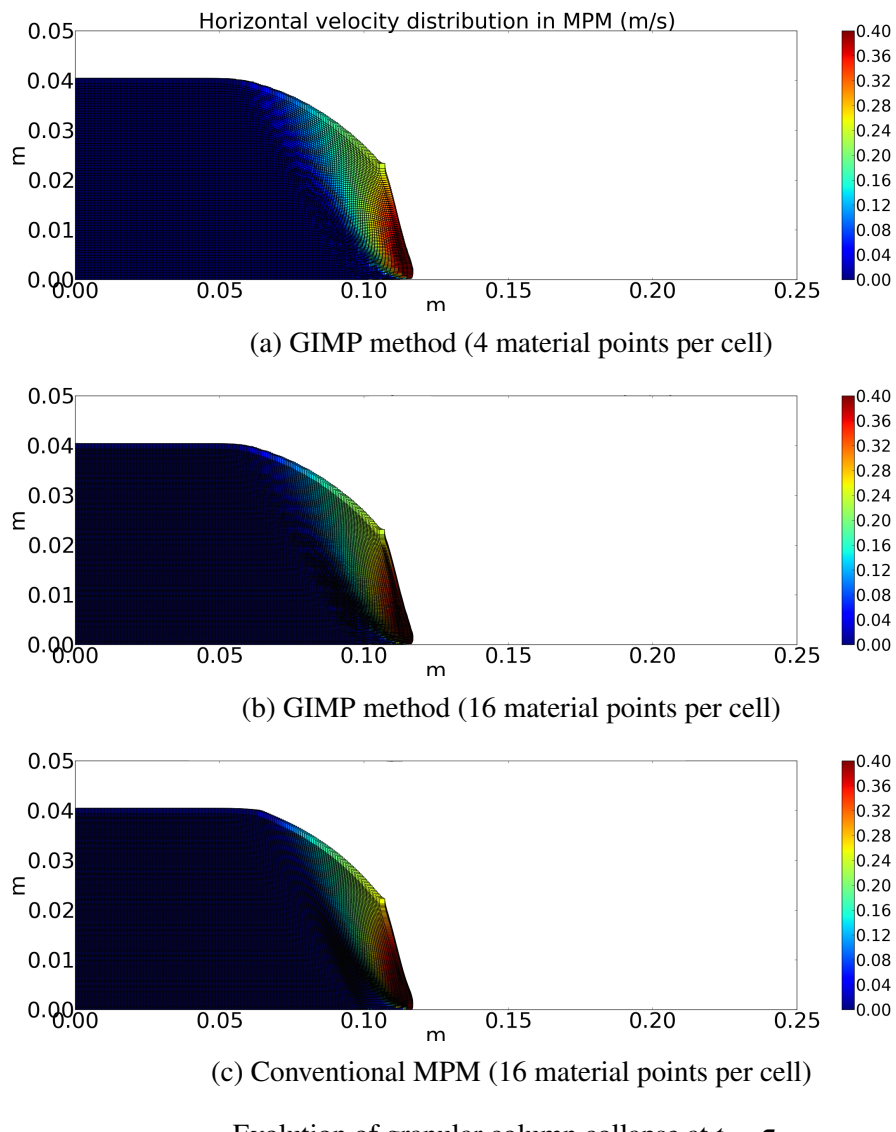
Figure 3.11 Schematic view of 1-D basis functions used in MPM (Steffen et al., 2008).

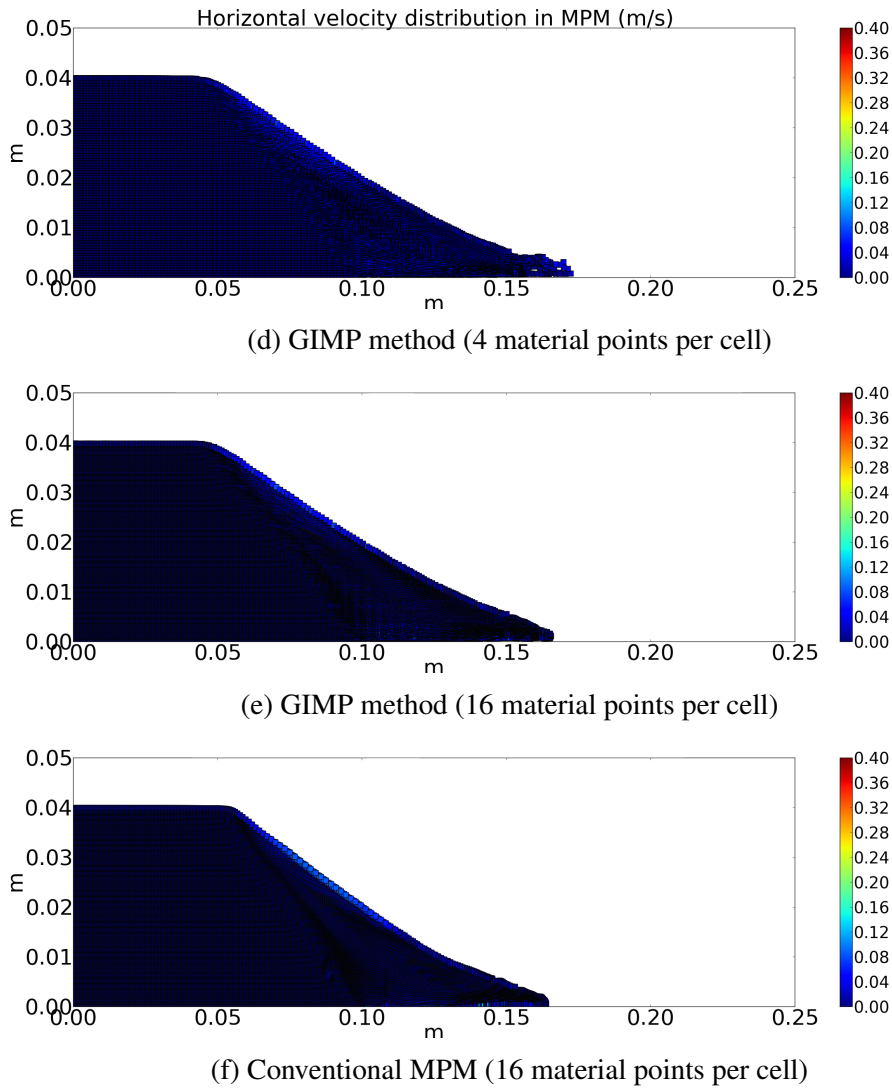
of the solution, simulation using 4 material points per cell with GIMP is also performed. The granular collapse experiment is performed for a column with an initial aspect ratio of 0.4 using both GIMP method and MPM with 16 material points per cell.

The evolution of run-out at time  $t = \tau_c$  and  $t = 6\tau_c$ , where  $\tau_c$  is the critical time when the potential energy is fully mobilised, are presented in figure 3.12. At the initial stage of collapse  $t = \tau_c$ , both MPM and GIMP give almost the same behaviour. The run-out observed in the case of 4 material points per cell is similar to the run-out behaviour for 16 material points per cell. At the end of the flow, GIMP with 4 material points show oscillations at the flow front due to fewer material points in a cell. However, both MPM and GIMP show a more smoother response at the flow front. The evolution of run-out and height with time for both MPM and GIMP are presented in figure 3.13. For a time up to  $t = 1.5\tau_c$  all approaches yield the exact same behaviour. However, as the flow progresses, the number of material points per cell at the flow front decreases and this results in oscillations. The oscillations with decrease in the number of material points can be seen in the case of 4 material points per cell. Hence, it is essential to have a larger number of material points, especially at the flow front. The difference in the normalised run-out between MPM and GIMP method is about 2.5%. This is due to the difference in the interpolation scheme adopted in both approaches. GIMP method offers a better approximation of the run-out behaviour as a result of the continuous basis function. This also results in a more smooth stress and velocity distribution in GIMP than MPM. With increase in the number of material points and the use of finer mesh size decrease the difference between both approaches. The computational effort using GIMP method is almost twice that of MPM, since GIMP method considers the particles at neighbouring cells due to the larger spread of the basis functions. In the present study, a very fine mesh and 16 material points per cell are used to simulate large deformation problems.

### 3.3.7 Application of MPM in geomechanics

The studies on using the material point method in modelling geotechnical problems are limited. The potential of Material Point Method in modelling granular flows, discharge of silos, was first recognised by Wieckowski et al. (1999). Bardenhagen et al. (2001) developed a frictional contact algorithm to model granular materials. The Mohr-Coloumb is used to describe the kinematics of the grains. In this model, a contact is defined when the nodal velocity interpolated from all material points in the cell differs from the nodal velocity interpolated from a single material point. Coetzee et al. (2005) applied this contact algorithm to understand the pull-out behaviour of anchors. Ma et al. (2014) developed a new contact algorithm with a penalty contact function and a limited maximum shear stress for soil-structure interaction, i.e, interaction of pipe-line with debris flow or submarine landslide.





$$t = 6\tau_c$$

Figure 3.12 Comparison between GIMP method and conventional MPM on the flow morphology of a granular column collapse ( $a = 0.4$ ).

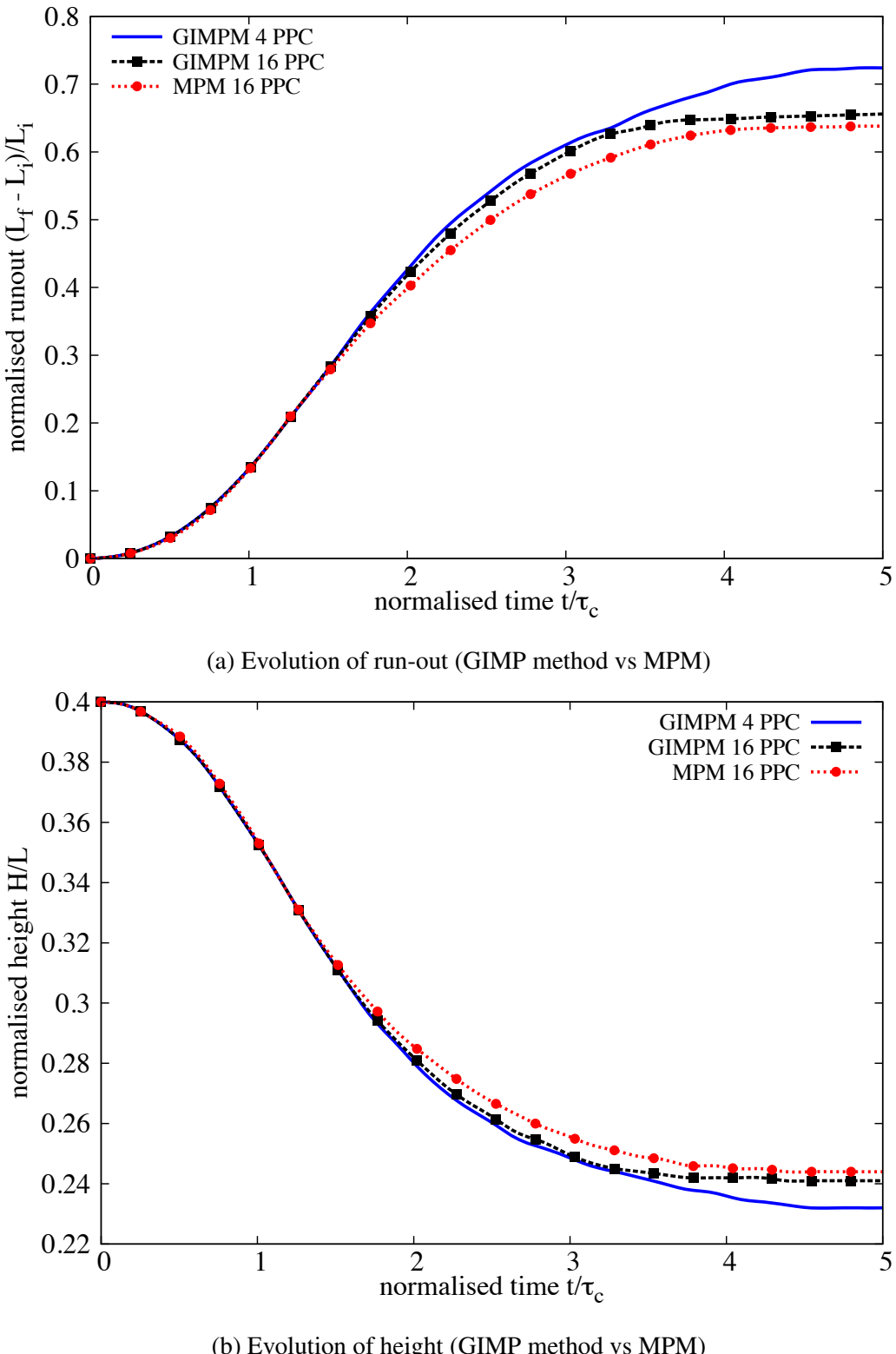


Figure 3.13 Comparison between GIMP method and conventional MPM on the evolution of run-out and height with time for a granular column collapse ( $a = 0.4$ ).

The penalty contact function behaves similar to numerical damping and thus reduces the oscillations during the impact.

Beuth et al. (2010) applied Gaussian integration in quasi-static MPM to model large strain problems. However in this approach, the conservation mass is not valid as a larger filled volume of material is considered. Andersen and Andersen (2010) used GIMP method with an elasto-plastic model to simulate slope failures. The solution is found to be dependant on the number of material points used to describe the slope geometry. Mast et al. (2014a) studied the behaviour of granular column collapse using a non-associative flow rule. They observed a significant increase in the run-out distance for large aspect ratio columns. Mast et al. (2014b) investigated the suitability of Material Point Method is realistic prediction of large deformation problems such as snow avalanches.

Guilkey et al. (2007) developed a coupled numerical scheme for fluid-structure interaction. The solid field is modelled in a Lagrangian frame, while an Eulerian frame, compressible CFD, is used for the fluid. As MPM computation grid is reset at every stage, the same Eulerian grid is adopted for both the solid and the fluid. Similar approach was adopted by Zhang et al. (2008) to model multiphase flows, where the interactions between the solid and gas are modelled using MPM background mesh as an Eulerian grid. Mackenzie-Helnwein et al. (2010) investigated various techniques to model multiphase drag forces. Both solid and the fluid are modelled as Lagrangian particles using the mixture theory. Abe et al. (2013) developed a soil–pore fluid coupled MPM algorithm based on Biot’s mixture theory for solving hydro-mechanical interaction problems. Bandara (2013) developed a unique approach in modelling solid-fluid interactions. Two sets of Lagrangian particles are used to represent soil skeleton and pore water, separately. Bandara (2013) applied the coupled MPM to solve large deformation problems such as slope failure due to seepage.

In the present study, the Material Point Method is used to model large deformation problems, such as collapse of dry columns and soil slopes subjected to impact loading. The suitability of continuum approach (MPM) in modelling large deformation problems is also investigated.

### **3.4 Particulate modelling of granular flows**

Granular materials often exhibit different behaviour under different circumstances. Fluidized granular material often resembles a liquid, and reveals surface waves. In certain situations, granular materials behave more like a solid exhibiting plastic deformations. Despite the wide variations in the physical and the chemical properties of the grains, the discrete granular struc-

ture has a rich generic phenomenology, which motivates us to understand the fundamental behaviour of these materials.

A granular material can be considered as a continuous material if it is viewed at a macroscopic scale, ignoring the fact that it is composed of grains. On a macroscopic scale, the behaviour of the granular material could be approximately defined using continuum mechanics. However, on a grain level, the granular materials exhibit complex solid-like and/or fluid like behaviour depending on the way the grains interact with each other. The analytical and finite element models, which consider granular materials as a continuum cannot take into account the local geometrical processes that govern the mechanical behaviour of a non-homogeneous soil. The application of continuum models to describe the granular flow poses subtle problems for statistical analysis (Mehta and Barker, 1994). The grain level description of the granular material enriches the macro-scale variables, which poorly account for the local rheology of the materials.

Numerical models such as the Discrete Element approach proposed by Cundall and Strack (1979) are capable of simulating the granular material as a discontinuous system. Although, modern measurement techniques can probe into the local granular variables, like grain position, velocities, contact forces, etc., they have inherent limitations in acquiring those variables. The *discrete-element* approach is a powerful and a reliable research tool to study the behaviour of granular materials at the grain-scale. This approach involves applying Newton's equation of motion simultaneously to all grains described as rigid solid bodies by considering the contact forces and the external forces acting on the grains. For a given boundary condition, the collective mechanical response of grains to the external force leads to the relative motion between grains constrained in a dense state and/or by in-elastic collisions in the loose state. Cundall and Strack (1979) applied this method to granular geomaterials, and called it the *Distinct Element Method*, to differentiate from the existing *Finite Element Method* used in geomechanics. The attribute "distinct" refers to the degrees of freedom of individual grains, but it was later replaced by "discrete" to underline the discrete nature of the system.

The interactions between the individual grains are governed by unilateral contact laws, and the mechanism of energy dissipation is through friction and inelastic collisions. Moreover, granular materials have a wide variation in their grain shape and size distribution that require appropriate numerical treatments. In DEM, the normal reaction force, which prevents the interpenetration of two grains is proportional to the depth of penetration. Thus, frictional contact between grains can be expressed as a function of the configuration variables, which describe the positions and velocities of the grains (Radjai and Dubois, 2011).

Discrete-Element methods, which describe interactions between grains based on the explicit overlap between the grains are termed as *smooth methods*. Another approach is the *non-smooth approach* (Jean, 1999), which describes the behaviour of discrete elements using the main features of uni-laterality and Coulomb friction, and by neglecting the finer details such as interpenetration and overlap between grains. The fundamental difference between the non-smooth method and the common discrete element method lies in the treatment of small length and time scales involved in the dynamics of granular media. In DEM, the grains are treated as rigid bodies but the contacts between grains are assumed to obey the visco-elastic constitutive law. The time-stepping schemes used for the numerical integration of the equations of motion in DEM, imply that the contact interactions involve smaller time and length scales. In the non-smooth Contact Dynamics (CD) method, these small scales are neglected and their effects are absorbed into the contact laws. In non-smooth formulation, the grain dynamics is described at a larger scale than the elastic response time and displacement scales (Jean, 1999; Radjai and Richefeu, 2009).

DEM simulations can easily capture the complex flow mechanics of large-deformation problems than the continuum approach. Tang et al. (2009) used 2D discrete element modelling to understand the mechanism of the Tsaoling landslide triggered by the Chi-Chi earthquake. The authors were able to establish the landslide characteristics to have a low-friction coefficient (about 0.15) and a medium strength. They were also able to back-calculate a maximum velocity of sliding reached 50 m/s. Similarly, Tang et al. (2013) performed 3D discrete-element simulations to understand the transportation and deposition of the 2009 Hsiaolin landslide. The authors estimated the friction coefficient of landslide-mass to have reached a critical value of 0.1, at which the mass begins to slide and reach a maximum velocity of 40 - 50 m/s. Two-dimensional DEM simulations have been used to analyse the temporal and spatial evolution of slope failure and landslides from the intact, pre-failure slope to the restabilised, post-failure slope composed of bonded material (Katz et al., 2014). The pre-failure slope material disintegration is found to be the fundamental element in determining the size and geometry of the resultant landslides. Liu and Koyi (2013) studied the kinematics and internal deformation of granular slopes, which experience flow-like behaviour. They observed that the Dilatant grain-shearing flow to be the dominating mechanism in the movement of granular slopes. DEM is capable of probing the material response in a detailed scale, where conventional experiments or field tests are not feasible. Hence, in the present study, 2D discrete element simulations are performed to understand the behaviour of granular flows.

## 3.5 Discrete Element Method

Discrete Element Method computes the equilibrium and the trajectories of a classical multi-body system. The Discrete Element Method is a simple and flexible discrete-element approach, which involves applying Newton's second law of motion to each grain to describe the deformation of the granular assembly.

$$m_i \frac{d^2 x_i}{dt^2} = \mathbf{F}_i, (i = 1, \dots, N), \quad (3.28)$$

where  $N$  is the number of grains in the simulation,  $m_i$  is the mass of a grain  $i$ ,  $x_i$  is its position, and  $\mathbf{F}_i$  is the force exerted on grain. The method consists of calculating the forces  $\mathbf{F}_i$  and then solving the ordinary differential in eq. 3.28. In general the system of coupled non-linear differential equations cannot be solved analytically. The approximate numerical solution of these equations, which describes the trajectories of all the grains of the system is called as Discrete Element Method.

DEM simulations are identical to the real experiments, this involve generation of samples (initial conditions) with  $N$  grains and solving the Newton's equation of motion for the system until the properties of the system no longer change with time (equilibration of the system). After equilibration, the actual analysis is performed.

The computation of the forces and torques is the central part of the Discrete Element Method simulation. The dynamics of the granular material is governed by Newton's equation of motion which depends on the centre-of-mass coordinates and the Euler angles of the grains  $i$  ( $i = 1, 2, \dots, N$ ):

$$\frac{\partial^2 \vec{r}_i}{\partial t^2} = \frac{1}{m_i} \vec{\mathbf{F}}_i(\vec{r}_j, \vec{v}_j, \vec{\varphi}_j, \vec{\omega}_j), \quad (3.29)$$

$$\frac{\partial^2 \vec{\varphi}_i}{\partial t^2} = \frac{1}{\hat{J}_i} \vec{\mathbf{M}}_i(\vec{r}_j, \vec{v}_j, \vec{\varphi}_j, \vec{\omega}_j), (j = 1, \dots, N). \quad (3.30)$$

The force  $\vec{\mathbf{F}}_i$  and the torque  $\vec{\mathbf{M}}_i$ , which act on grain  $i$  of mass  $m_i$  and the tensorial moment of inertia  $\hat{J}_i$  are (sometimes complicated) functions of the grain positions  $\vec{r}_j$ , their angular orientations  $\vec{\varphi}_j$ , and their corresponding velocities  $\vec{v}_j$  and  $\vec{\omega}_j$ . In a two-dimensional system, the angular orientation of a grain is described by a single (scalar) quantity  $\varphi_i$  and the moment of inertia reduces to a scalar value  $J_i$ .

For granular grains in the absence of long range fields, the force  $\vec{\mathbf{F}}_i$  and the torque  $\vec{\mathbf{M}}_i$  acting upon the grain  $i$  are given as sum of the pairwise interaction of grain  $i$  with all other

grains in the system:

$$\vec{\mathbf{F}}_i = \sum_{j=1, j \neq i}^N \vec{\mathbf{F}}_{ij}, \quad \vec{\mathbf{M}}_i = \sum_{j=1, j \neq i}^N \vec{\mathbf{M}}_{ij}. \quad (3.31)$$

The limitation to pairwise interaction is an abstraction, which is justified if the grains deformation at the contact is trivial. To describe the deformation of granular assemblies one has to take into account the effect of multi-grain interactions. This method is general and can be applied to a wide range of systems. The Discrete Element Method can be used to study the behaviour of grains in rapid flows to static assemblies. The method treats both the conditions in exactly the same way, it is not necessary to divide the system and then treat each condition differently. The simplest model for granular grain is a sphere. In a two-dimensions case, the sphere is reduced to a circular disk. Simulations using spherical grains are numerically very effective since grain collisions can be easily identified and described in a simple way (Poschel and Schwager, 2005).

### 3.5.1 The Forces

The force  $\mathbf{F}_i$  in eq. 3.28 represents both the grain to grain interaction force, and other external forces acting on the system. Therefore, the force  $\mathbf{F}_i$  is expressed as

$$\mathbf{F}_i = \sum_{j \neq 1} \mathbf{F}_{ij} + \mathbf{F}_{ext,i}, \quad (3.32)$$

where  $\mathbf{F}_i$  is the force exerted by grain  $j$  on  $i$ . The external force  $\mathbf{F}_{ext,i}$  is most often the force of gravity,  $\mathbf{F}_{ext,i} = m_i \mathbf{g}_i$ . The methodology to incorporate any other external forces in the simulation is the same. However, the computation of the interaction forces depends on the numerical method adopted in the study. The methodology used in the present study is described below.

Let us consider two grains  $i$  and  $j$ , in contact (figure 3.14). The contact force can be decomposed into two components, as the normal ( $F_n$ ) and the tangential ( $F_t$ ) components

$$\mathbf{F}_{ij} = F_n \mathbf{n} + F_t \mathbf{t}. \quad (3.33)$$

where  $\mathbf{n}$  and  $\mathbf{t}$  are unit vectors, pointing in the normal and the tangential directions. The procedure adopted to calculate the normal and tangential forces are discussed.

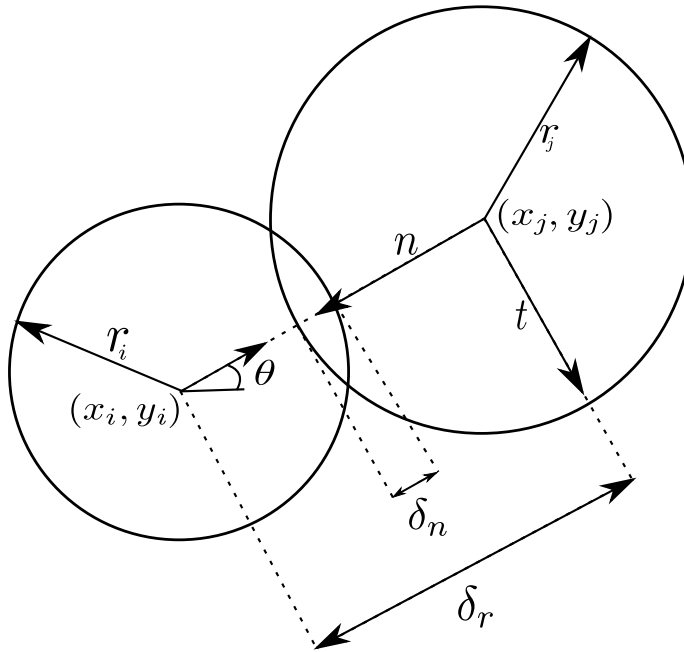


Figure 3.14 Grains *i* and *j* in contact, and the separation  $\delta_n$  is used to calculate the normal force

### Normal force

When grains collide, part of the kinetic energy is dissipated as heat and the other part causes deformation of the grain. These deformations generate interaction forces. The grains are considered to be rigid while their contact is assumed to be soft. Thus, the grains do not change their shape, instead they overlap. The shapes of the grains are conserved on an average, after many collisions. The overlap at the contact is limited to very small deformations, which are achieved by defining a repulsive normal force that opposes the overlap. The mutual compression ( $\delta_n$ ) of the grains *i* and *j* is defined as

$$\delta_n = |x_i - x_j| - r_i - r_j, \quad (3.34)$$

where  $x_i$  and  $x_j$  are the centres of the grains and  $r_i$  and  $r_j$  are their radii (figure 3.14). When  $\delta_n > 0$ , the two grains are not in contact, and there is no interaction. When  $\delta_n < 0$ , the two grains overlap, and there is a repulsive normal force that pushes the two grains apart. The simplest model is to consider the contact as a linear spring with damping. The repulsive force depends linearly on  $\delta_n$ , and is controlled by the stiffness of the grain. The energy dissipation due to the interaction between grains is an intrinsic characteristic of the granular material and is incorporated by adding a damping force that opposes the relative velocity for the duration of the contact. The interaction force at the contact is idealized as a simple spring-dashpot

system, with elastic and dissipative constants (Luding et al., 1994).

$$F_n = \begin{cases} 0, & \delta_n > 0 \\ -k_n \delta_n - \gamma_n \frac{d\delta_n}{dt}, & \delta_n < 0 \end{cases} \quad (3.35)$$

The constant  $k_n$  characterises the stiffness of the grain, and must be chosen sufficiently large so that the overlap between the grains remain small. Nevertheless, the solution has an undesirable property of generating an attractive force (Poschel and Schwager, 2005). It arises just before the two grains separate. In this case, we have  $d\delta_n/dt > 0$  while  $\delta_n$  approaches zero. To avoid the attractive force, the force is computed in two stages: a candidate force  $\hat{F}_n$  is calculated, and verified whether it is non-negative

$$\hat{F}_n = -k_n \delta_n - \gamma_n \frac{d\delta_n}{dt}, \quad F_n = \begin{cases} 0, & \hat{F} \leq 0 \\ \hat{F}_n, & \hat{F} > 0 \end{cases} \quad (3.36)$$

For pairwise collisions, the normal force ( $F_n$ ) represented as  $k_n \delta_n + \gamma_n$  causes a decrease in the relative normal velocity of the grains by a factor  $\epsilon$ . This factor is the *coefficient of restitution*, and is defined as  $\epsilon \approx g'/g$ , where  $g$  is the absolute normal relative velocity before the collision and  $g'$  corresponds to the post-collision value. The relative velocity,  $d\delta_n/dt > 0$ , can be obtained by differentiating eq. 3.34. Thus we obtain

$$\frac{d\delta_n}{dt} = (\mathbf{v}_i - \mathbf{v}_j) \cdot \mathbf{n}, \quad (3.37)$$

where  $\mathbf{v}_i = dx_i/dt$  is the velocity of grain  $i$  and  $\mathbf{v}_j = dx_j/dt$  is the velocity of grain  $j$ . The numerical integration of eq. 3.37 yields the separation  $\delta_n$  and permits us to generalise the model and treat the tangential forces as well, as explained in the next section. By integrating Newton's equation of motion it is found that the linear force corresponds to the co-efficient of restitution, which is defined as

$$\epsilon = \exp\left(-\frac{\pi \gamma_n}{2m^{eff}} / \sqrt{\frac{Y}{m^{eff}} - \frac{\gamma^2}{2m^{eff}}}\right). \quad (3.38)$$

### Tangential force

Grains are not perfect spheres, but have a complicated surface texture, therefore at oblique collisions, besides the normal force there is a tangential force too. Even perfectly smooth spheres exert a tangential force due to their bulk viscosity (Poschel and Schwager, 2005). To build a heap of spheres on a flat surface, the grains as well as the surface have to be

sufficiently rough, indicating the dependence of the tangential force on the surface properties of the granular materials. For realistic simulation of granular materials, it is important to consider the tangential force in DEM. The tangential force is considered in a similar fashion as the normal force, arising from a spring stretched by the relative motion of the grain. Tangential forces are modelled by considering the relevant relative tangential velocity of the grain surfaces at the point of contact. The point of contact is an approximation, as the description of the normal force assumes a compression  $\delta_n$ , which implies a contact surface in 3-D or a contact line in 2-D. Assuming a tangential spring of length  $\delta_t$  exerts an opposing force to the relative tangential displacements (ignoring the effect of relative rolling between the grains), the tangential force can be postulated similar to the normal force (eq. 3.37) as

$$\frac{d\delta_t}{dt} = (\mathbf{v}_i - \mathbf{v}_i) \cdot \mathbf{t}. \quad (3.39)$$

This equation must also be numerically integrated, just like eq. 3.28. The grains are in contact when  $\delta_t < 0$ , and when  $\delta_t = 0$ , the grains no longer exert a force on each other. With these assumptions,  $\delta_t$  can be calculated similar to the normal force. The tangential force is assumed to be governed by Coulomb's friction law.

$$|F_t| \leq \mu F_n, \quad (3.40)$$

where  $F_t$  is the tangential force and  $\mu$  is the friction coefficient. It is therefore necessary to constrain the tangential force to remain less than or equal to  $\mu F_n$ . To impose the condition in eq. 3.40, two-stages similar to the normal force computation is adopted. The first step is to evaluate the candidate force, and is then accepted if it obeys the condition in eq. 3.40.

$$\hat{F}_t = -k_t \delta_t - \gamma_t \frac{d\delta_t}{dt}, \quad F_t = \begin{cases} \text{sgn}(F_t), & |\hat{F}| \geq \mu F_n \\ \hat{F}_t, & |\hat{F}| < \mu F_n \end{cases} \quad (3.41)$$

where  $k_t$  is the stiffness of the tangential spring and  $\gamma_t$  is the damping constant. If  $|F_t| = \mu F_n$ , the contact is sliding, otherwise, it is non-sliding. It can be noted that the normal force (eq. 3.36) and the tangential force (eq. 3.41) are handled in the same way in DEM. When the grains slide against each other, they do not retain any memory of their initial position, and hence do not return to its original position. In order to model this behaviour, a limiting value of  $\delta_t$  is imposed. When the contact slides  $\delta_t = \pm \mu F_n / k_t$  is imposed.

In addition to sliding, the grains can roll relative to one another about their centre of mass due to the tangential force acting at their contact surface. In this case,  $d\delta_t/dt = 0$ . It is important to assume that the grains touch at a single point instead of overlapping, i.e.  $\delta_n = 0$ .

This point is located at  $x_i - r_i \mathbf{n} = x_j + r_j \mathbf{n}$ . If we consider that this point belongs to grain  $i$ , its velocity is  $v_i + r_i(\boldsymbol{\omega} \times \mathbf{n})$ . If it belongs to grain  $j$ , its velocity is  $v_j + r_j(\boldsymbol{\omega} \times \mathbf{n})$ . The relative velocity is the difference between these two velocities.

$$\frac{d\delta_t}{dt} = (\mathbf{v}_i - \mathbf{v}_j) \cdot \mathbf{t} - (r_i \boldsymbol{\omega}_i + r_j \boldsymbol{\omega}_j) \times \mathbf{n}. \quad (3.42)$$

It should be noted that the eq. 3.42 is only an approximation, as the grains in DEM do not touch at points, but overlap. It is therefore an approximation that produces an error of order  $O(\delta_n/r)$  (Radjai and Dubois, 2011). It is assumed that the contact forces are exerted at the point of contact. It implies that the tangential force is accompanied by torque acting on two grains. If the overlap is zero, these torques are

$$\tau_{ij} = -(a_i \mathbf{n}) \times (F_t \mathbf{t}), \quad (3.43)$$

$$\tau_{ji} = -(a_j \mathbf{n}) \times (F_t \mathbf{t}). \quad (3.44)$$

The torques modify the angular velocities of the grains. It is therefore necessary to incorporate the equation for the angular coordinates of the grains in eq. 3.28

$$I_j \frac{d\boldsymbol{\omega}_i}{dt} = \sum_{j \neq i} \tau_{ij}, \quad (3.45)$$

where  $I_j$  is the moment of inertia of grain  $j$ . The eq. 3.44 is only valid when  $\delta_n = 0$ . The torque is a vector product of the force and its lever arm. It is assumed that the lever arms have lengths equal to  $r_i$  and  $r_j$ , which is true only when the grains do not overlap, hence in this case they produce an error of order  $O(\delta_n/r)$ . It is nevertheless desirable to damp this type of motion (Radjai and Dubois, 2011). A rolling resistance is adopted in order to model the shape effect of non-spherical grains, which accounts for moments arising from the fact that the line of action of the normal contact force in the case of non-spherical particles no longer passes through the centre of mass of the particles and hence generates rotational moments.

The interaction between two solid bodies is much more complex than that is described by the simple linear model. Nevertheless, the linear force law has several advantages. It is simple to implement, and its harmonic behaviour is well understood, which makes it easier to interpret the results. The most common non-linear interaction law is the Hertz law (Hertz, 1882). In certain situations, such as a quasi-static packing, a non-linear law can have significant influence on the acoustic properties, and on the global stiffness (Agnolin and Roux, 2007). However, in case of rapid granular flows, the interaction force between the

grains has almost no effect on the phenomenon, and a linear law can be used to describe this kind of behaviour (Radjai and Dubois, 2011).

### 3.5.2 Numerical algorithm and integration scheme

The efficiency of a DEM algorithm is mainly determined by its efficiency to compute the interaction forces between grains. If we consider a model system with pairwise interactions, we have to consider the contribution of the force on grain  $i$  due to all its neighbours. If we consider only the interaction between a grain and the nearest image of another grain, then for a system of  $N$  grains, we must evaluate  $N \times (N - 1)/2$  pair distances. Consider a system of 1000 grains, at every time step all possible pairs of grains have to be considered to compute the interaction forces, hence,  $N(N - 1)/2 \approx 500,000$  force computations are required. For short-range grain interactions, the majority of these force evaluations is unnecessary as the corresponding grains are located far apart and do not necessarily touch each other. For a dense system of equally sized grains, the grains can have contacts with not more than 6 grains, this reduces the number of force computation required to  $3N \approx 3000$ . In the preliminary force computation scheme, at least 166 times more pair interactions are considered than necessary. Therefore, the numerical methods employed in the DEM should try to minimize the computation of interaction forces (Poschel and Schwager, 2005). There are three different methods for the efficient computation of the forces, the *Verlet* algorithm, the *link-cell* algorithm, and a *lattice* algorithm. The *Verlet* algorithm described in Grubmuller et al. (1991) is implemented in the present study.

#### Verlet list algorithm

The Verlet list algorithm assumes a cut-off value, so that only neighbouring grains that contribute to the energy of a grain  $i$  are considered. It is advantageous to exclude the grains that do not interact in the memory expensive energy computation. Verlet (1967) developed a book-keeping technique, commonly referred to as the Verlet list or neighbour list, which is illustrated in 3.15. In this method a second cut-off radius  $r_v > r_c$  is introduced, and before the interactions are calculated, a list is made (the Verlet list) of all grains within a radius  $r_v$  of the grain  $i$ . In the subsequent calculations of the interactions, only those grains in this list will be considered. The idea of the Verlet algorithm is based on a simple property of grain dynamics: neighbourhood relation between grains can only change slowly, i.e. two grains which are close to each other at a given time step will remain as neighbours, at least in the following few time steps. During initialization the neighbourhood relations between the grains, i.e. the distance of all close pairs of grains are computed. Two grains are considered as neighbours if

the distance of their surface is smaller than a predefined distance *Verlet distance*

$$(|\vec{r}_i - \vec{r}_j| - R_i - R_j) < \text{Verlet distance}. \quad (3.46)$$

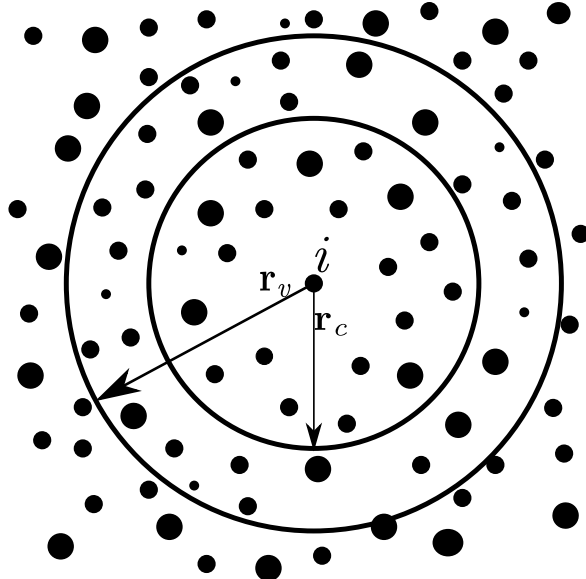


Figure 3.15 The Verlet list: a grain *i* interacts with those grains with the cut-off radius  $r_c$ , the Verlet list contains all the grains within a sphere with radius  $r_{v>r_c}$

For each grain there is a *Verlet list* in which the close neighbours are saved. To initialise the Verlet lists efficiently, a grid that covers the simulation area is defined. Its mesh size is larger than the largest grain. For construction of the lists only pairs whose grains reside in the same or adjacent grids are considered. This procedure guarantees the detection of all close pairs of grains (Poschel and Schwager, 2005). Redundancy in Verlet lists, i.e. if grain *i* is a neighbour of *j*, then grain *j* is a neighbour of *i*, are avoided by imposing a restriction on the list of grain *i* contains, such that it contains only neighbours with index  $j < i$ . For the computation of interaction forces, the Verlet list of grain *i* is scanned and only pairs which are recorded in one of the Verlet lists are considered. Hence, the Verlet list of each grain *i* is scanned and the interaction force of *i* with each entry *j* in its list is computed.

Initially to build the Verlet list, the grains are sorted into a grid of mesh size  $dx \times dy$ . For each grid there is a list of grains residing in the cell. During the simulation, the neighbourhood relation among the grains change, therefore, the Verlet lists have to be updated. The decision to update a Verlet list depends on how far the grains have travelled since the time when the present list was built. The Verlet list of a grain *i* must contain at any time all neighbours *j* with  $j < i$ . This assures that two grains *i* and *j* never touch and are not considered as neighbours,

i.e.  $j$  is not in the list of  $i$  and  $i$  is not in the list of  $j$ . Hence,

$$|\vec{r}_i - \vec{r}_j| - R_i - R_j > 0. \quad (3.47)$$

The above condition is required for all pairs  $(i,j)$  of grains which are *not* known as neighbours. This condition is a criterion to update the Verlet lists (Poschel and Schwager, 2005). Assume at the instant when the Verlet lists are constructed, the surfaces of the grains have the distance  $|\vec{r}_i - \vec{r}_j| - R_i - R_j >$  Verlet distance, i.e. they are not classified as neighbours. If the Verlet lists are updated before one of these grains has travelled the distance  $\text{Verlet distance}/2$  since the lists were constructed, they can never collide without being recognized as neighbours first. This is explained in figure 3.16. The impact of optimisation of the Verlet list algorithm has negligible effect on the computation time, as the algorithm is quite efficient already and only consumes a few percent of the total computation time in construction of the Verlet lists. The implementation of the Verlet list algorithm in force computation drastically reduces the computation time in comparison to the linear algorithm. The performance of the Verlet list algorithm is controlled by two crucial parameters: the number of cells  $N_c$ , for the construction of the Verlet lists and the Verlet distance  $r_v$  (Poschel and Schwager, 2005).

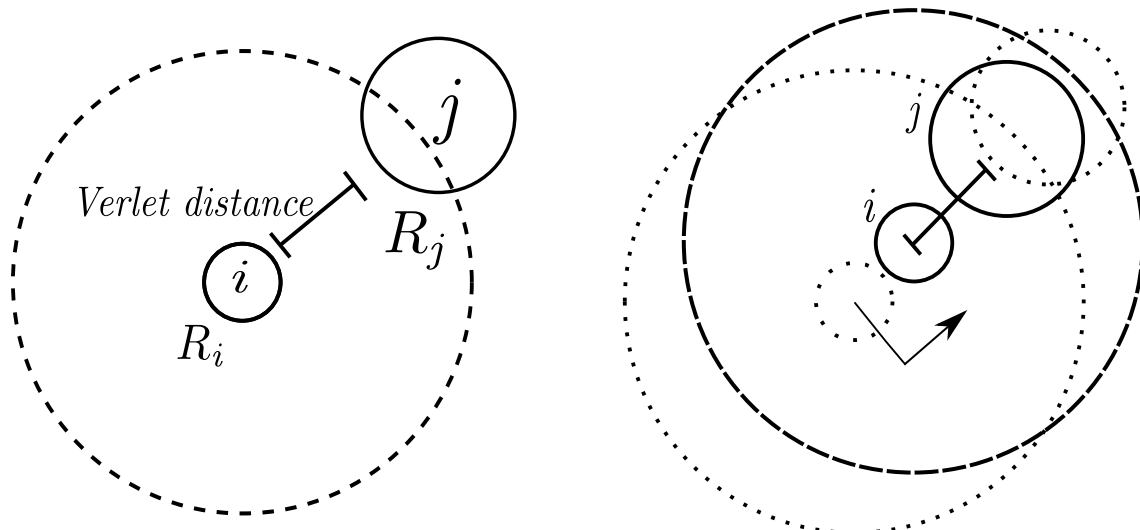


Figure 3.16 Checking the validity of Verlet lists. *Left:* the grains  $i$  and  $j$  are not recognized as neighbours since the distance of their surface is larger than the Verlet distance. The radius of the dashed circle is  $R_i + R_{max} + \text{Verlet distance}$ . *Right:* in the most unfortunate case the grains approach each other directly, travelling at the same velocity. As soon as one of the grains has travelled the distance  $\text{Verlet distance}/2$  (arrows), the Verlet lists have to be rebuilt. The grains  $i$  and  $j$  are now recognized as neighbours. Redrawn after Poschel and Schwager (2005).

### Leap frog or Verlet integration algorithm

Discrete Element Method involves numerically solving Newton's equation of motion eq. 3.28, which is an ordinary differential equation. Choosing an integration algorithm is important, as the forces are not always differentiable in time, and the temporary derivative of the force is discontinuous when the contact splits. It is also very essential to numerically integrate eq. 3.42 with the same precision as eq. 3.28. At first, computational speed seems important. It is usually not very relevant because the fraction of time spent on integrating the equation of motions (as opposed to computing the interactions) is small. Accuracy for large time steps is more important, because the larger the time step that we can use, the fewer evaluation of the forces are needed per unit of simulation time. Hence, this would suggest that it is advantageous to use a sophisticated algorithm that allows use of larger time step.

Algorithms that allow the use of large time steps, achieve this by storing information on increasingly higher-order derivatives of the grain coordinates. Consequently, they tend to require more memory storage. However, the most important aspect to consider is the energy conservation. It is important to distinguish between two kinds of energy conservation: the short time and long time. The sophisticated higher-order algorithms tend to have very good energy conservation at short times. However, they often have undesirable feature that results in drifting of the overall energy for longer times. In contrast, the Verlet style algorithms tend to have only moderate short term energy conservation, but little long-term drift (Frenkel and Smit, 1996). In this case, such algorithms are not useful. They are more complicated to program, and do not yield a more precise solution (Radjai and Dubois, 2011). It might seem important to have an algorithm that accurately predicts the trajectories of all grains for both short and long durations, however no such algorithm exists.

In certain cases, two trajectories that are initially very close may diverge exponentially as time progresses. Any integration error, however small it may be, would always diverge the predicted trajectory exponentially from the true trajectory. This phenomenon is called the Lyapunov instability, and it poses a serious threat to the whole idea of Discrete Element Method simulation. However, this problem might not be serious (Frenkel and Smit, 1996). The aim of DEM is not to predict precisely what will happen to a system, but to predict the average behaviour of the system that is prepared in an initial state about which we know something (initial position, velocity and energy), but not everything. Hence, DEM differs from other methods, which are used to predict the trajectories. However, considerable numerical evidence suggest that the shadow orbits exists, which is a true trajectory of a multi-body system that closely follows the numerical trajectory for a time that is longer in comparison with the time that is required for the Lyapunov instability to develop (Frenkel and Smit, 1996).

Newton's equations of motion are time reversible, and so should be the integration algorithm. The “leapfrog” algorithm or the Verlet integration algorithm is a numerical scheme used to integrate the Newton's equation of motion to calculate the trajectories of grains and is implemented in DEM by Verlet (1967). Verlet algorithm is fast and requires less storage memory, it is not particularly accurate for long time steps, and hence, we should expect to compute the forces on all grains rather frequently. Its short-term energy conservation is fair (in versions that use more accurate expression for velocity), but most importantly it exhibits little long-term energy drifts. This is related to the fact that the Verlet algorithm is time reversible and area preserving, however, it does not conserve the total energy of the system exactly (Frenkel and Smit, 1996). Verlet algorithm is simply based on a truncated Taylor expansion of grain co-ordinates.

$$t(t + \Delta t) = rt + \mathbf{v}(t)\Delta t + \frac{f(t)}{2m}\Delta t^2 + \dots \quad (3.48)$$

If we truncate this expansion beyond the term  $\Delta t^2$ , we obtain the Euler's algorithm, which looks similar to the Verlet Algorithm, but it does not preserve energy and have significant energy drifts. The simplest among the Verlet schemes is the *Leap frog algorithm*, which evaluates the velocities at half-integer time steps and uses these velocities to compute the new positions. The position of each grain is calculated at time  $t = 0, \Delta t, 2\Delta t, \dots$ , where  $\Delta t$  is the time step. On the other hand, their velocities are calculated at intermediate times, that is, at  $t = \Delta t/2, 3\Delta t/2, \dots$ . Let the position of a grain at time  $t = k\Delta t$  be written as  $x_k$ , and its velocity at time  $t = \Delta t(k + 1/2)$  be written  $\mathbf{v}_{k+1/2}$ , and its acceleration at  $t = k\Delta t$  be  $\mathbf{a}_k$ . Then the following equation is used to advance systematically

$$\mathbf{v}_{k+1/2} = \mathbf{v}_{k-1/2} + \mathbf{a}_k \Delta t, \quad (3.49)$$

$$x_{k+1} = x_k + \mathbf{v}_{k+1/2} \Delta t \quad (3.50)$$

This algorithm determines the new grain position with an error of order  $O(\Delta t^4)$ . But eq. 3.49 hides a difficulty in the application of this algorithm to granular materials (Radjaï and Dubois, 2011). The problem is that the acceleration must be calculated at time  $t = k\Delta t$ . But the velocities are known at  $t = (k - 1/2)\Delta t$ , and not at  $t = k\Delta t$ . One way to get around this problem is to write

$$\mathbf{v}_k = \mathbf{v}_{k-1/2} + \mathbf{a}_{k-1} \Delta t / 2. \quad (3.51)$$

The equation uses the acceleration of the preceding time step to estimate the velocity. This approximation does not diminish the order of the algorithm. eq. 3.51 estimates  $\mathbf{v}_k$  with an error of order  $O(\Delta t^2)$ , which produces an error of the same order in the calculation of the

force in eq. 3.49. But this causes only an error of order  $\mathbf{O}(\Delta t^3)$  in the velocity and an error of order  $\mathbf{O}(\Delta t^4)$  in the position. However, this problem does not exist in energy conservation systems, because the computed forces do not depend on the velocities of the grains. The heaviest computational task is the evaluation of forces and not the integration of equations. The Verlet integration scheme is summarized in eq. 3.52 and figure 3.17. To calculate the forces and acceleration, it requires the positions and velocities at time  $t$ :

$$\begin{aligned}\mathbf{v}(t + \Delta t/2) &= \mathbf{v}(t - \Delta t/2) + \mathbf{a}(t)\Delta t, \\ x(t + \Delta t) &= x(t) + \mathbf{v}(t + \Delta t/2)\Delta t, \\ \mathbf{v}(t) &= \mathbf{v}(t - \Delta t/2) + \mathbf{a}(t - \Delta t)\Delta t/2.\end{aligned}\quad (3.52)$$

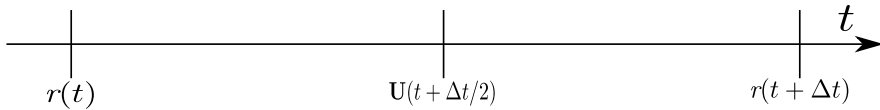


Figure 3.17 Verlet integration scheme

The analysis of the Discrete Element Method formulation reveals that the linear force law gives the model a harmonic character, showing that it is very closely related to simple models widely used in physics and mechanics. The shortest time scales often arise from the oscillations of one or two grains. The integration algorithm must resolve these movements with sufficient precision. Thus, the time steps used must be smaller than these time scales, the most rapid frequency is usually  $\omega_N$ , the characteristic oscillation frequency of very short waves. This frequency is proportional to  $\omega_0$ , which is easier to estimate. Therefore, it is essential to choose a time step  $\Delta t \approx \epsilon/\omega_0$ , where  $\epsilon$  is a constant that depends on the integration algorithm. Values such as  $\epsilon \approx 0.01$  are often a reasonable choice (Radjai and Dubois, 2011). In the case of rapid granular flows, the time step must be small enough so that the fastest grains move only by a small fraction of their size during one time step. The grains must be stiff enough so that violent collisions do not lead to large overlaps between grains.

### 3.5.3 Boundary conditions

In many cases, the dynamic and static properties of a granular system are substantially affected by the interaction of the granular material with the system boundaries, i.e. by the properties of the container or the surface on which the material is present. The effect of boundary conditions on the response of the granular assembly can be noticed in the convective motion of granular material in vibrating containers, the formation of density waves in pipes, the motion of granular material on conveyors, and the clogging of hoppers. In these and

many other cases, careful definition of the interaction between the granular material and the contact surface is essential. Of particular importance is the realistic modelling of the wall surface roughness. Unfortunately the mechanical interaction of a granular materials with a rough wall is poorly understood (Poschel and Schwager, 2005). A simple way to define the wall property is to build up the wall from grains, which obey the same rules of interaction as the grains of granular material. By varying the size and position of the wall grains, system boundaries of adjustable roughness can be described. However, the surface roughness that characterizes the frictional properties of the wall has to be arrived iteratively, and may not represent the real conditions. In the present case, a solid wall with corresponding stiffness, damping and frictional characteristics is introduced to model the interaction between grains and the wall. The interaction force is computed in a similar fashion to that of a pair of grains in contact and is divided into the normal and tangential components. The compression of the grain upon collision with the wall is calculated along the normal direction to the wall and the grain contact.

### **Periodic boundary**

The effect of a wall on the response of grains is very critical, especially in numerical simulation where the number of grains is relatively fewer in comparison to the experiments. The undesired effect of a wall can be eliminated using periodic boundary conditions, i.e. a periodic extension of the simulation area in one or more dimensions. Any grain leaving the system at one side is reintroduced at the opposite side, and correspondingly the interaction forces between grains at opposite sides of the simulation area are taken into account. In this framework, the simulation domain becomes a unit area containing grains with periodic copies paving the whole system. The periodic boundary conditions extend the system boundaries to infinity, so that the simulation cell simply plays the role of a coordinate system to locate grain positions 3.18.

The external stresses or displacements are applied on the simulation box by constraining the degrees of freedom of the wall, which are alternatively kept free or fixed depending on whether a stress or a displacement is monitored in a system. With periodic boundary conditions, this role is played by the collective degrees of freedom carried by the coordinate system, whose basis vectors become dynamic variables, and their conjugate stresses are expressed as a state function of the granular configuration (Parrinello and Rahman, 1980). In the case of granular systems, there is dissipation of energy during grain interactions. The kinematics, equation of dynamics, and the time-stepping schemes for DEM are discussed in detail in Radjai et al. (2011). The periodicity in position implemented in the present study is discussed below.

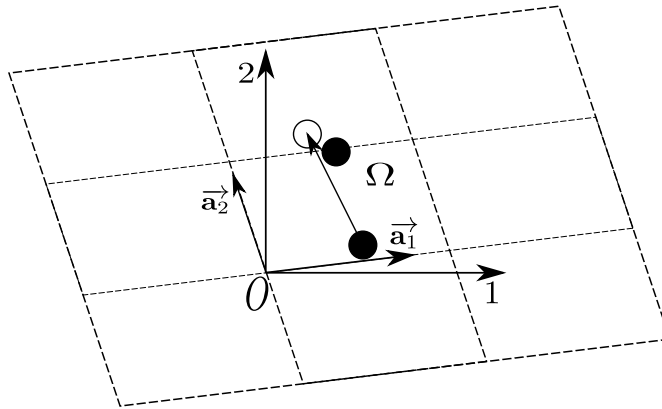


Figure 3.18 A 2D simulation cell  $\Omega$  with its basis vectors in an absolute frame. A grain located at the right boundary interacts with the image of another grain located at the left boundary.

Let us consider a collection of  $N_p$  grains with their centres contained in a cell of volume  $V$ . The cell can have any shape allowing for a periodic tessellation of space. The simplest shape is a parallelepiped i.e. parallelogram in 2D. The cell and its replicas define a regular lattice characterized by its basis vectors  $(\vec{a}_1, \vec{a}_2)$ . In the case of a parallelogram, the basis vectors may simply be the two sides of the parallelogram; figure 3.18. The origin  $O$  of the simulation cell is a vertex of the cell of coordinates  $(0, 0)$  and its replicas are defined by two indices  $(i_1, i_2)$  corresponding to a translation of the origin by the vector  $i_1 \vec{a}_1 + i_2 \vec{a}_2$ . Then, the coordinates  $\vec{r}(i)$  of the image  $i'$  of a grain  $i \in \Omega$  of coordinates  $\vec{r}(i')$  are given by:

$$\vec{r}(i') = \vec{r}(i) + \sum_{k=1}^2 i_k \vec{a}_k. \quad (3.53)$$

The grains belonging to the cell  $\Omega$ , characterized by  $i_1 = i_2 = 0$ , can interact with the grains of the same cell but also with image grains in the neighbouring cells characterized by  $i_k \in 1, -1$ . There are  $3^D - 1$  cells surrounding the simulation cell and they are involved in the search of contact partners for each grain. The distance between two grains  $i$  and  $j \in \Omega$  is the shortest distance separating  $i$  from  $j$  or from one of its images  $j'$ . As the system evolves in time, a grain  $i$  may leave but one of its images  $i'$  enters at the same moment. In order to keep all original grains in the cell, the status “original” should be reserved to the grains whose centres belongs to  $\Omega$ . Hence, whenever a grain  $i$  leaves the simulation cell, it becomes an image of  $i'$ , which then becomes the original. This means that a grain crossing a border of the simulation cell, returns to the cell by crossing another border.

### 3.5.4 Validation of DEM

It is essential to validate the developed DEM code. In the present study, a preliminary validation of the DEM code is performed by studying a ball rolling down an inclined plane. O’Sullivan et al. (2003) showed that the validation of DEM code using the above problem confirms the appropriate implementation of shear contact model in DEM. Theoretical solution for a ball rolling down an inclined plane is derived by Ke and Bray (1995). A disk is resting on a rigid inclined plane oriented at an angle  $\beta = 45^\circ$  to the horizontal plane (figure 3.19a). The disk has a radius  $r$  of 1m and a density of  $2650 \text{ kg/m}^3$ . The friction angle  $\phi$  between the disk and the rigid plane is varied. The disk rolls/slides down the plane due to gravity. The DEM solution for the sliding case ( $\phi = 0^\circ$ ) is compared with the theoretical solution by Ke and Bray (1995). The normal force, shear force, angular rotation, accelerations  $\ddot{a}$  and angular acceleration  $\ddot{\theta}$  are compared with the theoretical solution (table 3.1). The accumulation of disk rotation at time  $t = 0.2$  s versus the friction angle is presented in figure 3.19b. The angular rotation observed in the DEM matches the theoretical solution, which validates the shear contact model used in DEM. The DEM model implemented in the present study is further validated by comparing it with the granular column collapse simulations performed by Zenit (2005).

Table 3.1 Comparison of theoretical and DEM result for a disk on an inclined plane of  $45^\circ$

| $\phi = 0^\circ$ (sliding)      |                         |              |              |                   |
|---------------------------------|-------------------------|--------------|--------------|-------------------|
|                                 | $N = N/(Mg \cos \beta)$ | $S = S/(Mg)$ | $\ddot{a}/g$ | $\ddot{\theta}/g$ |
| Theoretical (Ke and Bray, 1995) | 1.000                   | 0.000        | 0.7071       | 0.000             |
| DEM                             | 1.000                   | 0.000        | 0.7071       | 0.000             |

### 3.5.5 Cumulative $\beta$ distribution

During a granular-metric analysis, the sample must be representative of the grain properties including the particle size distribution (PSD) both in volume (mainly for the smallest particles) and in number (for the largest particles). This representativeness of PSD is a condition for a sample to be a representative volume element. However, this condition cannot be satisfied in DEM for a poly-disperse sample, due to the upper limit on the computation capacity. It is important to extract a discrete ensemble of grain sizes such that a statistical representation of the size classes is obtained (Radjai and Dubois, 2011).

The  $\beta$  distribution in its cumulative form is able to satisfactorily model the size span (ratio of the largest to the smallest grain) and the shape descriptor (relative weights of the

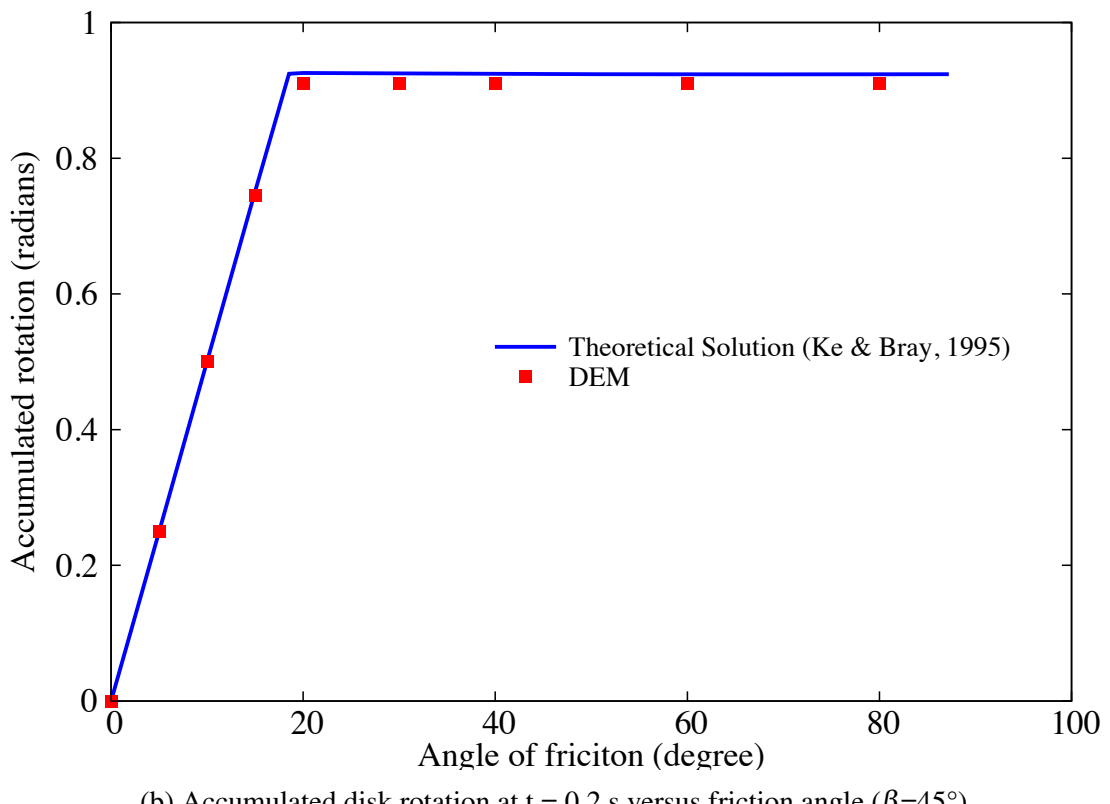


Figure 3.19 Validation of DEM using a disk rolling down an inclined plane

maximum and the minimum grain sizes). The cumulative  $\beta$  distribution (Voivret et al., 2007) is defined as

$$\beta(x, a, b) = \frac{1}{B(a, b)} \int_0^x t^{a-1} (1-t)^{b-1} dt, \quad (3.54)$$

where  $a > 0$  and  $b > 0$  are the two parameters of the distribution. The  $B(a, b)$  function is given by

$$B(a, b) = \frac{\Gamma(a)\Gamma(b)}{\Gamma(a+b)}, \quad (3.55)$$

where  $\Gamma$  is the gamma function defined by

$$\Gamma(x) = \int_0^\infty t^{x-1} e^{-t} dt. \quad (3.56)$$

The cumulative  $\beta$  (CB) distribution is defined and normalised in the interval [0,1] with  $\beta(0) = 0$  and  $\beta(1) = 1$ . To represent the grading curve of grain size range  $[d_{min}, d_{max}]$  with CB, the argument  $x$  is replaced by the reduced diameter  $d_r$

$$d_r(d) = \frac{d - d_{min}}{d_{max} - d_{min}}, \quad (3.57)$$

which varies in the range of [0,1]. The model grading curve  $h(d)$  is given by the CD distribution in terms of the reduced diameters as

$$h(d, a, b) = \beta(d_r(d); a, b). \quad (3.58)$$

The parameters  $a$  and  $b$  of the CB model allows the shape descriptor  $h(d)$  to vary easily. The size span is characterised by the ratio  $r = d_{max}/d_{min}$ . The size span can also be defined as

$$s = \frac{d_{max} - d_{min}}{d_{max} + d_{min}}. \quad (3.59)$$

A value of  $s = 0$  indicates a strictly mono-disperse grain size and a value of  $s = 1$  indicates an infinitely poly-disperse grain size distribution. Voivret et al. (2007) observed a well graded particle size distribution for  $a > 1$  and  $b > 1$ .

In the present study, a value of  $a = 4$  and  $b = 4$  is adopted to get a well graded curve. In the present study, samples with different poly-dispersity  $r = 1.5, 1.8, 2$  and  $6$  are used. Figure 4.1 shows a poly-disperse sample  $r = 1.5$  generated using the CB method, for  $a = 4$  and  $b = 4$ . The PSD curve of the generated sample is also presented.

### 3.5.6 Particle assembling methods

In order to simulate a granular assembly, it is essential to assign an initial position and velocity to all the grains in the system. Particle positions should be chosen to be compatible to the structure (granular fabric) we are trying to simulate. In any event, the grains should not be positioned such that there is an appreciable overlap between grains. In order to achieve the initial position of the grains, various grain-assembling methods can be adopted. The grain assembling methods can be classified into two broad categories: dynamic methods and geometrical approaches. The dynamic approach involves packing of grains using laws of mechanics and contacts, while in the geometrical method the grains are packed considering their geometry, i.e. grain size, shape and its position. In general, the packing of grains can be categorized into two types: crystal/lattice packing, like hexagonal or square pattern of mono-disperse grains, and random packing with varying density employing mono-disperse or poly-disperse grains. The crystalline packing arrangements, such as hexagon and square lattices, are easier to generate, however they have non-trivial effects on the response of the granular system (Staron et al., 2005). Hexagonal packing is the densest possible arrangement for mono-dispersed spherical grains. In 2D, the packing of mono-dispersed circles on a hexagonal lattice yields a packing density of  $\eta_h = \frac{1}{6}\pi\sqrt{3} \approx 0.9068$

The rheology of a granular material is controlled by the geometry of the assembly, which includes the grain shape, size distribution, and their arrangement. This prevailing role of geometry sometimes permits to simplify the dynamics in favour of a better description of the geometry and/or higher numerical efficiency (Radjai and Dubois, 2011). For example, dense granular packing may be efficiently constructed by replacing the equations of dynamics by simple displacement rules satisfying the geometrical constraints. Purely geometrical procedures can be much simpler and numerically faster than dynamic or quasi-static methods. Contrary to dynamic simulation methods, the geometrical methods allow for quick assembling of a large number of grains. Such packing may then be used as the initial state for dynamic simulations. The issue of the assembling methods is to construct configurations of grains as close as possible to a state of mechanical equilibrium with built-in packing properties. This can be a target packing density for a given grain size distribution. In the same way, the average connectivity of the grains (coordination number) and the anisotropy of the contact network are basic geometrical properties. The coordination number represents the mechanical response of packing. The homogeneity of the grain assembly in terms of packing fraction and connectivity is another important property, which depends on the assembling rules. In the present study, the initial grain packing is obtained using the ballistic deposition technique.

### Ballistic deposition

Initially a random arrangement of grains which do not touch each other is generated. The radii of the grains are chosen from the interval of  $(R_{min}, R_{max})$  in such a way that the total mass of all grains from a certain size interval is the same for all sizes, thus ensuring that neither larger nor smaller grains dominate the system. The grains are arranged randomly on a regular lattice. In the second step, the grains arranged in a regular lattice are allowed to fall down maintaining a constant potential head between layers of grains (figure 3.20).

The construction of the packing proceeds layer by layer from the substrate, hence this deposition model is also known as bottom-to-top restructuring model. In 2D, two contacts are sufficient to balance a grain if its centre of gravity lies between the two contacts. This corresponds to a position of local stable equilibrium. In this method, the order of deposited grains is generally random and independent of their sizes. The mechanically stable sample obtained from this method is presented in figure 3.21. Dense granular samples are prepared with zero initial friction angle. Zero frictional resistance ensures the densest possible packing. The friction angle is turned on during the analysis. To generate a dense sample, the sample is subjected to vibrations at varying frequencies.

Although there is no optimum specimen generation technique (O’Sullivan, 2011), there is a need to assess the homogeneity of the packing density generated (Jiang et al., 2003). The homogeneity of the sample is assessed by measuring the void-ratio within sub-volumes. The generated specimen is discretised into horizontal bands of  $2.5d_{50}$ . The homogeneity of the packing is calculated by the variance  $S$  in the void ratio.

$$S = \frac{1}{N_{layer} - 1} \sum_{i=1}^{N_{layer}} (e - e_i)^2, \quad (3.60)$$

where  $N_{layer}$  is the number of layers and  $e$  is the overall void ratio. A variance  $S$  of 2.74% is observed, which is less than 5% Jiang et al. (2003), indicating a homogeneous sample.

### 3.5.7 Voronoi tessellation

In order to extract bulk properties, such as packing density, stresses and strains, from a DEM simulation, it is important to quantify the granular texture. A useful geometrical representation of granular texture consists of dividing the space occupied by the particles into contiguous cells. This procedure is called ‘tessellation’. Voronoi tessellation is one of the mostly commonly used technique. For a finite set of points  $p_1, \dots, p_n$  in the Euclidean space, the domain/plane is discretised into convex polygons such that each polygon contains

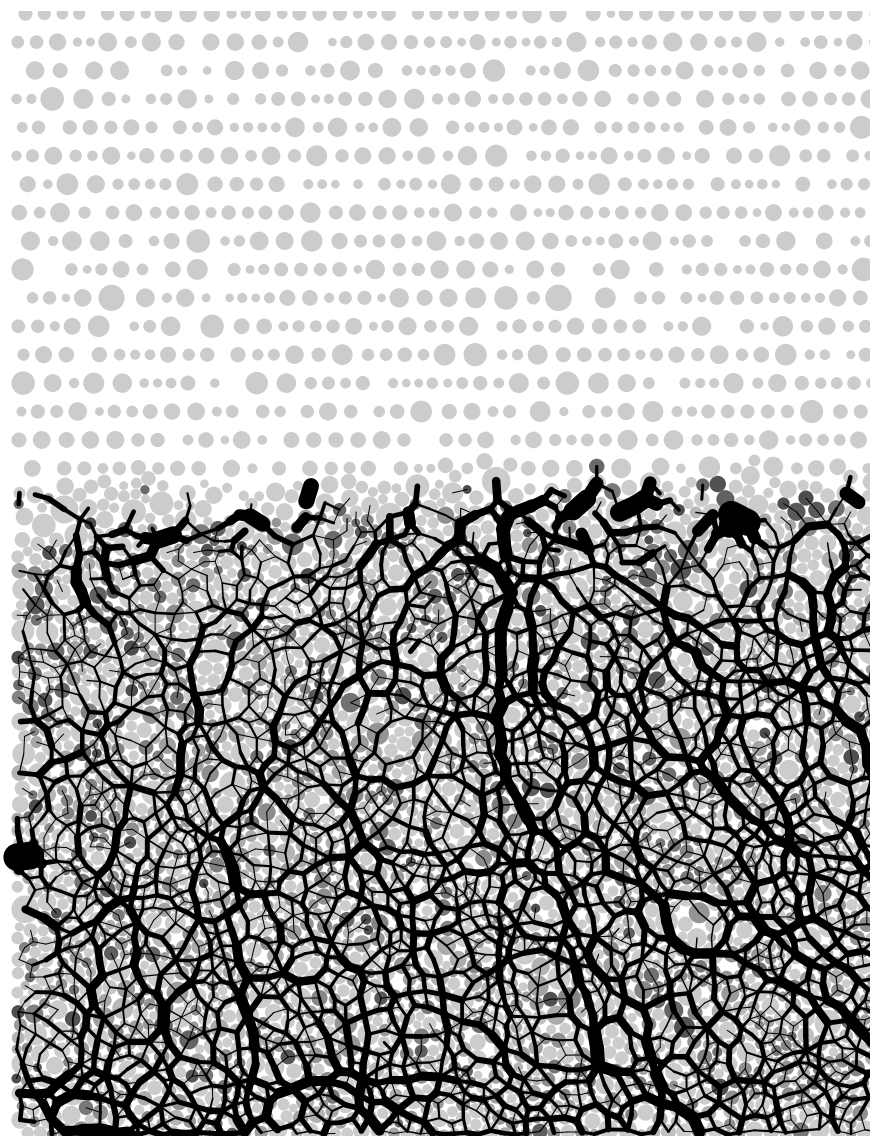


Figure 3.20 Generation of a poly-disperse sample using ballistic deposition technique

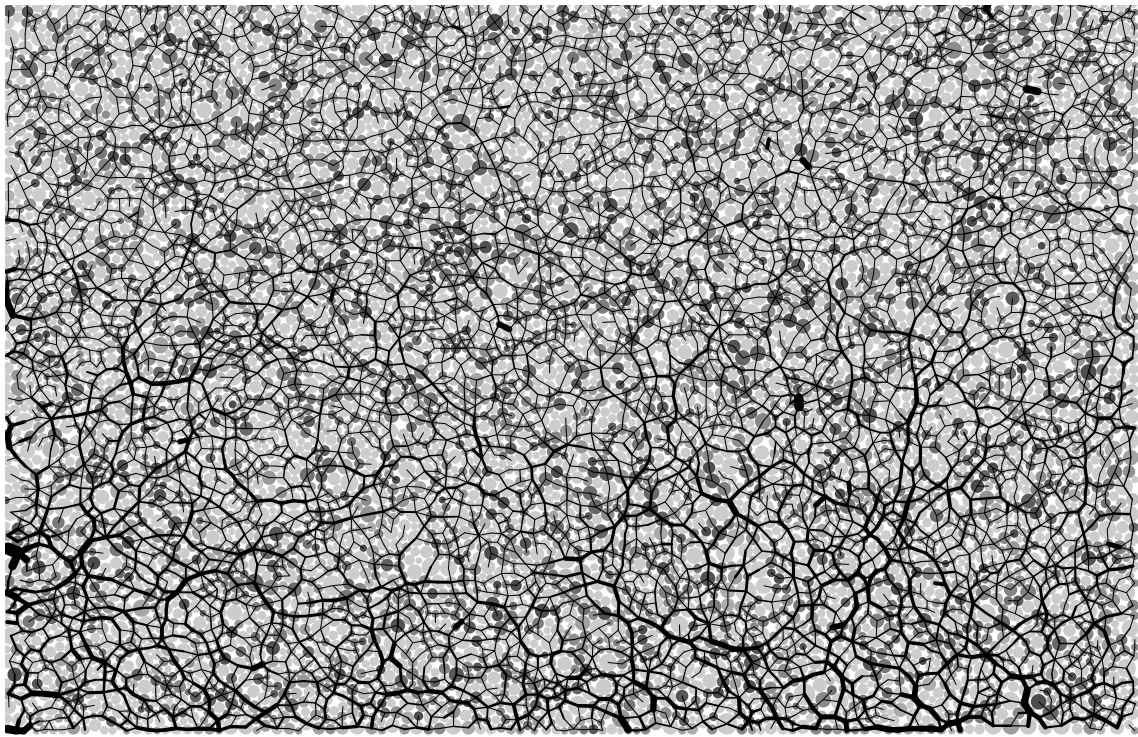


Figure 3.21 A poly-dispersed DEM sample generated using ballistic deposition technique

exactly one point  $p_i$  and every point in a given polygon is closer to its generating point  $p_i$  than to any other. The inverse of the Voronoi tessellation is the Delaunay triangulation.

In the present study, the Fortune (1992) sweep line algorithm is implemented to tessellate the region surrounding each grain in the geometry. Once each grain has a corresponding area, the macroscopic properties such as the bulk density and stresses can be extracted from micro-mechanical properties such as the local packing density and force chains.

Fortune sweep line algorithm involves a sweep line and a beach line, both of which move through the plane from left to right as the algorithm progresses. The sweep line is a straight line which moves from left to right across the plane. At any time during the algorithm, the points (grains) to the left of the sweep line will be incorporated into a Voronoi cell. While the points on the right of the sweep line are yet to be considered. The beach line is a complex curve, composed of pieces of parabolas that divides the plane within which the Voronoi diagram is known. As the sweep line crosses a point, a parabola evolves from the generating point. As the sweep line progresses, the vertices of the beach line, at which two parabolas cross, trace out the edges of the Voronoi diagram. The beach line progresses by keeping each parabola base exactly half way between the points initially swept over with the sweep line, and the new position of the sweep line. Figure 3.22 shows the Fortune sweep line algorithm in progress. In the present study, a modified version of the sweep-line algorithm is used to

construct an additively weighted Voronoi diagram, in which the distance to each site (grain) is offset by the weight of the site, i.e., the radius of the grain.

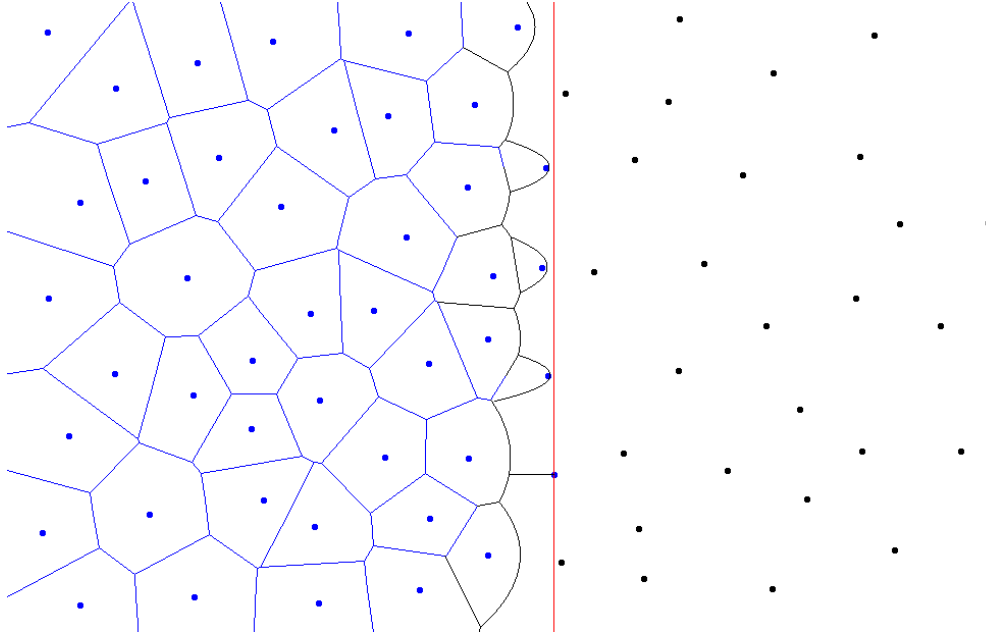


Figure 3.22 Fortune sweep line algorithm for generating Voronoi Tessellation. Generated from <http://www.diku.dk/hjemmesider/studerende/duff/Fortune/>.

The Voronoi tessellation is used to study the evolution of packing fraction during the collapse of a granular column. Figure 3.23a shows the Voronoi tessellation of the run-out for a granular column with an initial aspect ratio of 6 at time  $t = 3\tau_c$ . The distribution of local packing density for the run-out is shown in figure 3.23b. Dark regions represent dense packing, while loose regions are shown in white. The run-out at this stage has a bulk packing density of 81.23%. It is difficult to tessellate the free surface and the Voronoi cells on the free surface do not represent the actual packing density. Hence, during the evaluation of the macroscopic density, the packing density of surface grains that are larger than a threshold value are ignored. Voronoi Tessellation is a useful tool to extract continuum properties from DEM simulations. In the present study, the Voronoi tessellation is used to understand the evolution of packing density and entrainment of water in the flow front (due to hydroplaning) in granular flows.

## 3.6 Summary

A plane-strain Material Point Method is implemented in the present study to describe the continuum response of granular flows. When the material points move from one cell to

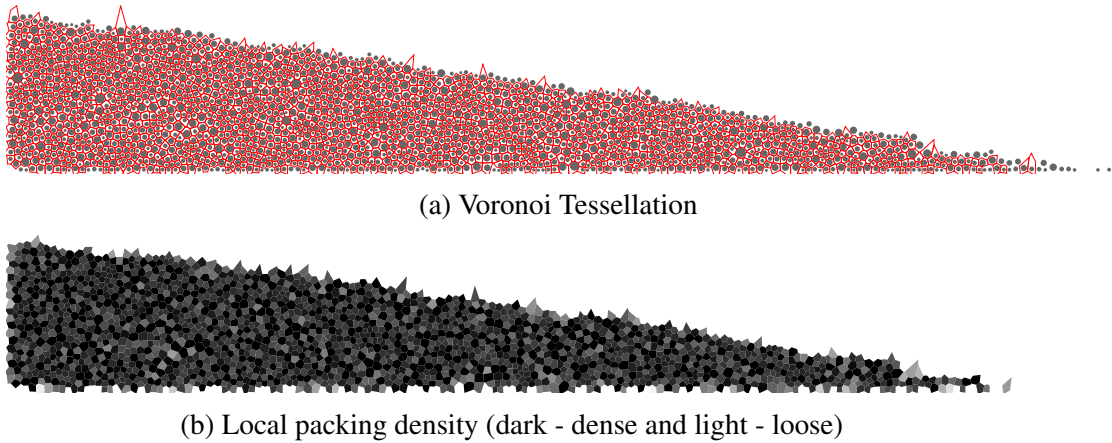


Figure 3.23 Voronoi tessellation of a run-out profile showing the local packing density

another, it results in numerical oscillations called as the cell-crossing noise. The Generalised Interpolation Material Point GIMP method is adopted to minimize these oscillations in large-deformation problems. The effect of mesh size and the number of material points per cell on the run-out behaviour is also investigated. The accuracy of the continuum approach improves with increase in the number of material points per cell and decrease in the mesh size. The grain-scale response is captured using a two-dimensional DEM code. The discrete grains are generated using a cumulative  $\beta$  distribution, which mimics the particle size distribution curves. The sample is generated using the ballistic deposition technique and the homogeneity of the generated sample is verified by investigating the variance in the void-ratio at different layers. A sweep-line Voronoi tessellation approach is adopted to extract macroscopic parameters such as stresses and packing density from micro-scale properties such as the local packing fraction. These multi-scale tools are used to understand the rheophysics of dry granular flows and to evaluate the suitability of MPM as a continuum approach in modelling granular flow behaviour.



# **Chapter 4**

## **Multi-scale modelling of dry granular flows**

### **4.1 Introduction**

In nature, instabilities of slopes or cliffs can manifest themselves in dramatic events involving sudden release of a large mass of soil. The prediction of these catastrophic events represents several challenges, one difficulty being our incomplete understanding of the granular flow dynamics (Rondon et al., 2011). Understanding the mechanics is of particular importance for risk assessment. Small scale laboratory experiments are usually unable to properly capture the dynamics of geophysical events. However, they can be useful to precisely study the physical mechanisms, which may play a crucial role in real flows (Iverson, 1997).

Conventionally, granular materials such as soils are modelled as a continuum. On a macroscopic scale, granular materials exhibit many collective phenomena and the use of continuum mechanics to describe the macroscopic behaviour can be justified. However on a grain-scale, the granular materials exhibit complex solid-like and/or fluid-like behaviour depending on how the grains interact with each other. Numerical studies at grain-scale allow a precise understanding of the internal flow structure. However, even in simplified geometries such as those investigated in the laboratory-scale experiments, DEM suffers from a serious short-coming in the number of grains that can be simulated in a reasonable time. This is a critical issue for more complex geometries or when granular processes which occur on a long time-scale are considered. For this reason, most numerical studies are performed in 2D or simple particles shapes and size distributions are considered.

Classical modelling strategies based on the finite element method (FEM) cannot be used for the simulation of very large deformations due to mesh distortion effects. In various

application of FEM, this problem is treated by means of technical tools such as re-meshing. These methods are, however, not robust and lead to round-off errors and are sensitive to the mesh characteristics. Recent works on granular materials suggest that a continuum law may be incapable of revealing in-homogeneities at the grain-scale level, such as orientation of force chains, collapse of local voids and grain rearrangements, which are purely micro-structural effects (Rycroft et al., 2009b). Discrete element approaches are capable of simulating the granular material as a discontinuous system allowing one to probe into local variables such as position, velocities, contact forces, etc. The fundamental question is how to model granular materials which exhibit complex phenomena. It is important to understand the mechanics of granular flows and the ability and limitations of continuum methods in modelling the granular flow dynamics.

## 4.2 Granular column collapse

The collapse of a granular column, which mimics the collapse of a cliff, has been extensively studied in the case of dry granular material (Hogg, 2007; Kerswell, 2005; Lajeunesse et al., 2004; Lo et al., 2009; Lube et al., 2005; Staron and Hinch, 2007; Zenit, 2005). The granular column collapse experiment involves filling a rectangular channel of height  $H_0$  and width  $L_0$  with a granular material of mass  $m$  (figure 2.7). The granular column is then released *en masse* by quickly removing the gate, thus allowing the granular material to collapse onto a horizontal surface, forming a deposit having a final height  $H_f$  and length  $L_f$ . Despite the complexity of the intermediate flow dynamics, experimental investigations have shown that the flow evolution, the spreading velocity, the final extent of the deposit, and the energy dissipation can be scaled in a quantitative way independent of the substrate properties, grain size, density, the shape of the granular material and the released mass (Lajeunesse et al., 2005; Lube et al., 2005; Staron and Hinch, 2007). The granular collapse has also been studied using discrete element method, which allows precise measurement of the internal flow structure (Lo et al., 2009; Staron and Hinch, 2007; Staron et al., 2005; Utili et al., 2014). Power laws relating the final run-out and height to the initial aspect ratio ( $a = H_0/L_0$ ) of the column were observed. These findings immediately pose a question: are these simple scaling laws fortuitous, an oversimplification, or in fact indicative of a simple dynamical balance?

Granular flows are conventionally modelled as a frictional dissipation process in continuum mechanics but the lack of influence of inter-particle friction on the energy dissipation and spreading dynamics (Lube et al., 2005) is surprising. However, Kerswell (2005) showed the run-out behaviour has a clear material dependence. Although, the collapse of a granular column on a horizontal surface is a simple case of granular flow, a proper model that describes

the flow dynamics is still lacking. Simple mathematical models based on conservation of horizontal momentum capture the scaling laws of the final deposit, but fail to describe the initial transition regime. From a theoretical point of view, the spreading has been described using depth averaged equations (Kerswell, 2005; Larrieu et al., 2006). The depth-averaged and Saint-Venant equations, however, struggle to recover the precise dynamic behaviour of the system (Warnett et al., 2013) and only succeeds in predicting the scaling observed for an aspect ratio less than one. Describing the behaviour of larger aspect ratio and capturing the initial stage of the collapse, when the grains experience a rapid change of direction from vertical to horizontal, remain an open challenge.

In the present study, multi-scale numerical modelling, i.e. grain-scale modelling and continuum analyses, of quasi-two-dimensional collapse of granular columns are performed using two-dimensional Discrete Element Method (DEM) and Generalised Interpolation Material Point Method (GIMP method). GIMP method, a hybrid Eulerian–Lagrangian approach, with a Mohr–Coloumb failure criterion is used to describe the continuum behaviour of the granular column collapse. Whereas, the micro-mechanics of the flow is captured using DEM simulations. In this section, the run-out behaviour of quasi-two-dimensional collapse using both MPM and DEM will be studied for initial aspect ratios varying from 0.2 to 10. The flow kinematics and the run-out behaviour between the grain-scale and the continuum simulations highlights the limitations of the continuum approach in modelling dense granular flows and their ability in capturing the complex flow kinematics which are due to micro-scale rheology.

### 4.2.1 Numerical set-up

In this study, the numerical set-up of granular column collapse is analogous to the experimental investigation performed by Lajeunesse et al. (2004). The experimental configuration of Lajeunesse et al. (2004) is shown in figure 2.7. Granular material of mass  $m$  is poured into a container to form a rectangular heap of length  $L_0$  and height  $H_0$ . The internal friction angle and the wall friction between the wall and the glass beads measured by Lajeunesse et al. (2004) are listed in table 4.1. The gate is then quickly removed to release the granular mass that spreads in the horizontal channel until it comes to rest. The final run-out distance  $L_f$  and the collapsed height  $H_f$  are measured. The run-out distance and collapse height exhibit a power law relation with the initial aspect ratio ‘ $a$ ’ ( $= H_0/L_0$ ) of the column.

Granular materials when released suddenly on a horizontal surface exhibit transient flow. In this study, the mechanism of flow initiation, spreading dynamics and energy dissipation are studied for varying initial aspect ratios of the granular column. The soil grain characteristics of the DEM sample match that of the experiment. The particle size distribution (PSD) is one

Table 4.1 Material properties of glass ballotini used in granular column collapse (Lajeunesse et al., 2004)

| Parameter           | Value                |
|---------------------|----------------------|
| Mean grain diameter | 1.15 mm              |
| Repose angle        | $22 \pm 0.5^\circ$   |
| Avalanche angle     | $27.4 \pm 0.5^\circ$ |
| Wall friction angle | $24.8 \pm 0.2^\circ$ |

of the most important factors controlling landslide initiation and soil permeability (Utili et al., 2014). Cumulative  $\beta$  distribution (described in section 3.5.5) is used to generate a graded sample with a mean grain diameter of 1.15mm (figure 4.1b). The DEM sample is composed of  $\sim 3000$  disks with a uniform distribution of diameters by volume fractions in the range  $[d_{min}, d_{max}] = 0.92 - 1.38$  mm with poly-dispersity  $r = \frac{d_{max}}{d_{min}} = 1.5$ . The granular column is prepared by allowing randomly placed grains to undergo ballistic deposition with a constant potential head between layers of soil grains. A snapshot of the sample generated is shown in figure 4.1a. A DEM sample with soil grains arranged in a regular hexagonal lattice is also used to understand the influence of crystallisation and jamming on the run-out behaviour.

The overlap between grains is determined by the stiffness  $k_n$  of the spring in the normal direction. Typically, an average overlap in the range 0.1 to 1.0% is desirable (Zenit, 2005) and the spring constant is chosen to produce grain overlaps in this range. The stiffness is determined as

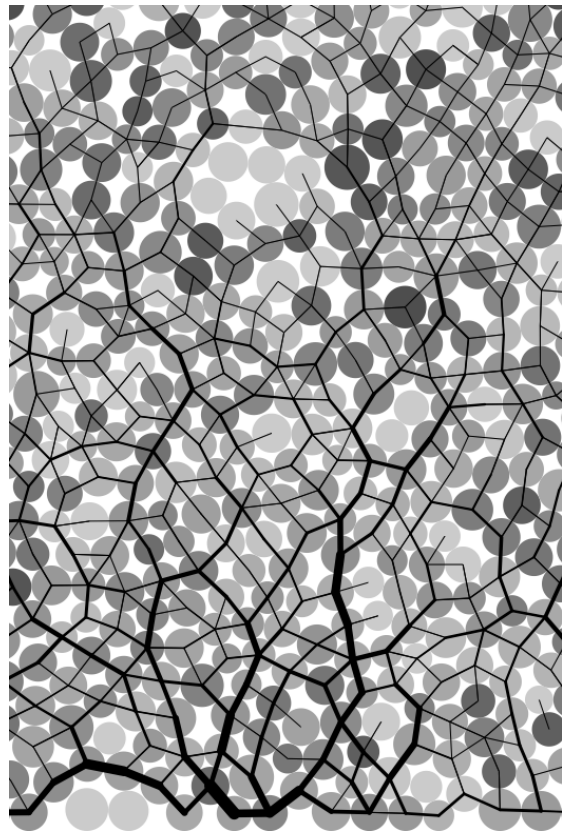
$$k_n = \frac{2\pi G}{(1-\nu)[2\ln(\frac{2r}{A}) - 1]} \quad (4.1)$$

$$A = \left[ \frac{2r(1-\nu)f_n}{\pi G} \right]^{\frac{1}{2}}, \quad (4.2)$$

where  $f_n$  is the normal contact force;  $G$  is the shear modulus;  $\nu$  is the Poisson's ratio and  $r$  is the radius of the grain. A simpler form of stiffness for a spherical grain is defined as

$$k_n = 4ER, \quad (4.3)$$

where  $E$  is the Young's modulus of the material and  $R$  is the radius of the grain. Cambou et al. (2009) observed that the contact model has negligible influence on the run-out behaviour of rapid granular flows. The granular collapse simulations performed using non-linear Hertz-Mindlin contact model and the linear-elastic contact model showed no significant difference in the granular flow behaviour (Utili et al., 2014). Linear-elastic contact model is used in the



(a) DEM sample prepared using ballistic deposition

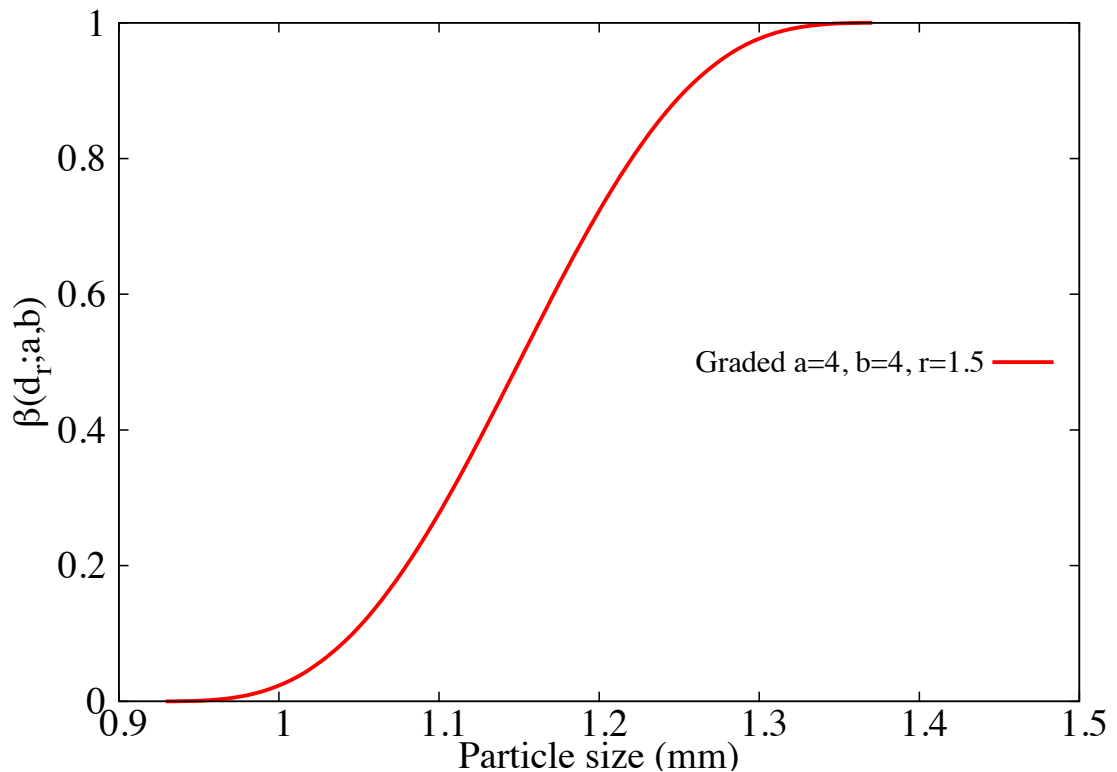
(b) DEM grains generated using the cumulative  $\beta$  distribution

Figure 4.1 DEM sample used for the granular column collapse and its grain size distribution curve

Table 4.2 Micro-mechanical parameters used in DEM simulations of granular column collapse

| Parameter                                  | Value                          |
|--|--------------------------------|
| Young's modulus of glass bead              | $70 \times 10^9 \text{ N/m}^2$ |
| Poisson's ratio                            | 0.22 - 0.24                    |
| Diameter of glass beads                    | 0.92 to 1.38 mm                |
| Normal and shear stiffness of grains       | $1.6 \times 10^8 \text{ N/m}$  |
| Normal and shear stiffness of wall         | $4 \times 10^8 \text{ N/m}$    |
| Inter-particle friction coefficient, $\mu$ | 0.53                           |
| Wall friction coefficient                  | 0.466                          |
| Coefficient of restitution, $\varepsilon$  | 0.75                           |

present study due to its simplicity and lower computation time requirement. The maximum tangential force is limited by the Mohr-Coloumb criterion.

Staron and Hinch (2007) observed that the coefficient of restitution  $\varepsilon$  dramatically changes the behaviour of the system for  $\varepsilon \rightarrow 1$ ; in particular, this dramatic change is expected to become more important for increasing values of  $a$ . On the contrary, for  $\varepsilon \leq 0.8$ , the influence of the coefficient of restitution becomes negligible. In the present study, a value of 0.75 is adopted as the coefficient of restitution, similar values of restitution coefficient was adopted by Girolami et al. (2012) and Zenit (2005). The normal damping coefficient  $C_n$  is appropriately chosen to achieve the required coefficient of restitution  $\varepsilon$ :

$$C_n = 2\gamma\sqrt{m_{ij}k_n}, \quad (4.4)$$

$$\text{where } \gamma = -\frac{\ln(\varepsilon)}{\sqrt{\pi^2 + \ln^2(\varepsilon)}}, \quad \text{and} \quad m_{ij} = \frac{m_i m_j}{m_i + m_j}. \quad (4.5)$$

The micro-mechanical parameters used in this study are presented in table 4.2. A rolling resistance is adopted in order to model the shape effect of non-spherical grains. Due to the unsteady nature of the flow, the grains get dispersed on the horizontal plane as discrete bodies start to separate from the main mass, hence the run-out distance is calculated as the position of the farthest grain which has at least one contact with the main mass.

The configuration of the granular column collapse using DEM is show in figure 4.2 for a column with an initial aspect ratio of 0.8. The soil grains are packed using ballistic deposition technique, once a stable state is reached, the gate is opened allowing the granular column to collapse and flow. Frictional boundaries are specified on the left and the bottom boundaries.

GIMP method with a Mohr-Coloumb constitutive model is used to simulate plane strain collapse of granular columns. Crosta et al. (2009) observed that the Mohr-Coloumb model with non-associate flow rule is able to capture granular collapse dynamics and models the

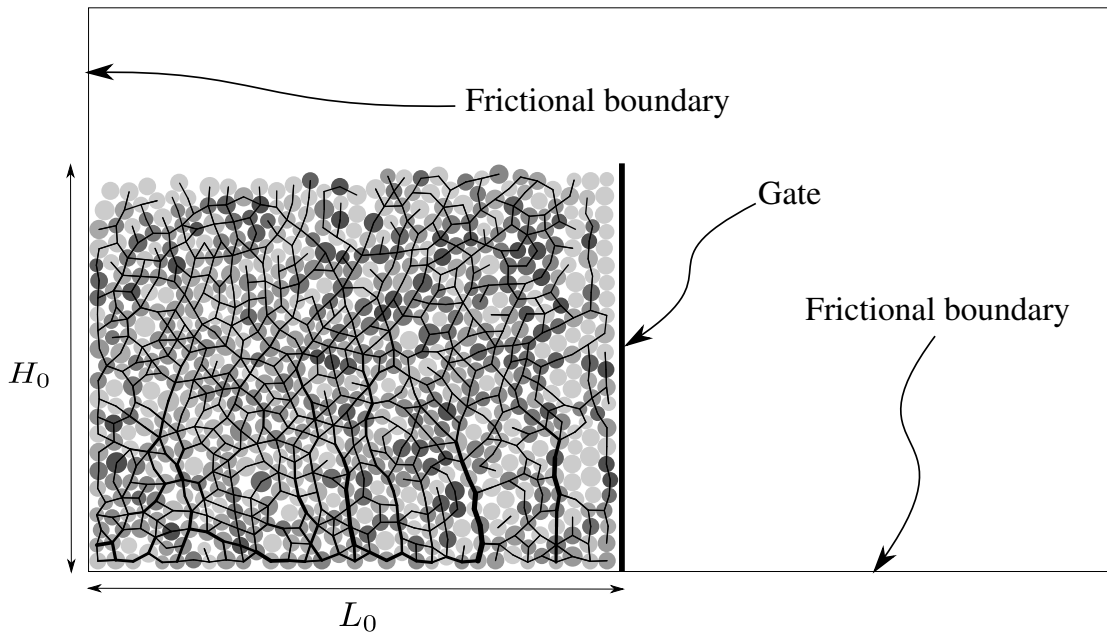


Figure 4.2 DEM set-up for a granular collapse simulation ( $a = 0.8$ ). Shows the grains in a stable state under the influence of gravity.

strong vertical motion. This method does not suffer the limitations of typical shallow water equation techniques. In order to understand the ability and limitations of continuum approaches in capturing the local rheology, it is important to scale the grain-scale material properties, such as the inter-particle friction and stiffness, to the continuum scale (macroscopic friction and Young's modulus). Crosta et al. (2009) observed that the friction angle plays a significant role on the run-out behaviour.

In MPM simulations, the granular flow is assumed to be in the critical state and the critical state friction angle is used as an input in the Mohr-Coloumb model. In order to obtain the critical state friction angle of the granular sample, a shear test is performed using 1078 DEM grains. A bi-periodic boundary condition is adopted on the sides of the sample (figure 4.3a). Two layers of fixed grains (shown in black) are placed at the top and the bottom of the shear sample. A normal pressure  $P$  and a horizontal velocity  $v$  is applied to the fixed grains at the top of the shear sample. As the normal effective stress is varied, the average shear stress in the sample is measured. The sample is sheared until the critical state is reached. The slope of shear stress versus normal effective stress gives the critical state friction angle. A critical state friction angle of  $22.2^\circ$  is obtained. The macroscopic friction angle is in the range observed by Estrada et al. (2008) and Mitchell and Soga (2005). The Young's modulus of the granular assembly is obtained as the initial slope of the stress-strain plot of a uni-axial compression of a laterally confined granular column using DEM.

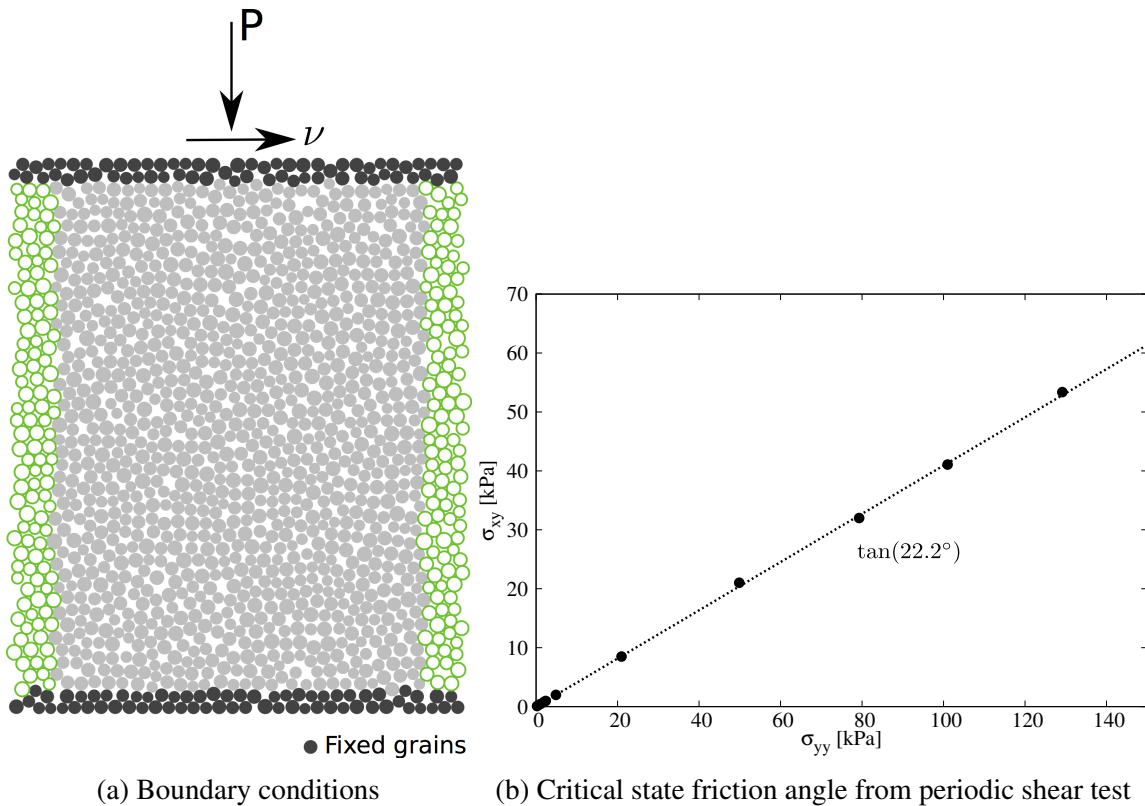


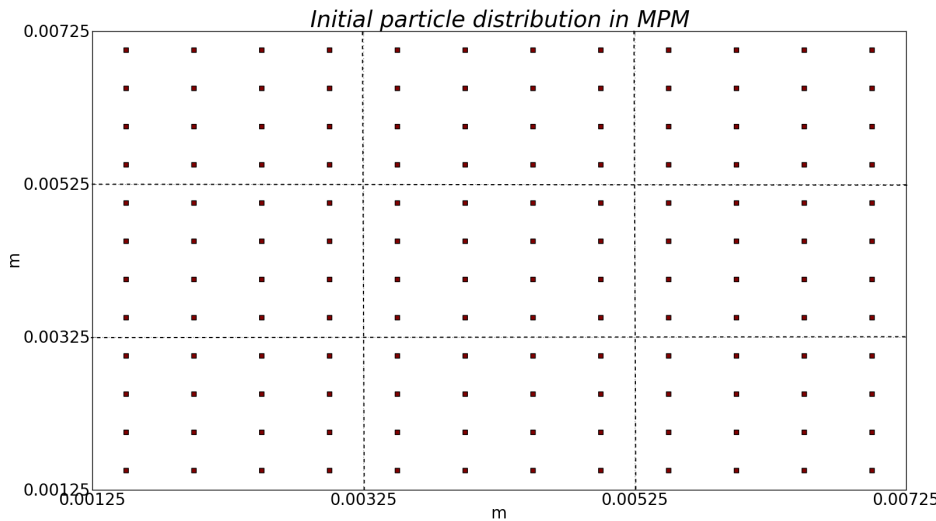
Figure 4.3 Periodic shear test using DEM to obtain macroscopic friction angle

Table 4.3 Parameters used in continuum simulations of granular column collapse

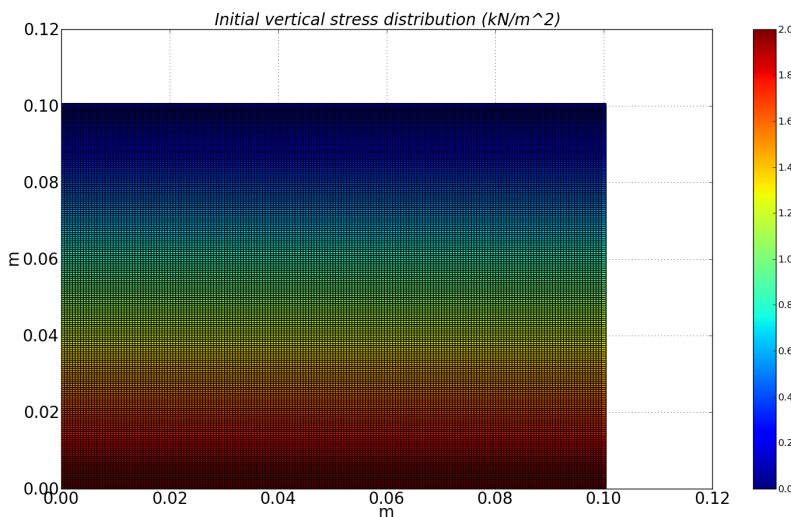
| Parameter                          | Value                               |
|------------------------------------|-------------------------------------|
| Material point spacing             | 0.5 mm                              |
| Number of material points per cell | 16                                  |
| Mesh length                        | $2 \times 10^{-3}$ m                |
| Young's Modulus, E                 | $1.98 \times 10^6$ N/m <sup>2</sup> |
| Poisson's ratio, $\nu$             | 0.22 to 0.24                        |
| Friction angle, $\phi$             | $22.2 \pm 0.2^\circ$                |
| Dilatancy angle, $\Phi$            | 0°                                  |
| Density, $\rho$                    | 1925 kg/m <sup>3</sup>              |
| Wall friction                      | 0.466                               |
| Time step increment                | $1.0 \times 10^{-6}$ s              |

Guilkey et al. (2003) suggests using at least four material points per cell for large deformation problems. In the present study, 16 material points per cell is adopted. If the mesh is too fine and the number of particles is too large, the particle size  $2lp$  decreases, and the GIMP interpolation function tends to approach the original MPM function, as shown by Bardenhagen and Kober (2004). Hence, GIMP loses the merit that it reduces the numerical noise due to material points crossing the background mesh. In addition, the probability of particles crossing the background mesh increases with decrease in the mesh size, hence, more noise may be produced (Abe et al., 2013). The effect of the number of material points per cell on the run-out behaviour is discussed in section 3.3.5.

The initial set-up of a granular column collapse ( $a = 1$ ) using MPM is shown in figure 4.4. For all MPM simulations, a cell size of  $2 \times 10^{-3}$  m with 16 material points per cell is adopted (figure 4.4a). The granular columns are discretised into 40,000 to 160,000 material points. Each material point represents one-eighth of a DEM soil grain. Since, the scale of the problem being modelled is small and it is important to precisely define the flow surface, a larger number of material points are used to represent the geometry. The initial vertical effective stress simulated in MPM, before the collapse stage, is shown in figure 4.4b. The extent of the background mesh in MPM is much larger than the initial column. In MPM, the material points move inside the grid, so it is important to have a sufficiently large domain for the collapse. Frictional boundaries are applied as constraints on the nodal accelerations on the left and the bottom boundaries. The parameters used for the continuum analyses are presented in table 4.3.



(a) Initial arrangement of material points in the mesh. Closer view of 16 material points per cell for a column with an initial aspect ratio of 1. Cell size of  $2 \times 10^{-3}$ m.



(b) Initial vertical effective stress in MPM for a column with an aspect ratio of 1.

Figure 4.4 MPM initial mesh and vertical stress for a granular column collapse simulation ( $a=1$ )

### 4.2.2 Deposit morphology

Two-dimensional plane-strain MPM and DEM simulations of granular column collapse are performed by varying the initial aspect ratio of the column from 0.2 to 10. The evolution of run-out and the flow kinematics observed in both approaches are compared to understand the ability and limitations of these approaches. The normalized final run-out distance,  $\Delta L = (L_f - L_0)/L_0$ , as a function of the initial aspect ratio  $a$  of the column is presented in figure 4.5. Similar to the experimental behaviour a power law relation between the run-out and the initial aspect ratio of the column is observed. Two distinct flow regimes can be seen: (a) for  $a < 2.7$  a linear relation between the spread and aspect ratio can be observed, and (b) for  $a > 2.7$  a power-law relationship exists. In the present study, the following scaling law for the run-out (using DEM) is observed:

$$\frac{L_f - L_0}{L_0} \approx \begin{cases} 1.67a, & a \lesssim 2.7 \\ 2.7a^{2/3}, & a \gtrsim 2.7 \end{cases} \quad (4.6)$$

Both, MPM and DEM simulations are able to capture the linear relationship for  $a < 2.7$ , and the simulation results agree with the experimental investigation (Lajeunesse et al., 2005). This shows that a simple frictional dissipation model is able to capture the flow dynamics for columns with small aspect ratios. For  $a < 2.7$ , the normalised run-out distance predicted using DEM simulations are very close to those observed in the experiment. DEM simulations with a hexagonal packing shows shorter run-out distances in comparison to the randomly packed sample. This difference in the run-out behaviour might be due to the crystallisation and jamming effects in hexagonal packing. The small difference in the final run-out between the DEM and the experimental results can be attributed to the variation in the packing of grains and the three-dimensional grain shape. Also, the experimental data corresponds to granular column collapse in a rectangular channel, where the collapse is not a pure two-dimensional collapse as in the case of numerical simulations. Most, aerial and sub-marine landslides have large lateral extent, i.e., plane-strain condition, hence in the present study two-dimensional simulations are performed. Although two-dimensional simulations don't capture movement of the grains perpendicular to the plane of the experiment, it simplifies the configuration so as to compare DEM simulations with MPM. Also, Balmforth and Kerswell (2005) observed that the side-walls in quasi-two-dimensional collapse does not influence the power-law behaviour but affects the numerical constant, which depends on the material properties.

A significant difference in the final run-out between MPM, which is based on a simple frictional model for dissipation of potential energy, and DEM simulations indicates a change in the mechanism of energy dissipation for columns with large aspect ratios ( $a > 2.7$ ). A

transition in the run-out behaviour at an aspect ratio of 2.7 indicates a change in the flow kinematics. Similar behaviour in the run-out distance was observed by Bandara (2013) for columns with large aspect ratios ( $a \geq 2$ ). Mast et al. (2014a) observed 40% increase in the final run-out distances, for large aspect ratios, than reported in the literature. Previous studies have failed to describe the mechanism of energy dissipation in continuum approaches and the reason for longer run-out distance. Section 4.2.4 discusses the reason behind the difference in the run-out behaviour between continuum and experimental findings.

The longer run-out distance in MPM simulations at large aspect ratios might be influenced by the amount of material mobilised during the collapse. In tall columns, the entire column participates in the flow, in contrast to short columns where the collapse is due to avalanching of flanks. It is possible that MPM simulations collapse more resulting in longer run-out distances. Figure 4.6 shows the normalized final height as a function of the initial aspect ratio of the column. Similar to the run-out behaviour, the normalised-height also shows two distinct regimes. The scaling of final height of the column with the initial aspect ratio of the column can be written as

$$\frac{H_f}{L_i} \propto \begin{cases} a, & a \lesssim 0.7 \\ a^{2/3}, & a \gtrsim 0.7 \end{cases} \quad (4.7)$$

The final height predicted by both DEM and MPM simulations match the experimental data for columns with smaller aspect ratios ( $a \leq 0.7$ ). Linear relationship between the final height and the aspect ratio indicates that only a part of the granular column is mobilised during the collapse. For tall columns, both approaches predict similar normalised height. However, the normalised height observed in MPM is higher than in DEM simulations, which is in contrast to the idea of increase in the amount of material mobilised during the collapse in MPM simulations resulting in longer run-out distance. Hence, the longer run-out observed in MPM simulations is due a change in the flow dynamics at higher aspect ratios, which is not captured in MPM simulations. The final height of a column is controlled by the amount of static region in the granular column collapse, while the run-out distance is essentially a function of the flowing mass. Hence, it is important to compare the evolution of flow and the internal flow structure in DEM and MPM simulations.

### 4.2.3 Flow evolution and internal flow structure

The normalised run-out and height as a function of the aspect ratio indicate that, for a given granular material and substrate properties, the flow dynamics and the final deposit morphology are independent of the volume of granular material released, but depend only

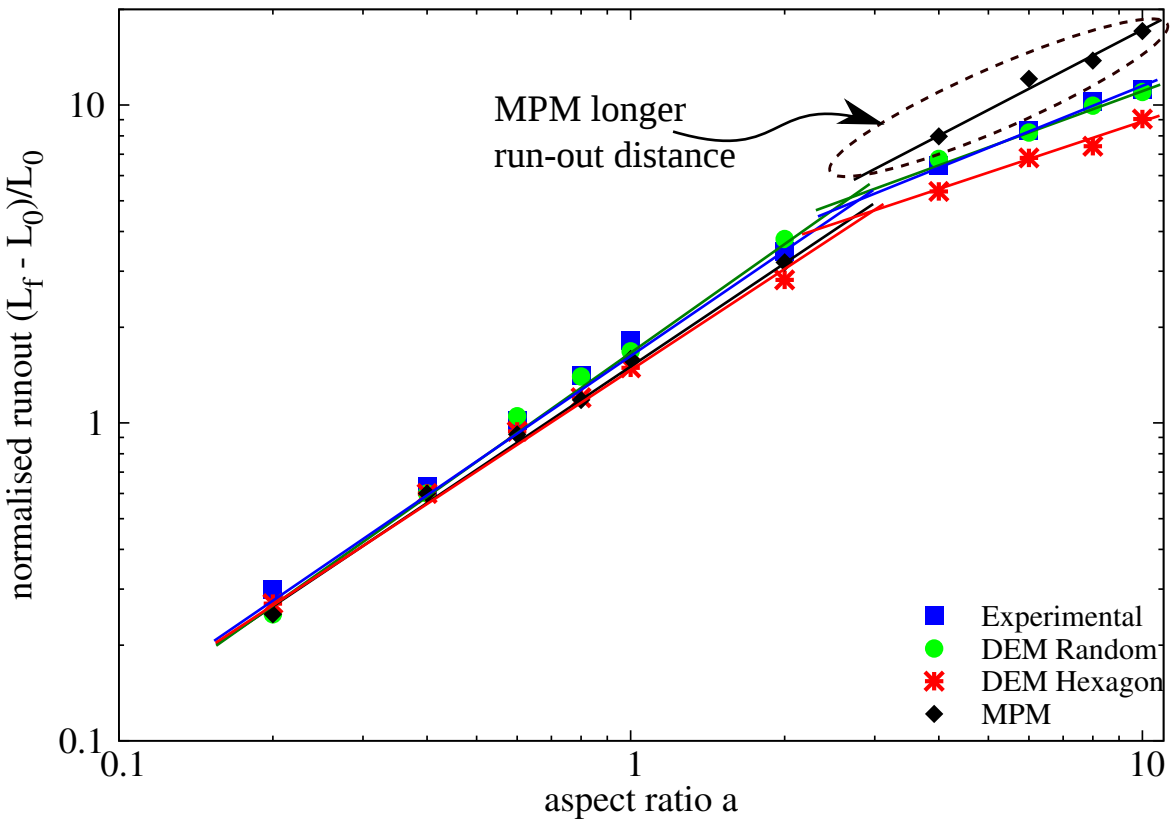


Figure 4.5 Normalised final run-out distance for columns with different initial aspect ratios.

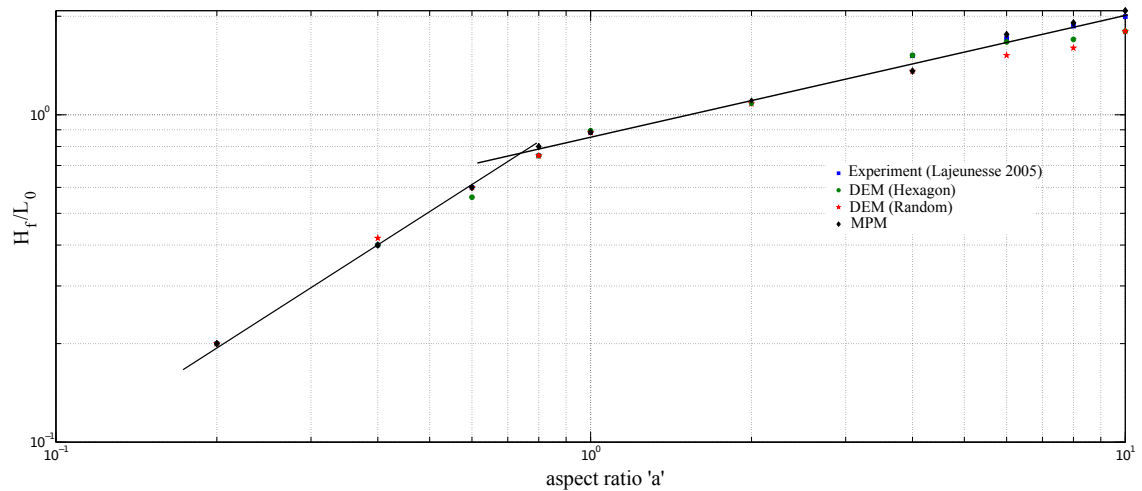


Figure 4.6 Normalised final collapse height for columns with different initial aspect ratios.

on the geometry of the column. A power law relationship is observed between the run-out distance and the initial aspect ratio of the column. A transition in the run-out behaviour at an aspect ratio of 2.7 indicates a change in the flow dynamics.

Dimensional analysis of granular column collapse reveals an intrinsic time defined as  $\sqrt{H_0/g}$ . This intrinsic time is a transient time of order  $\tau_c$ , at which the flow is fully developed, i.e., the potential energy available at the initial stage of collapse is now fully converted to kinetic energy. Numerical simulation of the velocity profile of a granular column ( $a=0.4$ ) at critical time  $\tau_c$  is presented in figure 4.7. At critical time, the velocity field depends only on the position of the grain along the sliding mass. The maximum velocity is observed at the front of the flowing mass corresponding to that of a plug flow in horizontal direction. Particulate and continuum simulations show similar run-out distance at the critical time. Both approaches show similar quantities of material destabilised above the failure surface. However, the crystalline arrangement of soil grains in a hexagonal packing results in a different flow mechanics, which also shows the effect of jamming at the flow front. The continuum nature of MPM results in a slightly different geometry of the material destabilised above the failure surface in comparison to DEM simulations. The velocity profile is similar to a steady granular surface flow observed by Lajeunesse et al. (2004).

For short columns ( $a < 2.7$ ), the flow is initiated by a failure at the edge of the pile along a well-defined shear-failure surface. The granular mass fails through avalanching of flanks producing a truncated cone-like deposit (' $a' < 0.7') or conical deposit (' $a' > 0.7'). The grains located above the failure surface move "*en masse*" leaving a static region underneath the failure surface. For columns with lower initial aspect ratios, the run-out distance is proportional to the mass flowing above the failure surface. The spreading results from a Coulomb-like failure of the edges and implies no free fall of the column. In this case, the effective friction properties of the flow can be simply predicted from the shape of the final deposit. The amount of mass mobilized during the collapse is significantly affected by the angle of the failure surface.$$

Figure 4.7 shows that both numerical techniques predict a distinct failure surface when the flow is fully developed at critical time  $\tau_c$ . The angle of the failure surface is found to be about  $55^\circ$ . The failure surface begins from the toe of the column and propagates inwards at an angle of  $50$  to  $55^\circ$ . The formation of the "truncated conical deposit" or "conical deposit" depends on the initial length of the column, as the angle of the failure surface is found to be independent of the aspect ratio. The failure angle is consistent with the interpretation in terms of *active Coulomb failure*, which leads to a predicted failure angle  $\theta_y = 45^\circ + \delta/2$ , where  $\delta$  is the friction angle of the granular material. In the present study, the macroscopic friction angle is  $22^\circ$ , which leads to  $\theta_y = 45^\circ + 22^\circ/2 = 56^\circ$ , which is in good agreement

with the numerical simulations and the experimental observations by Lajeunesse et al. (2004). The shear-failure angle has a direct effect on the transition between the truncated cone and the conical deposit occurring at an aspect ratio of 0.7.

The final profile of the granular column with an initial aspect ratio of 0.4 obtained from DEM and MPM simulations are shown in figure 4.8. Both MPM and DEM show similar run-out behaviour. The continuum approach is able to capture the flow dynamics of short columns, where the failure mechanism is active Coulomb failure. In dense hexagonal packing, the failure surface is steep due to crystallisation effects. The variation in the angle of the failure surface causes a difference in the amount of material destabilised, and in turn the run-out distance. This crystallisation phenomenon is found to have a significant influence on the final deposit of the granular column.

MPM and DEM simulations of the velocity profile of a granular column with an initial aspect ratio of 6 at critical time  $\tau_c$  is shown in figure 4.9. For tall columns ( $a > 2.7$ ), the flow is still initiated by a well defined failure surface as can be seen in figure 4.9. However, in this case the initial granular column is much higher than the top of the failure surface. Due to gravity most of the grains in the column experience free-fall consuming the column along their way. When they reach the vicinity of the failure surface, the flow gets deviated along the horizontal direction releasing a huge amount of kinetic energy gained during the free fall. For larger aspect ratio ( $a > 0.7$ ), the resulting static region is a cone, the final height of the cone  $H_f$  lies above the summit of the failure surface.

An initial failure surface starting from the toe end of the column at an angle of about  $55^\circ$  can be observed at the critical time  $\tau_c$ . As the collapse of the granular column progresses, successive failure planes parallel to the initial failure surface are formed and shear failure occurs along these planes. The presence of several shear bands in the final profile of the collapsed granular column confirms this behaviour. This observation throws light on the mechanics of propagation of shear bands in massive landslides such as the Storegga submarine landslide, where the propagation of shear band is found to have caused long run-out distances (Dey et al., 2012). After the initial stage of collapse in tall columns, the flow behaviour becomes similar to that of columns with lower initial aspect ratios as the flow starts descending along the failure plane. Hexagonal packing results in crystallisation, which has a significant effect on the run-out distance by forming a series of parallel shear bands, resulting in an unnatural flow kinematics. The final profile of the collapsed granular column with an initial aspect ratio of 6 is presented in figure 4.10. For tall columns, the dissipation process is more complex due to the free-fall dynamics. The vertical acceleration of the grains induces a non-trivial mass distribution in the flow during spreading. Staron and Hinch (2007)



Figure 4.7 Velocity profile of a granular column collapse ( $a = 0.4$ ,  $t = \tau_c$ ). Velocity is shown in m/s



Figure 4.8 Velocity profile of a granular column collapse ( $a = 0.4$ ,  $t = 3 \times \tau_c$ ). Velocity is shown in m/s

observed that the mass distribution plays a dominant role in the power-law scaling observed in the run-out.

Regardless of the experimental configuration and the initial aspect ratio of the columns, the flow is initiated by a well-defined rupture surface, above which the material slides down leaving a static region underneath the failure plane. Depending on the aspect ratio of the column, two asymptotic behaviours are observed. For smaller aspect ratios, the flow is dominated by friction where as the large aspect ratio columns are influenced by the pressure gradient.

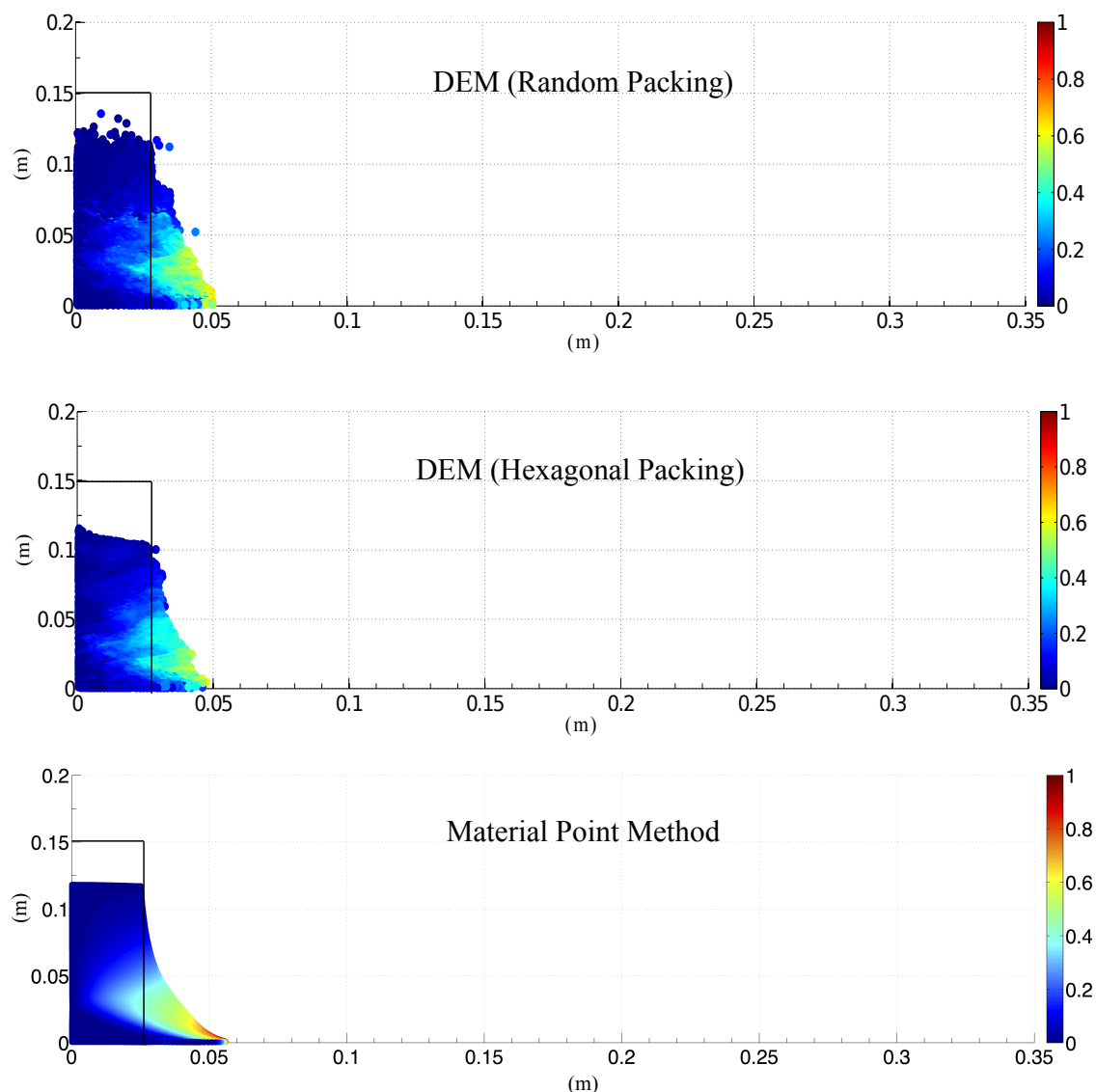


Figure 4.9 Velocity profile of a granular column collapse ( $a = 6, t = \tau_c$ ). Velocity is shown in m/s

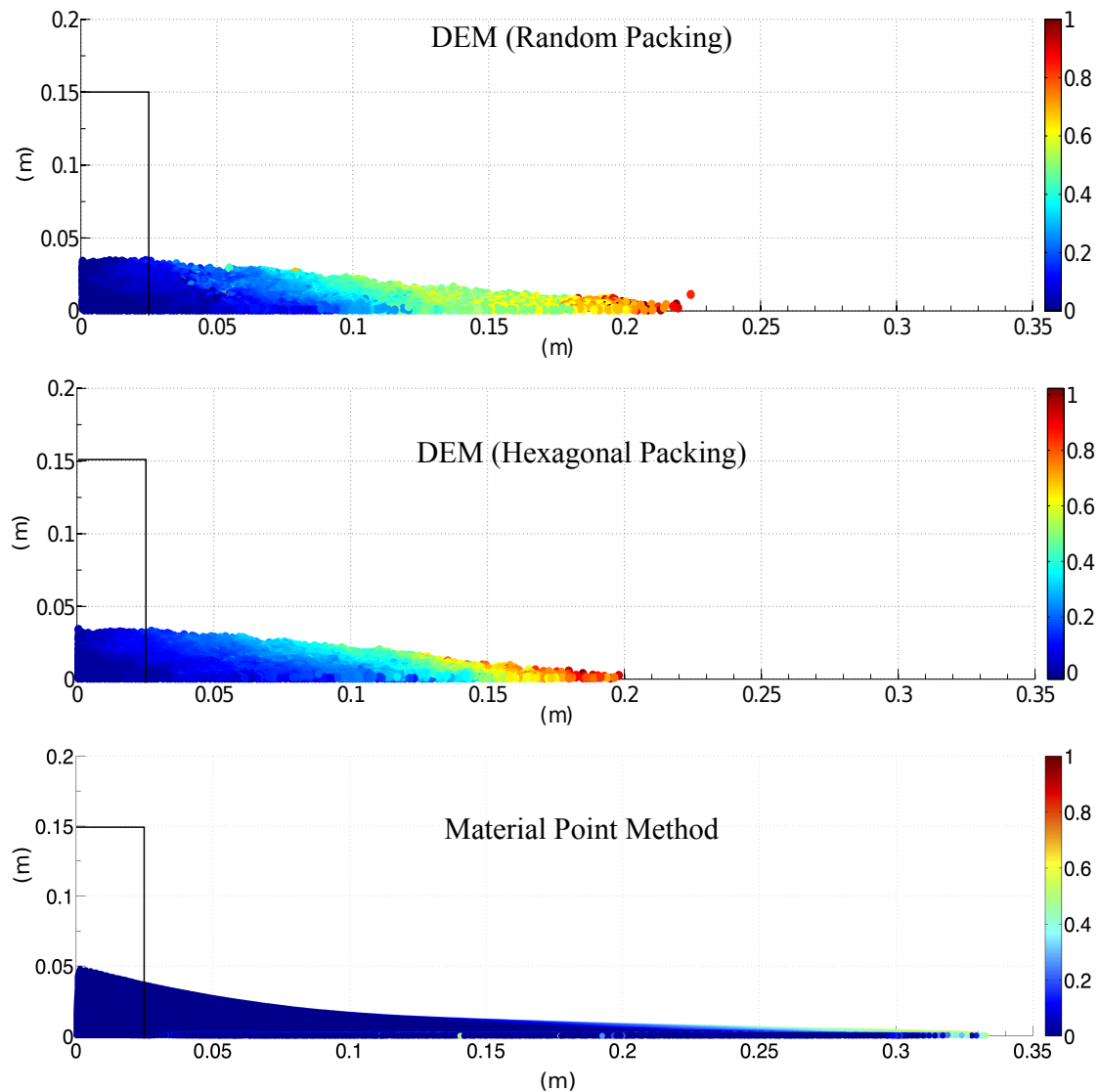


Figure 4.10 Velocity profile of a granular column collapse ( $a = 6, t = 3 \times \tau_c$ ). Velocity is shown in m/s

To study the influence of aspect ratio on the flow dynamics of granular columns, the flow front  $L(t)$  and the maximum height of column  $H(t)$  are tracked. The evolution of scaled height ( $H_f/L_0$ ) and the run-out distance  $(L_f - L_0)/L_0$  with time for granular columns with initial aspect ratios of 0.4 and 6 are presented in figure 4.11. Three distinct regions can be observed in the flow evolution of a granular column collapse regardless of the initial aspect ratio of the column. An initial transient acceleration phase is observed for a time  $0.8\tau_c$ . This phase is followed by a heap movement of granular materials at the foot of the column with a constant spreading velocity  $V$  for about  $2\tau_c$ . When time is longer than the critical time ( $t > \tau_c$ ), the velocity varies linearly with depth in the flowing layer and decreases exponentially with depth near the static layer. This velocity profile is similar to those observed in steady granular surface flows (Lajeunesse et al., 2004). Most of the run-out happens during this phase. The final phase involves deceleration of the flow front and the flow comes to rest after about  $0.6\tau_c$ . The spreading of the granular column ceases after a time on the order of about  $3\tau_c$ , however some motion still persists along the free surface behind the flow front for a much longer time due to internal rearrangement, the duration of which can last up to  $t \approx 6\tau_c$ .

The critical time is evaluated as the time at which the potential energy available for the flow has been converted to the kinetic energy. In short columns, the critical time observed in both hexagonal and random packing of grains matches the experimental observations. However, the material point method takes longer for the flow to be fully mobilized, this can be attributed to the continuum nature of MPM which takes  $\sim 20\%$  longer to destabilise the initial stress conditions. However, the actual run-out duration of the flow is similar to DEM and the granular mass comes to rest at about  $t = 3\tau_c$ , this is due to steeper decline in the potential energy in MPM compared to DEM simulations.

For columns with larger aspect ratios, the continuum and particulate approaches simulate similar flow evolution up to  $3\tau_c$ , beyond which particulate simulation decelerates and comes to rest, while the flow continues to evolve in MPM simulation resulting in longer run-out distance. The flow comes to rest at time  $t = 6\tau_c$ . The three phases in a granular flow can be distinctly observed in the flow evolution plot for a column with an initial aspect ratio of 6 (figure 4.11b). The flow evolution behaviour observed in the case of DEM simulation matches the experimental observation by Lajeunesse et al. (2004). Hexagonal packing predicts longer time for the flow to evolve, which can be attributed to jamming of grains. In MPM simulations, the failure starts at the toe of the column and slowly propagates up to form the failure surface. This results in slower initiation of the flow. In DEM, however, the initial stage of collapse is characterised by free-fall under gravity. It can be observed that MPM overestimates the critical time by 50%. Although, MPM and DEM simulations show the same run-out at time  $t = 3\tau_c$ , the flow evolution between both the approaches is

different. MPM simulation show that the granular flow continues to accelerate beyond  $3\tau_c$  and ceases at around  $6\tau_c$ . In order to understand the difference in the flow dynamics in the case of material point method, it is important to study the mechanism of energy dissipation.

#### 4.2.4 Energy dissipation mechanism

The energy dissipation mechanism during collapse provides useful insights into the flow dynamics. In the case of small aspect ratios, the columns undergo no free fall. The spreading mainly results from the failure of the edges, while the top of the column remains essentially undisturbed in the central area. The amount of energy dissipated during the spreading  $\delta E$  can be easily recovered using the simple shape of the final deposit and volume conservation (figure 4.12). The difference of potential energy between the initial and the final states gives

$$\delta E = \frac{1}{6}g\rho(L_f - L_0)H_0^2, \quad (4.8)$$

where  $\rho$  is the density of the packing. It is assumed that this energy is dissipated by the work of frictional forces  $W_\mu$  over the total run-out distance by the center of mass  $G$  of the spreading material. The collapse involves two regions of dissipation: the amount of mass destabilised  $\frac{1}{4}(L_f - L_0)H_0$  over two thirds of the run-out distance  $2(L_f - L_0)/3$  (considering the triangular shape of the final deposit and the initial and the final positions of the centre of mass). The effective coefficient of friction  $\mu_e$  characterizes the mean dissipation in the flow. The work of friction forces is

$$W_\mu = \frac{1}{6}\mu_e g\rho(L_f - L_0)^2 H_0. \quad (4.9)$$

Equating  $\delta E$  and  $W_\mu$  gives  $\mu_e(L_f - L_0) = H_0$ . The scaling of the runout leads directly to the relation  $\mu_e = \lambda^{-1}$ , where  $\lambda$  is the numerical constant in the power-law relation between the run-out and the initial aspect ratio, which depends on the material properties. The amount of energy  $\delta E$  dissipated during the spreading is compared with  $W = N_p g m_p r_p$ , where  $N_p$  is the total number of grains,  $m_p$  is their mass, and  $r_p$  is the total horizontal distance run by each of them. The dissipation energy  $\delta E$  is proportional to  $W$ . Staron and Hinch (2007) observed that the coefficient of proportionality gives a measure of the effective friction and observed a power law dependence between  $\mu_e$  and internal friction angle  $\mu$ :  $\mu_e = 0.425\mu^{0.2}$ . In this study, an effective friction angle  $\mu_e$  of  $21^\circ$  is observed, which is very close to the critical state friction angle of  $22^\circ$  used in MPM simulations. The global effective friction angle obtained from the simple macroscopic energy-dissipation analysis matches the critical state friction used in MPM simulations. This proves that the energy dissipation mechanism modelled in a

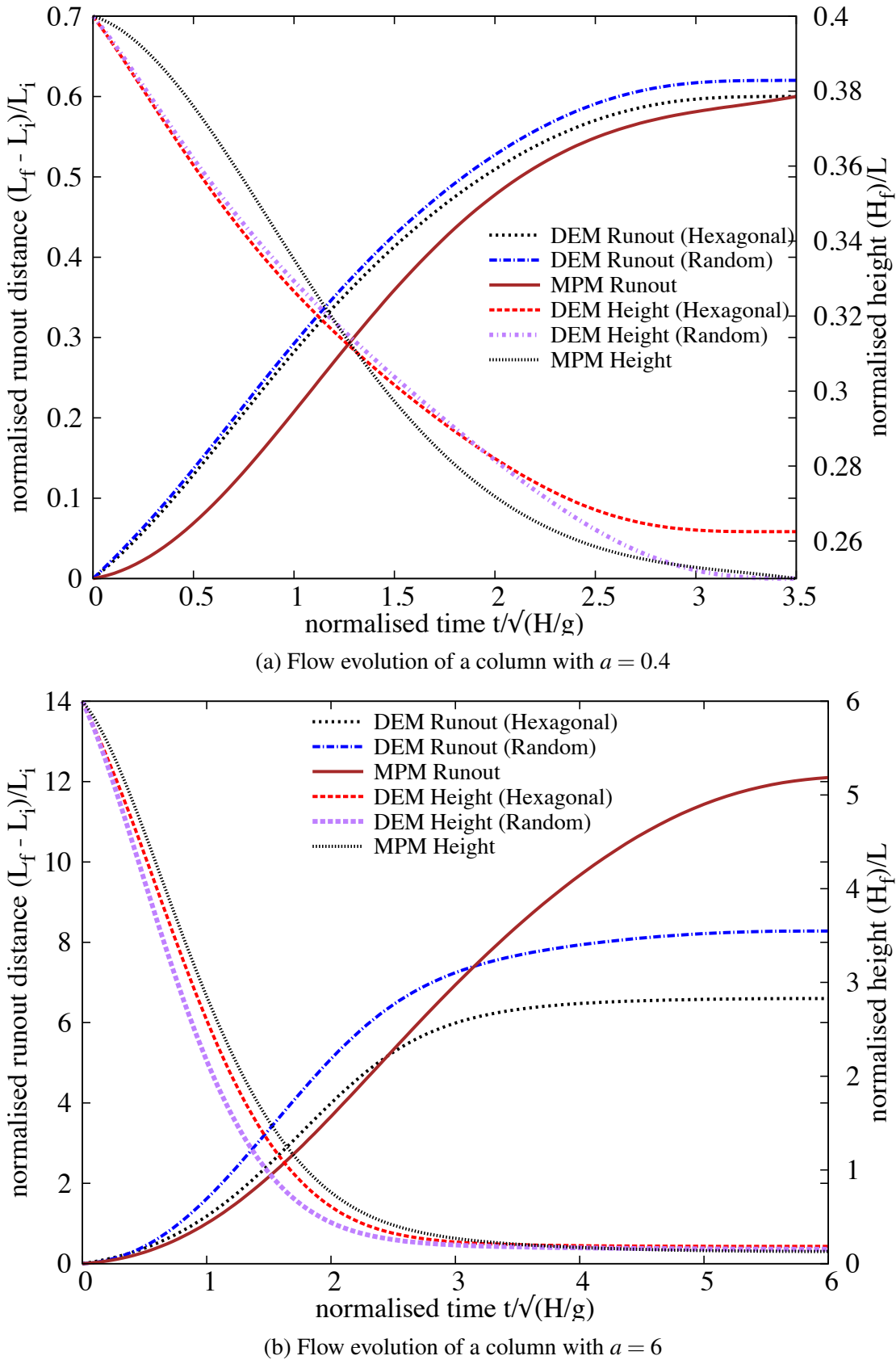


Figure 4.11 Flow evolution of granular column collapse ( $a = 0.4$  and  $6$ )

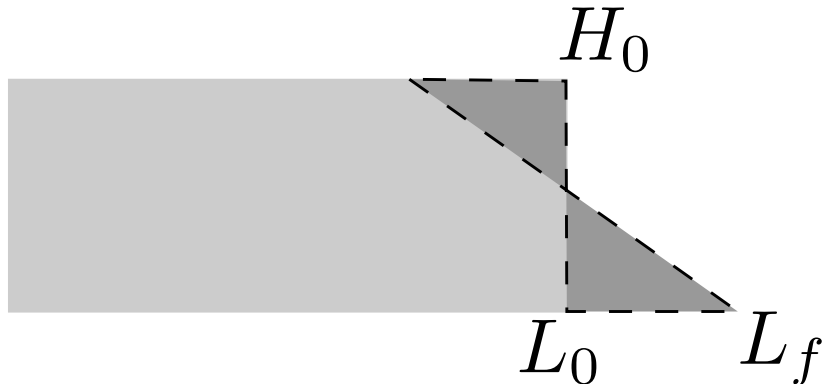


Figure 4.12 Scheme of collapse for small aspect ratio columns. The amount of energy  $\delta E$  lost in the process can be evaluated from the run-out distance  $L_f - L_0$  (Staron and Hinch, 2007).

continuum sense as a frictional dissipation process captures the flow kinematics observed in DEM and experiments for short columns.

Figure 4.13a shows the time evolution of the normalised potential energy ( $E_p/E_0$ ) and kinetic energy ( $E_k/E_0$ ) for granular columns with an initial aspect ratio  $a = 0.4$ . The normalised potential and kinetic energy are computed as

$$E_p = \sum_{p=1}^{N_p} m_p g h_p, \quad (4.10)$$

$$E_{ki} = \frac{1}{2} \sum_{p=1}^{N_p} m_p v_p^2, \quad (4.11)$$

where  $N_p$  is the total number of grains,  $m_p$  is the mass of a grain  $p$ ,  $h_p$  is the height and  $v_p$  is the velocity of the grain  $p$ . The cumulative dissipation energy is computed as

$$\frac{E_d}{E_0} = 1 - \frac{E_k}{E_0} - \frac{E_p}{E_0}. \quad (4.12)$$

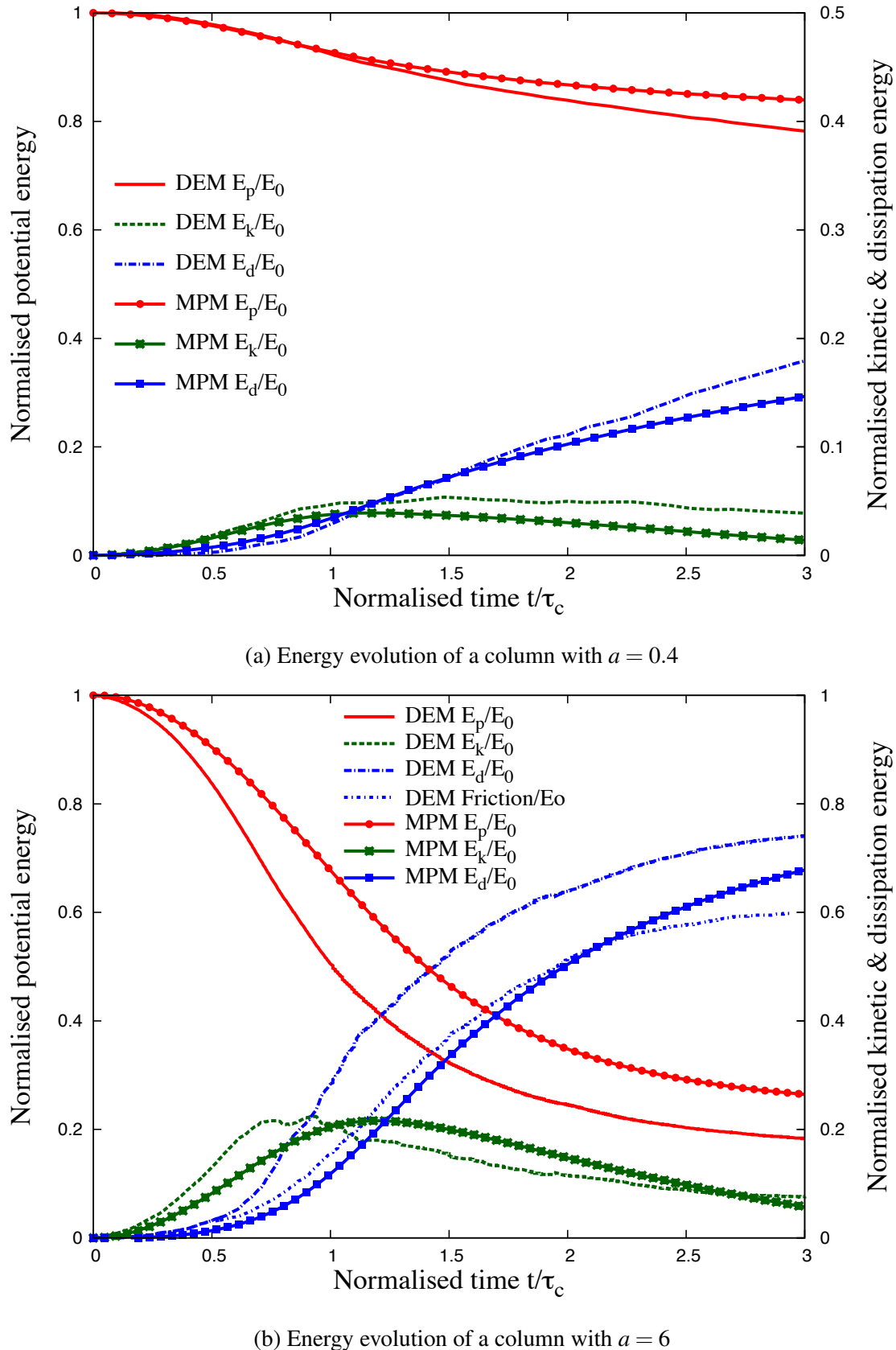
It can be observed that both MPM and DEM show similar energy dissipation mechanisms. The DEM simulation shows 3% more potential energy dissipation in comparison with MPM simulations. This small difference in the potential energy is due to grain rearrangements. This shows the ability of continuum approach in capturing the flow kinematics of columns with small aspect ratios ( $a \leq 2.7$ ).

The evolution of normalised kinetic and potential energy of a tall column collapse ( $a = 6$ ) are shown in figure 4.13b. It can be observed that the initial potential energy stored in the grains is converted to kinetic energy which is dissipated as the granular material flows down. Three successive stages can be identified in the granular column collapse. In the first stage,

similar to short columns, the flow is initiated by a well defined failure surface. However, the centre of gravity of the granular column is much higher than the top of the failure surface, which results in free fall of grains under gravity consuming the column along their way. In this stage which lasts for ( $t < 0.8\tau_c$ ), the initial potential energy stored in the grains is converted into vertical motion. In the second stage, when the grains reach the vicinity of the failure surface, they undergo collisions with the bottom plane and the neighbouring grains, thus causing the flow to deviate along the horizontal direction releasing a large amount of kinetic energy gained during the free fall (figure 4.10). In the third stage, the grains eventually leave the base area of the column and flow sideways (Lajeunesse et al., 2004). As the process involves collective dynamics of all the grains, it is difficult to predict the exact trajectory of a grain, however, the overall dynamics can be explained.

DEM simulations model both collisional and frictional dissipation process during the collapse of tall columns. However, MPM simulations assume that the total initial potential energy stored in the system is completely dissipated through friction over the entire run-out distance, which results in longer run-out distance. Figure 4.13b shows the evolution of normalised energies with time for MPM and DEM simulations. At the initial stage of collapse, characterised by free fall of grains under gravity, DEM simulation, due to its particulate nature shows a rapid reduction in the potential energy in comparison with MPM, where the failure begins from the toe of the column. The continuum nature of MPM simulations results in slower initiation of collapse (figure 4.11b). It can be also observed from figure 4.13b that dissipation energy in MPM is 25% less than DEM simulations. In order to understand the mechanism of energy dissipation, it is important to separate the contribution from the cumulative frictional and collisional parts. The frictional dissipation (basal and internal friction) observed in DEM is almost identical to the frictional dissipation observed in MPM (figure 4.13b). The difference in the dissipation energy is due to the collisional regime, which occurs at  $0.8\tau_c$ . The total dissipation and the frictional dissipation curves diverge around  $0.8\tau_c$  where the grains near the vicinity of the failure surface undergo collisions with the bottom plane and the neighbouring grains resulting in collisional dissipation of the stored potential energy. DEM simulation show drop in the peak kinetic energy at  $\approx 0.8\tau_c$ , which is at the beginning collisional dissipation stage. MPM lacks this collision dissipation mechanism, which results in longer run-out distances for columns with large aspect ratios.

The  $\mu(I)$  rheology, discussed in section 2.2.3, describes the granular behaviour using a dimensionless number, called the *inertial number I*, which is the ratio of inertia to the pressure forces. Small values of  $I$  correspond to the critical state in soil mechanics and large values of  $I$  corresponds to the fully collisional regime of kinetic theory.  $\mu(I)$  rheology is adopted in MPM simulations to understand the characteristics of the flow regime. Mohr-Coulomb model

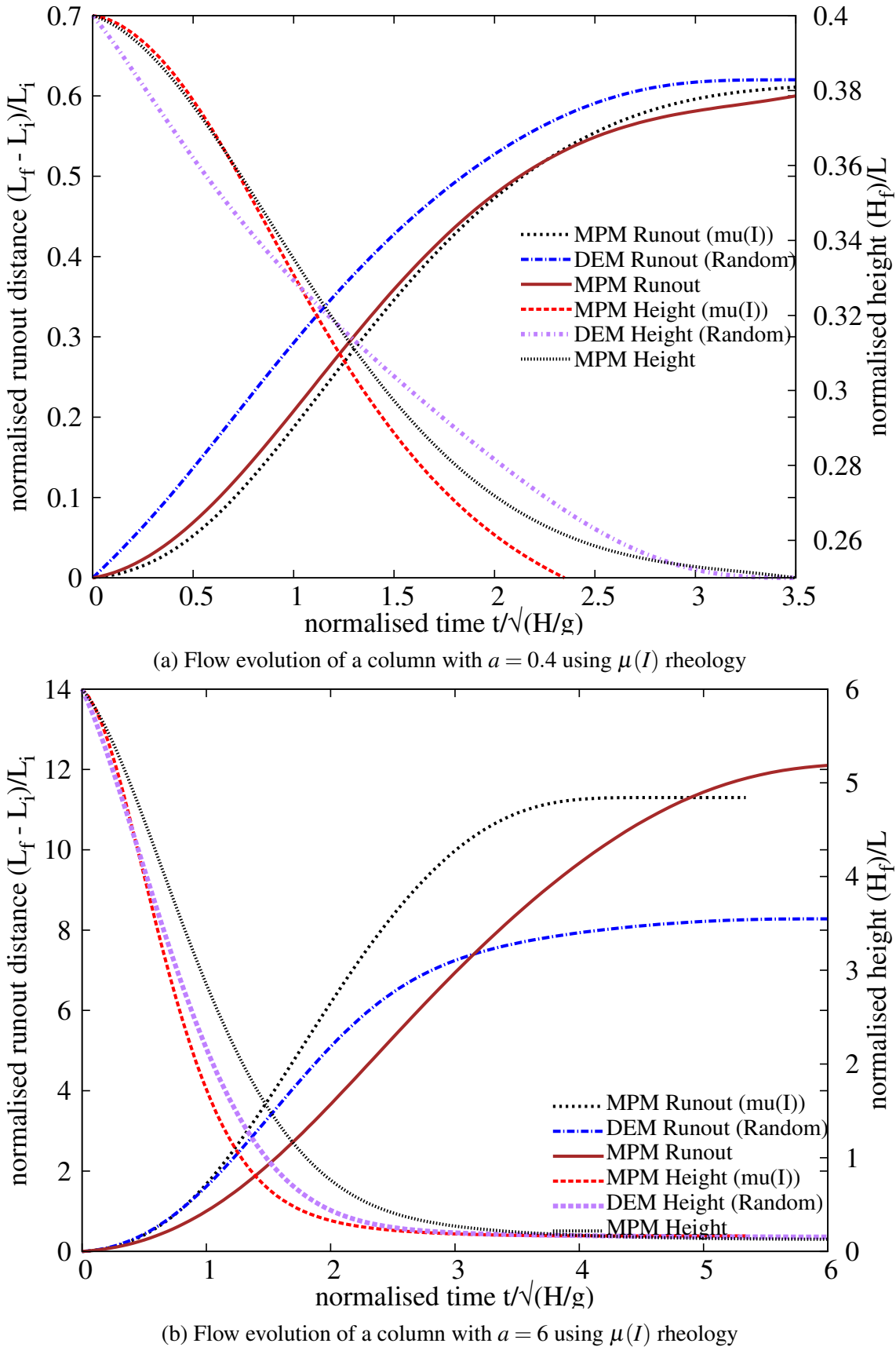
Figure 4.13 Energy evolution of granular column collapse ( $a=0.4$  and 6)

was used along with  $\mu(I)$  rheology. The friction angle is changed according to a friction law (Da Cruz et al., 2005) that is dependent on the inertial number  $I$  as  $\mu = \mu_{min} + bI$ , where  $\mu_{min} = 0.22$  and  $b = 1$ . Figure 4.14 shows the flow evolution of granular column collapse for aspect ratio  $a$  of 0.4 and 6 using  $\mu(I)$  rheology. For short columns, the evolution of flow based on  $\mu(I)$  rheology is identical to the MPM simulation using Mohr-Coloumb model. However, for tall columns,  $\mu(I)$  rheology evolves at the same rate as the DEM simulations up to  $t = 0.8\tau_c$ , after which MPM simulation continues to accelerate due to lack of collisional dissipation, while the DEM simulation decelerates with time.

Figure 4.25b shows that the short column attains a maximum inertial number of 0.012, which is in the dense granular flow regime, inertial number  $\approx 10^{-3} < I < 0.1$  (Da Cruz et al., 2005). However for tall column, the maximum inertial number  $I \approx 0.04$  is still within the dense granular flow regime. DEM simulations, however, showed a collisional regime that has inertial number higher than 0.1. This shows that continuum approach using frictional laws are able to capture the flow kinematics at small aspect ratios, however they are unable to precisely describe the flow dynamics of tall columns, which is characterised by an initial collisional regime. This suggests that triggering mechanisms play a crucial role in the case of modelling the natural flows. This stresses the necessity of accounting for initiation mechanisms while modelling the run-out behaviour using continuum approaches to predict realistic granular flow behaviour. The role of initiation mechanism on the run-out behaviour and the ability of MPM in modelling transient flows that does not involve collision are investigated in section 4.4. One of the important parameter is the initial material properties, such as the packing density, on the run-out behaviour. This aspect has attracted less research. In the next section, 2D DEM simulations are performed to understand the influence of initial grain properties on the collapse. This gives us a better understanding of the input parameters required in the continuum modelling.

### 4.3 Role of initial grain properties on the collapse of granular columns

The role of material properties and the distribution of mass in the system have been shown to have a non-trivial influence on the flow kinematics and the internal flow structure. Hence it is important to understand the role of initial packing density on the run-out behaviour in the case of granular column collapse. Lube et al. (2005) observed that the run-out distance scales with the initial aspect ratio of the column, independent of the material properties. The run-out evolution after the initial transition regime is a frictional dissipation process,

Figure 4.14 Flow evolution of granular column collapse using  $\mu(I)$  rheology ( $a=0.4$  and 6)

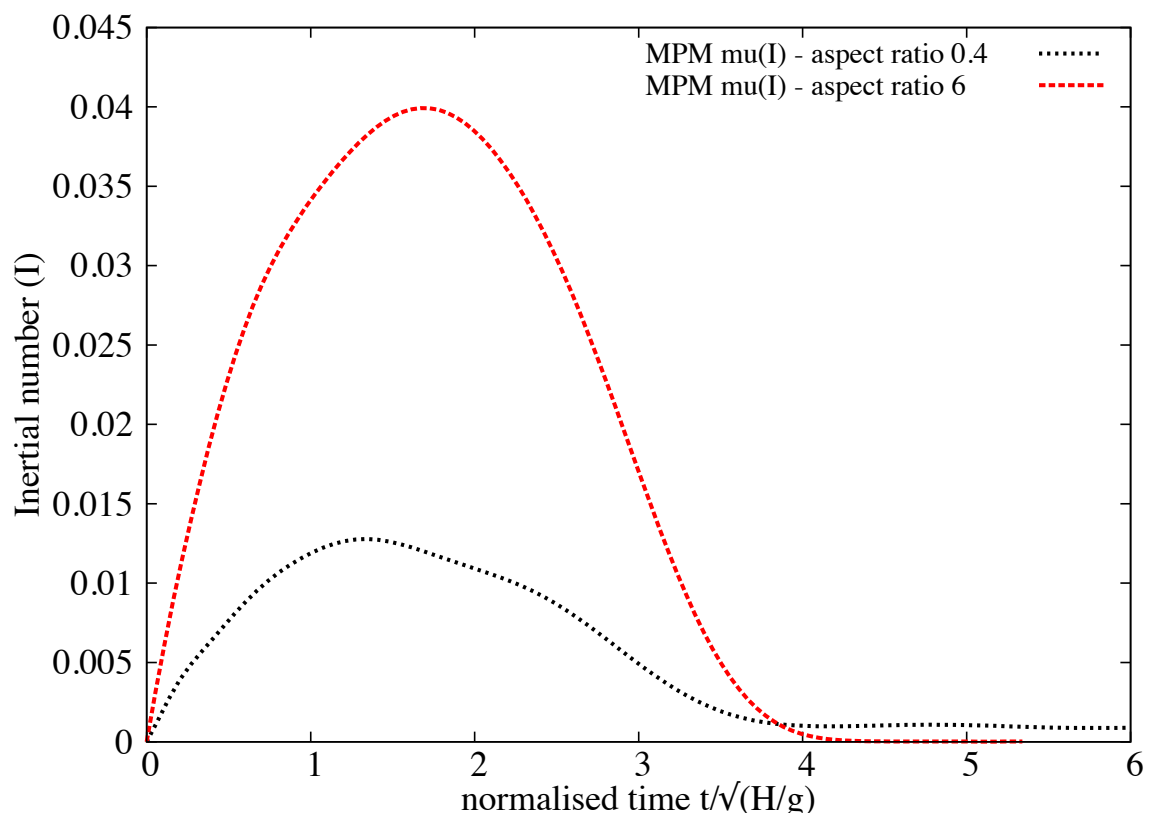


Figure 4.15 MPM simulation of evolution of inertial number with time for columns with  $a = 0.4$  and  $a = 6$

and the lack of influence of material properties on the run-out behaviour is inconsistent with frictional dissipation in continuum modelling of granular flow behaviour. Balmforth and Kerswell (2005) observed that the material properties have almost no influence on the exponent of the normalised run-out as a function of the initial aspect ratio. The numerical constant of proportionality, however, showed clear material dependence. This corroborates the conclusions of Lajeunesse et al. (2004) and refutes that of Lube et al. (2005). Daerr and Douady (1999) also observed strong influence of initial packing density and the internal structure on the behaviour of granular flows.

It should be noted that the collapse experiment is highly transient and no clear stationary regime is observed. On the contrary, the acceleration and the deceleration phases cover nearly the whole duration of the spreading. This makes it difficult to analyse the flow structure and its relation with other characteristic of the system. The knowledge of the final run-out is not a sufficient characterization of the deposit; one also needs to know how the mass is distributed during the flow to understand the dynamics and the dissipation process. This is expected to be true in natural contexts as well as in experiments. While the inter-grain friction does not affect the early vertical dynamics, nor the power-law dependence, it controls the effective frictional properties of the flow, and its internal structure (Staron and Hinch, 2007). It is interesting to note that the details of the structure of the flow do not influence the final run-out dependence, and thus seem to play a marginal role in the overall behaviour of the spreading. This could explain why a simple continuum model with a frictional dissipation could reproduce the run-out scaling for columns with small aspect ratios.

Most research have been focussed on the run-out behaviour of mono-disperse grain sizes. However, the influence of initial packing density and poly-dispersity have attracted less interest. In the present study, DEM simulations of collapse of a loose (79% packing density) and a dense (83% packing density) granular columns with an initial aspect ratio  $a$  of 0.8 are performed to understand the influence of material properties on the run-out behaviour. The evolution of normalised run-out with time for two different initial packing densities are presented in figure 4.16. At the initial stage of collapse  $t = \tau_c$ , the flow evolution is identical in both dense and loose conditions. However, the dense column flows 30% longer than the loose condition. Both the columns come to rest at around  $t = 4\tau_c$ . The columns, however, show similar evolution of the normalised height. This shows that only a part of the column is destabilised during the collapse.

Figure 4.18 shows the evolution of potential and kinetic energy with time. Similar potential energy evolution in both dense and loose conditions reveals that there is no change in the overall mechanism of collapse. The dense condition has a slightly higher peak kinetic energy than the loose column. In the free-fall phase, the dense column shows a steeper

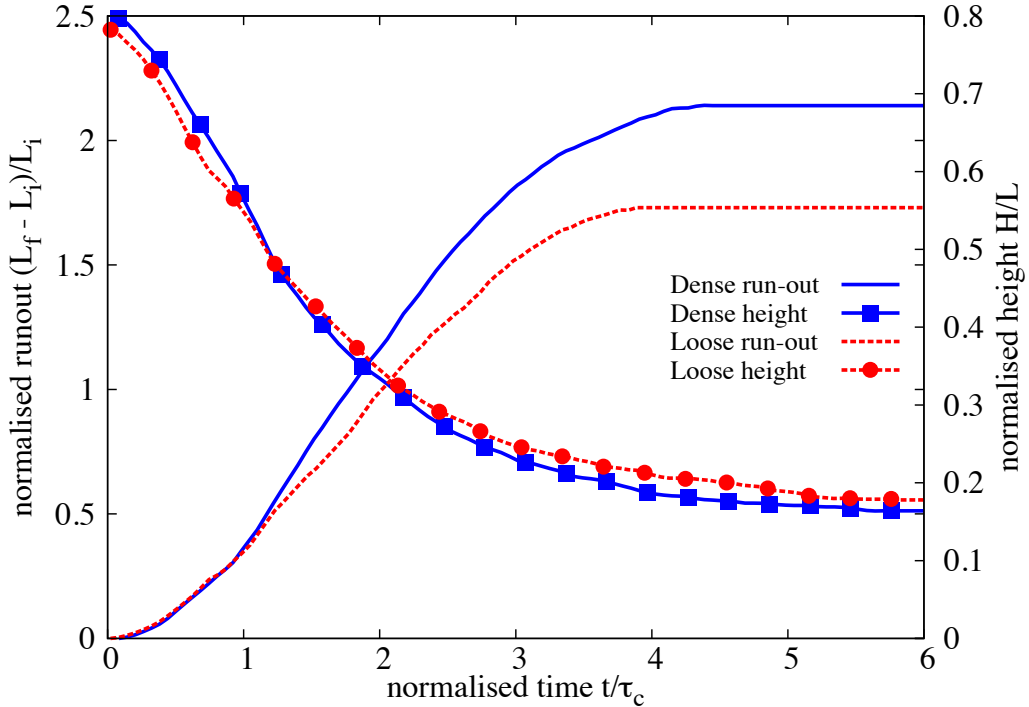


Figure 4.16 Effect of density on the run-out evolution  $\alpha = 0.8$

increase in the horizontal kinetic energy in comparison to the loose column. This indicates that dense granular mass is pushed farther away more quickly than the loose column. A loose column exhibits higher vertical kinetic energy which may be due to particle rearrangement resulting in densification of the granular mass. Figure 4.17 shows that the loose sample densifies as the flow evolves. Both dense and loose granular columns dilate during the initial stage of collapse, this is due to grains experiencing shear along the shear-failure surface. In both cases, the granular mass attains similar packing density at the end of the flow. The dense granular column dilates, while the loose column compacts to achieve the same critical density. The dense condition has higher mobilised potential energy during the initial stage of collapse, which yields higher horizontal kinetic energy for the flow. However in loose conditions, a higher proportion of the available energy is lost during compaction. This behaviour in addition to higher mobilised potential energy results in longer run-out distance in dense granular column. Lajeunesse et al. (2004) observed that the flow comes to rest at around  $3\tau_c$ , but the grains continue to re-arrange until  $6\tau_c$ . Similar behaviour is observed in DEM simulations.

In order to remove the effect of crystallisation on the run-out behaviour, a highly polydisperse sample ( $r = d_{max}/d_{min} = 6$ ) is used. The flow kinematics of a dense (relative density  $D_r = 74\%$ ) and a loose ( $D_r = 22\%$ ) granular column with aspect ratio of 0.8 is

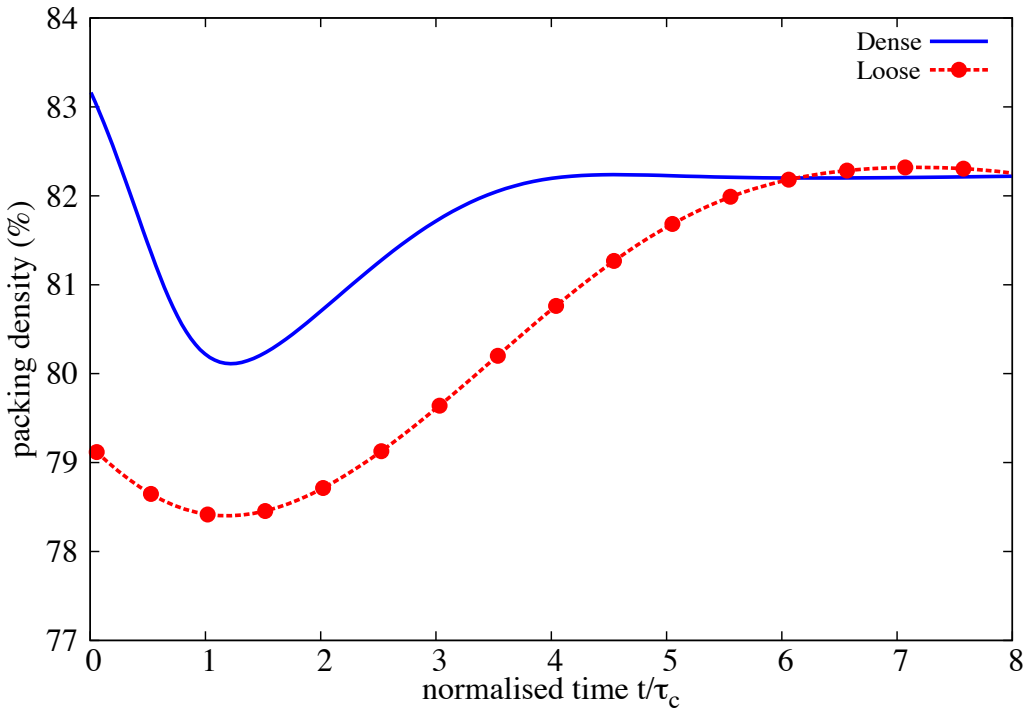


Figure 4.17 Evolution of local packing density with time  $a = 0.8$

studied. figure 4.19 shows the evolution of the normalised run-out with time for dense and loose granular columns with an initial aspect ratio of 0.4. Similar to the previous case, the dense granular column exhibits longer run-out distance (figure 4.19). Figure 4.21a show the evolution of energy with time for dense and loose conditions. The peak kinetic energy in the dense condition is  $\sim 20\%$  higher than the loose condition. Due to compaction of grains in loose condition, almost 20% of the normalised initial potential energy available for collapse is lost in densification due to grain rearrangements in comparison to the dense condition (figure 4.21). The compaction of grains in loose column and the dilation in dense column results in significantly different flow structure, especially at the flow front (figure 4.20). As the loose column densifies, more granular mass is pushed to the flow front resulting in higher vertical effective stress. The loose column exhibits a more parabolic final deposit profile in comparison to the dense column, which shows a triangular deposit at the front.

In short columns, only a part of the granular column above the failure surface participates in the flow. However, it appears that the collapse for large aspect ratios mixes two very different dynamics: the first stage shows a large vertical acceleration, while the second stage consists of a “conventional” horizontal granular flows. The effect of density on the run-out behaviour of tall columns is investigated. Similar to short columns, the dense granular column with an aspect ratio of 6 shows higher run-out distance in comparison to the loose condition.

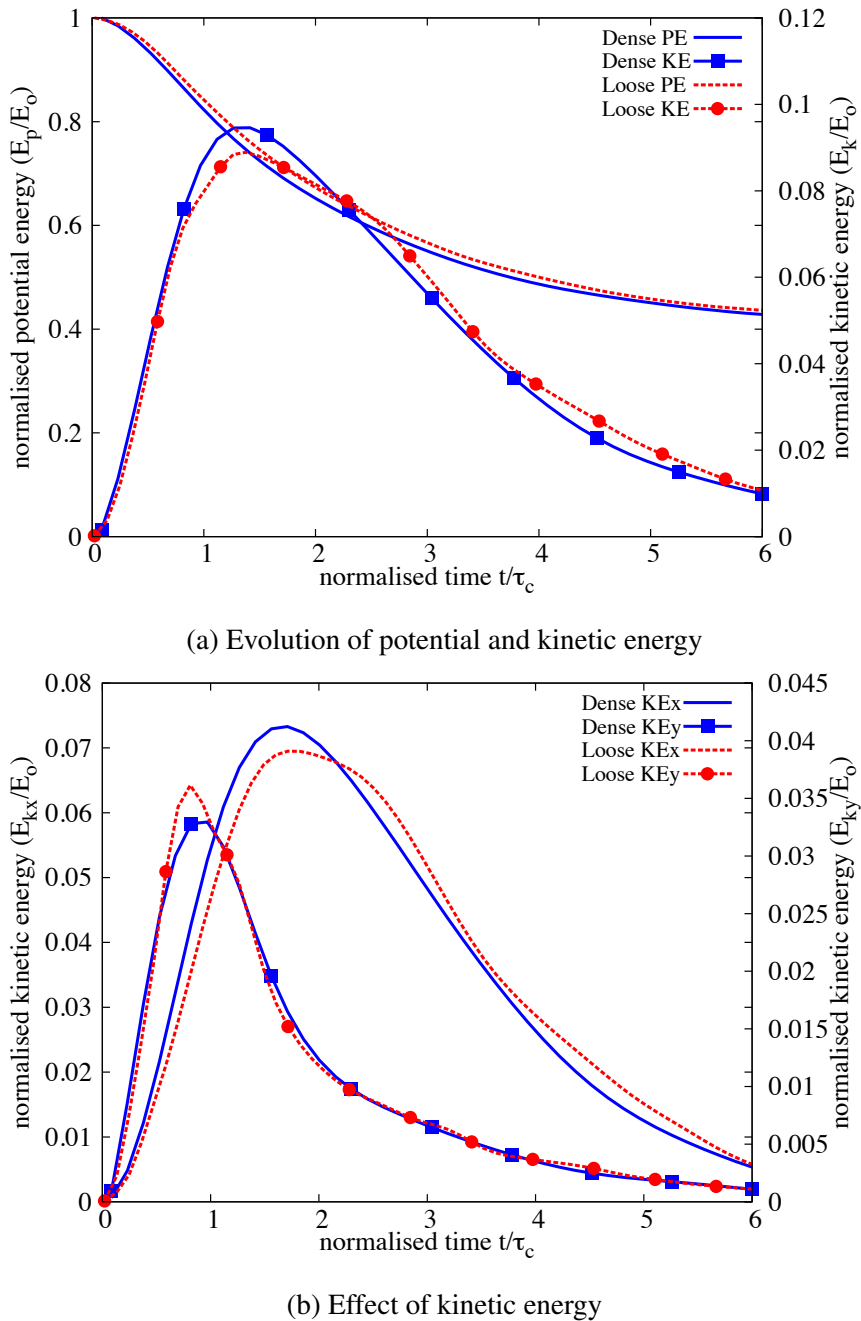
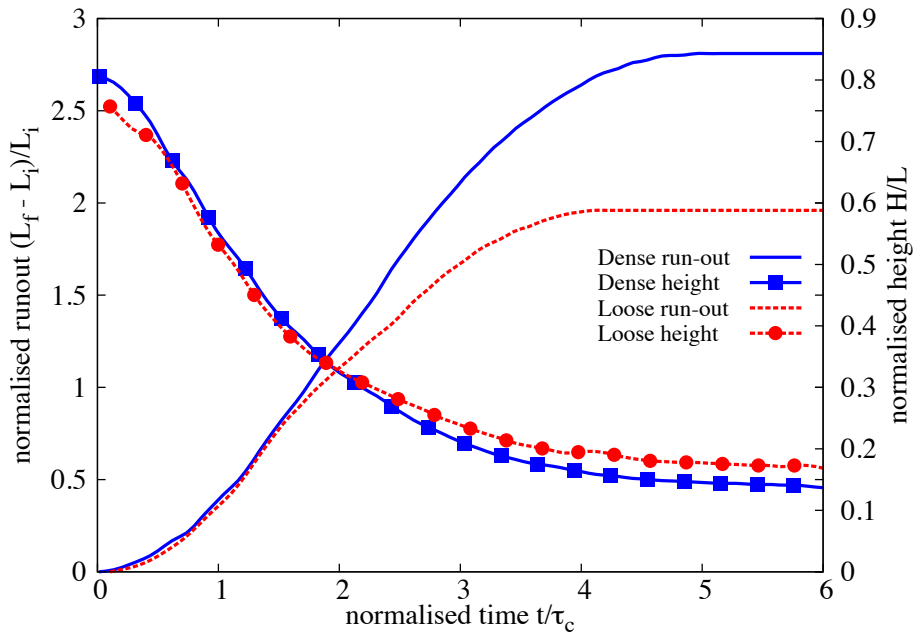
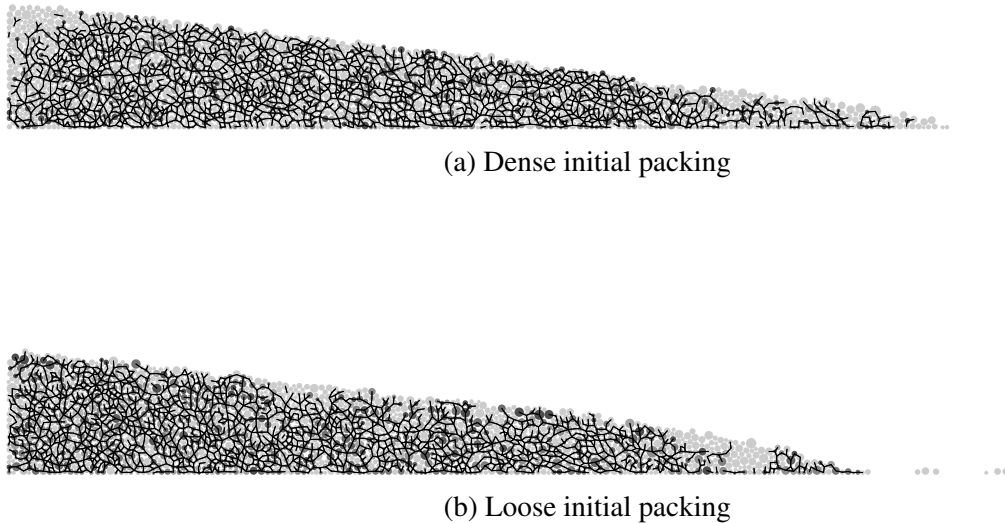


Figure 4.18 Effect of density on the energy evolution  $a = 0.8$

Figure 4.19 Effect of density on run-out evolution  $a = 0.8$  (poly-dispersity  $r = 6$ )Figure 4.20 Snapshots of granular column collapse at  $t = 6\tau_c$  ( $a = 0.8$ )

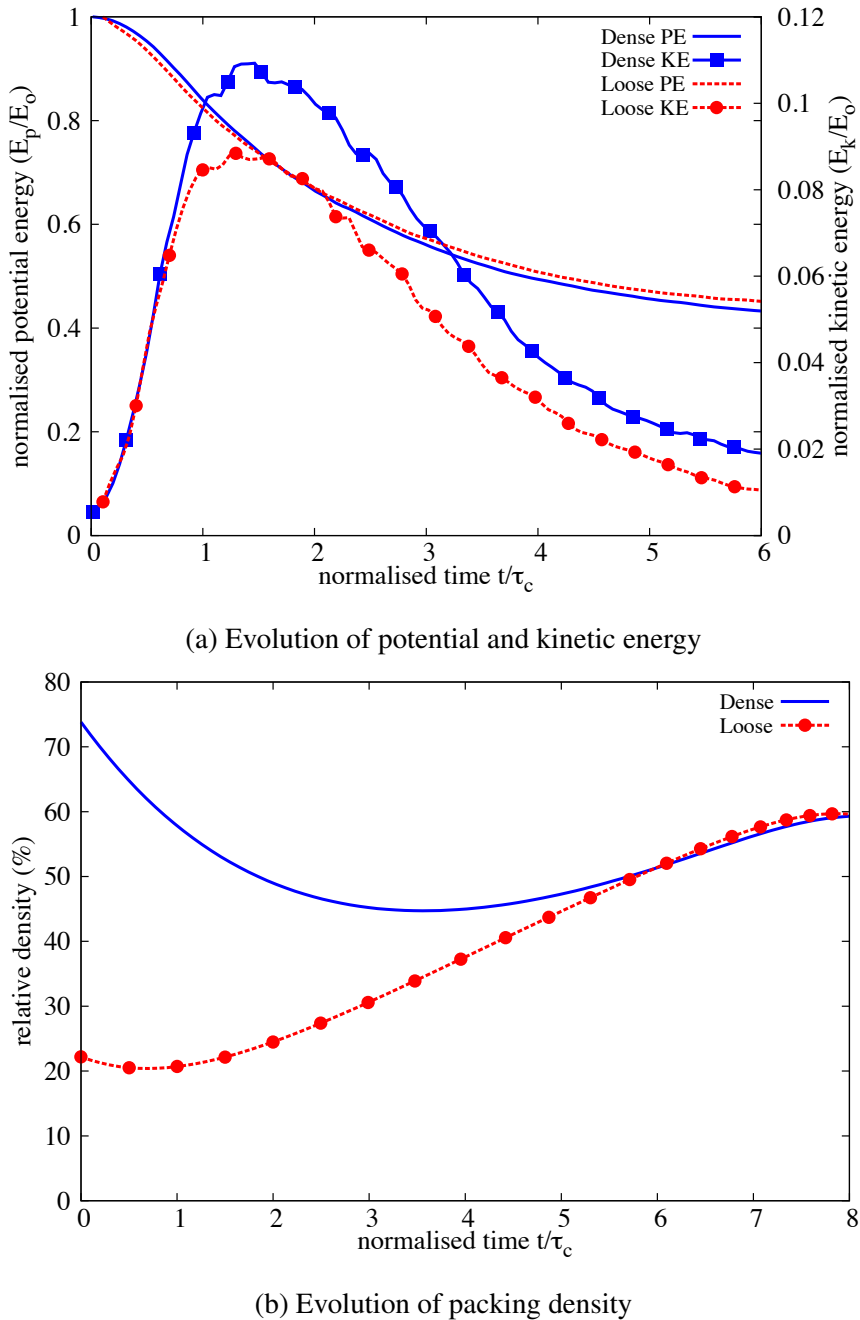


Figure 4.21 Effect of density on the evolution of energy and packing fraction  $a = 0.8$  (poly-dispersity 'r' = 6)

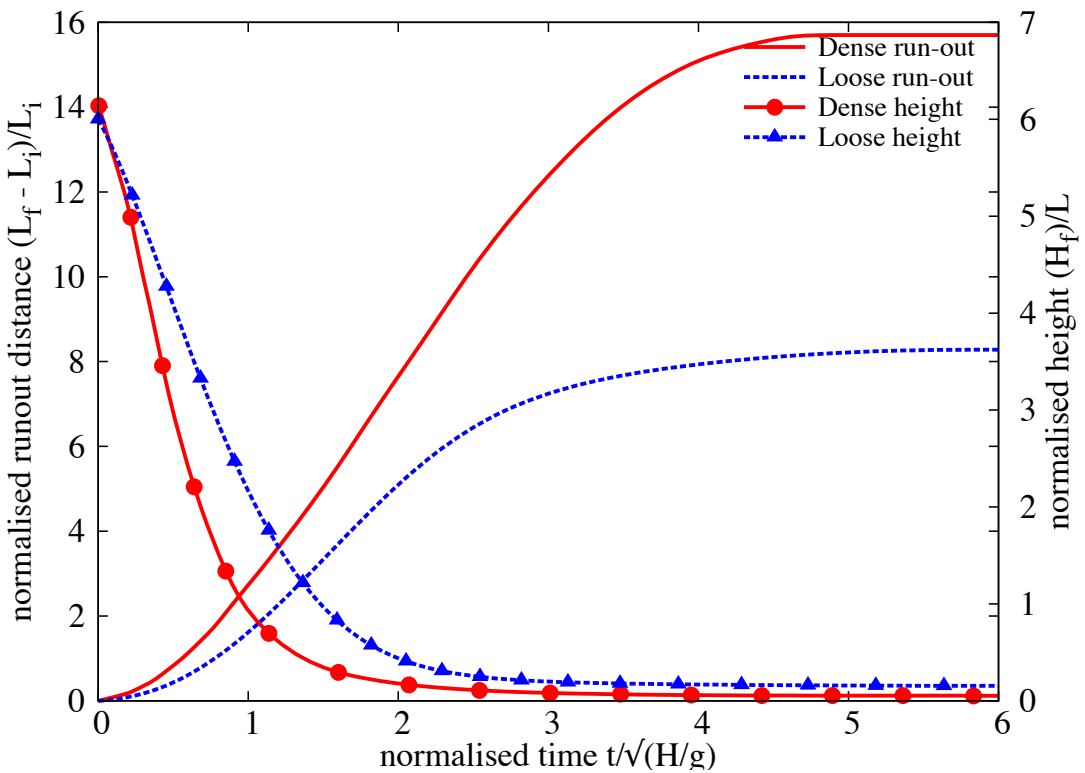
The dense granular column flows almost twice as much as that of the loose column. Unlike short columns, the evolution of run-out is different even at the initial stage of the collapse. The dense granular column, which has higher initial potential energy shows a rapid increase in the run-out due to free-fall and higher mobilised potential energy. During this stage of collapse, the dense granular column has 15 % higher normalised kinetic energy available for the horizontal push. This results in a longer run-out distance for a dense granular column in comparison to an initially loose granular column.

The initial packing fraction and the distribution of kinetic energy in the system has a significant influence on the flow kinematics and the run-out behaviour. The next section will discuss the influence of triggering mechanism and the distribution of the kinetic energy in the granular system on the run-out behaviour.

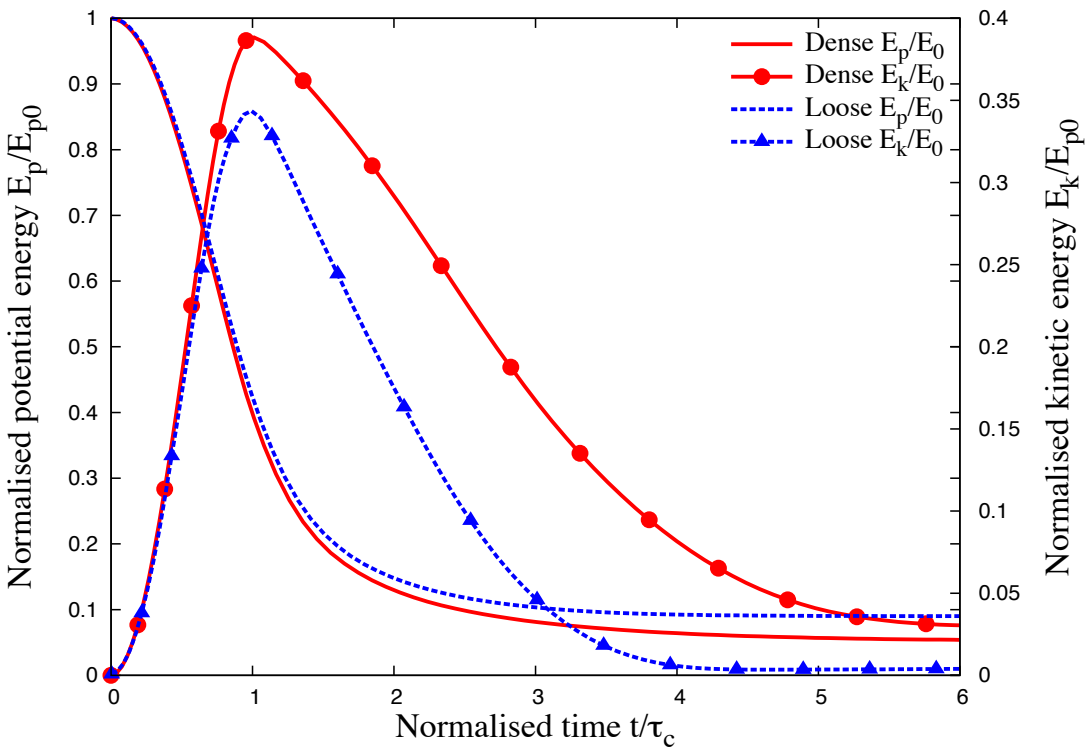
## 4.4 Slopes subjected to impact loading

Transient granular flows occur very often in nature. Well-known examples are rockfalls, debris flows, and aerial and submarine avalanches. In the geotechnical context, transient movements of large granular slopes is a substantial factor of risk due to their destructive force and the transformations they may produce in the landscape. Natural granular flows may be triggered as a result of different processes such as gradual degradation, induced by weathering or chemical reactions, liquefaction and external forces such as earthquakes. Most contemporary research on granular materials deals with the steady-state flow. Transients and inhomogeneous boundary conditions are much less amenable to observation and analysis, and have thus been less extensively studied despite their primary importance in engineering practice. In most cases of granular flow, an initially static pile of grains is disturbed by external forces, it then undergoes an abrupt accelerated motion and spreads over long distances before relaxing to a new equilibrium state. The kinetic energy acquired during destabilisation is dissipated by friction and inelastic collisions.

This section investigates the ability of MPM, a continuum approach, to reproduce the evolution of a granular pile destabilised by an external energy source. In particular, a central issue is whether power-law dependence of the run-out distance and time observed with respect to the initial geometry or energy can be reproduced by a simple Mohr-Coulomb plastic behaviour for granular slopes subjected an impact energy. The effects of different input parameters, such as the distribution of energy and base friction, on the run-out kinematics are studied by comparing the data obtained from DEM and MPM simulations.



(a) Effect of density on run-out evolution



(b) Effect of density on energy evolution

Figure 4.22 Effect of density on the run-out behaviour and energy evolution  $a = 0.6$

#### 4.4.1 Numerical set-up

The DEM sample is composed of  $\sim 13000$  disks with a uniform distribution of diameters by volume fractions ( $d_{max} = 1.5d_{min}$ ). The mean grain diameter and mass are  $d \simeq 2.455$  mm and  $m \simeq 0.0123$  kg, respectively. The grains are first poured uniformly into a rectangular box of given width and then the right-hand side wall is shifted further to the right to allow the grain to spread. A stable granular slope is obtained when all grains come to rest; see figure 4.23. This procedure leads to a mean packing fraction  $\simeq 0.82$ . Soil grains with mean density of  $2600$  kg/m<sup>3</sup> and internal friction coefficient of 0.4 between grains is adopted.

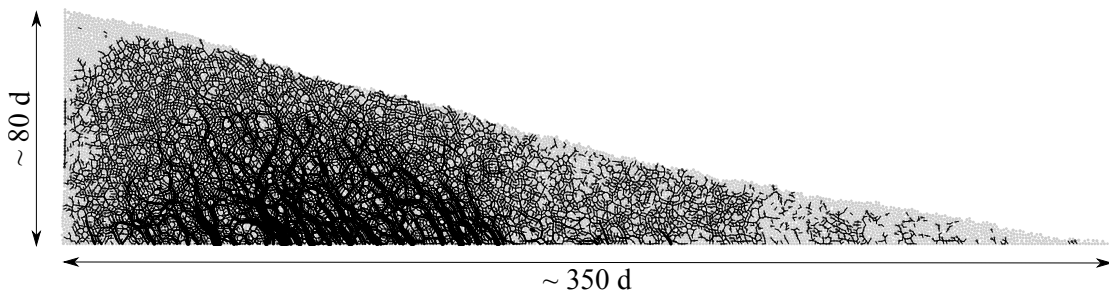


Figure 4.23 Initial geometry and dimensions of the pile subjected to an impact velocity

The initial static pile is set into motion by applying a horizontal gradient velocity  $v_{0x}(y) = k(y_{max} - y)$  with  $k > 0$ . Such a configuration mimics the energy transfer mechanism of a horizontal quake along the bottom of the pile. The evolution of pile geometry and the total kinetic energy as a function of the initial input energy  $E_0$  is studied. The run-out distance  $L_f$  is the distance of the rightmost grain, which is still in contact with the main mass when the pile comes to rest. The run-out will be normalized by the initial length  $L_0$  of the pile, as in the experiments of collapsing columns. The total run-out duration  $t_f$  is the time taken by the pile to reach its final run-out distance  $L_f$ .

For grain-scale simulations, classical DEM and Contact Dynamics approaches are used. This research is done in collaboration with Patrick Mutabaruka, University of Montpellier, who performed Contact Dynamics (CD) simulations that are presented in this section. A detailed description of the Contact Dynamics method can be found in Jean (1999); Moreau (1993); Radjai and Dubois (2011); Radjai and Richefeu (2009). The CD method is based on implicit time integration of the equations of motion and a non-smooth formulation of mutual exclusion and dry friction between particles. The CD method requires no elastic repulsive potential and no smoothing of the Coulomb friction law for the determination of forces. For this reason, the simulations can be performed with large time steps compared to discrete element simulations. The unknown variables are particle velocities and contact forces, which are calculated at each time step by taking into account the conservation of momenta and the

constraints due to mutual exclusion between particles and the Coulomb friction. An iterative algorithm based on a non-linear Gauss-Seidel scheme is used. The only contact parameters within the CD method are the friction coefficient  $\mu$ , the normal restitution coefficient  $\varepsilon_n$  and the tangential restitution coefficient  $\varepsilon_t$  between grains.

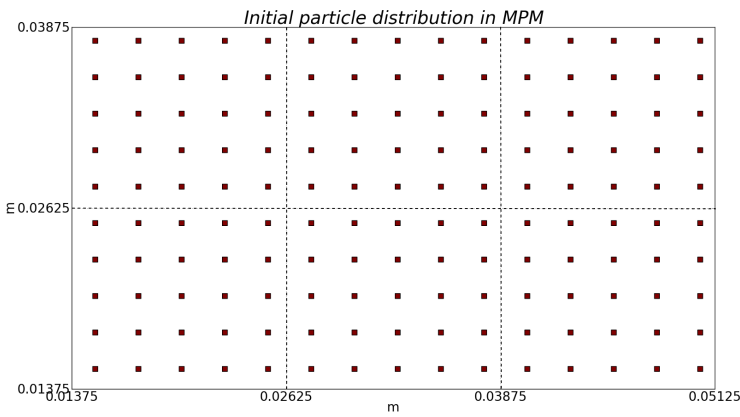
In MPM simulations, the material point spacing is adopted to be the same as the mean grain diameter in DEM. A mesh size of 0.0125m is adopted with 25 material points per cell. The effect of mesh size and the number of material points per cell is investigated in section 3.3.5. The initial configuration of the slope in MPM is shown in figure 4.24a. Frictional boundary condition is applied on the left and the bottom boundaries by applying constraints to the nodal acceleration. The initial vertical stress of the granular pile in equilibrium, before the impact, in the MPM simulation is shown in figure 4.24b. The distribution of the initial gradient impact energy of 50 J on the granular pile is shown in figure 4.24c. The Mohr-Coulomb model with no dilation is used to simulate the continuum behaviour of the granular pile. Periodic shear tests using CD (figure 4.25a), reveals a macroscopic friction coefficient of 0.22. The evolution of inertial number with friction is presented in figure 4.25b.

The natural units of the system are the mean grain diameter  $d$ , the mean grain mass  $m$  and acceleration due to gravity  $g$ . For this reason, the length scales are normalised by  $d$ , time by  $(d/g)^{1/2}$ , velocities by  $(gd)^{1/2}$  and energies by  $mgd$ .

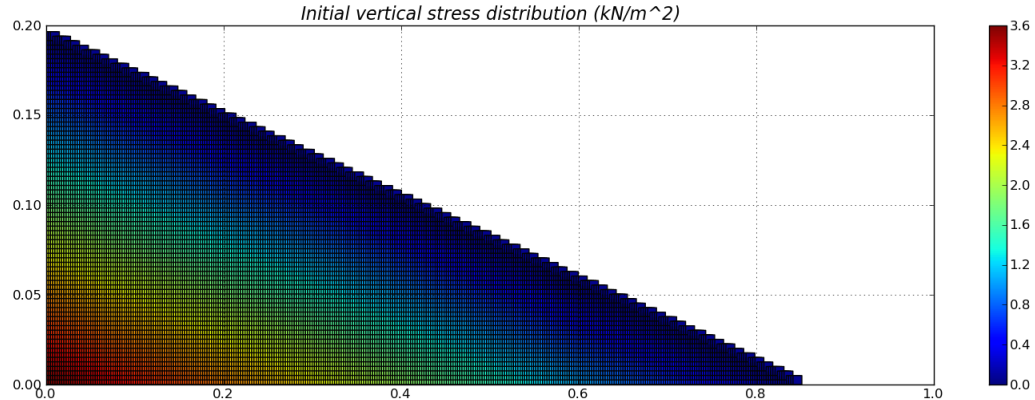
#### 4.4.2 Evolution of pile geometry and run-out

Figure 4.26 shows the initial evolution of granular slope subjected to an initial impact energy  $E_0 = 61$  (in dimensionless units) using MPM. As the granular slope is sheared along the bottom, the shear propagates to the top leaving a cavity in the vicinity of the left wall. This cavity gets partially filled as the granular mass at the top collapse behind the flowing mass due to inertia. Similar behaviour is observed during the initial stages of the flow evolution using DEM and CD techniques (figure 4.27). Due to inertia, the grains at the top of the granular heap roll down to fill the cavity, while the pile continues to spread.

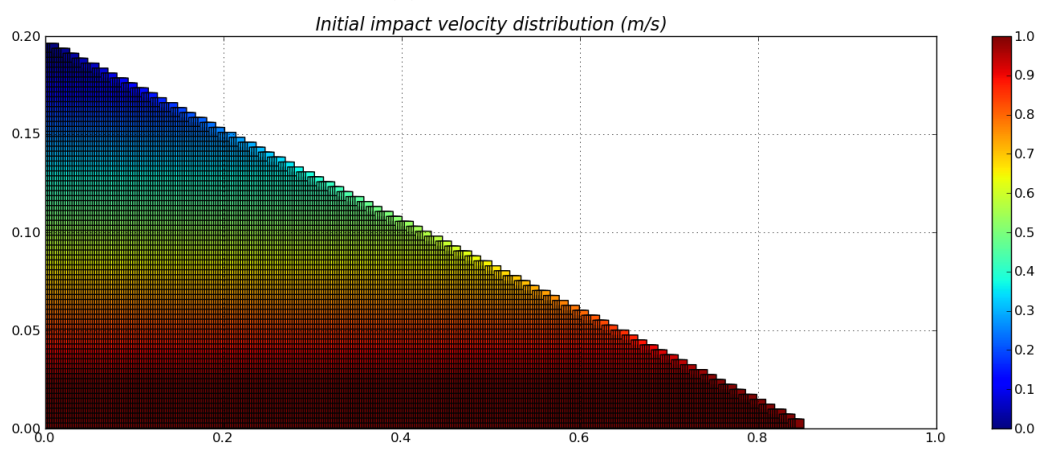
The flow involves a transient phase with a change in the geometry of the pile followed by continuous spreading. The gradient input energy applied to the granular slope mimics a horizontal quake. Despite the creation of a cavity behind the flowing mass, the granular heap remains in contact with the left wall irrespective of the input energy. Figure 4.28a shows the normalized run-out distance  $(L_f - L_0)/L_0$  and total run-out time  $t_f$  as a function of the input energy  $E_0$ . Two regimes characterized by a power-law relation between the run-out distance and time as a function of  $E_0$  can be observed. In the first regime, corresponding to the range of low input energies  $E_0 < 40 mgd$ , the run-out distance observed varies as  $L_f \propto (E_0)^\alpha$  with



(a) Initial configuration of material points per cell. 25 material points per cell. Cell size of 0.0125m.



(b) Initial stress in MPM



(c) Initial horizontal velocity for a pile subjected to an impact velocity of 50J.

Figure 4.24 Initial configuration for the MPM simulation of a pile subjected to impact velocities.

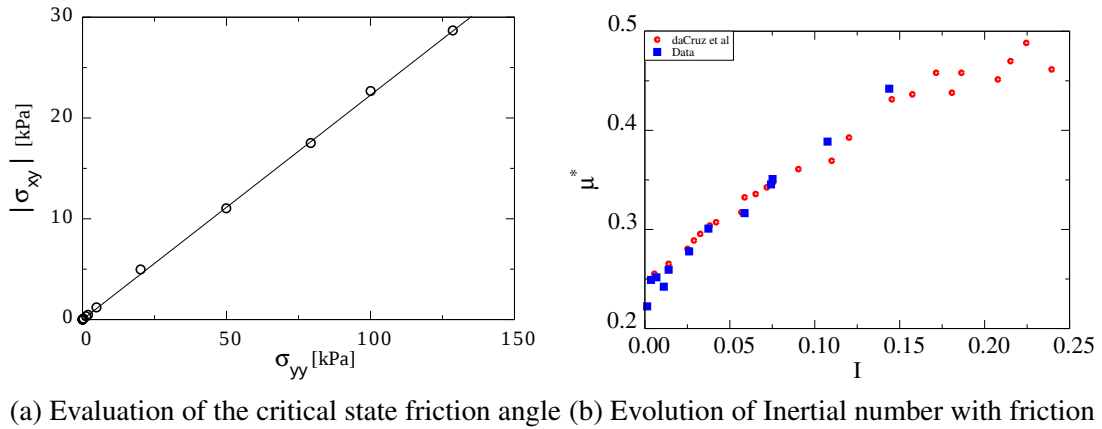


Figure 4.25 Periodic shear test using CD (Mutabaruka, 2013).

$\alpha \simeq 0.206 \pm 0.012$  over nearly one decade. Overall, the run-out distance predicted by the continuum approach matches the DEM simulations. At very low energies, DEM simulations show longer run-out distance due to local fluidisation. The difference in the run-out between DEM and CD arise mainly from the scales of description and the inelastic nature of Contact Dynamics. Similar behaviour between DEM and CD approaches was observed by Radjai et al. (1997).

While the run-out exhibits a power-law relation with the initial input energy, DEM simulations show that the flow duration remains constant at a value  $t_f \simeq 60 (d/g)^{0.5}$  irrespective of the value of  $E_0$ . The constant run-out time, in grain-scale simulations, indicates the collapse of grain into the cavity left behind the pile. An average run-out speed can be defined as  $v_s = (L_f - L_0)/t_f$ . According to the data,  $v_s \propto (E_0)^{0.52 \pm 0.012}$ . The error on the exponent represents the error due to the linear fit on the logarithmic scale. Since the initial average velocity varies as  $v_0 \propto (E_0)^{0.5}$ , this difference between the values of the exponents suggests that the mobilized mass during run-out declines when the input energy is increased.

In the second regime, corresponding to the range of high input energies  $E_0 > 40 \text{ mgd}$ , the run-out distance varies as  $L_f \propto (E_0)^{\alpha'}$  over one decade with  $\alpha' \simeq 0.56 \pm 0.04$  while the duration increases as  $t_f \propto (E_0)^{\beta'}$  with  $\beta' \simeq 0.33 \pm 0.02$ . Hence, in this regime the average run-out speed varies as  $v_s \propto (E_0)^{0.498 \pm 0.01}$ . This exponent is close to the value 0.5 in  $v_0 \propto (E_0)^{0.5}$ , and hence, within the confidence interval of the exponents. In the second regime, both DEM and MPM predict almost the same run-out behaviour. However, MPM predicts longer duration with increase in the input energy.

It is worth noting that a similar power-law dependence of the run-out distance and time were found in the case of granular column collapse with respect to the initial aspect ratio. In the column geometry, the grains spread away owing to the kinetic energy acquired during gravitational collapse of the column. Topin et al. (2012) found that the run-out distance varies

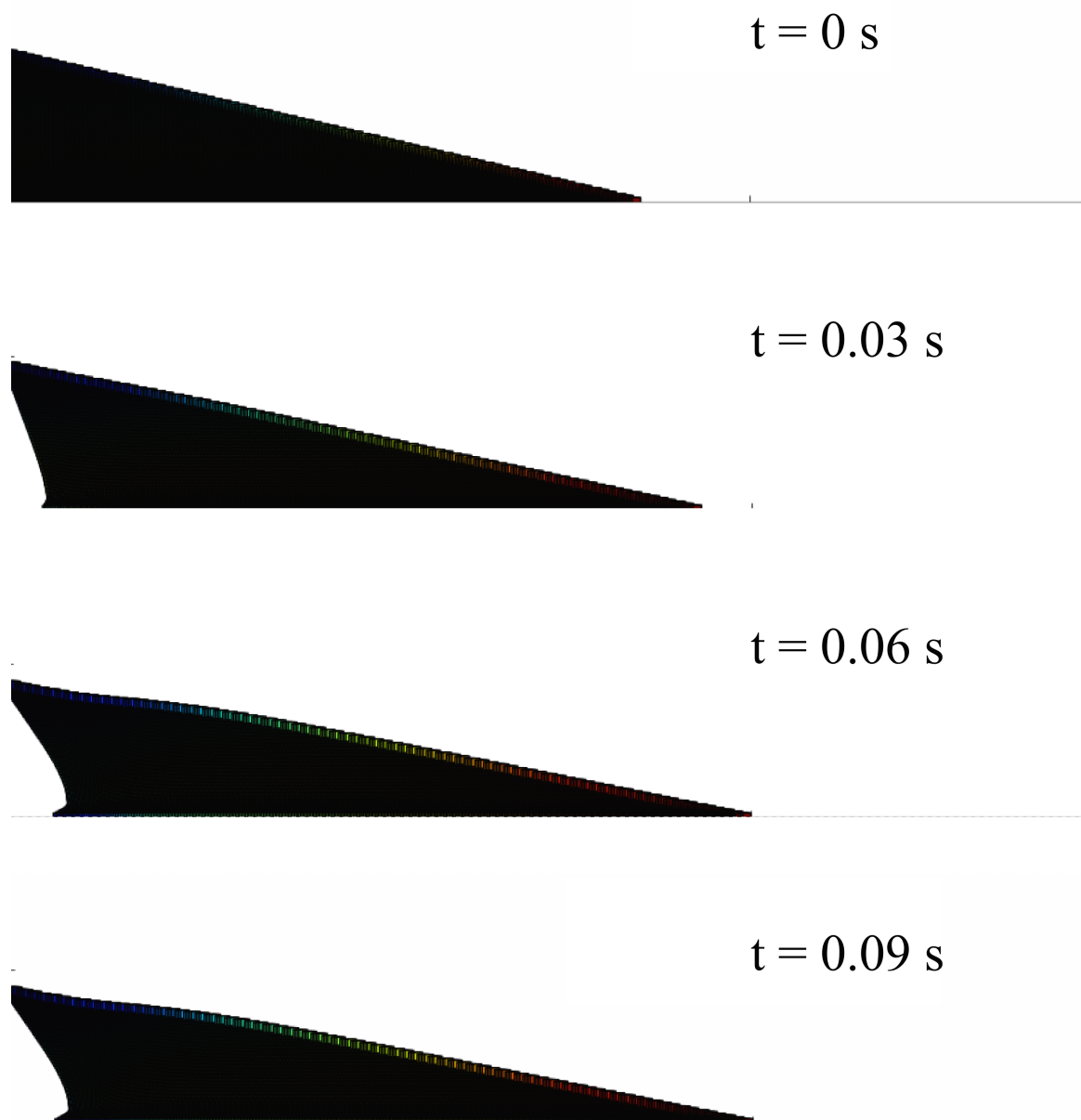


Figure 4.26 MPM simulation of the initial stages of granular pile subjected to a gradient impact energy.

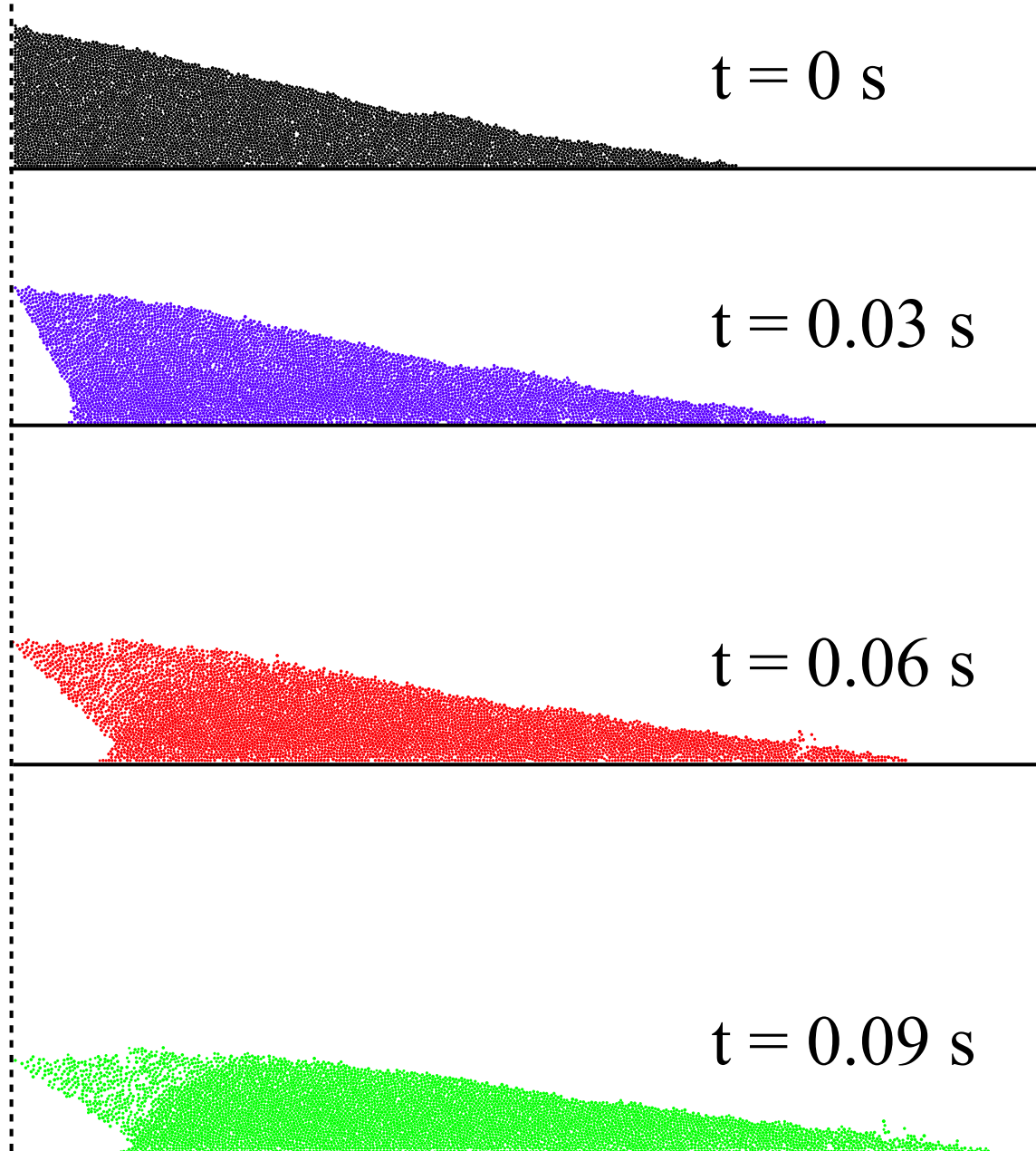
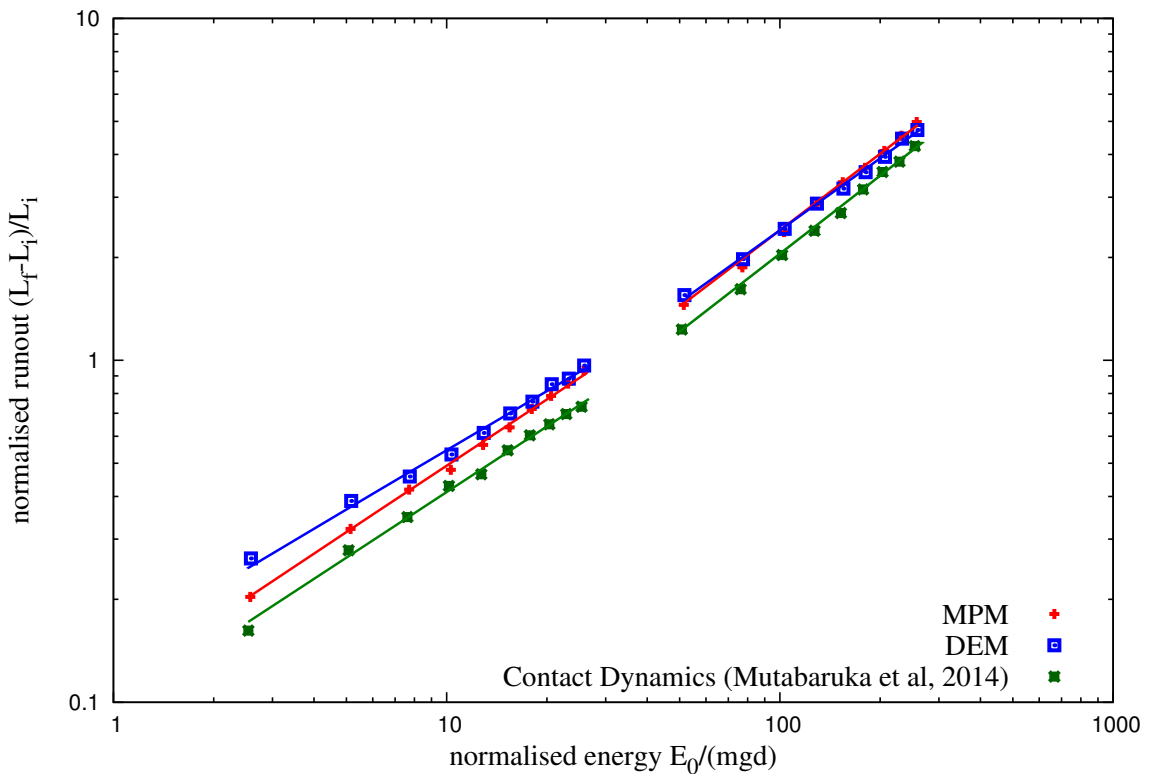
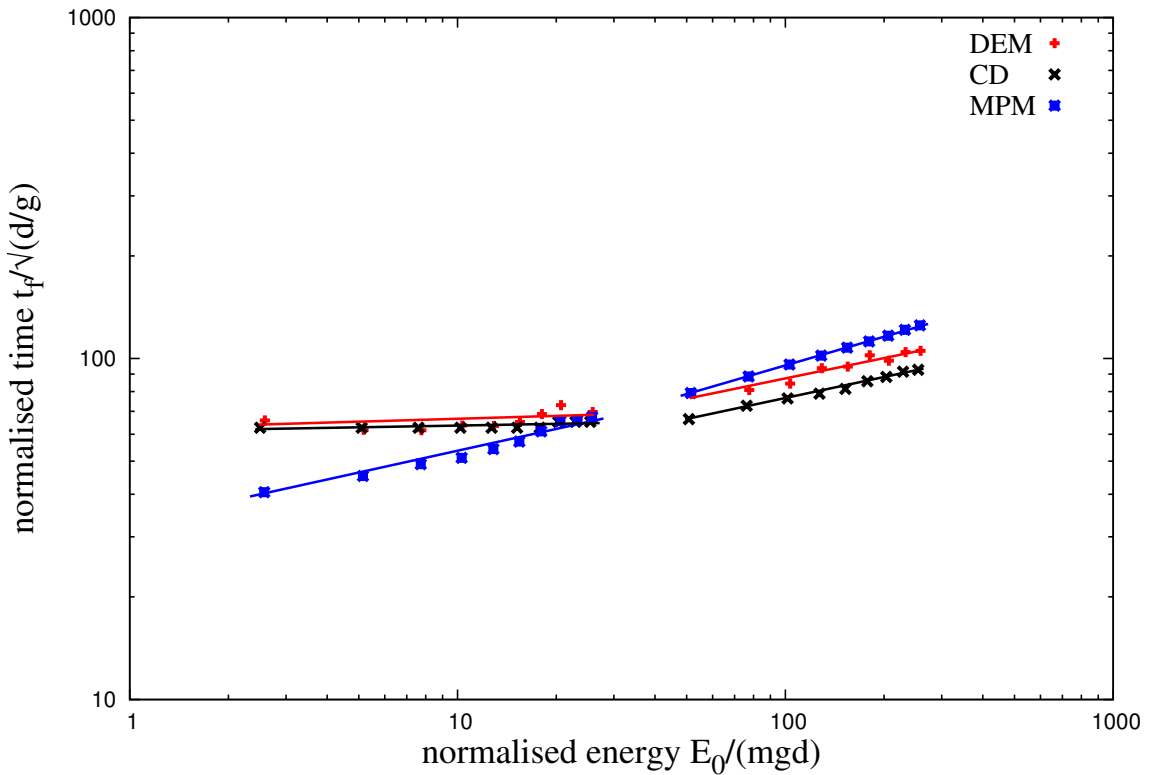


Figure 4.27 CD simulation of the initial stages of granular pile subjected to a gradient impact energy. (Mutabaruka, 2013).



(a) Run-out distance as a function of normalised input kinetic energy



(b) Duration of run-out as a function of normalised input kinetic energy

Figure 4.28 Evolution of run-out and time as a function of the normalised input energy for a pile subjected a gradient impact energy

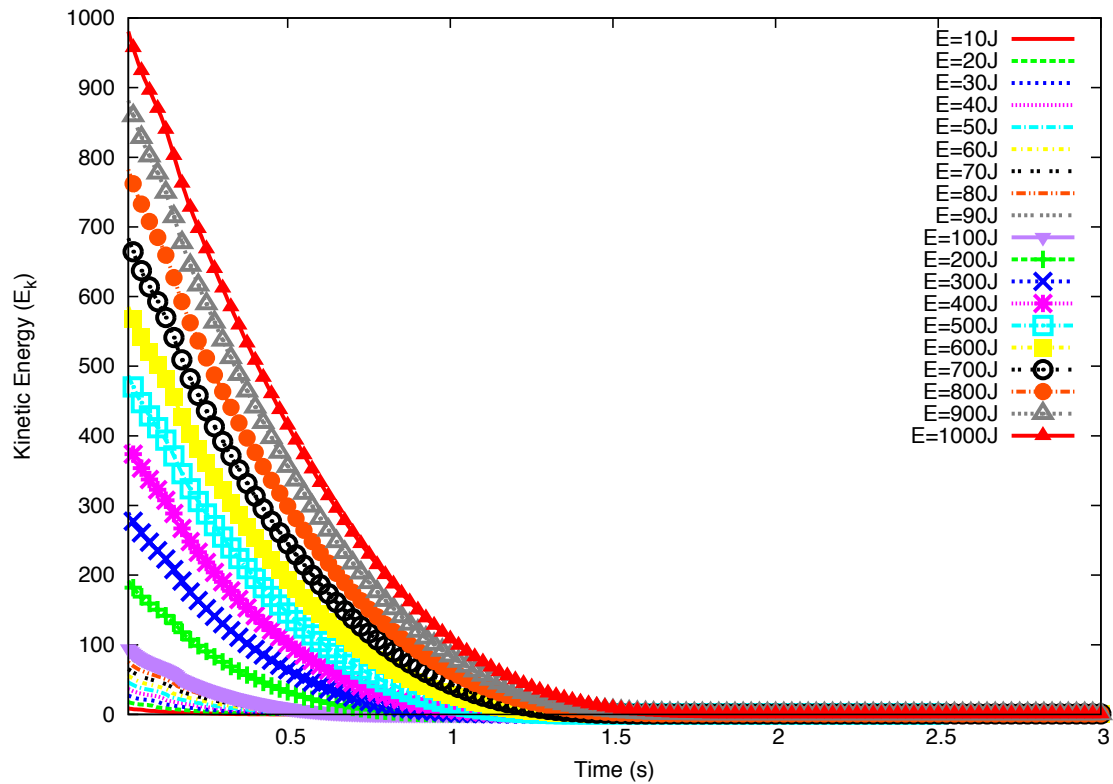
as a power-law of the available peak kinetic energy at the end of the free-fall stage with an exponent  $\simeq 0.5$ . This value of exponent is lower than the run-out evolution observed in the second regime. This is, however, physically plausible since the distribution of kinetic energies at the end of the collapse is more chaotic than in this case where the energy is supplied from the very beginning in a well-defined shear mode. As pointed out by Staron et al. (2005), the distribution of kinetic energies is an essential factor for the run-out distance.

#### 4.4.3 Decay of kinetic energy

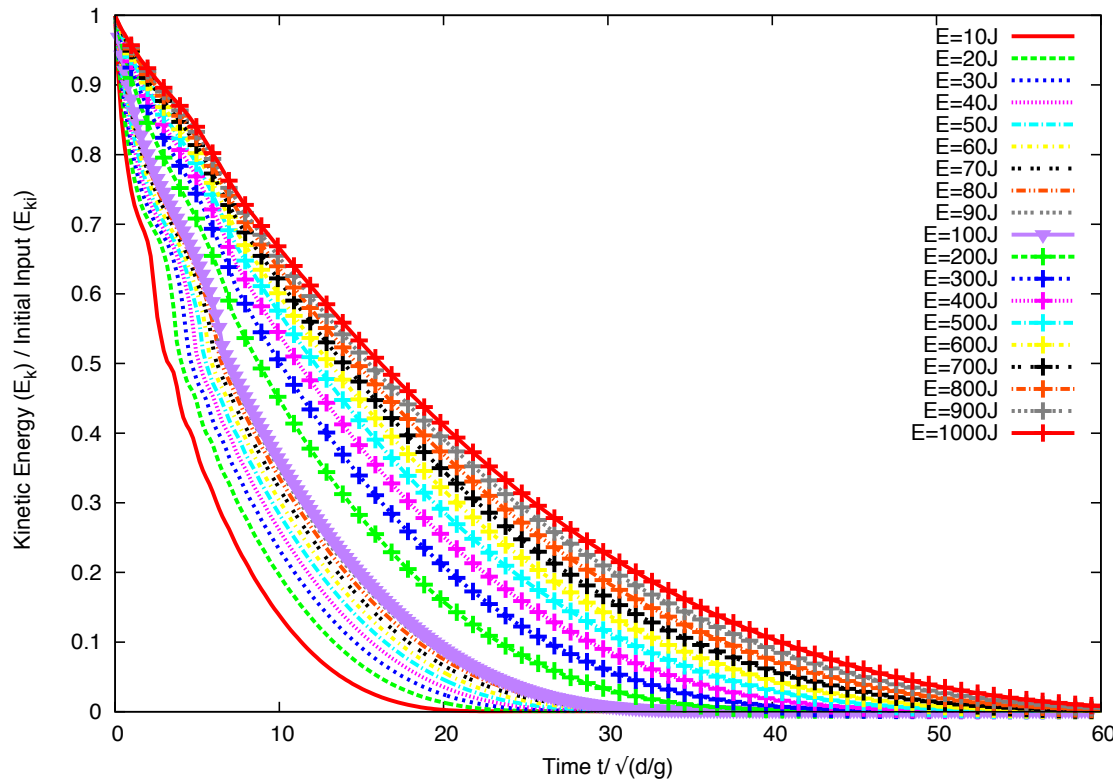
The non-trivial evolution of the pile geometry in two regimes suggests that the energy supplied to the pile is not simply dissipated by shear and friction along the bottom plane. It is important to split the kinetic energy into vertical and horizontal components ( $K_{Ex}$  and  $K_{Ey}$ ) of the velocity field. Although, the input energy is in the  $x$  component, a fraction of the energy is transferred to the vertical component of the velocity field and dissipated during the transient phase. The evolution of kinetic energy is studied to understand the behaviour of granular flow that is consistent with the evolution of the pile shape.

The evolution of total kinetic energies  $E_k$  with time for different values of the input energy  $E_{ki}$  based on MPM simulations are shown in figure 4.29. MPM simulation shows two distinct regimes in the normalised kinetic energy plot as a function of normalised time in figure 4.29b. However, DEM simulations (figure 4.30) show that the energy evolution corresponding to the low energy regime nearly collapse on to a single time evolution. This is consistent with the observation of run-out time  $t_f$  being independent of the input energy. In contrast, MPM simulations predict a power law relation between the run-out duration and input energy. However, the plots corresponding to the high energy regime (figure 4.29), collapse only at the beginning of the run-out i.e. for  $t < t_1 \simeq 7.5 (d/g)^{0.5}$ . Although MPM simulations show longer duration of run-out (figure 4.29), the total kinetic energy is completely dissipated at  $t = 60\sqrt{d/g}$ . DEM simulations predict  $t = 80\sqrt{d/g}$  for the kinetic energy to be completely dissipated. This is due to grain rearrangement at the free surface (figure 4.31). The granular mass densifies as the flow progresses, after the initial dilation phase for  $t = 20\sqrt{d/g}$ .

Figure 4.32 displays the evolution of kinetic energy in the translational ( $E_x$  and  $E_y$ ) degrees of freedom.  $E_x$  decays similar to the total energy dissipation, but  $E_y$  increases and passes through a peak before decaying rapidly to a negligible level. The transient is best observed for  $E_y$ , which has significant values only for  $t < t_1$ . This energy represents the proportion of kinetic energy transferred to the  $y$  component of the velocity field due to the destabilisation of the pile and collapse of grains in the cavity behind the pile. Higher proportion of vertical acceleration  $E_{ky}/E_0$  is observed for lower values of input energy  $E_0$ . This means that, at lower input energies a larger fraction of the energy is consumed in the



(a) Evolution of total kinetic energy with time



(b) Evolution of normalised kinetic energy with normalised time

Figure 4.29 Evolution of kinetic energy with time (MPM) for a pile subjected to gradient input velocities

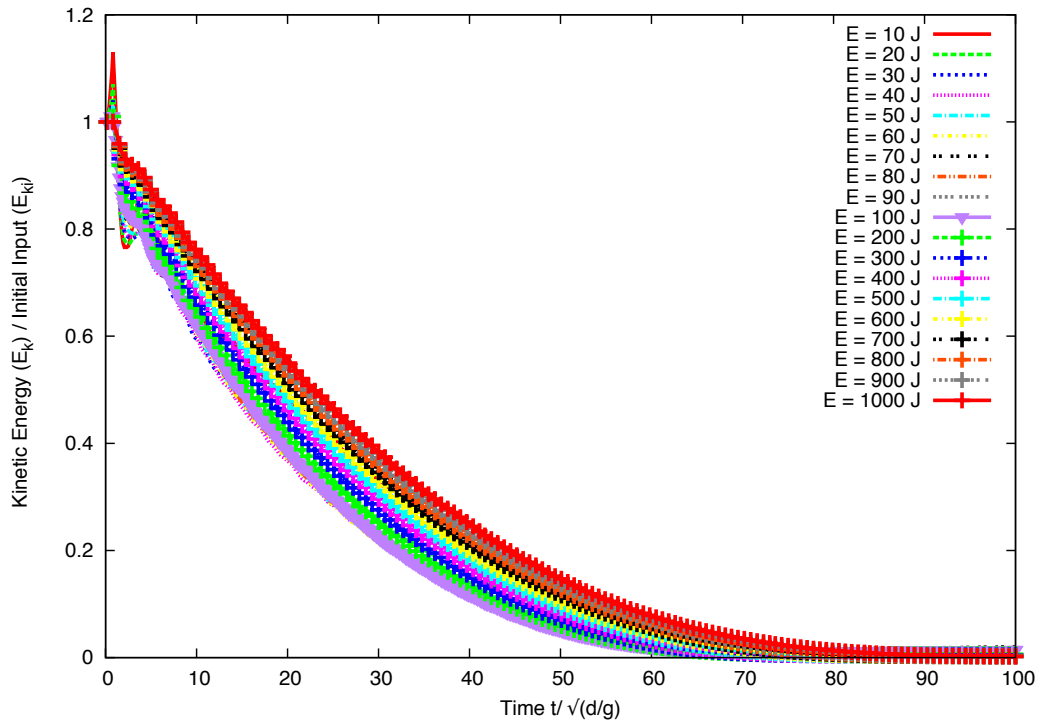


Figure 4.30 Evolution of normalised kinetic energy with normalised time for a pile subjected to gradient input velocities

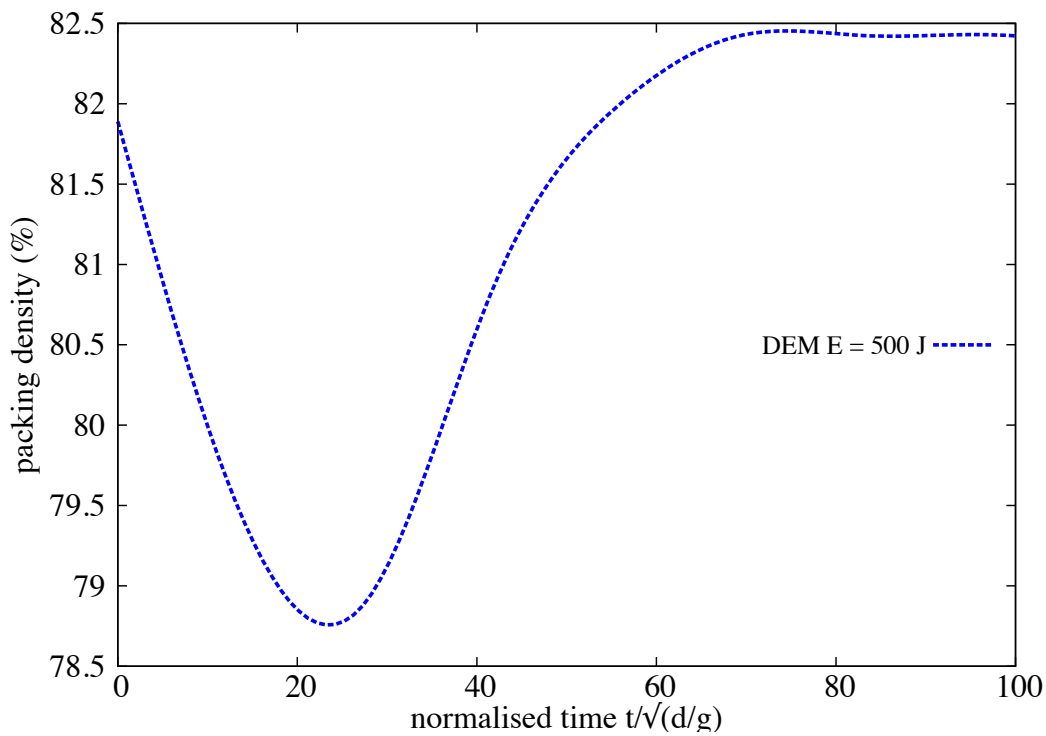


Figure 4.31 Evolution of packing density with time  $E_0 = 152mgd$  (DEM)

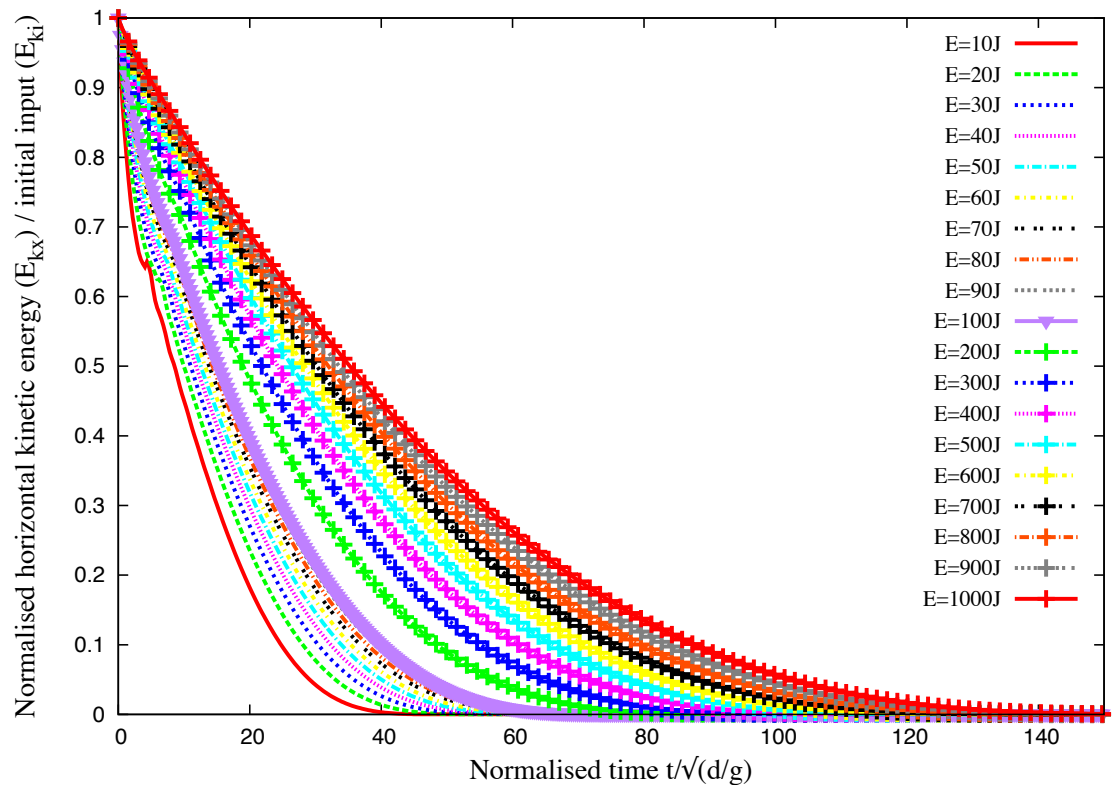
destabilisation process. Whereas at a higher input energies, most of the energy is dissipated in the spreading phase. For this reason, the total duration  $t_1$  of this destabilisation phase is nearly the same in both regimes and its value is controlled by gravity rather than the input energy. The height of the pile being of the order of  $80 d$ , the total free-fall time for a particle located at this height is  $\simeq 12 (d/g)^{0.5}$ , which is of the same order as  $t_1$ . DEM simulations show that the contribution of the rotational energy during the transient stage and the spreading stage is negligible.

To analyse the second phase for higher input energies, the kinetic energy  $E'_{kx0}$  available at the end of the transient phase is considered. This energy is responsible for most of the run-out, hence it is expected to control the run-out distance and time. Figure 4.33 shows the evolution of  $E_{kx}$  normalized by  $E'_{kx0}$  as a function of time. The plots have seemingly the same aspect but they show different decay times. A decay time  $\tau$  can be defined as the time required for  $E_{kx}$  to decline by a factor  $1/2$ . Figure 4.34 shows the same data in which the time  $t'$  elapsed since  $t_1$ , normalized by  $\tau$ . Interestingly, now all the data nicely collapse on to a single curve. However, this curve can not be fitted by simple functional forms such as variants of exponential decay. This means that the spreading of the pile is not a self-similar process in agreement with the fact that the energy fades away in a finite time  $t'_f$ .

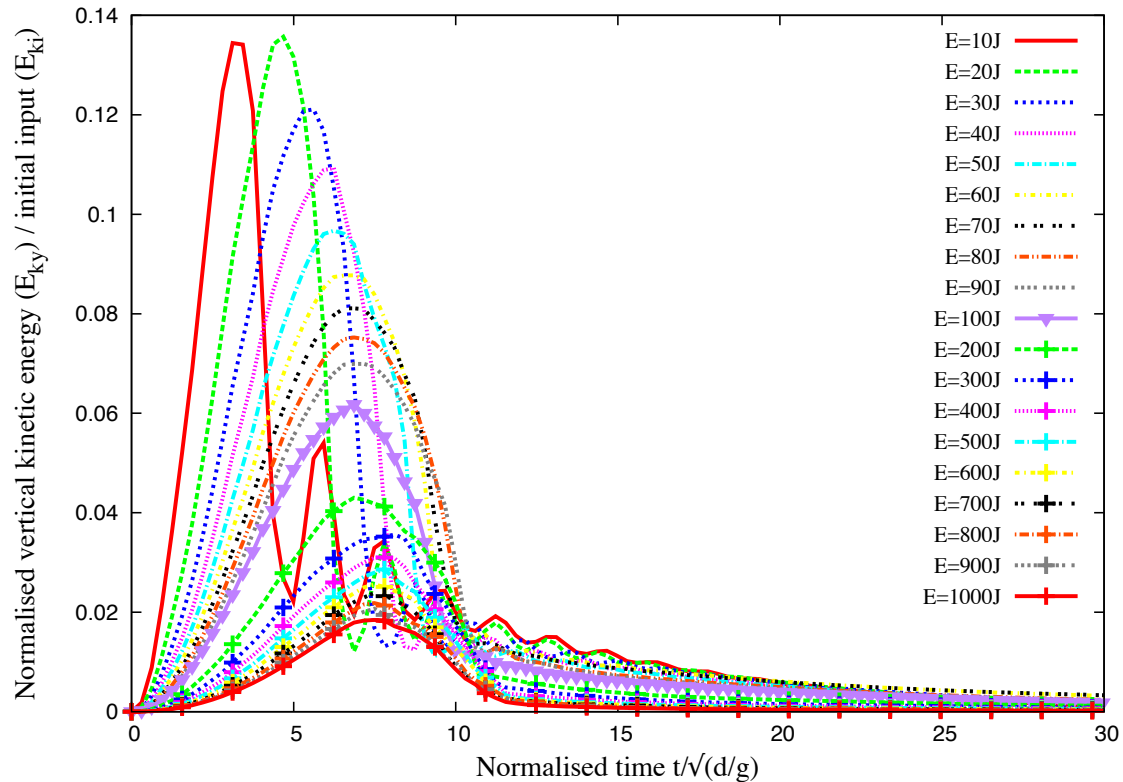
The scaling of the data with the decay time  $\tau$  suggests that the run-out time, since the beginning of the second phase,  $t'_f$  might be a simple function of  $\tau$ . Figure 4.35a shows both  $t'_f$  and  $\tau$  as a function of  $E'_{x0}$ , where a power-law relation can be observed for both time scales. The run-out time  $t'_f \propto (E'_{x0})^{\beta'}$  has the same exponent  $\beta' \simeq 0.33 \pm 0.02$  as  $t_f$  as a function of  $E_0$ . For the decay time we have  $\tau \propto (E'_{x0})^{\beta''}$  with  $\beta'' \simeq 0.38 \pm 0.03$ . The relation between the two times can thus be expressed as (figure 4.35b)

$$t'_f = k \tau (E'_{x0})^{\beta'' - \beta'}, \quad (4.13)$$

where  $k \simeq 5.0 \pm 0.4$  and  $\beta'' - \beta' \simeq 0.05 \pm 0.05$ . This value is small enough to be neglected. It is therefore plausible to assume that the run-out time is a multiple of the decay time and the spreading process is controlled by a single time. A weak dependence on the energy  $E'_{kx0}$  is consistent with the fact that the energy available at the beginning of the second phase is not dissipated in the spreading process (calculated from the position of the tip of the pile) since the pile keeps deforming by the movements of the grains at the free surface even when the tip comes to rest. This can explain the small difference between the two exponents as observed here.



(a) Evolution of normalised horizontal kinetic energy with time



(b) Evolution of normalised vertical kinetic energy with time

Figure 4.32 Evolution of vertical and horizontal kinetic energy with time (MPM) for a pile subjected to gradient input velocities

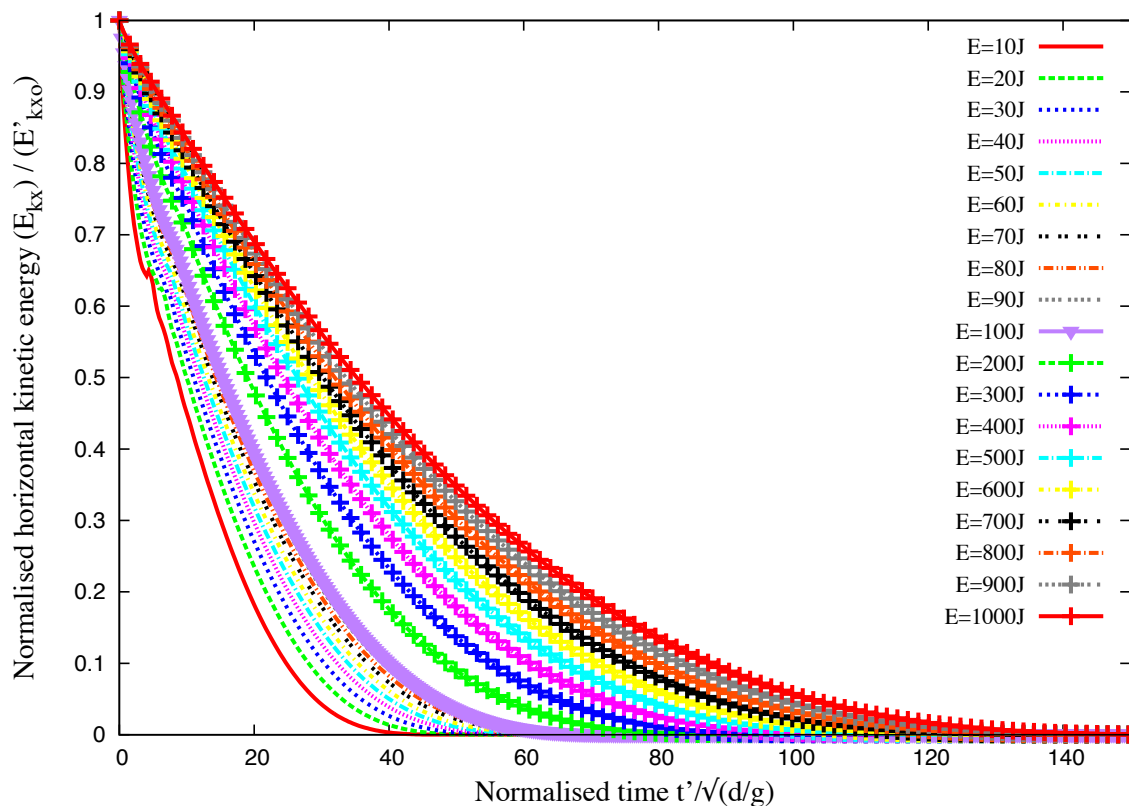


Figure 4.33 Evolution of kinetic energy in the  $x$  component of the velocity field normalized by the available kinetic energy at the end of the transient phase as a function of time elapsed since the same instant (MPM).

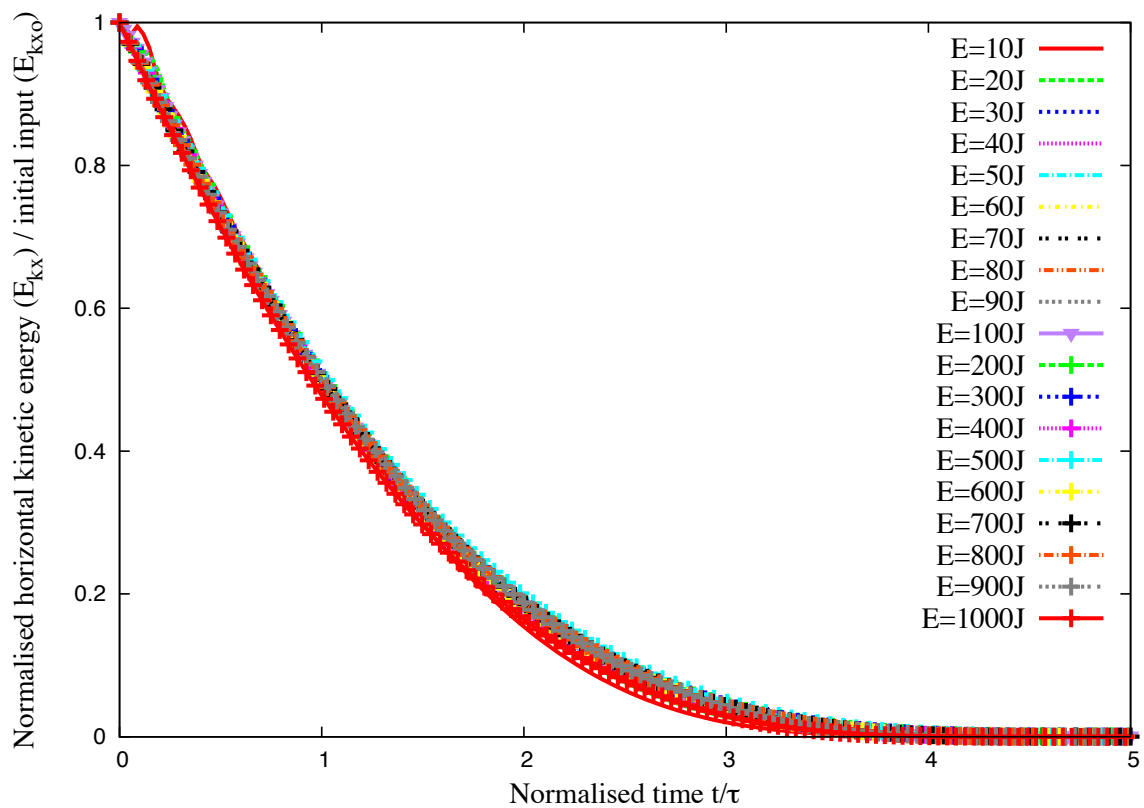
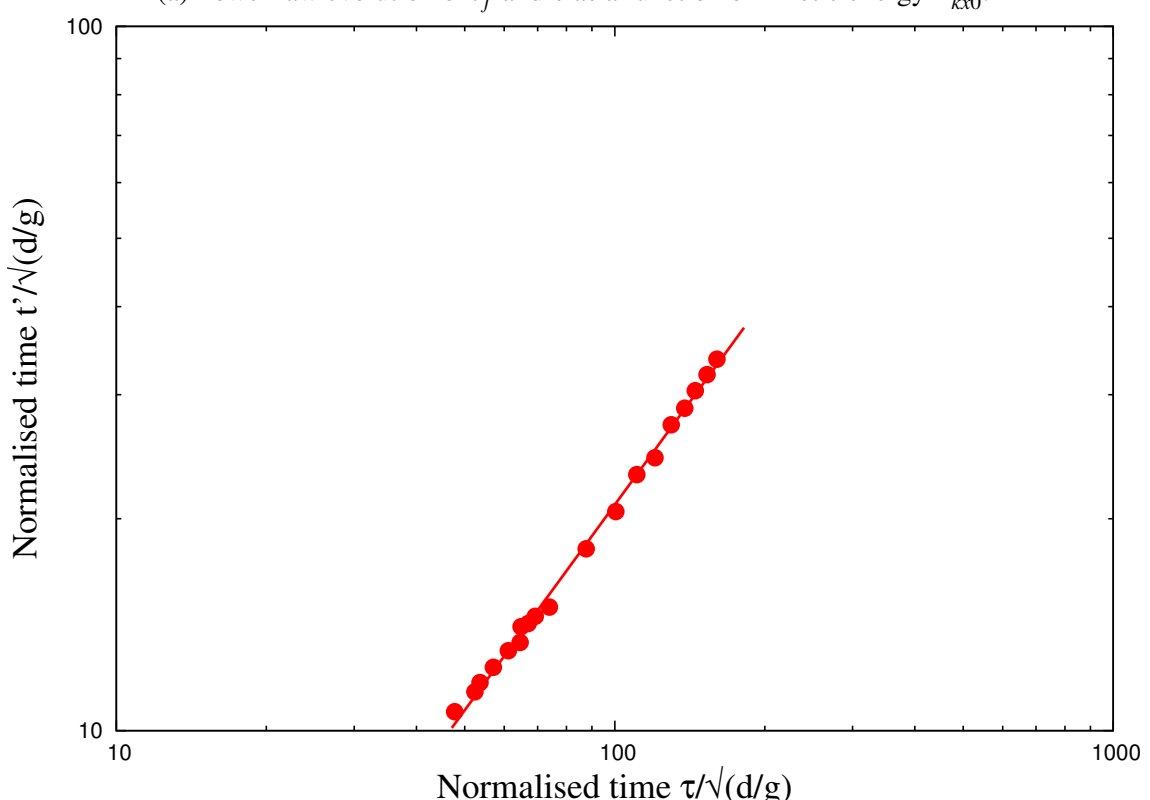
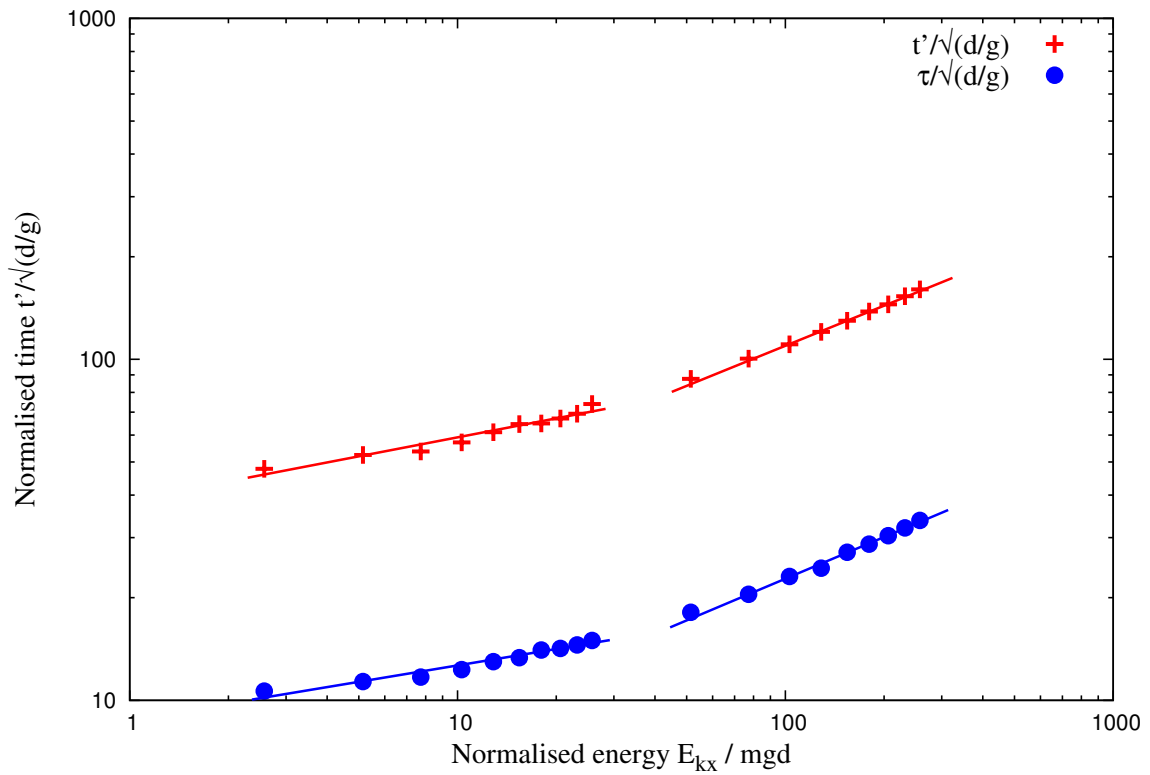


Figure 4.34 Evolution of kinetic energy in the  $x$  component of the velocity field normalized by the available kinetic energy at the end of the transient as a function of normalized time (MPM).



(b) Linear relationship between decay time and run-out time after the transient as a function of the normalised kinetic energy  $E_{kx0}$ .

Figure 4.35 Decay time and run-out time as a function of the normalised kinetic energy  $E_{kx0}$ .

#### 4.4.4 Effect of friction

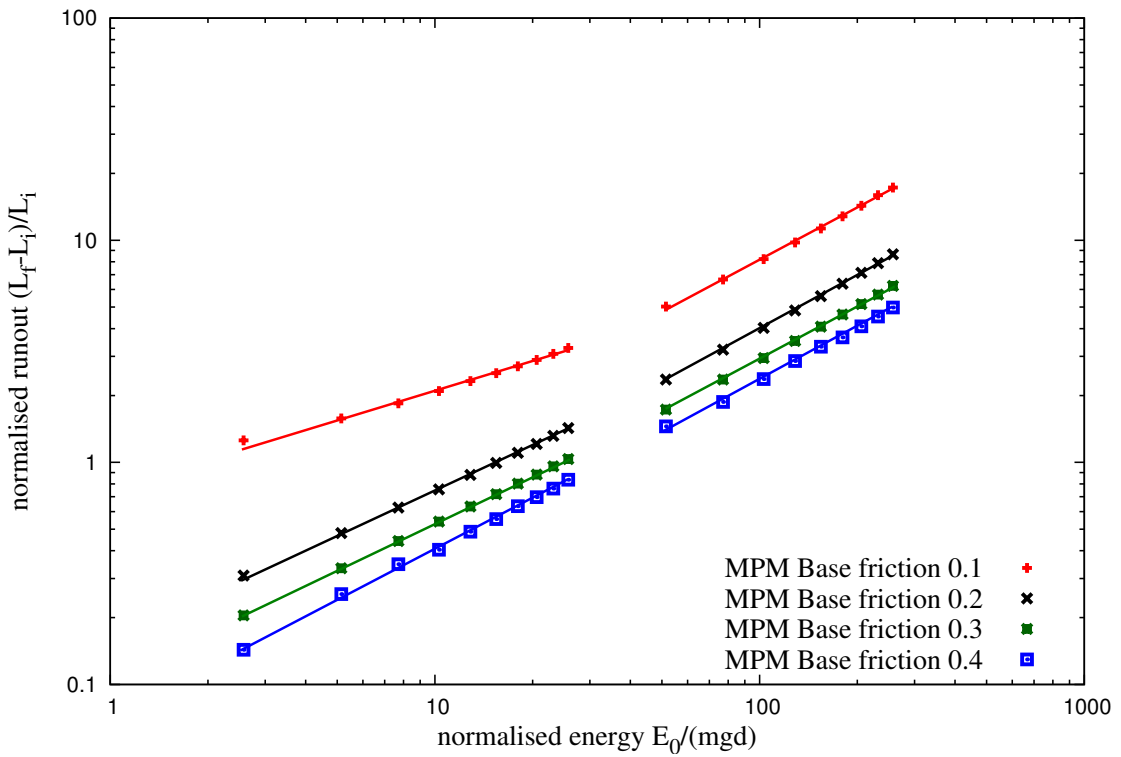
The run-out distance, duration of flow, and the dissipation of kinetic energy are controlled by the input energy and collective dynamics of the whole pile. However, the run-out behaviour is also expected to depend on the base friction. A series of simulations with different values of base friction was performed using MPM to analyse the influence of friction on the run-out behaviour. The influence of friction on the run-out behaviour for different input energies is shown in figure 4.36a. The run-out distance decreases with increase in the basal friction. The exponent of the power-law relation between the run-out and input energy has a weak dependence on the base friction, however, the proportionality constant is affected by the change in the base friction. This behaviour is similar to that observed in granular column collapse with varying initial properties (Balmforth and Kerswell, 2005; Lajeunesse et al., 2005).

CD simulations using different values of coefficient of restitution show no difference in the run-out behaviour. At large input energies, the pile remains in a dense state so that multiple collisions inside the pile occur at small time scales compared to the deformation time. When the restitution coefficients are increased, more collisions occur during a longer time interval but the overall energy dissipation rate by collisions remains the same. This effect is a seminal example of collective effects which erase the influence of local parameters at the macroscopic scale.

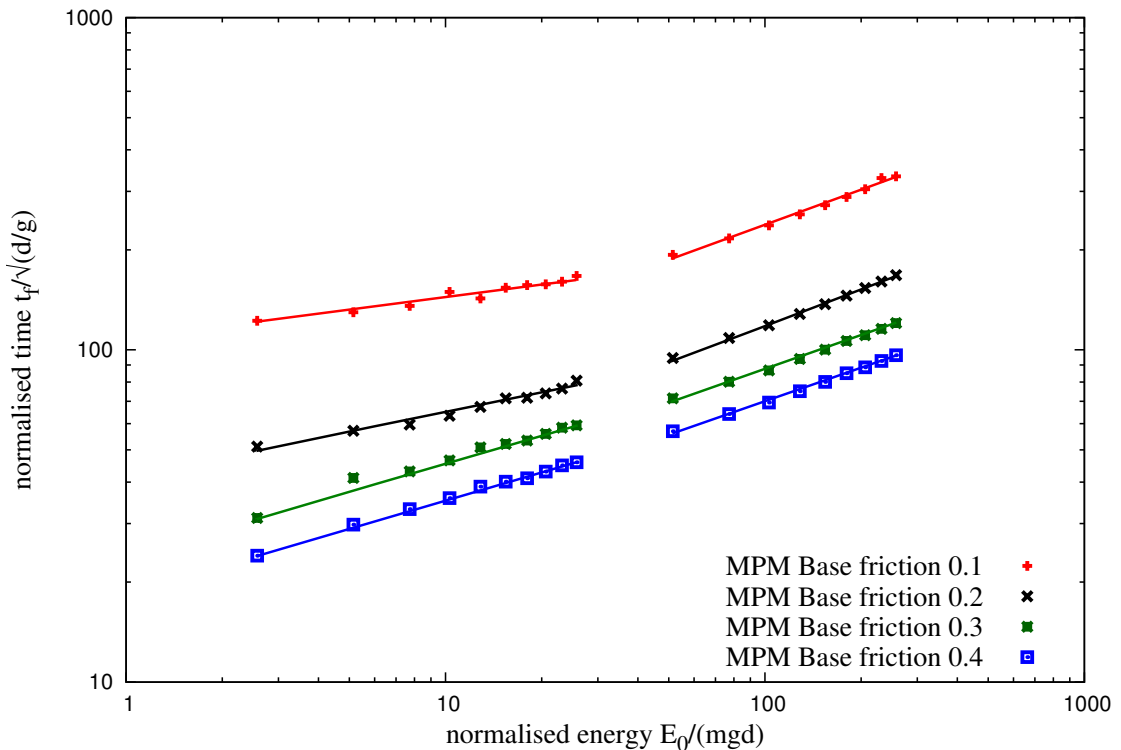
In contrast to the restitution coefficients, the effect of friction coefficient is quite important for the run-out. MPM simulations with varying friction coefficient shows that, both the run-out distance and the decay time decrease as the friction coefficient is increased. This effect is much more pronounced at low values of the friction coefficient. The run-out time, for example, is reduced by a factor of approximately 4 as  $\mu_s$  is increased from 0.1 to 0.2 while the change in the run-out and duration is less affected with increase in friction coefficient. This “saturation effect” can be observed in a systematic way in simple shear tests. The dissipation rate may reach a saturation point where the dilation of granular materials and rolling of the grains change in response to increase in friction coefficient (Estrada et al., 2008).

#### Effect kinetic energy distribution

Staron et al. (2005) observed that the distribution of kinetic energy in the granular system is an essential factor for the run-out distance. In order to understand the influence of energy distribution on the run-out behaviour, granular pile subjected to two different velocity fields were studied. A uniform velocity  $V_{xo}(y) = V_0$  is applied to the entire pile, in contrast to the gradient impact velocity. Snapshots of flow kinematics at initial stages are shown



(a) Effect of friction on the run-out distance



(b) Effect of friction on the duration of run-out.

Figure 4.36 MPM simulations of effect of friction on the run-out behaviour of slopes subjected to impact velocities.

in figure 4.37 (MPM simulations) and figure 4.38 (DEM). It can be observed from the figures that the continuum behaviour is identical to that of grain-scale simulations. As each grain experiences the same velocity, grains located at the top of the slope are pushed farther away and unlike the gradient input velocity, the cavity left behind the granular mass is not filled by the soil grains at the top.

Figure 4.39a shows the influence of velocity distribution on the run-out behaviour. At low input energy, the gradient velocity distribution shows significantly longer run-out in comparison to uniform velocity distribution. Section 4.4.3 shows that at low input energies a larger fraction of the energy is consumed in the destabilisation process. This means that the amount energy available for flow is less in uniform velocity distribution than the gradient velocity profile, this energy is even smaller as the initial velocity is distributed uniformly throughout the granular mass. However at higher input energy, where most of the energy is dissipated during the spreading phase, the run-out distance has a weak dependence on the distribution of velocity in the granular mass. The duration of the flow shows similar behaviour to the run-out, however, a slope subjected to a gradient velocity flows quicker than a slope subjected to a uniform impact velocity. The gradient velocity distribution provides more input energy at the initial stage to overcome the frictional resistance at the base. This shows that the material property and the distribution of kinetic energy in the system has a non-trivial influence on the flow kinematics and the internal flow structure.

#### 4.4.5 Comparison with granular column collapse

Figure 4.40 shows the run-out behaviour of granular column collapse and the slope subjected to impact velocities as a function of normalised kinetic energy. In the case of column collapse, the peak energy at  $\tau_c$  is used as the energy available for the flow. It can be observed that MPM and DEM predict similar run-out behaviour for low energy regime (short columns), which undergo frictional failure along the flanks. However MPM predicts longer run-out for high energy regime (corresponding to  $a > 2.7$ ), where the granular column experiences significant collisional dissipation. The lack of a collisional energy dissipation mechanism in MPM results in over prediction of run-out distances. In the case of granular column subjected to impact velocity, the dissipation is friction and MPM is able to predict the run-out response in good agreement with DEM simulations. At very low energy, DEM simulations show longer run-out in the case of slope subjected to impact due to local destabilisation at the flow front. Both granular flows, column collapse and slope subjected to impact, show power-law relation with the energy. This shows that the power-law behaviour is a granular flow characteristic.

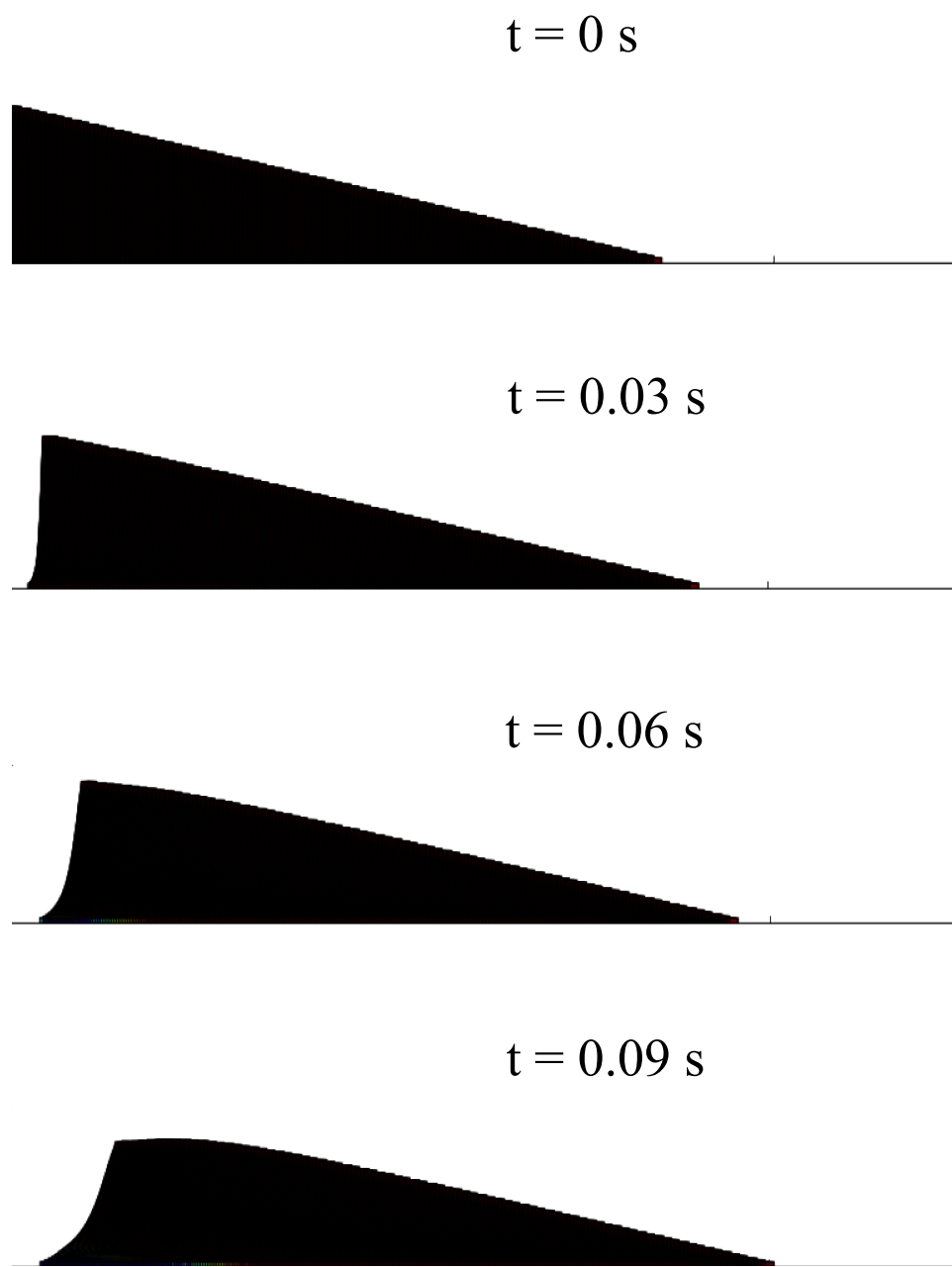


Figure 4.37 Snapshots of MPM simulations of the evolution of granular pile subjected to a gradient impact energy  $E_0 = 61 \text{ mgd}$ .

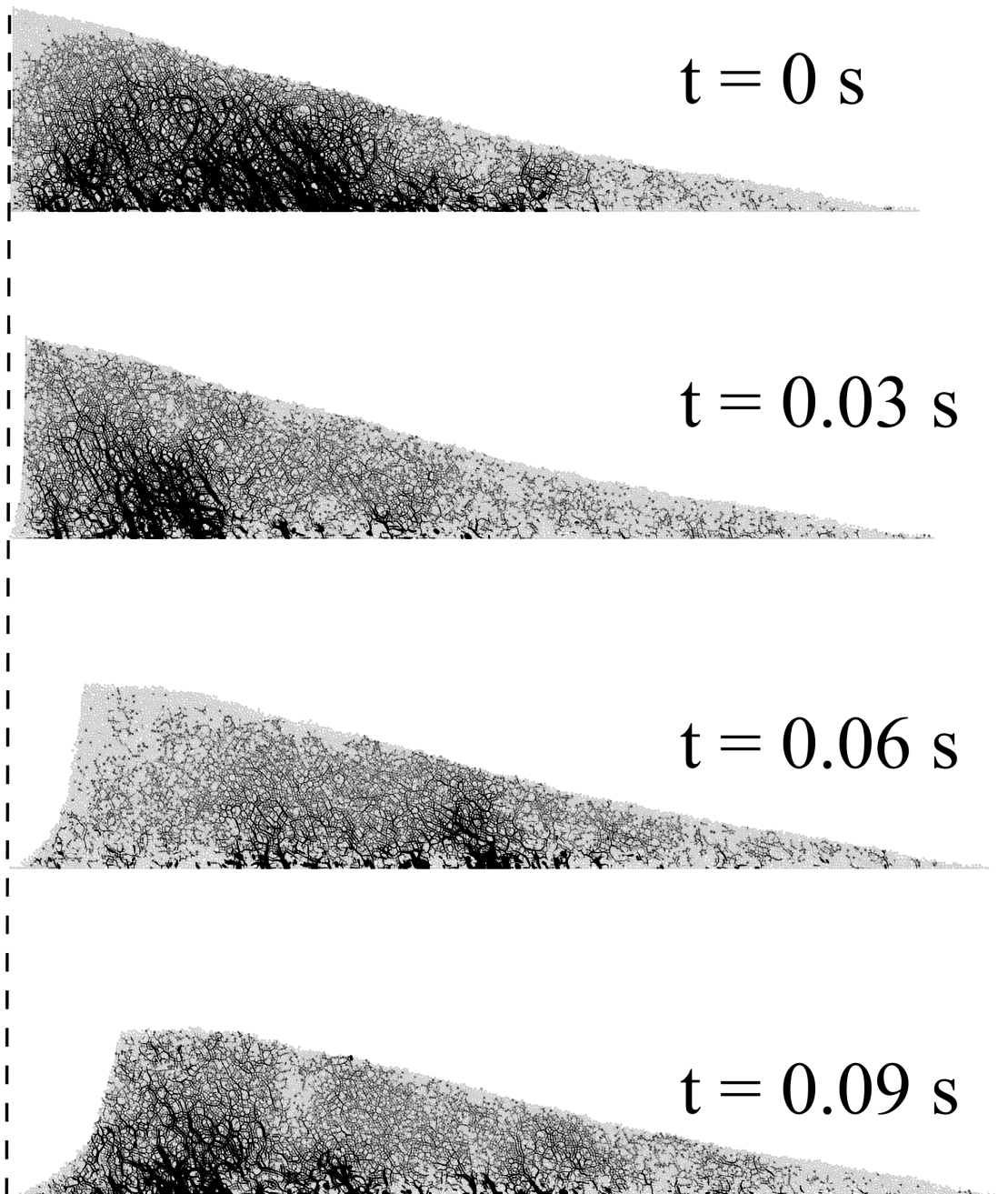
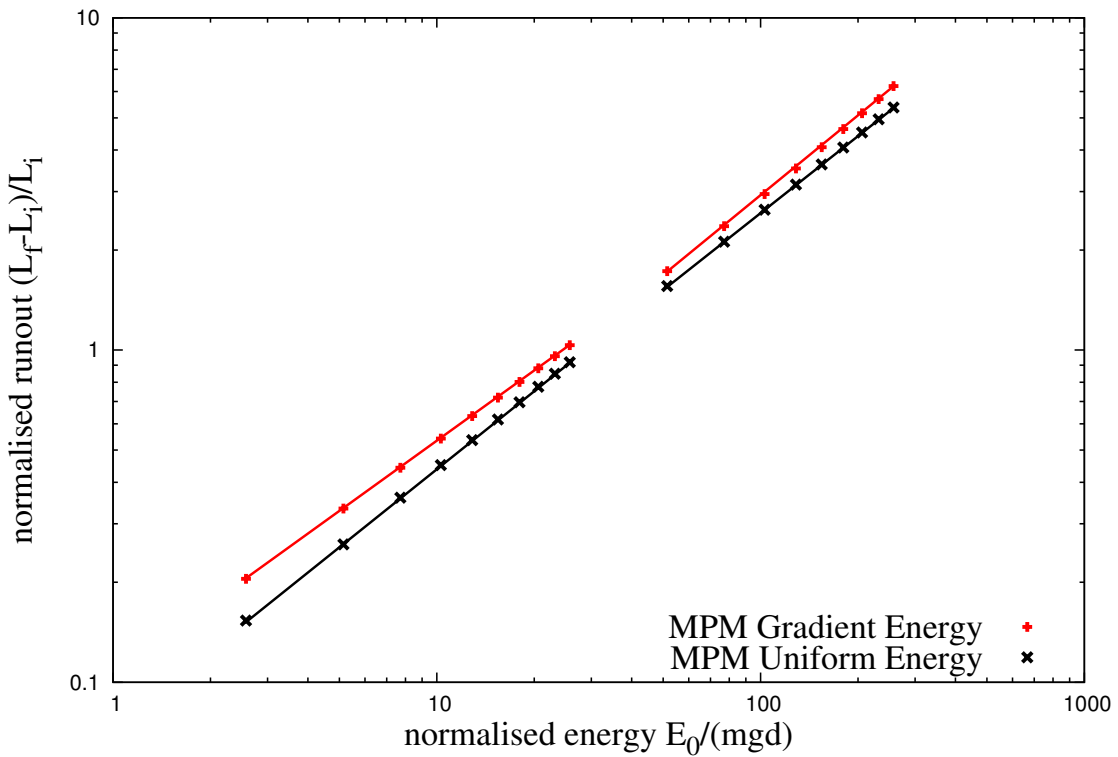
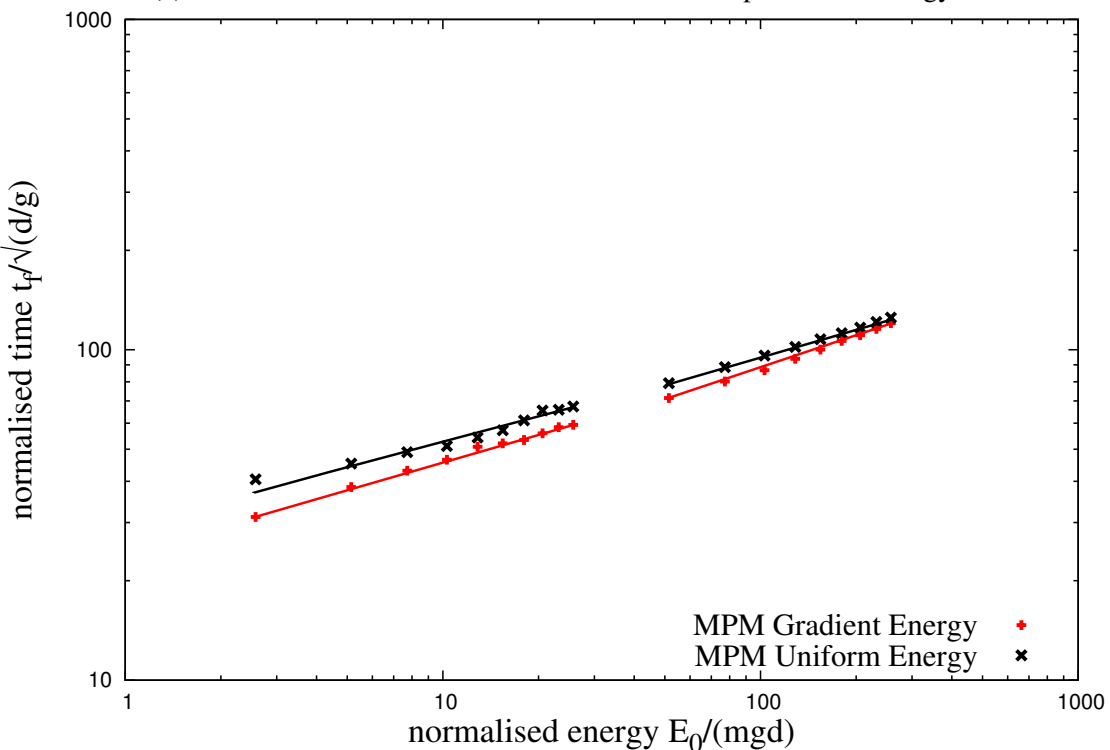


Figure 4.38 Snapshots of DEM simulations of the evolution of granular pile subjected to a gradient impact energy  $E_0 = 61 \text{ mgd}$ .



(a) Run-out distance as a function of normalised input kinetic energy



(b) Duration of run-out as a function of normalised input kinetic energy

Figure 4.39 Effect of input velocity distribution on the run-out behaviour of slopes subjected to impact velocities.

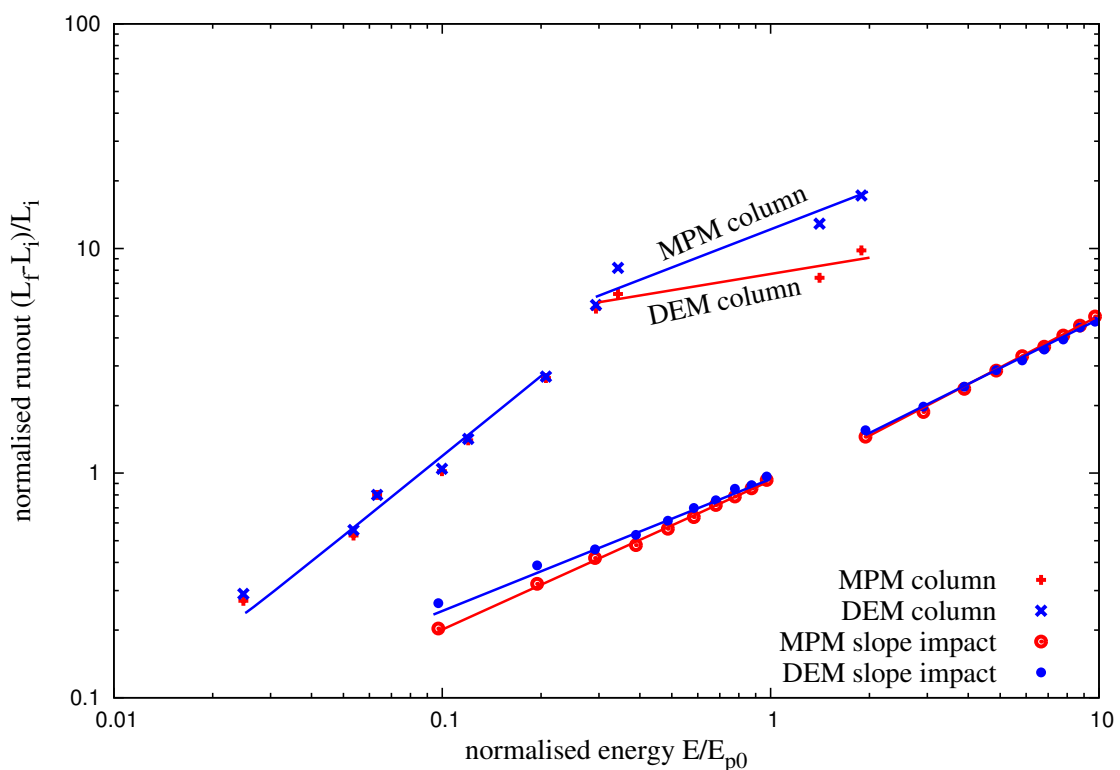


Figure 4.40 Comparison of the normalised run-out between the collapse of granular columns and granular slope subjected to impact loading.

## 4.5 Summary

Multi-scale simulation of dry granular flows were performed to capture the local rheology, and to understand the capability and limitations of continuum models in realistic simulation of granular flow dynamics. Previous studies on granular collapse have shown a power-law dependence between the run-out and the initial aspect ratio of the column. The change in the run-out behaviour for tall columns has remained unexplained. Also, the reason for longer run-out distance for tall column using continuum approach was still lacking. Most studies were focused on mono-disperse grain sizes. In the present study, a multi-scale simulations of granular column collapse are performed. Studies on the role of initial packing density and poly-disperse sample on the run-out behaviour are also performed. The following conclusions can be derived based on MPM and DEM simulations of granular column collapse:

- Both DEM and MPM simulations show a power-law dependence of the run-out and time with the initial aspect ratio of the column.
- Continuum approach, such as MPM with a simple frictional dissipation model is able to capture the flow kinematics of dry granular collapse for short columns. The collapse of short column is a frictional dissipation process.
- DEM simulations reveal collisional dissipation mechanism in the initial stage of collapse of tall columns.
- MPM simulations show longer run-out behaviour in the case of tall columns. MPM simulation assumes that the total initial potential energy stored in the system is completely dissipated through friction over the entire run-out distance. The lack of collisional dissipation in MPM results in longer run-outs for tall columns.
- The initial configuration and the material properties have a significant influence on the run-out behaviour. The run-out distance increases with increase in density of granular packing. This effect is significant in the case of tall columns.
- DEM simulations with different initial packing shows evolution of packing density with time. Hence it is important to consider macroscopic parameters like packing fraction and dilatancy behaviour, which are due to meso-scale grain arrangements, when modelling the granular system as a continuum.

Natural granular flows are triggered by different mechanisms. The distribution of kinetic energy in the granular mass is found to have an effect on the flow kinematics. A multi-scale

analyses of a granular slope subjected to impact velocities are performed and the following conclusions are derived:

- A power-law dependence of the run-out distance and time as a function of the input energy is observed. The power-law behaviour is found to be a generic feature of granular flow dynamics.
- The values of the power-law exponents are not simple functions of the geometry.
- Two regimes with different values of the exponents: a low-energy regime and a high-energy regime are observed.
- The low energy regime reflects mainly the destabilisation of the pile, with a run-out time independent of the input energy.
- The second regime is governed by the spreading dynamics induced by higher input energy. The evolution of granular slope in the high-energy regime can be described by a characteristic decay time, which is the time required for the input energy to decay by a factor of 0.5.
- The run-out distance and the decay time decrease as the friction increases. This effect is much more pronounced at low values of friction.
- At low input energy, the distribution of kinetic energy in the system is found have a significant effect on the run-out, as the energy is mostly consumed in the destabilisation process.
- At higher input energy, where most of the energy is dissipated during the spreading phase, the run-out distance has a weak dependence on the distribution of velocity in the granular mass.
- The duration of the flow shows similar behaviour to the run-out, however, a slope subjected to a gradient velocity flows quicker than a slope subjected to a uniform impact velocity.
- The material property and the distribution of kinetic energy in the system has a non-trivial influence on the flow kinematics and the internal flow structure.
- MPM is successfully able to simulate the transient evolution with a single input parameter, the macroscopic friction angle.

This study exemplifies the ability of MPM, a continuum approach, in modelling complex granular flow dynamics and opens the possibility of realistic simulation of geological-scale flows on complex topographies.



# Chapter 5

## Numerical modelling of fluid–grain interactions

### 5.1 Fluid simulation using lattice Boltzmann method

Grain–fluid systems can be found in many scientific and engineering applications, such as suspensions, fluidised beds, sediment transport, and geo-mechanical problems. In general, the fundamental physical phenomena in these systems are not well understood mainly due to the intricate complexity of grain–fluid interactions and the lack of powerful analysis tools (Han et al., 2007a). In addition to the interaction among soil grains, the motion of soil grains is mainly driven by gravity and the hydrodynamic force exerted by the fluid. The fluid flow pattern can be significantly affected by the presence of soil grains and this often results in a turbulent flow. Hence, the development of an effective numerical framework for modelling both the fluid flow patterns and the grain–fluid interactions is very challenging.

Development of a numerical framework depends crucially on the size of the soil grains relative to the domain/mesh size (Feng et al., 2007). Traditionally, the Navier-Stokes equation is solved by a grid-based Computational Fluid Dynamics (CFD) method, such as the Finite Volume Method, FVM, (Capelatro and Desjardins, 2013) or a mesh-free technique such as Smooth Particle Hydrodynamics (SPH) (Sun et al., 2013). The grid size in FVM or the smooth length in SPH for discretisation of the Navier-Stokes equation is at least an order of magnitude larger than the grain diameter (Xiong et al., 2014), thus ignoring the micro-scale interactions.

In situations where the average domain concentration phase is far from dilute, the computational effort is mostly devoted to the grain dynamics. The hydrodynamic forces on the soil grains are applied based on an empirical relation using the domain-averaged local

porosity of the soil grains in the grid. As a result, developing a fast fluid hydrodynamics solver is unimportant for dense flows. However, most geo-mechanical problems involve complex interactions between the solid and the fluid phase. This requires accurate modelling of the fluid flow pattern. Additionally, geophysical problems, such as submarine landslides and debris flow have a relatively large simulation domain, which requires parallel computation. Implementing traditional grid-based CFD methods face great challenges on multi-processor systems (Xiong et al., 2014). Although mesh-free approaches are free from the problem of parallel scalability, its modelling accuracy and speed are relatively low when compared to grid-based CFD methods. Therefore, an accurate, fast and a highly scalable scheme is required to model fluid - grain systems in geo-mechanics.

The Navier-Stokes equation describes the motion of a non-turbulent Newtonian fluid. The equation is obtained by applying Newton's second law to the fluid motion, together with an assumption that the fluid stress is the sum of the viscous term, proportional to the gradient of the velocity, and the pressure term. Conventional CFD methods compute pertinent flow fields, such as velocity  $u$  and pressure  $p$ , by numerically solving the Navier-Stokes equation in space  $x$  and time  $t$ . Alternatively, the transport equation or the Boltzmann equation, which deals with a single particle distribution function  $f(x, \xi, t)$  in phase space  $(x, \xi)$  and time  $t$ , can be used to solve various problems in fluid dynamics.

The Lattice Boltzmann Method (LBM) (Chen and Doolen, 1998; Han et al., 2007b; He and Luo, 1997a,b; Mei et al., 2000; Zhou et al., 2012) is an alternative approach to the classical Navier-Stokes solvers for fluid flows. LBM works on an equidistant grid of cells, called lattice cells, which interact only with their direct neighbours. In LBM, the discretisation of continuum equations is based on microscopic models and mesoscopic continuum theories. LBM is a special discretising scheme of the Boltzmann equation where the particle distribution functions (mass fractions) collide and propagate on a regular grid. The important aspect, however, is the *discretisation of the velocity*, which means that the particle velocities are restricted to a predefined set of orientations.

The theoretical premises of the LB equation are that (1) hydrodynamics is insensitive to the details of microscopic physics, and (2) hydrodynamics can be preserved so long as the conservation laws and associated symmetries are respected in the microscopic and mesoscopic level. Therefore, the computational advantages of LBM are achieved by drastically reducing the particle velocity space  $\xi$  to only a very few discrete points without seriously degrading the hydrodynamics (Mei et al., 2000). This is possible because LBM rigorously preserves the hydrodynamic moments of the distribution function, such as mass density and momentum fluxes, and the necessary symmetries (He and Luo, 1997a,b). LBM has evolved as a

comprehensive fluid solver and its theoretical aspects link well with the conventional central finite difference scheme (Cook et al., 2004).

### 5.1.1 Formulation

LBM is a ‘micro-particle’ based numerical time-stepping procedure for the solution of incompressible fluid flows. Consider a 2D incompressible fluid flow with density  $\rho$  and kinematic viscosity  $\nu$ , in a rectangular domain  $D$ . The fluid domain is divided into rectangular grids or lattices, with the same grid length ‘ $h$ ’ in both  $x$ - and  $y$ -directions (see figure 5.1).

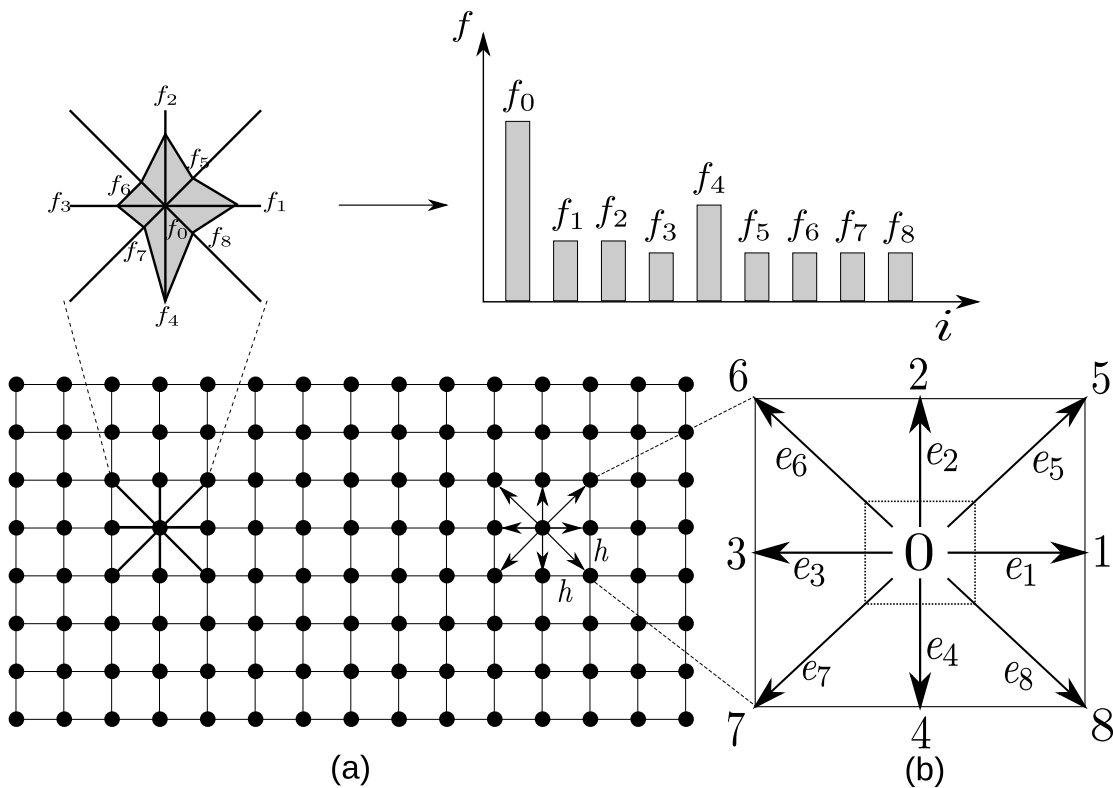


Figure 5.1 The Lattice Boltzmann discretisation and D2Q9 scheme: (a) a standard LB lattice and histogram views of the discrete single particle distribution function/direction-specific densities  $f_i$ ; (b) D2Q9 model.

These lattices are usually classified in the literature using the  $D\alpha Q\beta$ -notation, where  $\alpha$  denotes the space dimensionality and  $\beta$  is the number of discrete velocities (but also including the possibility of having particles at rest) within the momentum discretisation. The most common lattices are the  $D2Q9$  and the  $D3Q19$ -models, see He et al. (1997). The present study focuses on two-dimensional problems, hence the  $D2Q9$  momentum discretisation is adopted.

LBM discretises the Boltzmann equation in space to a finite number of possible particle spatial positions, microscopic momenta, and time. Particle positions are confined to the lattice nodes. The fluid particles at each node are allowed to move to their eight intermediate neighbours with eight different velocities  $e_i (i = 1, \dots, 8)$ . A particle can remain at its own node, which is equivalent to moving with zero velocity  $e_o$ . The particle mass is uniform, hence these microscopic velocities and momentum are always effectively equivalent (Han et al., 2007b). Referring to the numbering system shown in figure 5.1, the nine discrete velocity vectors are defined as

$$\begin{cases} e_0 = (0, 0); \\ e_1 = C(1, 0); e_2 = C(0, 1); e_3 = C(-1, 0); e_4 = C(0, -1); \\ e_5 = C(1, 1); e_6 = C(-1, 1); e_7 = C(-1, -1); e_8 = C(1, -1), \end{cases} \quad (5.1)$$

where  $C$  is the lattice speed that is defined as  $C = h/\Delta t$ , and  $\Delta t$  is the discrete time step. The primary variables in LB formulation are called the *fluid density distribution functions*,  $f_i$ , each representing the probable amount of fluid particles moving with the velocity  $e_i$  along the direction  $i$  at each node. The macroscopic variables are defined as functions of the particle distribution function (see figure 5.1)

$$\begin{cases} \rho = \sum_{i=0}^{\beta-1} f_i & \text{(macroscopic fluid density)} \\ \text{and} \\ \overrightarrow{u} = \frac{1}{\rho} \sum_{i=0}^{\beta-1} f_i \overrightarrow{e_i} & \text{(macroscopic velocity)}, \end{cases} \quad (5.2)$$

where  $i \in [0, \beta - 1]$  is an index spanning the discretised momentum space. There are nine fluid density distribution functions,  $f_i (i = 0, \dots, 8)$ , associated with each node in the *D2Q9* model. The evolution of the density distribution function at each time step for every lattice point is governed by

$$f_i(\mathbf{x} + \mathbf{e}_i \Delta t, t + \Delta t) = f_i(\mathbf{x}, t) - \frac{1}{\tau} [f_i(\mathbf{x}, t) - f_i^{eq}(\mathbf{x}, t)] \quad (i = 0, \dots, 8), \quad (5.3)$$

where for any grid node  $\mathbf{x}$ ,  $\mathbf{x} + \mathbf{e}_i \Delta t$  is its nearest node along the direction  $i$ .  $\tau$  is a non-dimensional relaxation time parameter, which is related to the fluid viscosity; and  $f_i^{eq}$  is

termed as the equilibrium distribution function that is defined as

$$\begin{cases} f_0^{eq} = w_0 \rho \left(1 - \frac{3}{2C^2} \mathbf{v} \cdot \mathbf{v}\right) \\ \text{and} \\ f_i^{eq} = w_i \rho \left(1 + \frac{3}{C^2} \mathbf{e}_i \cdot \mathbf{v} \frac{9}{2C^2} (\mathbf{e}_i \cdot \mathbf{v})^2 - \frac{3}{2C^2} \mathbf{v} \cdot \mathbf{v}\right) \quad (i = 0, \dots, 8), \end{cases} \quad (5.4)$$

in which,  $w_i$  represents the fixed weighting values:

$$w_0 = \frac{4}{9}, \quad w_{1,2,3,4} = \frac{1}{9}, \quad \text{and} \quad w_{5,6,7,8} = \frac{1}{36}. \quad (5.5)$$

The right-hand side of eq. 5.3 is often denoted as  $f_i(\mathbf{x}, t_+)$  and termed the post collision distribution. LBM ensures conservation of total mass and total momentum of the fluid particles at each lattice node (see eq. 5.3). The lattice Boltzmann modelling consists of two phases: *collision* and *streaming*. The collision phase computed in the right-hand side of eq. 5.3 involves only those variables that are associated with each node  $\mathbf{x}$ , and therefore is a local operation. The streaming phase then explicitly propagates the updated distribution functions at each node to its neighbours  $\mathbf{x} + e_i \Delta t$ , where no computations are required and only data exchange between neighbouring nodes are necessary. These features, together with the explicit time-stepping nature and the use of a regular grid, make LB computationally efficient, simple to implement and easy to parallelise (Han et al., 2007b).

The streaming step involves the translation of the distribution functions to their neighbouring sites according to the respective discrete velocity directions, as illustrated in figure 5.2 in the *D2Q9* model. The collision step, (see figure 5.3) consists of re-distribution the local discretised Maxwellian equilibrium functions in such a way that local mass and momentum are invariants. In incompressible flows, the energy conservation is equivalent to the momentum conservation (He et al., 1997).

The standard macroscopic fluid variables, such as density  $\rho$  and velocity  $v$ , can be recovered from the distribution functions as

$$\rho = \sum_{i=0}^8 f_i, \quad \text{and} \quad \rho \mathbf{v} = \sum_{i=0}^8 f_i \mathbf{e}_i. \quad (5.6)$$

The fluid pressure field ‘ $p$ ’ is determined by the equation of state

$$p = C_s^2 \rho, \quad (5.7)$$

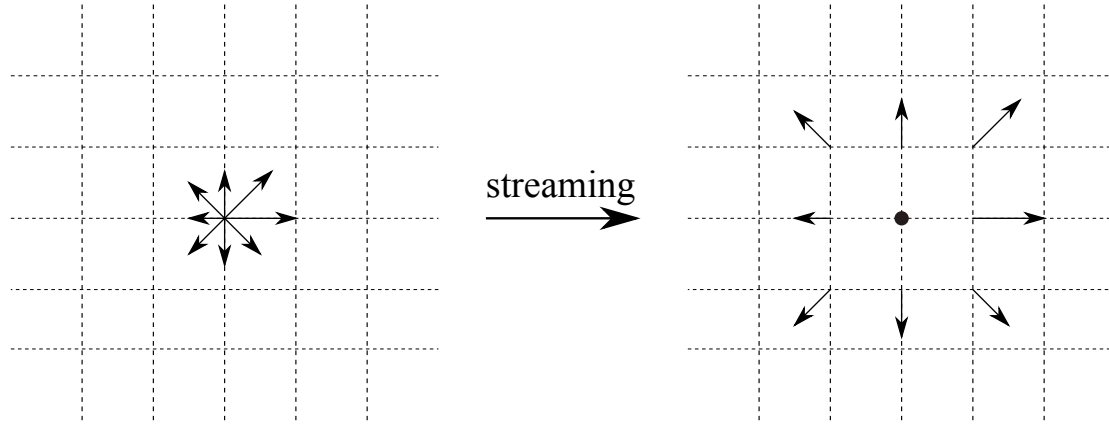


Figure 5.2 Illustration of the streaming process on a  $D2Q9$  lattice. The magnitude of the distribution functions remains unchanged, but they move to a neighbouring node according to their direction.

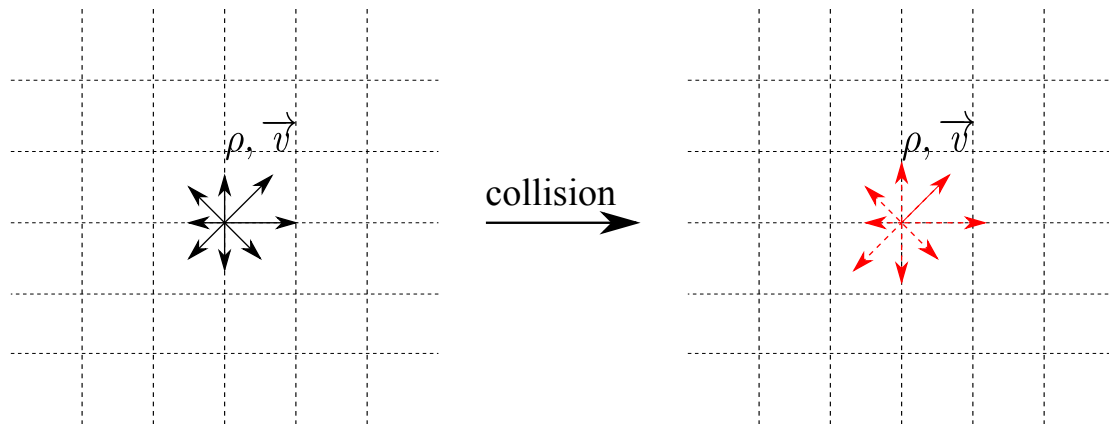


Figure 5.3 Illustration of the collision process on a  $D2Q9$  lattice. The local density  $\rho$  and velocity  $\mathbf{v}$  are conserved, but the distribution functions change according to the relaxation to local Maxwellian rule.

where  $C_s$  is termed the fluid speed of sound and is related to the lattice speed  $C$  as

$$C_s = C/\sqrt{3}. \quad (5.8)$$

The kinematic viscosity of the fluid  $\nu$  is implicitly determined by the model parameters  $h$ ,  $\Delta t$  and  $\tau$  as

$$\nu = \frac{1}{3}(\tau - \frac{1}{2})\frac{h^2}{\Delta t} = \frac{1}{3}(\tau - \frac{1}{2})Ch, \quad (5.9)$$

which indicates that these three parameters are related to each other and have to be appropriately selected to represent the correct fluid viscosity. An additional constraint to the parameter selection is the lattice speed  $C$ , which must be sufficiently large in comparison to the maximum fluid velocity  $v_{max}$ , to ensure accuracy of the solution. The ‘computational’ Mach number,  $M_a$ , defined as

$$M_a = \frac{v_{max}}{C}. \quad (5.10)$$

Theoretically, for an accurate solution, the Mach number is required to be  $<< 1$ . In practice,  $M_a$  should be at least smaller than 0.1 (He et al., 1997). From a computational point of view, it is more convenient to choose  $h$  and  $\tau$  as two independent parameters and  $\Delta t$  as the derived parameter

$$\Delta t = (\tau - \frac{1}{2})\frac{h^2}{3\nu}. \quad (5.11)$$

It can be observed that  $\tau$  has to be greater than 0.5 (He et al., 1997). Since there is no a priori estimation available to determine appropriate values of  $h$  and  $\tau$ , for a given fluid flow problem and a known fluid viscosity  $\nu$ , a *trial and error* approach is employed to ensure a smaller *Mach Number*. This is similar to choosing an appropriate Finite Element mesh size, without using automatic adaptive mesh techniques.

### 5.1.2 Lattice Boltzmann - Multi-Relaxation Time (LBM-MRT)

The Lattice Boltzmann Bhatnagar-Gross-Krook (LGBK) method is capable of simulating various hydrodynamics, such as multiphase flows and suspensions in fluid (Succi, 2001; Succi et al., 1989). However, LBM suffers from numerical instability when the dimensionless relaxation time  $\tau$  is close to 0.5. The Lattice Boltzmann Method – Multi-Relaxation Time (LBM-MRT) overcomes the deficiencies of linearised single relaxation LBM-BGK approach, such as the fixed Prandtl number ( $Pr=\nu/\kappa$ ), where the thermal conductivity ‘ $\kappa$ ’ is unity (Liu et al., 2003). LBM-MRT offers better numerical stability and has more degrees of freedom. In LBM-MRT the advection is mapped onto the momentum space by a linear transformation and the flux is finished within the velocity space (Du et al., 2006).

The lattice Boltzmann equation with multiple relaxation time approximation is written as

$$f_\alpha(\mathbf{x} + \mathbf{e}_i \Delta_t, t + \Delta_t) - f_\alpha(\mathbf{x}, t) = -\mathbf{S}_{\alpha i}(f_i(\mathbf{x}, t) - f_i^{eq}(\mathbf{x}, t)), \quad (5.12)$$

where  $\mathbf{S}$  is the collision matrix. The nine eigen values of  $\mathbf{S}$  are all between 0 and 2 so as to maintain linear stability and separation of scales. This ensures that the relaxation times of non-conserved quantities are much faster than the hydrodynamic time scales. The LGBK model is a special case in which the nine relaxation times are all equal and the collision matrix  $\mathbf{S} = \frac{1}{\tau} \mathbf{I}$ , where  $\mathbf{I}$  is the identity matrix. The evolutionary progress involves two steps, advection and flux:

$$f_\alpha^+(\mathbf{x}, t) - f_\alpha(\mathbf{x}, t) = -\mathbf{S}_{\alpha i}(f_i(\mathbf{x}, t) - f_i^{eq}(\mathbf{x}, t)) \quad (5.13)$$

$$f_\alpha(\mathbf{x} + e_\alpha \Delta_t, t + \Delta_t) = f_\alpha^+(\mathbf{x}, t). \quad (5.14)$$

The advection (eq. 5.13) can be mapped to the momentum space by multiplying with a transformation matrix  $\mathbf{M}$ . The evolutionary equation of LBM–MRT is written as

$$\mathbf{f}(\mathbf{x} + \mathbf{e}_i \Delta_t, t + \Delta_t) - \mathbf{f}(\mathbf{x}, t) = -M^{-1} \hat{\mathbf{S}}(\hat{\mathbf{f}}(\mathbf{x}, t) - \hat{\mathbf{f}}^{eq}(\mathbf{x}, t)), \quad (5.15)$$

where  $\mathbf{M}$  is the transformation matrix mapping a vector  $\mathbf{f}$  in the discrete velocity space  $\mathbb{V} = \mathbb{R}^b$  to a vector  $\hat{\mathbf{f}}$  in the moment space  $\mathbb{V} = \mathbb{R}^b$ .

$$\hat{\mathbf{f}} = \mathbf{M}\mathbf{f}, \quad (5.16)$$

$$\mathbf{f}(\mathbf{x}, t) = [f_0(\mathbf{x}, t), f_1(\mathbf{x}, t), \dots, f_8(\mathbf{x}, t)]^T. \quad (5.17)$$

The collision matrix  $\hat{\mathbf{S}} = M S M^{-1}$  in moment space is a diagonal matrix:

$$\hat{\mathbf{S}} = \text{diag}[s_1, s_2, s_3, \dots, s_9].$$

The transformation matrix  $\mathbf{M}$  can be constructed via Gram-Schmidt orthogonalisation procedure. The general form of the transformation matrix  $\mathbf{M}$  can be written as

$$\mathbf{M} = [|p\rangle, |e\rangle, |e^2\rangle, |u_x\rangle, |q_x\rangle, |u_y\rangle, |q_y\rangle, |p_{xx}\rangle, |p_{xy}\rangle]^T, \quad (5.18)$$

whose elements are,

$$|p\rangle = |e_\alpha|^0 \quad (5.19a)$$

$$|e\rangle_\alpha = Qe_\alpha^2 - b_2 \quad (5.19b)$$

$$|e^2\rangle_\alpha = a_1(Qe_\alpha^4 - b_6) + a_2(Qe_\alpha^4 - b_6) \quad (5.19c)$$

$$|u_x\rangle_\alpha = e_{\alpha,x} \quad (5.19d)$$

$$|q_x\rangle_\alpha = (b_1e_\alpha^2 - b_3)e_{\alpha,x} \quad (5.19e)$$

$$|u_y\rangle_\alpha = e_{\alpha,y} \quad (5.19f)$$

$$|q_y\rangle_\alpha = (b_1e_\alpha^2 - b_3)e_{\alpha,y} \quad (5.19g)$$

$$|p_{xx}\rangle_\alpha = de_{\alpha,x}^2 - e_\alpha^2 \quad (5.19h)$$

$$|p_{xy}\rangle_\alpha = e_{\alpha,x}e_{\alpha,y}, \quad (5.19i)$$

where  $d = 2$  and  $Q = 9$ ,  $b_1 = \sum_{\alpha=1}^Q e_{\alpha,x}^2$ ,  $b_2 = \sum_{\alpha=1}^Q e_\alpha^2$ ,  $b_3 = \sum_{\alpha=1}^Q e_\alpha^2 e_{\alpha,x}^4$ ,  $a_1 = ||e^2||^2$ , and  $a_2 = \sum_{\alpha=0}^{Q-1} (Qc_\alpha^2 - b_2) \times (Qc_\alpha^4 - b_6)$ .

Explicitly, the transformation matrix can be written as

$$\mathbf{M} = \begin{bmatrix} 1 & 1 & 1 & 1 & 1 & 1 & 1 & 1 & 1 \\ -4 & -1 & -1 & -1 & -1 & 2 & 2 & 2 & 2 \\ 4 & -2 & -2 & -2 & -2 & 1 & 1 & 1 & 1 \\ 0 & 1 & 0 & -1 & 0 & 1 & -1 & -1 & 1 \\ 0 & -2 & 0 & 2 & 0 & 1 & -1 & -1 & 1 \\ 0 & 0 & 1 & 0 & -1 & 1 & 1 & -1 & -1 \\ 0 & 0 & -2 & 0 & 2 & 1 & 1 & -1 & -1 \\ 0 & 1 & -1 & 1 & -1 & 0 & 0 & 0 & 0 \\ 0 & 0 & 0 & 0 & 0 & 1 & 1 & 1 & 1 \end{bmatrix}. \quad (5.20)$$

The corresponding equilibrium distribution functions in moment space  $\widehat{\mathbf{f}}^{eq}$  is given as

$$\widehat{\mathbf{f}}^{eq} = [\rho_0, e^{eq}, e^{2eq}, u_x, q_x^{eq}, q_y^{eq}, p_{xx}^{eq}, p_{xy}^{eq}]^T, \quad (5.21)$$

where

$$e^{eq} = \frac{1}{4}\alpha_2 p + \frac{1}{6}\gamma_2(u_x^2 + u_y^2) \quad (5.22a)$$

$$e^{2eq} = \frac{1}{4}\alpha_3 p + \frac{1}{6}\gamma_4(u_x^2 + u_y^2) \quad (5.22b)$$

$$q_x^{eq} = \frac{1}{2}c_1 u_x \quad (5.22c)$$

$$q_y^{eq} = \frac{1}{2}c_2 u_y \quad (5.22d)$$

$$p_{xx}^{eq} = \frac{3}{2}\gamma_1(u_x^2 - u_y^2) \quad (5.22e)$$

$$p_{xy}^{eq} = \frac{3}{2}\gamma_3(u_x u_y). \quad (5.22f)$$

To get the correct hydrodynamic equation, the values of the coefficients are chosen as  $\alpha_2 = 24$ ,  $\alpha_3 = -36$ ,  $c_1 = c_2 = -2$ ,  $\gamma_1 = \gamma_3 = 2/3$ ,  $\gamma_2 = 18$  and  $\gamma_4 = -18$ . The values of the elements in the collision matrix are:  $s_8 = s_9 = \tau$  and  $s_1 = s_4 = s_6 = 1.0$  and the others vary between 1.0 and 2.0 for linear stability. Through the Chapman-Enskog expansion (Du et al., 2006), the incompressible Navier-Stokes equation can be recovered and the viscosity is given as

$$\nu = c_s^2 \Delta t (\tau - 0.5). \quad (5.23)$$

### 5.1.3 Boundary conditions

Boundary conditions (BC) form an important part of any numerical technique. In many cases, the boundary conditions can strongly influence the accuracy of the algorithm. Velocity and pressure are not the primary variables in LBM, hence the standard pressure, velocity, and mixed boundary conditions cannot be imposed directly. Alternative conditions in terms of the distribution functions are adopted to describe the boundary conditions.

#### Periodic boundary condition

The simplest type of boundary condition is the periodic boundary. In this case, the domain is folded along the direction of the periodic boundary pair. For boundary nodes, the neighbouring nodes are on the opposite boundary, using the normal referencing of neighbours (see figure 5.1a). From the perspective of submarine landslide modelling, the periodic boundary conditions are useful for preliminary analysis, as they imply a higher degree of symmetry of the fluid domain. Further information on the periodic boundary condition can be found in Aidun et al. (1998).

### No-slip boundary condition

The most commonly adopted BC in the lattice Boltzmann approach is the no-slip BC, especially the simple bounce-back rule, which is quite elegant and surprisingly accurate. The basic idea is that the incoming distribution functions at a wall node are reflected back to the original fluid nodes, but with the direction rotated by  $\pi$  radians. The bounce-back boundary condition is one of the benefits of LBM, as it is trivial to implement and it allows one to effortlessly introduce obstacles into the fluid domain. However, the boundary conditions have been proven to be only first-order accurate in time and space (Pan et al., 2006). A straightforward improvement is to consider the wall-fluid interface to be situated halfway between the wall and the fluid lattice nodes (Ziegler, 1993). It involves defining the *solid* nodes as those lying within the stationary wall regions, and the *fluid* nodes otherwise. Then, if  $i$  is the direction between a fluid node  $n_1$  and a solid node  $n_2$ , the bounce-back rule requires that the incoming fluid particle from  $n_1$  to  $n_2$  be reflected back along the direction it came from, i.e.,

$$f_{-i}(\mathbf{x}, t + \Delta t) = f_i(\mathbf{x}, t_+), \quad (5.24)$$

where  $-i$  denotes the opposite direction of  $i$ . The bounce back rule is illustrated in figure 5.4. This simple rule ensures that no tangential velocity exists along the fluid-wall interface, thereby a non-slip condition is imposed, and can be extended to any shapes or objects in a fluid flow (Han et al., 2007a; Zou and He, 1997). The slip boundary conditions have similar treatment to the non-slip condition, except that the distribution functions are reflected in the boundary instead of bounce-back (Succi, 2001).

### Pressure and velocity boundary condition

The pressure (Dirichlet) boundary condition can be imposed in lattice Boltzmann by specifying a fluid density at the pressure boundary (Zou and He, 1997). To impose a pressure boundary along the y-direction (for example, consider the left hand side inlet boundary in figure 5.5), a density  $\rho = \rho_{in}$  is specified from which the velocity is computed. The vertical component of the velocity on the boundary is set as zero,  $u_y = 0$ . After streaming,  $f_2, f_3, f_4, f_6$ , and  $f_7$  are known,  $u_x$  and  $f_1, f_5, f_8$  are to be determined from eq. 5.2 as

$$f_1 + f_5 + f_8 = \rho_{in} - (f_0 + f_2 + f_3 + f_4 + f_6 + f_7) \quad (5.25)$$

$$f_1 + f_5 + f_8 = \rho_{in} u_x + (f_3 + f_6 + f_7) \quad (5.26)$$

$$f_5 - f_8 = f_2 - f_4 + f_6 - f_7, \quad (5.27)$$

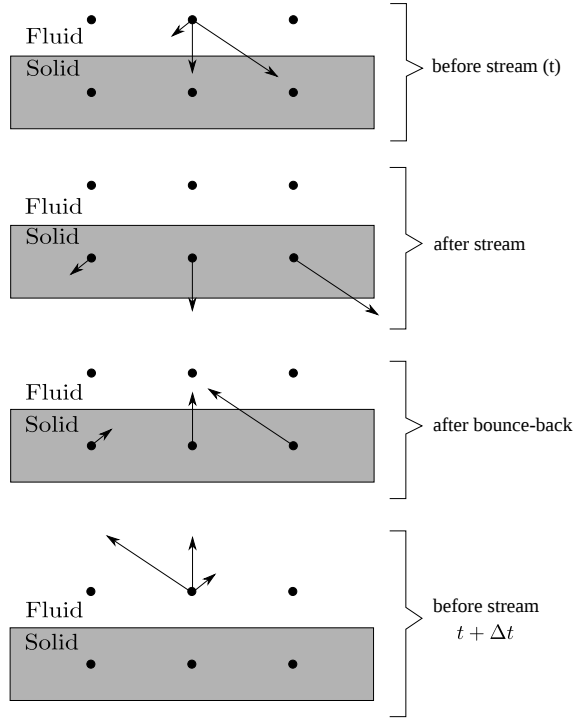


Figure 5.4 Half-way bounce back algorithm for the  $D2Q9$  model adopted after Sukop and Thorne (2006).

Consistency of equations (5.25) and (5.26) gives

$$u_x = 1 - \frac{[f_0 + f_2 + f_4 + 2 * (f_3 + f_6 + f_7)]}{\rho_{in}}. \quad (5.28)$$

The bounce-back rule for the non-equilibrium part of the particle distribution normal to the inlet is used to find  $f_1 - f_1^{eq} = f_3 - f_3^{eq}$ . The values of  $f_5$  and  $f_8$  can be obtained from  $f_1$ :

$$\begin{aligned} f_1 &= f_3 + \frac{2}{3}\rho_{in}u_x \\ f_5 &= f_7 - \frac{1}{2}(f_2 - f_4) + \frac{1}{6}\rho_{in}u_x \\ f_8 &= f_6 + \frac{1}{2}(f_2 - f_4) + \frac{1}{6}\rho_{in}u_x. \end{aligned} \quad (5.29)$$

The corner node at inlet needs some special treatment. Considering the bottom node at inlet as an example, after streaming,  $f_3, f_4, f_7$  are known;  $\rho$  is defined, and  $u_x = u_y = 0$ . The particle distribution functions  $f_1, f_2, f_5, f_6$ , and  $f_8$  are to be determined. The bounce-back rule for the non-equilibrium part of the particle distribution normal to the inlet and the

boundary is used to find

$$f_1 = f_3 + (f_1^{eq} - f_3^{eq}) = f_3 \quad (5.30)$$

$$f_2 = f_4 + (f_1^{eq} - f_3^{eq}) = f_4. \quad (5.31)$$

Using these we can compute

$$f_5 = f_7 \quad (5.32)$$

$$f_6 = f_8 = \frac{1}{2}[\rho_{in} - (f_1 + f_2 + f_3 + f_4 + f_5 + f_6 + f_7 + f_8)]. \quad (5.33)$$

Similar procedure can be applied to the top inlet node and the outlet nodes. Von Neumann boundary conditions constrain the flux at the boundaries. A velocity vector  $u = [u_0 \ v_0]^T$  is specified, from which the density and pressure are computed based on the domain. The velocity boundary condition can be specified in a similar way (Zou and He, 1997). The pressure and velocity boundary conditions contribute additional equation(s) to determine the unknown distribution functions. In the case of velocity boundary, the boundary condition equation is sufficient to determine the unknown distribution functions in the *D2Q9* model, however the pressure boundary conditions require additional constitutive laws to determine the unknown distribution functions.

## 5.2 Validation of the lattice Boltzmann method

To verify the incompressible LBM model implemented in the above section, numerical simulation of a transient development of steady state Poiseuille flow in a straight channel is performed. At  $t = 0$ , the LBM water particles ( $\rho = 1000 \text{ kg/m}^3$ ) are simulated to flow through a channel of width ‘H’ ( $= 0.4 \text{ m}$ ) and simulation length ‘L’ ( $2.5H$ ) under constant body force. Periodic boundary conditions are applied at either end of the channel and the pressure gradient is set to zero, which simulates the condition of a continuous flow of fluid in a closed circular pipe. The length ‘L’ has no effect on the simulation as no stream-wise variation is detected in the solution. The parameters adopted in LBM simulation are presented in table 5.1. Sufficient time is allowed for the flow to travel beyond the required development length so that the flow is laminar (Durst et al., 2005). The development length  $X_D$  required for a flow to be fully laminar is

$$X_D/H = [(0.619)^{1.6} + (0.0567R_e)^{1.6}]^{1/1.6}, \quad (5.34)$$

Table 5.1 LBM parameters used in simulating laminar flow through a circular pipe.

| Parameter                               | Value                                |
|---|--------------------------------------|
| Density $\rho$                          | 1000 kg/m <sup>3</sup>               |
| Relaxation parameter $\tau$             | 0.51                                 |
| Kinematic viscosity                     | $1 \times 10^{-6}$ m <sup>2</sup> /s |
| Grid resolution ‘h’                     | 1 <sup>-2</sup> m                    |
| Number of steps                         | 50,000                               |
| Error in predicting horizontal velocity | 0.009 %                              |

where  $R_e$  is the Reynolds number. The velocity profile at steady state is presented in figure 5.5. A maximum horizontal velocity of 0.037863 m/s is observed along the centre-line of the channel. The maximum horizontal velocity is compared with the closed-form based on the Hagen-Poiseuille flow equation for no-slip boundary condition (Willis et al., 2008)

$$U_x = \frac{\Delta P}{2\mu L} \left[ \frac{H^2}{4} - y^2 \right], \quad (5.35)$$

where  $v_x$  is the horizontal velocity (m/s);  $\Delta P$  is the pressure gradient,  $\mu$  dynamic viscosity of the fluid. LBM predicts the maximum horizontal velocity within an error of 0.009 %.

In order to further validate the accuracy of the lattice Boltzmann code, the transient development of the Poiseuille’s flow is compared with the CFD simulation performed using ANSYS Fluent. Finite Volume Method is a common CFD technique, which involves solving the governing partial differential equation (Navier-Stokes) over the discretised control volume. This guarantees the conservation of fluxes over a particular control volume. The finite volume equations yield governing equations of the form

$$\frac{\partial}{\partial t} \iiint Q d\mathbf{V} + \iint F d\mathbf{A} = 0, \quad (5.36)$$

where  $Q$  is the vector of conserved variables,  $F$  is the vector of fluxes in the Navier-Stokes equation,  $V$  is the volume of control volume element, and  $A$  is the surface area of the control volume element.

A 2D rectangular plane of length 1 m and height 0.04 m is discretised into 400 cells of size 1<sup>-2</sup> m (see figure 5.6). A constant velocity is applied at the inlet. Water ( $\rho = 998.2 \text{ kg/m}^3$ , viscosity ‘ $\eta$ ’ =  $1 \times 10^{-3} \text{ Ns/m}^2$ ) is allowed to flow through the channel and it develops into a fully laminar flow. The least squares approach was adopted to solve the gradient, and a maximum of 100 iteration steps were carried out until the solution converged.

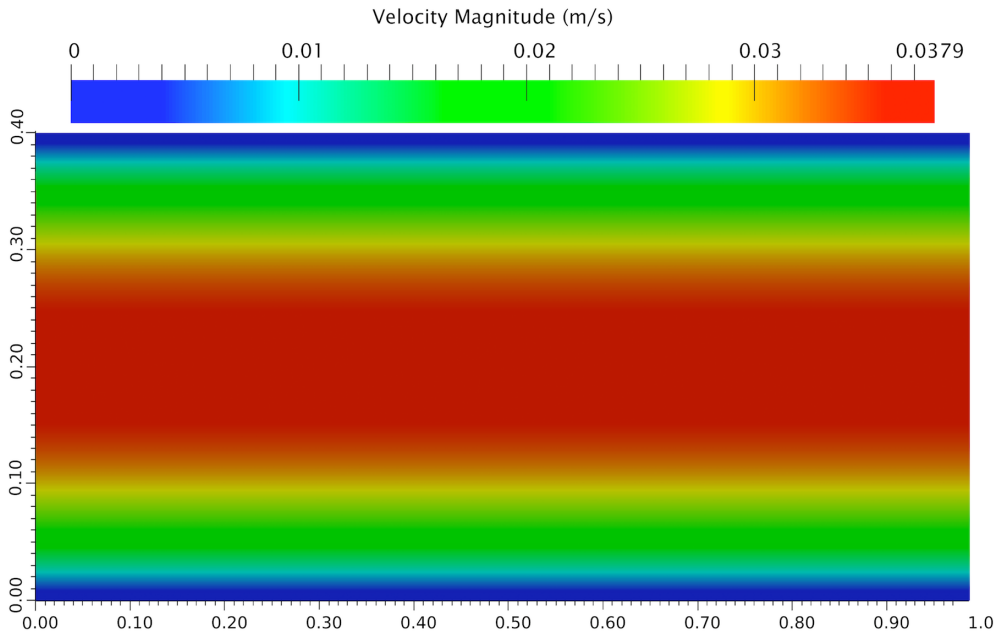


Figure 5.5 Velocity profile obtained from a LBM Simulation of a laminar flow through a channel.

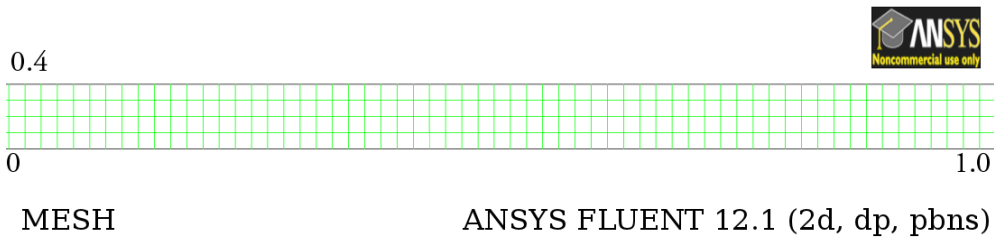


Figure 5.6 Finite Volume mesh used in the CFD analysis of laminar flow through a channel.

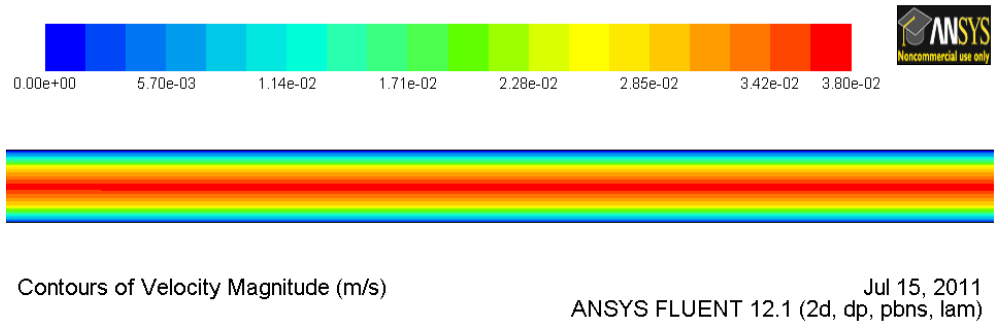


Figure 5.7 Velocity profile obtained from a CFD analysis of laminar flow through a channel.

The velocity profile obtained from the CFD simulation at cross-section ‘L/4’ is shown in figure 5.7. Figure 5.8 compares the development of computed velocity profiles with the analytical solution. At normalised time  $t = 1$ , the flow approaches steady state. It can be observed that LBM has excellent agreement with CFD and the analytical solution at various stages of flow evolution.

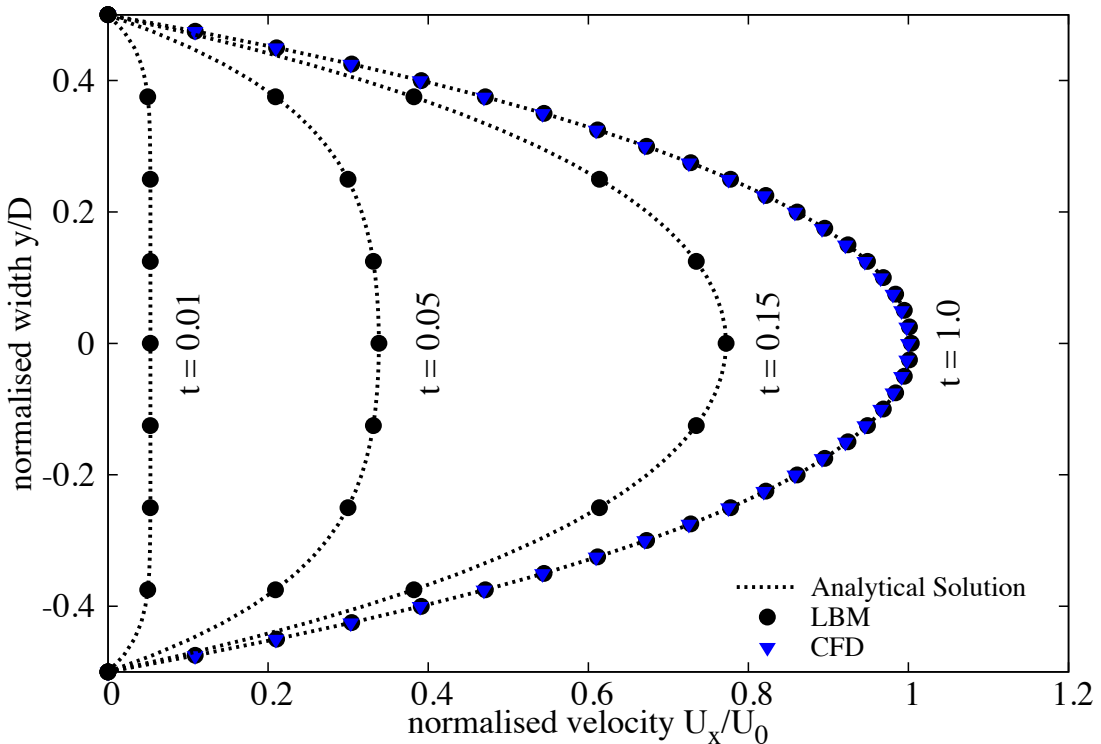


Figure 5.8 Development of the Poiseuille velocity profile in time: comparison between LBM simulation, CFD simulation and the analytical solution. Time is made dimensionless by  $H/U_0$ .

In order to study the capability of the lattice Boltzmann technique to simulate fluid–solid interaction, LB simulation of a fluid flow around a rectangular obstacle is compared with the CFD technique. A solid wall of height ‘ $H/2$ ’ is placed at length ‘ $L/4$ ’ in the channel. Bounce-back algorithm is employed to model the fluid-wall interaction in LBM. In the CFD model, the control volume is discretised into 10,000 cells. A constant velocity is applied in the inlet and the horizontal velocity profile is recorded. Both, CFD and LBM simulations were performed to study the influence of a solid wall on the fluid flow behaviour.

The horizontal velocity profile obtained after 50,000 LBM iterations is presented in figure 5.9. LBM is able to capture the velocity shedding around the edges of the wall. The velocity profile obtained from the CFD analysis is presented in figure 5.10. The horizontal velocity profile at ‘ $L/4$ ’ at  $t = 1$  is shown in figure 5.11. The maximum horizontal velocity from

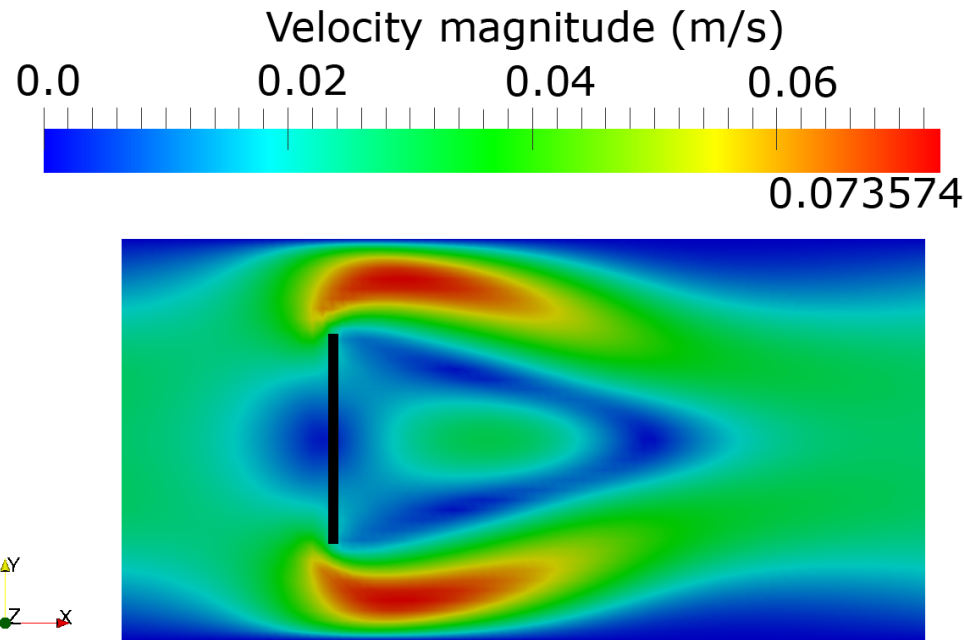


Figure 5.9 LBM simulation of velocity profile for a laminar flow through a pipe with an obstacle at L/4.

the CFD analysis is 0.3% higher in comparison with the LBM simulation. The discrepancy in the horizontal velocity profile (figure 5.11) can be attributed to the relaxation parameter used in the LBM, which is obtained by a trial and error procedure. The velocity profile obtained from the LBM simulation compares qualitatively with the FE analysis performed by Zhong and Olson (1991). Thus, it can be concluded that the lattice Boltzmann method is a suitable form of numerical representation of the Navier-Stokes equation to model fluid – solid interactions.

### 5.3 Turbulence in lattice Boltzmann method

The above formulation of lattice Boltzmann has been successfully applied to many fluid flow problems, however it is restricted to flows with low Reynolds number. Modelling fluids with low viscosity like water and air remains a challenge, necessitating very small values of  $h$ , and/or  $\tau$  very close to 0.5 (He et al., 1997). The standard lattice Boltzmann can deal with laminar flows, while practical problems with small kinematic viscosity are often associated with flows having large Reynolds numbers, i.e. flows which are unsteady or turbulent in

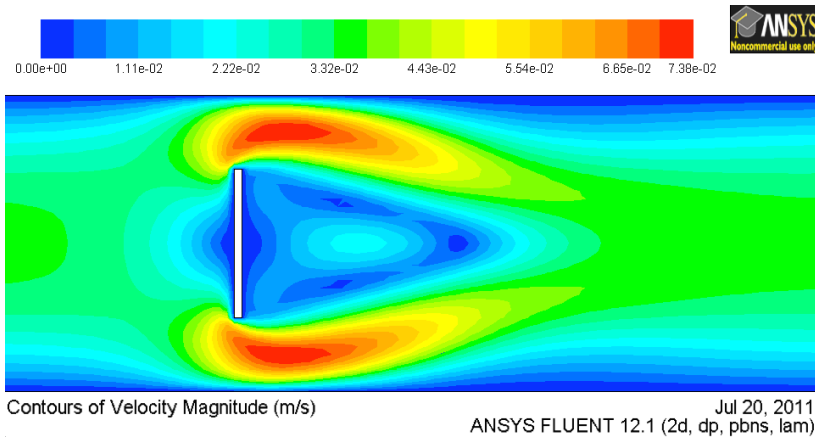


Figure 5.10 CFD simulation of velocity contour for a laminar flow through a pipe with an obstacle at L/4.

nature. The turbulent flows are characterised by the occurrence of eddies with multiple scales in space, time and energy.

The large eddy simulation (LES) is the most widely adopted approach to solve turbulent flow problems. It directly solves the large scale eddies, which carry the predominant portion of the energy, and the smaller eddies are modelled using a sub-grid approach. The separation of scales is achieved by filtering of the Navier-Stokes equations, from which the resolved scales are directly obtained. The unresolved scales are modelled by a one-parameter Smagorinski sub-grid methodology, which assumes that the Reynolds stress tensor is dependent only on the local strain rate (Smagorinsky, 1963). It involves parametrising the turbulent energy dissipation in the flows, where the larger eddies extract energy from the mean flow and ultimately transfer some of it to the smaller eddies which, in turn, pass the energy to even smaller eddies, and so on up to the smallest scales. At the smallest scale, the eddies convert the kinetic energy into the internal energy of the fluid. At this scale, the viscous friction dominates the flow (Frisch and Kolmogorov, 1995).

In the Smargonisky model, the turbulent viscosity  $\nu$  is related to the strain rate  $S_{ij}$  and a filtered length scale ‘ $h$ ’ as follows

$$S_{ij} = \frac{1}{2}(\partial_i u_j + \partial_j u_i) \quad (5.37)$$

$$\nu_t = (S_c h)^2 \bar{S} \quad (5.38)$$

$$\bar{S} = \sqrt{\sum_{i,j} \tilde{S}_{i,j} \tilde{S}_{i,j}}, \quad (5.39)$$

where  $S_c$  is the Smargonisky constant, which is close to 0.03 (Yu et al., 2005). The effect of the unresolved scale motion is taken into account by introducing an effective collision

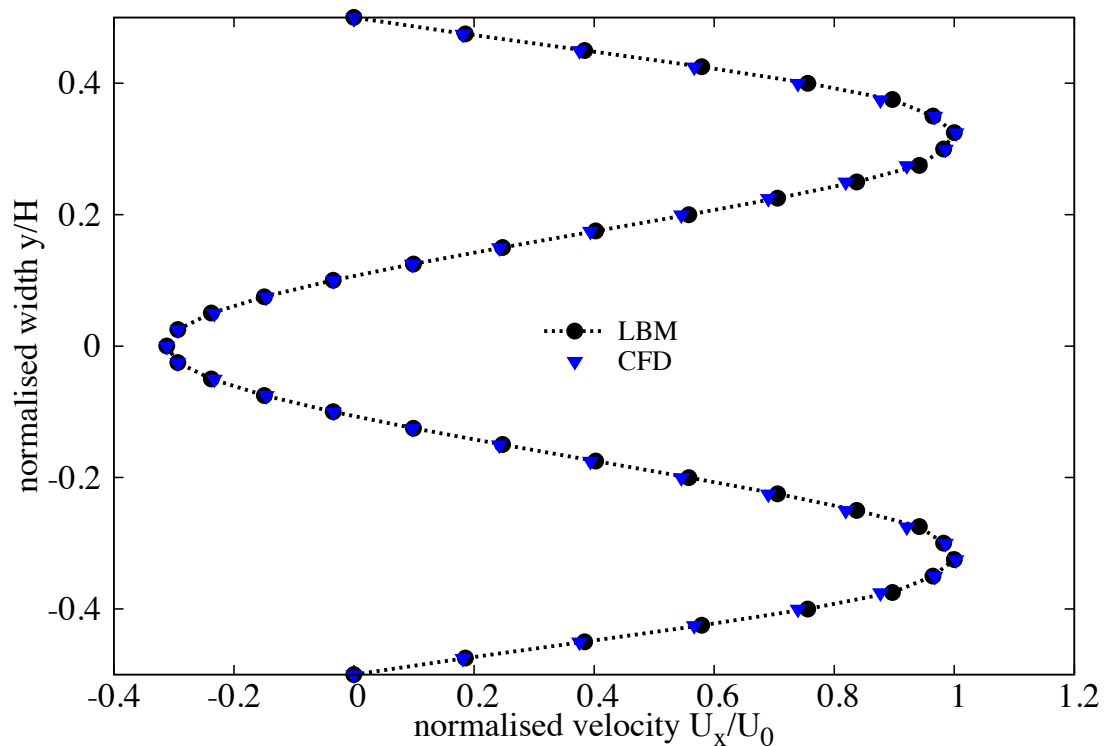


Figure 5.11 LBM and CFD simulation of the velocity contour at  $L/2$  for a flow around an obstacle at  $L/4$ .

relaxation time scale  $\tau_t$ , so that the total relaxation time  $\tau_*$  is written as

$$\tau_* = \tau + \tau_t, \quad (5.40)$$

where  $\tau$  and  $\tau_t$  are respectively the standard relaxation times corresponding to the true fluid viscosity  $\nu$  and the turbulence viscosity  $\nu_t$ , defined by a sub-grid turbulence model. The new viscosity  $\nu_*$  corresponding to  $\tau_*$  is defined as

$$\begin{aligned} \nu_* &= \nu + \nu_t \\ &= \frac{1}{3}(\tau_* - \frac{1}{2})C^2\Delta t = \frac{1}{3}(\tau + \tau_t - \frac{1}{2})C^2\Delta t \end{aligned} \quad (5.41)$$

$$\nu_t = \frac{1}{3}\tau_t C^2\Delta t. \quad (5.42)$$

The Smargonisky model is easy to implement and the lattice Boltzmann formulation remains unchanged, except for the use of a new turbulence-related viscosity  $\tau_*$ . The component  $s_1$  of the collision matrix becomes  $s_1 = \frac{1}{\tau + \tau_t}$ .

The effectiveness of LBM-LES model in simulating unsteady flows is verified by modelling the Kármán vortex street. In fluid dynamics, a Kármán vortex street is a repeating pattern of vortices caused by unsteady separation of fluid flow around circular obstacles. A vortex street will only be observed above a limiting value of Reynolds number of 90. The Reynolds number is computed based on the cylinder diameter ‘D’ and the mean flow velocity  $U$  of the parabolic inflow profile:

$$Re = \frac{UD}{\nu}. \quad (5.43)$$

LBM particles are simulated to flow through a 2D rectangular channel with an aspect ratio ‘L/H’ of 2.5. A cylinder of diameter ‘d’ = 0.27H is placed at H/2. The pressure gradient at the inlet and the outlet is varied to create flows with different mean velocities. Numerical simulations of vortex shedding behind a circular obstacle are carried out for three different fluid flow regimes (Reynolds number of 55, 75, and 112). The fully developed fluid flows for different Reynolds numbers are shown in figure 5.12. It can be observed from figure 5.12 that the Von Kármán vortex street can only be observed at high a Reynolds number of 112 ( $Re > 90$ ), which shows the ability of the LBM turbulence model to capture instabilities in fluid flow.

One important quantity taken into account in the present analysis is the Strouhal number  $St$ , a dimensionless number describing oscillating unsteady flow dynamics. The Strouhal number is computed from the cylinder diameter D, the measured frequency of the vortex

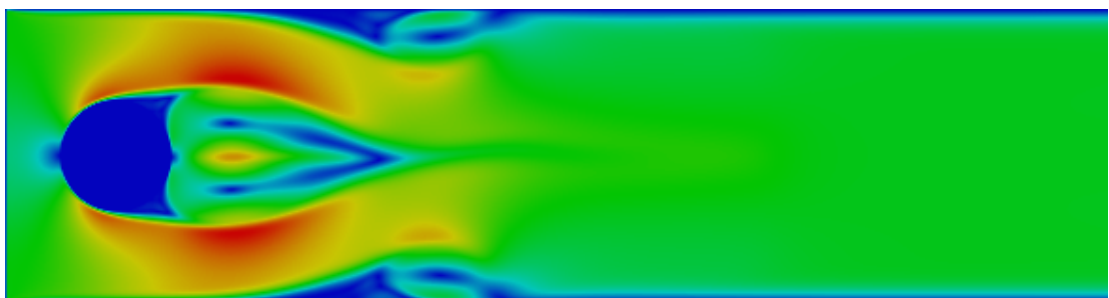
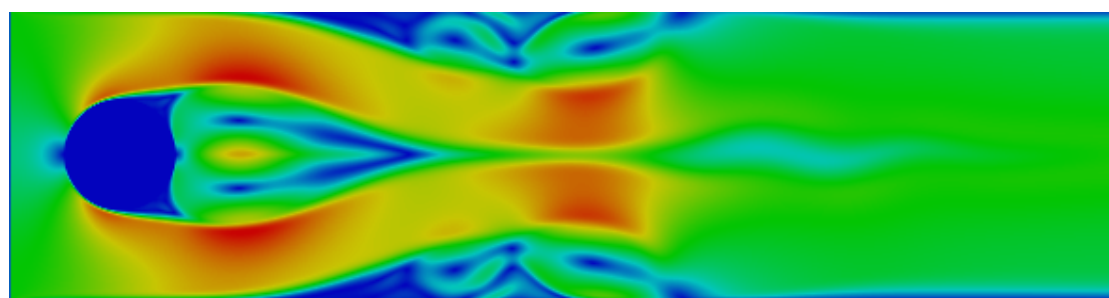
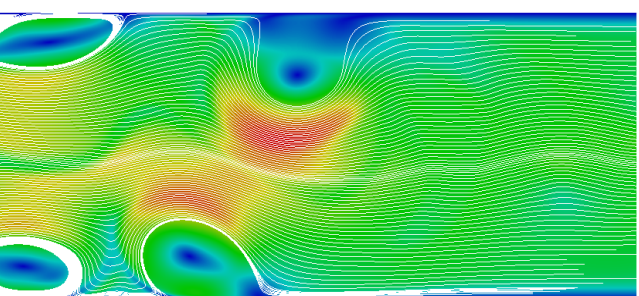
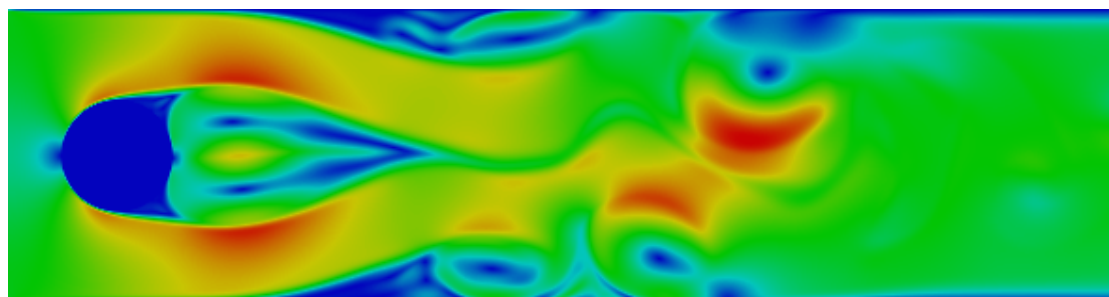
(a)  $\text{Re} = 55$ (b)  $\text{Re} = 75$ (c)  $\text{Re} = 112$ 

Figure 5.12 Development of Kármán vortex street around a circular obstacle, for different Reynolds number.

shedding  $f$ , and the maximum velocity  $U_{max}$  at the inflow plane:

$$St = \frac{fD}{U_{max}}. \quad (5.44)$$

The characteristic frequency  $f$  is determined by a spectral analysis (Fast Fourier Transform - FFT) of time series of the fluid pressure. Table 5.2 shows that the Strouhal numbers computed from LBM simulations have a very good agreement with FVM results obtained by Breuer et al. (2000). This shows the ability of LBM-LES in capturing unsteady flow dynamics.

Table 5.2 Computed Strouhal number for fluid flows with different Reynolds number

| Reynolds number | Strouhal number |       |
|-----------------|-----------------|-------|
|                 | LBM             | FVM   |
| 55              | 0.117           | 0.117 |
| 75              | 0.128           | 0.129 |
| 112             | 0.141           | 0.141 |

\* FVM results are from Breuer et al. (2000)

## 5.4 Coupled LBM and DEM for fluid-grain interactions

Modelling fluid–grain interactions in submarine landslides requires the ability to simulate the interactions at the dynamic fluid – solid boundaries. In principle, the conventional FE and FVM based approaches for solving the Navier-Stokes equations with moving boundaries and/or structural interaction (Bathe and Zhang, 2004) can be applied to particle fluid interaction problems. The common feature of these approaches is to model the interaction between the fluid and the solid to a high degree of accuracy. However, the main computational challenge is the need to continuously generate new geometrically adapted meshes to circumvent severe mesh distortion, which is computationally very intensive (Han et al., 2007b).

The lattice Boltzmann approach has the advantage of accommodating large particle sizes and the interaction between the fluid and the moving grains can be modelled through relatively simple fluid - grain interface treatments. Further, employing DEM to account for the grain/grain interaction naturally leads to a combined LB – DEM solution procedure. The Eulerian nature of the lattice Boltzmann formulation, together with the common explicit time step scheme of both LBM and DEM makes this coupling strategy an efficient numerical procedure for the simulation of fluid – grain systems.

LBM – DEM technique is a powerful predictive tool for gaining insights into many fundamental physical phenomena in fluid-solid systems. Such a coupled methodology was first proposed by (Cook et al., 2004) for simulating fluid-grain systems dominated by fluid-grain and grain-grain interactions. To capture the actual physical behaviour of the fluid-grain system, it is essential to model the boundary condition between the fluid and the grain as a non-slip boundary condition, i.e. the fluid velocity near the grain should be similar to the velocity of the grain boundary. The soil grains in the fluid domain are represented by lattice nodes. The discrete nature of the lattice will result in stepwise representations of the surfaces, which are otherwise circular, this is neither accurate nor smooth, unless sufficiently small lattice spacing is adopted.

### Modified bounce back rule

To accommodate the movement of solid particles in the commonly adopted bounce-back rule (see section 5.1.3), Ladd (1994) modified the ‘no-slip’ rule for a given boundary link  $i$  to be

$$f_i(\mathbf{x}, t + \Delta t) = f_i(\mathbf{x}, t_+) - \alpha_i e_{\mathbf{i}} \cdot \mathbf{v}_b \quad (\alpha_i = 6w_i \rho / C_s^2), \quad (5.45)$$

where  $f_i(\mathbf{x}, t_+)$  is the post collision distribution at the fluid or solid boundary node  $\mathbf{x}$ , and  $v_b$  is the velocity at the nominal boundary point at the middle of the boundary link  $i$

$$\mathbf{v}_b = \mathbf{v}_c + \boldsymbol{\omega} \times (\mathbf{x} + e_{\mathbf{i}} \Delta t / 2 - \mathbf{x}_c), \quad (5.46)$$

in which  $v_c$  and  $\boldsymbol{\omega}$  are the translational and angular velocities at the mass centre of the solid particle, respectively.  $\mathbf{x}_c$  and  $\mathbf{x} + e_{\mathbf{i}} \Delta t / 2$  are the coordinates of the centre and the nominal boundary point, respectively. The impact force on the soil grain from the link is defined as

$$\mathbf{F}_{\mathbf{i}} = 2[f_i(\mathbf{x}, t_+) - \alpha_i e_{\mathbf{i}} \cdot \mathbf{v}_b] / \Delta t. \quad (5.47)$$

The corresponding torque  $\mathbf{T}_i$ , produced by the force with respect to the centre of the particle is computed as

$$\mathbf{T}_i = \mathbf{r}_c \times \mathbf{F}_i (\mathbf{r}_c = \mathbf{x} + e_{\mathbf{i}} \Delta t / 2 - \mathbf{x}_c). \quad (5.48)$$

Then the total hydrodynamic force and torque exerted on the particle can be calculated by summing up the forces and torques from all the related boundary links:

$$\begin{aligned} \mathbf{F} &= \sum_i \mathbf{F}_i \\ \mathbf{T} &= \sum_i \mathbf{T}_i. \end{aligned} \quad (5.49)$$

Ladd and Verberg (2001) described a methodology that minimises the oscillations resulting from soil grains crossing lattices at a very high speed. The methodology involves combining several extensions for the fluid simulation like the treatment of moving curved boundaries with the scheme of Yu et al. (2003) and a fluid/grain force interaction method with the momentum exchange method of Ladd and Verberg (2001). The simulation of the moving curved grain surfaces results in the intersection of links between two nodes at arbitrary distances (Iglberger et al., 2008). These distance values are referred to as delta values:

$$\delta = \frac{\text{Distance between fluid node and soil surface}}{\text{Distance between fluid node and soil node}} \in [0, 1]. \quad (5.50)$$

For each pair of a fluid and grain node, a delta value has to be calculated. Delta values of zero are not possible as the nodes on the surface are considered as solid nodes. The algorithm for computation of the  $\delta$  value is presented in Iglberger et al. (2008). Figure 5.13 shows the three possible situations for delta values between 0 and 1. The fluid particles in LBM are always considered to be moving at the rate of one lattice per time step ( $\delta\mathbf{x}/\delta t$ ), for delta values smaller than 0.5. For  $\delta$  values larger than 0.5, the fluid particles would come to rest at an intermediate node  $\mathbf{x}_i$ . In order to calculate the reflected distribution function in node  $\mathbf{x}_f$ , an interpolation scheme has to be applied. The linear interpolation scheme of Yu et al. (2003) is used in the present study, which uses a single equation, irrespective of the value of  $\delta$  being smaller or larger than 0.5, to the reflected distribution function that is computed as

$$\begin{aligned} f_{\bar{\alpha}}(\mathbf{x}_f, t + \delta t) = & \frac{1}{1 + \delta} \cdot [(1 - \delta) \cdot f_{\alpha}(\mathbf{x}_f, t + \delta t) + \delta \cdot f_{\alpha}(\mathbf{x}_b, t + \delta t) \\ & + \delta \cdot f_{\bar{\alpha}}(\mathbf{x}_{f2}, t + \delta t) - 2w_a \rho_w \frac{3}{c^2} e_a \cdot \mathbf{u}_w], \end{aligned} \quad (5.51)$$

where  $w_{\alpha}$  is the weighting factor,  $\rho_w$  is the fluid density in node  $\mathbf{x}_f$ , and  $\mathbf{u}_w$  is the velocity at the bounce-back wall. In order to couple the fluid-grain interaction, the LBM approach is extended by adopting a force integration scheme, to calculate the fluid force acting on the grain surface, and the momentum exchanged method described earlier. The physical force acting on grain agglomerates is calculated as the sum over all fluid/grain node pairs, resulting in

$$F = \sum_{\mathbf{x}_b} \sum_{\alpha=1}^{19} \mathbf{e}_{\alpha} [f_{\alpha}(\mathbf{x}_b, t) + f_{\bar{\alpha}}(\mathbf{x}_f, t)] \delta\mathbf{x}/\delta t. \quad (5.52)$$

After the force calculations, the coupled rigid body physics can be simulated in order to move the grains / grain-agglomerates according to the applied forces. The total hydrodynamic forces and torque exerted on a grain can be computed as (Cook et al., 2004; Noble and

Torczynski, 1998)

$$\mathbf{F}_f = Ch \left[ \sum_n \left( \beta_n \sum_i f_i^m e_i \right) \right] \quad (5.53)$$

$$\mathbf{T}_f = Ch \left[ \sum_n \left( \mathbf{x}_n - \mathbf{x}_c \right) \times \left( \beta_n \sum_i f_i^m e_i \right) \right]. \quad (5.54)$$

The summation is over all lattice nodes covered by the soil grain, and  $\mathbf{x}_n$  represents the coordinate of the lattice node  $n$ .

When grains are not in direct contact among themselves, but are driven by the fluid flow and body force, i.e. gravity, their motion can be determined by Newton's equation of motion

$$m\mathbf{a} = \mathbf{F}_f + m\mathbf{g} \quad (5.55)$$

$$J\ddot{\theta} = \mathbf{T}_f, \quad (5.56)$$

where  $m$  and  $J$  are respectively the mass and the moment of inertia of a grain,  $\ddot{\theta}$  is the angular acceleration,  $\mathbf{g}$  is the gravitational acceleration,  $\mathbf{F}_f$  and  $\mathbf{T}_f$  are respectively the hydrodynamic forces and torque. The equation can be solved numerically by an explicit numerical integration, such as the central difference scheme.

The interaction between the soil grains, and the soil grains with the walls are modelled using the DEM technique. To solve the coupled DEM–LBM formulation, the hydrodynamic force exerted on soil grains and the static buoyancy force are considered by reducing the gravitational acceleration to  $(1 - \rho/\rho_s)\mathbf{g}$ , where  $\rho_s$  is the density of the grains. When taking into account all forces acting on an element, the dynamic equations of DEM can be expressed as

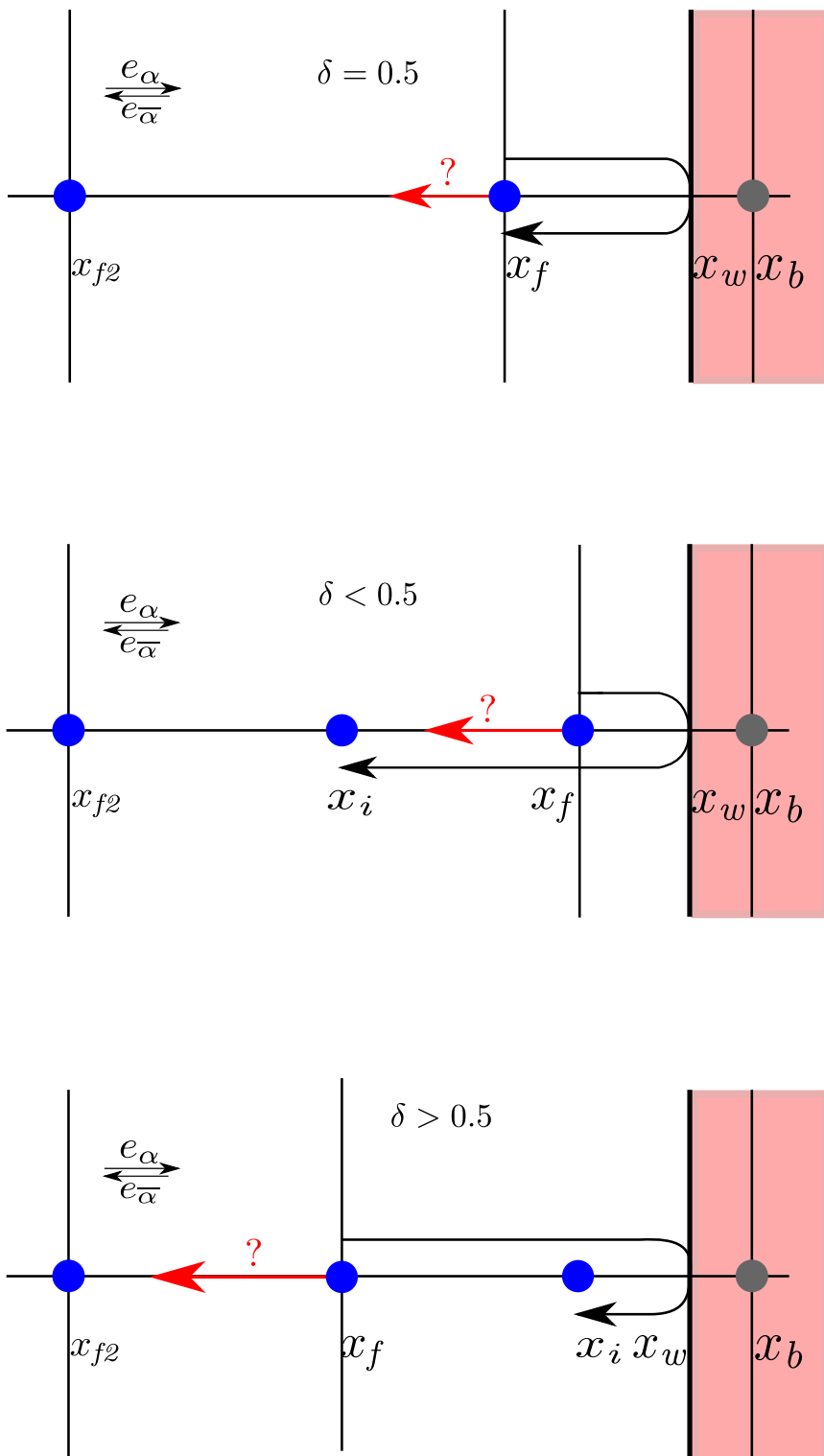
$$m\mathbf{a} + c\mathbf{v} = \mathbf{F}_c + \mathbf{F}_f + m\mathbf{g}, \quad (5.57)$$

where  $\mathbf{F}_c$  denotes the total contact forces from other elements and/or the walls, and  $c$  is a damping coefficient. The term  $c\mathbf{v}$  represents a viscous force that accounts for the effect of all possible dissipation forces in the system including energy lost during the collision between grains. Considering a linear contact model

$$\mathbf{F}_c = k_n \delta, \quad (5.58)$$

where  $k_n$  is the normal stiffness and  $\delta$  is the overlap, the critical time step associated with the explicit integration is determined as (He et al., 1997)

$$\Delta t_{cr} = 2(\sqrt{1 + \xi^2} - \xi)/\omega, \quad (5.59)$$

Figure 5.13 LBM bounce back boundaries for different values of  $\delta$

where  $\omega = \sqrt{k_n/m}$  is the local contact natural frequency and  $\xi = c/2m\omega$  is the critical damping ratio. The actual time step used for the integration of the Discrete Element equations is

$$\Delta t_D = \lambda \Delta t_{cr}. \quad (5.60)$$

The time step factor  $\lambda$  is chosen to be around 0.1 to ensure both stability and accuracy (He et al., 1997).

When combining the Discrete Element modelling of the grain interactions with the LB formulation, an issue arises. There are now two time steps:  $\Delta t$  for the fluid flow and  $\Delta t_D$  for the particles. Since  $\Delta t_D$  is normally smaller than  $\Delta t$ ,  $\Delta t_D$  is slightly reduced to a new value  $\Delta t_s$  so that  $\Delta t$  and  $\Delta t_s$  have an integer ratio  $n_s$

$$\Delta t_s = \frac{\Delta t}{n_s} \quad (n_s = [\Delta t/\Delta t_D] + 1). \quad (5.61)$$

This results in a sub-cycling time integration for the Discrete Element part. At every step of the fluid computation,  $n_s$  sub-steps of integration are performed for the Discrete Element Method (5.57) using the time step  $\Delta t_s$ . The hydrodynamic force  $\mathbf{F}_f$  is unchanged during the sub-cycling.

### 5.4.1 Draft, kiss and tumbling: Sedimentation of two grains

In multiphase flows, fundamental mechanisms of fluid – grain and grain – grain interactions are very important for accurately predicting the flow behaviours. The sedimentation of two circular grains in a viscous fluid serves as the simplest problem to study these two types of interactions, and many experimental and numerical studies have been carried out to investigate this behaviour (Komiwas et al., 2005; Wang et al., 2014). Fortes (1987) observed experimentally that in the sedimentation of two grains under gravity in a Newtonian fluid, the two grains would undergo the draft, kiss and tumbling (DKT) phenomenon.

The *draft*: grain 2 is first placed within the hydrodynamic drag above grain 1. As the hydrodynamic drag of grain 1 is a depression zone, grain 2 is attracted inside. The *kiss*: grain 2 increases its vertical velocity until it touches grain 1. The horizontal velocity of grain 1 increases and its vertical velocity decreases below that of grain 2. *Tumbling*: grain 2 having the same horizontal velocity and higher vertical velocity than grain 1, overtakes grain 1.

LBM-DEM simulation of two grains under gravity in a viscous Newtonian fluid reproduces the draft, kiss and tumble effect (see figure 5.14). They are in agreement with the experimental description of the DKT effect. For better understanding of the DKT effect, the time history of three distances between the grains (normalised to the diameter of the grain D)

are tracked i.e., the difference in the transverse coordinates  $\delta_x/D$  and longitudinal coordinates  $\delta_y/D$  of the two grain centres, and the gap between the two surfaces  $\delta = \sqrt{\delta_x^2 + \delta_y^2} - 1$  (see figure 5.15c).

As shown in figure 5.14, grain 1 trails grain 2. As grain 2 approaches the depression zone, corresponding to negative fluid pressure behind grain 1, the velocity of the trailing grain increases as the grains approach closer, this is in agreement with the experimental description of the draft. Grain 2 increases its vertical velocity more than grain 1 until it touches grain 1. The kiss happens at a normalised time  $(t/\sqrt{(D/g)}) = 25$ . At this stage, the gap  $\delta$  between the grains is zero, but the actual gap is about one lattice spacing for the LBM collision model. After this time, the vertical velocity of grain 1 decreases and its horizontal velocity increases as the grains tumble. At this stage, the grains still remain in contact, i.e., the gap remains unchanged  $\delta = 0$ . Subsequently, the two grains separate and move away from each other. Figure 5.15b shows that the terminal velocities of the two grains are in good agreement with the terminal velocity of a single grain found by an independent simulation and calculated using the empirical Schiller and Nauman formula (Komiwes et al., 2005).

## 5.5 GP-GPU Implementation

Graphics Processing Unit (GPU) is a massively multi-threaded architecture that is widely used for graphical and now non-graphical computations. Today’s GPUs are general purpose processors with support for an accessible programming interface. The main advantage of GPUs is their ability to perform significantly more floating point operations (FLOPs) per unit time than a CPU. General Purpose computations on GPUs (GPGPUs) often achieve speed-ups of orders of magnitude in comparison with optimised CPU implementations.

A GPU consists of several *Streaming Multiprocessors* (SMs). Each SM contains 32 CUDA processors. Each CUDA processor has a fully pipelined integer arithmetic logic unit (ALU) and a floating point unit (FPU). The FPU complies with the IEEE 754-2008 industry standard for floating-point arithmetic, capable of double precision computations. The SM schedules work in groups of 32 threads called warps. Each SM features two warp schedulers and two instruction dispatch units, allowing two warps to be issued and executed concurrently. Each thread has access to both L1 and L2 caches, which improves the performance for programs with random memory access.

The occupancy rate of the SPs, i.e. the ratio between the number of threads run and the maximum number of executable threads, is an important aspect to take into consideration for the optimisation of a CUDA kernel. Even though a block may only be run on a single SM, it is possible to execute several blocks concurrently on the same SM. Hence, tuning the

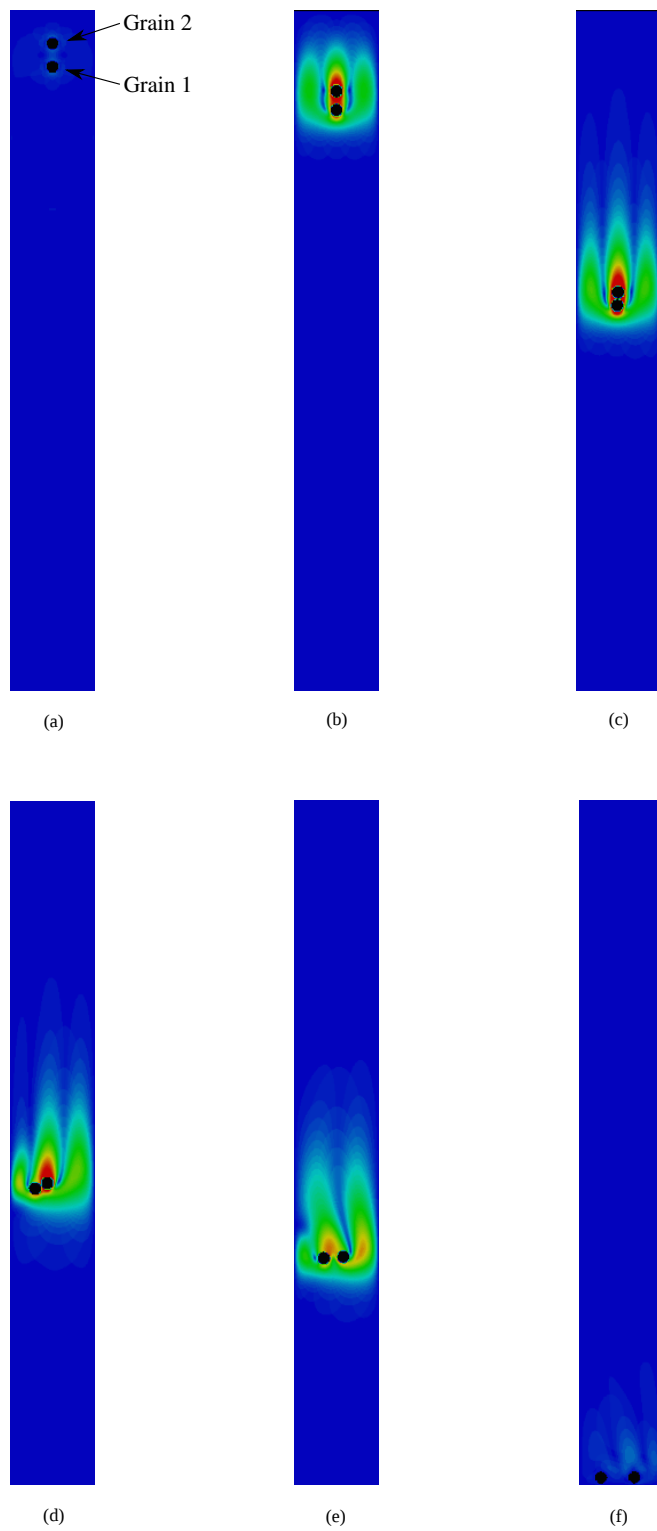


Figure 5.14 Time series of draft, kiss and tumble of two grains during sedimentation in a viscous fluid.

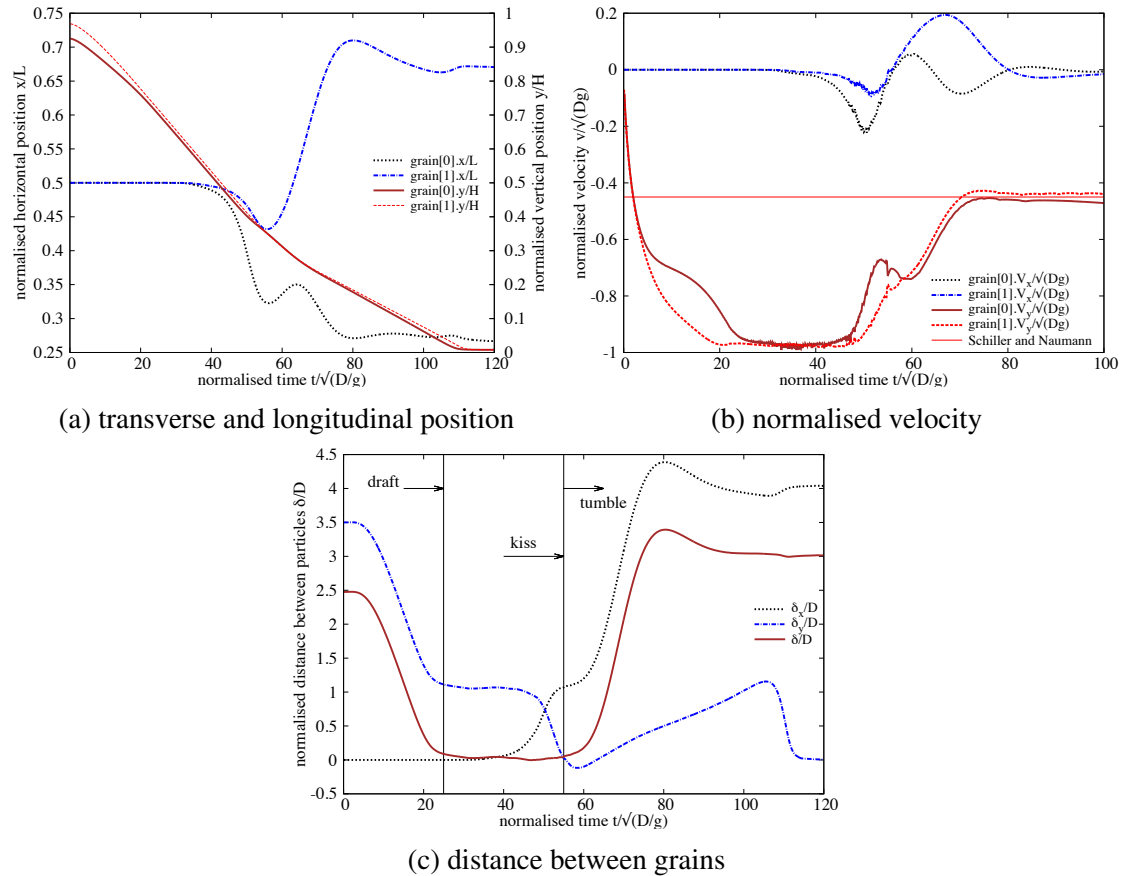


Figure 5.15 Time history of sedimentation of two circular grains.

execution grid layout allows one to increase the occupancy rate. Nevertheless, reaching the maximum occupancy is usually not possible, as the threads executed in parallel on one SM have to share the available registers (Obrecht and Kuznik, 2011).

Many-core processors are promising platforms for intrinsically parallel algorithms such as the lattice Boltzmann method. Since the global memory for GPU devices shows high latency and LBM is data intensive, the memory access pattern is an important issue for achieving good performances. Whenever possible, global memory loads and stores should be coalescent and aligned, but the propagation phase in LBM can lead to frequent misaligned memory accesses. Also, the data transfer between the host and the device is very expensive. In the present study, the LBM implementation follows carefully chosen data transfer schemes in global memory.

There are three ways to accelerate GPGPU applications: (a) Using ‘drop-in’ libraries, (b) using directives by exposing parallelism, and (c) using dedicated GPGPU programming languages. OpenACC (Open Accelerators) is an open GPU directives programming standard for parallel computing on heterogeneous CPU/GPU systems. Unlike conventional GPU programming languages, such as CUDA, OpenACC uses directives to specify parallel regions in the code and performance tuning works on exposing parallelism. OpenACC targets a host-directed execution model where the sequential code runs on a conventional processor and computationally intensive parallel pieces of code (kernels) run on an accelerator such as a GPU (see figure 5.16).

The original GPGPU LBM – DEM code was implemented in C using OpenACC API v1.0, which was released in November 2011. The current implementation in C++ uses OpenACC API v2.0a (OpenACC-Members, 2013) and has two compute constructs, the kernels construct and the parallel construct. LBM – DEM implementation predominantly uses the OpenACC gang and vector parallelism. The LBM – DEM code runs sequential and computationally less intensive functions on the CPU, OpenMP multi-threading is used when possible. Computationally intensive functions are converted to a target accelerator specific GPU parallel code. Schematics of a heterogeneous CPU/GPU system is shown in figure 5.16.

OpenACC offers kernel and parallel constructs to parallelise algorithms on CUDA kernels. The loop nests in a kernel construct are converted by the compiler into parallel kernels that run efficiently on a GPU. There are three steps to this process. The first is to identify the loops that can be executed in parallel. The second is to map that abstract loop parallelism onto a concrete hardware parallelism. In OpenACC terms, gang parallelism maps to grid-level parallelism (equivalent to a CUDA blockIdx), and vector parallelism maps to thread-level parallelism (equivalent to a CUDA threadIdx). The compiler normally maps a single loop

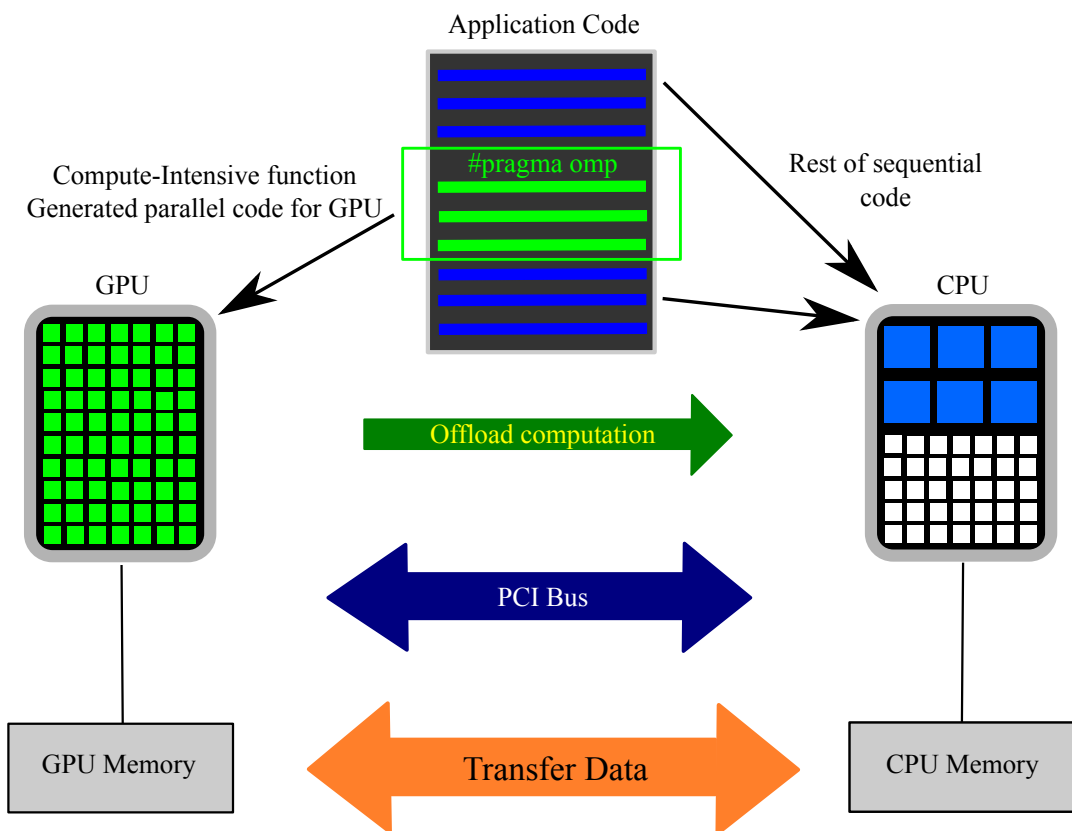


Figure 5.16 Schematics of a heterogeneous CPU/GPU system.

across multiple levels of parallelism using strip-mining. Finally, in step three the compiler generates and optimizes the actual code to implement the selected parallelism mapping.

An OpenACC parallel construct creates a number of parallel threads that immediately begin executing the body of the parallel construct redundantly. When a thread reaches a work-sharing loop, that thread will execute some subset of the loop iterations, depending on the scheduling policy as specified by the program or at the runtime. The code generation and optimization for a parallel construct is essentially the same as for the kernel construct. A key difference is that unlike a kernel construct, the entire parallel construct becomes a single target parallel operation, aka a single CUDA kernel. Both constructs allow for automatic vectorization within the loops (Wolfe, 2012).

An excerpt from the LBM-DEM code showing the OpenACC GPU implementation of the hydrodynamic force computation is presented in Listing 5.1. The kernels loop construct tells the compiler to map the body of the following loop into an accelerator kernel. The GPU implementation uses a two-dimensional grid splitting the iterations across both the vector and gang modes. The kernel is mapped to a vector mode mapped (aligned with CUDA `threadidx%x`) with a vector length (thread block size) of 128. The kernel is also mapped to gang parallelism, aligned to CUDA `blockidx%x`, to avoid partition camping by mapping the stride-1 loop to the x dimension. The compiler strip-mines the loop into chunks of 256 iterations, mapping the 256 iterations of a chunk in vector mode across the threads of a CUDA thread block, and maps the  $n/256$  chunks in gang mode across the thread blocks of the CUDA grid. The consecutive iterations ( $i$  and  $i+1$ ), which refer to contiguous array elements (`fhf[i]` and `fhf[i+1]`), are mapped to adjacent CUDA threads in the same thread block, to optimize for coalesced memory accesses.

Memory transaction optimisation is more important than computation optimisation. Registers do not give rise to any specific problem apart from their limited amount. Global memory, being the only one accessible by both the CPU and the GPU, is the critical path as it suffers from high latency. However, this latency is mostly hidden by the scheduler which stalls inactive warps until data are available. For data intensive LBM, this aspect is generally the limiting factor (Obrecht and Kuznik, 2011). To optimise the global memory transactions, the memory access is coalesced and aligned, as explained above. The memory transactions between the host and the target through a PCI bus are kept to a minimum.

Listing 5.1 OpenACC GPU implementation of the hydrodynamic force computation.

```

1 //OpenACC Kernels copy data between the host and the device
2 #pragma acc kernels
3 copyout(fhf1 [0: nbgrains ], f hf2 [0: nbgrains ], f hf3 [0: nbgrains ])
4 copyin(obst [0:][0:], g [0: nbgrains ], ey [0:], f [0:][0:][0:], ex [0:])
5 //Create individual threads for each DEM grain
6 #pragma acc parallel for
7 for (i=0; i<nbgrains ;i++) {
8     // Reset hydrodynamic forces to zero at the start of time step
9     f hf1 [i]=f hf2 [i]=f hf3 [i ]=0.:
10    // Iterate through all lattice nodes
11    for (y=0; y<l y;y++) {
12        for (x=0; x<l x;x++) {
13            if (obst [x ][y]==i) {
14                // generate code to execute the iterations in parallel with
15                // no synchronization
16                #pragma acc for independent
17                for (iLB=1; iLB<Q; iLB++) {
18                    next_x=x+ex[iLB];
19                    next_y=y+ey[iLB];
20                    if (iLB<=half) halfq=half;
21                    else halfq= -half;
22                    if (obst [next_x ][next_y ]!=i) {
23                        f nx=(f [x ][y ][iLB+halfq]+f [next_x ][next_y ][iLB])*ex[iLB+halfq];
24                        f ny=(f [x ][y ][iLB+halfq]+f [next_x ][next_y ][iLB])*ey[iLB+halfq];
25                        f hf1 [i]=f hf1 [i]+f nx;
26                        f hf2 [i]=f hf2 [i]+f ny;
27                        f hf3 [i]=f hf3 [i]-f nx*(y-(g[i].x2-wall_bottom_y)/dx)
28                            +f ny*(x-(g[i].x1-wall_left_x)/dx);
29                    }
30                }
31            }
32        }
33    }
34 }
```

A two-dimensional fluid – grain system, which consists of 7.2 million LBM nodes and 2500 DEM grains is used to demonstrate the ability of the GPGPU LBM – DEM code. The wall time required to compute 100 iterations of the given LBM – DEM problem is compared for executions running on a single CPU thread, multi-threaded CPU (using OpenMP) and the GPGPU implementations (see table 5.3). The speed-up of parallel implementations are measured against the single CPU thread execution time. OpenMP parallelised multi-threaded CPU execution running on 12 cores achieved a speed-up of 13.5x in comparison to a serial implementation. GPGPU implementation using OpenACC delivered an impressive 126x speed-up in comparison to a single thread CPU execution and about 10 times quicker than a CPU parallel code. In other words, a simulation that would have ordinarily taken 126 days to compute, could now be finished in a day using a GPU.

Table 5.3 GPU vs CPU parallelisation

| Execution             | Computational Time (s) | Speedup |
|-----------------------|------------------------|---------|
| CPU 1 OpenMP thread   | 2016                   | –       |
| CPU 2 OpenMP threads  | 1035                   | 1.5 x   |
| CPU 4 OpenMP threads  | 660                    | 3.0 x   |
| CPU 12 OpenMP threads | 150                    | 13.5 x  |
| GPU OpenACC           | 16                     | 126.0 x |

# Wall time for 100 iteration for 7.2 Million LBM nodes and 2500 DEM grains.

\* CPU OpenMP threads - 6 core Intel Xeon @ 3.3GHz

† GPU threads - GeForce GTX 580 - 512 CUDA cores

Scalability is an important criterion when developing high-performance computing codes. Scalability in GPUs is measured in terms of SM utilisation. It is important to distribute sufficient work to all SMs such that on every cycle the warp scheduler has at least one warp eligible to issue instructions. In general, sufficient warps on each SM should be available to hide instruction and memory latency and to provide a variety of instruction types to fill the execution pipeline. Figure 5.17 shows the scalability of GPGPU implementation as the LBM domain size is increased from 500,000 to 9 million nodes. With increase in LBM nodes the computation time increases linearly with a slope of about 2, which shows that the LBM-DEM implementation algorithm scales with the domain size.

A two-dimensional coupled LBM-DEM technique is developed to understand the local rheology of granular flows in fluid. The coupled LBM-DEM technique offers the possibility to capture the intricate micro-scale effects such as the hydrodynamic instabilities. The Smargonisky turbulence model is implemented in LBM to capture the unsteady flow dynamics in underwater granular avalanches. The GPGPU implementation of the coupled LBM – DEM

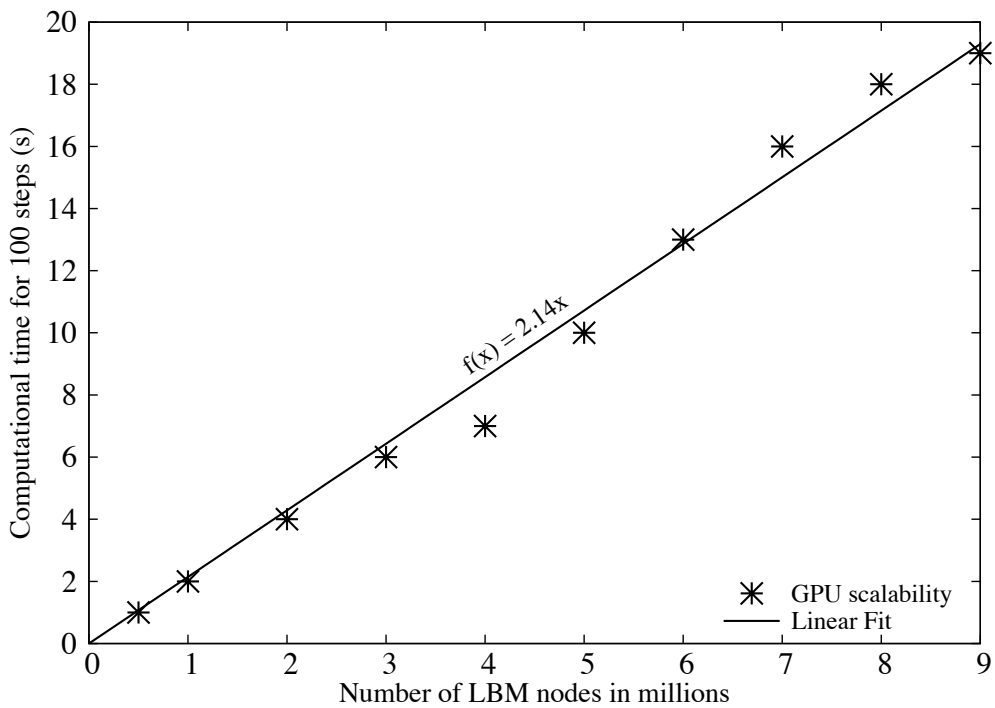


Figure 5.17 GPU scalability with increase in LBM nodes

technique offers the capability to model large scale fluid – grain systems, which are otherwise impossible to model using conventional computation techniques. Efficient data transfer mechanisms that achieve coalesced global memory ensure that the GPGPU implementation scales linearly with the domain size.

# Chapter 6

## Underwater granular flows

### 6.1 Introduction

Avalanches, landslides, and debris flows are geophysical hazards, which involve rapid mass movement of granular solids, water, and air as a single phase system. Globally, landslides cause billions of pounds in damage, and thousands of deaths and injuries each year. Hence, it is important to understand the triggering mechanism and the flow evolution. The momentum transfer between the discrete and the continuous phases significantly affects the dynamics of the flow as a whole (Topin et al., 2012). Although certain macroscopic models are able to capture the simple mechanical behaviours (Peker and Helvacı, 2007), the complex physical mechanisms occurring at the grain scale, such as hydrodynamic instabilities, formation of clusters, collapse, and transport (Topin et al., 2011), have largely been ignored. In particular, when the solid phase reaches a high volume fraction, the strong heterogeneity arising from the contact forces between the grains, and the hydrodynamic forces, are difficult to integrate into the homogenization process involving global averages.

In order to describe the mechanism of immersed granular flows, it is important to consider both the dynamics of the solid phase and the role of the ambient fluid (Denlinger and Iverson, 2001). The dynamics of the solid phase alone are insufficient to describe the mechanism of granular flows in fluid. It is important to consider the effect of hydrodynamic forces that reduce the weight of the solids inducing a transition from dense-compacted to dense-suspended flows, and the drag interactions which counteract the movement of the solids (Meruane et al., 2010). Transient regimes characterized by a change in the solid fraction, dilation at the onset of flow and the development of excess pore-pressure, result in altering the balance between the stress carried by the fluid and that carried by the grains, thereby changing the overall behaviour of the flow.

The presence of a fluid phase in a granular medium has profound effects on its mechanical behaviour. In dry granular media, the rheology is governed by grain inertia and static stresses sustained by the contact network depending on the shear-rate and the confining pressure, respectively (Midi, 2004). As the fluid inertia and viscosity come into play, complications arise as a result of contradictory effects. On one hand, the fluid may delay the onset of granular flow or prevent the dispersion of the grains by developing negative pore-pressure (Pailha et al., 2008; Topin et al., 2011). On the other hand, the fluid lubricates the contacts between grains, enhancing the rate of granular flow, but it has a retarding effect at the same time by inducing drag forces on the grains. The objective of the present study is to understand the differences in the mechanism of flow initiation and kinematics between dry and submerged granular flows. In the present study, a coupled 2D Lattice-Boltzmann and Discrete Element Method is used to model the fluid-soil interactions in underwater granular flows. The 2D geometry does not take into account the movement of grains perpendicular to the plane. Also, due to the 2D nature of the geometry fluid flows and fluid-solid interactions in the direction perpendicular to the plane are not considered. However, the movement of fluid in the plane normal to the direction of flow is minimal and the choice of 2D geometry is justified. LBM - DEM approach is computationally expensive as it models the fluid - solid interaction at a scale that is orders of magnitude smaller than the grain size. It is important to consider the representative volume element that is large enough to capture the granular flow dynamics in fluid. The 2D geometry has the advantage of cheaper computational effort than a 3D case, making it feasible to simulate very large systems. The configuration and parameters studied in this chapter are presented in table 6.1.

## 6.2 LBM-DEM permeability

In a 3D granular assembly, the pore spaces between the grains are interconnected, whereas in a 2-D assembly, a non-interconnected pore-fluid space is formed as the grains are in contact with each other. This means that the fluid enclosed between the grains cannot flow to the neighbouring pore-spaces. This results in an unnatural no flow condition in a 2-D case (figure 6.1). In order to overcome this effect, a reduction in radius is assumed only during the LBM computation (fluid and fluid – solid interaction) steps. The reduced radius of the soil grain, i.e., the *hydrodynamic radius*  $r$ , allows for interconnected pore space through which the pore-fluid can flow similar to the 3D behaviour. The reduction in the radius is assumed only during LBM computations, hence this technique has no effect on the grain – grain interactions computed using DEM.

Table 6.1 Configurations for LBM-DEM simulations of granular collapse in fluid

| Simulations                             | Aspect ratio | Hydrodynamic radius                    | Packing density (%) | Slope angle (°) |
|---|--------------|--|---------------------|-----------------|
| <b>Collapse on a horizontal surface</b> |              |  |                     |                 |
| Effect of initial aspect ratio          | 0.2 - 6      | r = 0.7 R                              | 83                  | 0               |
| Effect of permeability                  | 0.2 - 6      | r = 0.7, 0.75, 0.8, 0.85, 0.9 & 0.95 R | 83                  | 0               |
| Effect of initial density               | 0.8          | r = 0.7, 0.75, 0.8, 0.85, 0.9 & 0.95 R | 79 & 83             | 0               |
| <b>Collapse on an inclined plane</b>    |              |  |                     |                 |
| Effect of initial density               | 0.8          | r = 0.9 R                              | 79 & 83             | 0, 2.5, 5 & 7.5 |
| Effect of permeability                  | 0.8          | r = 0.7, 0.75, 0.8, 0.85 & 0.9 R       | 79 & 83             | 0 & 5           |
| Tall columns                            | 6            | r = 0.85 R                             | 79 & 83             | 0, 2.5, 5 & 7.5 |

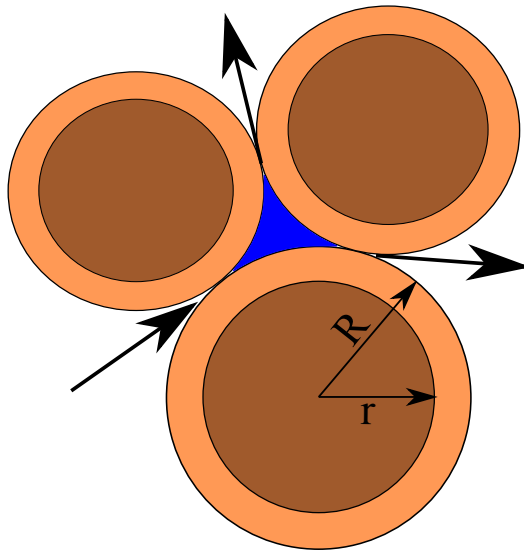


Figure 6.1 Schematic representation of the hydrodynamic radius in LBM-DEM computation.

Realistically, the hydrodynamic radius can be varied from  $r = 0.7R$  to  $0.95R$ , where  $R$  is the grain radius. Different permeabilities can be obtained for any given initial packing by varying the hydrodynamic radius of the grains, without having to change the actual granular packing. This introduces a new parameter into the system. In a physical sense, a hydrodynamic radius represents the three-dimensional permeability of a granular assembly simulated as a two-dimensional geometry. The hydrodynamic radius can also be assumed to represent the irregularities on the granular surface. The hydrodynamic radius represents asperities on the grain surface, which represents a channel for the fluid to flow between the grains.

In order to understand the relation between the hydrodynamic radius and the permeability of the granular assembly, horizontal permeability tests are performed by varying the hydrodynamic radius as  $0.7 R$ ,  $0.75 R$ ,  $0.8 R$ ,  $0.85 R$ ,  $0.9 R$  and  $0.95 R$ . A square sample of  $50 \text{ mm} \times 50 \text{ mm}$  filled with poly-disperse ( $d_{\max}/d_{\min} = 1.8$ ) grains having a mean diameter of  $1.7 \text{ mm}$  is used to determine the relation between the hydrodynamic radius and the permeability. Dirichlet boundary condition (discussed in section 5.1.3), i.e., density constraint, is applied along the left and the right boundaries of the sample. The fluid density on the left boundary is increased in small steps ( $10^{-4} \Delta P$ ), while a constant density is maintained on the right boundary. This results in a pressure gradient (figure 6.2a) causing the fluid to flow through the pore-space. Figure 6.2b show the horizontal velocity of flow through the interconnected pore-space.

For a given hydrodynamic radius, the pressure gradient  $\Delta P$  is varied to obtain different flow rates. Probing the fluid space showed a Poiseuille flow behaviour between the grains.

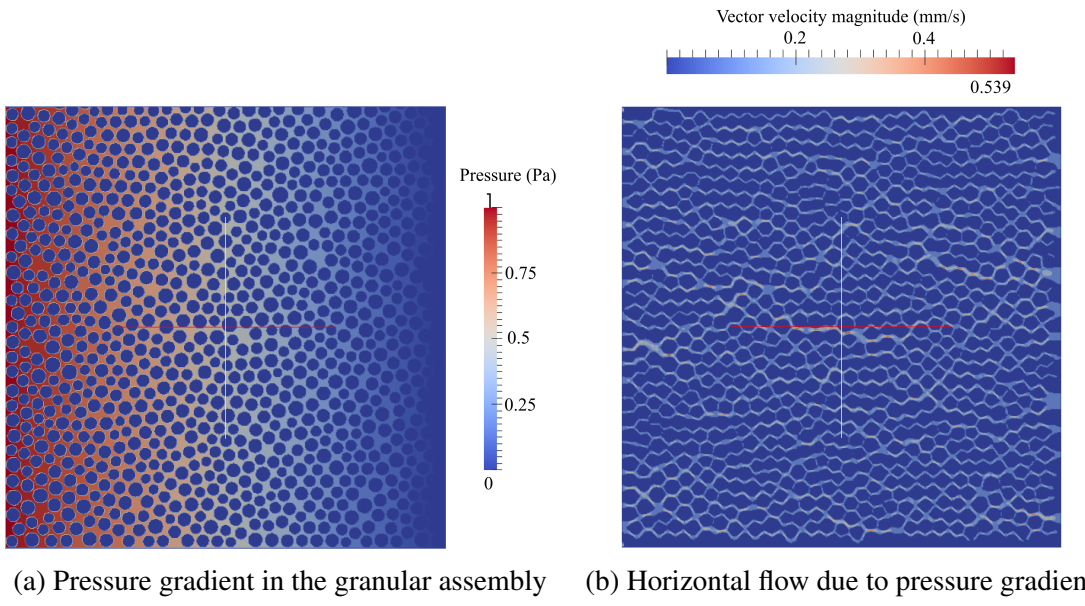


Figure 6.2 Evaluation of the horizontal permeability for a hydrodynamic radius of 0.7 R.

The flow is still within the Darcy's laminar flow regime. Figure 6.3 shows the linear relationship between the applied mean pressure to the mean horizontal flow velocity for different hydrodynamic radii, this proves that the flow is laminar. From the mean flow velocity ( $v$ ), the transverse permeability ( $k$ ) of the sample is computed as

$$k = v \cdot \mu \cdot \frac{\Delta x}{\Delta P}, \quad (6.1)$$

where  $\mu$  is the dynamic viscosity of the fluid (Pa s),  $\Delta x$  is the thickness of the bed of porous medium m, and  $\Delta P$  is the applied pressure difference Pa. It can be observed that with increase in the hydrodynamic radius the permeability decreases, i.e., the slope of the mean flow velocity to the pressure gradient decreases. At very low pressure gradients ( $\Delta P \leq 0.1$ ), both 0.9 R and 0.95 R have no flow. Even at higher pressure gradients, a hydrodynamic radius of  $r = 0.95R$  shows almost no flow behaviour. A high value of hydrodynamic radius  $r > 0.95R$  results in unnatural flow/no-flow behaviour. Hence in the present study, a hydrodynamic radius in the range of 0.7 to 0.95 R is adopted.

Increase in the hydrodynamic radius from 0.7 to 0.95 reduces the quasi-porosity from 0.60 to 0.27. The permeability computed from LB – DEM method is verified by comparing it with the analytical solution. One of the widely used analytical solution for permeability is the Carman – Kozeny equation (CK Model), which is based on the Poiseuille's flow through a pipe and is mainly used for 3D, homogeneous, isotropic, granular porous media at moderate porosities. In the present study, a modified Carman – Kozeny equation that takes

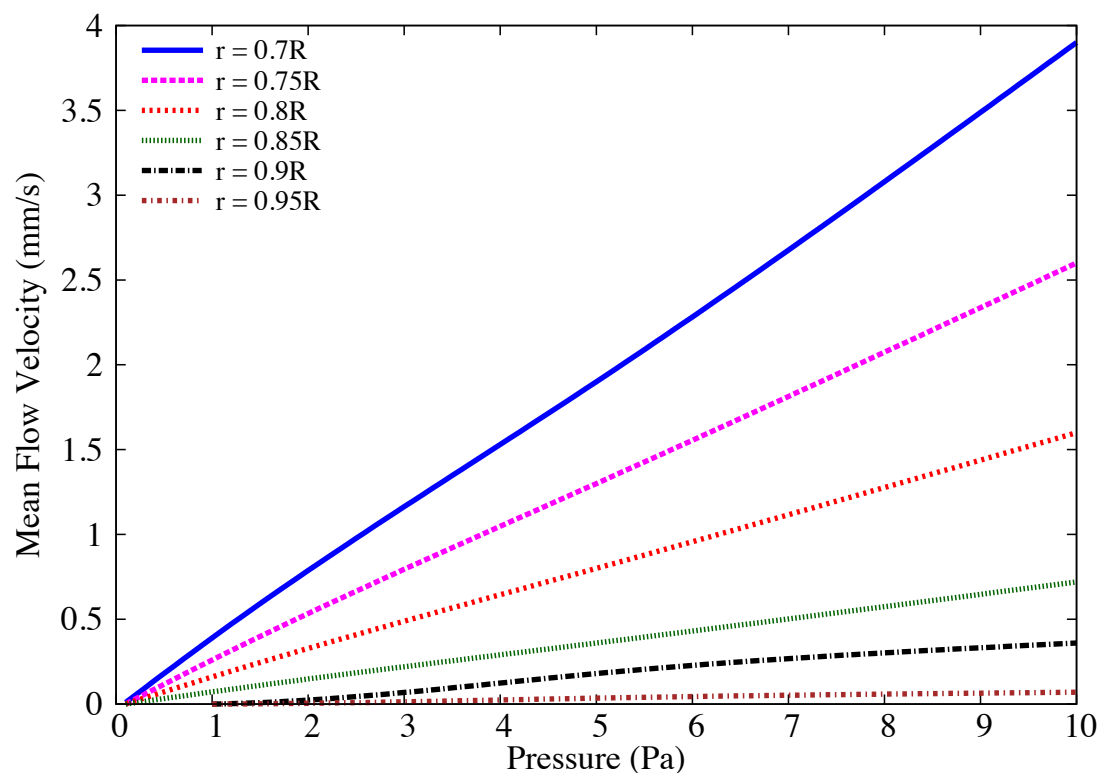


Figure 6.3 Variation of the mean flow velocity with pressure gradient for different hydrodynamic radius.

into account of the micro-structure of the fibres and that is valid in a wide range of porosities is adopted (Yazdchi et al., 2011). The normalized permeability is defined as

$$\frac{k}{d^2} = \frac{\varepsilon}{\psi_{CK}(1-\varepsilon)^2}. \quad (6.2)$$

In the CK model, the hydraulic diameter  $D_h$ , is expressed as a function of measurable quantities: porosity and specific surface area

$$D_h = \frac{4\varepsilon V}{S_v} = \frac{\varepsilon d}{(1-\varepsilon)}, \quad (6.3)$$

$$a_v = \frac{\text{grain surface}}{\text{grain volume}} = \frac{S_v}{(1-\varepsilon)V} = \frac{4}{d}, \quad (6.4)$$

where  $S_v$  is the total wetted surface, and  $a_v$  is the specific surface area. The above value of  $a_v$  is for circles (cylinders) - for spheres  $a_v = 6/d$ .  $\psi_{CK}$  is the empirically measured CK factor, which represents both the shape factor and the deviation of flow direction from that in a duct. It is approximated for randomly packed beds of spherical grains. The variation of normalized permeability with porosity, obtained by varying the radius from 0.7 R to 0.95 R, is presented in figure 6.4. The permeability values obtained from LBM - DEM simulations are found to match the qualitative trend of the Carman-Kozeny equation. The LB - DEM permeability curve lies between the permeability curves for spherical and cylindrical grain arrangements implying a better simulation of three-dimensional permeability using a 2D granular assembly. Thus using a hydrodynamic radius, realistic 3D fluid - grain interactions can be simulated in a 2D geometry.

### 6.3 Granular collapse in fluid

The collapse of a granular column, which mimics the collapse of a cliff, has been extensively studied in the case of dry granular material, when the interstitial fluid plays no role (section 4.2). The problem of the granular collapse in a liquid, which is of importance for submarine landslides, has attracted less attention (Rondon et al., 2011). Thompson and Hupper (2007) observed that the presence of liquid dramatically changes the way a granular column collapses compared to the dry case. The destabilization of a granular pile strongly depends on the initial volume fraction. For dense packings the granular flow is localized at the free surface of the pile, whereas for loose packings the destabilization occurs in the bulk of the material and has a parabolic profile (Bonnet et al., 2010; Iverson, 2000; Topin et al., 2011).

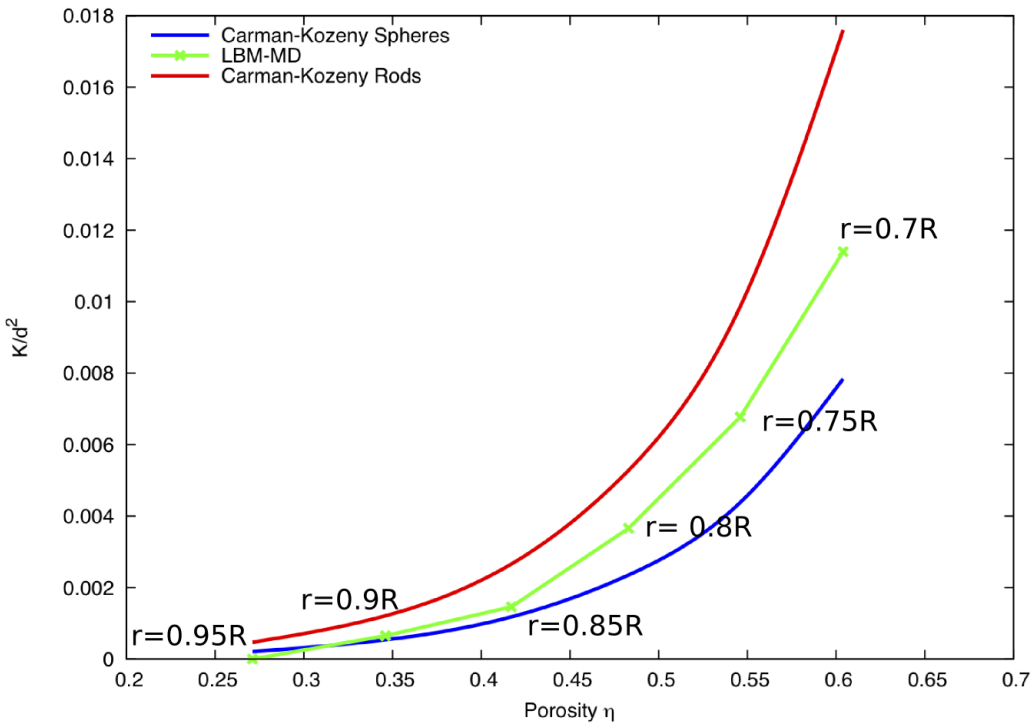
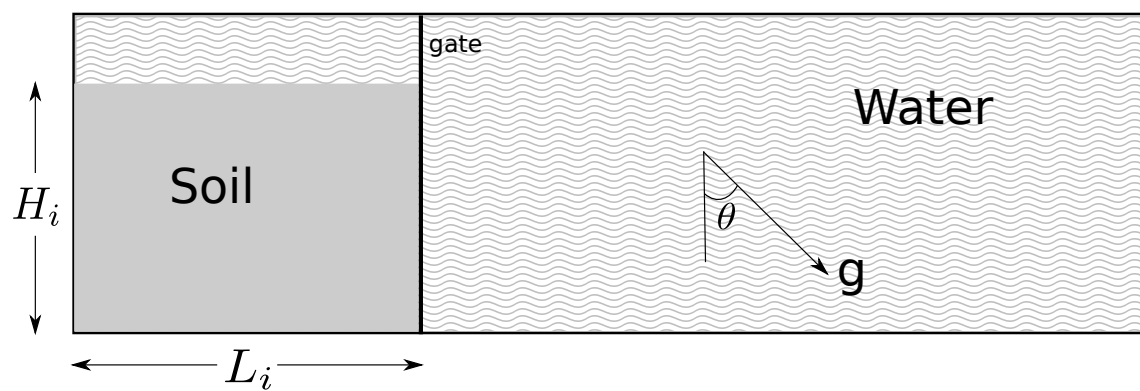


Figure 6.4 Relation between permeability and porosity for different hydrodynamic radius and comparison with the analytical solution.

### 6.3.1 LBM-DEM set-up

In the present study, the collapse of a granular column in fluid is studied using 2D LBM - DEM. The effect of initial aspect ratio on the run-out behaviour is investigated. The flow kinematics are compared with the dry and buoyant granular collapse to understand the influence of hydrodynamic forces and lubrication on the run-out. Unlike dry column, the permeability and the initial volume fraction are expected to have a significant influence on the flow dynamics. Hence the effect of these parameters on the run-out behaviour is investigated.

The granular column collapse set-up in fluid is very similar to the dry granular column collapse. A rectangular channel of length  $L_0$  and height  $H_0$  is filled with poly-dispersed discs,  $d_{max}/d_{min} = 1.8$  (figure 6.5a). Once the DEM soil grains reach equilibrium in the dry condition, the granular sample is then placed in the fluid domain simulated using LBM. The LBM-DEM set-up of a granular column with an aspect ratio  $a$  of 6 in fluid is shown in figure 6.5b. The fluid has a density of  $1000 \text{ kg/m}^3$  and a kinematic viscosity of  $1 \times 10^{-6} \text{ m}^2/\text{s}$ . The gate supporting the right-hand side boundary of the granular column is opened allowing the column to collapse and flow in a fluid. The final run-out distance is measured as  $L_f$  and final collapse height as  $H_f$ . The collapse takes place on a horizontal surface. The initial aspect ratio of the column is varied as 0.2, 0.4, 0.6, 0.8, 1, 2, 4 and 6.



(a) Schematic view of underwater granular collapse set-up.

(b) LBM-DEM simulation of underwater granular collapse set-up ( $a = 6$ ).

Figure 6.5 Underwater granular collapse set-up.

The cumulative  $\beta$  distribution is adopted to generate grains with  $d_{max}$  and  $d_{min}$  as 2.2 mm and 1.25 mm, respectively. The soil column is modelled using  $\sim 2000$  discs of density  $2650 \text{ kg/m}^3$  and a contact friction angle of  $26^\circ$ . A linear-elastic contact model is used in the DEM simulations. The granular assembly has a packing fraction of 83%. The critical time step for DEM is computed based on the local contact natural frequency and damping ratio. A sub-cycling time integration is adopted in DEM (section 5.4). A fluid flow (LBM) time step of  $\Delta t = 2.0 \times 10^{-5} \text{ s}$  is determined based on the viscosity and the relaxation parameter  $\tau = 0.506$ . An integer ratio  $n_s$ , between the fluid flow time step  $\Delta t$  and the DEM time step  $\Delta t_D$  is determined as 15, i.e., every LBM iteration involves a sub-cycle of 15 DEM iterations.

In order to capture the realistic physical behaviour of the fluid – grain systems, it is essential to model the boundary condition between the fluid and the grain as a non-slip boundary condition, i.e. the fluid near the grain should have similar velocity as the grain boundary. The solid grains inside the fluid are represented by lattice nodes. The discrete nature of the lattice results in a stepwise representation of the surfaces (figure 6.6), which are otherwise circular, hence sufficiently small lattice spacing  $h$  is required. The smallest DEM grain in the system controls the size of the lattice. In the present study, a very fine discretisation of  $d_{min}/h = 10$  is adopted, i.e., the smallest grain with a diameter  $d_{min}$  in the system is discretised into 100 lattice nodes ( $10h \times 10h$ ). This provides a very accurate representation of the interaction between the solid and the fluid nodes. A hydrodynamic radius of 0.7 R is adopted during the LBM computations. The fluid pressure on the top and right boundaries are maintained constant. Hence, any pressure wave that is generated during the collapse is absorbed in the boundary. Frictional boundary constraint is applied along the bottom boundary.

### 6.3.2 Collapse in fluid: Flow evolution

Two-dimensional plane-strain LBM-DEM simulations of granular column collapse are performed by varying the initial aspect ratio of the column from 0.2 to 6. The normalized final run-out distance is measured as  $\Delta L = (L_f - L_0)/L_0$ . Similar to the dry granular collapse, the duration of collapse is normalised with a critical time  $\tau_c = \sqrt{H/g}$ , where  $H$  is the initial height of the granular column and  $g$  is the acceleration due to gravity. Dry and buoyant analyses of granular column collapse are also performed to understand the effect of hydrodynamic forces on the run-out distance.

Snapshots of the flow evolution of a granular column collapse with an initial aspect ratio of 0.4 are shown in figure 6.7. The failure begins at the toe end of the column, and the shear-failure surface propagates into the column at an angle of about  $50^\circ$ , similar to the dry column collapse. For the short column, the failure is due to collapse of the flank. Once the

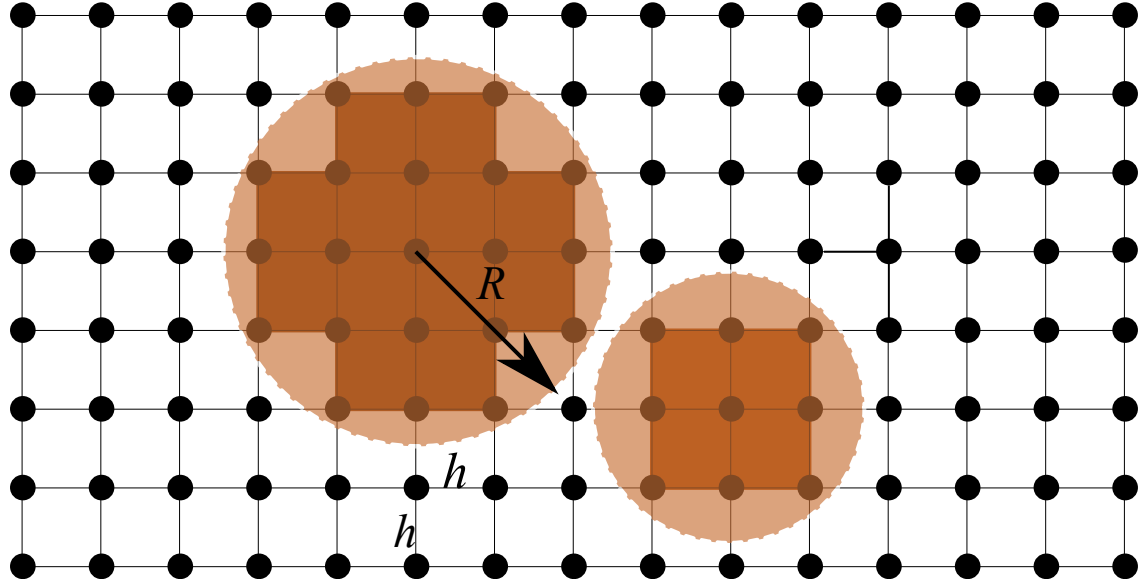


Figure 6.6 Discretisation of solid grains in LBM grid. Shows the step-wise representation of circular disks in the lattice.

material is destabilised, the granular mass interacts with the surrounding fluid resulting in formation of turbulent vortices. These vortices interact with the grains at the surface resulting in an irregular free surface. Force chains can be observed in the static region of collapse, which indicates the granular flow in fluid can still be described using continuum theories. As the granular material ceases to flow, force chains develop at the flow front, revealing consolidation of the granular mass resulting in an increase in the shear strength.

The evolution of normalised run-out  $(L_f - L_0)/L_0$  with normalised time  $t/\tau_c$  for a short column ( $a = 0.4$ ) in dry and submerged conditions is presented in figure 6.8a. The dry column exhibits longer run-out distance in comparison to the submerged column. The collapse of a dry column using DEM represents a collapse in a vacuum, without any influence of drag forces or viscosity of air. A LBM-DEM simulation of a granular column collapse using the kinematic viscosity of air is performed to compare the dry column with the collapse in air. Although the effect of viscous drag can be observed in the collapse in the air, both the “dry” condition and the collapse in air show almost the same run-out behaviour. However, the collapse in fluid (water) results in a much shorter run-out distance. The granular mass in fluid has the buoyant mass, in contrast to the dry density. A dry granular collapse with the buoyant unit weight also exhibits longer run-out behaviour than the collapse in fluid. However, due to decrease in the initial potential energy, the run-out observed in the buoyant condition is shorter than the dry condition. The column collapse in fluid takes longer to evolve, which might be due to the development of large negative pore water pressure that is generated

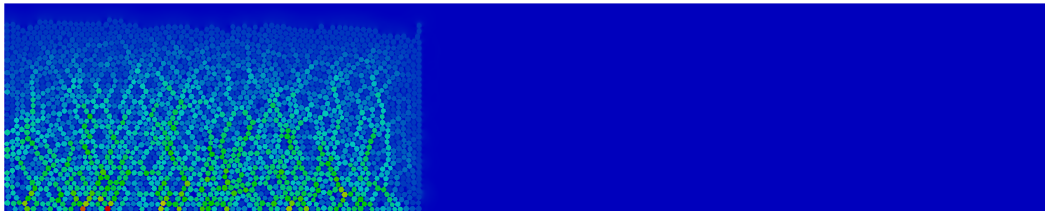
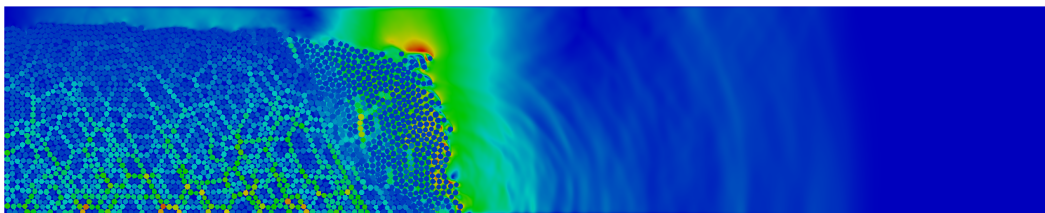
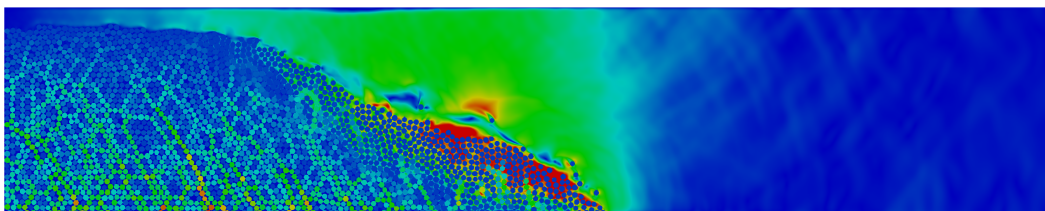
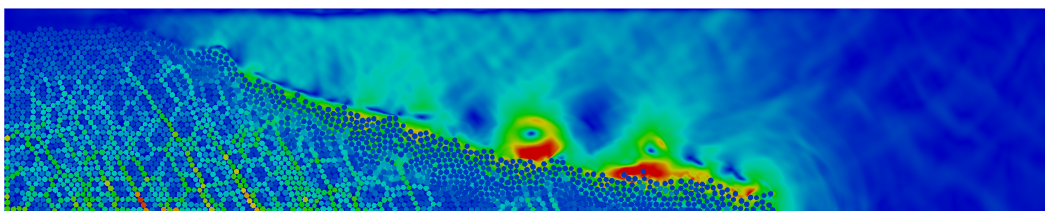
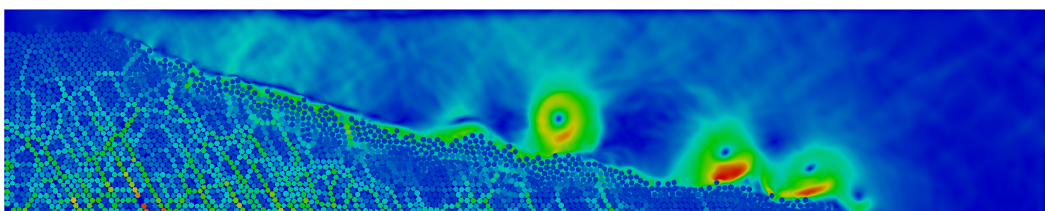
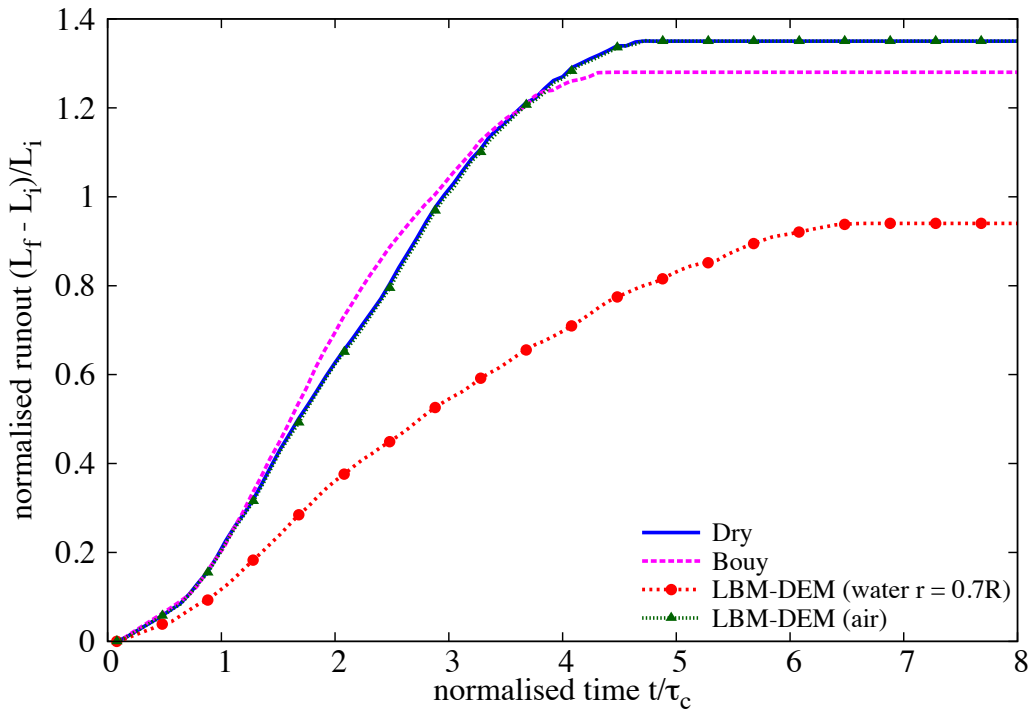
(a)  $t = 0\tau_c$ (b)  $t = 1\tau_c$ (c)  $t = 3\tau_c$ (d)  $t = 6\tau_c$ (e)  $t = 8\tau_c$ 

Figure 6.7 Flow evolution of a granular column collapse in fluid ( $a = 0.4$ ). Shows the velocity profile of fluid due to interaction with the grains (red - higher velocity).

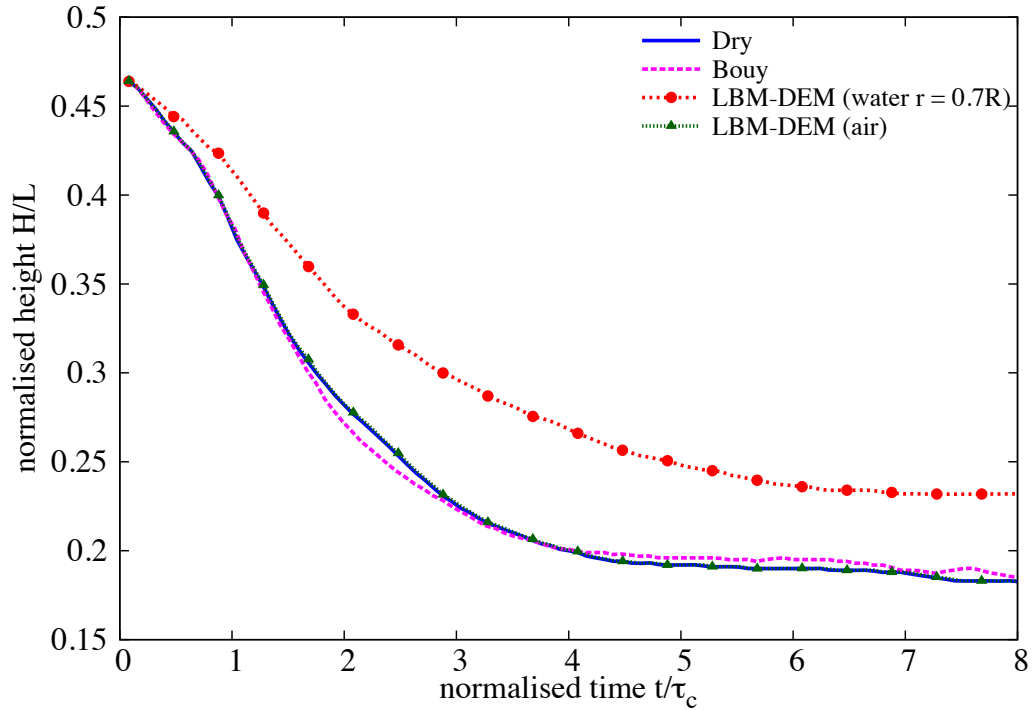
during the shear failure along the shear-failure surface. This large negative pore-pressure has to be dissipated before the granular mass, above the shear-failure surface, can collapse and flow. The shorter run-out distance in the fluid case, in comparison with the dry and buoyant conditions, shows that the collapse in fluid is significantly affected by the hydrodynamic drag forces acting on the soil grains. The evolution of normalised height  $H/L$  with time under dry and submerged conditions is presented in figure 6.8b. Since the failure of the column is only at the flank, the central static region remains unaffected. Hence, the final height of the column is the same in dry and submerged conditions.

The evolution of the normalised kinetic energy  $E_k/E_{p0}$  with time under dry and submerged conditions for a column with an initial aspect ratio of 0.4 is shown in figure 6.9. It can be observed that the peak kinetic energy is attained later in the submerged condition than the dry collapse. This can be attributed to the time required to overcome the negative pore-pressure generated during the shear along the shear-failure surface. For short columns the critical time  $\tau_c$  is controlled by the vertical kinetic energy. The amount of kinetic energy in submerged case is significantly lower than the dry condition. Also, the evolution of the normalised potential energy  $E_p/E_{p0}$  with time under dry and submerged conditions is presented in figure 6.10. The potential energy drops faster in dry and buoyant conditions in comparison to submerged condition. This shows a significant influence of the hydrodynamic forces on the amount of material destabilised during the collapse. The drag forces on the soil grains reduce and slow down the amount of material that undergo collapse resulting in a shorter run-out distance for the collapse of short columns in fluid.

Snapshots of the flow evolution of a granular column collapse with an initial aspect ratio of 4 is shown in figure 6.11. For a tall column, the collapse mechanism changes. The entire column is involved in the collapse. The height of the static region, which is below the shear-failure surface, is shorter than the total height of the column. This results in a free-fall of grains above the shear-failure surface. As the grains experience free-fall they interact with the surrounding fluid. However, no vortices are observed during the initial stage of collapse. In the second phase, when the grains reach the base, the vertical acceleration gained during the free-fall is converted into horizontal velocity. As the grains are ejected horizontally, the free surface of the granular mass interacts with the fluid resulting in the formation of turbulent vortices. Unlike short columns, these vortices have significant influence on the mass distribution along the run-out. Heaps of granular material can be observed in front of each vortex. The number of vortices formed during a collapse is found to be proportional to the amount of material destabilised, i.e., the length of free-surface interacting with the fluid influences the number of vortices generated during the collapse. The reappearance of force

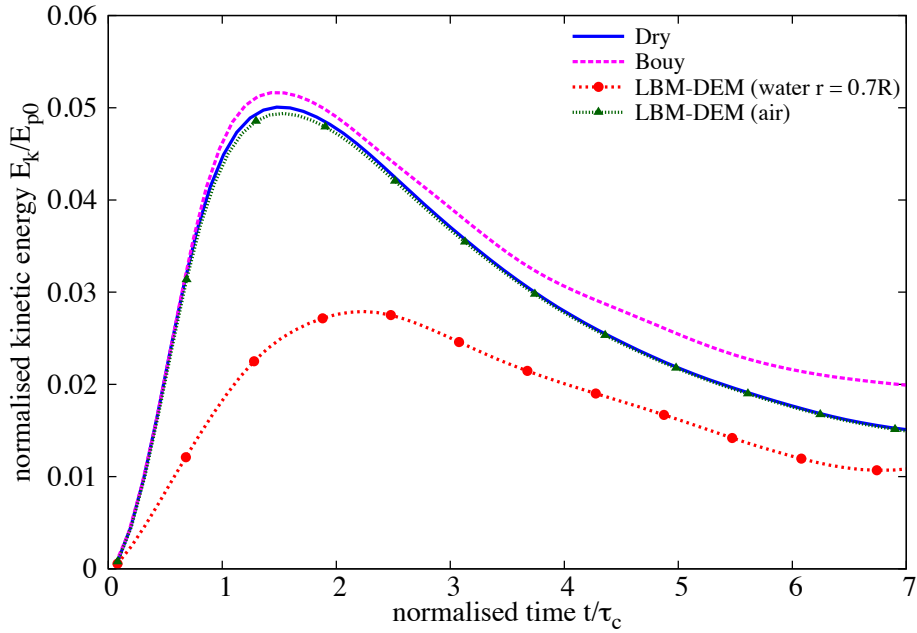


(a) Evolution of run-out with time

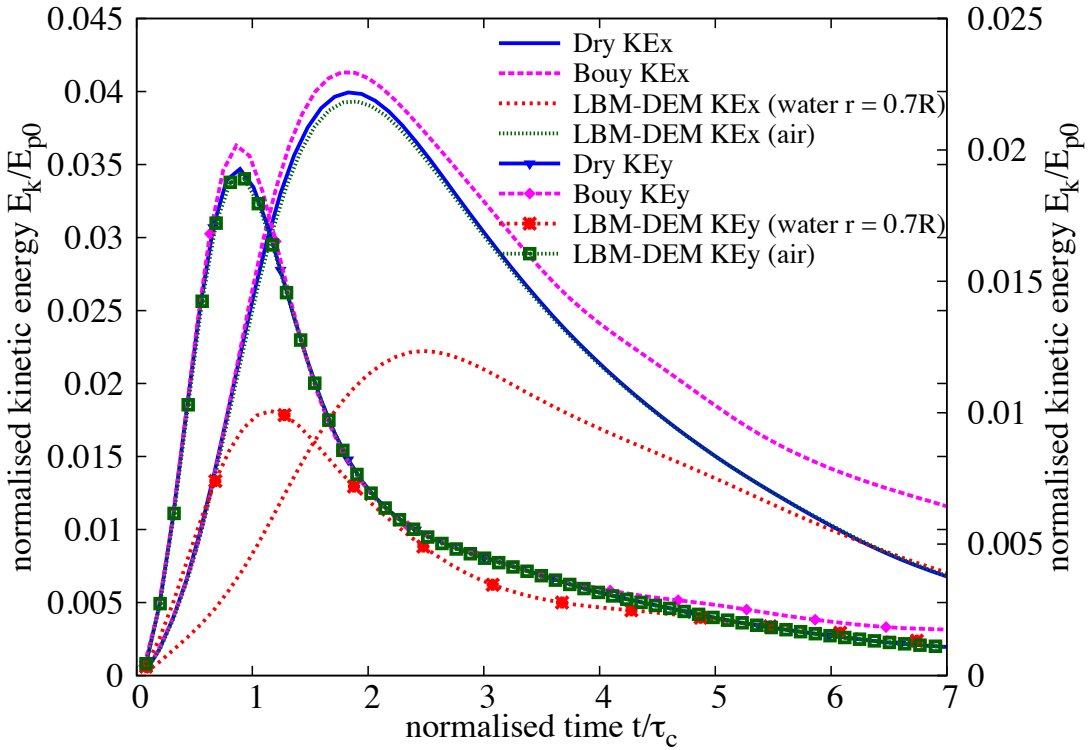


(b) Evolution of height with time

Figure 6.8 Evolution of height and run-out with time for a column collapse in fluid ( $a = 0.4$ ).



(a) Evolution of the total kinetic energy.



(b) Evolution of horizontal and vertical kinetic energies.

Figure 6.9 Evolution of kinetic energies with time for a granular column collapse in fluid ( $a = 0.4$ )

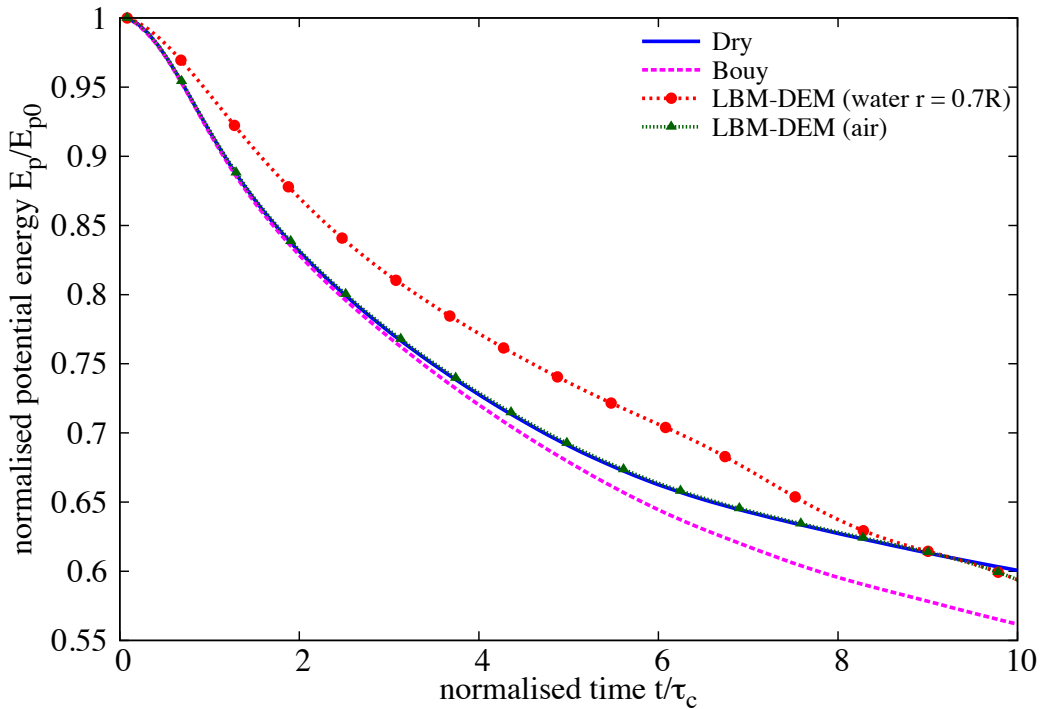
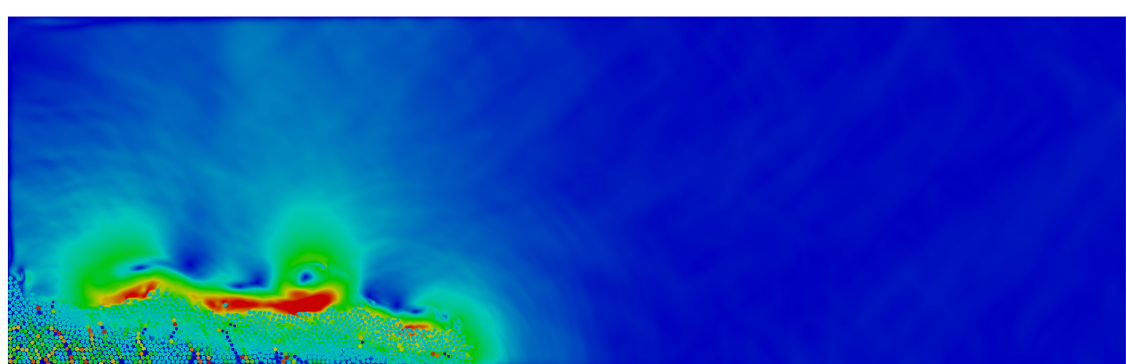


Figure 6.10 Evolution of the potential energy with time for a granular column collapse in fluid ( $a = 0.4$ )

chains at  $t = 6\tau_c$  and  $8\tau_c$  indicates the granular mass is consolidating resulting in an increase in the shear strength.

The time evolution of the run-out and the height of a tall column ( $a = 4$ ) is presented in figure 6.12a and figure 6.12b, respectively. Similar to the short column, the run-out observed in the dry condition is much longer than that observed in the submerged condition. Also, the evolution of run-out is slower in the case of submerged condition, which indicates the influence of drag force on the run-out evolution. Figures 6.12b and 6.13 shows the evolution of normalised height and potential energy with time. The submerged column collapse at a slower rate than its dry counterpart. The hydrodynamic forces in fluid causes an increase in the drag force thus reducing the amount of material destabilised during the collapse.

The evolution of kinetic energies with time for an initial aspect ratio 4 is presented in figure 6.14. Even during the free-fall stage, the peak vertical kinetic energy is delayed in the case of fluid, which shows the influence of viscosity on the flow evolution. Almost half of the kinetic energy that is available in the case of dry granular collapse is dissipated through the drag forces experienced by the grains. This shows that the influence of viscous drag on the run-out evolution is significantly higher than the effect of lubrication.

 $t = 0\tau_c$  $t = 1\tau_c$  $t = 3\tau_c$

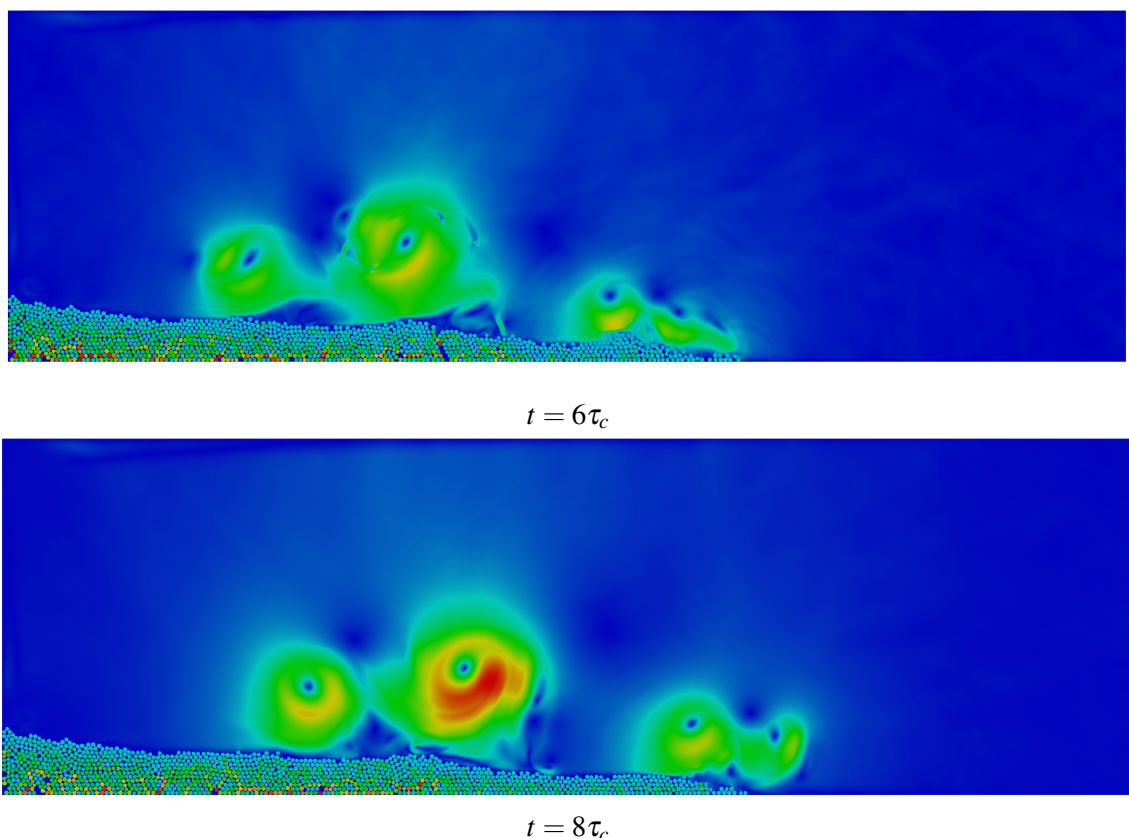


Figure 6.11 Flow evolution of a granular column collapse in fluid ( $a = 4$ ). Shows the velocity profile of fluid due to interaction with the grains (red - higher velocity).

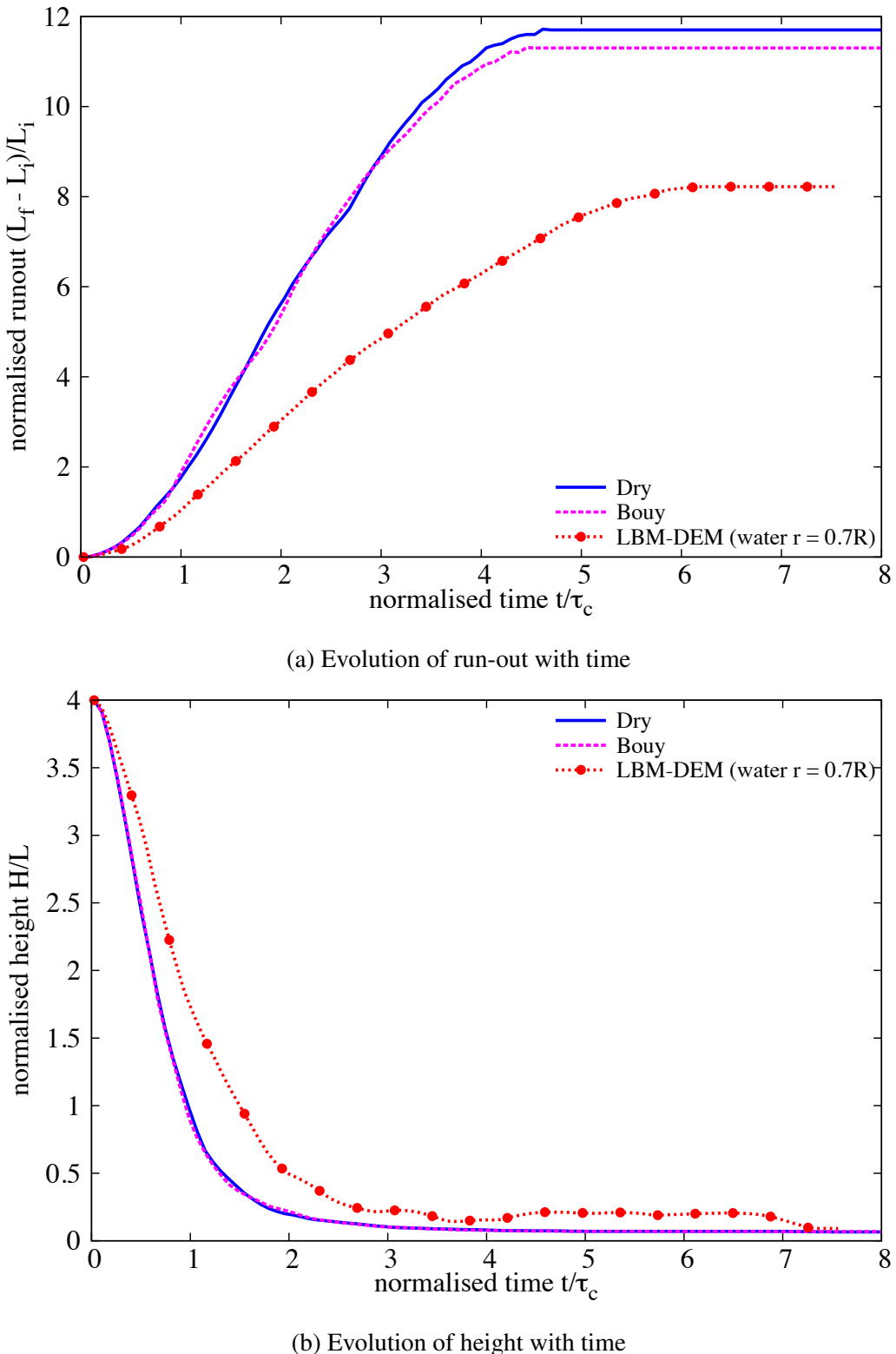


Figure 6.12 Evolution of run-out and height with time for a column collapse in fluid ( $a = 4$ )

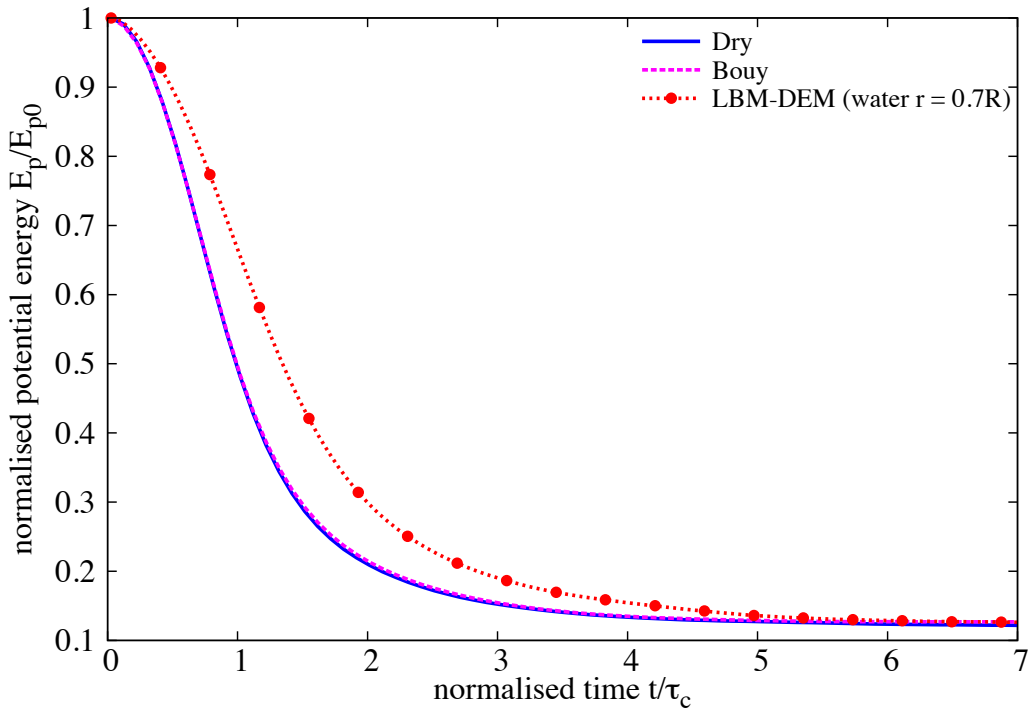


Figure 6.13 Evolution of the potential energy with time for a granular column collapse in fluid ( $a = 4$ )

The normalised final run-out distance as a function of the initial aspect ratio of the column under dry and submerged conditions is presented in figure 6.15a. For all aspect ratios, the run-out observed in the dry case is significantly higher than the submerged condition. For short columns, the run-out distance is found to have a linear relationship with the initial aspect ratio of the column. A power law relation is observed between the run-out and the initial aspect ratio of the column.

$$\frac{L_f - L_0}{L_0} \propto \begin{cases} a, & a \lesssim 2.7 \\ a^{2/3}, & a \gtrsim 2.7 \end{cases} \quad (6.5)$$

The normalised final height as a function of the initial aspect ratio of the column under dry and submerged conditions is presented in figure 6.15b. It can be observed that the final collapse height is much higher in the submerged condition than the dry collapse. The drag force on the granular column reduces the amount of granular mass participating in the collapse, resulting in a shorter run-out distance. The drag force seems to have a predominant influence on the run-out behaviour than the lubrication effect in fluid.

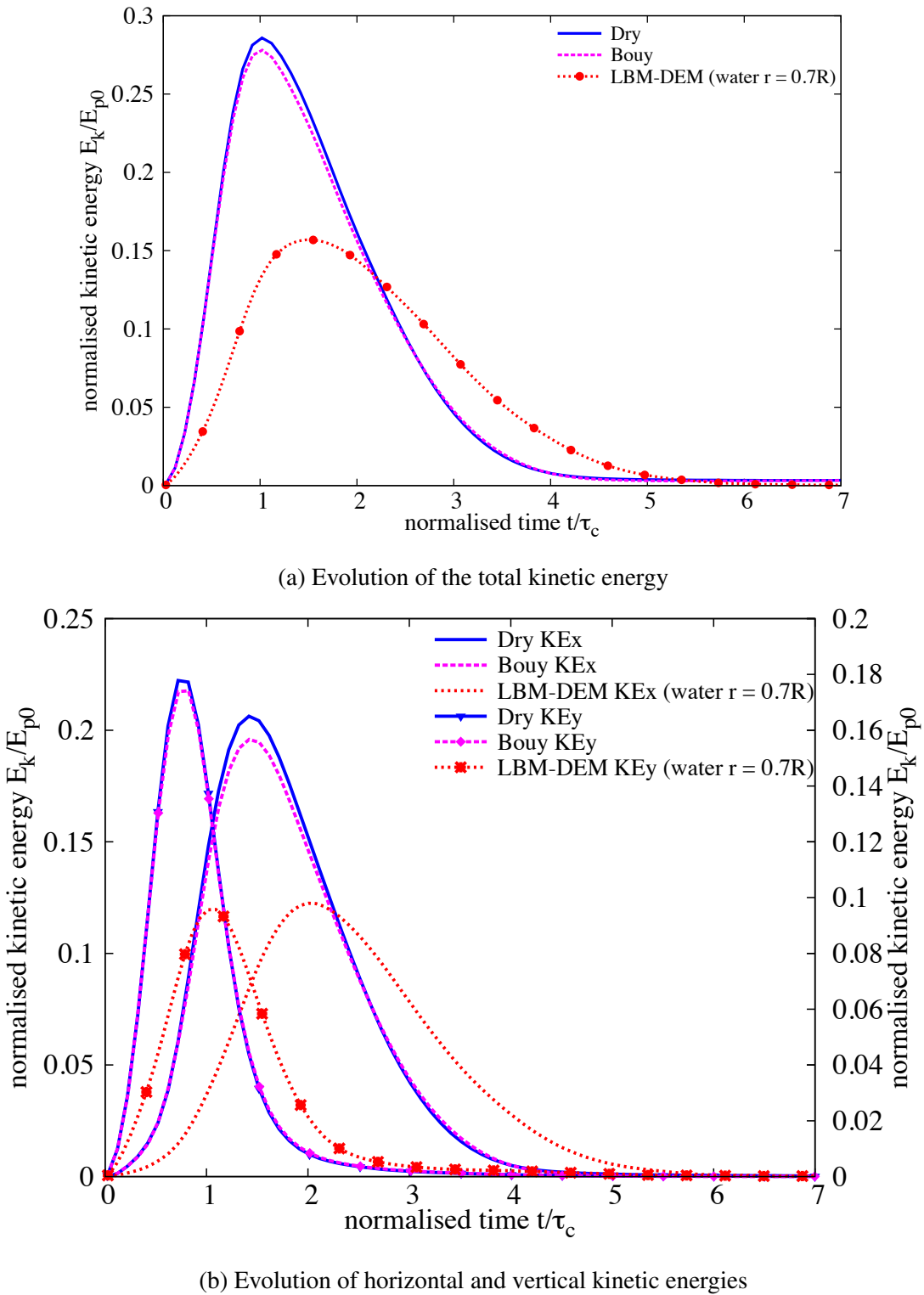
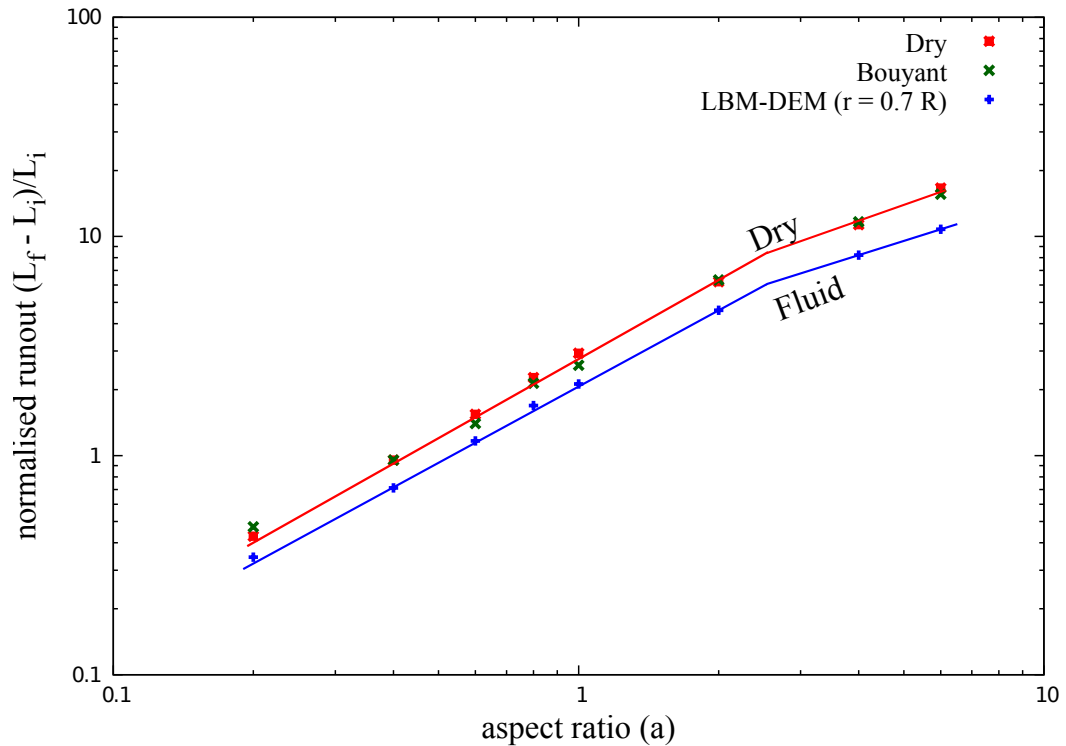
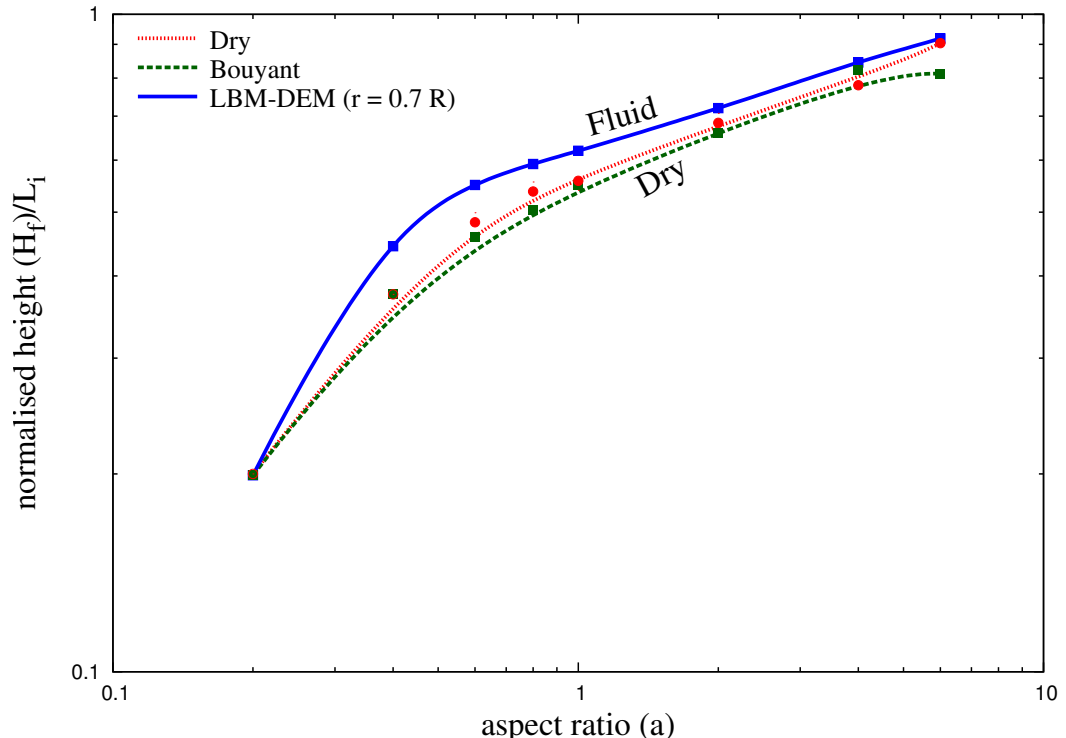


Figure 6.14 Evolution of kinetic energies with time for a granular column collapse in fluid ( $a = 4$ )



(a) Normalised final run-out distance for columns with different initial aspect ratios. Comparison of dry and submerged granular column collapse.



(b) Normalised final collapse height for columns with different initial aspect ratios. Comparison of dry and submerged granular column collapse.

Figure 6.15 Normalised final collapse run-out and height for columns with different initial aspect ratios.

### 6.3.3 Effect of permeability

Topin et al. (2011) observed development of large negative pore-pressure during dispersion of grains. The rate of dissipation of the negative pore-pressure is directly proportional to the permeability of the granular assembly. In the previous section, the evolution of run-out with the initial aspect ratio is studied using a constant hydrodynamic radius  $r = 0.7 R$ . In order to understand the effect of permeability on the run-out behaviour, the hydrodynamic radius  $r$  is varied from  $0.7 R$  to  $0.95 R$  for all aspect ratios. Increase in the hydrodynamic radius decreases the permeability of the granular assembly resulting in a longer duration for the dissipation of negative pore-pressure.

The normalised run-out for different hydrodynamic radii for a granular column with an initial aspect ratio of 0.8 are presented in figure 6.16. The run-out increases with decrease in the permeability, which is equivalent to an increase in the hydrodynamic radius. An increase in the hydrodynamic radius from  $0.7$  to  $0.95 R$  increases the normalised run-out by 25%. However, even under a very low permeability condition ( $r = 0.95 R$ ), the run-out observed in fluid is shorter than the dry and the buoyant conditions.

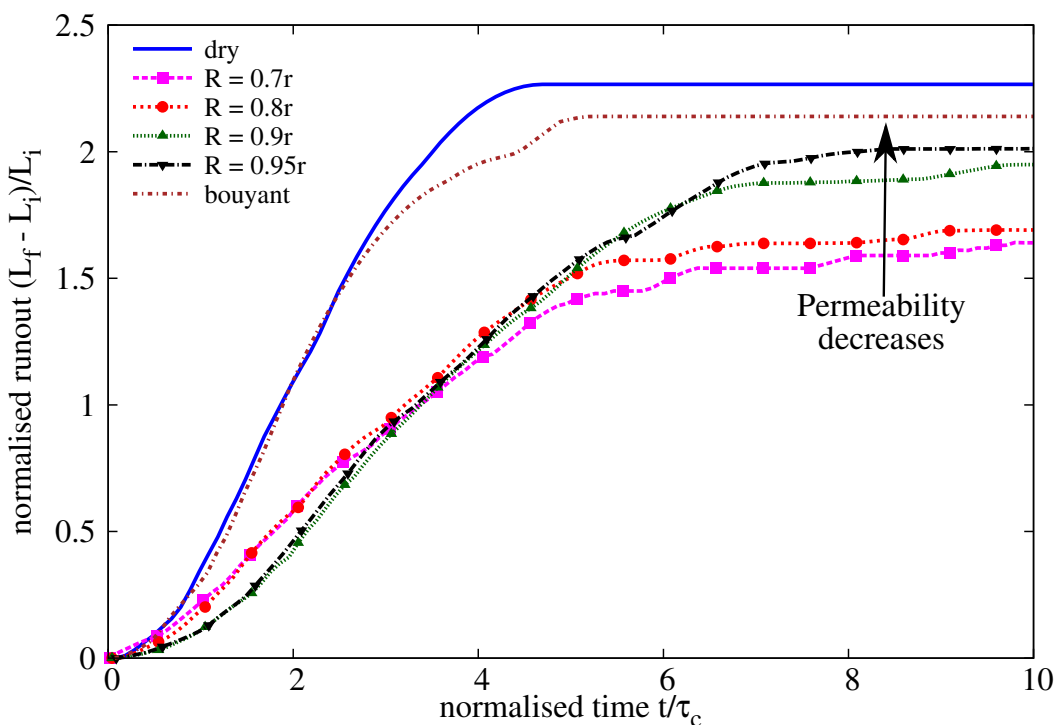


Figure 6.16 Effect of permeability on the evolution of run-out for a column collapse in fluid ( $\alpha = 0.8$ )

At a high permeability ( $r = 0.7 R$ ), the evolution of run-out at the initial stage is quicker, which means that the negative pore-pressure that is developed during the shearing along the shear-failure surface is dissipated faster. Even though the negative pore-pressure is dissipated,

due to the development of negative pore-pressure the evolution of run-out in fluid is slower than its dry counterpart. The rate of pore-pressure dissipation decreases with decrease in the permeability. This can be observed by a flatter slope in the run-out evolution with decrease in the permeability. Figure 6.17 shows the distribution of pore-pressure in high and low permeable granular media along the horizontal direction at a height of  $10 \times d$  from the base. In LBM, the pore-pressure in fluid is a function of fluid density distribution functions. At time  $t = \tau_c$ , the highly permeable ( $r = 0.7 R$ ) granular column shows smaller negative pore-pressure in comparison to large negative pore-pressures observed in the shearing zone of a low permeable column ( $r = 0.9 R$ ). This shows that not only does it take longer for the pore-pressure to dissipate with a decrease in permeability, but also results in almost twice the negative pore-pressure than what is observed in the high permeable case (figure 6.17b).

Although the low permeable granular columns require a longer duration for the run-out to evolve, the final run-out distance is found to be much longer than the high permeable condition. Figure 6.18 shows that the potential energy available for the flow of a low permeable column is 20% smaller than the collapse of a high permeable granular column. The normalised kinetic energy evolution with time (figure 6.19) shows that the low permeable column has a wider peak kinetic energy distribution in comparison to a sharp peak observed in the high permeable condition. This indicates the influence of lubrication, i.e., hydroplaning of the granular flow in low permeable conditions. The evolution of the horizontal kinetic energy with time reveals that the peak kinetic energy is sustained longer as the permeability of the granular material decreases (figure 6.19b). Although the peak kinetic energy is smaller in the low permeability case, the hydroplaning of the flowing granular mass results in a longer run-out distance. Figure 6.20b shows the distribution of pore-pressure for a dense granular column collapse in fluid along the bottom plane. A high positive pore-pressure is observed at the base of the granular flow at the flow front in low permeability condition indicating the occurrence of hydroplaning. The positive pore-pressure at the flow front decreases the effective stress thus the creating lubrication effect. The evolution of local packing density with time shows that the packing density decreases with decrease in permeability (figure 6.21). This drop in the value of packing density between  $t = 2\tau_c$  and  $t = 3\tau_c$  corroborates with the duration of hydroplaning during which a large amount of water is entrained at the flow front.

High permeable granular column shows lower water entrainment (figure 6.21), which indicates that for highly permeable flows the drag force acting on the soil grains predominates over the lubrication effect on the run-out behaviour. In both the low and high permeable granular flows, the granular material consolidates at the final stage of the flow (figure 6.21). This can be observed by the increase in the packing density at the final stage due to settlement of grains and expulsion of entrained water. The final deposit profile for both low and high

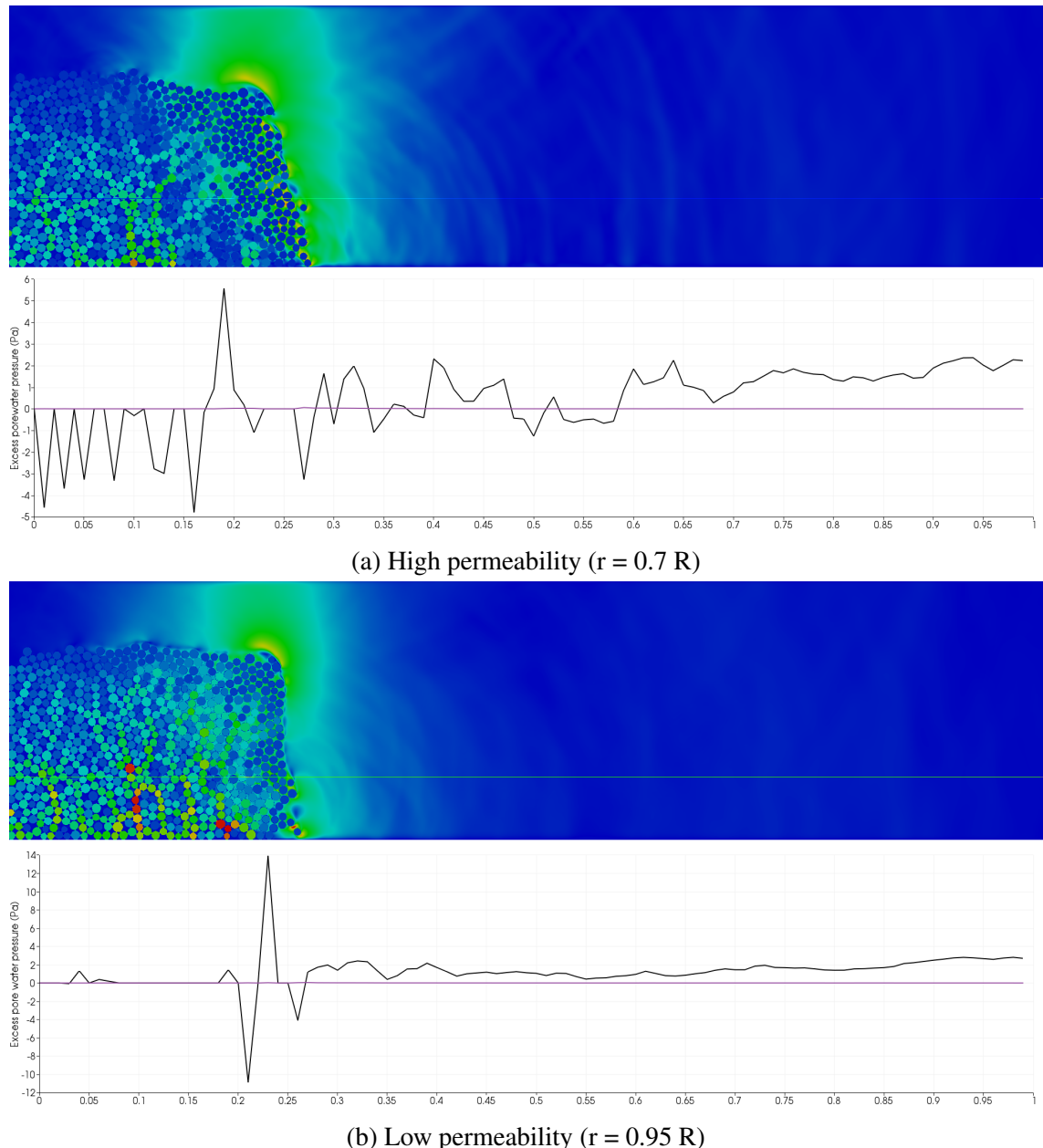


Figure 6.17 Effect of permeability on the excess pore water pressure distribution for a granular column collapse in fluid ( $a = 0.8$  & dense packing) at  $t = \tau_c$  along the horizontal direction at a height of 10d from the base.

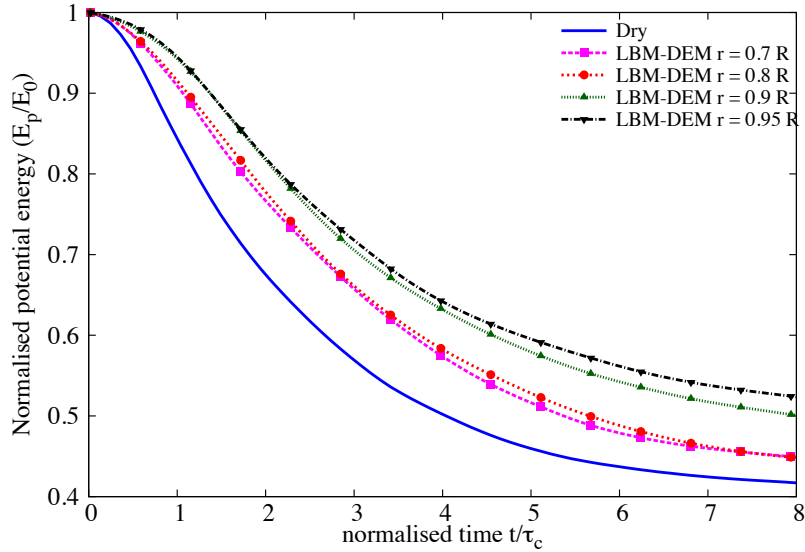


Figure 6.18 Effect of permeability on the evolution of the potential energy with time for a granular column collapse in fluid ( $a = 0.8$ )

permeability conditions are shown in figure 6.22. The high permeable collapse show a more parabolic (convex) deposit profile in contrast to the more concave profile observed in the low permeability condition. In high permeable condition, once the granular mass is mobilised, the drag forces slows down the rate of flow, which allows the grains to densify resulting in a more parabolic profile. This is in contrast to the hydroplaning observed in low permeability condition, where the granular mass thickness is smaller than the dense condition. The observation of hydroplaning in the low permeable condition may be due to the difference in the distribution of granular mass at the flow front. Instigation of hydroplaning is controlled by the balance of gravity and inertia forces at the debris front and is suitably characterized by the densimetric Froude's number:

$$Fr_d = \frac{U}{\sqrt{(\frac{\rho_d}{\rho_w} - 1)gH \cos \theta}}, \quad (6.6)$$

where  $U$  is the average velocity of sliding mass,  $\rho_d$  and  $\rho_w$  are the densities of soil and water, respectively,  $H$  is the thickness of the sliding mass,  $g$  is acceleration due to gravity and  $\theta$  represents the slope angle. Harbitz (2003) observed hydroplaning above a critical value of densimetric Froude's number of 0.4. A Froude's  $Fr_d$  value of 0.427 is observed for the low permeable flow ( $r = 0.95 R$ ), which indicates the occurrence of hydroplaning. Whereas, a  $Fr_d = 0.273$  is observed for the high permeable granular flow indicating absence

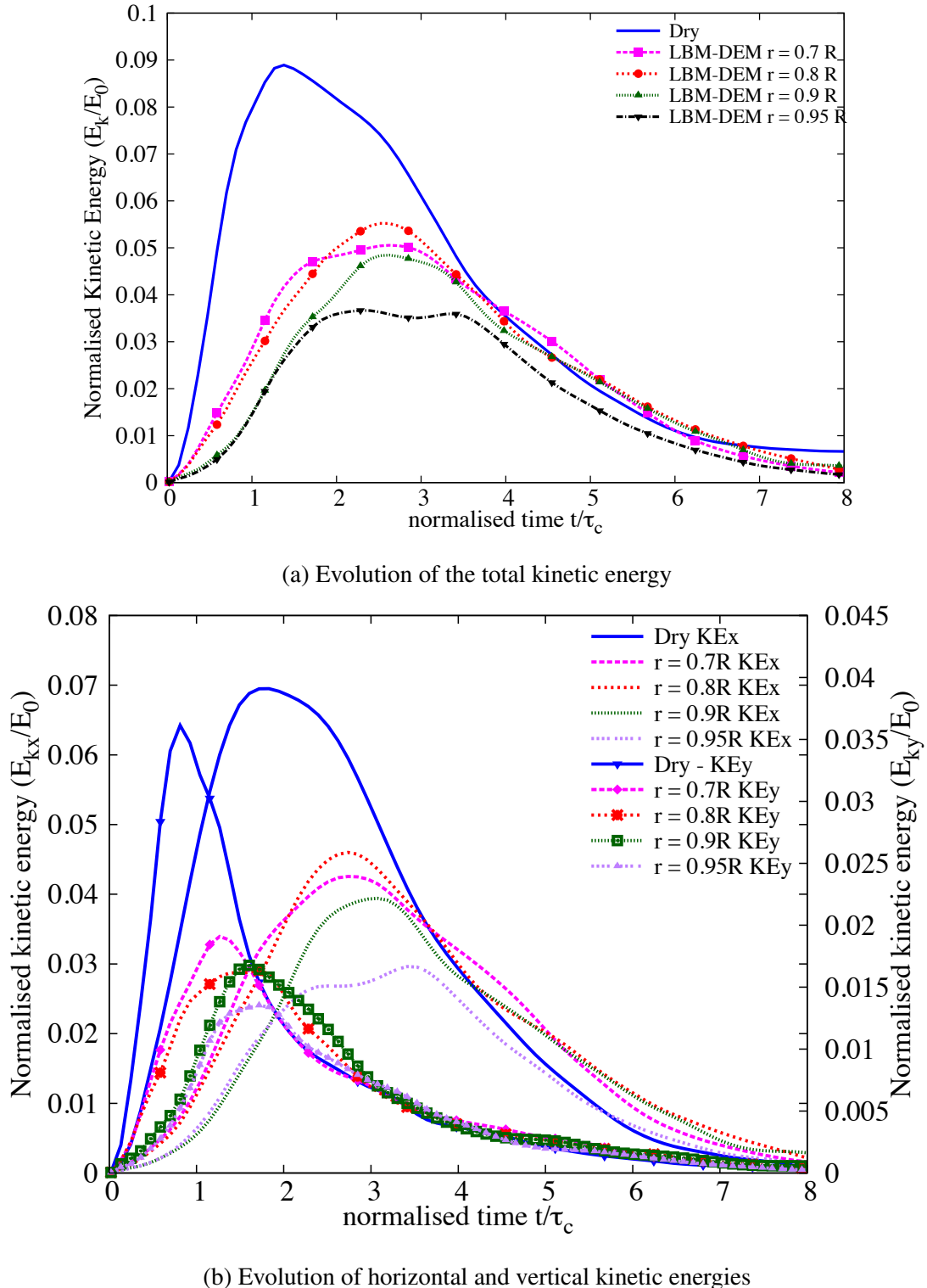


Figure 6.19 Effect of permeability on the evolution of kinetic energies with time for a granular column collapse in fluid ( $a = 0.8$ )

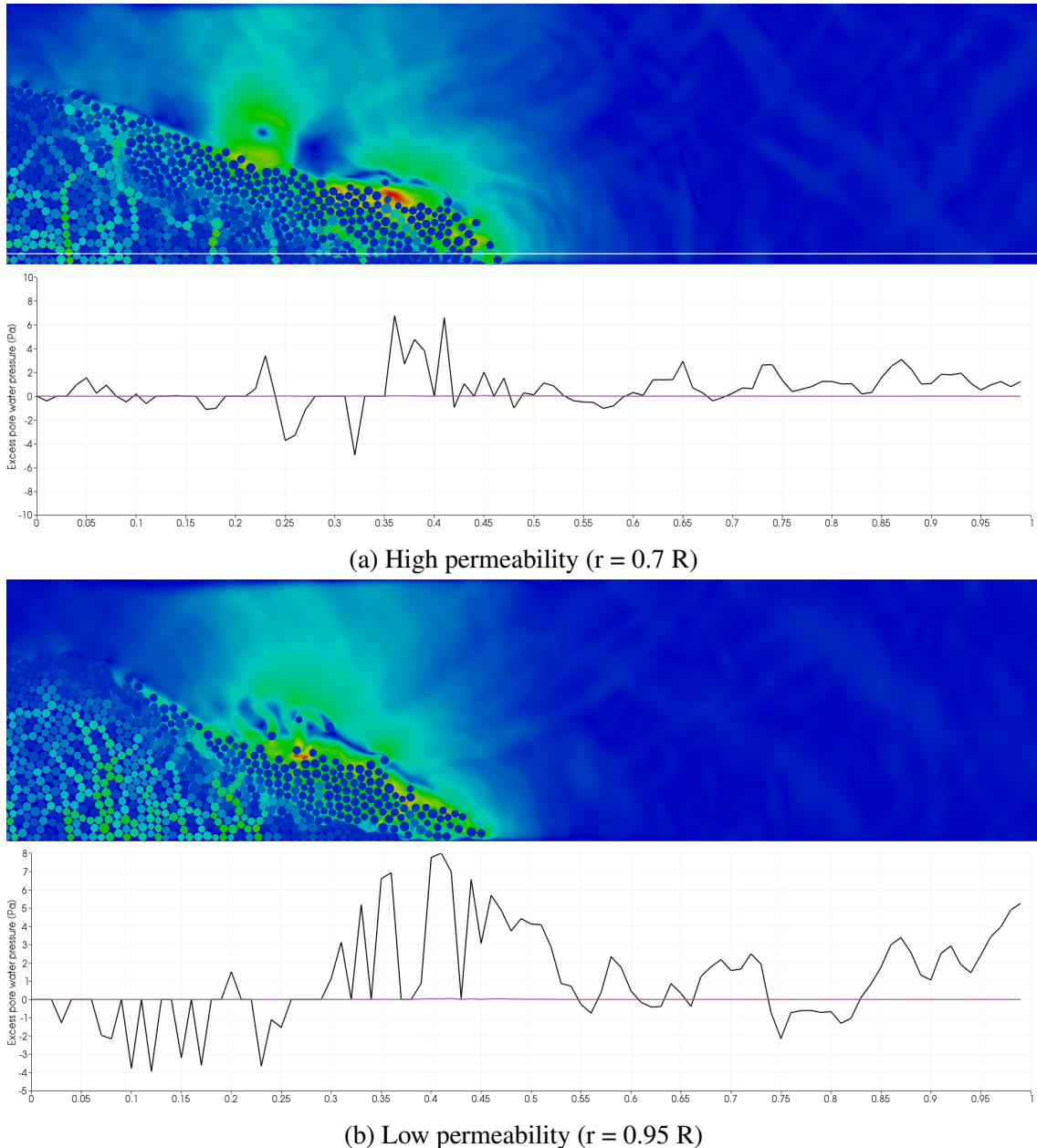


Figure 6.20 Effect of permeability on the excess pore water pressure distribution along the bottom plane for a granular column collapse in fluid ( $a = 0.8$  & dense packing) at  $t = 2\tau_c$ .

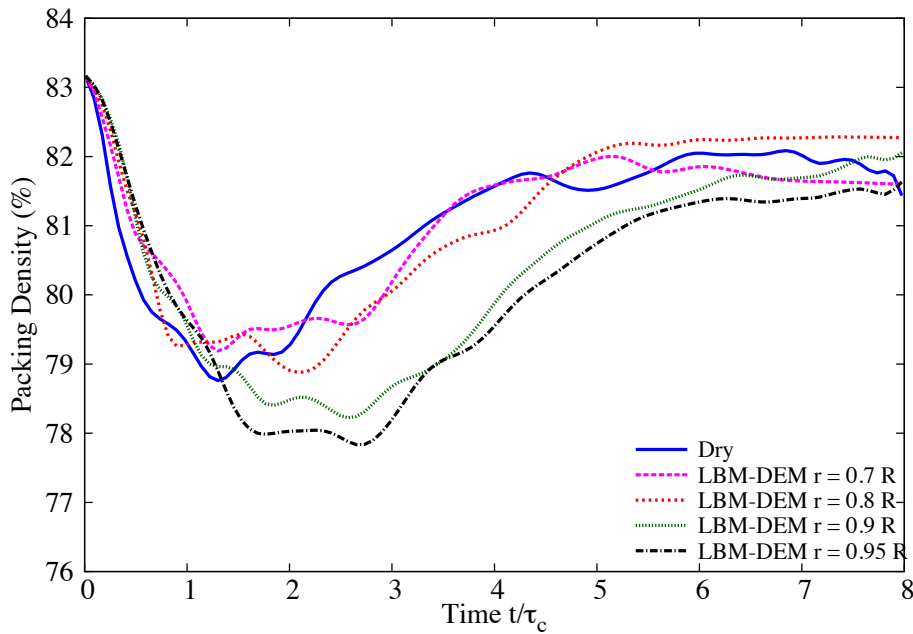
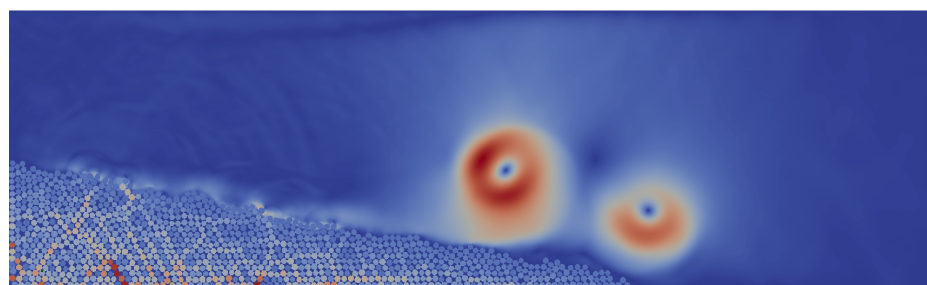


Figure 6.21 Effect of permeability on the evolution of packing density for a granular column collapse in fluid ( $a = 0.8$  & dense initial packing)

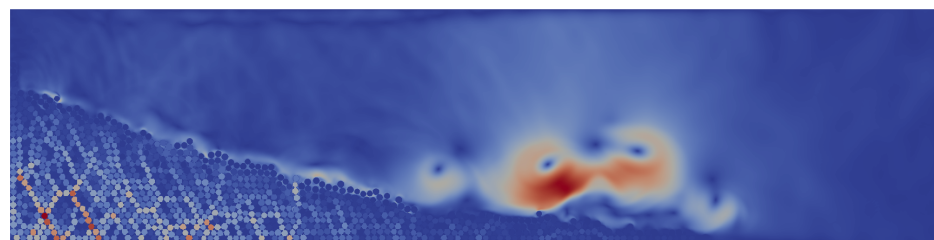
of hydroplaning, the low permeable collapse is predominated by the viscous drag force resulting in a parabolic profile and shorter run-out distance.

The normalised final run-out distance as a function of the initial aspect ratio of the column for different values of permeability and in dry case is presented in figure 6.23. For all aspect ratios, the dry condition yields the farthest run-out distance. For a given aspect ratio, the dry collapse acquires the highest peak kinetic energy due to the lack of viscous dissipation during vertical collapse. This extra kinetic energy is high enough to propel the heap, in spite of a high frictional dissipation, over a distance that is longer than the run-out distance in the fluid regime. In the submerged condition, for the same aspect ratio, the kinetic energy available for spreading is lower and the dissipation due to viscous drag is higher, thus leading to a much shorter run-out distance.

For short columns, with decrease in permeability the run-out distance increases, however, the run-out distance is not higher than the dry condition. At higher aspect ratios, decrease in permeability from  $r = 0.8 R$  to  $r = 0.9 R$  does not have a significant influence on the run-out behaviour. This can be attributed to the turbulent nature of the granular flows for tall columns. The run-out behaviour is a result of transformation of (part of) the initial potential energy to the peak kinetic energy, which in turn controls the subsequent run-out along the plane. For dry and submerged conditions with different values of permeability, the run-out distance is plotted as a function of the normalised peak kinetic energy in figure 6.24. It can be observed



(a) High permeability ( $r = 0.7 R$ )



(b) Low permeability ( $r = 0.95 R$ )

Figure 6.22 Effect of permeability on the deposit morphology of a granular column collapse in fluid  
( $a = 0.8$ )

that for the same aspect ratio, the peak kinetic energy is higher in the case of dry column. This represents grain inertial regime in dry granular collapse, which indicates that a part of the potential energy, in the presence of the fluid, is dissipated during the vertical collapse due to viscous friction. In all regimes, the run-out distance increases as a power law  $L_f \propto KE_{max}^\gamma$ . For the same value of peak kinetic energy, the run-out distance in fluid is longer than the dry column collapse. Also, with decrease in permeability the run-out distance increases for the same peak kinetic energy.

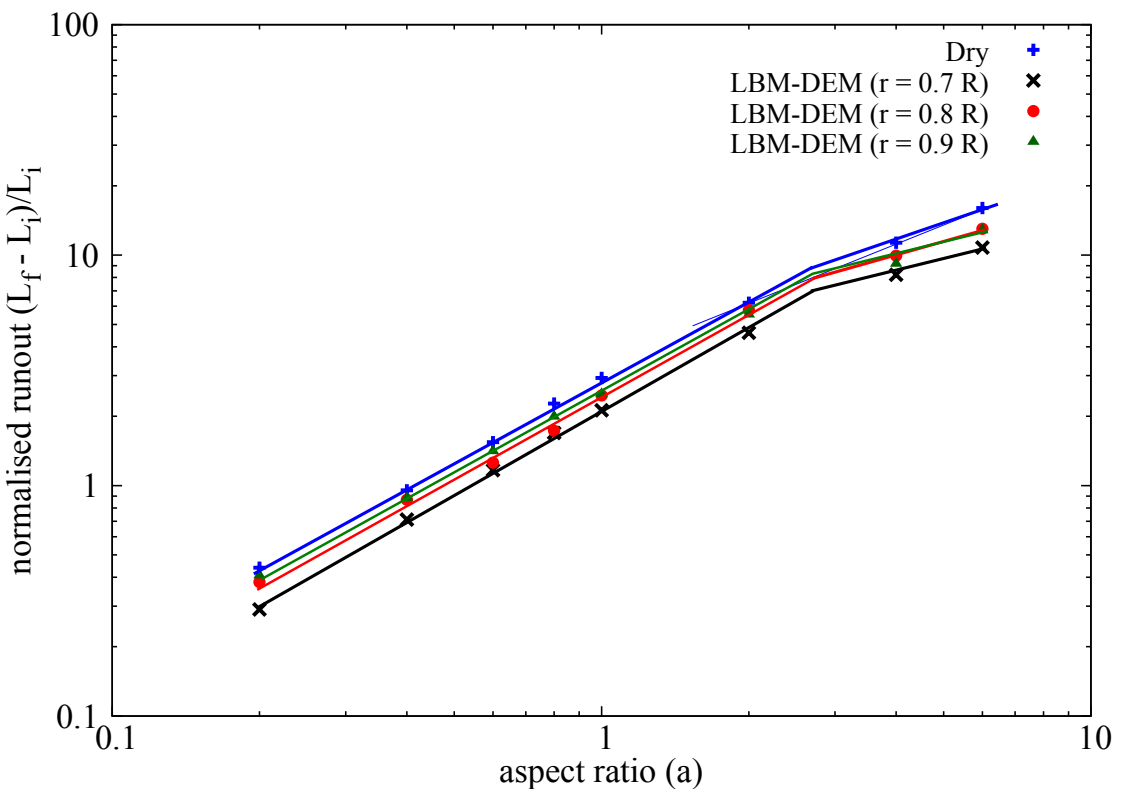


Figure 6.23 Normalised final run-out distance for columns with different initial aspect ratios. Comparison of dry and submerged granular column collapse for different hydrodynamic radius ( $0.7 R$ ,  $0.8 R$  and  $0.9 R$ ).

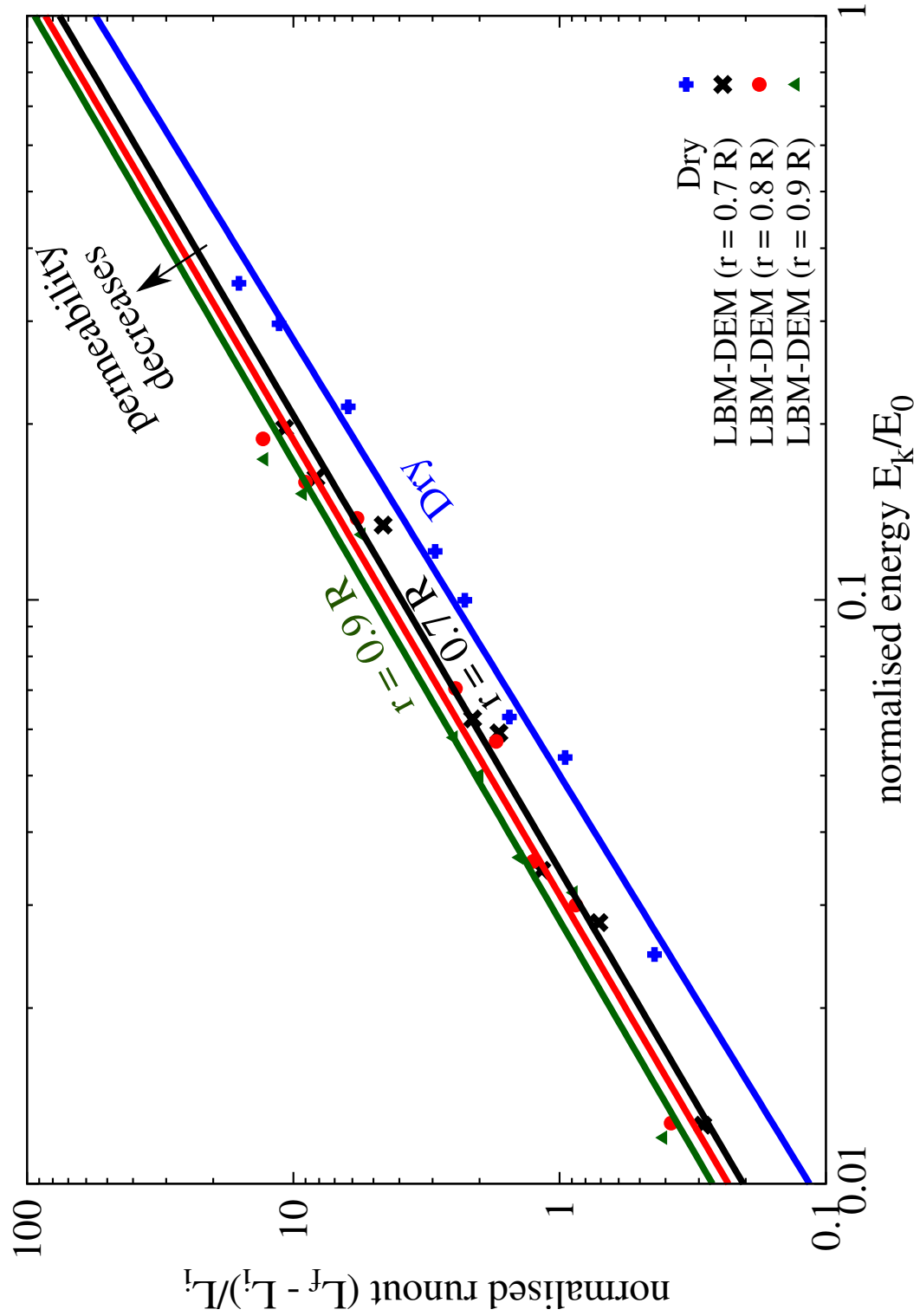


Figure 6.24 Normalised final run-out distance for columns as a function of peak kinetic energy. Comparison of dry and submerged granular column collapse for different hydrodynamic radius (0.7 R, 0.8 R and 0.9 R).

### 6.3.4 Effect of initial packing density

Rondon et al. (2011) observed that the loose packings flow rapidly on a time scale proportional to the initial height and results in longer run-out distance in comparison to the dense packing. Hydroplaning occurs above a critical Froude's number of 0.4. The Froude's number is inversely related to the thickness of the flow and its density. Hence, for the same thickness of flow, a loose granular column will experience more hydroplaning than a dense granular flow. This effect might result in longer run-out behaviour in fluid than the dry condition for the same initial aspect ratio. The initial packing density and the permeability of a 2D granular column, with an aspect ratio of 0.8, are varied to understand their influence on the run-out behaviour. The run-out behaviour of the dense case (83% packing density), discussed in the previous section, is compared with a loose granular column (79% packing fraction). The permeability is varied by changing the hydrodynamic radius from 0.7 R to 0.95 R.

The normalised run-out evolution with time for a loose initial packing (79% packing fraction) with different hydrodynamic radii 0.7 R, 0.8 R, 0.9 and 0.95 R are presented in figure 6.25. The run-out evolution of dry and a column with grains in suspension with an initial aspect ratio of 0.8 are also presented to understand the influence of hydrodynamic forces on the flow kinematics. Similar to the dense granular column, the run-out distance increases with increase in the hydrodynamic radius (i.e., decrease in permeability). At low permeabilities ( $r = 0.9$  and  $0.95$  R), the run-out distance is longer than the dry condition. This shows that the lubrication effect in low permeability condition overcomes the influence of the drag force and the development of large negative pore-pressure resulting in a longer run-out distance. Although the suspended granular masses experience higher drag forces and turbulent effects, the run-out evolves almost at the same rate in comparison with granular columns with high permeability. This shows the effect of permeability on the dissipation rate of negative pore-pressure developed during the initial stage of collapse.

Figure 6.26 shows the development of negative pore-pressure in low permeability ( $r = 0.95$  R) and dissipation of negative pore-pressure in high permeability ( $r = 0.7$  R) at the same time  $t = \tau_c$ . This difference in the quantity and the rate of dissipation of negative pore-pressure results in a difference in the rate of flow evolution. A low permeable column requires a longer duration to evolve. Figure 6.27 shows the distribution of the excess pore-pressure along the bottom for low and high permeability conditions. As the flow progresses, the low permeability of the granular column causes hydroplaning to occur at the base of the column, which can be observed by high positive pore-pressure at the base of the flow front, resulting in a longer run-out distance.

The evolution of the potential energy with time (figure 6.28) reveals that at a very low permeability ( $r = 0.95$  R), the initial potential energy mobilised is smaller than at  $r = 0.9$  R.

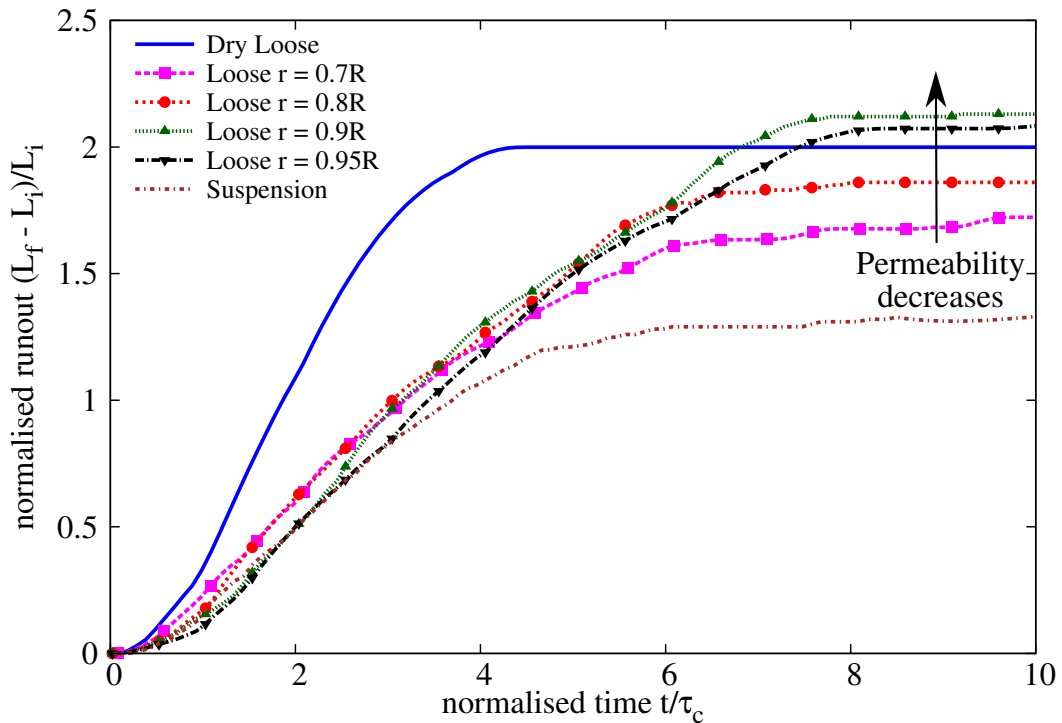


Figure 6.25 Effect of permeability on the evolution of run-out for a column collapse in fluid ( $a = 0.8$  & loose packing)

Also with decrease in permeability, the time required to dissipate the negative pore-pressure increases. This results in a shorter run-out distance in the case of  $r = 0.95 R$  to that of  $r = 0.9 R$ . As the quantity of material destabilised is small, the flow is thinner and thus has a high Froude's number (0.59). Figure 6.29b shows that the peak horizontal kinetic velocity observed in the case of  $r = 0.9 R$  is higher than  $r = 0.95 R$ . A Froude's number of 0.59 for  $r = 0.9 R$  is observed in contrast to 0.46 for  $r = 0.95 R$ . Both values of hydrodynamic radii result in a Froude's number that indicate the occurrence of hydroplaning. However, the difference in the amount of material destabilised for  $r = 0.95 R$  and the decreased effect of hydroplaning results in a shorter run-out distance for  $r = 0.95 R$  in comparison to  $r = 0.9 R$ .

Figure 6.30 shows the evolution of packing fraction with time for different values of permeability. As the column collapses, water is entrained at the flow front. This can be observed by the decrease in the packing fraction during  $t = \tau_c$  and  $t = 3\tau_c$ . As the flow progresses, the entrained water is expelled and the soil grains consolidate to reach a critical packing density at the end of the flow. The permeability (i.e., hydrodynamic radius) plays a crucial role in the rate of dissipation of the entrained water. As the permeability decreases, the water entrained at the flow front takes longer time to be dissipated resulting in lubrication of the flow at

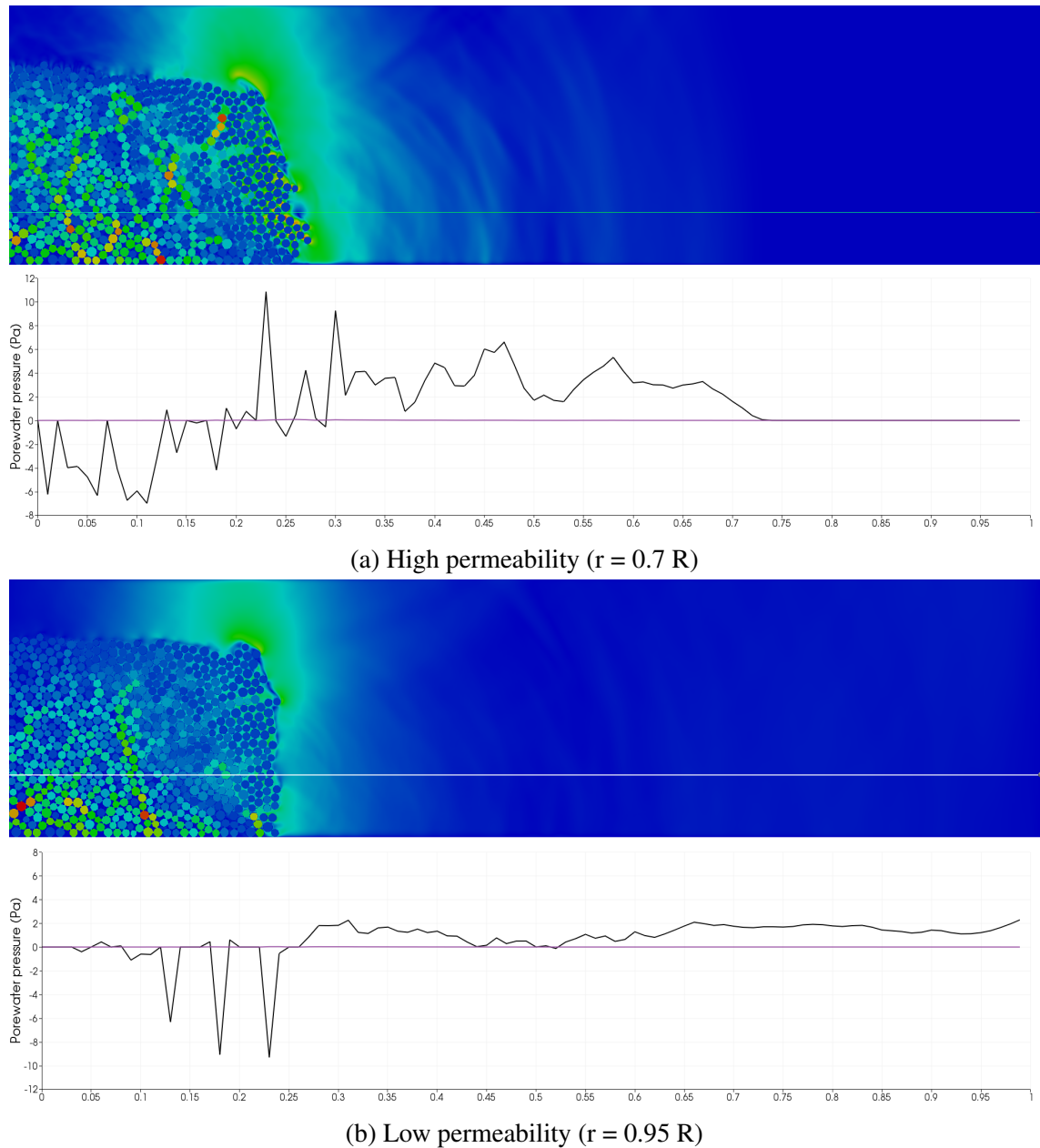


Figure 6.26 Effect of permeability on the excess pore water pressure distribution along the base of a granular column collapse in fluid ( $a = 0.8$  & loose packing) at  $t = \tau_c$

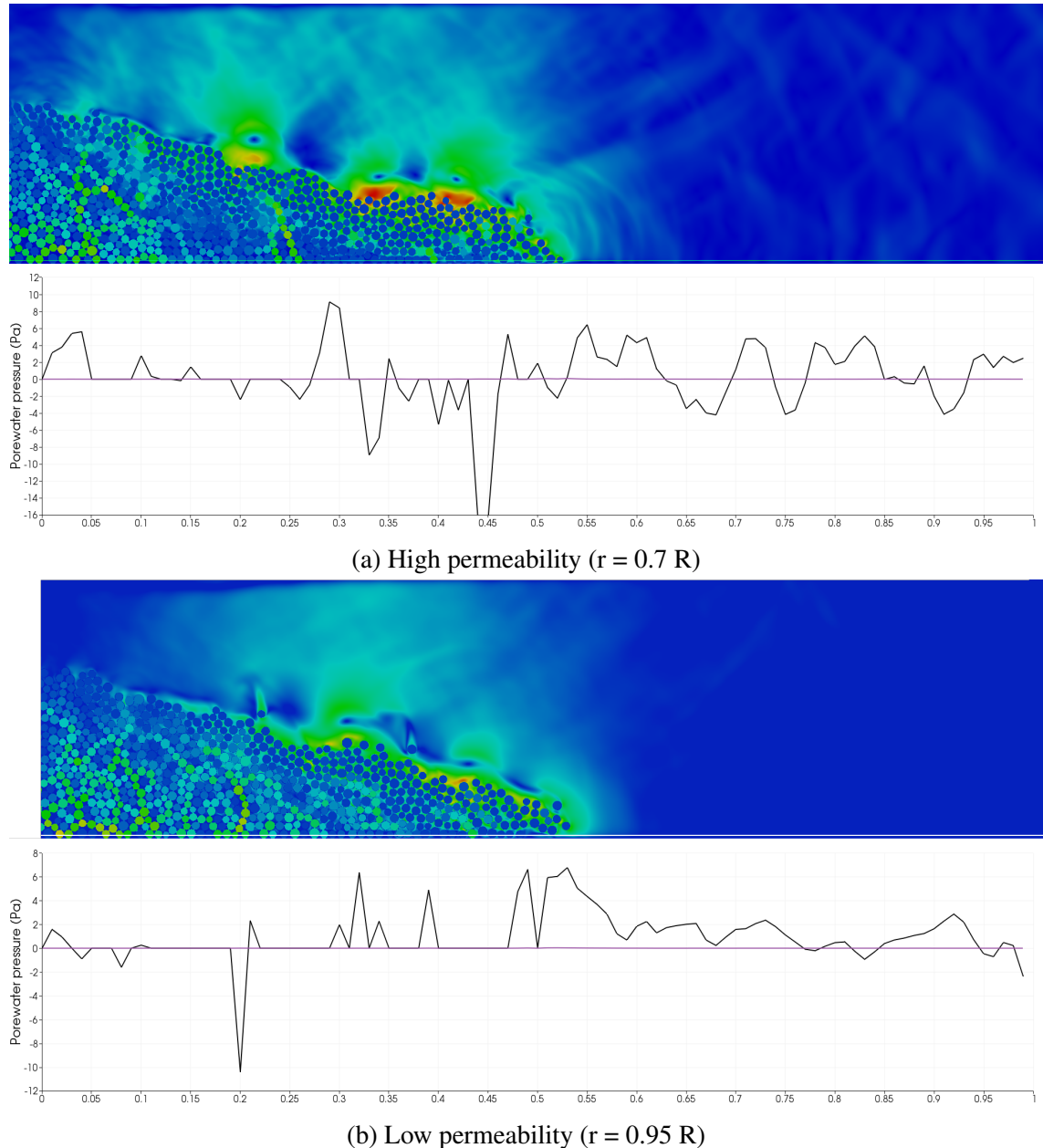


Figure 6.27 Effect of permeability on the excess pore water pressure distribution for a granular column collapse in fluid ( $a = 0.8$  & loose packing) at  $t = 2\tau_c$

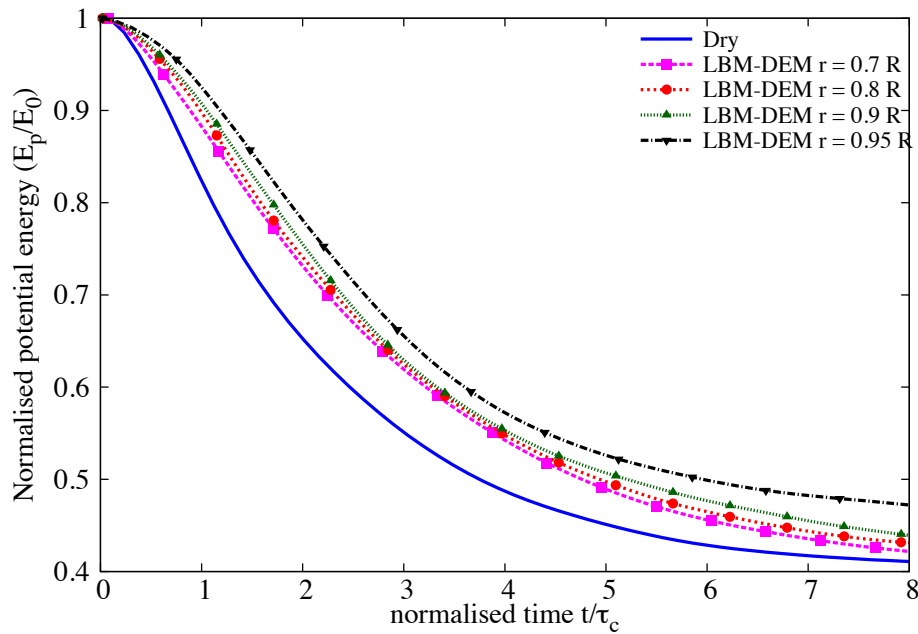


Figure 6.28 Effect of permeability on the evolution of the potential energy with time for a granular column collapse in fluid ( $a = 0.8$  & loose packing)

low permeabilities. This lubrication effect results in an increase in the run-out distance for columns with low permeabilities.

The evolution of grain trajectories with time are presented in figure 6.31 for low ( $r = 0.95$  R) and high ( $r = 0.9$  R) permeability conditions. It can be observed that a high permeability column shows a parabolic (convex) final profile in contrast to the more concave profile observed in low permeability condition, due to the effect of drag forces on the flow front. This difference in the flow thickness results in a higher value of Froude's number (0.59) and the occurrence of hydroplaning in the low permeability condition. Due to the high permeability, the water entrained at the flow front is dissipated quicker and thus no lubrication effect is observed. A Froude's number of 0.272 (no hydroplaning) is observed for the high permeability condition ( $r = 0.7$  R). The thick flow front in dense condition results in higher effective stress, in contrast to the low effective stress in loose condition due to positive pore-pressure at the flow front. The higher effective stress results in more frictional dissipation in dense condition, while the loose column experiences lubrication effect. This shows that the drag force predominates at high permeability, while the low permeability condition is characterised by hydroplaning and lubrication.

Figure 6.32 shows the normalised pressure at the base for the low and high permeability flows at  $t = 2\tau_c$ . The normalised effective stress plotted is obtained as the average over 5 time steps at  $2\tau_c$ . The effective stress at the base is normalised to the effective stress of a

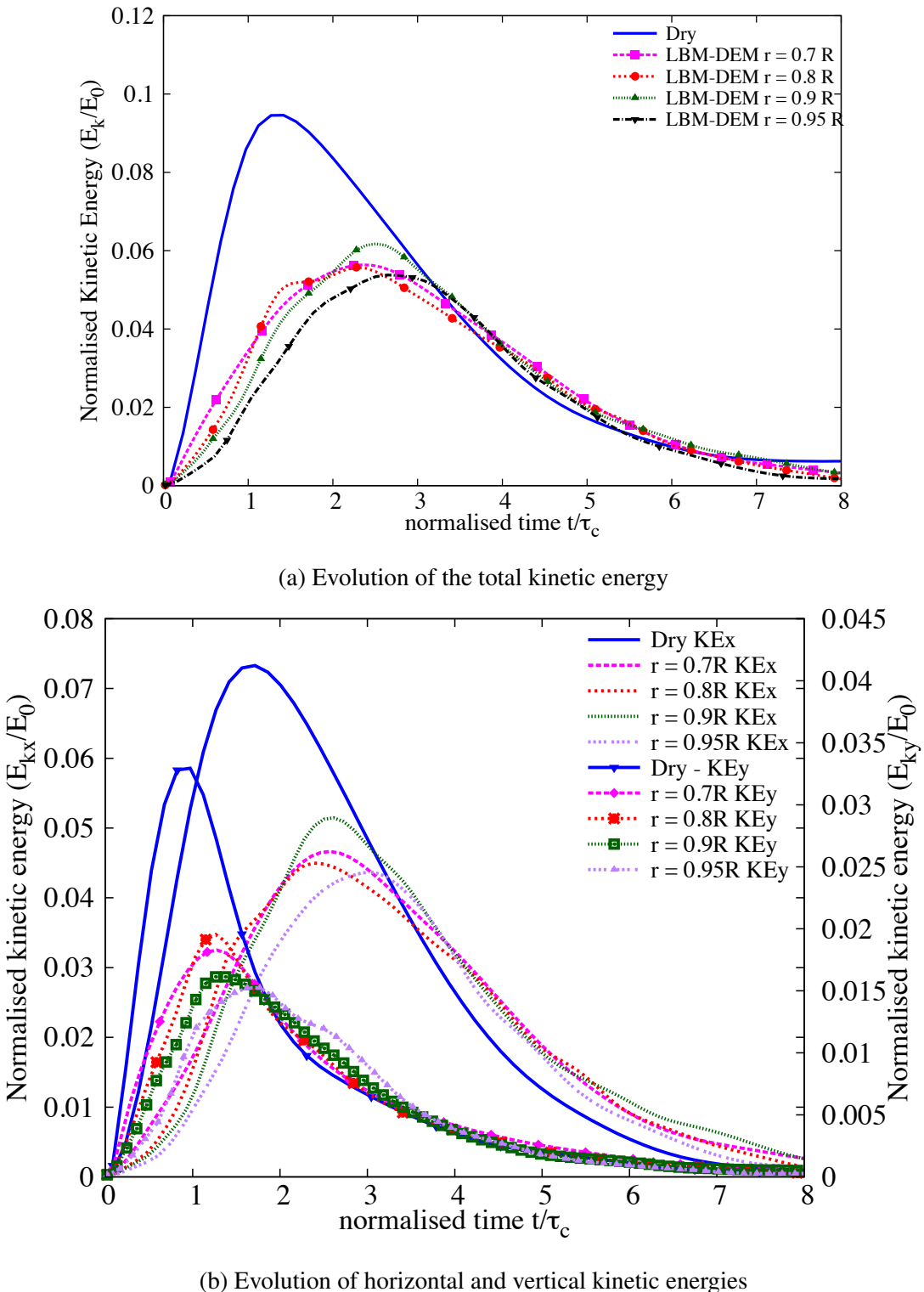


Figure 6.29 Effect of permeability on the evolution of kinetic energies with time for a granular column collapse in fluid ( $a = 0.8$  & loose packing)

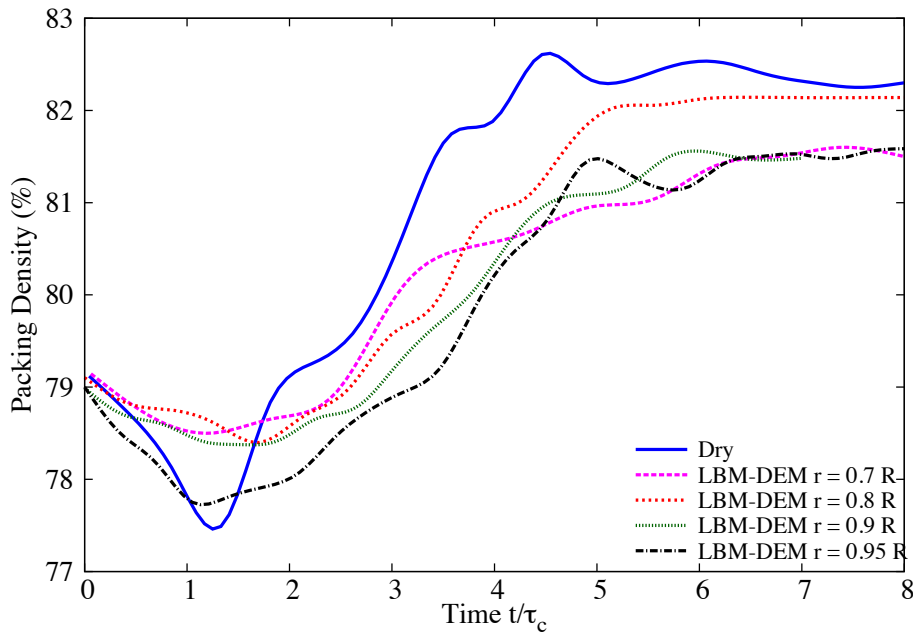
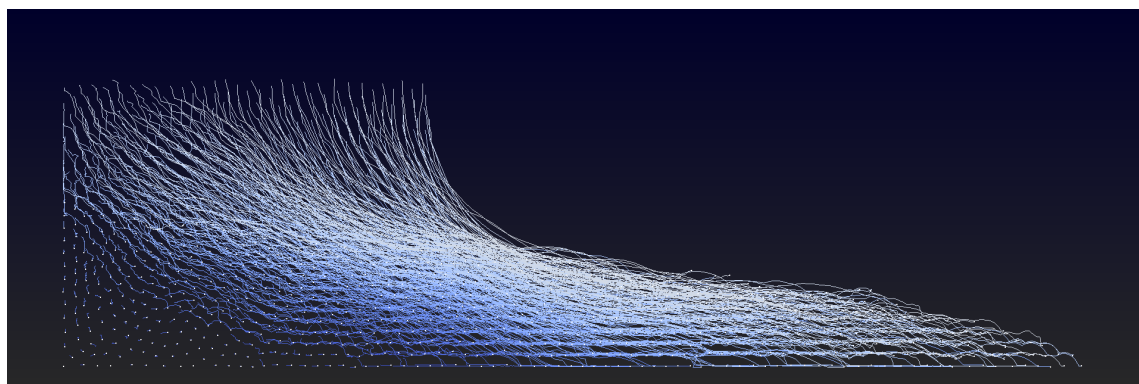


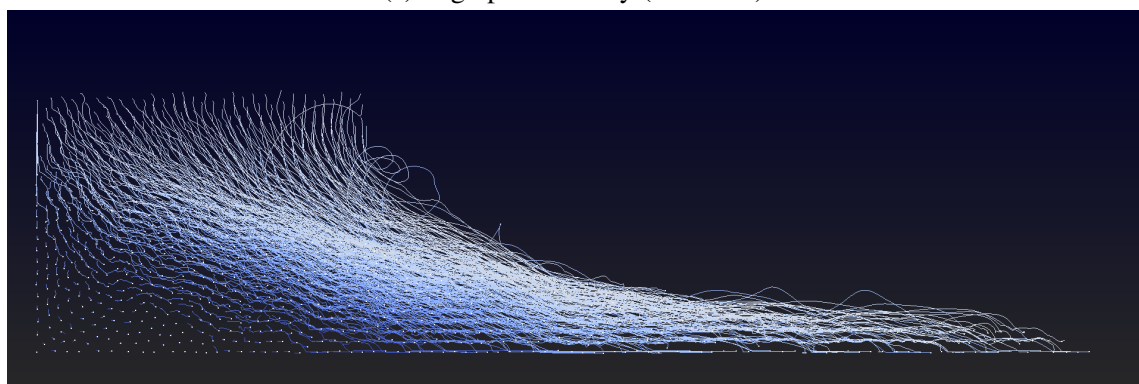
Figure 6.30 Effect of permeability on the evolution of packing density for a granular column collapse in fluid ( $a = 0.8$  & loose initial packing)

static granular column before the collapse. A value of 1 indicates that the effective stress hasn't changed, which can be observed in the static region of the granular column. It can be observed that the normalised effective stress is significantly higher for the high permeability condition at the flow front in comparison to the almost non-existence of effective stress in the low permeability condition. The observation of trivial effective stress at the flow front corroborates the lubrication effect observed at low permeability conditions.

Figure 6.33 shows the grain trajectories of a dense and a loose initial packing for a hydrodynamic radius ( $r = 0.95 R$ ). It can be observed that the dense initial packing results in a lot of turbulent behaviour at the flow surface in contrast to the more uniform flow behaviour in the loose condition. The thickness of the deposit in both dense and loose condition is almost the same, however the density of the flow results in a Froude's number of 0.59 and 0.429 for loose and dense conditions, respectively. The low initial density results in more hydroplaning in the loose condition. The effect of water entrainment at the flow front in dense and loose conditions can be seen in figure 6.34. Water entrainment at the flow front can be observed in the loose condition, this is shown by white-coloured (empty voronoi cells) at the flow front. This empty region in the granular packing between the granular mass and the base at the flow front represents the entrained water, which results in hydroplaning. Comparing the evolution packing densities in dense and loose conditions (figures 6.21 and 6.30) reveal almost the same packing density when the flow is fully mobilised. Hence, it is the density of the flowing



(a) High permeability ( $r = 0.7 R$ )



(b) Low permeability ( $r = 0.95 R$ )

Figure 6.31 Particle tracking of the deposit morphology for a granular column collapse in fluid ( $a = 0.8$  & loose packing), influence of permeability

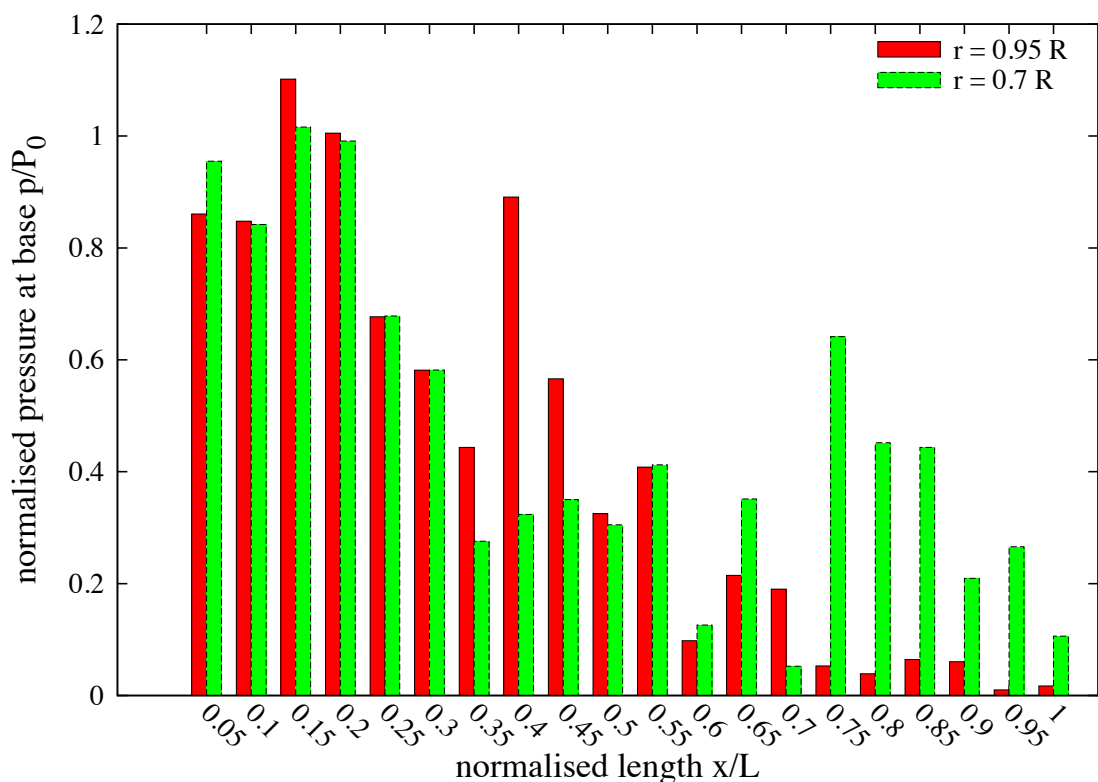
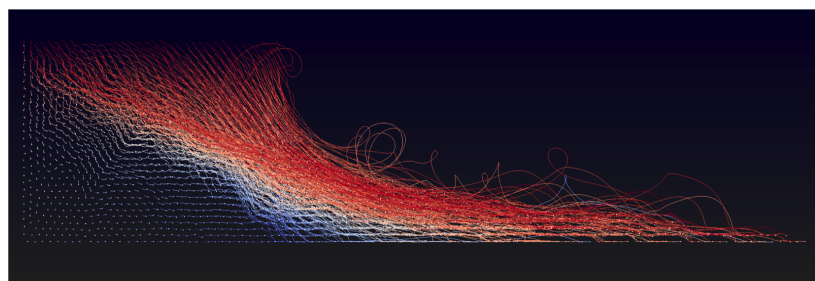


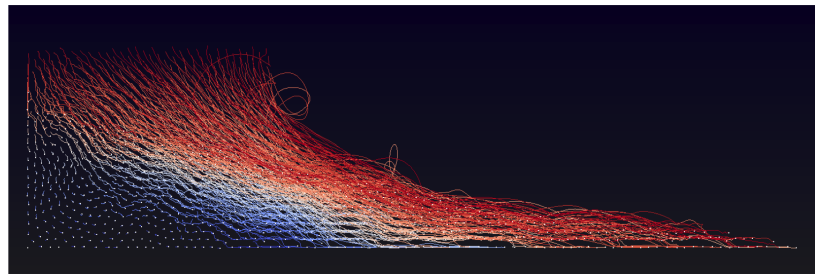
Figure 6.32 Effect of permeability on the normalised effective stress for loose initial packing at  $t = 2\tau_c$

granular mass that controls the influence of hydroplaning for a given hydrodynamic radius and initial aspect ratio. A loosely packed granular column with low permeability entrains more water at the flow front, resulting in a hydroplaning effect that overcomes the influence of viscous drag forces and thereby yields a higher run-out distance than the dry condition.

Rondon et al. (2011) also observed that the collapse of a granular column in a viscous fluid is mainly controlled by the initial volume fraction and not by the aspect ratio of the column. The role of the initial volume fraction observed explains the pore pressure feedback mechanism proposed by (Iverson, 2000; Schaeffer and Iverson, 2008) in the context of landslides. The compaction or dilation of grains can cause additional stress in the grains which can stabilise or destabilise the soil. The flow is thus controlled by the coupling between the dilatancy of the granular layer and the development of pore pressure in the fluid phase (Pailha et al., 2008). The dense column needs to dilate in order to flow. When it starts to fall, liquid is then sucked into the column, which is then stabilized by the additional viscous drag (Rondon et al., 2011; Topin et al., 2012). By opposition the loose column when it starts flowing expands and ejects liquid, leading to a partial fluidisation of the material.



(a) Dense initial packing (83%)

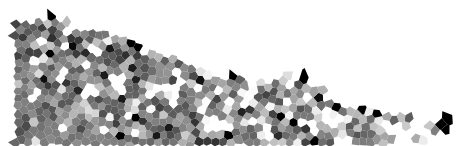


(b) Loose initial packing (79%)

Figure 6.33 Effect of initial density on the deposit morphology for a granular column collapse in fluid ( $a = 0.8$ ). Dense vs loose initial packing fraction ( $r = 0.95 R$ ). Darker means dense packing, white indicates loose packing density.



(a) Dense initial packing (83%)



(b) Loose initial packing (79%)

Figure 6.34 Evolution of packing fraction at  $t = \tau_c$  for dense and loose initial packing fraction. Black means dense packing, while white colour denotes loose packing in the voronoi cell.

## 6.4 Submarine granular flows down incline plane

Slope failure is a problem of high practical importance for both civil engineering structures and natural hazards management. Catastrophic events such as landslides, debris flows, rock avalanches or reservoir embankment failures exemplify the potential consequences of a soil gravitational instability. One of the most critical situations concerns a submerged sandy slope as pore pressure changes, seepage or earthquakes can cause significant damages to off-shore structures and may generate a tsunami.

The influence of slope angle on the effect of permeability and the initial packing density on the run-out behaviour are studied. In this study, a 2D poly-disperse system ( $d_{max}/d_{min} = 2$ ) of circular discs forming a granular column in fluid is used to understand the behaviour of granular flows down inclined planes (figure 6.5). The soil column is modelled using  $\sim 1000$  to  $2000$  discs of density  $2650 \text{ kg/m}^3$  and a contact friction angle of  $26^\circ$ . The collapse of the granular column is simulated inside a fluid with a density of  $1000 \text{ kg/m}^3$  and a kinematic viscosity of  $1 \times 10^{-6} \text{ m}^2/\text{s}$ . A granular column with an initial aspect ratio  $a$  of  $0.8$  is used. A hydrodynamic radius  $r = 0.9 R$  is adopted during the LBM computations. Dry analyses are also performed to study the effect of hydrodynamic forces on the run-out distance. The numerical configuration used in this study is shown in figure 6.5a. The slope angle  $\theta$  is varied as  $0^\circ$ ,  $2.5^\circ$ ,  $5^\circ$ , and  $7.5^\circ$ . The influence of permeability (with hydrodynamic radius varied as  $0.7$ ,  $0.75$ ,  $0.8$ ,  $0.85$  and  $0.9 R$ ) on the run-out behaviour of collapse of granular columns on to an inclined plane with a slope angle of  $5^\circ$  is also analysed.

### 6.4.1 Effect of initial density

In order to understand the influence of the initial packing density on the run-out behaviour, a dense sand column (initial packing density,  $\Phi = 83\%$ ) and a loose sand column ( $\Phi = 79\%$ ) are considered. The granular columns collapse and flow down slopes of varying inclinations. The run-out behaviour is compared with the collapse of a granular column in fluid on a horizontal surface. For all slope angles, the flow kinematics in the submerged condition is compared with its dry counterpart to understand the influence of lubrication and viscous drag. A hydrodynamic radius of  $r = 0.9 R$  is adopted in all cases, because low permeability conditions result in longer run-out distance as observed in the previous section.

The evolution of the normalised run-out with time for the collapse of a dense sand column in dry and submerged conditions for varying slope inclinations is presented in figure 6.35a. For all slope angles, the run-out distances in the dry condition are longer than those observed in the submerged condition. Similar to the case of collapse on a horizontal plane, the dense granular columns experience drag forces that have a significant influence than the lubrication

effect. The difference in the run-out between the dry and the submerged condition decreases with increase in the slope angle. At a slope angle of  $5^\circ$  the difference in the run-out between the dry and the submerged condition is the smallest. This is due to hydroplaning of a thin flowing layer, the occurrence of hydroplaning can be observed by a sustained peak kinetic energy (figure 6.35b). At higher slope angles ( $> 5^\circ$ ), the drag force predominates over the lubrication effect and results in significantly shorter run-out distance than the dry condition. This can be observed by the difference in the kinetic energy evolution between the dry and the submerged conditions.

Similar to the case of collapse on a horizontal surface, the dense granular columns in fluid require a longer time to collapse and flow, due to the development of large negative pore-pressure. Large negative pore-pressure are developed as the dense granular material dilates due to shearing along the shear-failure surface in the initial phase of the flow. The snapshots of the dense granular column collapse down slopes of varying inclinations at the time ( $t = \tau_c = 3\sqrt{H/g}$ ), are shown in figure 6.36. It can be observed that the amount of water entrainment increases with increase in slope angle. At a slope of  $7.5^\circ$ , a layer of entrained water (thickness  $\sim 2d$ ) along the bottom of the flow front can be observed. However, with increase in slope angle, the surface area of granular mass experiencing the hydrodynamic drag increases, which results in shorter run-out distance than the dry condition.

Figure 6.35b shows the evolution of normalised kinetic energy with time for dry and submerged collapse on different slope angles. It can be seen that the viscous drag on the dense column tends to predominate over the influence of hydroplaning on the run-out behaviour. This influence can be observed in the smaller peak kinetic energy for submerged granular in comparison to the dry condition. With increase in the slope angle, the volume of material that dilates increases. This results in large negative pore-pressure and more viscous drag on the granular material. Hence, the difference in the run-out between the dry and the submerged conditions, for a dense granular assembly, increases with increase in the slope angle above an inclination of  $5^\circ$ .

In contrast to the dense granular columns, the loose granular columns (packing fraction of 79%) show longer run-out distance in immersed conditions (figure 6.37a). The snapshots at  $t = 3\tau_c$  of a loose granular column ( $a = 0.8$ ) collapse down slopes inclined at an angle of  $2.5^\circ$ ,  $5^\circ$  and  $7.5^\circ$  are presented in figure 6.38. The run-out distance in fluid increases with increase in the slope angle in comparison to the dry cases. The loose granular flow tends to entrain more water at the base of the flow front, creating a lubricating surface, which results in a longer run-out distance. For the same thickness of the flow, the loose granular flow has smaller density and hence a higher Froude's number than the dense flow resulting in a higher

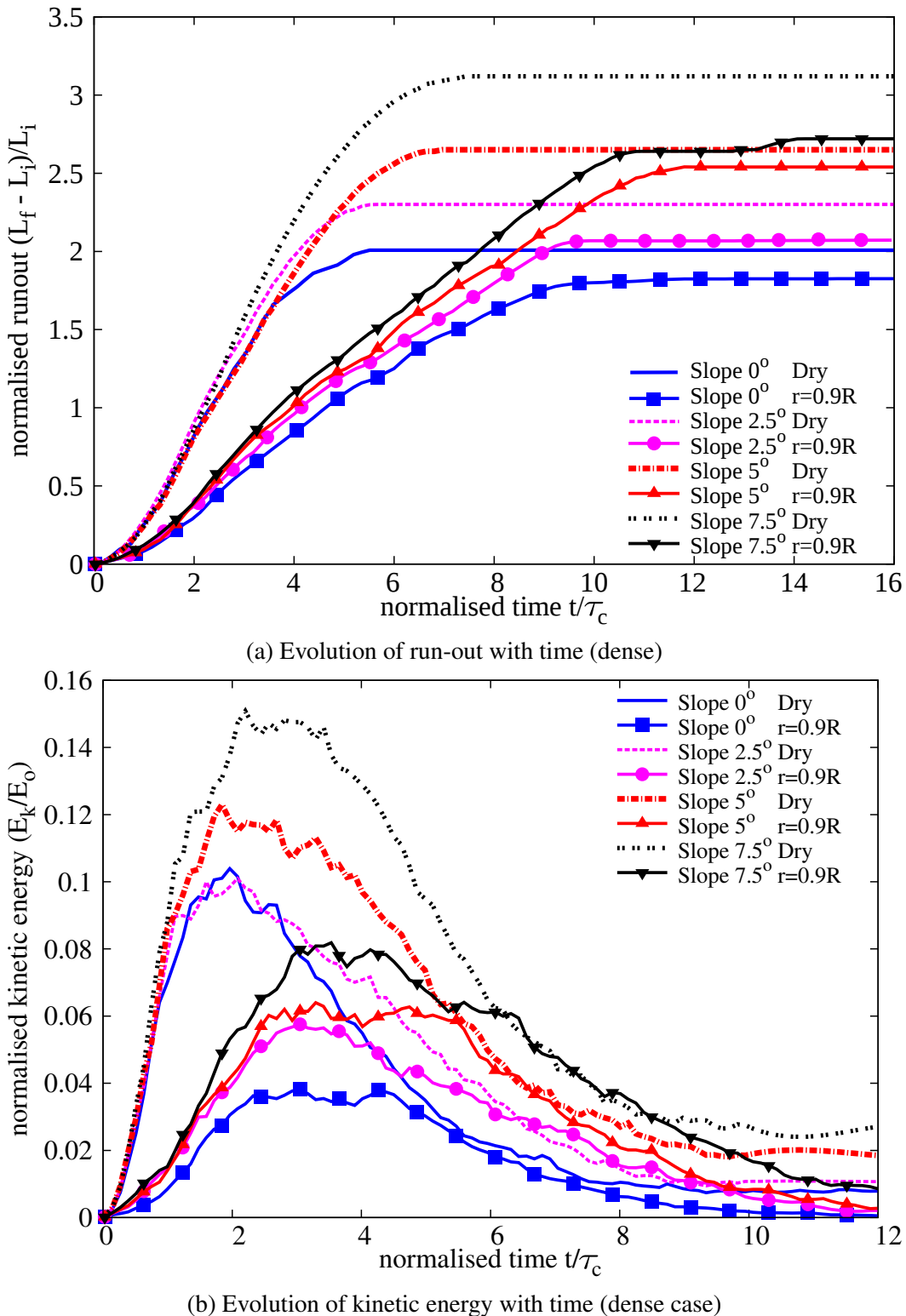


Figure 6.35 Evolution of run-out and kinetic energy with time (dense)

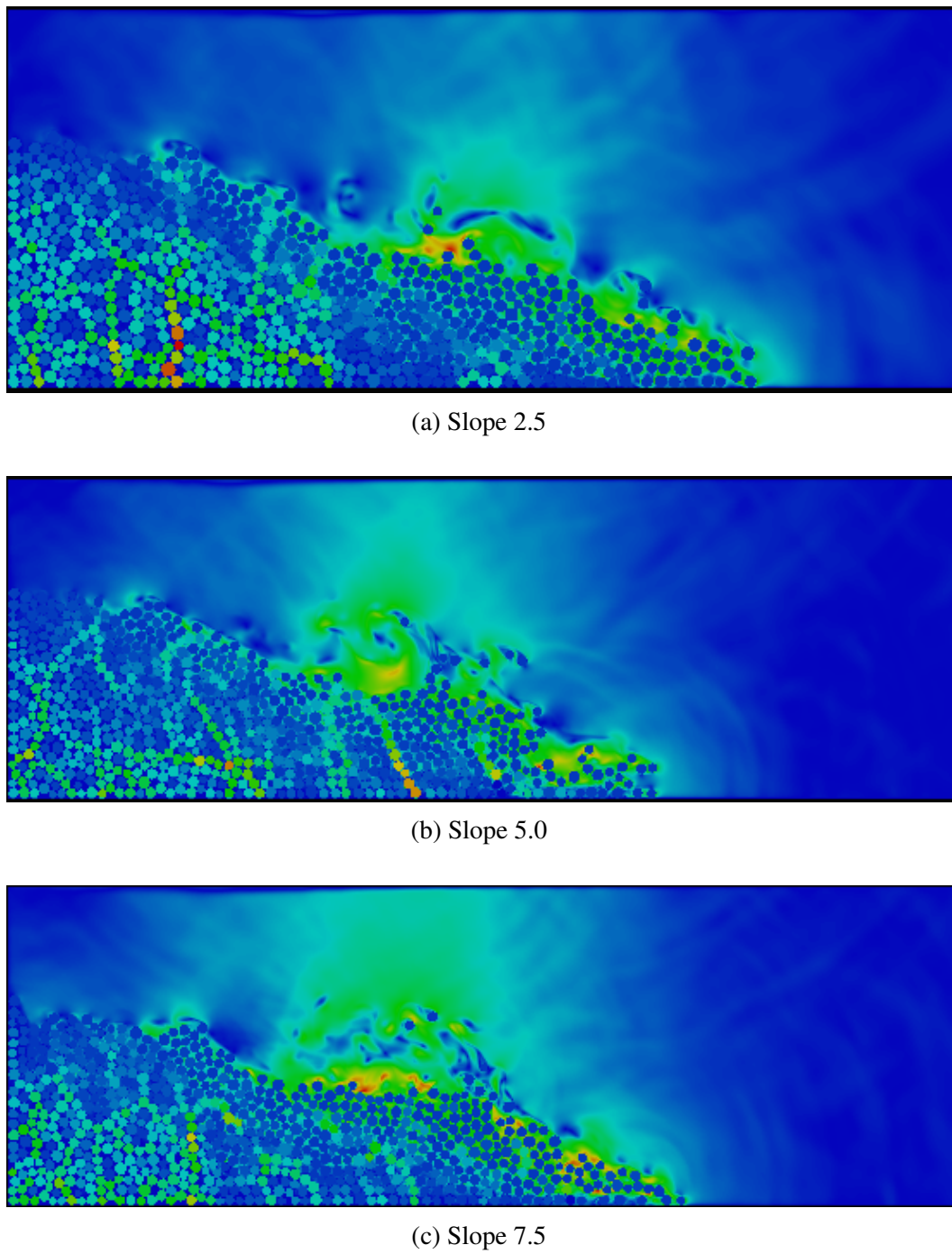


Figure 6.36 Flow morphology at  $t = 3\tau_c$  for different slope angles (dense)

probability of hydroplaning. The hydroplaning effect causes an increase in the flow velocity for the loose granular material in comparison with the dense condition (figure 6.37b).

In contrast to dense granular flows, loose granular flow exhibits a plug-like flow (figure 6.37a). Due to the low permeability, the water entrapped in the flow front results in a drop in the density of the flowing mass, which causes lower effective stress thus enabling lubrication. The turbulence effect observed on the surface of the dense granular flow is absent in the loose granular collapse. This, along with the lubrication effect, results in a longer run-out distance in the submerged condition for a loose granular column than the dry collapse.

The evolution of packing density for dry and loose collapse in fluid on different slope angles (figure 6.39) shows that, at the end of the flow, both the dense and the loose conditions reach similar packing density. The dense granular column dilates more, which results in large negative pore-pressure that is to be dissipated so as the granular mass is able to flow. Whereas in the loose condition, a positive pore-pressure is observed at the base of the flow, indicating entrainment of water at the base, i.e. lubrication and drop in the effective stress resulting in a longer run-out distance. The amount of water entrained in the loose granular column is higher than the dense condition, this can be observed by the low packing fraction observed between  $2\tau_c$  and  $5\tau_c$ .

Figure 6.40a shows the evolution of run-out with slope angle for an initially dense granular column. With increase in the slope angle, the run-out increases in both dry and submerged conditions. For all slope angles, the run-out in the dry condition is higher than the submerged conditions. As the slope angle increases, the drag force experienced by the dense granular column predominates over the lubrication effect on the run-out behaviour, this results in an increase in the difference between the dry and the submerged conditions with increase in the slope angle. Whereas with increase in slope angle, the loose granular column flows longer than the dry conditions. The longer run-out in the loose granular column collapse is due to hydroplaning experienced at the flow front as a result of entrainment of water. Figure 6.41 shows that for a given initial aspect ratio and slope angle, the run-out distance in the loose granular collapse in fluid is higher than the dense condition. This observation in fluid is in contrast to the dry condition, where the dense granular column flows longer due to higher initial potential energy. The low permeability observed in the loose granular flow ensures that water entrained at the base of the flow front is retained resulting in sustained lubrication effect. Also, the low permeability ensures that the density of the flowing mass remains in a slurry state resulting in a longer duration of hydroplaning. These effects in the loose granular column with low permeability condition result in a longer run-out distance.

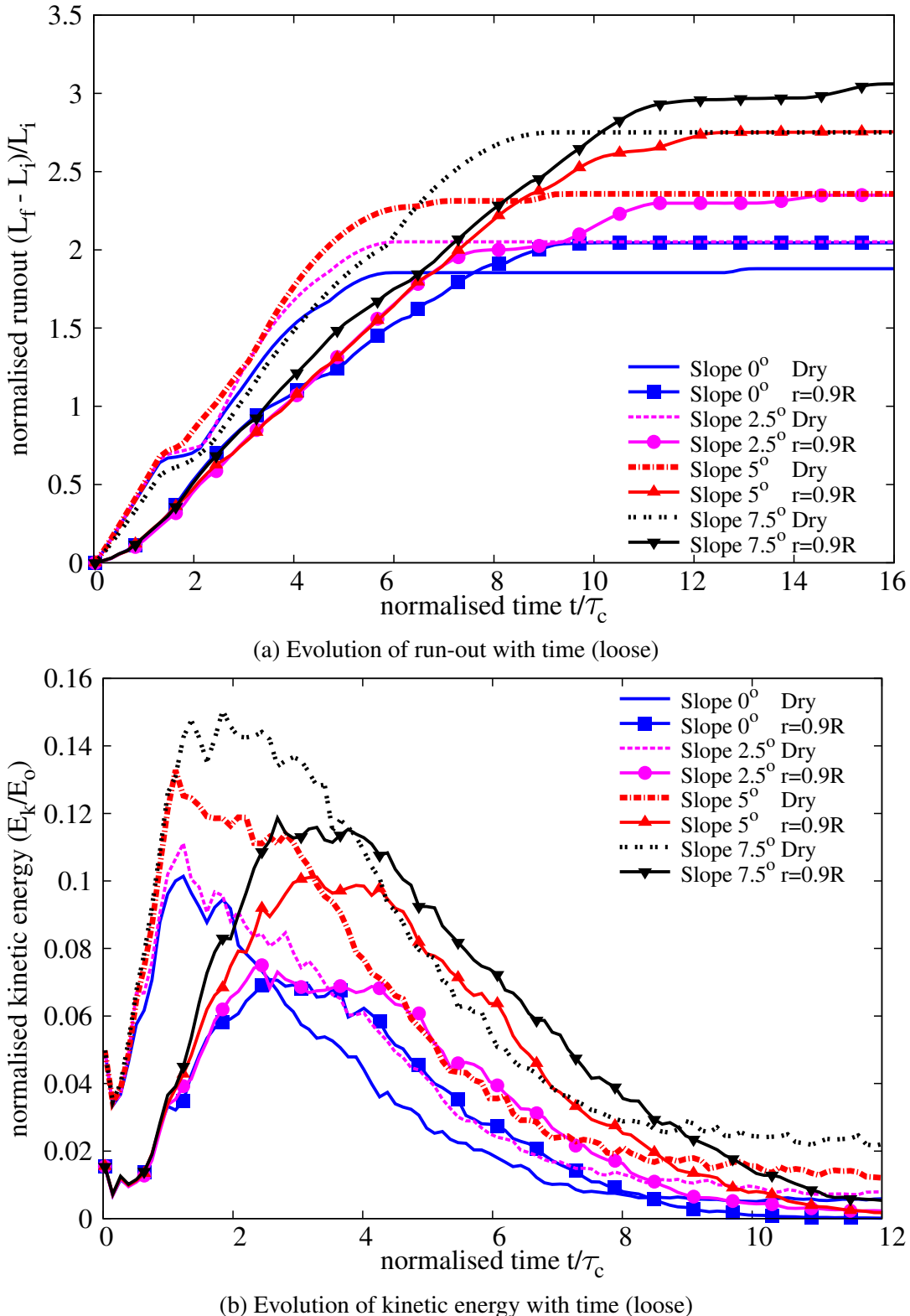
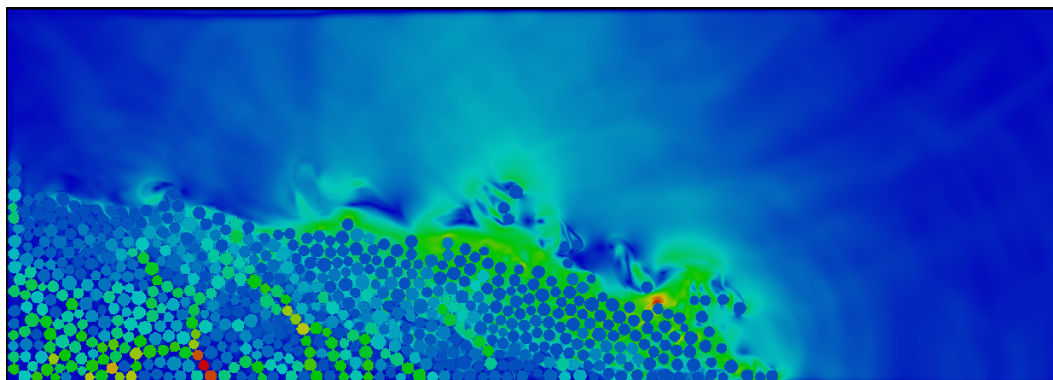
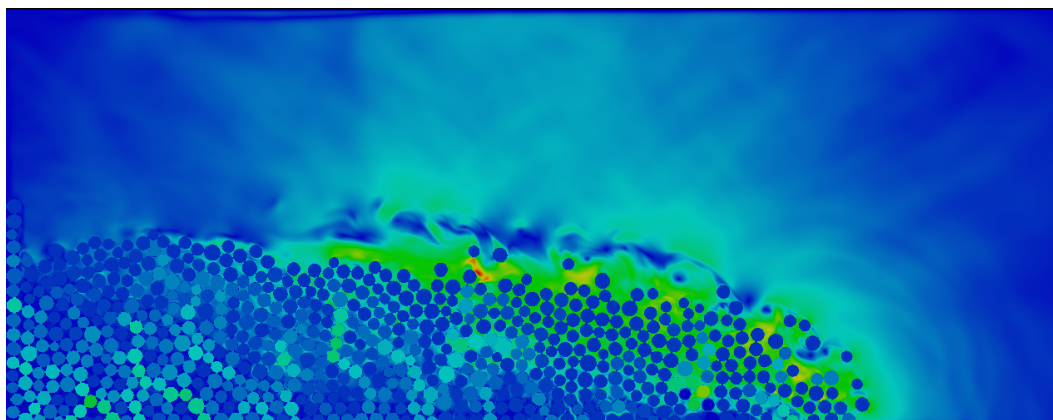


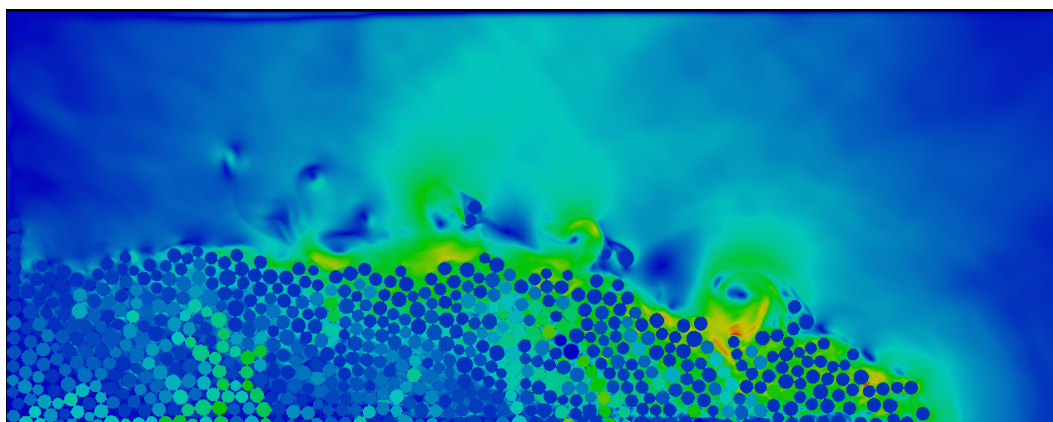
Figure 6.37 Evolution of run-out and kinetic energy with time (loose)



(a) Slope 2.5



(b) Slope 5.0



(c) Slope 7.5

Figure 6.38 Flow morphology at time  $t = 3\tau_c$  for different slope angles (loose)

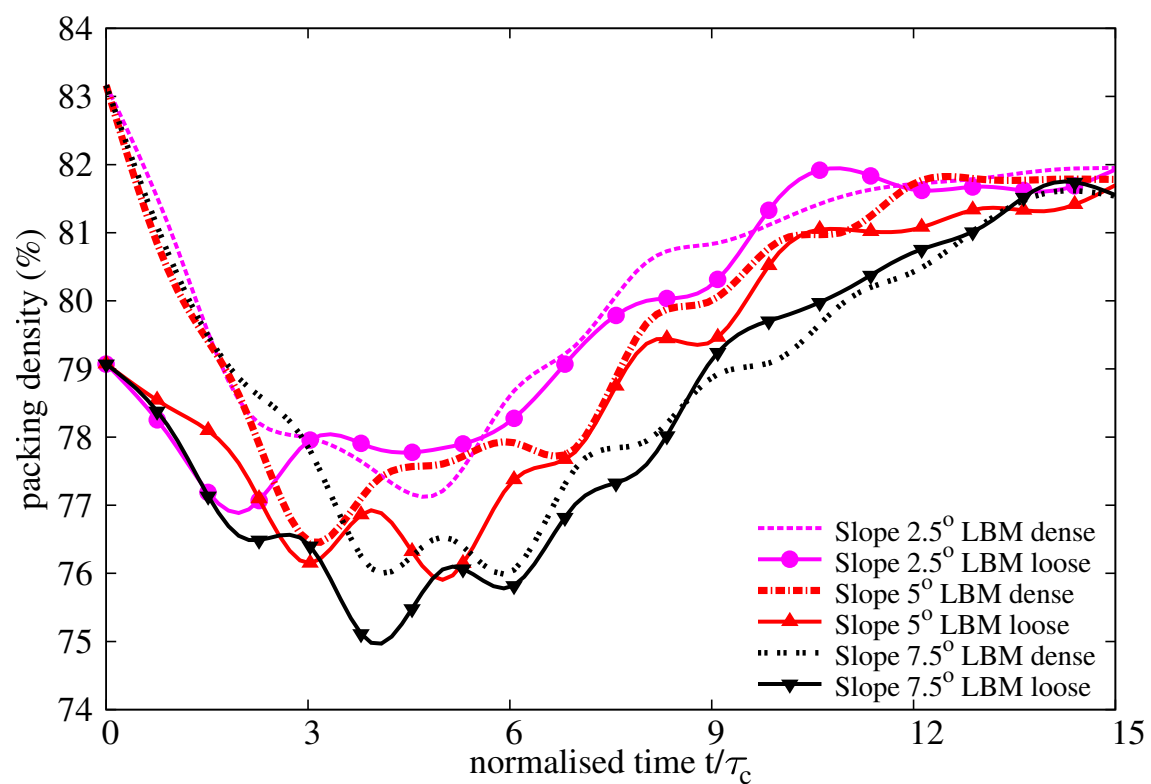
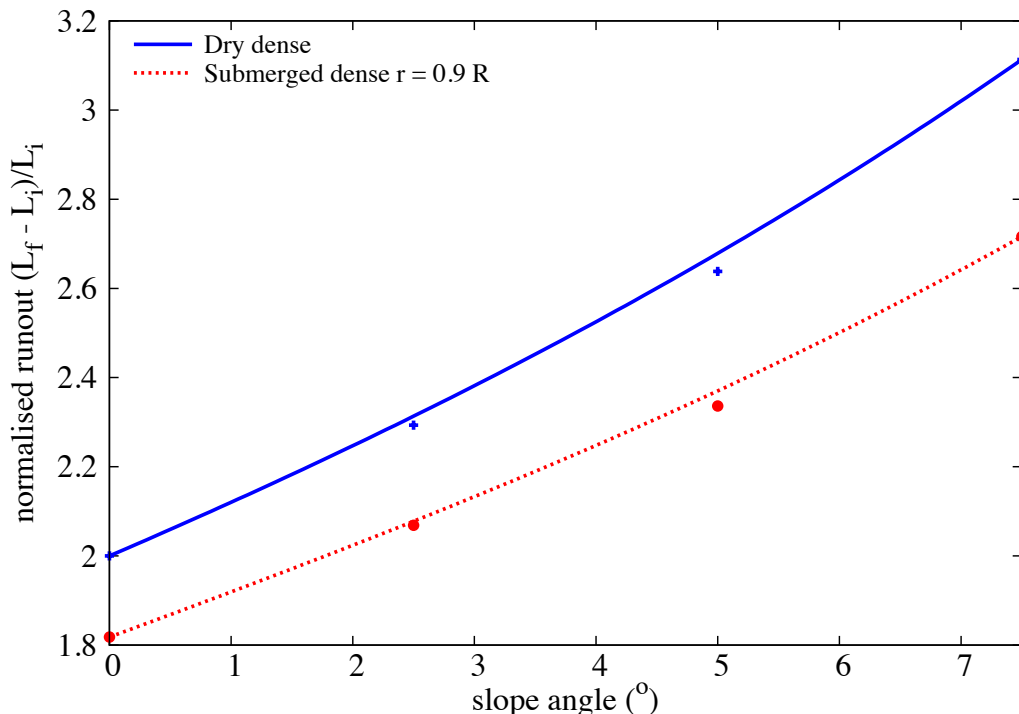
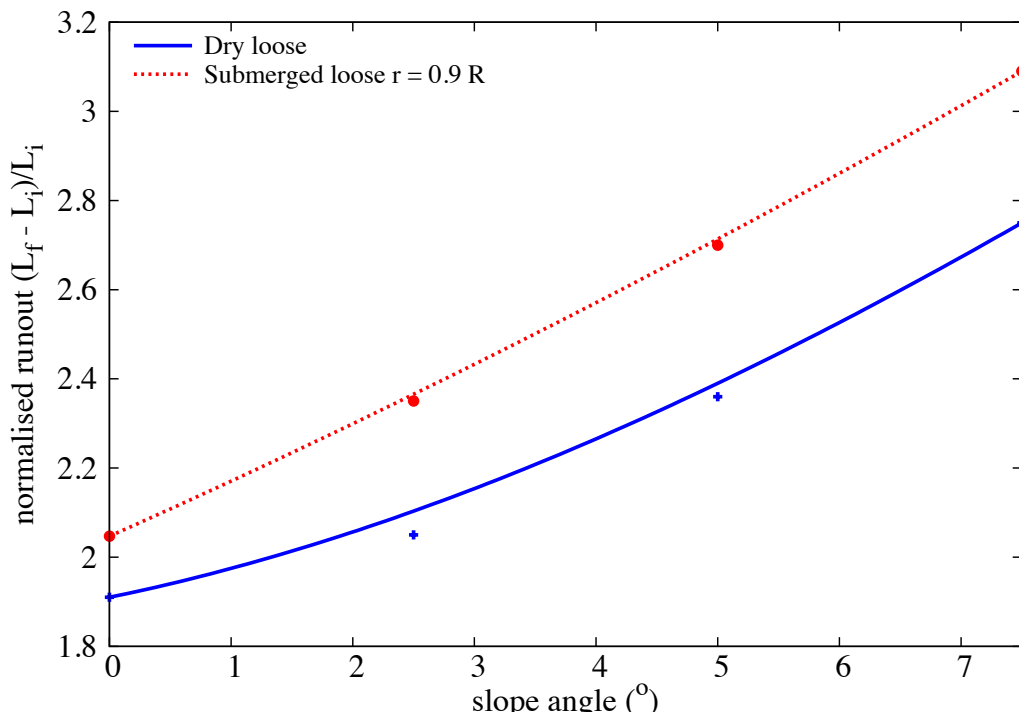


Figure 6.39 Evolution of packing density with time for different slope angles



(a) Dense



(b) Loose

Figure 6.40 Comparison between dry and submerged granular column on the effect of slope angle on the run-out distance (Dense and Loose).

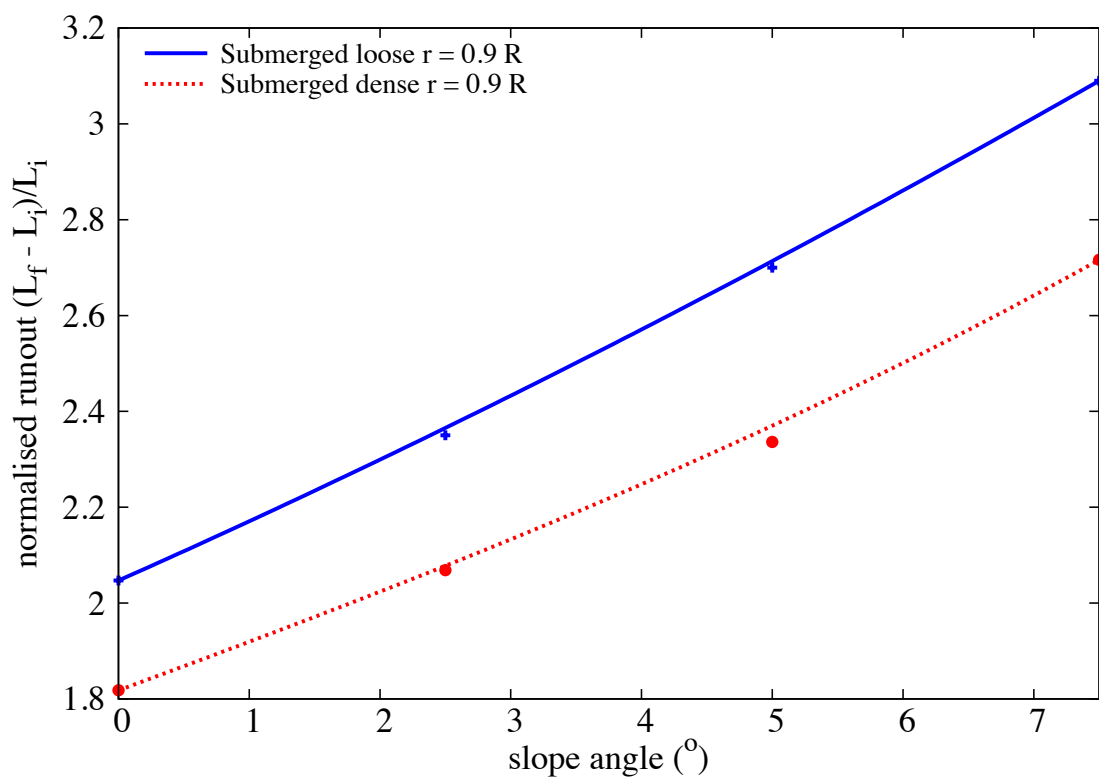


Figure 6.41 Effect of slope angle on the run-out behaviour for different initial packing density.

### 6.4.2 Effect of permeability

In order to understand the effect of permeability at a slope angle of  $5^\circ$ , the collapse of a granular column with an initial aspect ratio of 0.8 is simulated with different permeabilities. The hydrodynamic radius of a loosely packed granular column is varied from  $r = 0.7 R$  (high permeability), 0.75 R, 0.8 R, 0.85 R to 0.9 R (low permeability). The run-out distance is found to increase with decrease in the permeability of the granular assembly (figure 6.42a). The run-out distance for high permeable conditions ( $r = 0.7 R - 0.8 R$ ) are lower than their dry counterparts. Although, decrease in permeability resulted in an increase in the run-out distance, no significant change in the run-out behaviour is observed for a hydrodynamic radii of up to 0.8 R.

With further decrease in permeability ( $r = 0.85 R$  and  $0.9 R$ ), the run-out distance in the fluid is longer than that observed in the dry condition. At a very low permeability ( $r = 0.9 R$ ), the flowing granular mass entrains more water at the base, which causes a reduction in the effective stress accompanied by a lubrication effect. This can be seen by a significant increase in the peak kinetic energy and the sustained duration of the peak energy, in comparison to the dry and the highly permeable conditions (figure 6.43a). However, the permeability of the granular column did not have an influence on the evolution of height during the flow. But, the dry granular column tends to collapse more than the immersed granular column due to the lack of viscous dissipation (figure 6.42b).

Positive pore-pressure generation at the base of the flow is observed for low permeable conditions. Inspection of the local packing density showed entrainment of water at the base of the flow, which can also be observed by the steep decrease in the packing density (figure 6.43b) for the very low permeability condition ( $r = 0.9 R$ ). At the end of the flow ( $t \geq 10 \times \tau_c$ ), the excess pore-pressure dissipates and the granular flows, irrespective of their permeability, reach almost the same packing density.

Figure 6.45 shows the effect of permeability on the run-out behaviour for a dense and a loose granular column collapse on a slope of  $5^\circ$  and  $0^\circ$ . In both cases, the run-out distance increases with increase in the hydrodynamic radius (decrease in permeability). However in the dense case, the run-out distance observed in the fluid is shorter than the dry condition. Whereas in the loose condition, the run-out distance increases significantly at low permeabilities and results in a longer run-out distance in the submerged condition in comparison to the dry granular collapse. The comparison of loose and dense collapse on a slope of  $0^\circ$  and  $5^\circ$  shows that the initial packing density plays a significant role in the case of collapse on a horizontal plane, however at a slope of  $5^\circ$ , the run-out distance is unaffected by the initial packing density at high permeability conditions. This shows that at high permeabilities, the viscous drag forces predominate resulting in almost the same run-out

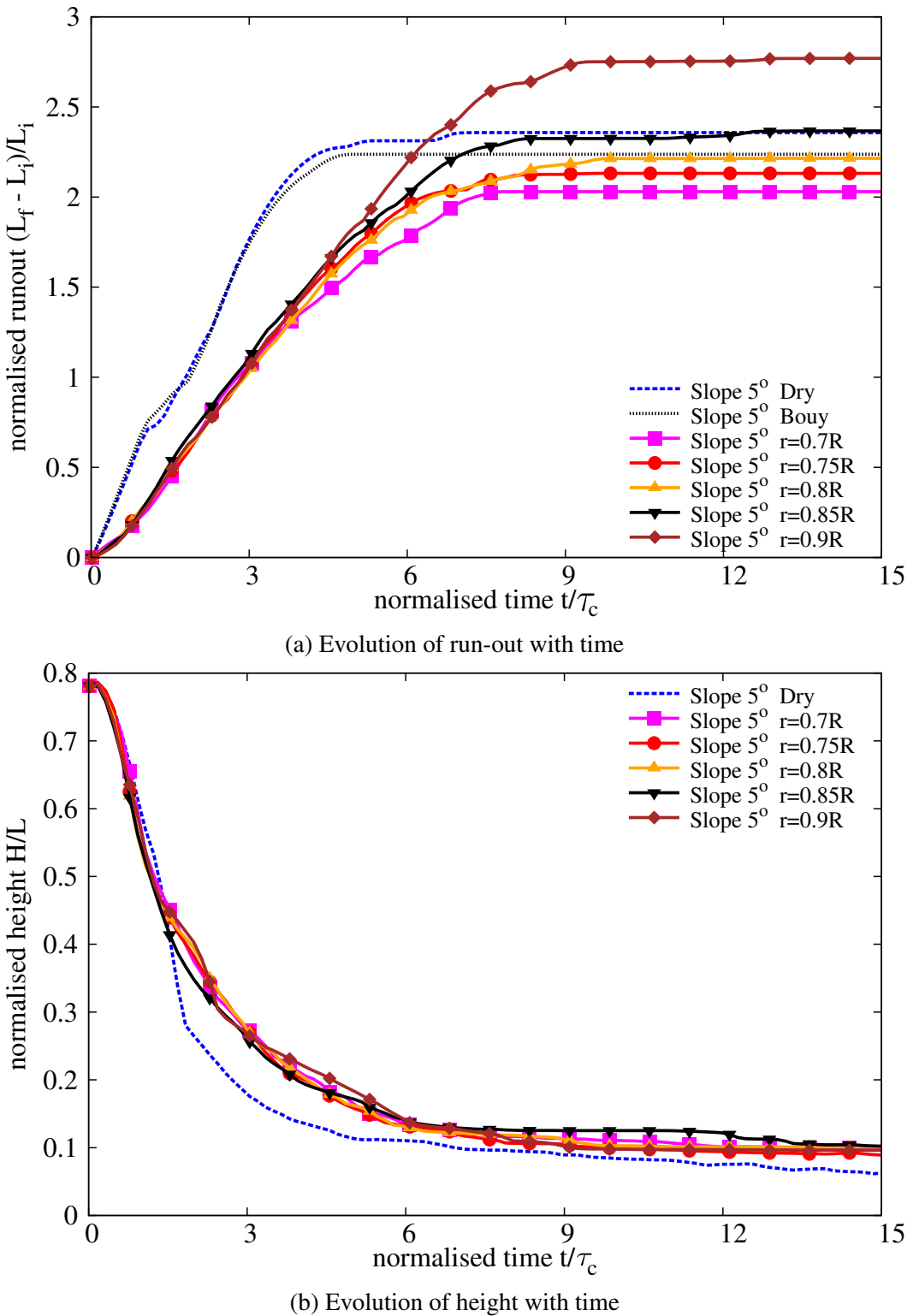


Figure 6.42 Evolution of run-out and height with time for different permeability (loose slope  $5^\circ$ )

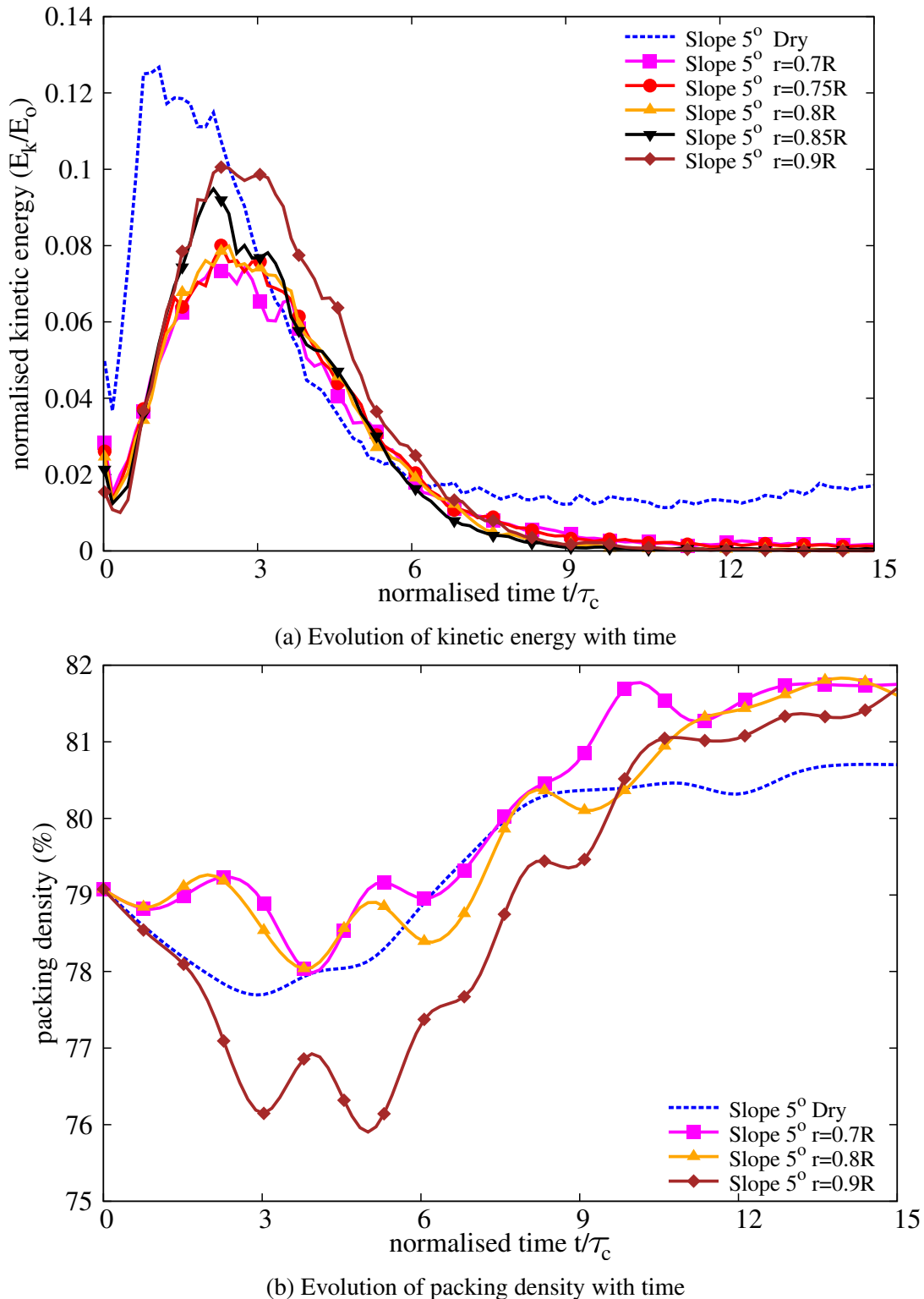


Figure 6.43 Evolution of kinetic energy and packing density with time for different permeability (loose slope  $5^\circ$ )

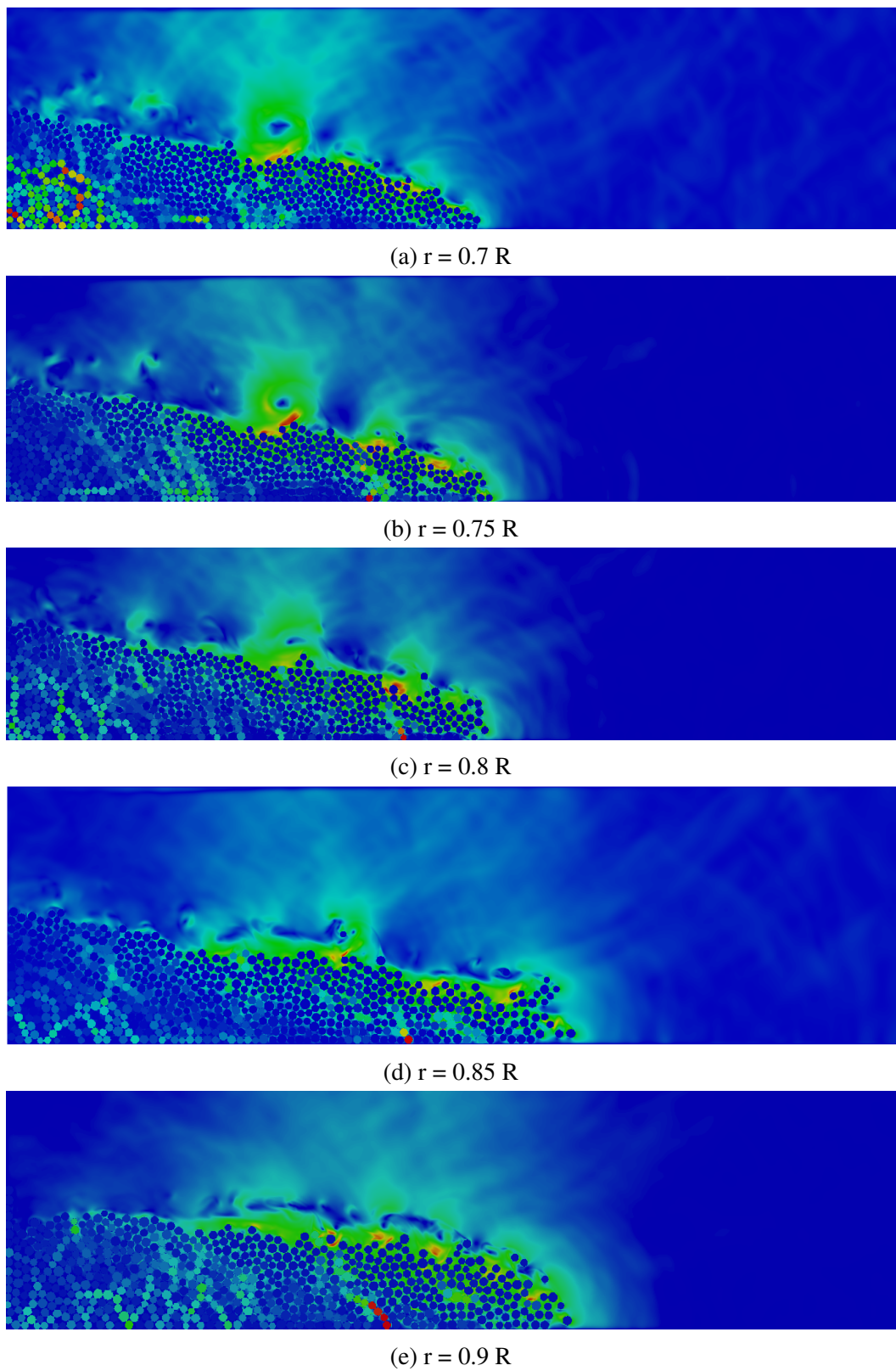


Figure 6.44 Evolution of the flow front at  $t = 3\tau_c$  for different permeabilities (loose slope  $5^\circ$ ).

distance for both dense and loose conditions. However at a low permeability ( $r = 0.9 R$ ), hydroplaning is observed in the case of loose granular column resulting in a substantially longer run-out distance than the dense granular column in submerged condition.

## 6.5 Tall columns

In the case of tall columns, the amount of material destabilised above the failure plane is larger than that of the short column. Hence in tall columns, the surface area of the mobilised mass that interacts with the surrounding fluid is significantly higher than the short columns. This increase in the area of soil - fluid interaction results in an increase in the formation of turbulent vortices that alter the deposit morphology during the collapse. It is observed that the vortices result in formation of heaps that significantly affects the distribution of mass in the flow (section 6.3.2). Staron and Hinch (2007) observed that the distribution of the mass in the granular flow plays a crucial role in the flow kinematics. In order to understand the behaviour of tall columns, the run-out behaviour of a dense granular column with an initial aspect ratio of 6 is studied. The collapse of a tall granular column on slopes of  $0^\circ$ ,  $2.5^\circ$ ,  $5^\circ$  and  $7.5^\circ$  are studied. A hydrodynamic radius of  $r = 0.85 R$  is adopted.

Snapshots of the collapse of an aspect ratio 6 column in fluid on a horizontal surface are shown in figure 6.47. The initial stage of collapse is characterised by the free-fall of grains above the failure surface. Unlike the dry condition, as the grains undergo free-fall due to gravity, they interact with the surrounding fluid experiencing drag forces. This results in a significant drop in the kinetic energy available for the flow. As the grains reach the static region, they interact with the neighbouring grains and the energy gained during the free fall is converted into horizontal acceleration. Uniquely during this stage ( $t = 3\tau_c$ ) the interactions between the soil grains on the surface with the surrounding fluid result in the formation of eddies. The number of eddies formed during the flow is proportional to the surface area of the granular mass interacting with the fluid. Hydroplaning can be observed at the flow front ( $t = 3\tau_c$ ). Two large vortices with almost the same size can be observed at the final stage of collapse. The soil grains on the surface experience suction due to formation of eddies and this results in formation of heaps of granular mass in front of each vortex. The formation of heaps, although in evidence, doesn't significantly affect the distribution of mass in the case of collapse on a horizontal plane.

Snapshots of the collapse of a granular column ( $a = 6$ ) on a inclined plane at angle of  $5^\circ$  are shown in figure 6.48. The collapse on a slope of  $5^\circ$  show flow evolution behaviour similar to the case of collapse on a horizontal plane. The vortices are formed only during the horizontal spreading stage  $t = 3\tau_c$ , but the number of vortices formed during the collapse

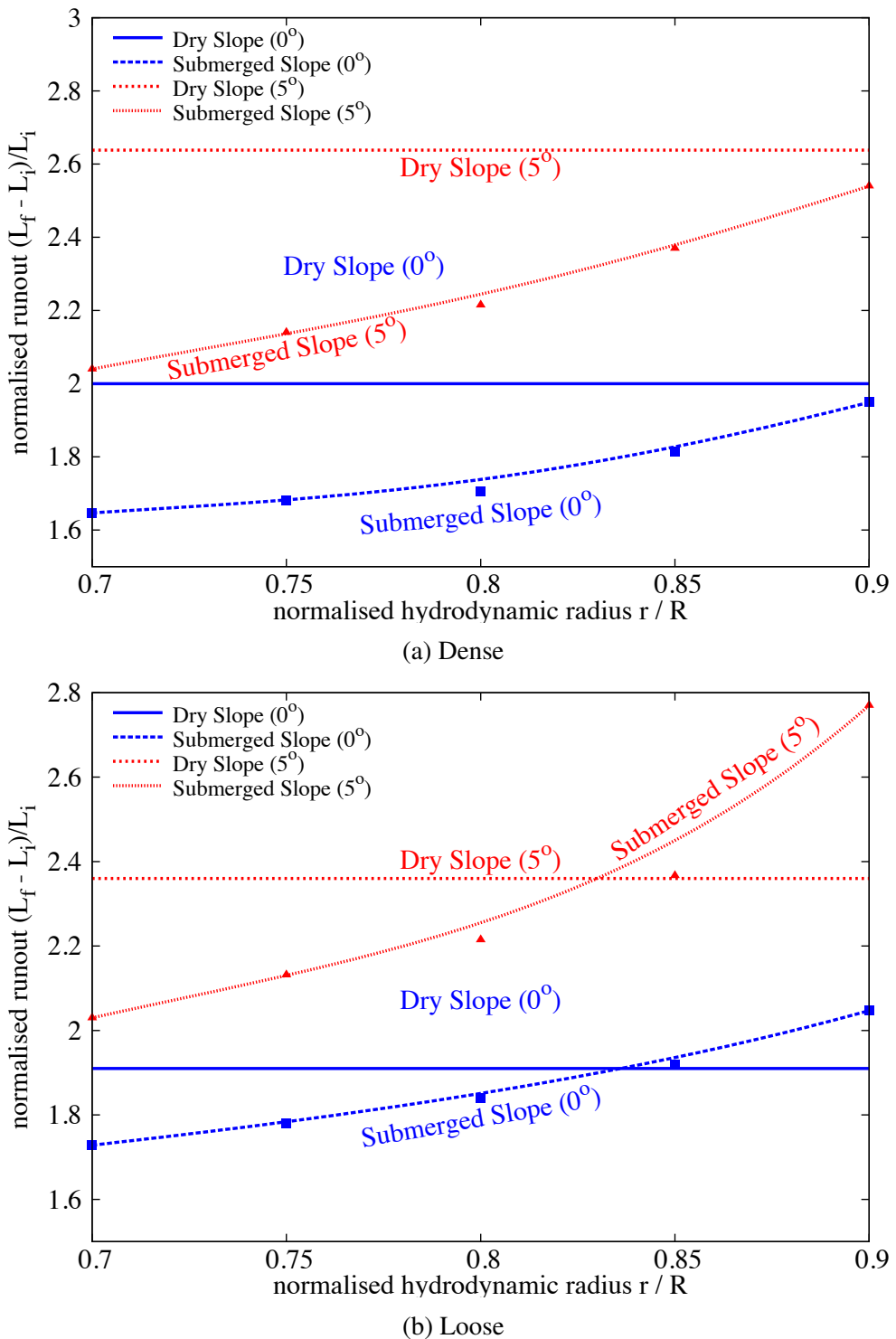


Figure 6.45 Comparison between dry and submerged granular column for a slope angle of  $0^\circ$  and  $5^\circ$  on the effect of permeability on the run-out distance (Dense and Loose).

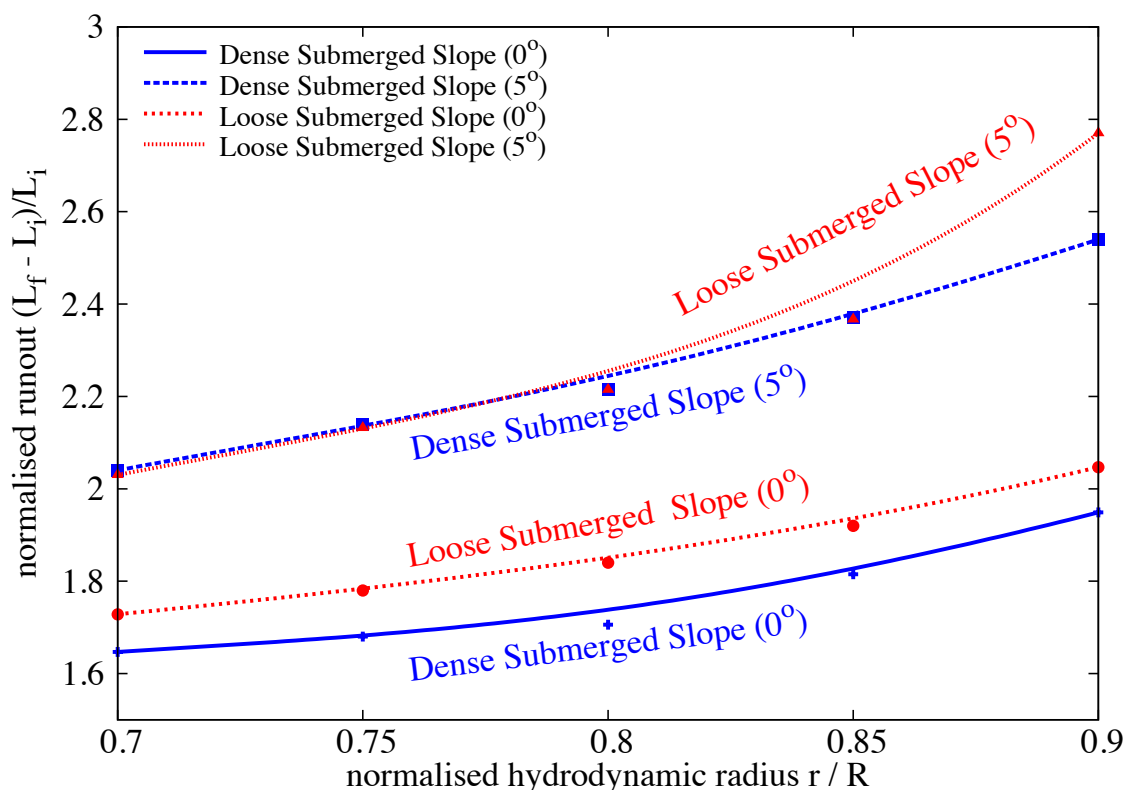


Figure 6.46 Effect of permeability on the run-out behaviour for different slope angle and the initial packing density.

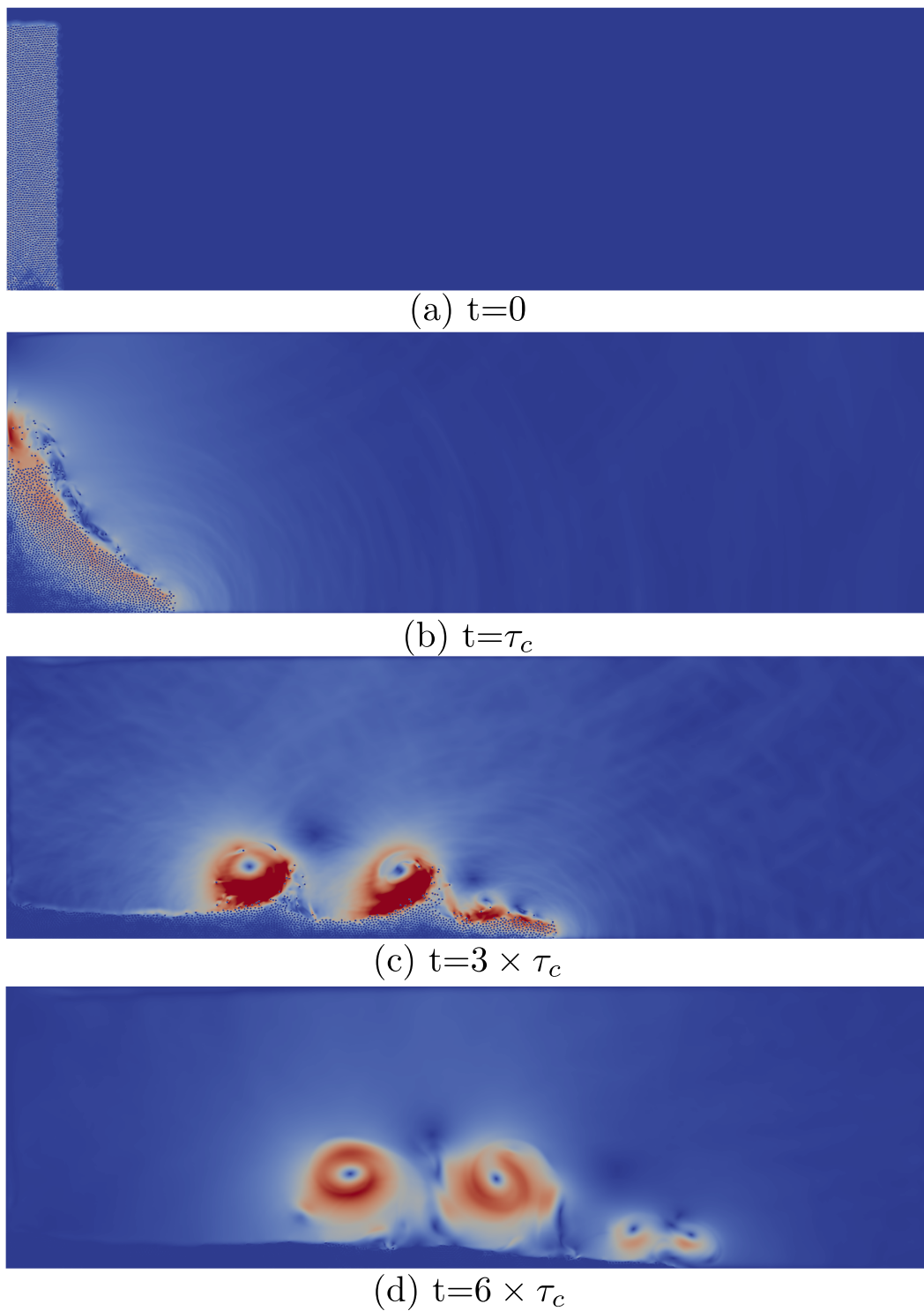


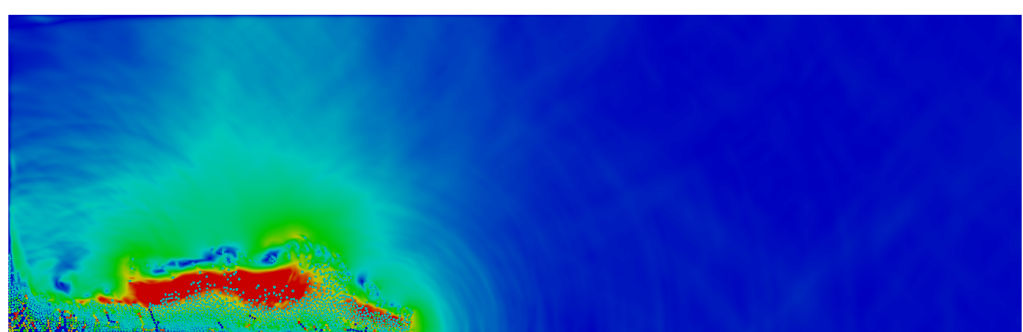
Figure 6.47 Flow evolution of a granular column collapse in fluid ( $a = 6$ ) on a horizontal surface

is higher than the collapse on a horizontal plane. However, as the flow progresses a single large vortex engulfs other smaller vortices, thus having a significant influence on the mass distribution. Figure 6.49 shows the distribution of mass and the packing density at  $t = 6\tau_c$  and  $t = 8\tau_c$ . A heap can be observed in front of the large vortex almost at the middle of the flow. The height of the heap is higher than the collapse height next to the wall. However, when the flow comes to rest and the vortex moves away from the flowing surface, the mass present in the heap gets redistributed (as seen at  $t = 8\tau_c$ ). This behaviour is significantly different from that observed in the case of short columns.

In order to understand the influence of slope angles on the run-out behaviour, the collapse of a granular column with an initial aspect ratio of 6 is performed on slopes of  $0^\circ$ ,  $2.5^\circ$ ,  $5^\circ$  and  $7.5^\circ$ . The run-out evolution with time for different slope angles are presented in figure 6.50a. The run-out distance increases with increase in the slope angle, however the run-out distance in the fluid is significantly shorter than the dry condition. The slow evolution of run-out in the submerged condition is due to the delay in the dissipation of large negative pore-pressure developed during the initial stage of the collapse. The formation of eddies during the flow indicates that most of the potential energy gained during the free-fall is dissipated through viscous drag and turbulence. This effect predominates over the hydroplaning that is observed during the flow resulting in a shorter run-out distance in the case of fluid. The evolution of the normalised height with time (figure 6.50b) for collapse on different slope angles indicates that the amount of material destabilised in fluid is less than the dry conditions due to the drag forces experienced by the grains, which retards the quantity and the rate of collapse.

Figure 6.51a shows the evolution of the normalised kinetic energy for a granular column ( $a = 6$ ) collapse in fluid on different slope angles. The amount of kinetic energy available for the flow in the submerged condition is almost half that of the dry condition. It can be seen from the figure that the vertical kinetic energy in the fluid condition is dissipate over a longer duration, in contrast to the free-fall release observed in the dry condition. The slower dissipation is attributed to the viscous drag force experienced by the grains and through formation of eddies.

The behaviour of tall columns are significantly different from that observed in the case of short columns. The slope angle has a strong influence on the number and size of eddies during the flow. The eddies interact with the surface of the granular flow and forms heaps in front of each vortex. This significantly affects the mass distribution and in turn the run-out evolution. Although tall cliffs are quite rare in submarine condition in comparison to short cliffs or slopes, further research is required to understand the influence of permeability and packing density on the run-out evolution of tall columns.

 $t = 0\tau_c$  $t = 1\tau_c$  $t = 3\tau_c$

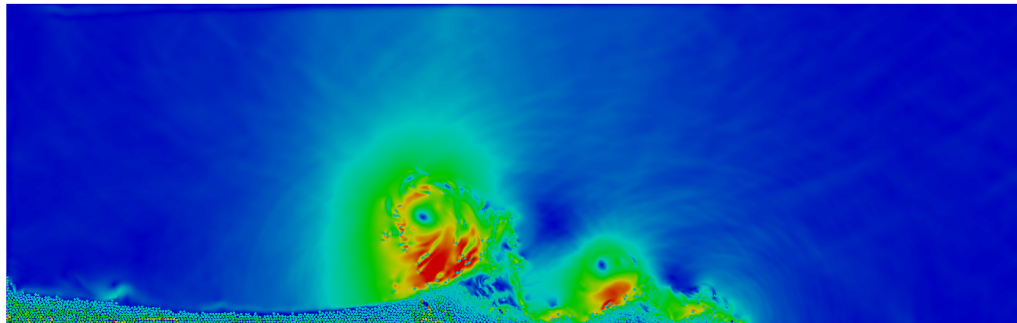
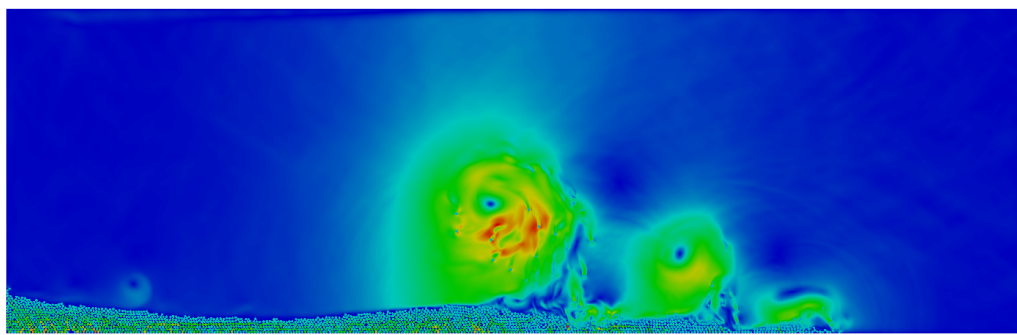
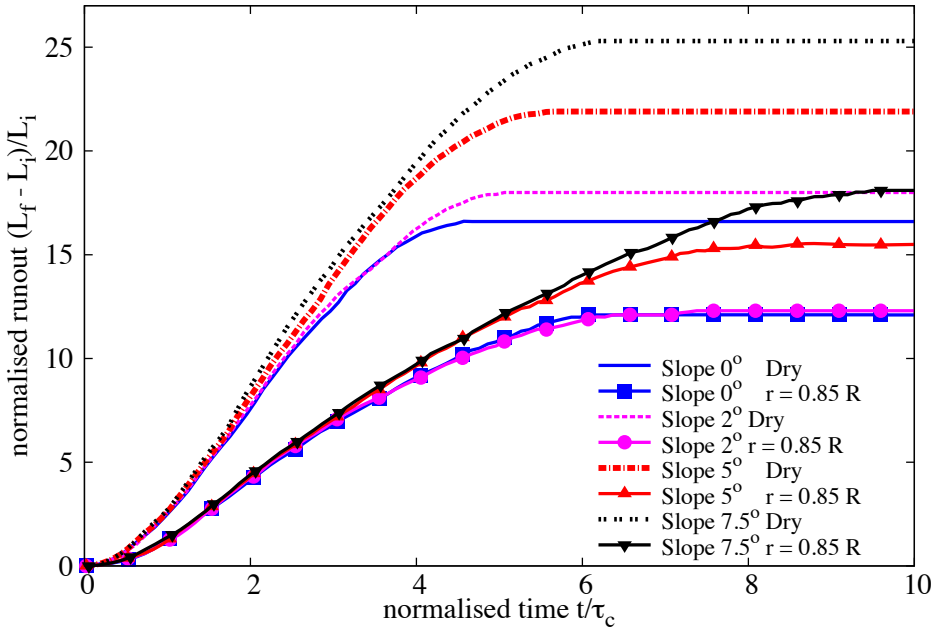
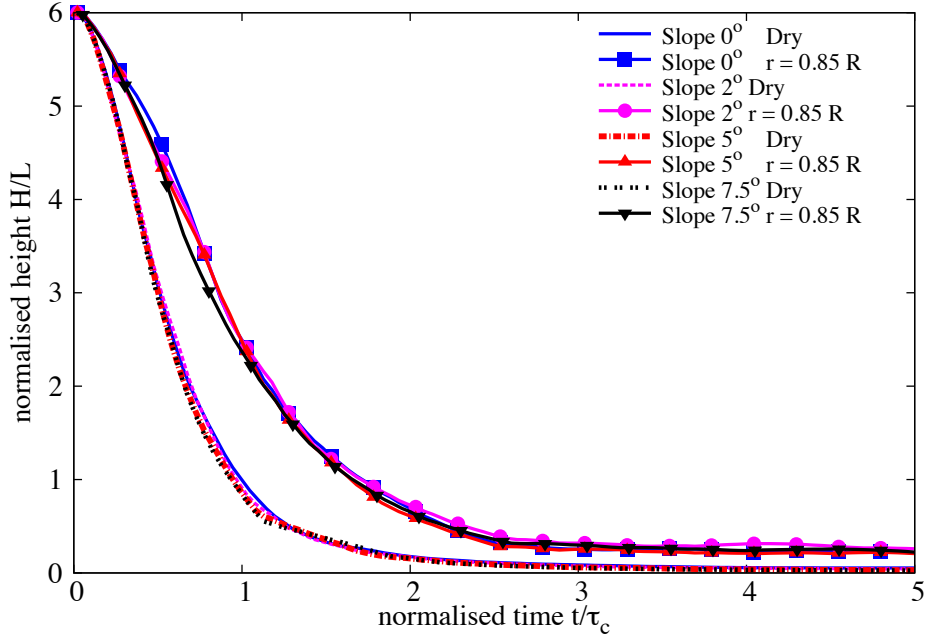
 $t = 6\tau_c$  $t = 8\tau_c$ 

Figure 6.48 Flow evolution of a granular column collapse in fluid ( $a = 6$ ) on a slope of  $5^\circ$ . Shows the velocity profile of fluid due to interaction with the grains (red - higher velocity).

 $t = 6\tau_c$  $t = 8\tau_c$ 

Figure 6.49 Packing density of a granular column collapse in fluid ( $a = 6$ ) on a slope of  $5^\circ$ .

(a) Evolution of run-out for a column collapse in fluid ( $a = 6$ ) on a slope of  $5^\circ$ (b) Evolution of height with time for a column collapse in fluid ( $a = 6$ ) on a slope of  $5^\circ$ Figure 6.50 Evolution of run-out and height for a column collapse in fluid ( $a = 6$ ) on a slope of  $5^\circ$

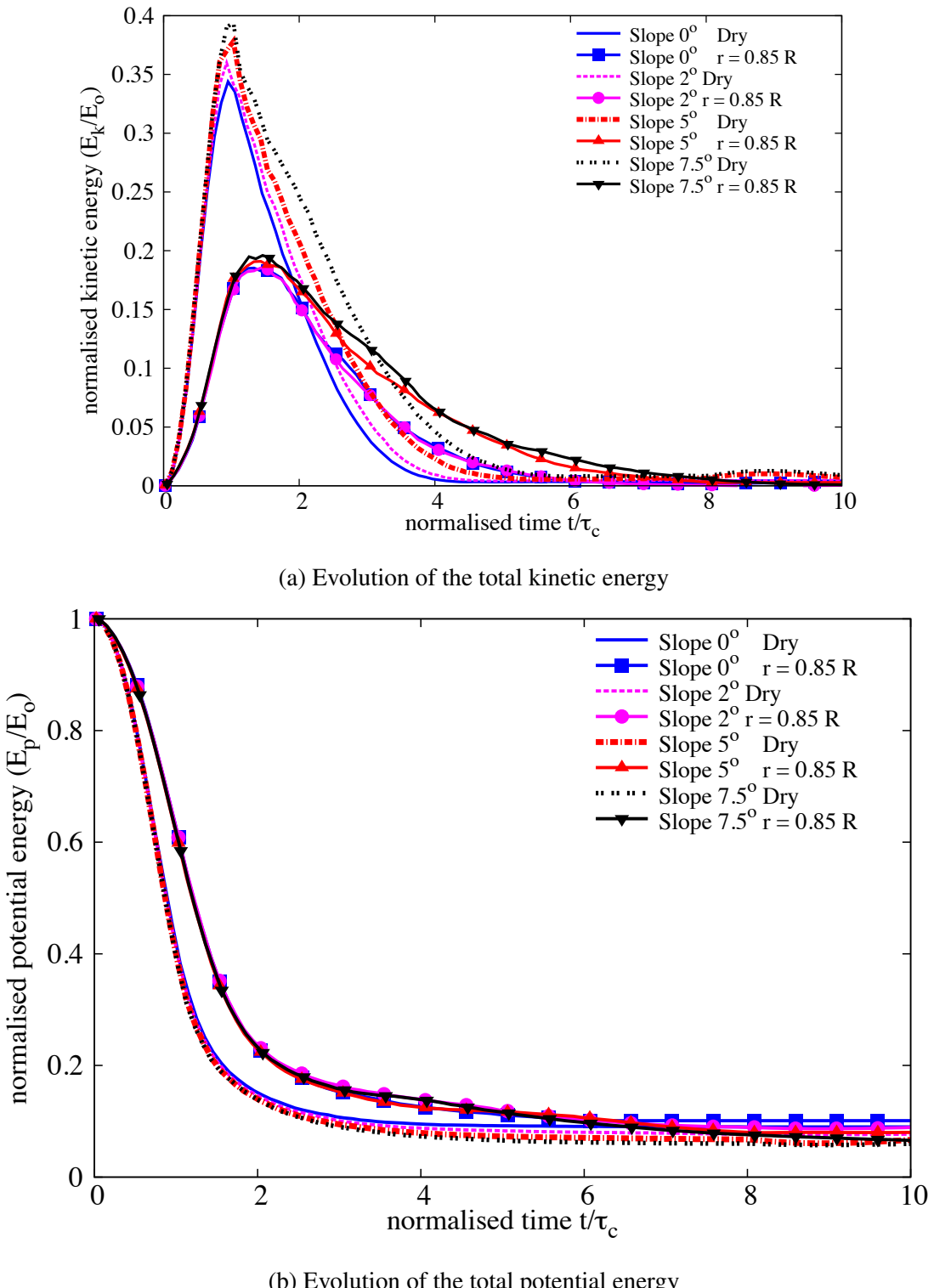


Figure 6.51 Evolution of the kinetic and the potential energy with time for a granular column collapse in fluid ( $a = 6$ ) on a slope of  $5^\circ$

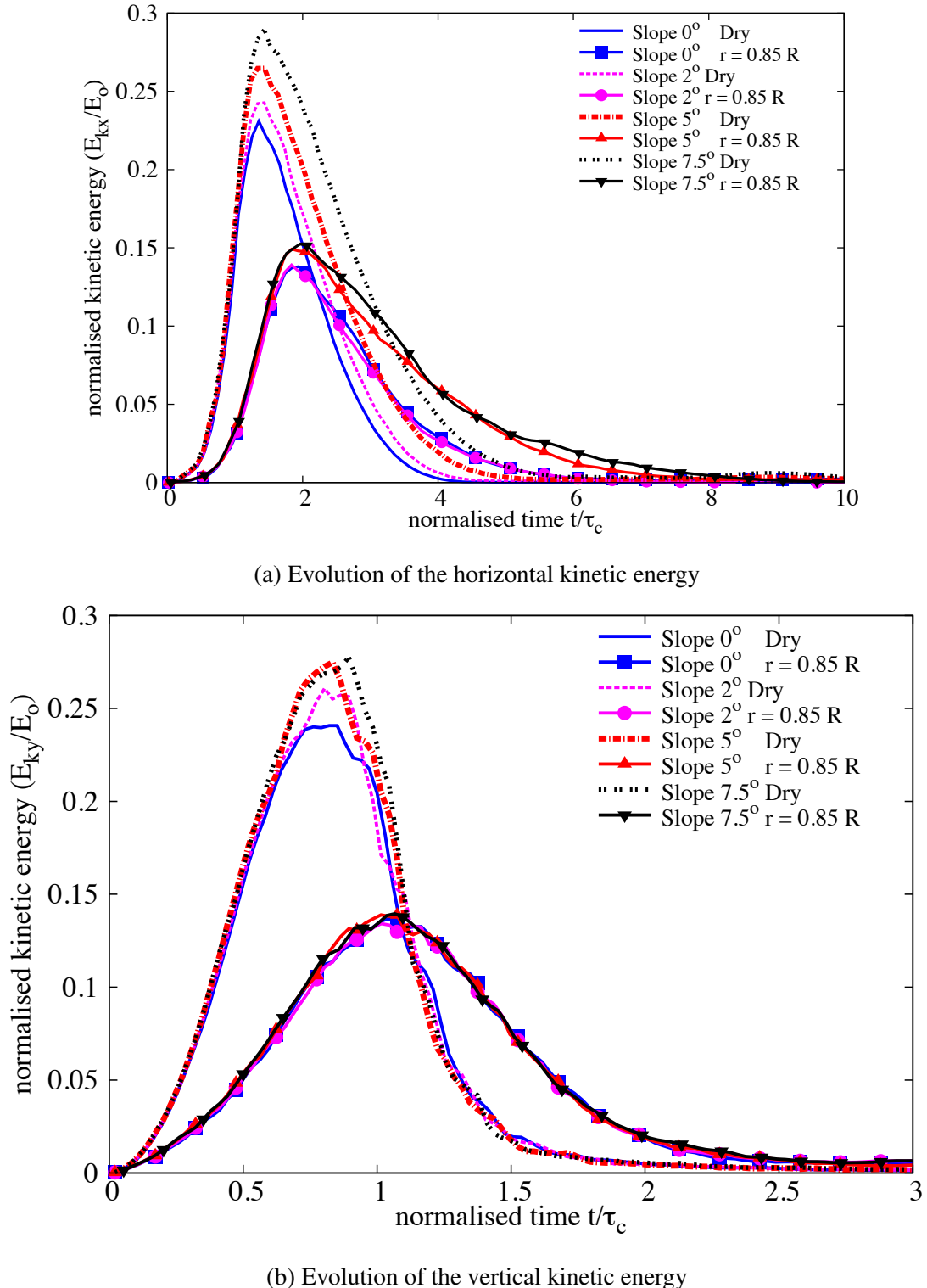


Figure 6.52 Evolution of the kinetic energies with time for a granular column collapse in fluid ( $a = 6$ ) on a slope of  $5^\circ$

## 6.6 Summary

Two-dimensional LB-DEM simulations are performed to understand the behaviour of submarine granular flows. Unlike dry granular collapse, the run-out behaviour in fluid is dictated by the initial volume fraction. Although previous studies have shown the influence of initial packing density on the run-out behaviour, a precise understanding of density, permeability and presence of fluid on the run-out behaviour was lacking. The following conclusion are derived based on this study:

- For dense columns, at all aspect ratios, the run-out in the dry case is significantly higher than the submerged condition.
- Granular columns with loose packing and low permeability tend to flow farther in comparison to dense columns and dry conditions, due to entrainment of water at the base of the flow front resulting in lubrication and/or hydroplaning.
- For the same thickness and velocity of the flow, the potential of hydroplaning is influenced by the density of the flowing mass. Loose columns are more likely to hydroplane than the dense granular masses, as they entrain more water at the flow front, leading to partial fluidisation.
- In both dense and loose conditions, the run-out distance increases with decrease in the permeability. An increase in the hydrodynamic radius from 0.7 to 0.95 R increases the normalised run-out by 25%.
- For the same value of peak kinetic energy, the run-out distance in fluid is longer than the dry column collapse. Also, with decrease in permeability the run-out distance increases for the same peak kinetic energy.
- The low permeability of the granular mass results in entrainment of water causing hydroplaning. At higher aspect ratios, decrease in permeability does not have a significant influence on the run-out behaviour, due to the turbulent nature of collapse of tall columns.
- With decrease in permeability, the duration for the flow to initiate increases as the time required to dissipate the large negative pore-pressure increases.
- The number of vortices formed during a collapse in fluid is found to be proportional to the amount of material destabilised. The vortices are formed only during the spreading stage of collapse.

- The formation of eddies during the collapse of tall columns indicates that most of the potential energy gained during the free-fall is dissipated through viscous drag and turbulence.
- For dense granular columns at various slope angles, the run-out in the dry condition is higher than the submerged conditions. Whereas with increase in slope angle, the loose granular column flows longer than the dry conditions.
- The initial packing density plays a significant role in the case of collapse on a horizontal plane, however at slope greater than  $5^\circ$ , the run-out distance is unaffected by the initial packing density at high permeability conditions.
- At high permeabilities, the viscous drag forces predominate for both dense and loose conditions. However at a low permeability ( $r = 0.9 R$ ), hydroplaning is observed in the case of loose condition.
- The behaviour of tall columns are significantly different from that observed in the case of short columns. The slope angle has a strong influence on the number and size of eddies during the flow. The eddies interact with the surface of the granular flow and forms heaps in front of each vortex. This significantly affects the mass distribution and in turn the run-out evolution of tall columns.



# **Chapter 7**

## **Conclusions and recommendations for future research**

### **7.1 Conclusions**

This PhD has made advances in several aspects of multi-scale modelling of granular flows and understanding the complex rheology of dry and submerged granular flows. The significant contributions of this PhD are summarised in this chapter.

#### **7.1.1 Multi-scale modelling of dry granular flows**

A multi-scale approach is adopted to study the granular flow behaviour. The material point method, a continuum approach, is used to model the macro-scale response, while the grain-scale behaviour is captured using a discrete element technique. In the present study, a two-dimensional DEM code is developed in C++ to study the micro-scale rheology of dry granular flows. The Verlet-list algorithm is implemented for neighbourhood detection to improve the computational efficiency. A linear-elastic model with a frictional contact behaviour is used to model dense rapid granular flows. A sweep-line Voronoi tessellation algorithm is implemented, in the present study, to extract continuum properties such as bulk density from the local grain-scale simulations.

In order to capture the macro-scale response, a template-based three-dimensional C++11 Material Point Method code, an Eulerian-Lagrangian approach, developed at the University of Cambridge, is modified and extended to study granular flows as a continuum. In the present study, the Generalised Interpolation Material Point GIMP method is implemented to reduce the cell-crossing noise and oscillations observed during large-deformation problems,

when using the standard MPM. The three-dimensional MPM code is parallelised to run on multi-core systems, thus improving the computational efficiency.

### **Granular column collapse**

Previous studies on granular collapse have shown a power-law dependence between the run-out and the initial aspect ratio of the column. However, the origin of power-law behaviour and the change in the run-out behaviour for tall columns have remained unexplained. Also, the reason for longer run-out distance for tall column using continuum approach was still lacking. Most studies were focused on mono-disperse grain sizes.

Multi-scale simulations of dry granular flows are performed to capture the local rheology, and to understand the capability and limitations of continuum models in realistic simulation of granular flow dynamics. For short columns, the run-out distance is found to be proportional to the granular mass destabilised above the failure surface. The spreading results from a Coulomb-like failure of the edges and is a frictional dissipation process. The continuum approach, using a simple frictional dissipation model, is able to capture the flow dynamics of short columns. Unlike short columns, the collapse of tall columns is characterised by an initial collisional regime and a power-law dependence between the run-out and the initial aspect ratio of the granular column is observed. MPM simulations show longer run-out behaviour in the case of tall columns. MPM simulation assumes that the total initial potential energy stored in the system is completely dissipated through friction over the entire run-out distance. The energy evolution study reveals that the lack of collisional dissipation mechanism in MPM results in a substantially longer run-out distance for large aspect ratio columns. The continuum approaches using frictional laws are able to capture the flow kinematics at small aspect ratios, which is characterised by an inertial number  $I$  less than 0.2 indicating a dense granular flow regime. However, a continuum approach like MPM is unable to precisely describe the flow dynamics of tall columns, which is characterised by an initial collisional regime ( $I > 0.2$ ). DEM studies on the role of initial material properties reveal that the initial packing fraction and the distribution of the kinetic energy in the system have a significant influence on the flow kinematics and the run-out behaviour. For the same material, a dense granular packing results in a longer run-out distance in comparison to the initially loose granular column. Hence it is important to consider macroscopic parameters like packing fraction and dilatancy behaviour, which are due to meso-scale grain arrangements, when modelling the granular system as a continuum.

### Granular slopes subjected to impact loading

The ability of MPM in modelling transient flows that do not involve collision is further investigated. In the present study, a multi-scale analyses of a granular slope subjected to impact velocities reveals a power-law dependence of the run-out distance and time as a function of the input energy with non-trivial exponents. The power-law behaviour is found to be a generic feature of granular dynamics. Two different regimes are observed depending on the input energy. The low energy regime reflects mainly the destabilisation of the pile, with a run-out time independent of the input energy. Whereas, the high energy regime involves spreading dynamics, which is characterised by a decay time that is defined as the time required for the input energy to decline by a factor 1/2.

The distribution of the kinetic energy in the system is found to have a significant influence in the low energy regime, where a large fraction of the input energy is consumed in the destabilisation process. However at higher input energy, where most of the energy is dissipated during the spreading phase, the run-out distance has a weak dependence on the distribution of velocity in the granular mass. The duration of the flow shows similar behaviour to the run-out, however, a slope subjected to a gradient velocity flows quicker than a slope subjected to a uniform impact velocity. The material characteristics of the granular slope affect the constant of proportionality and not the exponent in the power-law relation between the run-out and the input energy. The run-out distance and the decay time decrease as the friction increases. This effect is much more pronounced at low values of friction.

MPM is successfully able to simulate the transient evolution of granular flow with a single input parameter, the macroscopic friction angle. This study exemplifies the suitability of MPM, as a continuum approach, in modelling large-deformation granular flow dynamics and opens the possibility of realistic simulations of geological-scale flows on complex topographies.

#### 7.1.2 Granular flows in fluid

A two-dimensional coupled lattice Boltzmann - DEM technique is developed in C++ to understand the local rheology of granular flows in fluid. A multi-relaxation time LBM approach is implemented in the present study to ensure numerical stability. The coupled LBM-DEM technique offers the possibility to capture the intricate micro-scale effects such as the hydrodynamic instabilities. Coupled LBM-DEM involves modelling interactions of a few thousand soil grains with a few million fluid nodes. Hence, in the present study the LBM-DEM approach is implemented in the General Purpose Graphics Processing Units. The GPGPU implementation of the coupled LBM – DEM technique offers the capability

to model large scale fluid – grain systems, which are otherwise impossible to simulate using conventional computational techniques. In the present study, simulations involving up to 5000 soil grains interacting with 9 million LBM fluid nodes are modelled. Efficient data transfer mechanisms that achieve coalesced global memory ensure that the GPGPU implementation scales linearly with the domain size. Granular flows in fluid involve soil grains interacting with fluid resulting in formation of turbulent vortices. In order to model the turbulent nature of granular flows, the LBM-MRT technique is coupled with the Smargonisky turbulent model. The LBM-DEM code offers the possibility to simulate large-scale turbulent systems and probe micro-scale properties, which are otherwise impossible to capture in complex fluid - grain systems.

### **Granular collapse in fluid**

Unlike dry granular collapse, the run-out behaviour in fluid is dictated by the initial volume fraction. Although previous studies have shown the influence of initial packing density on the run-out behaviour, the effect of initial density, permeability, slope angle, aspect ratio and presence of fluid on the run-out behaviour have largely been ignored. The difference in the mechanism of flow behaviour between dense and loose granular column was not precisely understood. Previous studies have shown that only the dry collapse results in the farthest run-out in comparison with submerged conditions. Two-dimensional LB-DEM simulations are performed to understand the behaviour of submarine granular flows and the influence of various parameters on the flow dynamics.

Two-dimensional LB-DEM simulations pose a problem of non-interconnected pore-space between the soil grains, which are in contact with each other. In the present study, a hydrodynamic radius, a reduction in the radius of the grains, is adopted during the LBM computation stage to ensure continuous pore-space for the fluid flow. A relation between the hydrodynamic radius and the permeability of the granular media is obtained.

In order to understand the difference in the mechanism of granular flows in the dry and submarine conditions, LBM-DEM simulations of granular column collapse are performed and are compared with the dry case. Unlike the dry granular collapse, the run-out behaviour in fluid is found to be dictated by the initial volume fraction. For dense granular columns, the run-out distance in fluid is much shorter than its dry counterpart. Dense granular columns experience significantly high drag force and develop large negative pore-pressure during the initial stage of collapse resulting in a shorter run-out distance. On the contrary, granular columns with loose packing and low permeability tend to flow further in comparison to dry granular columns. This is due to entrainment of water at the flow front leading to hydroplaning.

In both dense and loose initial packing conditions, the run-out distance is found to increase with decrease in the permeability. An increase in the hydrodynamic radius from 0.7 to 0.95 R increases the normalised run-out by 25%. With decrease in permeability, the duration required for the flow to initiate takes longer due to the development of large negative pore-pressure. However, the low permeability of the granular mass results in entrainment of water at the flow front causing hydroplaning. For the same thickness and velocity of the flow, the potential for hydroplaning is influenced by the density of the flowing mass. Loose columns are more likely to hydroplane than the dense granular masses resulting in a longer run-out distance. This is in contrast to the behaviour observed in the dry collapse, where dense granular columns flow longer in comparison to loose columns.

Similar to the dry condition, a power-law relation is observed between the initial aspect ratio and the run-out distance in fluid. For a given aspect ratio and initial packing density, the run-out distance in the dry case is usually longer than the submerged condition. However, for the same kinetic energy, the run-out distance in fluid is found to be significantly higher than the dry conditions. The run-out distance in the granular collapse has a power-law relation with the peak kinetic energy. For the same peak kinetic energy, the run-out distance is found to increase with decrease in the permeability. The permeability, a material property, affects the constant of proportionality and not the exponent of the power-law relation between the run-out and the peak kinetic energy.

The number of vortices formed during a collapse in fluid is found to be proportional to the amount of material destabilised. The vortices are formed only during the spreading stage of collapse. The formation of eddies during the collapse of tall columns indicates that most of the potential energy gained during the free-fall is dissipated through viscous drag and turbulence

### **Granular collapse down inclined planes**

The influence of slope angle on the effect of permeability and the initial packing density on the run-out behaviour are studied. For increase in slope angle, the viscous drag on the dense column tends to predominate over the influence of hydroplaning on the run-out behaviour. The difference in the run-out between the dry and the submerged conditions, for a dense granular assembly, increases with increase in the slope angle above an inclination of 5°. In contrast to the dense granular columns, the loose granular columns show a longer run-out distance in immersed conditions. The run-out distance increases with increase in the slope angle in comparison to the dry cases. The low permeable loose granular column retains the water entrained at the base of the flow front resulting in sustained lubrication effect. In

contrast to the dry granular collapse, for all slope inclinations, the loose granular column in fluid flows further than the dense column.

For granular collapse on inclined planes, the run-out distance is unaffected by the initial packing density at high permeability conditions. For collapse down inclined planes at high permeabilities, the viscous drag forces predominate resulting in almost the same run-out distance for both dense and loose initial conditions. However, at low permeability the entrainment of water at the flow front and the reduction in the effective stress of the flowing mass result in a longer run-out distance in the loose condition than the dense case as the slope angle increases.

In tall columns, the run-out behaviour is found to be influenced by the formation of vortices during the collapse. The interaction of the surface grains with the surround fluid results in formation of vortices uniquely during the horizontal acceleration stage. The vortices result in redistribution of granular mass and thus affect the run-out behaviour. This effect is predominant on steeper slopes.

## 7.2 Recommendations for future research

Further research can be pursued along two directions: *a.* improvement of the numerical tools and constitutive models to realistically simulate large-deformation problems and *b.* investigation of the rheology of granular flows using experimental and numerical tools.

### 7.2.1 Development of numerical tools

#### Discrete element method

The two-dimensional discrete element method, developed in the present study, can be extended to three-dimensions to model realistic soil flow problems. Although the linear-elastic contact model is found to be sufficient to describe rapid granular flows, further research using Hertz-Mindlin or other advanced contact model shall be performed. DEM is limited by the number of grains that can be simulated. Hence, it is important to be able to run DEM simulations on multi-core systems or on GPUs to model large-scale geometries. The initial grain properties are found to have a significant influence on the run-out behaviour, hence, it is vital to model grains of different shapes to understand their influence on the run-out distance. Agglomerates can also be used to study the effect of grain-crushing as the flow progresses down slope.

### Material point method

The present MPM code is capable of solving both 2D and 3D granular flow problems. Further research should focus on modelling three-dimensional granular flow problems and validate the suitability of MPM in modelling geological scale run-out behaviours. As the scale of the domain increases, the computational time increases especially when using GIMP method. To improve the computational efficiency, the material point method developed in the present study shall be modified to run on large clusters. The dynamic re-meshing technique (Shin, 2010) shall be implemented to efficiently solve large deformation problems. The dynamic meshing approach is useful for problems involving motion of a finite size body in unbounded domains, in which the extent of material run-out and the deformation is unknown *a priori*. The approach involves searching for cells that only contain material points, thereby avoiding unnecessary storage and computation.

The current MPM code is capable of handling fluid-solid interactions in two-dimensions. Further research shall be pursued to implement fully coupled 3D material point method. The MPM code can also be extended to include the phase-transition behaviour in a continuum domain for partially fluidized granular flows (Aranson and Tsimring, 2001, 2002; Volfson et al., 2003). Fluid - solid interactions result in pressure oscillations. Further research is essential to explore advanced stabilisation methods that can be used to avoid the oscillations that occur due to incompressibility.

### Lattice Boltzmann - DEM coupling

The GPGPU parallelised 2D LBM-DEM coupled code, developed in the present study, shall be extended to three-dimensions. This would require a very high computational cost and hence it is important to parallelise the LBM-DEM code across multiple GPUs through a Message Passing Interface (MPI) similar to a large cluster parallelisation. A three-phase system of granular solids, water and air can be developed to realistically capture debris flow behaviour. The LB code can be extended to include a free surface, which can be used to investigate the influence of submarine mass movements on the free surface, such as tsunami generation.

### Constitutive models

DEM simulations of granular flow problems reveal that the initial material properties play a crucial role on the run-out evolution. The granular materials experience change in the packing fraction as the flow progresses. Hence, it is important to consider advanced models such as Nor-Sand, a critical state based model, and  $\mu(I)$  to model the dense granular flows.

The behaviour of the soil under large deformations can be better expressed with a critical state model. The modified Nor-Sand constitutive model (Robert, 2010) implemented in the present study can be used in large-deformation flow problems. The  $\mu(I)$  rheology, which is capable of capturing the complex rheology of dense granular flow, can be extended to include the effect of fluid viscosity (Pouliquen et al., 2005) to model granular flows in fluids.

### 7.2.2 Understanding the rheology of granular flows

#### Granular column collapse

Although, two-dimensional simulations provide a good understanding of the physics of granular flows, it is important to perform three-dimensional analysis to understand the realistic granular flow behaviour. Multi-scale simulations of three dimensional granular collapse experiments can be performed in dry and submerged conditions to understand the flow kinematics. Further research is essential to quantify the influence of initial packing density, shape and size of grains on the run-out behaviour for different initial aspect ratios. This would provide a basis for macro-scale parameters that are required to model the granular flow behaviour in a continuum scale.

#### Slopes subjected to impact

This work may be pursued along two directions: *a.* experimental realization of a similar set-up with different modes of energy injection and *b.* investigating the effect of various particle shapes or the presence of an ambient fluid. Although numerical simulations are generally reliable with realistic results found in the past studies of steady flows, the transient phases are more sensitive than steady flows and hence experimental investigation are necessary for validation. This configuration is also interesting for the investigation of the behaviour of a submerged slope subjected to an earthquake loading.

#### Granular flow down inclined planes

Multi-scale analyses of large deformation flow problems such as the flow of dry granular materials down an inclined flume can be performed. This analysis will provide an insight on the limits of the continuum approach in modelling large deformation problems, which involve high shear-rates. The influence of parameters, such as particle size, density, packing and dilation, on the flow dynamics can be explored. These studies will be useful in describing the granular flow behaviour using the  $\mu(I)$  rheology.

**Granular flows in fluid**

Three dimensional LBM-DEM simulations of granular collapse in fluid can be carried out with varying shape, friction angle and size of particles to understand the influence of initial material properties on the run-out behaviour. Parametric analyses on the initial properties can be used to develop a non-dimensional number that is capable of delineating different flow regimes observed in granular flows in a fluid. Further research can be carried out on the collapse of tall columns and the influence of vortices on the run-out behaviour and re-distribution of the granular mass during the flow.

**flow** collapse  
**run-out**  
**material**  
**grains**  
**granular**  
**behaviour**  
**MPM** initial grain stress  
study critical evolution packing dense horizontal effect  
distribution points order simulation deformation high  
case ratio model dynamics dry  
influence boundary condition large  
continuum lattice understand  
However particle failure significant  
important friction fraction capture  
two soil resulting fraction  
results applied scale found capture  
front simple

# References

- Abe, K., Johansson, J., and Konagi, K. (2006). A new method for the run-out analysis and motion prediction of rapid and long travelling landslides with MPM. *Doboku Gakkai Ronbunshuu*, 63:93–109 (in Japanese).
- Abe, K., Soga, K., and Bandara, S. (2013). Material Point Method for Coupled Hydromechanical Problems. *Journal of Geotechnical and Geoenvironmental Engineering*.
- Agnolin, I. and Roux, J.-N. (2007). Internal states of model isotropic granular packings. I. Assembling process, geometry, and contact networks. *Phys. Rev. E*, 76(6):061302.
- Aidun, C., Lu, Y., and Ding, E. (1998). Direct analysis of particulate suspensions with inertia using the discrete Boltzmann equation. *Journal of Fluid Mechanics*, 373(-1):287–311.
- Andersen, S. and Andersen, L. (2010). Modelling of landslides with the material-point method. *Computational Geosciences*, 14(1):137–147.
- Aranson, I. S. and Tsimring, L. S. (2001). Continuum description of avalanches in granular media. *Physical Review E - Statistical, Nonlinear, and Soft Matter Physics*, 64(2 I):203011–203014.
- Aranson, I. S. and Tsimring, L. S. (2002). Continuum theory of partially fluidized granular flows. *Physical Review E*, 65(6):061303.
- Augarde, C. and Heaney, C. (2009). The use of meshless methods in geotechnics. In *Proceedings of the 1st International Symposium on Computational Geomechanics*, France.
- Bagnold, R. (1954). Experiments on a gravity-free dispersion of large solid spheres in a Newtonian fluid under shear. *Proceedings of the Royal Society of London. Series A. Mathematical and Physical Sciences*, 225(1160):49.
- Balmforth, N. J. and Kerswell, R. R. (2005). Granular collapse in two dimensions. *Journal of Fluid Mechanics*, 538:399–428.
- Bandara, S. (2013). *Material Point Method to simulate Large Deformation Problems in Fluid-saturated Granular Medium*. PhD thesis, University of Cambridge.
- Bardenhagen, S. (2002). Energy Conservation Error in the Material Point Method for Solid Mechanics. *Journal of Computational Physics*, 180:383–403.
- Bardenhagen, S. and Kober, E. (2004). The generalized interpolation material point method. *Computer Modeling in Engineering and Sciences*, 5(6):477–496.

- Bardenhagen, S. G., Brackbill, J. U., and Sulsky, D. (2000). The material-point method for granular materials. *Computer Methods in Applied Mechanics and Engineering*, 187(3-4):529–541.
- Bardenhagen, S. G., Guilkey, J. E., Roessig, K. M., Brackbill, J. U., Witzel, W. M., and Foster, J. C. (2001). *An improved contact algorithm for the material point method and application to stress propagation in granular material*, volume 2. Tech Science Press.
- Bareschino, P., Lirer, L., Marzocchella, A., Petrosino, P., and Salatino, P. (2008). Self-fluidization of subaerial rapid granular flows. *Powder Technology*, 182(3):323–333.
- Bathe, K. and Zhang, H. (2004). Finite element developments for general fluid flows with structural interactions. *International Journal for Numerical Methods in Engineering*, 60(1):213–232.
- Belytschko, T., Lu, Y. Y., and Gu, L. (1994). Element-free Galerkin Method. *International Journal for Numerical Methods in Engineering*.
- Beuth, L., Wieckowski, Z., and Vermeer, P. A. (2010). Solution of quasi-static large-strain problems by the material point method. *International Journal for Numerical and Analytical Methods in Geomechanics*, pages n/a–n/a.
- Bigler, J., Guilkey, J., Gribble, C., Hansen, C., and Parker, S. (2006). A case study: Visualizing material point method data. *Proceedings of Euro Vis 2006*, pages 299–306.
- Bonet, J. and Kulasegaram, S. (2000). Correction and stabilization of smooth particle hydrodynamics methods with applications in metal forming simulations. *International Journal for Numerical Methods in Engineering*.
- Bonnet, F., Richard, T., and Philippe, P. (2010). Sensitivity to solid volume fraction of gravitational instability in a granular medium. *Granular Matter*.
- Breuer, M., Bernsdorf, J., Zeiser, T., and Durst, F. (2000). Accurate computations of the laminar flow past a square cylinder based on two different methods: lattice-Boltzmann and finite-volume. *Journal of Heat and Fluid Flow*, 21(2):186–196.
- Cambou, B., Jean, M., and Radjaï, F. (2009). *Micromechanics of granular materials*. Wiley-ISTE.
- Campbell, C. (1986). The effect of microstructure development on the collisional stress tensor in a granular flow. *Acta Mechanica*, 63(1):61–72.
- Campbell, C. and Brennan, C. (1985). Computer simulation of granular shear flows. *Journal of Fluid Mechanics*, 151:167–88.
- Campbell, C. S. (1990). Rapid Granular Flows. *Annual Review of Fluid Mechanics*, 22(1):57–90.
- Campbell, C. S. (2002). Granular shear flows at the elastic limit. *Journal of Fluid Mechanics*, 465:261–291.
- Campbell, C. S. (2006). Granular material flows - An overview. *Powder Technology*, 162(3):208–229.

- Capecelatro, J. and Desjardins, O. (2013). An Euler–Lagrange strategy for simulating particle-laden flows. *Journal of Computational Physics*, 238(0):1–31.
- Cassar, C., Nicolas, M., and Pouliquen, O. (2005). Submarine granular flows down inclined planes. *Physics of Fluids*, 17(10):103301–11.
- Cawthor, C. J. (2006). The flow of granular media. Technical report, University of Cambridge, Department of Applied Mathematics and Theoretical Physics.
- Chen, S. and Doolen, G. G. D. (1998). Lattice Boltzmann method for fluid flows. *Annual review of fluid mechanics*, 30(1):329–364.
- Chen, Z. and Brannon, R. (2002). An evaluation of the material point method. *Sandia National Laboratories (SAND2002-0482)*.
- Choi, J. (2005). *Transport-limited aggregation and dense granular flow*. Phd, Massachusetts Institute of Technology.
- Coetzee, C. J., Vermeer, P. A., and Basson, A. H. (2005). The modelling of anchors using the material point method. *International Journal for Numerical and Analytical Methods in Geomechanics*, 29(9):879–895.
- Cook, B., Noble, D., and Williams, J. (2004). A direct simulation method for particle-fluid systems. *Engineering Computations*, 21(2/3/4):151–168.
- Courrech du Pont, S., Gondret, P., Perrin, B., and Rabaud, M. (2003). Granular Avalanches in Fluids. *Physical Review Letters*, 90(4):044301.
- Crosta, G. B., Imposimato, S., and Roddeman, D. (2009). Numerical modeling of 2-D granular step collapse on erodible and nonerodible surface. *Journal of Geophysical Research*, 114(F3):F03020.
- Cundall, P. A. and Strack, O. D. L. (1979). A discrete numerical model for granular assemblies. *Geotechnique*, 29(1):47–65.
- Da Cruz, F., Emam, S., Prochnow, M., Roux, J. N., and Chevoir, F. (2005). Rheophysics of dense granular materials: Discrete simulation of plane shear flows. *Physical Review E - Statistical, Nonlinear, and Soft Matter Physics*, 72(2):1–17.
- Daerr, A. and Douad, S. (1999). Sensitivity of granular surface flows to preparation. *Europhys. Lett.*, 47(3):324–330.
- Daerr, A. and Douady, S. (1999). Two types of avalanche behaviour in granular media. *Nature*, 399(6733):241–243.
- Daniel, R. C., Poloski, A. P., and Eduardo Saez, A. (2007). A continuum constitutive model for cohesionless granular flows. *Chemical Engineering Science*, 62(5):1343–1350.
- Denlinger, R. and Iverson, R. (2001). Flow of variably fluidized granular masses across three-dimensional terrain, ii: Numerical predictions and experimental tests. *J. Geophys. Res.*, 106(B1):553–566.

- Dey, R., Hawlader, B., Philips, R., and Soga, K. (2012). Effects of Shear Band Propagation on Submarine Landslide. In *Proceedings of the twenty-second International Offshore and Polar Engineering Conference*, Greece. e International Society of Offshore and Polar Engineers (ISOPE).
- Donea, J., Giuliani, S., and Halleux, J. (1982). An arbitrary Lagrangian-Eulerian finite element method for transient dynamic fluid-structure interactions. *Computer Methods in Applied Mechanics and Engineering*.
- Du, R., Shi, B., and Chen, X. (2006). Multi-relaxation-time lattice Boltzmann model for incompressible flow. *Physics Letters A*, 359(6):564–572.
- Durst, F., Ray, S., Unsal, B., and Bayoumi, O. (2005). The development lengths of laminar pipe and channel flows. *Journal of fluids engineering*, 127:1154.
- Estrada, N., Taboada, A., and Radjai, F. (2008). Shear strength and force transmission in granular media with rolling resistance. *Physical Review E*, 78(2):021301.
- Feng, Y. T., Han, K., and Owen, D. R. J. (2007). Coupled lattice Boltzmann method and discrete element modelling of particle transport in turbulent fluid flows: Computational issues. *International Journal for Numerical Methods in Engineering*, 72(9):1111–1134.
- Forsterre, Y. and Pouliquen, O. (2008). Flows of Dense Granular Media. *Annual Review of Fluid Mechanics*, 40(1):1–24.
- Fortes, A. (1987). Nonlinear mechanics of fluidization of beds of spherical particles. *Journal of Fluid Mechanics*.
- Fortune, S. (1992). Voronoi diagrams and Delaunay triangulations. *Computing in Euclidean geometry*.
- Frenkel, D. and Smit, B. (1996). *Understanding molecular simulation: From algorithms to applications*. Academic Press.
- Frisch, U. and Kolmogorov, A. (1995). *Turbulence: the legacy of AN Kolmogorov*. Cambridge University Press.
- Girolami, L., Hergault, V., Vinay, G., and Wachs, A. (2012). A three-dimensional discrete-grain model for the simulation of dam-break rectangular collapses: comparison between numerical results and experiments. *Granular Matter*, pages 1–12.
- Goldhirsch, I. (2003). Rapid granular flows. *Annual Review of Fluid Mechanics*, 35:267–293.
- Grubmuller, H., Heller, H., Windemuth, A., and Schulten, K. (1991). Generalized verlet algorithm for efficient molecular dynamics simulations with long-range interactions. *Molecular simulations*, 6:121–142.
- Guilkey, J., Harman, T., and Banerjee, B. (2007). An Eulerian–Lagrangian approach for simulating explosions of energetic devices. *Computers & Structures*, 85(11-14):660–674.
- Guilkey, J., Harman, T., Xia, A., Kashiwa, B., and McMurtry, P. (2003). An Eulerian–Lagrangian approach for large deformation fluid structure interaction problems, Part 1: algorithm development. *Advances in Fluid Mechanics*, 36:143–156.

- Guilkey, J. and Weiss, J. (2003). Implicit time integration for the material point method: Quantitative and algorithmic comparisons with the finite element method. *International Journal for Numerical Methods in Engineering*.
- Gumhold, S. (2003). Splatting illuminated ellipsoids with depth correction. In *VMV*, volume 2003, pages 245–252.
- Han, K., Feng, Y., and Owen, D. (2007a). Coupled lattice Boltzmann and discrete element modelling of fluid–particle interaction problems. *Computers & Structures*, 85(11-14):1080–1088.
- Han, S., Zhu, P., and Lin, Z. (2007b). Two-dimensional interpolation-supplemented and Taylor-series expansion-based lattice Boltzmann method and its application. *Communications in Nonlinear Science and Numerical Simulationin Nonlinear Science and Numerical Simulation*, 12(7):1162–1171.
- Harbitz, C. B. (2003). Hydroplaning of subaqueous debris flows and glide blocks: Analytical solutions and discussion. *Journal of Geophysical Research*, 108(B7):2349.
- Harlow, F. H. (1964). The particle-in-cell computing method for fluid dynamics. *Computer Methods in Physics*, 3:319–343.
- He, X. and Luo, L. L.-S. (1997a). Theory of the lattice Boltzmann method: From the Boltzmann equation to the lattice Boltzmann equation. *Physical Review E*, 56(6):6811.
- He, X. and Luo, L.-S. (1997b). A priori derivation of the lattice Boltzmann equation. *Physical Review E*, 55(6):R6333–R6336.
- He, X., Zou, Q., Luo, L. S., and Dembo, M. (1997). Analytic solutions of simple flows and analysis of nonslip boundary conditions for the lattice Boltzmann BGK model. *Journal of Statistical Physics*, 87(1):115–136.
- Hertz, H. (1882). Über die Berührung fester elastischer Körper. *Journal für die Reinen und Angewandte Mathematik*, 92:156–171.
- Hogg, A. J. (2007). Two-dimensional granular slumps down slopes. *Physics of Fluids*, 19(9):9.
- Hutter, K., Koch, T., Pluuss, C., and Savage, S. (1995). The dynamics of avalanches of granular materials from initiation to runout. Part II. Experiments. *Acta Mechanica*, 109(1):127–165.
- Hutter, K., Wang, Y., and Pudasaini, S. P. (2005). The Savage–Hutter Avalanche Model: How Far Can It be Pushed? *Philosophical Transactions: Mathematical, Physical and Engineering Sciences*, 363(1832):1507–1528.
- Iddir, H. and Arastoopour, H. (2005). Modeling of multitype particle flow using the kinetic theory approach. *AICHE Journal*, 51(6):1620–1632.
- Iglberger, K., Thurey, N., and Rude, U. (2008). Simulation of moving particles in 3D with the Lattice Boltzmann method. *Computers & Mathematics with Applications*, 55(7):1461–1468.

- Iverson, R. (2003). The debris-flow rheology myth. In Rickenmann and Chen, editors, *Debris-Flow Hazards Mitigation: Mechanics, Prediction, and Assessment*, pages 303–314, Rotterdam.
- Iverson, R. M. (1997). The physics of debris flows. *Rev. Geophys.*, 35(3):245–296.
- Iverson, R. M. (2000). Acute Sensitivity of Landslide Rates to Initial Soil Porosity. *Science*, 290(5491):513–516.
- Iverson, R. M., Reid, M. E., and LaHusen, R. G. (1997). Debris-flow mobilization from landslides. *Annual Review of Earth and Planetary Sciences*, 25(1):85–138.
- Jaeger, H., Nagel, S., and Behringer, R. (1996). Granular solids, liquids, and gases. *Reviews of Modern Physics*, 68(4):1259–1273.
- Jean, M. (1999). The non-smooth contact dynamics method. *Computer Methods in Applied Mechanics and Engineering*, 177(3-4):235–257.
- Jenkins, J. T. and Savage, S. B. (1983). A theory for the rapid flow of identical, smooth, nearly elastic, spherical particles. *Journal of Fluid Mechanics*, 130:187–202.
- Jiang, M., Konrad, J., and Leroueil, S. (2003). An efficient technique for generating homogeneous specimens for DEM studies. *Computers and Geotechnics*, 30(7):579–597.
- Johnson, A. (1965). *A model for debris flow*. PhD thesis, The Pennsylvania State University.
- Jop, P., Forterre, Y., and Pouliquen, O. (2006). A constitutive law for dense granular flows. *Nature*, 441(7094):727–730.
- Josserand, C., Lagree, P. Y., and Lhuillier, D. (2004). Stationary shear flows of dense granular materials: A tentative continuum modelling. *European Physical Journal E*, 14(2):127–135.
- Kafaji, I. (2013). *Formulation of a dynamic material point method (MPM) for geomechanical problems*. PhD thesis, University of Stuttgart.
- Kamrin, K. (2008). *Stochastic and deterministic models for dense granular flow*. PhD thesis, Massachusetts Institute of Technology.
- Kamrin, K. (2010). Nonlinear elasto-plastic model for dense granular flow. *International Journal of Plasticity*, 26(2):167–188.
- Kamrin, K., Rycroft, C. H., and Bazant, M. Z. (2007). The stochastic flow rule: a multi-scale model for granular plasticity. *Modelling and Simulation in Materials Science and Engineering*, 15(4):S449–S464.
- Katz, O., Morgan, J., Aharonov, E., and Dugan, B. (2014). Controls on the size and geometry of landslides: Insights from discrete element numerical simulations. *Geomorphology*.
- Ke, T.-C. and Bray, J. (1995). Modeling of Particulate Media Using Discontinuous Deformation Analysis. *Journal of Engineering Mechanics*, 121(11):1234–1243.
- Kerswell, R. (2005). Dam break with Coulomb friction: A model for granular slumping? *Physics of Fluids*, 17:057101.

- Komiwas, V., Mege, P., Meimon, Y., and Herrmann, H. (2005). Simulation of granular flow in a fluid applied to sedimentation. *Granular Matter*, 8(1):41–54.
- Krogh, M., Painter, J., and Hansen, C. (1997). Parallel sphere rendering. *Parallel Computing*, 23(7):961–974.
- Kuester, F., Bruckschen, R., Hamann, B., and Joy, K. (2001). Visualization of particle traces in virtual environments. In *Proceedings of the ACM symposium on Virtual reality software and technology*, pages 151–157.
- Lacaze, L., Phillips, J. C., and Kerswell, R. R. (2008). Planar collapse of a granular column: Experiments and discrete element simulations. *Physics of Fluids*, 20(6).
- Ladd, A. J. (1994). Numerical simulations of particulate suspensions via a discretized Boltzmann equation. Part 1. Theoretical foundation. *Journal of Fluid Mechanics*, 271:285–309.
- Ladd, A. J. C. and Verberg, R. (2001). Lattice-Boltzmann Simulations of Particle-Fluid Suspensions. *Journal of Statistical Physics*, 104(5):1191–1251.
- Lajeunesse, E., Mangeney-Castelnau, A., and Villette, J. P. (2004). Spreading of a granular mass on a horizontal plane. *Physics of Fluids*, 16(7):2371.
- Lajeunesse, E., Monnier, J. B., and Homsy, G. M. (2005). Granular slumping on a horizontal surface. *Physics of Fluids*, 17(10).
- Larrieu, E., Staron, L., and Hinch, E. J. (2006). Raining into shallow water as a description of the collapse of a column of grains. *Journal of Fluid Mechanics*, 554:259–270.
- Lemiale, V., Muhlhaus, H. B., Meriaux, C., Moresi, L., and Hodkinson, L. (2011). Rate effects in dense granular materials: Linear stability analysis and the fall of granular columns. *International Journal for Numerical and Analytical Methods in Geomechanics*, 35(2):293–308.
- Levoy, M. (1988). Display of surfaces from volume data. *Computer Graphics and Applications, IEEE*, 8(3):29–37.
- Li, S. and Liu, W. (2002). Meshfree and particle methods and their applications. *Applied Mechanics Reviews*, 55:1.
- Liu, S. H., Sun, D. A., and Wang, Y. (2003). Numerical study of soil collapse behavior by discrete element modelling. *Computers and Geotechnics*, 30(Compindex):399–408.
- Liu, Z. and Koyi, H. (2013). Kinematics and internal deformation of granular slopes: insights from discrete element modeling. *Landslides*.
- Lo, C. Y., Bolton, M., and Cheng, Y. P. (2009). Discrete element simulation of granular column collapse. In *AIP Conf. Proc. Powders and Grains 2009*, volume 1145 of *6th International Conference on Micromechanics of Granular Media, Powders and Grains 2009*, pages 627–630.
- Locat, J. and Lee, H. (2002). Submarine landslides: advances and challenges. *Canadian Geotechnical Journal*.

- Lorensen, W. and Cline, H. (1987). Marching cubes: A high resolution 3D surface construction algorithm. *ACM Siggraph Computer Graphics*, 21(4):163–169.
- Love, E. and Sulsky, D. L. (2006). An unconditionally stable, energy-momentum consistent implementation of the material-point method. *Computer Methods in Applied Mechanics and Engineering*, 195(33-36):3903–3925.
- Lube, G., Huppert, H. E., Sparks, R. S. J., and Freundt, A. (2005). Collapses of two-dimensional granular columns. *Physical Review E - Statistical, Nonlinear, and Soft Matter Physics*, 72(4):1–10.
- Luding, S., Clément, E., and Blumen, A. (1994). Anomalous energy dissipation in molecular-dynamics simulations of grains: The "detachment" effect. *Physical Review*, 50:4113.
- Ma, J., Wang, D., and Randolph, M. (2014). A new contact algorithm in the material point method for geotechnical simulations. *International Journal for Numerical and Analytical Methods in Geomechanics*, 38(11):1197–1210.
- Mackenzie-Helnwein, P., Arduino, P., Shin, W., Moore, J. A., and Miller, G. R. (2010). Modeling strategies for multiphase drag interactions using the material point method. *International Journal for Numerical Methods in Engineering*, 83(3):295–322.
- Maeda, K. and Sakai, H. (2010). Seepage failure and erosion of ground with air bubble dynamics. In *Geoenvironmental Engineering and Geotechnics: Progress in Modeling and Applications*, pages 261–266. ASCE.
- Mangeney, A., Roche, O., and Hungr, O. (2010). Erosion and mobility in granular collapse over sloping beds. *Journal of Geophysical Research*, 115(F3):F03040.
- Mast, C. M., Arduino, P., Mackenzie-Helnwein, P., and Miller, G. R. (2014a). Simulating granular column collapse using the Material Point Method. *Acta Geotechnica*.
- Mast, C. M., Arduino, P., Miller, G. R., and Mackenzie-Helnwein, P. (2014b). Avalanche and landslide simulation using the material point method: flow dynamics and force interaction with structures. *Computational Geosciences*, 18(5):817–830.
- Mehta, A. (2011). *Granular Physics*. Cambridge University Press.
- Mehta, A. and Barker, G. (1994). The dynamics of sand. *Reports on Progress in Physics*, 57:383.
- Mei, R., Shyy, W., Yu, D., and Luo, L.-S. (2000). Lattice Boltzmann Method for 3-D Flows with Curved Boundary. *Journal of Computational Physics*, 161(2):680–699.
- Meruane, C., Tamburrino, A., and Roche, O. (2010). On the role of the ambient fluid on gravitational granular flow dynamics. *Journal of Fluid Mechanics*, 648:381–404.
- Midi, G. D. R. (2004). On dense granular flows. *European Physical Journal E*, 14(4):341–365.
- Mitchell, J. K. and Soga, K. (2005). *Fundamentals of soil behavior*. John Wiley & Sons.

- Monaghan, J. (2005). Smoothed particle hydrodynamics. *Reports on progress in physics*.
- Moreau, J. J. (1993). New computation methods in granular dynamics. In Thornton, C., editor, *Powders and Grains*, page 227. A. A. Balkema.
- Mori, H. (2008). *The SPH method to simulate river levee failures*. Msc thesis, University of Cambridge.
- Mutabaruka, P. (2013). *Modelisation numerique des milieux granulaires immergés : initiation et propagation des avalanches dans un fluide*. Phd thesis, University of Montpellier 2.
- Nedderman, R. M. (1992). *Statics and Kinematics of Granular Materials*. Cambridge University Press.
- Ng, B. H., Ding, Y., and Ghadiri, M. (2008). Assessment of the kinetic-frictional model for dense granular flow. *Particuology*, 6(1):50–58.
- Noble, D. and Torczynski, J. (1998). A lattice-Boltzmann method for partially saturated computational cells. *International Journal of Modern Physics C-Physics and Computer*, 9(8):1189–1202.
- Obrecht, C. and Kuznik, F. (2011). A new approach to the lattice Boltzmann method for graphics processing units. *Computers & Mathematics*.
- Okada, Y. and Ochiai, H. (2008). Flow characteristics of 2-phase granular mass flows from model flume tests. *Engineering Geology*, 97(1-2):1–14.
- OpenACC-Members (2013). The OpenACC Application Programming Interface Version 2.0 (June, 2013; Corrected: August, 2013). Technical report, OpenMP Standard Group.
- O’Sullivan, C. (2011). *Particulate discrete element modelling*. Taylor and Francis.
- O’Sullivan, C., Bray, J., and Li, S. (2003). A new approach for calculating strain for particulate media. *International Journal for Numerical and Analytical Methods in Geomechanics*, 27(10):859–877.
- Pailha, M., Pouliquen, O., and Nicolas, M. (2008). Initiation of Submarine Granular Avalanches: Role of the Initial Volume Fraction. *AIP Conference Proceedings*, 1027(1):935–937.
- Pan, C., Luo, L., and Miller, C. (2006). An evaluation of lattice Boltzmann schemes for porous medium flow simulation. *Computers & fluids*, 35(8-9):898–909.
- Parrinello, M. and Rahman, A. (1980). Crystal structure and pair potentials: a molecular-dynamics study. *Physics Review Letters*, 45:1196.
- Peker, S. and Helvacı, S. (2007). *Solid-liquid two phase flow*. Elsevier.
- Pitman, E. B. and Le, L. (2005). A Two-Fluid Model for Avalanche and Debris Flows. *Philosophical Transactions: Mathematical, Physical and Engineering Sciences*, 363(1832):1573–1601.

- Popken, L. and Cleary, P. W. (1999). Comparison of Kinetic Theory and Discrete Element Schemes for Modelling Granular Couette Flows. *Journal of Computational Physics*, 155(1):1–25.
- Poschel, T. and Schwager, T. (2005). *Computational Granular Dynamics*. Springer-Berlin.
- Potapov, A. and Campbell, C. (1996). Computer simulation of hopper flow. *Physics of Fluids*, 8:2884.
- Pouliquen, O. (1999). Scaling laws in granular flows down rough inclined planes. *Physics of Fluids*, 11(3):542–548.
- Pouliquen, O., Cassar, C., Forterre, Y., Jop, P., and Nicolas, M. (2005). How do grains flow: Towards a simple rheology of dense granular flows. In *Powders and Grains*.
- Pouliquen, O., Cassar, C., Jop, P., Forterre, Y., and Nicolas, M. (2006). Flow of dense granular material: towards simple constitutive laws. *Journal of Statistical Mechanics: Theory and Experiment*, 2006(07):P07020–P07020.
- Pouliquen, O. and Chevoir, F. (2002). Dense flows of dry granular material. *Comptes Rendus Physique*, 3(2):163–175.
- Pouliquen, O. and Forterre, Y. (2002). Friction law for dense granular flows: Application to the motion of a mass down a rough inclined plane. *Journal of Fluid Mechanics*, 453:133–151.
- Qiu, G., Henke, S., and Grabe, J. (2011). Application of a Coupled Eulerian–Lagrangian approach on geomechanical problems involving large deformations. *Computers and Geotechnics*.
- Radjai, F. and Dubois, F. (2011). *Discrete-element modeling of granular materials*. ISTE Wiley, London; Hoboken, N.J.
- Radjai, F. and Richéfeu, V. (2009). Contact dynamics as a nonsmooth discrete element method. *Mechanics of Materials*, 41(6):715–728.
- Radjai, F., Schafer, J., Dipple, S., and Wolf, D. (1997). Collective Friction of an Array of Particles: A Crucial Test for Numerical Algorithms. *Journal de Physique I*, 7(9):1053–1070.
- Radjai, F., Voivret, C., and McNamara, S. (2011). Discrete-element modelling of granular materials. In Radjai, F. and Dubois, F., editors, *Discrete-element modelling of granular materials*, chapter Periodic B, pages 181–198. ISTE Wiley.
- Robert, D. (2010). *Soil-pipeline interaction in unsaturated soil*. PhD thesis, University of Cambridge.
- Rondon, L., Pouliquen, O., and Aussillous, P. (2011). Granular collapse in a fluid: Role of the initial volume fraction. *Physics of Fluids*, 23(7):073301–073301–7.
- Roscoe, K. (1970). The influence of strains in soil mechanics. *Geotechnique*.

- Roux, J. and Combe, G. (2002). Quasistatic rheology and the origins of strain. *Comptes Rendus Physique*, 3(2):131–140.
- Rycroft, C. H., Bazant, M. Z., Grest, G. S., and Landry, J. W. (2006). Dynamics of random packings in granular flow. *Physical Review E*, 73(5):051306.
- Rycroft, C. H., Kamrin, K., and Bazant, M. Z. (2009a). Assessing continuum postulates in simulations of granular flow. *Journal of the Mechanics and Physics of Solids*, 57(5):828–839.
- Rycroft, C. H., Orpe, A. V., and Kudrolli, A. (2009b). Physical test of a particle simulation model in a sheared granular system. *Physical Review E*, 80(3):031305.
- Savage, S. and Hutter, K. (1991). The dynamics of avalanches of granular materials from initiation to runout. Part I: Analysis. *Acta Mechanica*, 86(1):201–223.
- Savage, S. and Jeffrey, D. (1981). The stress tensor in a granular flow at high shear rates. *Journal of Fluid Mechanics*, 110(1):255–272.
- Savage, S. and Sayed, M. (1984). Stresses developed by dry cohesionless granular materials sheared in an annular shear cell. *Journal of Fluid Mechanics*, 142:391–430.
- Savage, S. B. (1984). The Mechanics of Rapid Granular Flows. *Advances in Applied Mechanics*, 24(C):289–366.
- Schaefer, D. G. (1990). Instability and ill-posedness in the deformation of granular materials. *International Journal for Numerical and Analytical Methods in Geomechanics*, 14(4):253–278.
- Schaeffer, D. G. (1987). Instability in the evolution equations describing incompressible granular flow. *Journal of Differential Equations*, 66(1):19–50.
- Schaeffer, D. G. and Iverson, R. M. (2008). Steady and Intermittent Slipping in a Model of Landslide Motion Regulated by Pore-Pressure Feedback. *SIAM Journal on Applied Mathematics*, 69(3):769–786.
- Schofield, A. and Wroth, P. (1968). *Critical state soil mechanics*. European civil engineering series. McGraw-Hill.
- Shin, W. (2010). *Numerical simulation of landslides and debris flows using an enhanced material point method*. Phd thesis, University of Washington.
- Smagorinsky, J. (1963). General circulation experiments with the primitive equations. *Monthly weather review*, 91(3):99–164.
- Staron, L. and Hinch, E. J. (2007). The spreading of a granular mass: Role of grain properties and initial conditions. *Granular Matter*, 9(3-4):205–217.
- Staron, L., Radjai, F., and Villette, J. P. (2005). Multi-scale analysis of the stress state in a granular slope in transition to failure. *The European physical journal. E, Soft matter*, 18(3):311–20.

- Steffen, M., Wallstedt, P., Guilkey, J., Kirby, R., and Berzins, M. (2008). Examination and analysis of implementation choices within the material point method. *Computer Modeling in Engineering and Sciences*, 32:107–127.
- Succi, S. (2001). *The lattice Boltzmann equation for fluid dynamics and beyond*. Oxford University Press.
- Succi, S., Foti, E., and Higuera, F. (1989). Three-Dimensional Flows in Complex Geometries with the Lattice Boltzmann Method. *Europhysics Letters (EPL)*, 10(5):433–438.
- Sukop, M. and Thorne, D. (2006). *Lattice Boltzmann modeling: An introduction for geoscientists and engineers*. Springer Verlag.
- Sulsky, D., Chen, Z., and Schreyer, H. (1994). A particle method for history-dependent materials. *Computer Methods in Applied Mechanics and Engineering*, 118(1-2):179–196.
- Sulsky, D., Zhou, S.-J., and Schreyer, H. L. (1995). Application of a particle-in-cell method to solid mechanics. *Computer Physics Communications*, 87(1-2):236–252.
- Sun, X., Sakai, M., and Yamada, Y. (2013). Three-dimensional simulation of a solid–liquid flow by the DEM–SPH method. *Journal of Computational Physics*, 248(0):147–176.
- Tang, C., Hu, J., Lin, M., and Angelier, J. (2009). The Tsaoling landslide triggered by the Chi-Chi earthquake, Taiwan: insights from a discrete element simulation. *Engineering Geology*.
- Tang, C., Hu, J., and Yuan, R. (2013). The transportation and deposition of the 2009 Hsiaolin landslide in Taiwan revealed from 3D granular discrete element simulation. In *EGU General Assembly*.
- Thompson, E. L. and Hupper, H. E. (2007). Granular column collapses: Further experimental results. *Journal of Fluid Mechanics*, 575:177–186.
- Topin, V., Dubois, F., Monerie, Y., Perales, F., and Wachs, A. (2011). Micro-rheology of dense particulate flows: Application to immersed avalanches. *Journal of Non-Newtonian Fluid Mechanics*, 166(1-2):63–72.
- Topin, V., Monerie, Y., Perales, F., and Radjaï, F. (2012). Collapse Dynamics and Runout of Dense Granular Materials in a Fluid. *Physical Review Letters*, 109(18):188001.
- Utili, S., Zhao, T., and Housby, G. (2014). 3D DEM investigation of granular column collapse: Evaluation of debris motion and its destructive power. *Engineering Geology*.
- Van Wachem, B., Schouten, J., Van den Bleek, C., Krishna, R., and Sinclair, J. (2001). Comparative analysis of CFD models of dense gas–solid systems. *AICHE Journal*, 47(5):1035–1051.
- Verlet, L. (1967). Computer "Experiments" on Classical Fluids. I. Thermodynamical Properties of Lennard-Jones Molecules. *Phys. Rev.*, 159(1):98.
- Vovret, C., Radjai, F., Delenne, J. Y., and El Youssoufi, M. S. (2007). Space-filling properties of polydisperse granular media. *Physical Review E*, 76(2):021301.

- Volfson, D., Tsimring, L. S., and Aranson, I. S. (2003). Partially fluidized shear granular flows: Continuum theory and molecular dynamics simulations. *Physical Review E*, 68(2):021301.
- Wallstedt, P. and Guilkey, J. (2008). An evaluation of explicit time integration schemes for use with the generalized interpolation material point method. *Journal of Computational Physics*, 227:9628–9642.
- Wang, L., Guo, Z., and Mi, J. (2014). Drafting, kissing and tumbling process of two particles with different sizes. *Computers & Fluids*.
- Ward, S. and Day, S. (2002). Suboceanic landslides. In 2002 Yearbook of Science and Technology. *McGraw-Hill*, 349:352.
- Warnett, J. M., Denissenko, P., Thomas, P. J., Kiraci, E., and Williams, M. A. (2013). Scalings of axisymmetric granular column collapse. *Granular Matter*, 16(1):115–124.
- Wieckowski, Z., Youn, S.-K., and Yeon, J.-H. (1999). A particle-in-cell solution to the silo discharging problem. *International Journal for Numerical Methods in Engineering*, 45(9):1203–1225.
- Willis, A., Peixinho, J., Kerswell, R., and Mullin, T. (2008). Experimental and theoretical progress in pipe flow transition. *Philosophical Transactions of the Royal Society A: Mathematical, Physical and Engineering Sciences*, 366(1876):2671.
- Wolfe, M. (2012). PGInsider August 2012: OpenACC Kernels and Parallel Constructs.
- Xiong, Q., Madadi-Kandjani, E., and Lorenzini, G. (2014). A LBM–DEM solver for fast discrete particle simulation of particle–fluid flows. *Continuum Mechanics and Thermodynamics*.
- Xu, H., Louge, M., and Reeves, A. (2003). Solutions of the kinetic theory for bounded collisional granular flows. *Continuum Mechanics and Thermodynamics*, 15(4):321–349.
- Yazdchi, K., Srivastava, S., and Luding, S. (2011). Microstructural effects on the permeability of periodic fibrous porous media. *International Journal of Multiphase Flow*.
- Yu, D., Mei, R., Luo, L., and Shyy, W. (2003). Viscous flow computations with the method of Lattice Boltzmann equation. *Progress in Aerospace Sciences*, 39(5):329–367.
- Yu, H., Girimaji, S., and Luo, L. (2005). Lattice Boltzmann simulations of decaying homogeneous isotropic turbulence. *Physical Review E*, 71(1):016708.
- Yu, H. and Yuan, X. (2006). On a class of non-coaxial plasticity models for granular soils. *Proceedings of the Royal Society A: Mathematical, Physical and Engineering Sciences*, 462(2067):725–748.
- Zenit, R. (2005). Computer simulations of the collapse of a granular column. *Physics of Fluids*, 17(Compendex):031703–1–031703–4.
- Zhang, D. Z., Zou, Q., Vanderheyden, W. B., and Ma, X. (2008). Material point method applied to multiphase flows. *Journal of Computational Physics*, 227(6):3159–3173.

- Zhang, H. W., Wang, K. P., and Chen, Z. (2009). Material point method for dynamic analysis of saturated porous media under external contact/impact of solid bodies. *Computer Methods in Applied Mechanics and Engineering*, 198(17-20):1456–1472.
- Zhang, Y. and Campbell, C. S. (1992). The interface between fluid-like and solid-like behaviour in two-dimensional granular flows. *Journal of Fluid Mechanics*, 237:541–568.
- Zhong, Q. and Olson, M. (1991). Finite element-algebraic closure analysis of turbulent separated-reattaching flow around a rectangular body. *Computer methods in applied mechanics and engineering*, 85(2):131–150.
- Zhou, H., Mo, G., Wu, F., Zhao, J., Rui, M., and Cen, K. (2012). GPU implementation of lattice Boltzmann method for flows with curved boundaries. *Computer Methods in Applied Mechanics and Engineering*, 225-228(null):65–73.
- Ziegler, D. (1993). Boundary conditions for Lattice Boltzmann simulations. *Journal of Statistical Physics*, 71(5):1171–1177.
- Zou, Q. and He, X. (1997). On pressure and velocity boundary conditions for the Lattice Boltzmann BGK model. *Physics of Fluids*, 9(6):1591–1598.